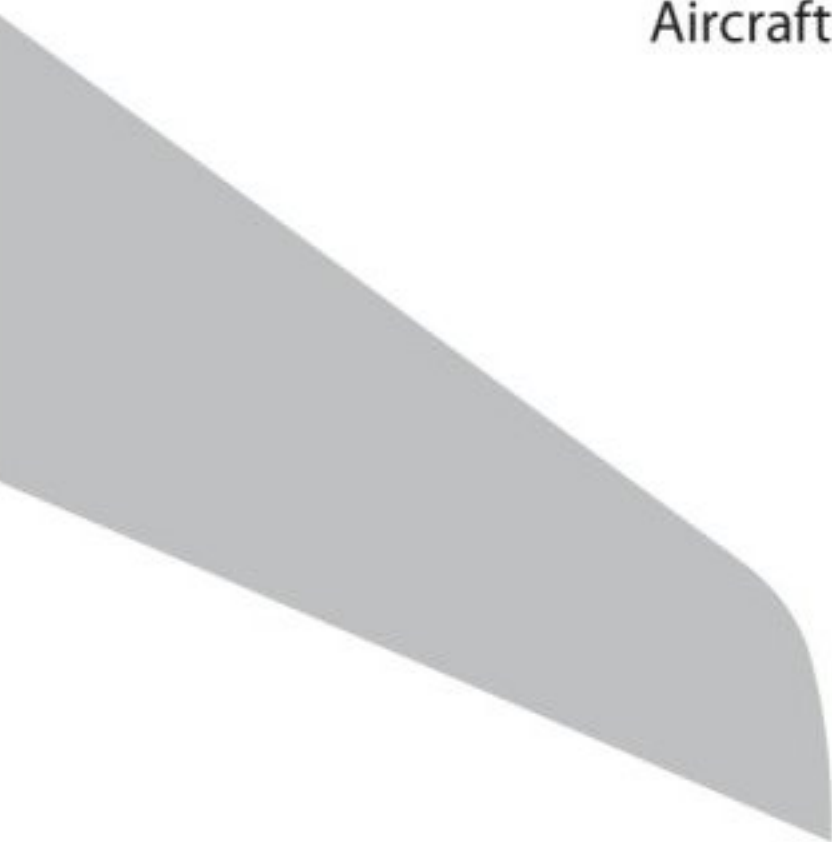# Aerodynamic Design of Transport Aircraft

Ed Obert

AERODYNAMIC DESIGN OF TRANSPORT AIRCRAFT

Aerodynamic Design of Transport Aircraft

Ed Obert

Based on the original lecture series by Ed Obert amended by:

Ronald Slingerland

Format designed and executed by:

Debbie J.W. Leusink

Tobie van den Berg

Justin H. Koning

LEGAL NOTICE

The publisher is not responsible for the use which might be made of the following information.

PRINTED IN THE NETHERLANDS

This book is dedicated to the memory of Dr. Ronald Slingerland and Prof. Ir. Hans Wittenberg. The latter stimulated the author to join Fokker and later to become a part-time professor at the Aerospace Faculty of Delft University of Technology.

Ed Obert

Preface

The impetus for this book stems from the time when the author was appointed part-time professor in the Aerospace Faculty of Delft University of Technology. At the time his main activities were those of leading the departments of Aerodynamics, Performance and Preliminary Design at Fokker Aircraft Company.

The book has had a long period of gestation. It started in 1987 as a series of lecture notes consisting mainly of pictorial material with a minimum of English explanatory text. The course was titled "Aerodynamic Design and Aircraft Operation". After the demise of Fokker in 1996 it was feared at the faculty that interest in aeronautical engineering would strongly diminish and the course was discontinued and the relationship between the author and the faculty came to an end.

Two years later the situation was reappraised, and the interest in aeronautical engineering remained, so the course was reinstated. The course was renamed "Aerodynamic Design of Transport Aircraft" with a former Fokker colleague Ronald Slingerland as lecturer. Ronald largely used the author's lecture notes but took the initiative to make video recordings of his own lectures. Three student-assistants, Debbie Leusink, Tobie van den Berg and Justin Koning took on the difficult task of transcribing the recorded English-spoken lectures on which they did an excellent job. In the Summer of 2007 this work had proceeded far enough to warrant the production of a preliminary version of the new lecture notes in time for the new study year in the Autumn.

In October 2007 Ronald Slingerland died tragically in a mid-air collision in a light plane. As a stop-gap solution the author was requested to complete the lecture course and to review the new lecture notes.

Independent of these sad developments it had been decided at the faculty that the lecture notes should be published as a textbook. This required a re-consideration on the contents of the book. First it had to be updated as it was basically twenty years old. Second the language used had to be formalised if it was made accessible to larger circles than the Aerospace Faculty. The author took on this task with the present result. But it would not have had the excellent

layout and general appearance without the unremitting energy and dedication of the author's three assistants named above.

This book is mainly descriptive. For detailed aerodynamic design procedures and the associated computer programmes or for detailed quantitative performance analyses the reader should consult other sources. However, the reader is assumed to be familiar with the basic elements of theoretical aerodynamics, aircraft stability and control and performance analysis. The illustrations and examples presented were taken from a large number of sources mentioned in the captions and at the end of the book. Some of the information presented may be considered outdated but has been retained for its historical value.

Some figures do not mention any source. In a time when some aircraft types are operated in thousands by hundreds of operators spread all over the world it is unrealistic to assume that manufacturer's data remain within the intended small circles. Performance engineers' manuals, flight simulator handbooks, sales presentations, etc. are distributed to various parties. Modern production programmes depend on close contacts between partners, subcontractors, vendors, etc. with extensive data exchange. Manufacturer's sales representatives and representatives of operator's fleet acquisition departments have both formal and informal contacts. Just as in military and political intelligence communities sensitive information remains in close circles unknown to the outside world but it is often known to the party who has the greatest interest in it, the competition. Although for some information in this book no source is mentioned the reader may rest assured that it has a sound basis.

Proof reading has been done by the author's good friend and former colleague Carl P. Stocks, latterly with BAe Systems Warton. In order to expedite the presentation of this book only his comments which saved the author from the biggest linguistic blunders have been incorporated. Any further lack in the proper use of the English language and any inaccurate information provided is entirely the responsibility of the author.

Finally the author thanks Bram Elsenaar (ret.) of NLR for deriving the relation between local static pressure and local Mach number as presented in chapter 10 and Nico Voogt (formerly with the Fokker Aircraft Company, now with the Boeing Company) checking and correcting the author's view on the use of modern CFD methods as described in chapter 24.

<div align="right">Ed Obert</div>

Table of contents

Notations

Notation		Unit
a	Velocity of sound	m/sec or ft/sec
A, A_w	Wing aspect ratio,	-
A_h	Horizontal tailplane aspect ratio	-
A_v	Vertical tailplane aspect ratio	-
A_∞	Intake stream tube cross-sectional area infinitely far ahead	m^2 or ft^2
A_E, A_e	Exhaust area	m^2 or ft^2
A_{HL}	Highlight area	m^2 or ft^2
A_{TH}	Throat area	m^2 or ft^2
b, b_w	Wing span	m or ft.
c	Chord	m or ft.
$\bar{c}$	Mean aerodynamic chord	m or ft.
c_d	Airfoil section drag coefficient, $c_d = D \,/\, \frac{1}{2}\rho V^2 c$	-
c_r	Rudder chord	m or ft.
c_v	Vertical tailplane chord	m or ft.
C_D	Drag coefficient, $C_D = D \,/\, \frac{1}{2}\rho V^2 S$	-
C_D	Discharge coefficient	-
C_{Di}	Induced drag coefficient, $C_{Di} = D_i \,/\, \frac{1}{2}\rho V^2 S$	-
C_{D0}	Zero-lift drag coefficient, $C_{D_0} = D_0 \,/\, \frac{1}{2}\rho V^2 S$	-
C_{Dp}	Profile drag coefficient	-
C_{Dtrim}	Trim drag coefficient	-
C_{DPmin}	Minimum profile drag coefficient	-
c_f	Average friction coefficient, $c_f = frictionforce \,/\, \frac{1}{2}\rho V^2 l$	-
$\bar{c}_f, C_F$	Equivalent flat-plate friction drag coefficient	-
c_l	Airfoil section lift coefficient, $c_l = L \,/\, \frac{1}{2}\rho V^2 c$	-
c_{lmax}	Maximum airfoil section lift coefficient	-
C_{ha}	Aileron hinge moment coefficient	-
C_{hr}	Rudder hinge moment coefficient	-
C_{he}	Elevator hinge moment coefficient	-
C_l	Rolling moment coefficient	-
C_L	Lift coefficient, $C_L = L \,/\, \frac{1}{2}\rho V^2 S$	-

$C_{L_{app}}$	Approach lift coefficient	-
C_{L_h}	Horizontal tailplane lift coefficient, $C_{L_h} = L_h / \frac{1}{2}\rho V^2 S_h$	-
C_{L_v}	Vertical tailplane lift coefficient, $C_{L_v} = L_v / \frac{1}{2}\rho V^2 S_v$	-
$C_{L_{max}}$	Maximum lift coefficient	-
$C_{L_{T-O}}$	Tail-off lift coefficient	-
$C_{L_{trim}}$	Trimmed lift coefficient	-
$C_{L\alpha}$	Lift curve gradient	deg^{-1} or rad^{-1}
ΔC_L	Change in lift coefficient due to flap deflection	-
$(\Delta C_L)_{\alpha=0}$	Change in lift coefficient due to flap deflection at $\alpha = 0$	-
C_m	Pitching moment coefficient, $C_m = M / \frac{1}{2}\rho V^2 S \overline{c}$	-
C_{m_0}	Zero-lift pitching moment coefficient for the aircraft tail-off	-
$C_{m_{T-O}}$	Tail-off pitching moment coefficient	-
$C_{m_{30}}$	Pitching moment coefficient with moment ref. centre at $0.30\ \overline{c}$	-
c_n	Section normal force coefficient	-
C_n	Yawing moment coefficient, $C_n = N / \frac{1}{2}\rho V^2 S b$	-
C_p, c_p	Static pressure coefficient, $c_p = p - p_0 / \frac{1}{2}\rho V_0^2$	-
c_{pcrit}, c_p^*	Static pressure coefficient for $M_{local} = 1.0$	-
c_{pmin}	Minimum static pressure coefficient	-
$c_{p_{TE}}$	Static pressure coefficient at the trailing edge	-
C_T	Specific fuel consumption	kg/kg/hr or lb/lb/hr
C_T	Total propeller thrust coefficient, $C_T = T / \frac{1}{2}\rho V^2 S_w$	-
C_T	Thrust coefficient, $C_T = actual\ gross\ thrust / ideal\ gross\ thrust$	-
C_V	Velocity coefficient	-
c.g.	Centre of gravity	-
D	Drag	N, kg or lb
D_i	Induced drag	N, kg or lb
D_0	Zero-lift drag	N, kg or lb
D_{prop}	Propeller diameter	m or ft.
D_{HL}	Inlet highlight diameter	m or ft.

D_{TH}	Inlet throat diameter	m or ft.
e	"Oswald" efficiency factor	-
F	Gross thrust	N, kg or lb
F_e	Elevator control force	N, kg or lb
g	Gravitational constant	m/sec^2 or ft/sec^2
h	Height, altitude	m or ft.
i_h	Horizontal tailplane (stabiliser) setting	deg or rad
J	Propeller advance ratio, $J = V/nD_{prop}$, where n = r.p.m.	-
k, k_S	Distributed or equivalent sand roughness grain size	mm or in
K	Shape or form factor	-
L	Lift	N, kg or lb
L, l	Length	m or ft.
L_h	Horizontal tailplane lift	N, kg or lb
l_h	Horizontal tailplane moment arm	m or ft.
L_V	Vertical tailplane lift (side force)	N, kg or lb
m	Mass	kg or lb
$\dot{m}, W_A$	Mass flow	kg/sec or lb/sec
M	Pitching moment	Nm, kgm or lbft
M, Ma	Mach number	-
M_0, M_∞	Free stream Mach number	-
M_L, M_{loc}	Local Mach number	-
M_{MO}	Maximum Operating Mach number	-
M_D	Design dive Mach number	-
$M_{S.B.O.}$	Local Mach number in front of the shock wave at buffet onset	-
n	Normal load factor	-
N	Yawing moment	Nm, kgm or lbft
p	Roll rate	deg/sec or rad/sec
p	Static pressure	N/m^2, kg/m^2 or lb/sq.ft.
p_0, p_∞	Free stream static pressure	N/m^2, kg/m^2 or lb/sq.ft.
p_t, p_T	Total pressure	N/m^2, kg/m^2 or lb/sq.ft.
$P_{T\infty}$	Free stream total pressure	N/m^2, kg/m^2 or lb/sq.ft.
P_{T_2}	Total pressure at the compressor face	N/m^2, kg/m^2 or lb/sq.ft.
q	Dynamic pressure, $q = \frac{1}{2}\rho V^2$	N/m^2, kg/m^2 or lb/sq.ft.
q_0	Free stream dynamic pressure	N/m^2, kg/m^2 or lb/sq.ft.
q_h	Average dynamic pressure at the horizontal tail	N/m^2, kg/m^2 or lb/sq.ft.
r	Yaw rate	deg/sec or rad/sec

r	Radius of curvature	m or ft.
R	Universal gas constant	-
R	Range	km or NM
Re, R	Reynolds number	-
Δs	Area on elementary air particle	m² or sq.ft.
S	Distance covered	km or NM
S, S_w	Wing area	m² or sq.ft.
S_h	Horizontal tailplane area	m² or sq.ft.
S_v	Vertical tailplane area	m² or sq.ft.
S_{wet}	Wetted area	m² or sq.ft.
t	Airfoil section thickness	m or ft.
T	Temperature	deg C.
T	Thrust	N, kg or lb
T_C	Single propeller thrust coefficient $C_T = T/\tfrac{1}{2}\rho V^2 \dfrac{\pi}{4} D_{prop}^2$	-
T_T	Total temperature	deg C.
u	Flow velocity in the boundary layer	m/sec or ft/sec
U	Flow velocity at the edge of the boundary layer	m/sec or ft/sec
V	Airspeed, flow velocity	m/sec or ft/sec
V_0	Free stream velocity	m/sec or ft/sec
V_1	Engine failure recognition speed	m/sec or kts
V_2	Initial climb-out speed with a failed engine	m/sec or kts
V_e	Exhaust velocity	m/sec or ft/sec
$\overline{V}_h$	Horizontal tailplane volume coefficient, $\overline{V}_h = S_h L_h / S_w \overline{c}$	-
V_{APP}	Approach speed	m/sec or kts
V_D	Design dive speed	m/sec or kts
V_{LO}	Lift-off speed	m/sec or kts
V_{MC}	Minimum control speed	m/sec or kts
V_{MO}	Maximum operating speed	m/sec or kts
V_{MU}	Minimum unstick speed	m/sec or kts
V_S	Stall speed	m/sec or kts
W	Weight	N, kg or lb
X, x	Distance from the origin along the X-axis	m or ft
$x_{a.c.}$	Aerodynamic centre position	m or ft
$x_{c.g.}$	Centre-of-gravity position	m or ft
$x_{n.p.}$	Neutral point position	m or ft
Y, y	Distance from the origin along the Y-axis	m or ft

Z, z	Distance from the origin along the Z-axis	m or ft
α	Angle of attack	deg or rad
α_0	Zero-lift angle of attack for the aircraft tail-off	deg or rad
α_h	Average horizontal tailplane angle of attack	deg or rad
α_v	Average vertical tailplane angle of attack	deg or rad
$\alpha_{C_{L=0}}$	Zero-lift angle of attack	deg or rad
α_R	Angle of attack relative to a reference line, usually the fuselage centre line	deg or rad
β	Sideslip angle	deg or rad
β	Blade angle	deg or rad
γ	Flight path angle	deg or rad
γ	Specific heat ratio	-
δ	Atmospheric pressure ratio, $\delta = p / p_0$	-
δ_a	Aileron angle	deg or rad
δ_e	Elevator angle	deg or rad
δ_f	Flap angle	deg or rad
δ_r	Rudder angle	deg or rad
δ_s	Slat angle	deg or rad
δ_{sa}	Spoiler aileron angle	deg or rad
δ_{sp}	Spoiler angle	deg or rad
δ^*	Boundary layer displacement thickness	m or ft.
ε	Downwash angle	deg or rad
ε_0	Downwash angle at $\alpha = 0$	deg or rad
λ	Taper ratio	-
Λ	Sweep angle	deg or rad
v	Kinematic viscosity	m^2/sec or ft^2/sec
μ	Friction coefficient (friction between runway and tire)	-
ρ	Air density	kg/m^3, $kgsec^2/m^4$ or $lbsec^2/ft^4$
σ	Atmospheric density ratio $\sigma = \rho / \rho_0$	-
θ	Atmospheric static temperature ratio, $\theta = T / T_0$	-
θ	Diffuser angle	deg or rad
θ	Momentum thickness	m or ft.
η	Relative spanwise wing station, $\eta = y / b / 2$	-
φ	Wing sweep angle – U.K. notation	deg or rad
ω	Rotational speed	deg/sec or rad/sec

PART 1

INTRODUCTION

1 *Introduction*

During the last century, three design methods have been developed in the aerodynamic design process. Until the early 1960's, only two methods were available: empirical and – rather elementary – mathematical methods. Since the 1960's, a third method has been developed: computational fluid dynamics, which can be considered as a combination of the two earlier methods. These three methods and their history will be discussed briefly in this chapter.

Empirical methods

Based on either theory or experiments or a combination of both, the empirical methods consist of handbooks which are essentially a collection of graphs and equations. They are meant to give a relation between elementary parameters of the geometry of the aircraft and the desired characteristics of the aircraft (such as forces acting on components). However, these books provide no insight into the physics of the problem.

This is the oldest method of aerodynamic design; until about 1940, it was the only practical tool available. Nevertheless, it is still in use today as it is very convenient in the preliminary design phase. For the initial sizing study, for example, it gives a first indication of the geometry needed to obtain the desired characteristics of the aircraft. It is also still the standard tool for sizing studies and for performance and stability and control analyses.

Examples of such collections of graphs and formulae are ESDU data sheets and the USAF Datcom.

Analytical methods

These methods are actually the opposite of the first method: the aerodynamic characteristics of the detailed geometry are obtained by physical insight – in other words, through pressure distributions.

In the first quarter of the 20th century mathematical modelling of flow physics played practically no role in the overall design of aircraft. Although Prandtl had

formulated both his lifting-line theory and his boundary-layer theory prior to the first World War, up to the late twenties practical aerodynamic design was almost entirely an empirical activity. The reasons for this were twofold: not only were the theoretical design tools of a rather elementary nature, but they were also rather tedious to apply because of the lack of suitable computing equipment.

In the late thirties, Theodorsen at NACA used theory for the first time in history to generate a family of airfoil sections suitable for practical use. In his work, he used the theory of conformal mapping, and the result was the well-known NACA 6-series of airfoils. In the design of these sections the boundary layer was neglected. Therefore a large number of sections had to be tested in the windtunnel to provide practical and reliable design data.

This approach in the design of airfoil sections was soon followed by research institutes and large aircraft manufacturing companies in other countries; through the 1930's and 1940's, institutes such as NACA (USA), RAE (UK), DVL and AVA (Germany) produced a vast amount of systematic design data based on both windtunnel test data and on computations.
The best known example of such data collections is Abbott and Von Doenhoff's "Theory of Wing Sections". Other examples are the USAF Datcom and the RAE (now ESDU) data sheets, as well as many NACA reports and the British "Reports & Memoranda" (R & M's).

Modern method – Computational fluid dynamics

With the development of computers, more and more powerful numerical methods became available to aircraft designers. These numerical methods are known as computational fluid dynamics. It allows them to obtain the intended characteristics of the aircraft (or one of its major components) by directly determining the required detailed aerodynamic shape through the use of fluid dynamics and the associated pressure distribution.

The foundations for this design method have been laid by Hess and Smith of Douglas with their initial subsonic panel method and by Garabedian, Korn, Bauer and Jameson of the University of New York with their computer codes for transonic flow.

CFD methods have progressed enormously over the years, and today they are the most important aerodynamic design tool in all phases of the design, with

the exception of the preliminary phase. A huge range of codes is available, varying in complexity from incompressible 2D flow to the full Navier-Stokes equations.

The advent of the numerical methods is a clear example that the emphasis in aerodynamic design has moved ever more towards a theoretical approach. The great advantage of this has been that, through a better understanding of basic flow physics, one has to rely much less on previous experience and the final design can now be optimized much closer to its specific design requirements than before.

Yet despite this development, each new design needs a large amount of wind tunnel testing. This is due to the unavoidable shortcomings of CFD: it may be very difficult or even impossible to predict the effects of the boundary layer or separated flow with sufficient accuracy. If one is not thoroughly familiar with these shortcomings, it can lead to a "blind" use of the software which may result in completely erroneous results and consequently produce some very disappointing surprises later on in the design process or during flight tests.

2 *Classification of fixed-wing aircraft*

An elementary understanding of the basic classification of fixed-wing aircraft is required before contemplating on the most suitable approach in the aerodynamic design of a particular project. Table 2.1 illustrates this by showing various types of fixed-wing aircraft and their functions.

Classification of fixed-wing aircraft				
			Type	Functions
Civil	A		Private	Training, leasure flying Aerobatics
	B		Transport	Revenue passenger transportation Business flying
	C		Special purpose	Agricultural spraying
Military	D		"Transport" type	Cargo, troops transportation Patrol
	E		"Fighter" type	Air-superiority Interception
		E1	Airforce	
		E2	Navy	Ground-attack / Reconnaissance Training
	F		"Bomber" type	Bombing missions

Table 2.1 - Classification of fixed-wing aircraft

One of the great challenges in the design of an aircraft lies in **finding a balance between the aircraft's performance and capabilities on the one hand and its complexity and hence its costs, both to purchase and to operate it, on the other hand**.

For instance, a light aircraft designed for training and touring will have as main requirements:

- Low purchase and operating costs
- Ruggedness
- Reliability

In other words, simplicity will be the key word. This means that a minimum of double curvature will be pursued in its exterior shapes. Also the need for taper in the wings and tail surfaces may not be justified. Such an aircraft may well be designed with "handbook" methods.

For the upper-range, four- to six-seat single-engined aircraft, the matter may already be different, however. It will be different again for a private owner or businessman who wants to fly his aircraft regularly over longer distances over the Rocky Mountains, in which case a pressurized cabin may be required. This means that the fuselage can no longer have a simple shape with slab fuselage sides and simple wing-fuselage junctions.

In civil transport aircraft one may for example have to consider whether the use of double curvature in the upper and lower skins of wing, tail surface torsion boxes or in engine pylons justifies the additional manufacturing costs.
Military transport aircraft have basically the same requirements as civil ones, except that there will probably also be requirements that the loading and unloading has to be done in a short amount of time.

In military front-line aircraft the emphasis will be almost entirely on its capabilities. The resulting high costs will usually mainly reflect in the number of aircraft purchased within the nation's available defence budget. Very complex shapes are generally justified here.

To give an impression of the cost of aircraft in various categories, table 2.2 has been provided. The above given examples of design requirements are summarized in table 2.3.

Type	Acquisition cost
Private	From $50,000
Transport	From $200,000 per person
Extra 400	$500,000
Gulfstream IV	15 M$
Fokker F100	20 M$
Airbus A380	285 M$
Aerobatic (Extra 300)	$150,000
Military	
F16	$\approx$ 20 M$
F14 / F15	$\approx$ 60 M$
Panavia Tornado	$\approx$ 90 M$
B2	$\approx$ 500 M$

Table 2.2 - Examples of acquisition costs of various aircraft

Significant characteristics of the various classes of aircraft	
Private aircraft	"Poor people" / Flying clubs Costs are dominant
	"Rich people" / business men Costs / performance
Business aircraft	Balance between costs, comfort and performance
Agricultural aircraft	Very specialized, good balance between costs and revenue with probably accent on costs
Aerobatic aircraft	Very specialized, performance (manoeuvrability) is dominant, often very expensive
Civil transport aircraft	Costs may be high if, given a certain fare structure, revenues are higher
Military aircraft (non-transport types)	Costs may be high, military capabilities and operational readiness are dominant
	Most military aircraft have apart from load-carrying requirements high demands on both manoeuvrability ("dog-fighting") and stability ("aiming platform")

Table 2.3 - Main design requirements of various aircraft categories

3 *Design requirements and objectives of transport aircraft*

In this chapter, the design requirements and objectives of a transport aircraft will be detailed.

The general design objective of a transport aircraft is **to transport a payload A over a distance B between airports of category C against minimum costs (i.e. at an optimum speed D).**
The driving parameters to accomplish this goal are:

 • Engine characteristics
 • Lift/drag ratio, $C_{L_{max}}$, buffet boundary
 • Weight

It should be emphasised that estimating the weight and aerodynamic characteristics with sufficient accuracy at an early stage of the design is really an art – but an important one and a crucial one: it determines the initial quality of the design.

The airworthiness requirements then require the aircraft to be **safe**, i.e. its flight handling characteristics (stability and control) must be satisfactory.

The aircraft should also be reliable, which implies that:

 • Systems (such as navigation equipment) must be adequate.
 • Systems shall be reliable and sufficiently redundant (minimum no-go items).

In civil air transport, designing a family of aircraft has become a standard procedure. Two approaches can be recognised.

In the first approach, several versions of the aircraft are developed more or less simultaneously from the start of a programme. These different versions can have different take-off weights, fuselage lenghts, etc. Examples of this approach are the Boeing 787 family (787-3, 787-8 and 787-9) and the Airbus A350XWB family (A350-800, A350-900, A350-1000).

In the second approach, growth versions of the aircraft are developed (long) after the first development round has been completed. These growth versions usually have considerable modifications and associated costs. An example of this approach is the Airbus A340-500/600, in which $ 2.5 billion was invested.

Table 3.1 shows some more design objectives and constraints for civil and military transport aircraft.

Issues	Civil	Military
Dominant design criteria	Economics and safety	Mission accomplishment and survivability
Performance	Maximum economic cruise	Adequate range and response
	Minimum off-design penalty in wing design	Overall mission accomplishment
Airfield environment	Moderate-to-long runways	Short-to-moderate runways
	Paved runways	All types of runway surfaces
	High-level ATC and landing aides	Often spartan ATC, etc
	Adequate space for ground manoeuver and parking	Limited space available
System complexity and mechanical design	Low maintenance - economic issue	Low maintenance — availability issue
	Low system cost	Acceptable system cost
	Safety and reliability	Reliability and survivability
	Long service life	Damage tolerance
Government regulations and community acceptance	Must be certifiable (FAA, etc.) • Safety oriented	Military standards • Performance and safety • Reliability oriented
	Low noise mandatory	Low noise desirable • Good neighbour in peace • Reduced Detectability in war

Table 3.1 - Transport aircraft design objectives and constraints. Source: AIAA Paper No 77-1795

4 *The aircraft design process*

In the aircraft design process five elements can be recognized:

1. The specification
2. Preliminary design
3. The aerodynamic shape
4. Flight handling characteristics
5. Filling the "empty shell"

1. The specification

Setting up a specification requires insight in:

a. The market and its operational requirements (networks, traffic flow etc., numbers and types of existing aircraft and their condition)
b. The economic situation (What is the economic growth projection? Who has the money? What is the tariff structure? Which new opportunities exist for generating additional revenues?)

Knowledge and insight is required of performance aerodynamics, the achievable engine performance and all weight aspects.

The development of the Boeing 747 shows how important weight is. The first ideas were that 350 passengers could be transported over 5100 nm at a MTOW of 550,000 lb. The increase in weight during the development had a "snowball effect", a small increase in weight of some component resulted in a further increase in total weight and so on. The first aircraft was certificated at a MTOW of 710,000 lb, which is an increase of 29%.

In general a good insight is required in projected economic and social development in the not-too-near future. Note that between the initial project definition and first aircraft delivery 5 to 7 years may pass after which the aircraft will have an operational life of at least 30 years. The aviation sector is very sensitive to the state of the economy, during a recession the aviation sector may collapse.

Examples of wrong specification

Dassault Mercure:

Instead of designing the aircraft for a maximum range, Dassault chose to design the Mercure for the average range demanded by airlines. This range was only a fourth of the maximum range, resulting in a design that was not flexible in range and consequently it was an economic failure.

Figure 4.1 - Dassault Mercure. Source: Andrew Hunt

VFW 614:

This aircraft was technically too complicated for the intended market section at its time of introduction and therefore not affordable. The lesson to be learned from this is that applying (new) technologies does not necessarily pay, particularly when politics are heavily involved.

Figure 4.2 - VFW 614. Source: J. de Groot

F-28 Mk6000:

The Fokker F-28 Mk. 6000 was designed to operate from short runways and low-to-medium-altitude airfields. It required high C_L-values at $1.2V_s$ but the high induced drag together with the extra drag from the slats also led to relatively low lift-drag ratios in the take-off. This resulted in a lack of excess thrust for operations from airfields at higher altitude with the engines available.

Figure 4.3 - F-28 Mk. 6000. Source: G. Helmer

2. Preliminary design (The sizing study)

When a good set of specifications is obtained, it is possible to proceed with the next element in the aircraft design process, the preliminary design. Preliminary design is in the first place the finding of a balance between:

- Required volumes
- Weight distribution
- Main dimensions
- Engine performance

As the primary performance characteristics of the aircraft are handled with "mass point mechanics" it is absolutely of prime importance that the relatively simple relationships between prime dimensions, weights and aerodynamics have maximum accuracy. Empirical databases must therefore continuously be updated. Furthermore it is implicitly assumed through these relationships that the designer will succeed in realizing a design that is in accordance with the state-of-the-art. (For example no flow separation or transonic aerodynamic interference of any significance should occur).

Preliminary design is in the first place a formulation of requirements which have to be fulfilled in the detail design of the aircraft by the various specialist disciplines. It is not just filling in formulae; it is the actual numbers of the various coefficients that matter. When a given number is ascribed to the zero-lift drag coefficient C_{D_0} or to the wing weight this means that the design specialists need to achieve this level of drag or wing weight. In preliminary design these numbers are not realized, they are given as minimum goals.

Often the goals set by the preliminary design are too optimistic. Modifying the design is very costly, compensation will have to be paid and customers may be lost.

An aircraft designer should develop a good feeling for what is realizable. Knowing a bit of every aspect is not enough; the designer must have detailed knowledge about (almost) every aspect. The preliminary design must be realistic, not too optimistic as this will result in a disappointing design and not too conservative because then the competition will have a better design. The preliminary designer, at least when it comes to weight, drag and performance, does not design but predict.

Finally, if high but realistic requirements are obtained, the next element can be addressed.

3. The aerodynamic shape

Once the required basic characteristics of the aircraft have been determined, the detailed aerodynamic shape, which both contains the required volumes and produces the desired aerodynamic characteristics, is determined. The aerodynamic shape is obtained through

    a.   Theory (Computational aerodynamics, including CFD)
    b.   Wind tunnel testing
    c.   Taking selected data from empirical data bases (Handbooks)

During the last 30 years, most of the development has been in the field of Computational Fluid Dynamics (CFD). With CFD it is possible to compute the static pressure at any point on a complicated shape for any airspeed. There are two families of CFD methods:

The first family concerns direct analytical methods. With these methods the properties of a given aerodynamic shape are computed. The shape is optimized either by means of trial and error or, more and more often nowadays, by optimization techniques.

The second, most wanted but more difficult method, consists of the inverse methods. With these methods a certain shape is computed based on required properties.

Wind tunnel testing is expensive and its use is limited as much as possible. But their use remains necessary as theoretical calculations do not give a good enough representation of reality, especially at the boundaries of the flight envelope.

Some examples of empirical methods are: DATCOM, ESDU, Abbott & Von Doenhoff.

4. Flight handling characteristics

The prime aim of aerodynamic design is finding an external shape that optimizes lift and drag characteristics for performance purposes. Obtaining satisfactory flight handling characteristics requires attention directed primarily to tailplane, fin and control surfaces. Concerning the size of these components there are conflicting requirements for performance (tail and control surfaces as small as possible) and flight handling (large surfaces). Therefore there is a balance between performance and flight handling.

Generally, the performance is optimized within the boundaries that satisfactory flight handling requires. The flight handling characteristics are not optimized, they are boundary conditions.

Figure 4.4 shows a diagram of the ratio of the horizontal tailplane area over the wing area S_h/S versus the chordwise position of the centre of gravity $(x/c)_{cg}$. The boundary to the left is the control boundary; the right boundary is the stability limit.
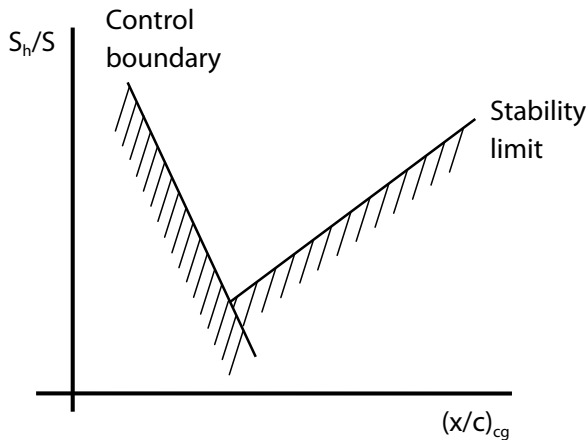
Figure 4.4 - Control and stability limits

In short, as a general rule a designer must:

- Optimize performance
- Produce satisfactory flight handling characteristics

The situation is different with combat aircraft and aerobatic aircraft . For these types of aircraft the controllability can be more important than the mass-point performance.

An example of this is the horizontal tail of the F-18 Hornet; this control surface is larger than is necessary for stability. This is done in order to increase controllability. The deflections during a manoeuvre are also smaller leading to less profile drag at the tail and thus to a higher lift-drag ratio.

Another example of this is the horizontal tail of the F-16, it was designed to have sufficient stability but had a lack of manoeuvrability when performing highly dynamic manoeuvres. When performing these highly dynamic manoeuvres or "jinking" the horizontal tail stalled. To overcome this problem the tail area was enlarged as can be seen in figure 4.5.
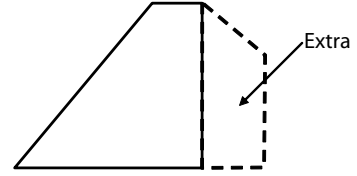
Figure 4.5 - Horizontal tail of the F-16

5. Filling the "empty shell"

Once the aerodynamic shape is determined detail design is performed on:

- Cabin and cockpit arrangement
- All aircraft systems
- Aircraft structure

This is where the more abstract results from the previous parts of the aircraft design process are converted into hardware. This last part of the aircraft design process is the most labour intensive. In 1995 at Fokker for example, 15 persons worked on the preliminary design of an aircraft and 45 on the aerodynamic design. But the rest of the engineering work took up 940 persons.

Evidently there is a large degree of interaction between items 4 and 5.
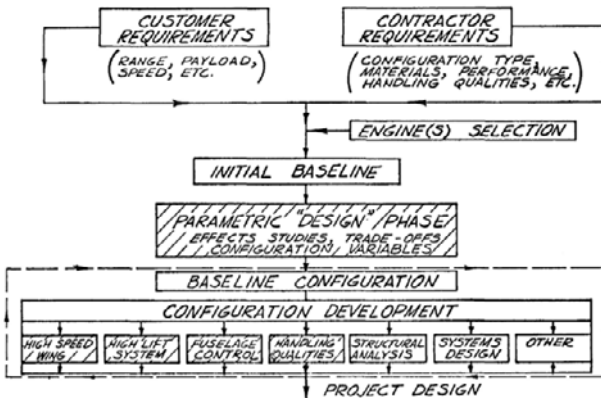
Figure 4.6 - Preliminary design process. Source: AGARD LS-37, paper no. 6

Figure 4.6 shows a block diagram of a preliminary design process. The requirements on the design are set by both the customer (upper left) and the contractor (upper right). The customer sets requirements on transport capacity and the contractor on what can be realized.

Figure 4.7 shows a thrust-to-weight ratio vs. wing loading diagram. Such a diagram is used to determine the design point of an aircraft design. There are various requirements on the design such as the Take-Off Field Length (TOFL), the Engine-Out Altitude (EOA) and the approach airspeed. Parameters that can be optimized by choosing a certain design point are the Minimum Block Fuel (MBF), the minimum Direct Operating Costs (DOC) and the minimum Take-Off Gross Weight (TOGW). Where the design point is chosen depends on expectations of fuel prices, inflation, purchase price, number of aircraft to sell, etc. In this diagram a lower MBF would lead to a larger wing and bigger engine. Suppose the fuel price

Figure 4.7 - EET Baseline design selection chart.
Source: AIAA Paper No. 79-1795
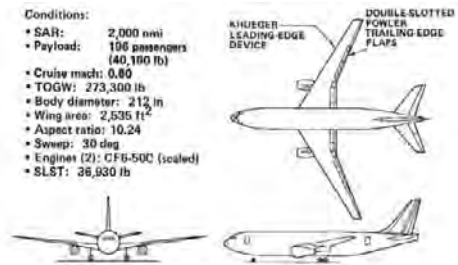
Figure 4.8 - Baseline aircraft.
Source: AIAA Paper No. 79-1795

would increase, then the design point would be shifted to the MBF area. In this case the design point is chosen such that at a given take-off field length the DOC are minimal. This study from Boeing is from 1979, after the second oil crisis when it was expected that the fuel price would increase from $ 0.60 to $ 2.00 per gallon. As this did not happen (at the time) the design was fuel efficient but expensive.

The typical mission phases of an aircraft are: take-off , climb, cruise, descend and landing. The performance during the cruise phase can be estimated with the Breguet formula

$$R = K \frac{V}{SFC} \frac{L}{D} \ln \frac{W_1}{W_2}$$

(4.1)

where

$\dfrac{V}{SFC}\dfrac{L}{D}$	=	Range factor	$\dfrac{L}{D}$	=	Lift over drag ratio
K	=	Constant	SFC	=	Specific fuel consumption
R	=	Range	W_1	=	Weight at start
V	=	Airspeed	W_2	=	Weight at end

In order to increase the range the airspeed could be increased. But today aircraft do not fly at very high airspeeds: a maximum airspeed of Mach = 0.85 is typical. For higher airspeeds flying becomes more expensive because of the high fuel consumption, highly swept wings become necessary and the aircraft becomes heavier which reduces the range. The parameter that can then be changed to influence the range is the lift - drag ratio. The lift - drag ratio is a function of the span b and the wetted area S_{wet}. Figure 4.9 shows a diagram of the maximum lift - drag ratio versus the aerodynamic efficiency of 13 existing aircraft. Note that A_{wet} indicates the wetted surface.
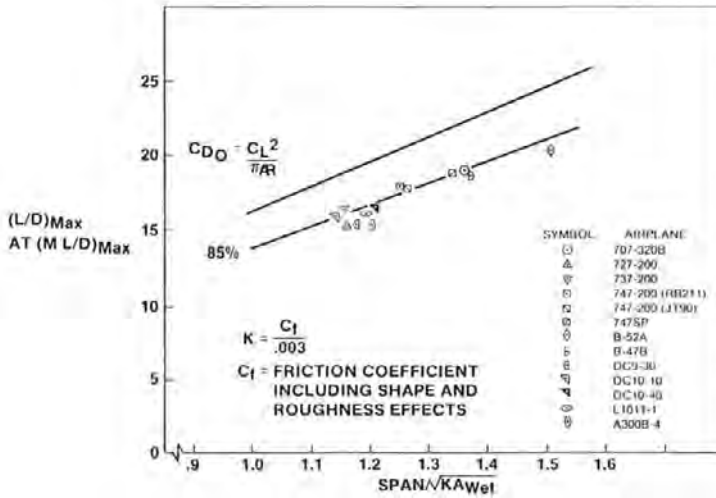
Figure 4.9 - Aerodynamic efficiency at $(L/D)_{max}$. Source : AGARD report no. 712, Paper No. 6

Note that the aspect ratio is only of importance if the wing area is fixed. If not, the span loading $\dfrac{W}{b^2}$ should be used:

$$\frac{D_i}{W} = \frac{C_{D_i}}{C_L} = \frac{C_L}{\pi\,Ae} = \frac{WS}{\pi\,qSb^2e} = \frac{1}{\pi\,qe}\frac{W}{b^2} \tag{4.2}$$

The derivation of the figure will be further discussed in chapter 40. It can be seen that the B-52 is unsurpassed; it is approximately where the designs of the Airbus A340 and Boeing 777 would be in the diagram.

The certification requirements for a civil transport aircraft with respect to take-off and landing relate basically to the safety aspects of the acceleration during take-off from standstill to $1.2V_S$ and the deceleration during landing from $1.3V_S$ to standstill by braking.

Take-Off

A requirement for civil transport aircraft is that it must be possible to continue the take-off after an engine has failed at a critical moment during the ground run. For that case certain climb requirements must be met. Consequently the aircraft must be equipped with a minimum of two engines.

A 2-engined aircraft must be able to continue the take-off after an engine failure on one engine, or 50% of the installed power. The required minimum climb gradient for this configuration is 2.4%. Similarly, an aircraft with 3 engines must be able to continue the take-off on two engines (67% of the power installed) with a minimum climb gradient of 2.7% and for a 4-engined aircraft a continued take-off must be possible on three engines (75% of the power installed) with a minimum climb gradient of 3.2% . From the above it can be concluded that the everyday climb performance (with all engines operational) of a 2-engined aircraft will be considerably better than the performance of a 4-engined aircraft. This is an important factor when considering the noise characteristics of a particular aircraft from a certification point of view.

At take-off, the objective is to achieve a $(C_L)_{V_2}$ as high as possible, combined with a $(L/D)_{V_2}$ as high as possible. At landing achievement of a high maximum lift coefficient is dominant but modern noise requirements limit the acceptable drag levels in the landing configuration.
Therefore, many flap settings are required; figure 4.10 shows the variation of $(L/D)_{V_2}$ with $(C_L)_{V_2}$ for different aircraft.
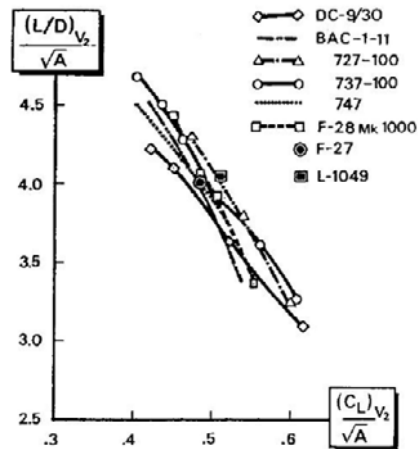
Figure 4.10 - Generalized take-off.
Source : E. Torenbeek, Synthesis of Aircraft Design

The pattern of low-speed drag polars for a transport aircraft is given in figure 4.11. The diagram shows how the lift-drag polar shifts up and to the right with increased flap setting: an increase in maximum lift comes with an increase in drag.
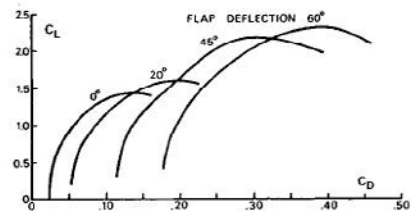
Figure 4.11 - Low-speed polars for a transport aircraft

The main parameters for take-off are the take-off lift coefficient $C_{L_{TO}}$, the drag coefficient and the thrust to weight ratio which gives the aircraft acceleration and determines the climb gradient. Just as the cruise performance the climb performance is strongly influenced by wing span. Figures 4.12, 4.13 and 4.14 give more information about the take-off ground run and climb out phases.
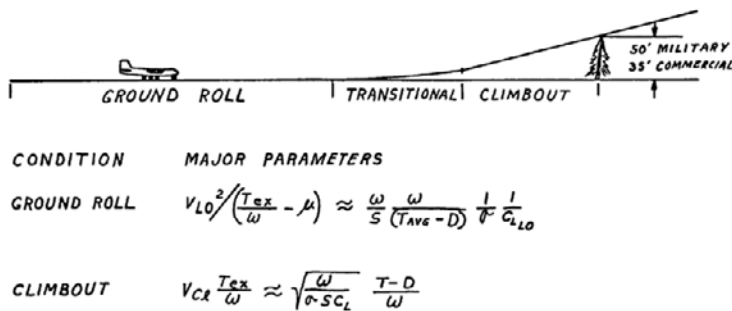
Figure 4.12 - Take-off profile and major parameters. Source : AGARD LS-37, paper no. 6
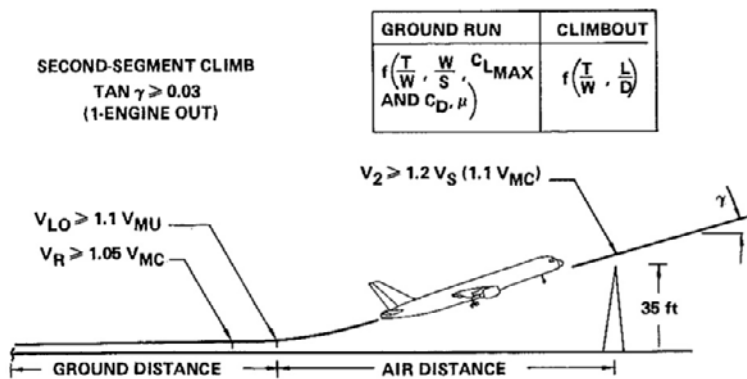
Figure 4.13 - Take-off profile. Source: AGARD CP-365, paper no. 9
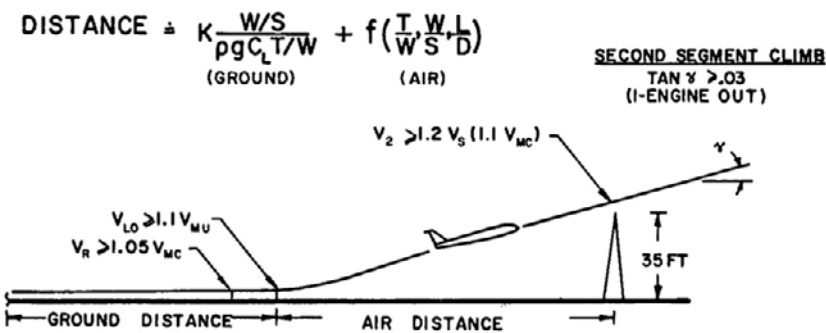
Figure 4.14 - Take-off profile. Source : AGARD LS-43, paper no. 7

Landing

Climb requirements have not only been formulated for take-off but also for landing. This is shown schematically in figure 4.15. The requirement for the approach is that with one engine out (N-1) and approach flaps, the aircraft must be able to reach a climb gradient of at least 2.7% at the certificated minimum approach speed. With landing flaps deployed and all engines running, the aircraft must be able to achieve in a go-around a climb gradient of at least 3.2%. When an engine failure occurs during flight it is possible to have a missed approach when approach flaps have been selected, but a go-around should not be attempted when landing flaps are deployed. Once landing flaps are selected the landing must be continued .

The climb and descent performance requirements set operational restrictions to the take-off and landing weight depending on altitude and temperature (WAT limit) and obstacles. Examples of these limitations are mountains, towers, buildings (Hong Kong), the airfield altitude (La Paz: 14,000 ft), the engine performance, etc. Therefore it is an important design objective to make operational flexibility as wide as possible. This is the reason why the Boeing 737 and the McDonnell Douglas MD-80 for example have a range of certified flap settings.
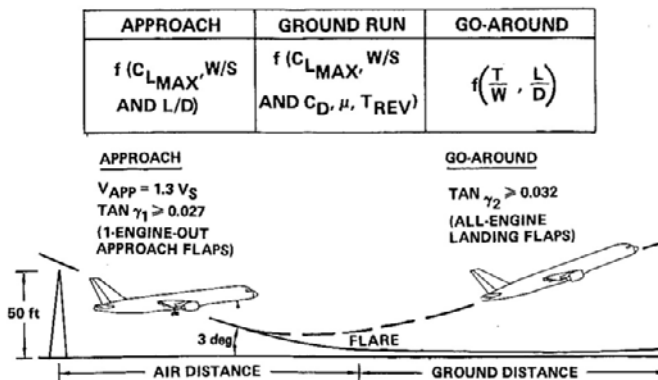
Figure 4.15 - Landing profile. Source: AGARD CP-365, paper no. 9

To illustrate the importance of an accurate estimation of the coefficients of an aircraft the effect of the lift coefficient on the weight and the take-off and landing field lengths are shown in figures 4-16 and 4-17. For a certain flap setting the weight-versus-field-length plots are limited by the WAT limit. The climb gradient is a function of the thrust-to-weight ratio and the lift-drag ratio:

$$\tan \gamma = \frac{T}{W} - \frac{D}{L} \qquad\qquad (4.3)$$

Suppose an aircraft is designed for an initial climb lift coefficient $C_L = 1.2$ and has an available take-off field length of 10000 ft leading to a maximum take-off weight MTOW = 400,000 lb. Now the aircraft suffers from stalling problems that must be solved by lowering the lift coefficient to $C_L = 1.1$. This then leads to a maximum take-off weight MTOW = 380,000 lb, a reduction of about 5%. This may not seem much, but an aircraft like the Boeing 767 has an empty weight fraction of 50% of the maximum take-off weight, a fuel fraction of 35% and a payload fraction of just 15%. The reduction in take-off weight reduces the payload weight to 10% of the original take-off weight. This decrease in revenue of 30% is unacceptable for operators and makes the aircraft economically unattractive for this particular operation.
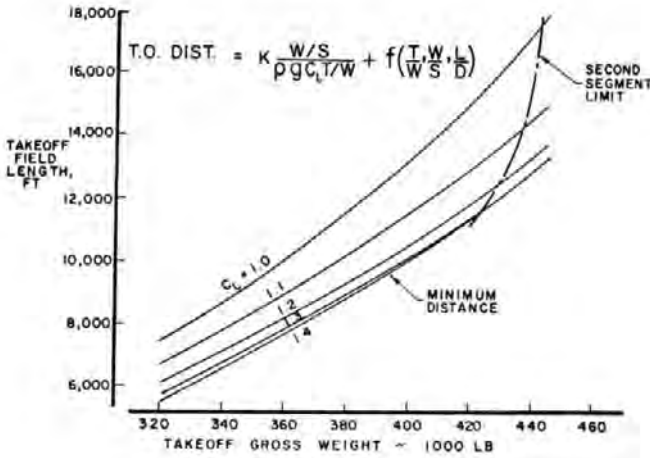
Figure 4.16 - Take-off performance. Source: AGARD LS-43
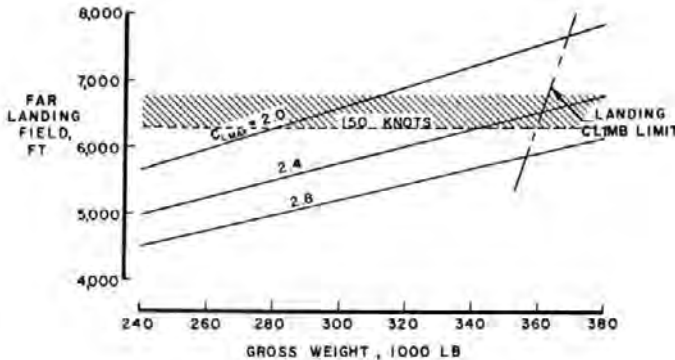
Figure 4.17 - Landing performance. Source: AGARD LS-43

Figures 4.18 to 4.26 present some further information that should be of use for the estimation of the take-off and landing performance.
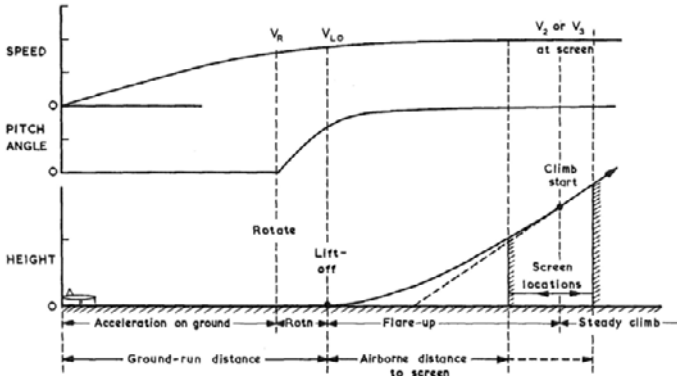
Figure 4.18 - Basic take-off framework. Source: AGARD LS-56, paper no. 2
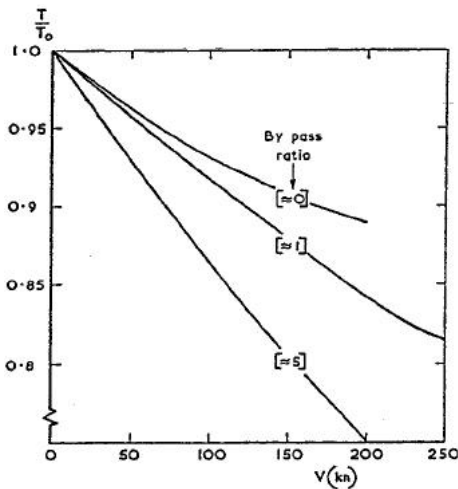
Figure 4.19 - Engine thrust decay with speed. Source: AGARD LS-56, paper no. 2
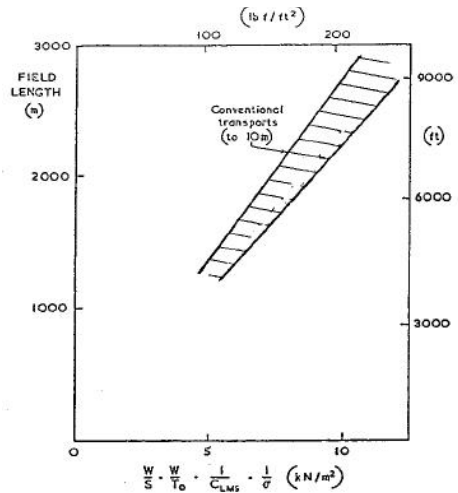
Figure 4.20 - Take-off distance to screen. Source: AGARD LS-56, paper no. 2
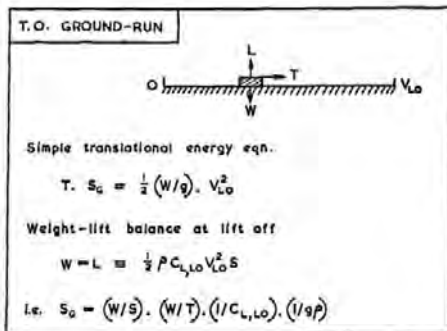
Figure 4.21 - Take-off ground run. Source: AGARD LS-56, paper no. 2
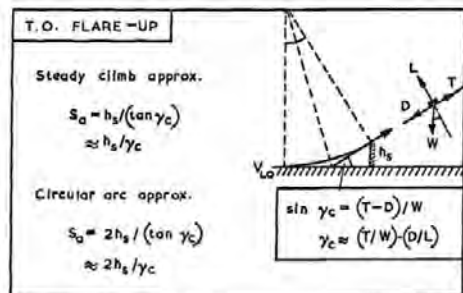
Figure 4.22 - Take-off flare-up. Source: AGARD LS-56, paper no. 2
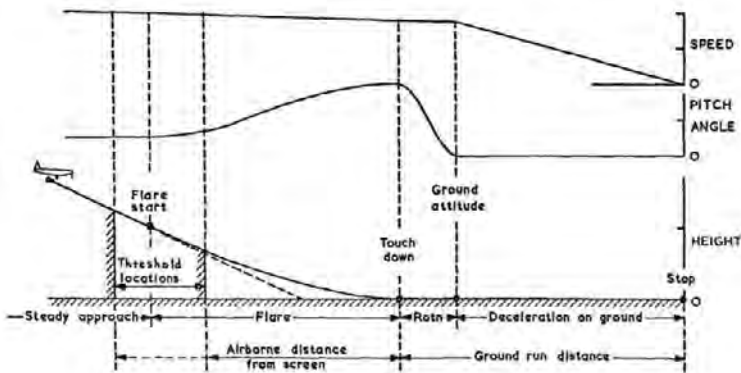
Figure 4.23 - Basic landing framework.
Source: AGARD LS-56, paper no. 2
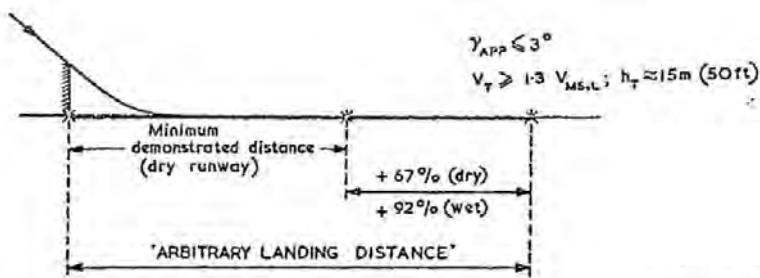
Figure 4.24 - Landing distance.
Source: AGARD LS-56, paper no. 2
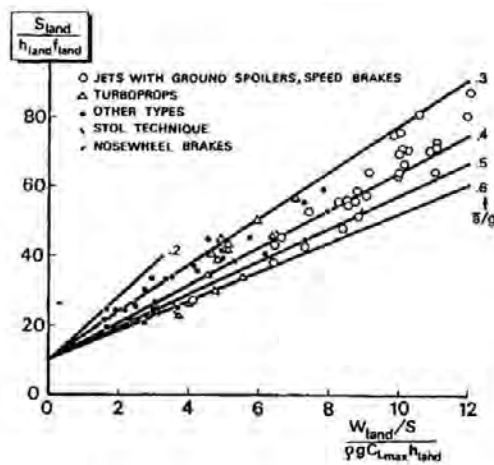
Figure 4.25 - Statistical correlation of the unfactored
landing distance. Source: E. Torenbeek

Assume Overall Mean deceleration d

i.e. $S_{Ldg} \approx \frac{1}{2} d \, V_A^2 = \frac{1}{2} d . (KV_{S,1g})^2$

$= d \, K^2 . (W/S) . (1/q C_{Lmax})$

where $K \approx 1.3$ typically.
          $d \approx 0.40 \, g$ typically

Figure 4.26 - Elementary kinematic relations. Source: AGARD LS-56, paper no. 2

Figure 4.27 is an example of a set of requirements and the corresponding characteristics of the resulting design. The iterative procedure followed in designing an aircraft is illustrated in figures 4.28 and 4.29.

Mission Requirements

• Still air range	= 3704 km (2000 nmi)
• Payload	= 196 passengers, 18 225 kg (40 180 lb)
• Initial cruise altitude	$\geqslant$ 10 668m (35 000 ft)
• Cruise Mach number	= 0.80
• Takeoff field length	$\leqslant$ 2290m (7500 ft)
• Approach speed	$\leqslant$ 231.5 km/h (125 kn)
• Reserves	= 1967 ATA domestic

Airplane size and geometry characteristics	
Wing area	235.51 m^2 (2535.0 ft^2)
Wing span	49.11m (161.12 ft)
MAC	5.23m (17.15 ft)
Aspect ratio	10.24
Sweep$_{c/4}$	0.52 rad (30 deg)
Taper ratio	0.3158
t/c, SO8/tip*	15%/10.3%
Horizontal tail area	51.65 m^2 (556.0 ft^2)
Vertical tail area	36.14 m^2 (389.0 ft^2)
Body length	47.55m (156.0 ft)
Body diameter	5.39m (17.67 ft)
Engines	2 scaled CF6-50C
Bypass ratio	4.4
Sea level static thrust (uninstalled)	164.27 kN (36 930 lb)

*Based on gross chord length

Airplane performances	
Takeoff gross weight	120 719 kg (266 140 lb)
Operating empty weight	76 861 kg (169 450 lb)
Block fuel	19 051 kg (42 000 lb)
Reserves	6827 kg (15 050 lb)
Mission landing weight	101 913 kg (224 680 lb)
Thrust/weight	2.726 N/kg (0.278 lb/lb)
Wing loading	512.67 kg/m^2 (105.0 lb/ft^2)
Initial cruise altitude capability	11 113m (36 460 ft)
Average cruise altitude	11 723m (38 460 ft)
Range factor	22 909m (12 370 nmi)
Lift/drag	18.2
Specific fuel consumption	0.069 kg/hr/N (0.674 lb/hr/lb)
$C_{D_{P_{MIN}}}$	0.01791
FAR TOFL, SL, 29°C (84°F)	2290m (7500 ft)
$C_{L_{V_2}}$	1.506
$V_{APP}(1.3 V_s)$	62 m/s (120 kn)
$C_{L_{APP}}$	1.81

Figure 4.27 - Sized EET Airplane Performance and Characteristics (Model 768-785B). Source: AIAA Paper No. 79-1795
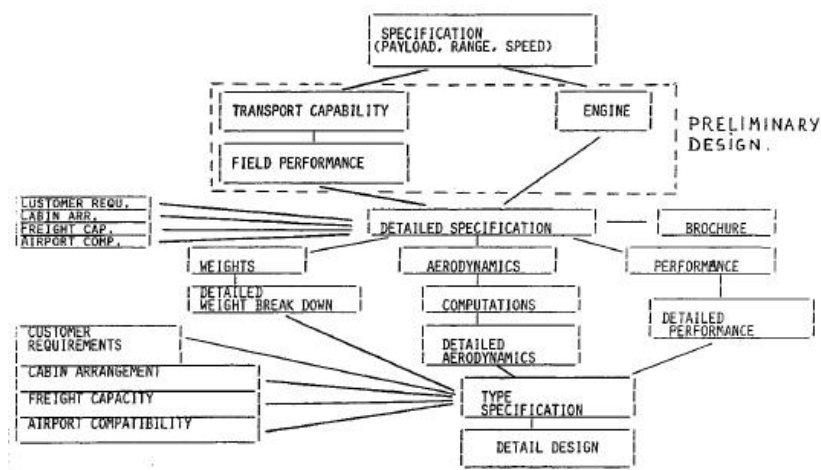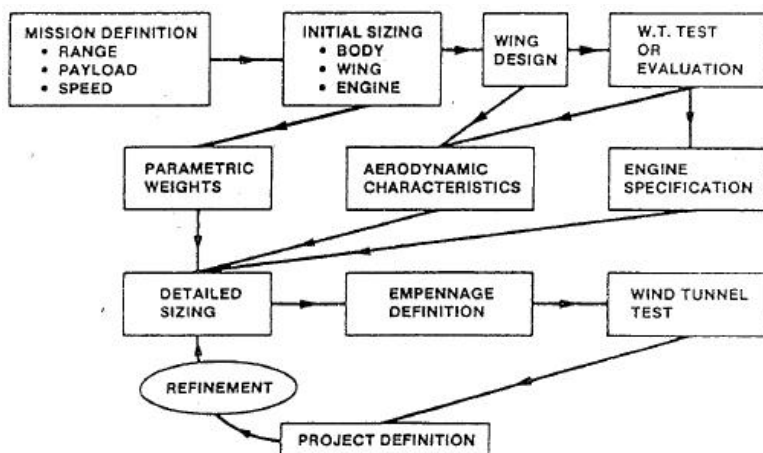
Figure 4.28 - The design process

Figure 4.29 - Aircraft design cycle. Source: AGARD R-712, paper no. 6

5 *Geometry*

The geometry of the aircraft is defined by four elements, which are:

1. The **internal geometry** with respect to:
    a. Required volume, by taking into account
        • Cargo volume (including overhead bins)
        • Dimensions of seats, legroom, headroom
        • Inflight entertainment
    b. The shape, i.e. the usefulness of the volume
        • Non-cylindrical fore and aft fuselage
        • Inclined floor in rear, such as on the Airbus A300
        • Under-floor cargo hold - especially with respect to containers)
    c. Access to the available volume - very important for quick loading and unloading, i.e. short turn-around times.

This will lead to the definition of various important parts, such as:
    • Fuselage cross-section
    • Cabin and freight hold length and internal arrangement
    • Required fuel volume
    • Required space for equipment
      (avionics, APU, undercarriage, control surface mechanisms, etc.).

2. The **internal geometry** with respect to structural (strength and stiffness) considerations:
    • Thickness distribution along the span of the wing and tail surface torsion boxes
    • Thickness of flaps (DC-8 did not have fairings for flaps, DC-10 and B747 did have fairings to cater for sophisticated flap movements)
    • Thickness of engine struts and pylons.

3. The **external geometry** with respect to aerodynamic considerations (determining the thickness for the desired supervelocities).

4. The **external geometry** with respect to producibility and cost control
A classical example would be to avoid double curved surfaces when possible. However, this depends much on the material used: composites are very suitable for double curved shapes, but cannot handle kinks very well.

6 *Design of the external geometry*

The external geometry of the aircraft should be designed such that it leads to **optimum aircraft performance** and **satisfactory flight handling characteristics**, whilst fulfilling the requirements on the **internal geometry** and **producibility**.

The various flight phases and different airworthiness and flight handling requirements lead to conflicting design requirements concerning basic design data such as wing loading, $C_{L_{max}}$ versus L/D and weight.

In fact, aircraft design is always about finding a compromise between opposing requirements. In this chapter, we shall further discuss the design of the external geometry as determined by *aerodynamic* design requirements and objectives.

Up to about 1940, the relation between the geometry of aircraft components and aerodynamic characteristics was heavily based on experimental data (wind tunnel and flight tests). Well-known examples are the NACA 4-digit and 5-digit series airfoils and the NACA engine cowlings.
The experience of the designer also played a role here, with some "signature" designs – such as the vertical tail on the De Havilland Hornet Moth and the Vickers Viscount. See figure 6.1 for a picture of the tail of the Hornet Moth.

Figure 6.1 - De Havilland Hornet Moth. Source : Mick Bajcar

After 1940, (limited) theoretical analysis, with an emphasis on airfoils, was done by those that had "computing power" – large research institutes and airframe manufacturers. This resulted in, for example, the NACA 6-series laminar flow airfoils.

With the advent of jet engines and aircraft flying near the speed of sound, a return to windtunnel experiments took place, as the computer codes of that time were not capable of handling transonic (mixed subsonic and supersonic) flow. However, a limited use of theory was made to determine the next step on the experimental process.
The "peaky" airfoil sections (by Pearcey et al.) that have been widely applied in the 1960's are a good example of research results in this era.

Today, the prime aerodynamic design tools are various design and analysis computer codes, together indicated as computational fluid dynamics (CFD). For the design flight condition – the cruise – these methods work quite well. The initial climbout (high-lift devices extended) can also be treated accurately.

However, CFD still does not produce sufficiently accurate results in case of separated flow. And it is exactly in that area that the designers want to have accurate results, as this determines the limits of the design. These so-called "off-design" conditions include low-speed stall (important for airfield performance), the buffet boundary and the flight regime between M_{MO} and M_D (which are both important for cruise performance).

Consequently, the crucial question in aerodynamic design is at present:

What is the proper design (= target) pressure distribution?

Or, in other words, which pressure distribution should one try to obtain in the design flight condition which will fulfil *all* design requirements?

In order to postpone flow separation as far as possible and to minimise drag, the **general goal in aerodynamic design should be**:

- For components that do *not* have to produce resultant forces, local supervelocities should be minimised.

- For components that *do* need to produce resultant forces (such as the wing or rudder), the pressure distribution at the relevant flight conditions should be optimised such that the momentum loss in the boundary layer and behind the shockwave is minimal.

- Finally, for components that must tolerate a large variation in local flow direction (such as tail surfaces and engine intakes), leading-edge shapes and design pressure distributions must be found, which cope with this variation.

7 Computing velocity and pressure distributions on fixed bodies in attached flow conditions

Calculations on velocity and pressure distributions have two objectives:

- Optimise the pressure distribution, preferably over the complete aircraft.
- Determine the overall characteristics of the aircraft, including stability and control derivatives, such as C_L - α, C_L - C_m, C_{l_β}, C_m - δ_e, etc.

Although in general accuracy is improved when boundary layer effects are incorporated, neglecting them together with thickness effects on wing and tail surfaces, and using a relatively coarse panelling, produces quick and surprisingly good results.

The simplest computation of velocity and pressure distribution takes place by means of potential flow theory (which uses sources, sinks, dipoles and vortices). However, it should be kept in mind that potential flow in itself does not take lift into effect. This is covered by the so-called Kutta-Joukowski boundary condition.

The Kutta-Joukowski condition is an empirical boundary condition and as such is not unique - for each case a choice has to be made. Physically, the Kutta-Joukowski condition is tied to the boundary layer flow at the body's trailing edge and consequently for the proper choice of the Kutta-Joukowski condition the boundary layer has to be incorporated in the computations when lift is involved and when detailed knowledge of the pressure distribution is required.

In order to take boundary layer effects into account in calculation, the concept of displacement thickness, δ^*, is used. The definitions of the boundary layer are shown in figure 7.1.
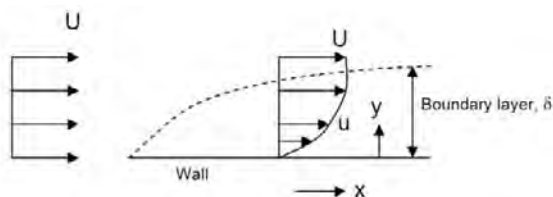
Figure 7.1 - Boundary layer definitions

Through the mass conservation law, the following relation can be found:

$$\delta^* \cdot U \cdot \rho = \rho \int_{y=0}^{y=\infty} (U - u)dy \tag{7.1}$$

Typically, $\delta^* = \frac{1}{6}\delta$.

Another important boundary layer quantity, in particular in questions concerning drag computation and flow separation, is the momentum thickness, θ.

Through the momentum conservation law, the following relation is found:

$$\theta \cdot U \cdot \rho \cdot U = \rho \int_{y=0}^{y=\infty} u(U - u)dy \tag{7.2}$$

Finally, a last important factor in boundary layer analysis, combining both the displacement thickness and the momentum thickness, is the shape factor, H. It is defined as:

$$H = \frac{\theta}{\delta^*} \tag{7.3}$$

As both δ^* and θ are highly dependent on the shape of the velocity distribution in the boundary layer, the shape factor H is even more so (hence its name). The shape of the velocity distribution in the turbulent boundary layer has been determined experimentally.

Finally, when the displacement thickness has been determined the detailed pressure distribution can be obtained by analysing an equivalent body in potential flow. The equivalent body is obtained by adding the displacement thickness to the actual body.
The Kutta-Joukowski condition is also determined on the basis of the equivalent body.

8 *The limitations of boundary layer theories*

In this chapter, various issues concerning the quality of boundary layer theories will be addressed briefly.

Laminar boundary layer theory started in the early 1900's by Prandtl. Nowadays it is a well-established theory.
However, the situation concerning the turbulent boundary layer is different. Based on experimental data, models have been developed, which rely heavily on the boundary layer velocity profile and the flat-plate (zero pressure gradient) drag as a function of Reynolds number. Despite long periods of research, turbulence models have not yet reached an acceptable accuracy for proper analysis of flows with large pressure gradients.

Turbulent separation at the trailing-edge of an airfoil can be handled reasonably well in many cases, at least in two-dimensional flow, but much work has to be performed before it can be claimed to be fully understood.
On the other hand, the understanding of separation at or near the leading edge is still lacking sufficient accuracy for design purposes and "design" is based purely on empirical results. The same holds for the boundary layer transition, including the transition bubble.

Interaction between shockwaves and the boundary layer can be treated analytically but only for nominally weak shockwaves. In practice, up to boundary-layer separation reasonable 2D results are obtained. Separation itself is determined with rather crude empirical criteria.

Until about 30 years ago, for practical design purposes, in most cases only full-potential theory was used with two-dimensional or axially-symmetric boundary-layer theory. Computations with Euler and time-averaged Navier-Stokes codes were mostly performed in a laboratory environment.

However, today, even small companies can afford to buy and use these codes. For example, the Brazilian aircraft manufacturer Embraer has used Navier-Stokes codes in designing its regional jets.

9 Computations with separated flow

Computations with separated flow find application in two main categories at present.

The first of the applications is on wings with sharp-swept leading edges. These wings generate leading-edge vortices, which produce additional lift; however, this comes at the expense of additional drag. These wings are mainly used on military aircraft – fighters in particular, as they have a large amount of thrust to overcome the extra drag, and can put the extra lift to good use.
As for the computation, results with Euler codes give good results.

The second application is in the prediction of $C_{l_{max}}$ of 2D airfoils (including airfoils with slats and/or flaps deflected). This started with a combination of full-potential and boundary-layer theory. It is expected that the use of Euler codes (i.e. including rotation effects) and Navier-Stokes codes in the future will show improvements. However, up to now empirical data remain necessary for maximum lift prediction.

PART 2

PRESSURE DISTRIBUTIONS

10 The relation between supervelocity and pressure coefficient

In this chapter, the relation between ΔV and C_p will be derived from known theory. First, for incompressible flow with small disturbances, from Bernoulli's law:

$$p_t = p_0 + \tfrac{1}{2}\rho V_0^2 = \text{constant} \tag{10.1}$$

From equation (10.1) follows that:

$$p_t = p_{local} + \tfrac{1}{2}\rho V_{local}^2$$

or

$$p_t = p_{local} + \tfrac{1}{2}\rho \left(V_0 + \Delta V\right)^2$$

or

$$p_t = p_{local} + \tfrac{1}{2}\rho V_0^2 + \rho V_0 \Delta V + \tfrac{1}{2}\rho\left(\Delta V\right)^2$$

The last term can be neglected because only small disturbances are considered here. Rewriting this last result gives:

$$p_t = p_{local} + \tfrac{1}{2}\rho V_0^2 \left(1 + 2\frac{\Delta V}{V_0}\right) \tag{10.2}$$

Since (10.1) must be equal to (10.2), this yields:

$$p_0 + \tfrac{1}{2}\rho V_0^2 = p_{local} + \tfrac{1}{2}\rho V_0^2 \left(1 + 2\frac{\Delta V}{V_0}\right) \tag{10.3}$$

By definition, the pressure coefficient is equal to:

$$C_p = \frac{p_{local} - p_0}{\tfrac{1}{2}\rho V_0^2} \tag{10.4}$$

Combining (10.3) and (10.4) results in the desired relations:

$$p_{local} - p_0 = -\tfrac{1}{2}\rho V_0^2 \frac{2\Delta V}{V_0} \tag{10.5}$$

and

$$C_p = -\frac{2\Delta V}{V_0} \tag{10.6}$$

When compressibility effects are included the relation between pressure coefficient and supervelocity becomes more complicated. Figure 10.1 shows the relation between pressure coefficient, free stream Mach number and local Mach number according to Kármán-Tsien. Note that in this figure the C_p shown should be read as the negative C_p.

As an example of how to use this figure, consider the following example. Consider an airfoil where at a certain point on the airfoil $C_p = 0.32$ at $M_0 = 0.6$. The critical Mach number for this airfoil, neglecting compressibility effects, can be found on the horizontal axis, which is 0.84. Taking compressibility into account, the curved line of $C_p = 0.32$ is followed, until it reaches the point where M_{local} is 1.0. Then, it follows that for this point, the critical Mach number is 0.77.
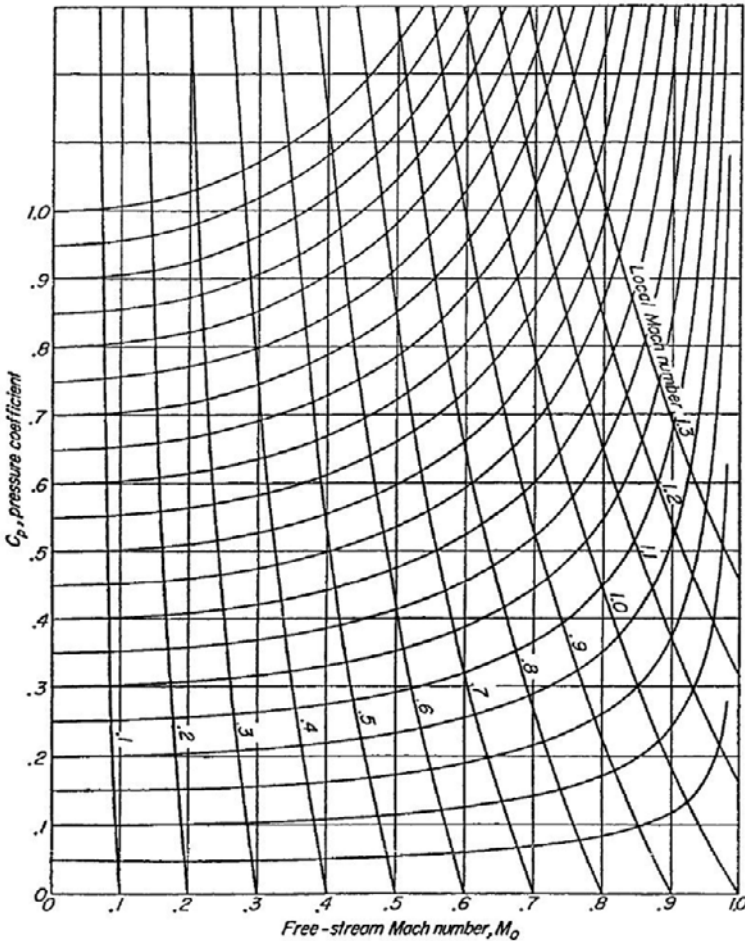
Figure 10.1 - Variation of local pressure coefficient and local Mach number with free stream Mach number according to Kármán-Tsien. Source: Abbott & Von Doenhoff, Theory of Wing Sections

The relation between local Mach number, M_{local} and static pressure coefficient c_p as a function of free stream Mach number M, including local Mach number above $M_{local} = 1$

The relation presented below is strictly speaking only valid for isentropic flow. This means that compressibility effects are included but not the entropy increase due to shock waves. In practice, however, this relation applies very well to the flow around transonic airfoils.

As stated above, the static pressure coefficient is defined as:

$$C_p = \frac{p_{local} - p_0}{\frac{1}{2}\rho V_0^2} = \frac{p - p_0}{q_0}$$

where p is the local static pressure, p_0 is the free stream static pressure and q_0 is the free stream dynamic pressure.

Furthermore, the following isentropic relation applies:

$$p_t = p\left(1 + \frac{\gamma - 1}{2} M_{local}^2\right)^{\frac{\gamma}{\gamma - 1}} = p_0\left(1 + \frac{\gamma - 1}{2} M^2\right)^{\frac{\gamma}{\gamma - 1}} \tag{10.7}$$

Where p_t is the total pressure

Equation 10.7 gives the relation between p and p_0.

With the aid of the gas law $p = \rho RT$ and the equation for the speed of sound, $a^2 = \gamma RT$, the free stream dynamic pressure q_0 can be written as:

$$q_0 = \tfrac{1}{2}\rho_0 V_0^2 = \tfrac{1}{2}\rho_0 \gamma RTM^2 = \tfrac{1}{2} p_0 \gamma M^2 \tag{10.8}$$

Where ρ_0 is the free stream air density, V_0 is the free stream velocity, T is the static temperature and R is the universal gas constant.

After some manipulation this leads to the following relation:

$$M_{local}^2 = \frac{2}{\gamma - 1}\left[\frac{1 + \frac{\gamma - 1}{2} M^2}{\left(1 + \tfrac{1}{2}\gamma M^2 c_p\right)^{\frac{\gamma - 1}{\gamma}}} - 1\right] \tag{10.9}$$

As noted above, for the analysis of the flow around transonic airfoils this relation can be used for local Mach numbers up to $M_{local} = 1.4$ to 1.5.

11 The relation between geometry and pressure distribution

The pressure distribution on any closed body in steady flow has, in general, the following characteristics:

- A stagnation point (where $C_P = 1$ in incompressible flow) at or near the leading edge or nose.
- A stagnation point at or near the trailing edge or tail.
- A point on upper and/or lower surfaces, or a line on the periphery of the body, where the supervelocities reach a maximum (and the static pressure coefficient C_P a minimum)

Note that the latter applies only to pressure distributions with maximum positive supervelocities. On lifting surfaces, the pressure distribution on the lower surface often shows a minimum positive C_P-value, indicating a minimum negative supervelocity.

Away from the stagnation areas there exists a direct relationship between surface curvature and pressure coefficient: the stronger the (convex) curvature, the higher the (positive) supervelocities and the (negative) C_P-values. This is explained in more detail in figure 11.2.

Consequently, if a local change in pressure coefficient is required then the curvature must be increased (made more convex or less concave) if C_P has to become more negative or less positive and the curvature should be decreased if C_P has to be changed in a positive sense.

Note that if locally the shape is changed through a "bulge" or a "dent" blending into the original geometry, this always leads to a change in curvature forward and aft of the "bulge" or "dent", opposite to the bulge or dent itself. See figure 11.1.
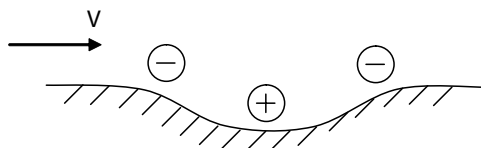
Figure 11.1 - Relation between geometry and pressure coefficient

The prime questions in design concerning the relation between geometry and pressure distribution then reduce to:

- Given certain required characteristics: what should the design pressure distribution be and what is the associated geometry and resulting volume?

- Given a required shape and volume: what are the minimal changes required to produce the most favourable pressure distribution?

For answers to these questions see chapter 6.
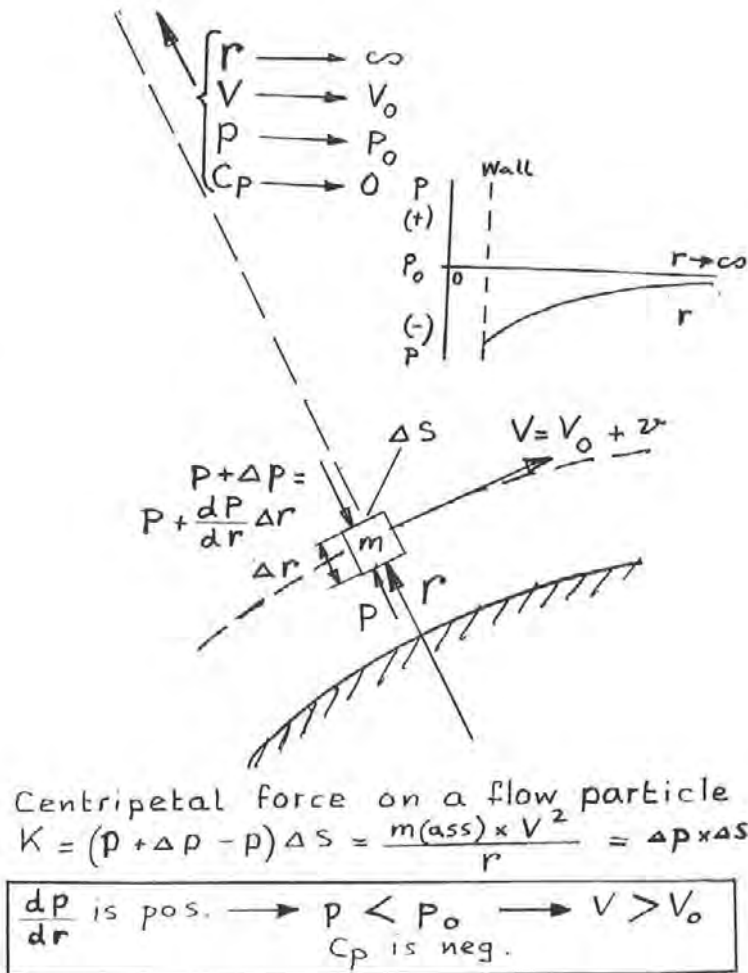
Figure 11.2 - Relation between local velocity and local curvature

12 Pressure distributions on components which are not intended to generate aerodynamic forces

Air flowing over a body causes a pressure distribution on that body. A locally convex curvature causes the pressure to decrease and a locally concave curvature will lead to an increase in pressure.

This is illustrated in figures 12.1 and 12.2. The dotted curve in figure 12.1 shows the calculated pressure distribution without annular bump. Note the large suction peaks over areas where the local radius of convex curvature is very small and the locally strong increase in the pressure where the local radius of concave curvature is very small.
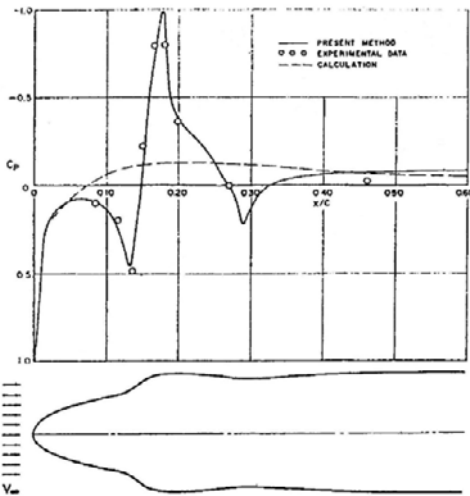
Figure 12.1 - Comparison of calculated and experimental pressure distributions on a prolate spheriod with an annular bump.
Source: Canadian Aeronautics and Space Journal, Febr. 1970
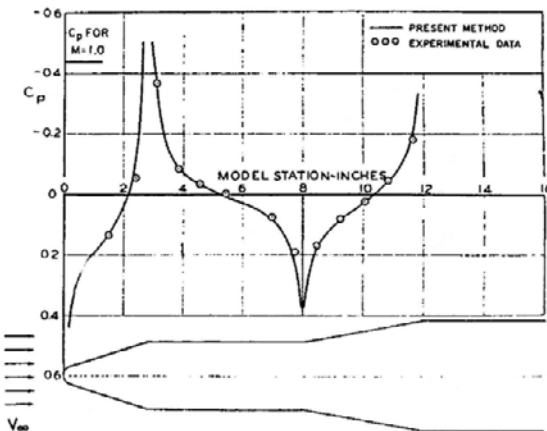
Figure 12.2 - Comparison of calculated and experimental pressure distribution on a Skybolt missile at a free-stream Mach number of 0.8.
Source: Canadian Aeronautics and Space Journal, Febr. 1970
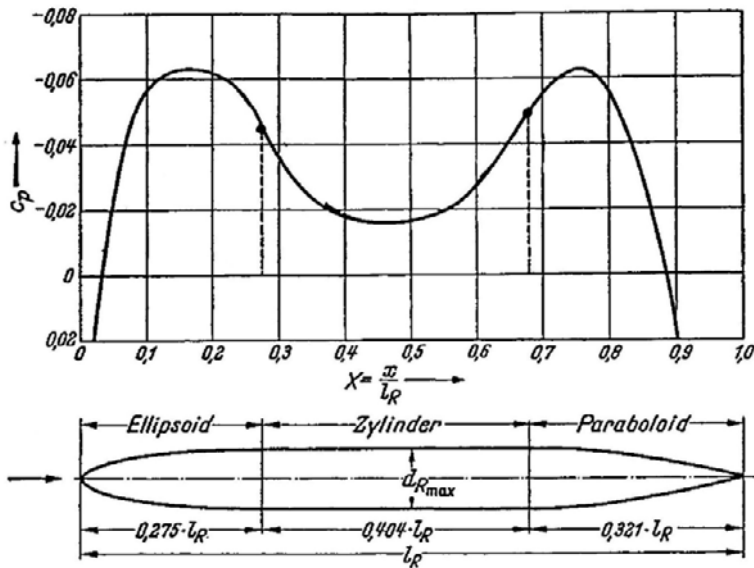
Figure 12.3 - Pressure distribution on a rotational body with cylindrical middle part. Ratio body diameter to length: 0.09. Source: Schlichting und Truckenbrodt: Aerodynamik des Flugzeuges Band II, 9.2

On a part with no axial curvature, for example on the cylindrical part of the body in figure 12.3 the pressure coefficient tends towards zero.

Also figure 12.4 shows that higher local convex curvature leads to higher supervelocities (near the front and the rear end on the ellipsoid and near the middle of the paraboloid).

Pressure distributions over aircraft components

The pressure distribution over an aircraft fuselage shows the same characteristics as explained here and on the previous page. This is illustrated in figure 12.5. The difference in theoretical and experimental pressure distribution at the position of the tail is caused by the theory not taking the vertical tail into account. Notice the increase in pressure between cockpit and wing.

Because here the fuselage has a cylindrical shape the pressure coefficient increases towards zero, for $\theta = 0°$ and $90°$. For $\theta = 180°$ the pressure coefficient even becomes positive shortly before the wing because of the proximity of the stagnation area at the wing leading edge. For $\theta = 0°$ the effect of the rapid changes in the cockpit contour can be seen. The flow accelerates, decelerates and accelerates again rapidly at these locations.

Figure 12.4 - Pressure distribution over rotational bodies (paraboloid and ellipsoid) at incompressible, axial flow. Ratio body thickness over length: 0.1. Source: Schlichting und Truckenbrodt: Aerodynamik des Flugzeuges Band II, 9.2
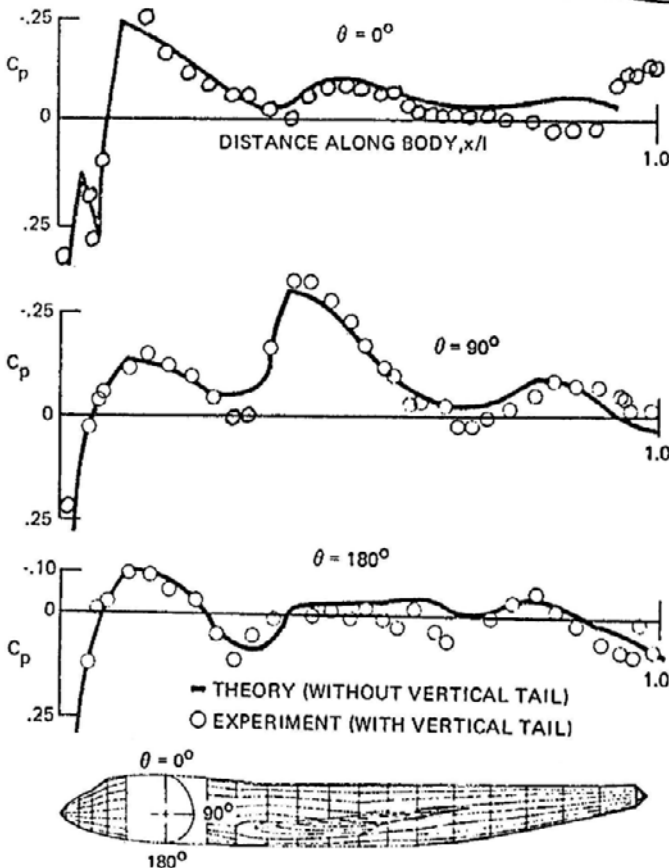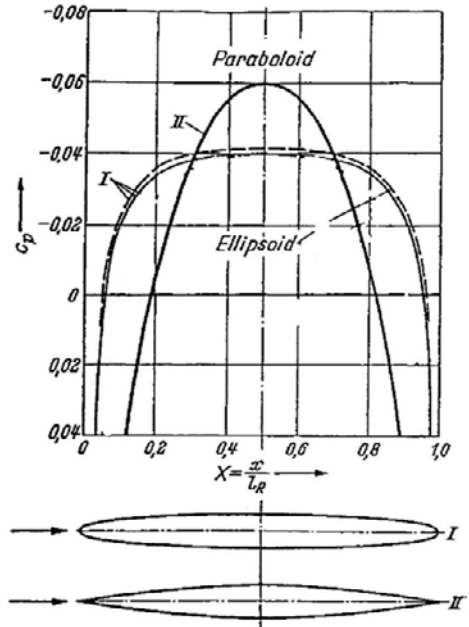
Figure 12.5 - Fuselage pressure distribution comparison, Boeing 747. Source: AIAA Paper No 72-188

Figure 12.6 shows a comparison between the pressure distribution from wind tunnel tests and as obtained with a numerical method. Apparently, the method used was not sufficiently sophisticated to handle the high local velocities at the cockpit canopy resulting in large discrepancies between the data from the tests and the calculations.
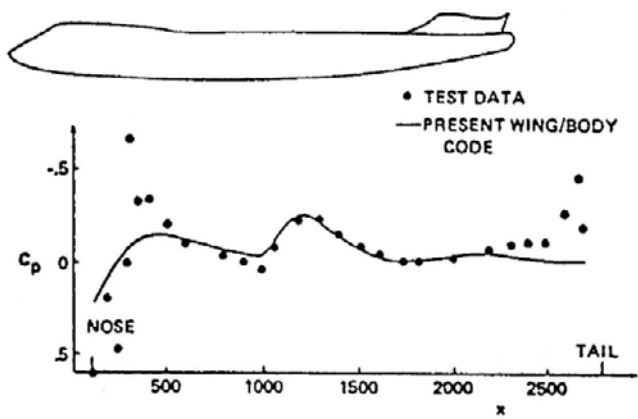
Figure 12.6 - Comparisons of crown line pressure distributions for a low wing transport configuration at $M_\infty = 0.84$ and $\alpha = 2.8°$, Boeing 747. Source: AIAA Paper No 72-188
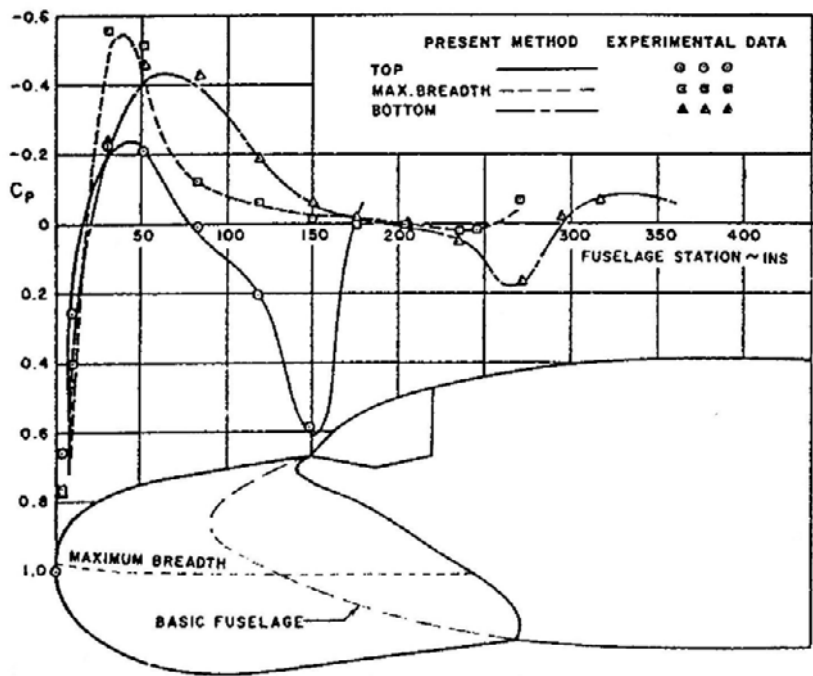
Figure 12.7 - Comparison of calculated and experimental pressure distributions on a C-135 fuselage with a large radome at zero angle of attack. Source: Canadian Aeronautics and Space Journal, Febr. 1970
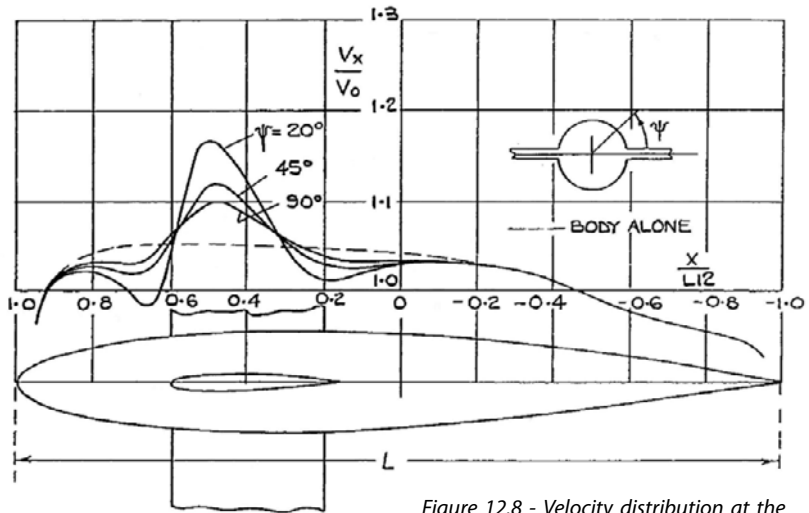
Figure 12.8 - Velocity distribution at the body of a wing fuselage combination. Source: RAE Report No Aero 2219, 1947
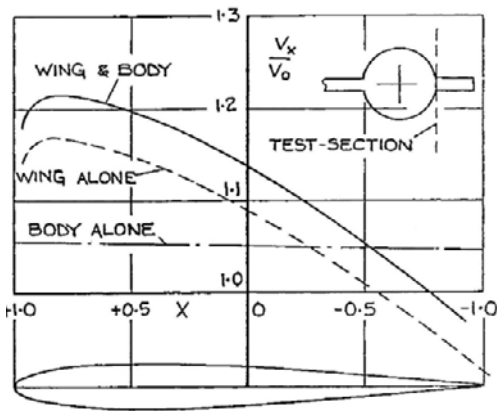
Figure 12.9 - Velocity distribution at the wing root of a wing fuselage combination, t/c = 0.1. Source: RAE Report No Aero 2219, 1947
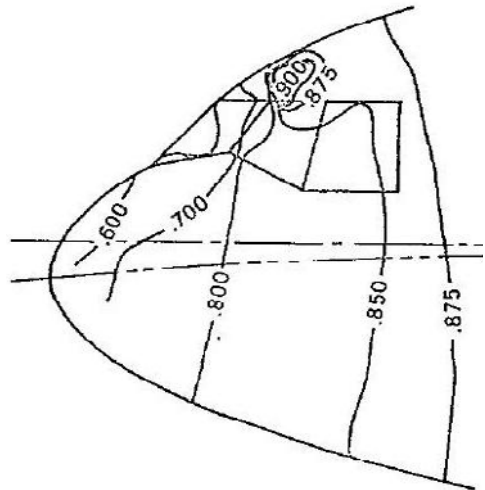
Figure 12.10 - Mach number distribution on fuselage nose, McDonnell-Douglas DC-10, M = 0.85
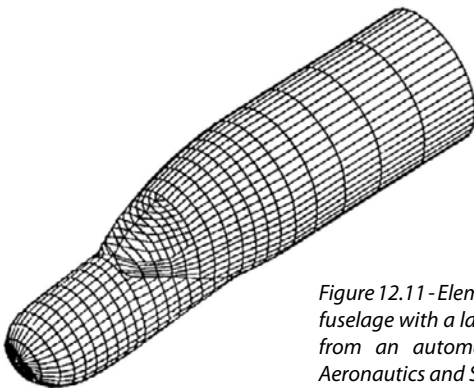
Figure 12.11 - Elements used to approximate a C-135 fuselage with a large radome (unretouched output from an automatic plotter). Source: Canadian Aeronautics and Space Journal, Febr. 1970

Components not required to generate aerodynamic forces

A number of aircraft components are not intended to generate aerodynamic forces. On these components local supervelocities should be minimized. Such components are:

- Front fuselage including cockpit canopies
- Centre and rear fuselage sections
- Engine struts and pylons
- Fins in cruise flight
- Tailplane-fin fairings
  etc.

Figures 12.7 to 12.16 present pressure distributions on various front and centre fuselages.

In figure 12.10 the pressure distribution over a cockpit is shown, expressed as a local Mach number distribution. Due to the convex shape the area over the cockpit windows shows an increase in local Mach number up to velocities close to the supersonic regime.
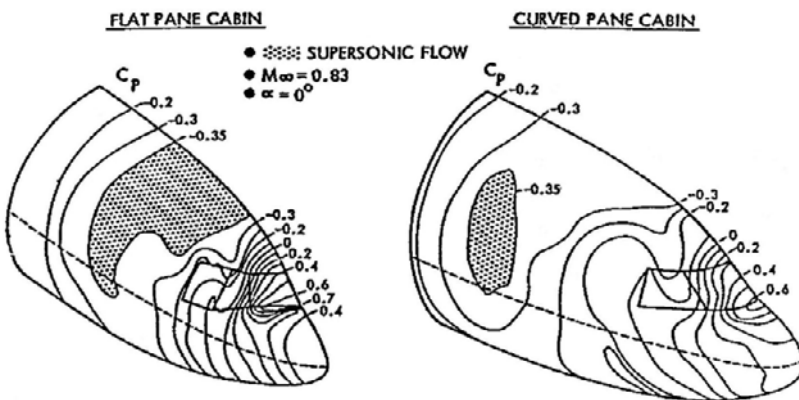
Figure 12.12 - Potential flow - pilot cabin evaluation, Boeing. Source: AGARD LS-67, Paper 4

Using Computational Fluid Dynamics (CFD) calculations, local supervelocities can be analysed and improvements could be made to minimise these. For example the shape of the cockpit, as illustrated in figure 12.12, can be altered to reduce the size of areas with supersonic flow, resulting in less drag and cockpit noise.

Figure 12.13 illustrates the need for numerical methods to predict local supervelocities accurately. Sonic airspeeds are nearly reached. Also figure 12.14 shows the difference in calculated and measured pressure distribution, illustrating the need for correct calculation methods. Especially regions with supersonic flow are of importance, as these regions will highly influence drag.
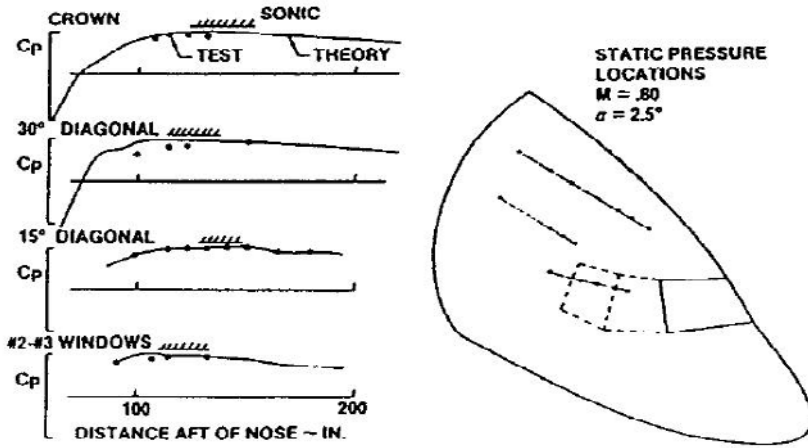
Figure 12.13 - Comparison of analysis and test for cab. Source: ICAS 1982 Paper 5.7.2.
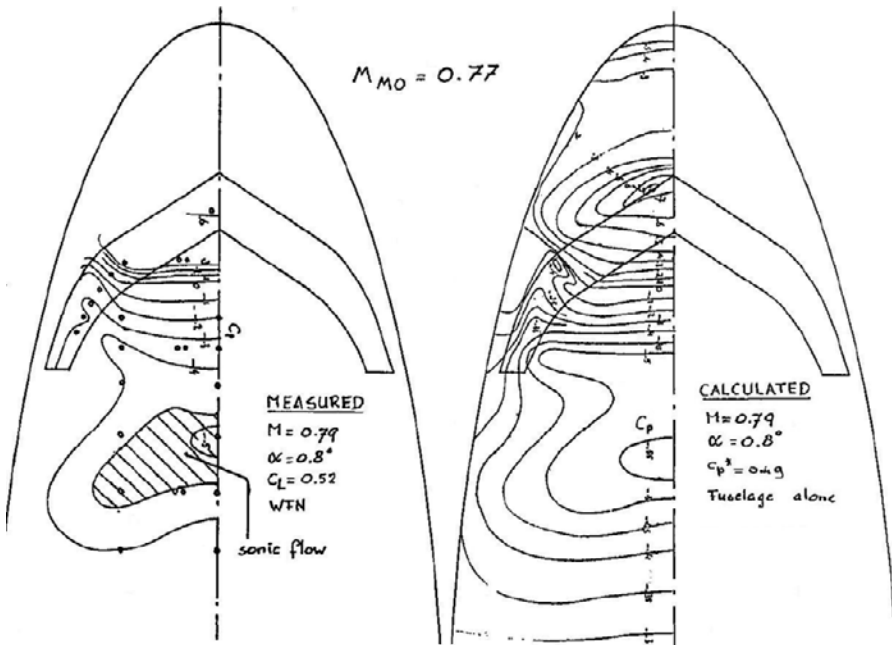
Figure 12.14 - Comparison between measured and calculated isobar pattern on cockpit.
Source: Fokker Report L-29-135

Besides reducing sections with local supersonic flow, also momentum thickness can be controlled in the design phase. A more or less continuous momentum thickness distribution will result in lower drag than with large variations. This is illustrated in figure 12.15.

Using CFD calculations, more can be done to improve the drag characteristics of the aircraft. In figure 12.17 the outer flow velocity vectors are shown on the front fuselage of the Boeing 757. Being able to predict these vectors, designers can design a rain protector (rain guide) above the cabin door in the direction of the flow. If this guide is not parallel to the local flow direction the flow may separate and increase drag. An example of such a rain guide is shown in figure 12.16.

Figure 12.15 - Effect of cab fairing on the boundary layer momentum thickness of a Boeing 737. Source: AGARD LS-67 Paper 4
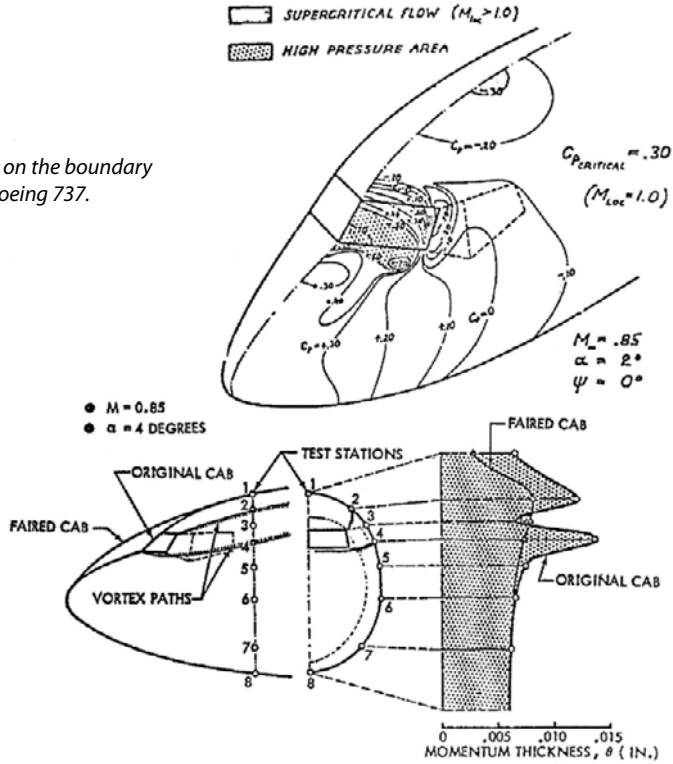
Figure 12.16 - Picture of rain guides on a Boeing 777. Source: Justin Koning
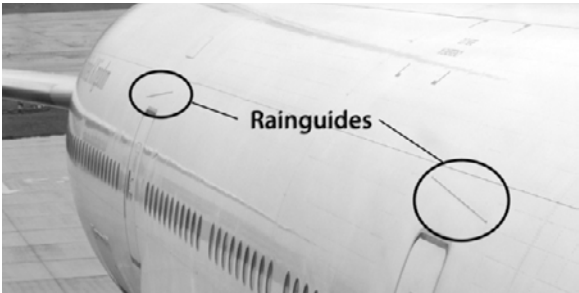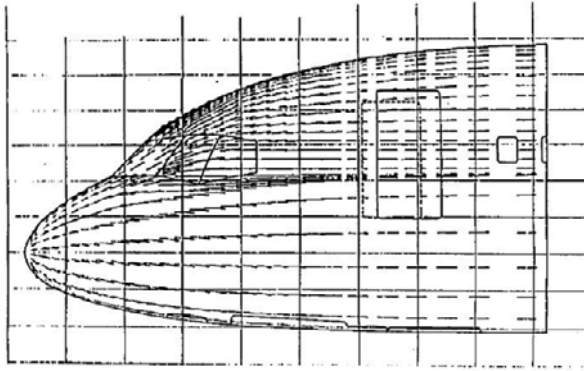
Figure 12.17 - Outer flow velocity vectors. M = 0.80, α = 2.5°. Source: AIAA 83-2060

When wing and fuselage are considered together, supervelocities of the individual components are added. Before CFD came in general use this effect was called an interference effect. The lift over the wing, for example, is increased due to the presence of the fuselage, as can be seen in figure 12.18 (section 1). Further illustrations of this effect are presented in figures 12.19, 12.20 and 12.21. The panel distribution used to calculate the pressure distribution of this aircraft is shown in figure 12.20.
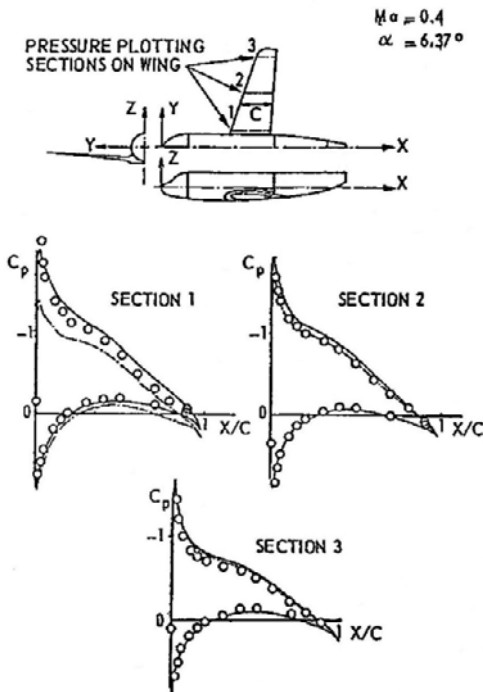
Figure 12.18 - Wing pressure distributions for a typical, short range, subsonic transport configuration. Source: AGARD CP-71, paper no. 11
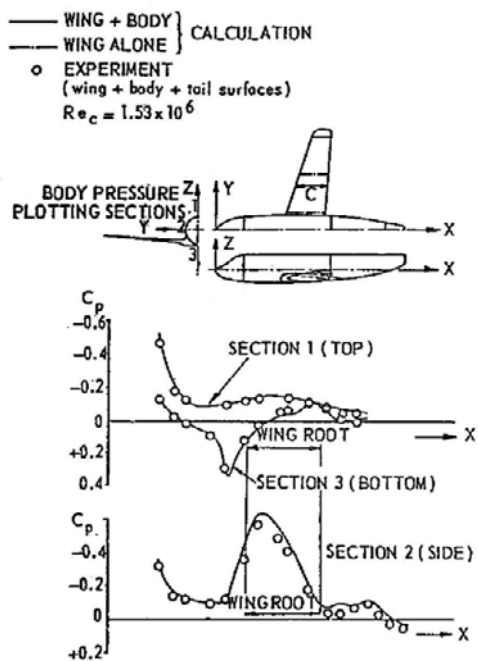
Figure 12.19 - Body pressures for a typical, short range, subsonic transport configuration. Source: AGARD CP-71, paper no. 11
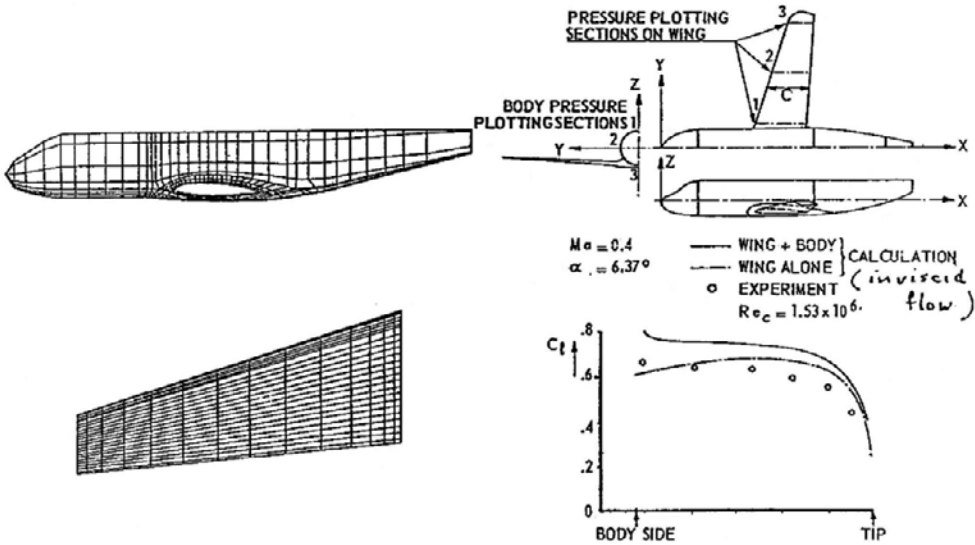
Figure 12.20 - Panel arrangement for a typical short range, subsonic transport configuration.
Source: AGARD CP-71, paper no. 11

Figure 12.21 - Spanwise lift distribution for a typical short range, subsonic transport configuration.
Source: AGARD CP-71, paper no. 11

Adding the supervelocities of the fuselage to those of the wing alters the variation of the local lift coefficient over the wing span. The lift is increased due to the presence of the fuselage. Also noticeable is the difference between experimental data and calculations, which is due to the calculations having been performed for inviscid flow, whereas the experiments concern viscous flow.

When comparing data from calculations and experiments, the differences found can be reduced by adding both thickness as well as viscosity effects. If only one of these two is applied, the result in lift will not be consistent with results found from experiments.

Another example of the superposition of supervelocities when a wing is fitted on a fuselage is presented in figures 12.8 and 12.9. The unfavourable summation of supervelocities causes interference drag. In the design process shapes should therefore be pursued such that a proper interposition of the various components leads to a favourable summation of supervelocities. This means that if one component has a negative pressure coefficient, the intersecting component should at that location have a low negative or even positive C_P.

This can be done by local shape modifications but in some cases this may not be sufficient. At the tailplane-fin interaction for example a "waisted" body may be necessary such as on the Tupolev Tu-154, see figure 12.22.

Figure 12.22 - Tupolev 154. Source: Biel Gomila

In figures 12.23 to 12.25 some results of design activities on the Douglas DC-10 are presented. Studies were performed on reducing the peak pressure coefficients between the fuselage and centre nacelle at the fuselage aft-end. The original configuration showed supersonic flow and the associated drag due to shock waves. In the final configuration, this has been reduced considerably.
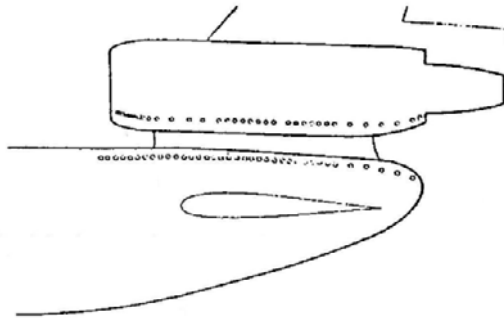
Figure 12.23 - Pressure survey locations. Source: AIAA Paper No 69-830
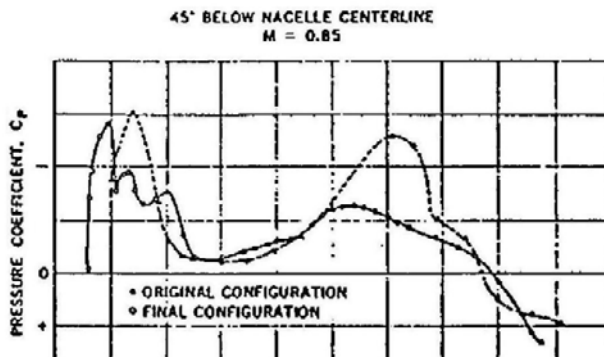
Figure 12.24 - Aft-nacelle pressure distribution of a McDonnell Douglas DC-10. Source: AIAA Paper No 69-830

M = 0.85
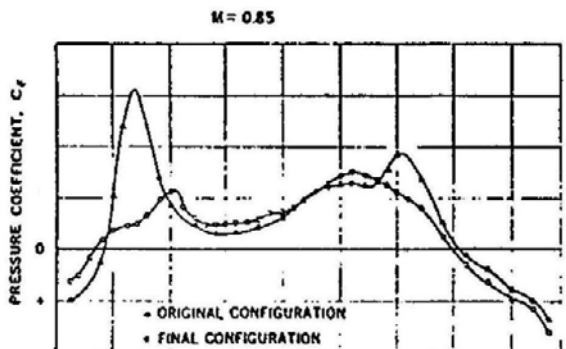
Figure 12.25 - Fuselage aft-end pressure distribution of a McDonnell Douglas DC-10. Source: AIAA Paper No 69-830

In figures 12.26 to 12.28 the unexpectedly high drag that was found during flight tests on the Douglas DC-8 are analysed. This high drag occurred at cruise Mach numbers and was not found in the wind tunnel tests (see figure 12.27). This was due to the unfavourable channel flow between the wing and the nacelles which in flight showed a stronger supersonic flow and shock waves than in the wind tunnel tests. Figure 12.26 shows that in the wind tunnel tests a maximum local Mach number $M_{local} = 1.16$ was found whereas the flight tests showed a maximum Mach number $M_{local} = 1.28$. On the DC-8 up to the 50 Series the drag was reduced to an acceptable level by modifying the wing leading edge.
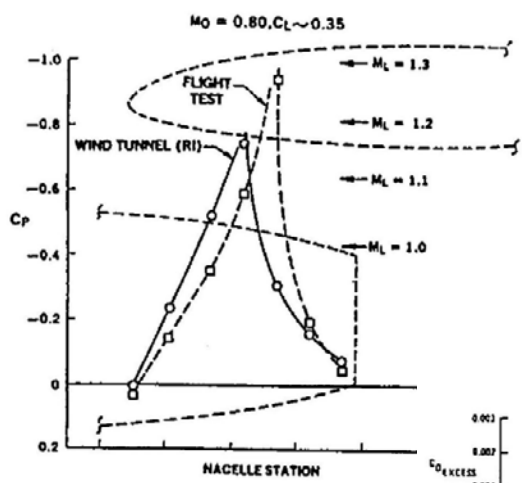
Figure 12.26 - Comparison of wind tunnel and flight pressure distribution for DC-8 prototype long duct nacelle installation. Source: Douglas Paper No 7026
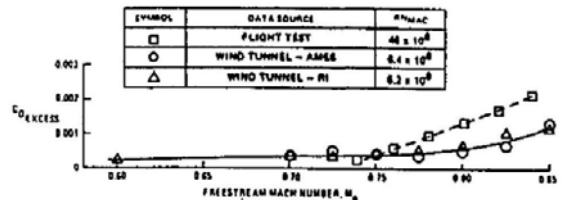
Figure 12.27 - Interference drag of DC-8 prototype long duct nacelle installation. Source: Douglas Paper No 7026
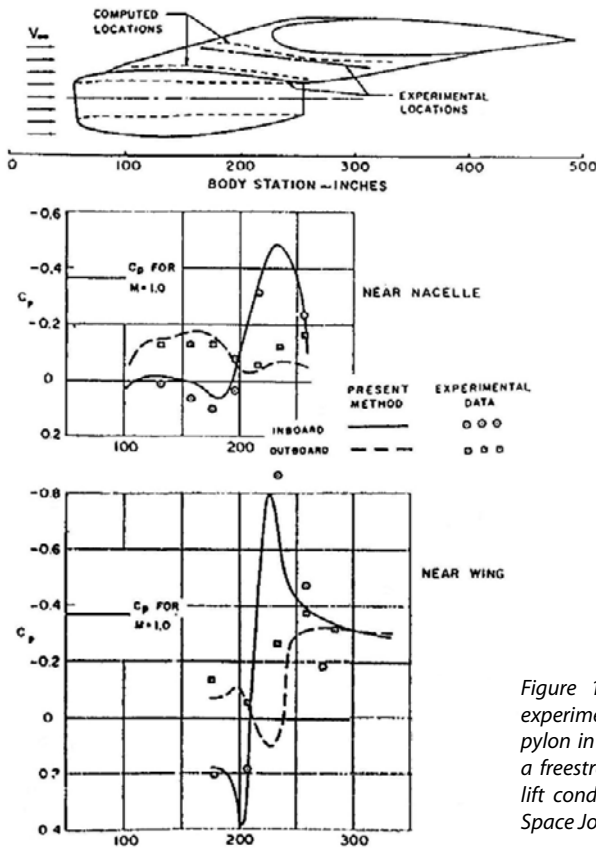
Figure 12.28 - Comparison of calculated and experimental pressure distributions on a DC-8 pylon in the proximity of the nacelle and wing at a freestream Mach number of 0.825 for the zero-lift condition. Source: Canadian Aeronautics and Space Journal, Febr. 1970

The DC-8 was not the only first-generation jet transport aircraft having initially a disappointing drag level. The Convair 990 went through an extensive drag reduction programme.

Figures 12.29 to 12.33 present some data on a number of modifications which Convair investigated in order to reduce drag, as well as the effect this had on the drag coefficient, see figure 12.33. Note that one drag count is $\Delta C_D = 0.0001$.

Wing-pylon-nacelle integration offers a real challenge in minimising interference drag. The nacelle must be positioned at a certain distance (in longitudinal and vertical sense) away from the wing as shown in figure 12.34. This relation is based on a history of wind tunnel test data.

Using CFD techniques, it has become possible to move the nacelle closer to the wing, even to previously thought-to-be unacceptable positions as shown in figure 12.35.
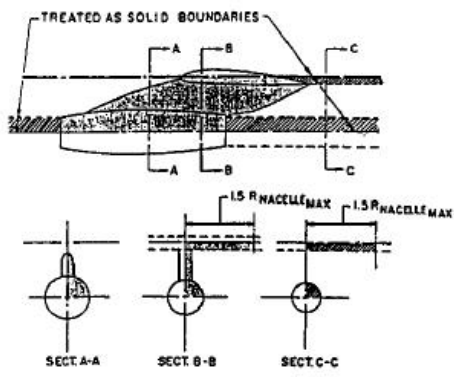
Figure 12.29 - Initial area distribution boundaries applied to each side of each nacelle. Source: Journal of Aircraft, Jan-Febr 1964
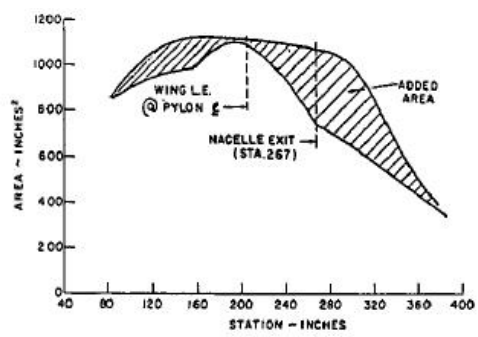
Figure 12.30 - Illustration of concept of desired distribution modification. Source: Journal of Aircraft, Jan-Febr 1964
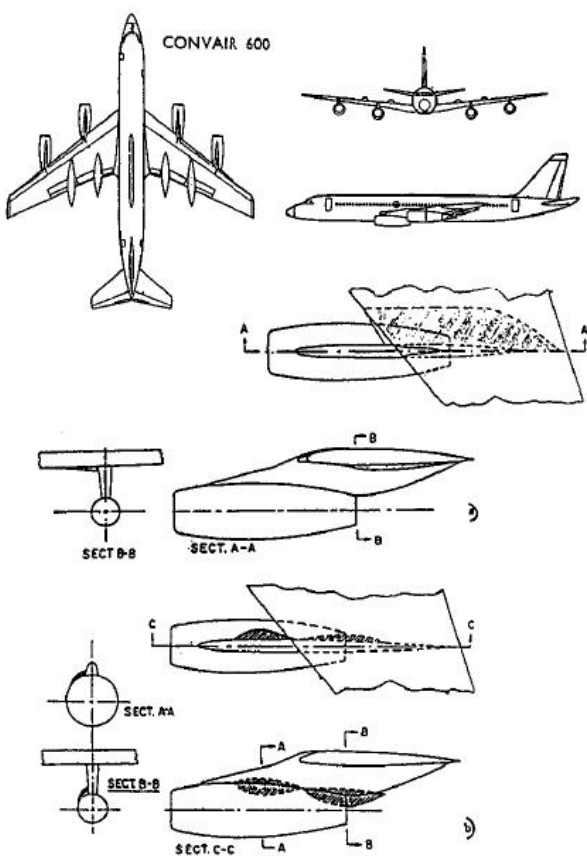
Figure 12.31 - a) Wing leading edge and lower surface fairing concept, b) Nacelle fairing concept. Source: Journal of Aircraft, Jan-Febr 1964
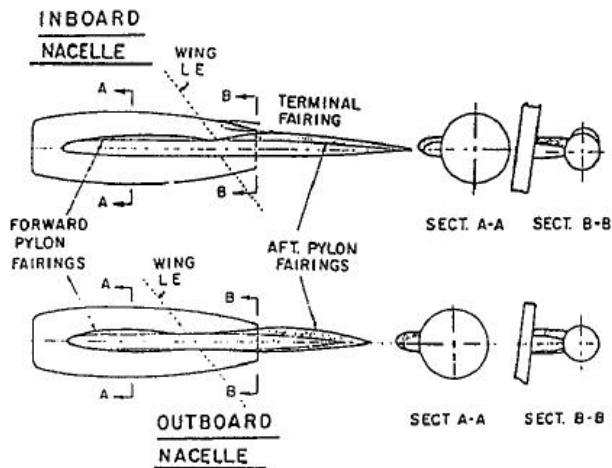
*Figure 12.32 - Illustration of most effective configuration
modification. Source: Journal of Aircraft, Jan-Febr 1964*
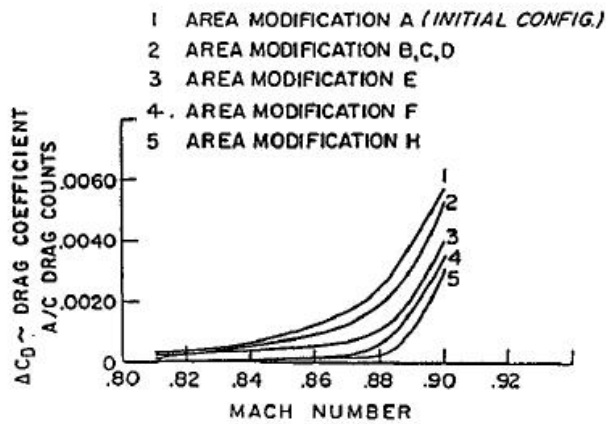
*Figure 12.33 - Effect of distribution modifications.
Source: Journal of Aircraft, Jan-Febr 1964*
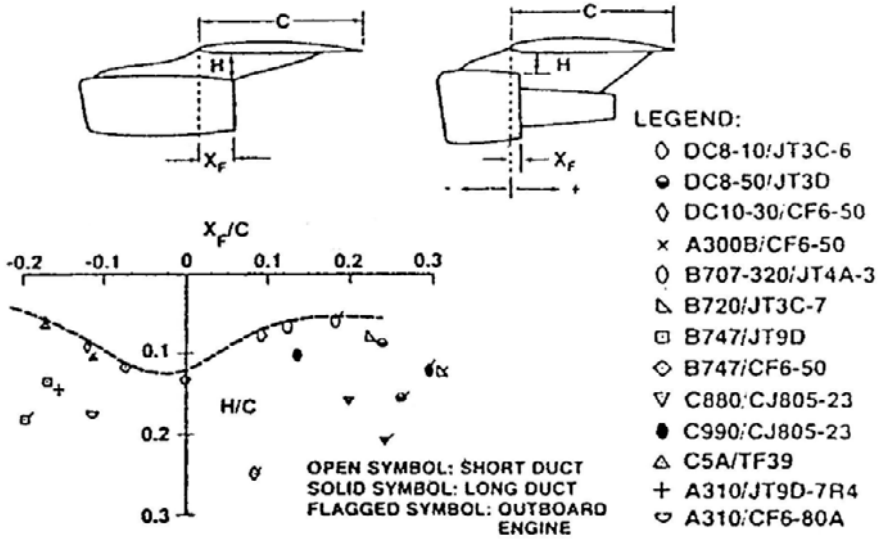
Figure 12.34 - Baseline via wind tunnel test methodology. Source: AIAA Paper No 83-2060
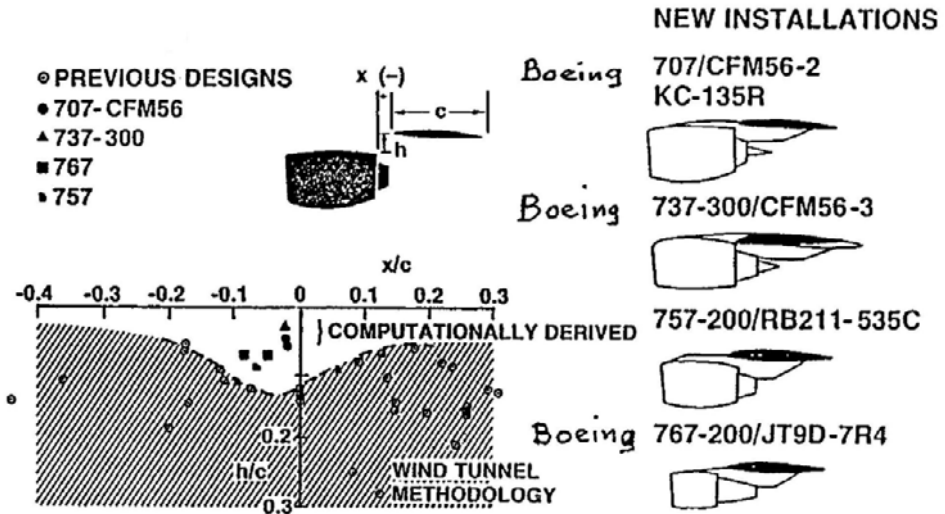
Figure 12.35 - Computationally derived close-coupled nacelle positions. Source: AIAA Paper No 83-2060

Small improvements in aerodynamic quality in order to lower the drag on aircraft in production is an ongoing process with most aircraft manufacturers. When further development within a programme takes place a considerable reduction in drag is sometime realised. When the upper deck of the Boeing 747 was extended the cross-sectional area distribution according to the transonic area rule was improved. This improved the drag rise Mach number as is shown in figures 12.36 and 12.37.
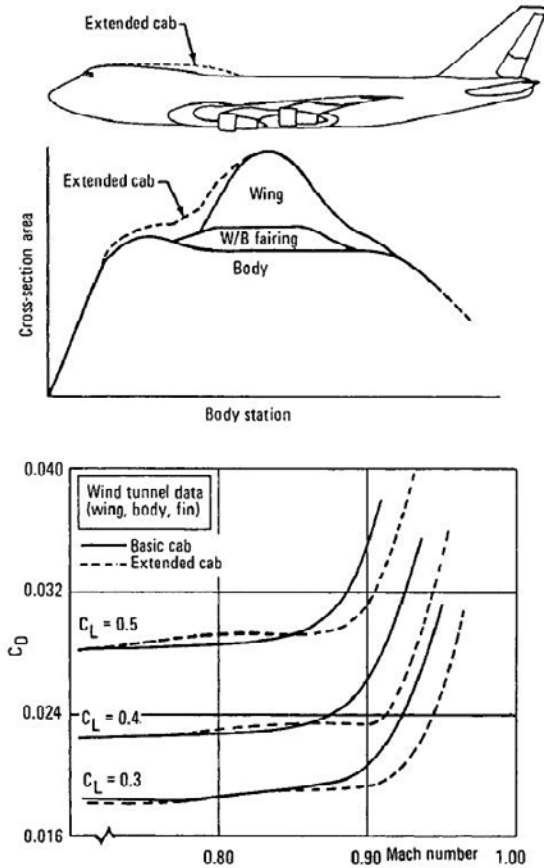
Figure 12.36 - Boeing 747 cab extension, subsonic area ruling. Source: Aeronautics and Astronautics, Dec. 1973

Swissair Orders Improved 747 Version

Seattle - Swissair has kicked off Boeing's latest improved 747 version with an order for five of the wide-body transports with a strechted upper deck and improved engines (AW&ST Apr. 28, p. 24).

The Swiss carrier ordered 747 versions with the upper deck stretched 280 in. to allow it to carry 56 economy passengers, although the area can seat as many as 69. It also ordered the aircraft equipped with the 54,750-lb. thrust Pratt & Whitney JT9D-7R4G-2 engine, a variation of the more fuel-efficient JT9D series used to power some of Boeing's new 767 transports.

Shaded area indicates stretched upper deck area in new Boeing 747 transport offering.
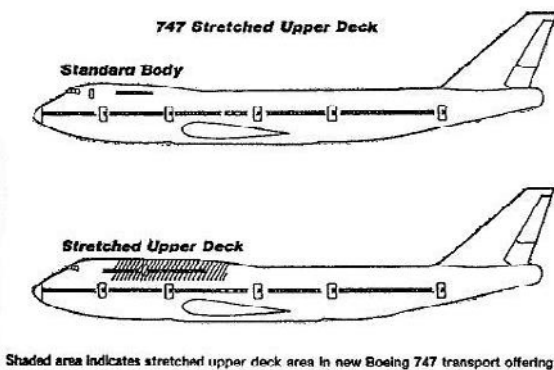
Figure 12.37 - Boeing 747-200 and 747-300. Source: Aviation Week & Space Technology, June 16, 1980

In the 70's interest in minimising drag received a new impulse because of the first oil crisis.

One area which received renewed attention was rear fuselage drag. The effect of rear-fuselage upsweep on drag is shown in figures 12.38 and 12.39. This is why, for example, the Boeing 767 has little upsweep in the rear fuselage (see figures 12.40 and 12.41).
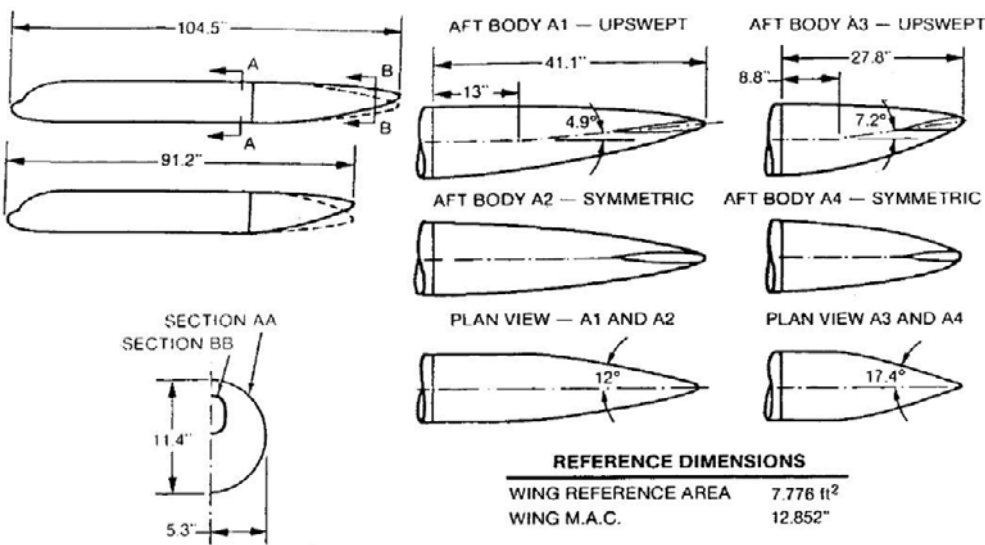
Figure 12.38 - Model geometry and reference dimensions. Source: AIAA Paper No 84-0614

C_D drag coefficient, based on free stream dynamic pressure and a model reference area of 7.776 ft^2

C_{Dp} coefficient of profile drag

C_{Dv} coefficient of vortex drag
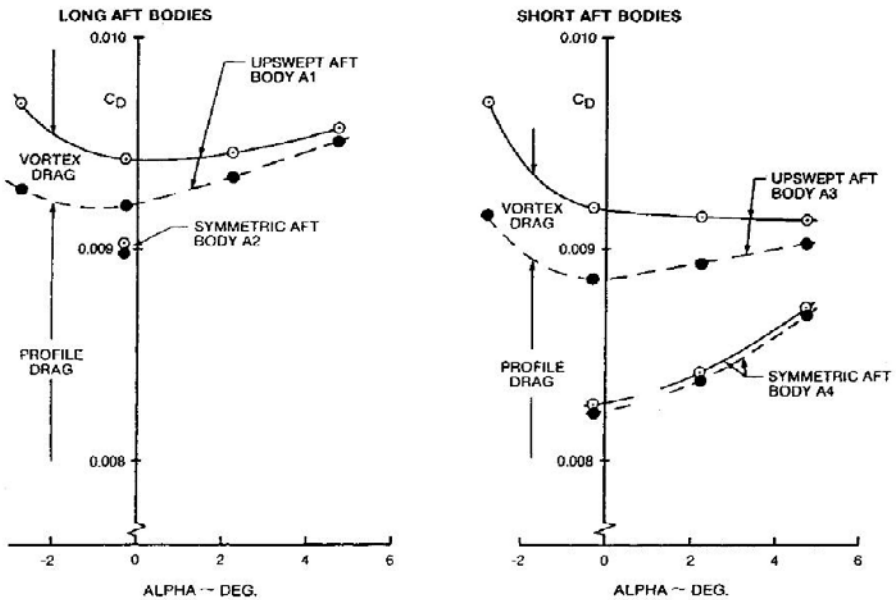
Figure 12.39 - Profile and vortex drag from wake measurements. Source: AIAA Paper No 84-0614
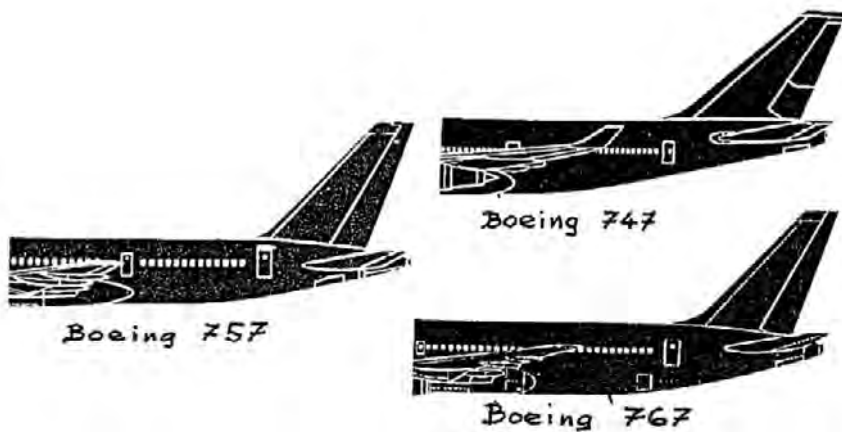
Figure 12.40 - Shape of aft-fuselage of Boeing 747, 757 and 767. Source: AIAA Paper No 84-0614

Comparison of Drag Measurements With Predictions

The figure below shows the effect of aft body length on the measured and predicted drag of the complete body. The results are presented at α = -0.25 degrees, where body profile drag is near minimum.
Wake survey measurements for the symmetric aft bodies A2 and A4 are compared to predictions made using ESDU Data Sheet No. 78019, which is based on boundary layer calculations made for bodies of revolution with attached flow. Agreement with the wake survey measurements is excellent, within about 2 percent.

Aft body slenderness ratio = aft-body-length / maximum-diameter ratio.
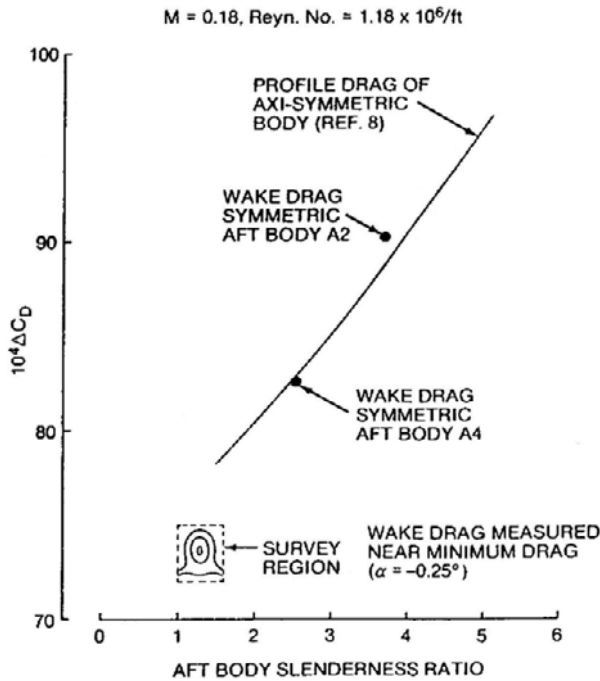
Figure 12.41 - Comparison of predicted profile drag of symmetric bodies with wake survey measurements. Source: AIAA Paper No 84-0614

13 Pressure distributions on components which are required to generate aerodynamic forces

Aerodynamic forces are required to be generated by:

- Wing
- Stabilizer (horizontal tailplane)
- Fin (vertical tailplane)
- Control surfaces (elevator, ailerons, rudder, spoiler panels, speed brakes)

Lift-producing surfaces should have the following characteristics, at an acceptable weight, wetted area and internal volume:

1. An as high as possible lift-curve gradient (C_L vs α)
2. An as high as possible maximum lift coefficient
3. An as low as possible drag
4. An as high as possible angle-of-attack where flow separation occurs.

For different lifting surfaces the order of importance of these points is not identical (for example: for a fin the C_{Lmax} has the lowest priority but not so for a wing).

14 *Pressure distributions on wings*

In this chapter some general design considerations for the pressure distribution on wings designed for transonic flight conditions (the focus of this book is on this kind of aircraft) are given.

In defining the wing shape the following aerodynamic parameters have to be taken into consideration:

1. In cruising flight:
 • C_L
 • C_D
 • drag creep

2. Around the boundaries of cruise flight conditions:
 • buffet boundary
 • maximum buffet penetration
 • stability and control above buffet onset (both pitch and roll)
 • margin between M_{MO} and M_D
 • stability and control between M_{MO} and M_D

3. At low speeds:
 • $C_{L_{max}}$ for all aircraft configurations
 • stalling characteristics for all aircraft configurations over the complete C.G. range (both pitch and roll)
 • lift/drag ratio at one-engine-out initial climb speed $(L/D)_{V2}$

4. For structural and trim drag reasons:
 • section zero-lift pitching moment distribution along the span (C_{m_0} versus C_l or for cruise conditions C_m versus C_l)
 • C_{m_0} or C_m at $C_{L_{cruise}}$ for the aircraft-less-tail.

The prime characteristics defining the wing design are:

 a. M_{design} and $C_{L_{design}}$ (the latter due to wing loading W/S and cruise altitude)
 b. Aspect ratio (A), sweep angle (Λ) and the basic airfoil section in the outboard wing.

Defining these characteristics is of most importance for the outboard wing, because when minimum induced drag is pursued, then the spanwise lift distribution (C_l x chord versus wing span) has to be elliptical. Consequently, on a tapered wing, $C_{l_{max}}$ is found at 60-70% of the semi-span. This is then the section with the most severe design requirements (see also chapter 23).

PART 3

AIRFOILS

15 *The pressure distribution on airfoil sections*

The pressure distribution on an airfoil section has the following characteristics:

1. A stagnation point at or near the leading edge ($C_P \geq 1$)
2. The magnitude and location of the maximum super velocity ($C_{P_{min}}$)
3. The ratio between $C_{P_{min}}$ and the pressure coefficient for $M_{local} = 1$ (C_P^* or $C_{P_{crit}}$)
4. The pressure gradient behind the point where $C_P = C_{P_{min}}$, i.e. in the recompression region
5. The trailing edge pressure. In non-viscous flow $C_{P_{TE}} \geq 1$ (a stagnation point). The pressure coefficient at the trailing edge ($C_{P_{TE}}$) ranges between 0.1 and 0.3, depending on Re-number in real attached flow and $C_{P_{TE}} < 0$ when flow separation occurs at the trailing edge. In the latter case often a region with constant C_P will exist.

To be able to determine the overall characteristics of the pressure distribution over an airfoil section, characteristics of the boundary layer have to be considered, which are the displacement thickness δ^*, the momentum thickness θ and the local friction coefficient C_f.

To illustrate the characteristics mentioned above, figures 15.1 to 15.8 give examples of pressure distributions and their characteristics. They show the effects of varying features of the airfoil (airfoil thickness, angle-of-attack and Reynolds number).

Figures 15.1 to 15.4 show the pressure distributions for the NACA 0006 airfoil (symmetric airfoil, maximum thickness is 6% of the chord), whereas figures 15.5 to 15.8 show the same, but now for the NACA 0018 airfoil (symmetric, 18% max t/c). Then, figures 15.1 and 15.2 as well as 15.5 and 15.6 present the figures for a Reynolds number of $2 \cdot 10^6$, whereas figures 15.3, 15.4, 15.7 and 15.8 display this for a Reynolds number of $20 \cdot 10^6$. Finally, on each page, the pressure distributions are shown for both an angle of attack of 0 and 6 degrees.
All pressure distributions shown were calculated at a low Mach number.

Note the following when comparing the pressure distributions:

1. At $C_l = 0$ ($\alpha = 0$) C_{Pmin} is proportional to the sections relative thickness.
2. With increasing α, the leading edge suction peak increases much faster and is followed by a much stronger adverse pressure gradient for the airfoil section with the small leading edge radius than for the section with the large leading edge radius.
3. On the thick section, boundary layer effects are much stronger than on the thin section and flow separation ($C_f = 0$) is approached much quicker.
4. Increasing Reynolds-number causes boundary layer effects to decrease (higher C_l vs α, lower drag, less de-cambering effects).
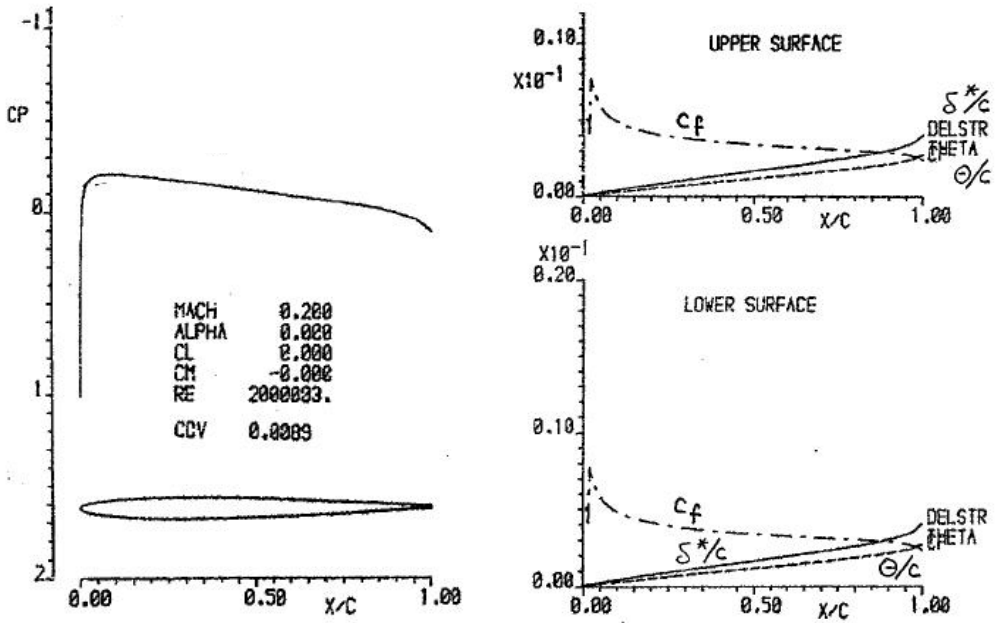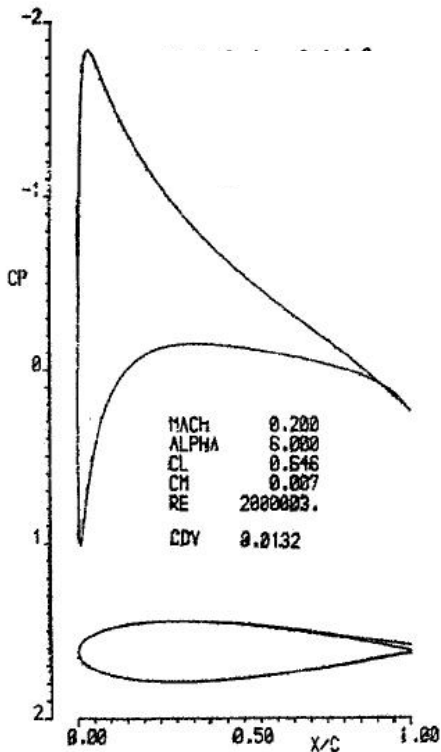
Figure 15.1 - Pressure distribution for NACA 0006 airfoil section at $\alpha = 0^o$ and Re = $2 \cdot 10^6$
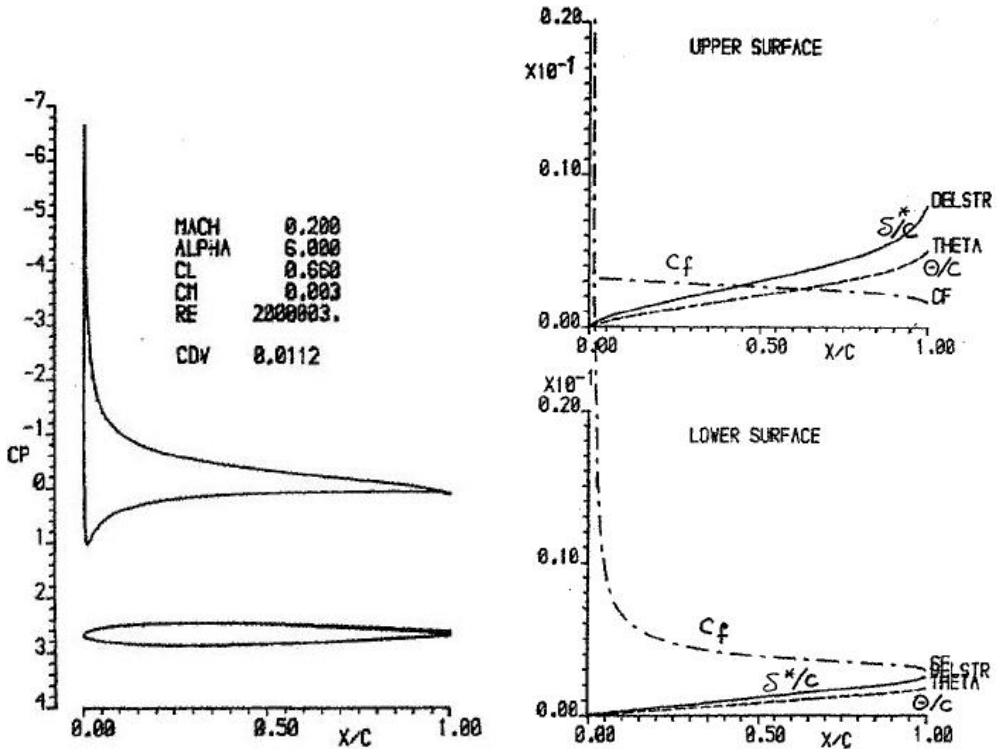
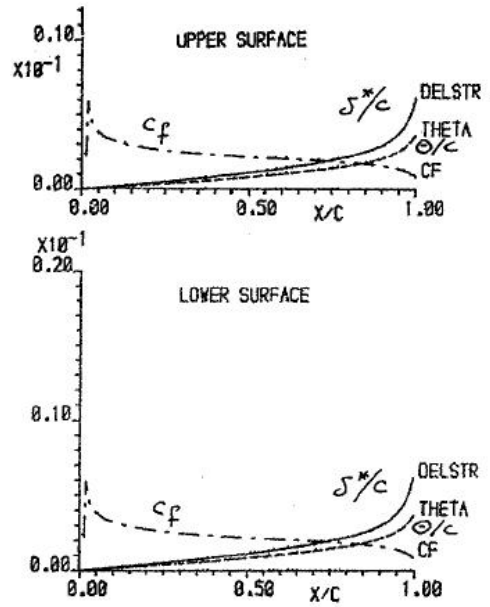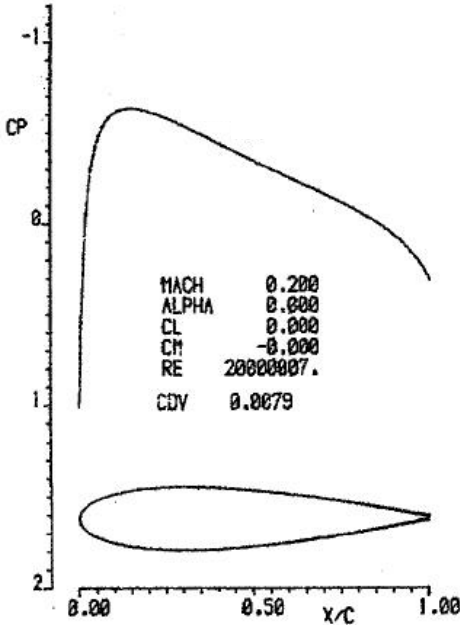Figure 15.2 - Pressure distribution for NACA 0006 airfoil section at $\alpha = 6^o$ and Re = $2 \cdot 10^6$
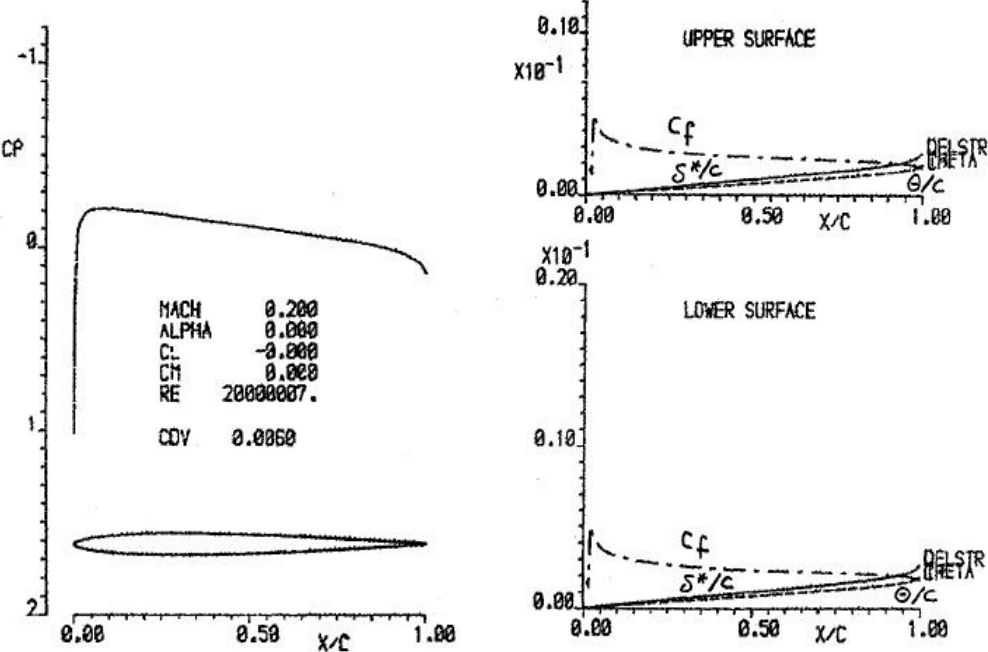
Figure 15.3 - Pressure distribution for NACA 0006 airfoil at α = 0° and Re = 20 · 10⁶
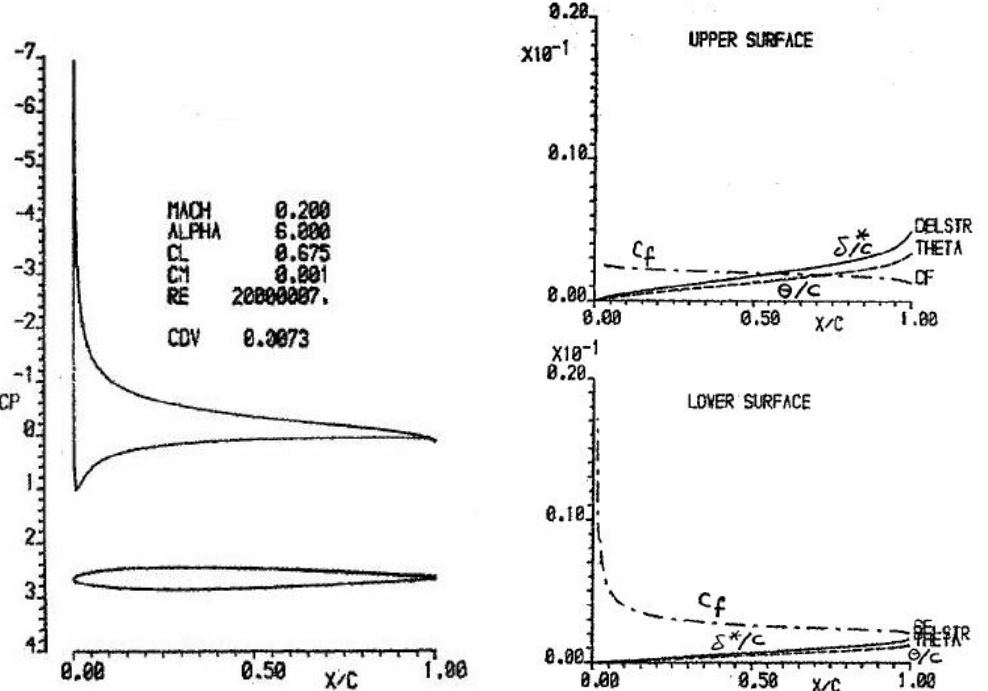
Figure 15.4 - Pressure distribution for NACA 0006 airfoil at α = 6° and Re = 20 · 10⁶
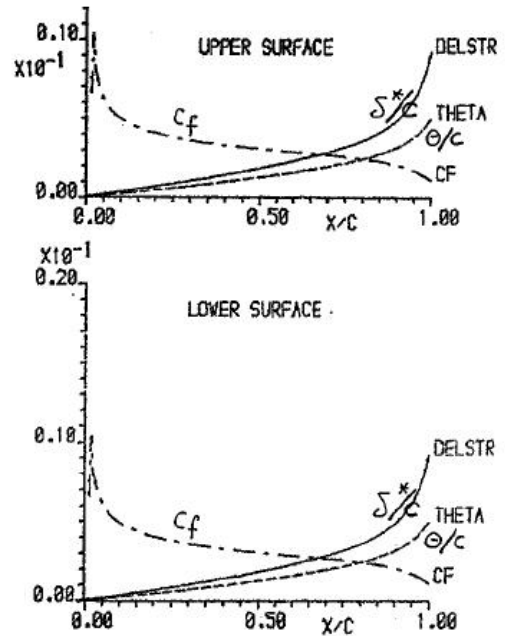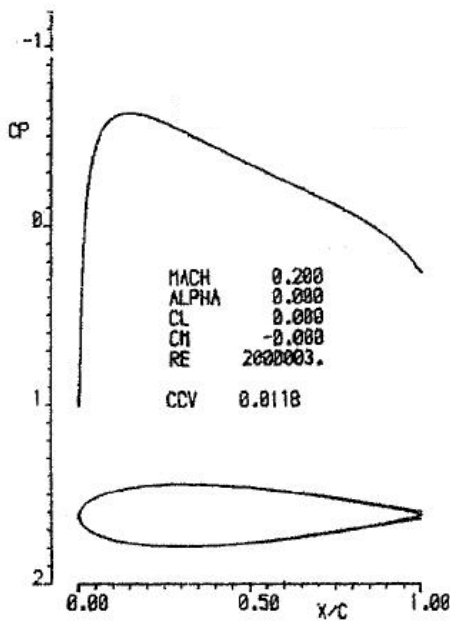
Figure 15.5 - Pressure distribution for NACA 0018 airfoil section at α = 0° and Re = 2·10⁶
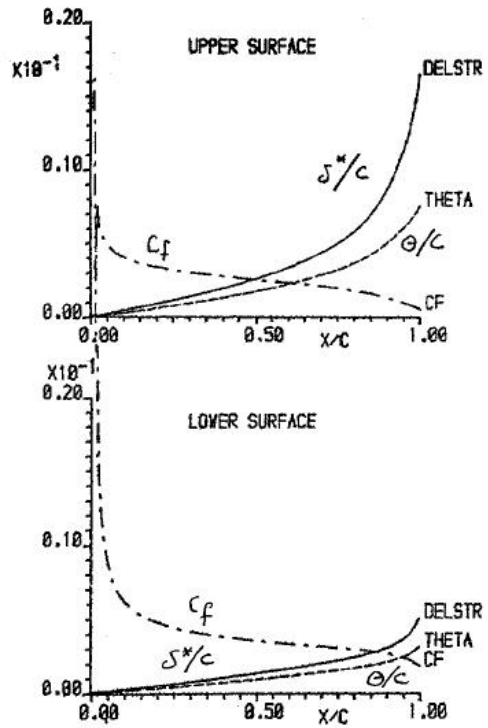
Figure 15.6 - Pressure distribution for NACA 0018 airfoil section at α = 6° and Re = 2·10⁶

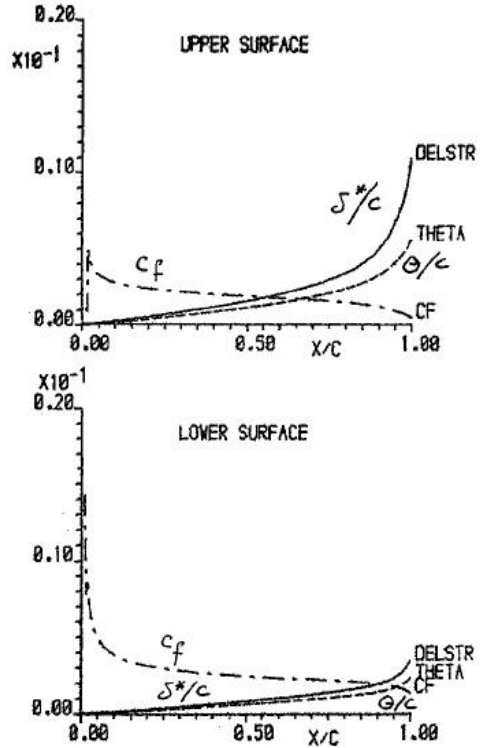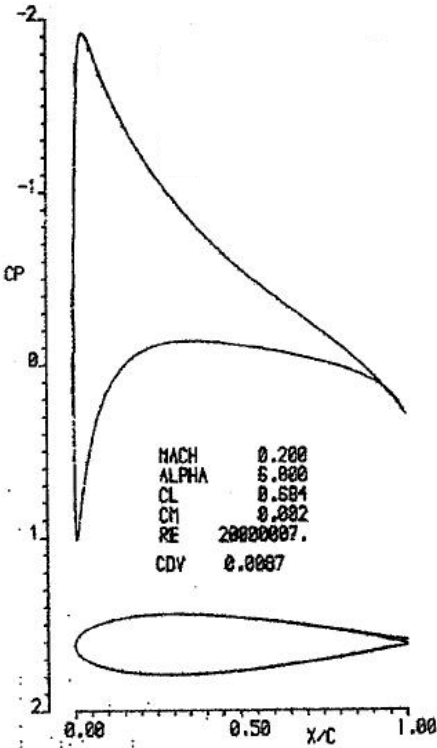Figure 15.7 - Pressure distribution for NACA 0018 airfoil at α = 0° and Re = 20 · 10⁶

Figure 15.8 - Pressure distribution for NACA 0018 airfoil at α = 6° and Re = 20 · 10⁶

If a control surface is deflected, the pressure distribution over that control surface will change. Control surfaces on thick sections with large trailing edge angles often produce unsatisfactory control characteristics, as combined effects of the changing pressure distribution and thickness easily lead to trailing edge flow separation. This can manifest itself even at small control deflections. Figures 15.9 to 15.11 illustrate the change in pressure distribution with changing control deflection and angle-of-attack (α_h).
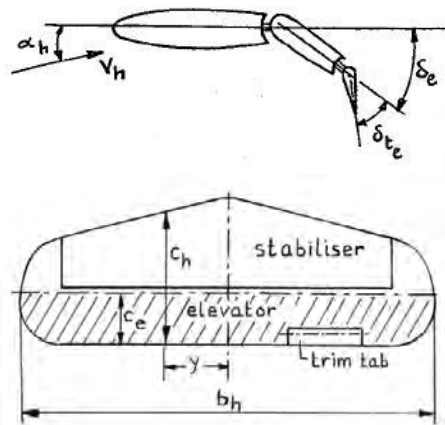

Figure 15.9 - The horizontal tail surface.
Source: Lecture notes Airplane Performance, Delft, 1955 (in Dutch)
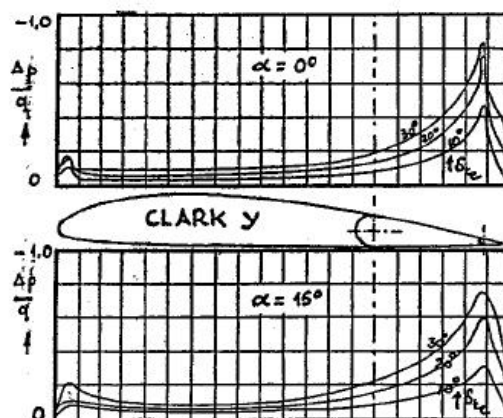

Figure 15.10 - Alteration in chordwise lift distribution caused by trim tab deflection.
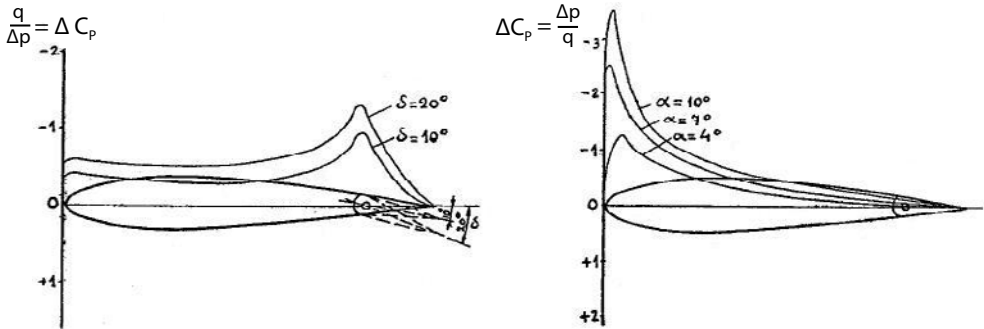Source: Lecture notes Airplane Performance, Delft, 1955 (in Dutch)

Figure 15.11 - Chordwise lift distribution on a tail surface at varying δ (left) and α (right).
Source: Lecture notes Airplane Performance, Delft, 1955 (in Dutch)

To avoid any drag creep due to local supersonic flow at higher Mach numbers up to the cruise condition, but at the same time to obtain an airfoil section with the maximum relative thickness possible, a design pressure distribution on the airfoil upper surface may be selected with a so-called "sonic roof top" shape. The pressure distribution on a sonic roof top airfoil is characterized by a constant (or almost constant on a section of a tapered swept wing) value of $C_p = C_p^*$ from the leading edge up to a point at $x/c = 0.30 – 0.60$ depending on the design Mach number.

Airfoil sections with a sonic roof top pressure distribution in the design cruise condition were developed in the UK in the 60's when the so-called "peaky airfoil sections ", which initially looked promising, showed some unpredictable characteristics, in particular at varying Reynolds numbers.

Sonic roof top sections were applied in the wing design of the BAC – 111 and the Airbus A – 300B. This is illustrated in figure 15.12 and 15.13.
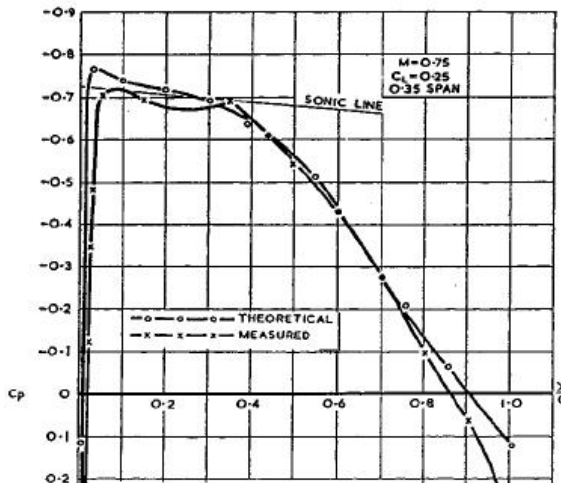

Figure 15.12 - BAC - 111, comparison of theoretical and measured chordwise upper surface distribution on the chosen wing section. Source: Aircraft Engineering, May 1963
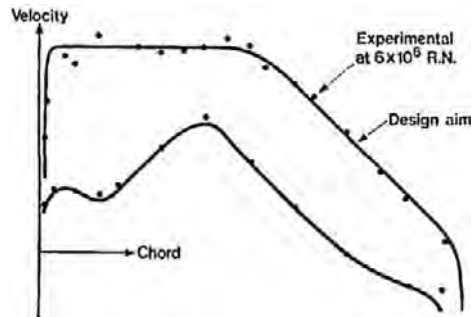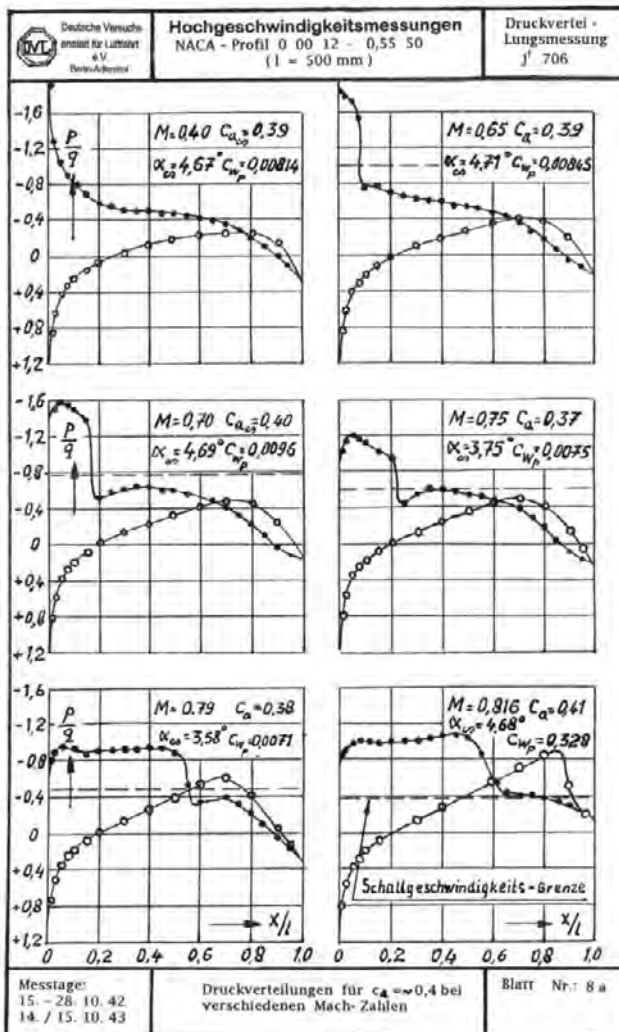
Figure 15.13 - Pressure distribution on the airfoil section at cruise condition applied in the wing design of the Airbus A300B. Source: Aircraft Engineering, October 1969

During the Second World War extensive research was performed in Germany on both airfoil sections and straight and swept wings suitable for very high flying speeds. One family of airfoil sections investigated was the series of Modified Four-Digit sections originally developed before the war by Stack at NACA for high-speed propellers. Test data on one such section is presented in figures 15.14 and 15.15.

Figure 15.14 - Development of the pressure distribution with increasing Mach number on section NACA 00012 - 0.55 - 50 at $C_l \approx 0.40$
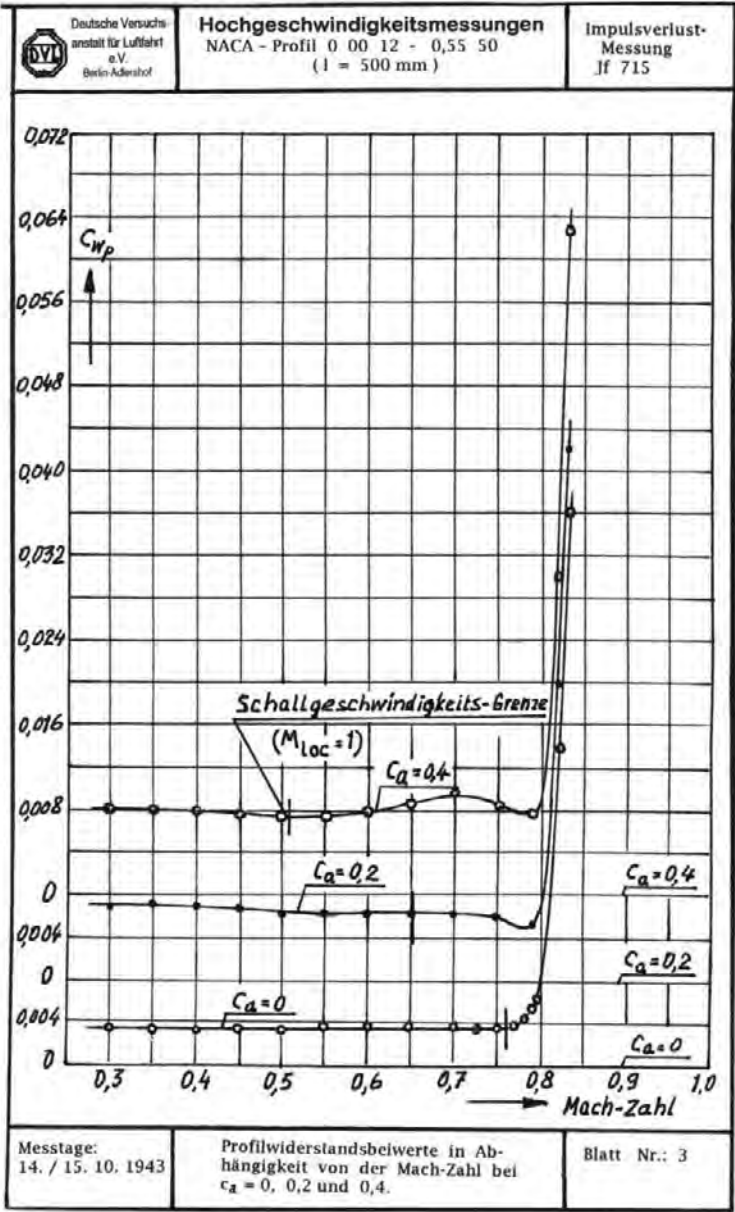Source: UM 1167 (1944), B. Göthert

Figure 15.15 - High-speed drag characteristics of airfoil section NACA 0012 - 0.55 - 50.
Source: UM 1167 (1944), B. Göthert

In the early 40's airfoil section development was concentrated on finding and investigating section shapes with pressure distributions which were favourable for developing a laminar boundary layer. It was thought that the resultant lower drag would lead to better aircraft performance. These developments led to the well-known NACA 6-series airfoil sections.

When aircraft speeds increased and compressibility effects received more attention, it turned out that these laminar flow sections had unfavourable characteristics as soon as the speed of sound was surpassed locally.

These characteristics exist because on laminar sections in the design condition, the supervelocities reach a maximum near mid chord. A small increase in Mach number then produces a sharp increase in supersonic local velocity, resulting in a strong shock wave and flow separation at the foot of the shock. This led to the (wrong) conclusion that the Critical Mach number in terms of flow condition (when locally $M = 1$ is reached) is also the Critical Mach Number for the airfoil section in terms of drag and controllability.

Stack at NACA, and later German researchers, modified some of the standard parameters of the old NACA 4-digit sections such that in sub-critical flow conditions the highest supervelocities were concentrated near the leading-edge (i.e. a "suction peak"), followed by an area with almost constant pressure. They found that locally $M = 1$ was reached at a lower free stream Mach number, but with increasing Mach number a region of supersonic flow developed which was terminated by a (weak) shock without flow separation. In conclusion, although locally $M = 1$ was reached earlier, the Drag Diversion Mach number (the Mach number where drag rises rapidly) was increased in comparison to those of earlier profile sections.

This is very convincingly illustrated in figures 15.14 and 15.15 where at $c_l = 0.4$ locally $M = 1$ is reached at a free-stream Mach number $M = 0.51$ and the sharp drag rise occurs first at $M = 0.78$.

The definitions of the parameters which determine the Modified Four-Digit airfoil sections can be found in Abbott and Doenhoff's "Theory of Wing Sections". The important parameters are leading-edge radius and position of maximum thickness.

In the 50's and 60's Modified Four-Digit sections were applied in a number of aircraft designs such as the Fokker F-28, the Lockheed Viking and the Lockheed C-141. Figure 15.16 shows test data of one of the airfoil sections investigated during the development of the F-28.

The airfoil sections as applied in the wing design of the C-141 are presented in figure 15.17. Lockheed performed an investigation into possible drag improvements for the wing of the C-141.
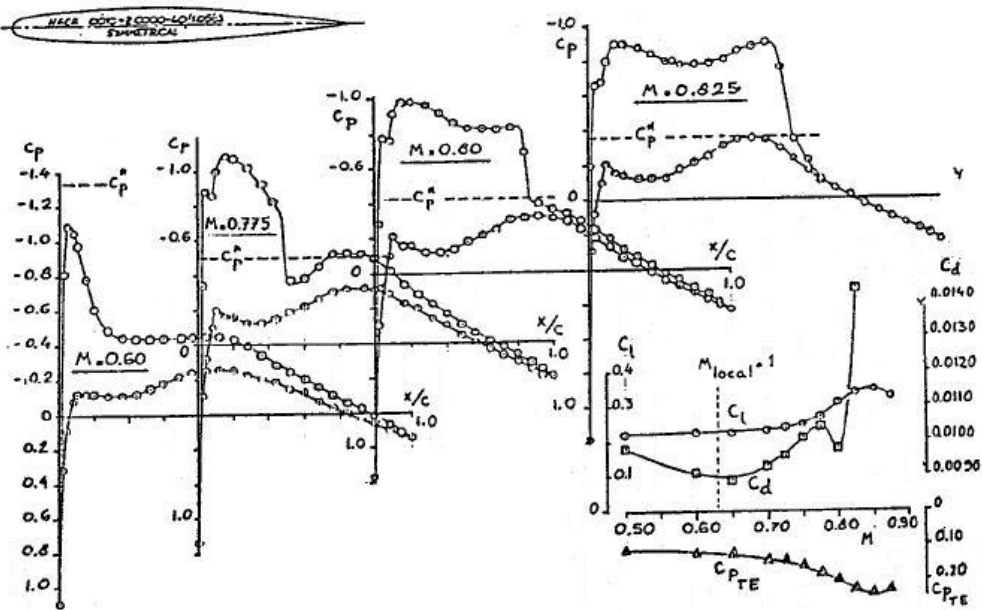
Figure 15.16 - Lift, drag and pressure distribution of NACA 0010 - 2.000 - 40/1.0563 profile at α = 2°

Airfoil section
Root	NACA 0013.0-1.10-40/1.575 (MOD) $α_o$ = 0.8 (MOD) C_{li} = 0.153
Inboard break	NACA 0011.2-1.10-40/1.575 (MOD) $α_o$ = 0.8 (MOD) C_{li} = 0.194
Outboard break	NACA 0011.0-1.10-40/1.575 (MOD) $α_o$ = 0.8 (MOD) C_{li} = 0.201
Tip	NACA 0010.0-2.20-40/1.575 (MOD) mean line 1/2
	(NACA 66 at C_{li} = 1.0- NACA 230 at C_l = 1.0 C_{li} = 0.452)

Incidence, deg
Root	4.89
Construction break	2.25
Tip	-0.69

Dihedral, deg
Inboard of construction break	-0.94
Outboard of construction break	-1.195

Chord lengths, inches
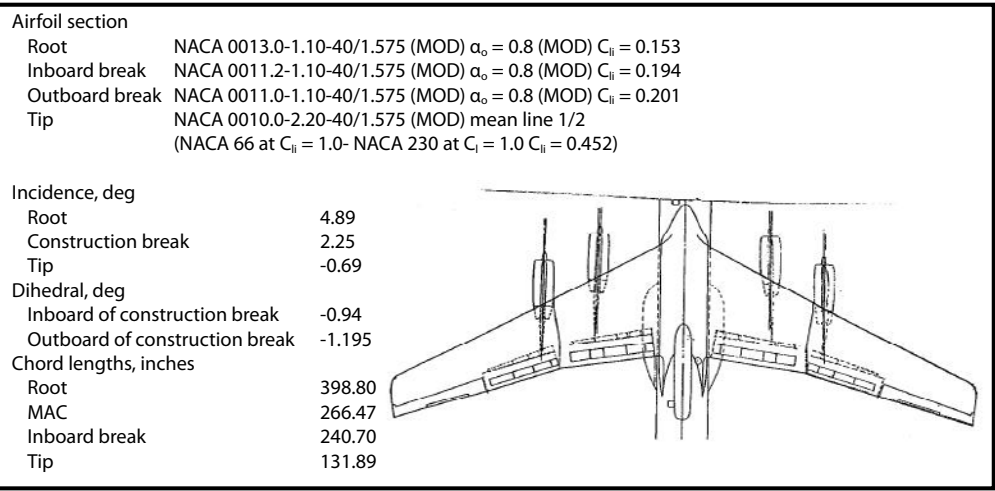|	
Root	398.80
MAC	266.47
Inboard break	240.70
Tip	131.89

Figure 15.17 - Airfoil sections defining the wing of the Lockheed C-141.
Sources: NACA CR-2333 and AIAA Paper No 79-0066

Some results of the drag improvements are presented in figures 15.18 to 15.24. Figure 15.18 shows three different leading-edge shapes that were investigated on a two-dimensional wind tunnel model, the original (base) shape and two modified shapes. Figure 15.19 shows that both modified shapes have better drag divergence characteristics than the original leading edge. This is due to the

partial isentropic recompression on the upper surface behind the leading-edge suction peak and the weaker shock wave (smaller pressure jump) terminating the area of supersonic flow as shown in figure 15.20. Wind tunnel tests on a complete three-dimensional model with both the original and a modified wing leading-edge produced the lift curves, pressure distributions and drag data as shown in figures 15.21, 15.22 and 15.23. Figure 15.24 presents the high-speed drag data for a different (apparently less successful) modification. The improvements in drag may be small but they are not insignificant in particular at the higher lift coefficients.

Note that the geometry modifications presented were obtained in an intuitive way (it was the pre-CFD era) and consequently the whole development process was much a process of trial and error.
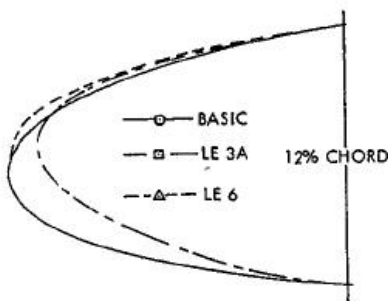

Figure 15.18 - Leading edge shape options of Lockheed C-141. Source: AIAA Paper No. 79-0066
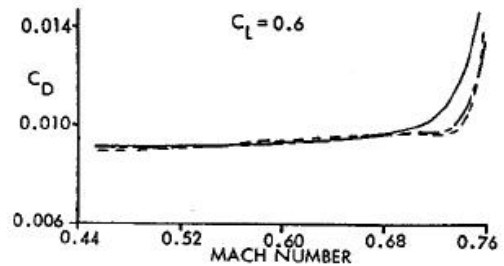

Figure 15.19 - Experimental drag of leading edge modification to C-141 2-D airfoil for drag reduction. Source: AIAA Paper No. 79-0066
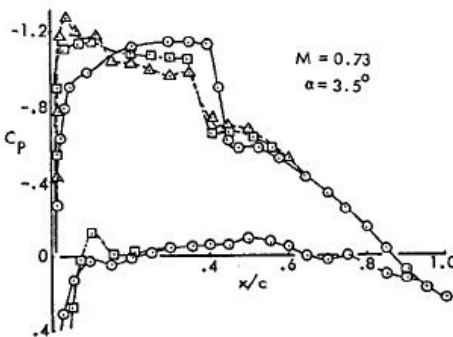

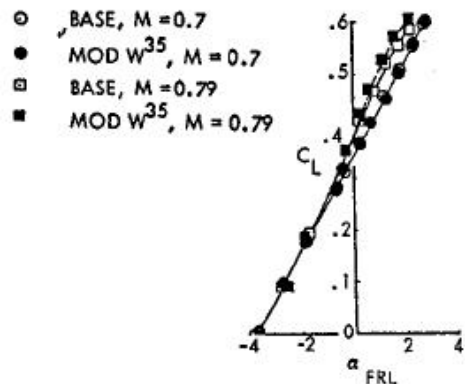Figure 15.20 - Experimental pressure distributions. Source: AIAA Paper No. 79-0066

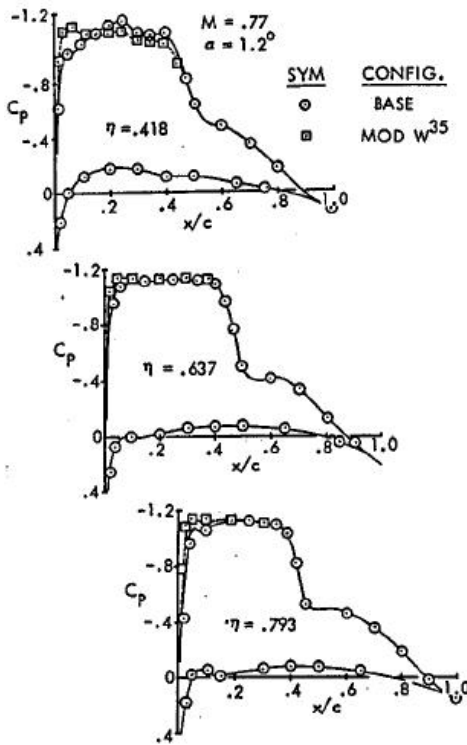Figure 15.21 - Experimental lift-alpha curve. Source: AIAA Paper No. 79-0066

Figure 15.23 - Test drag rise for the base wing, W^{12C}, and modified wing, W^{35}. Source: AIAA Paper No 79-0066

Figure 15.22 - Comparison of experimental chordwise pressure distributions for the base and modified leading edge W^{35}. Source: AIAA Paper No 79-0066
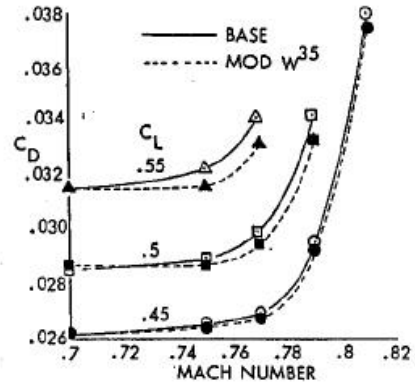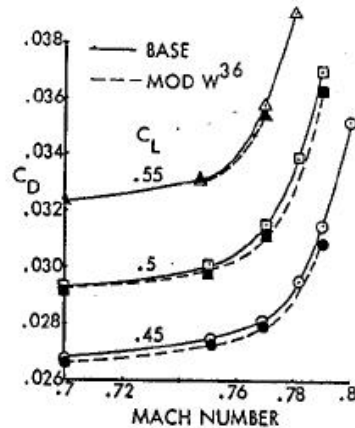

Figure 15.24 - Test drag rise for the base wing, W^{12C} and modified wing, W^{36}. Source: AIAA Paper No 79-0066

Based on the German experience with the NACA Modified Four-Digit series of airfoil sections, development of low drag sections with transonic flow was continued in England by Pearcey et al. Their general conclusions were:

1. A sharp suction peak had to be present at the leading edge in subsonic flow conditions at the particular angle of attack.
2. Behind the suction peak rapid deceleration had to occur in subsonic flow.
3. Behind the leading edge the curvature distribution had to be such that the expansion waves in the supersonic region, the sonic line and the "reflected" compression occurred behind the suction peak. This would then cause a very weak or no shock wave at all at the end of the supersonic region in the flow around the airfoil.

This is visually explained in figures 15.25 to 15.27.

In this paper the development [first at the National Physical Laboratory (NPL) from 1965 to 1970, then at RAE] is described of a series of aerofoils, intended to exploit the potential benefits of using relatively large regions of controlled supersonic flow over the upper surface of a wing at high subsonic free-stream Mach numbers.

The exciting possibilities of this concept had already been demonstrated by Pearcey at the NPL in the early 1960s. He had shown in a number of experiments how, by careful design of the shape of the upper surface of an aerofoil, the flow could be constrained to decelerate isentropically from a maximum local Mach number as high as 1.4 without breaking down into the shock wave that usually terminates such a supersonic flow region, and hence without incurring any wave drag penalty. Such an ideal situation could admittedly occur, for any particular aerofoil, only at one isolated "design point", corresponding to a particular pair of values (M∞, α) of the free-stream Mach number and angle of incidence; but fortunately it was found that the rate of growth of shock waves in any departure from the design condition was usually slow, so that practical benefits could undoubtedly be obtained.
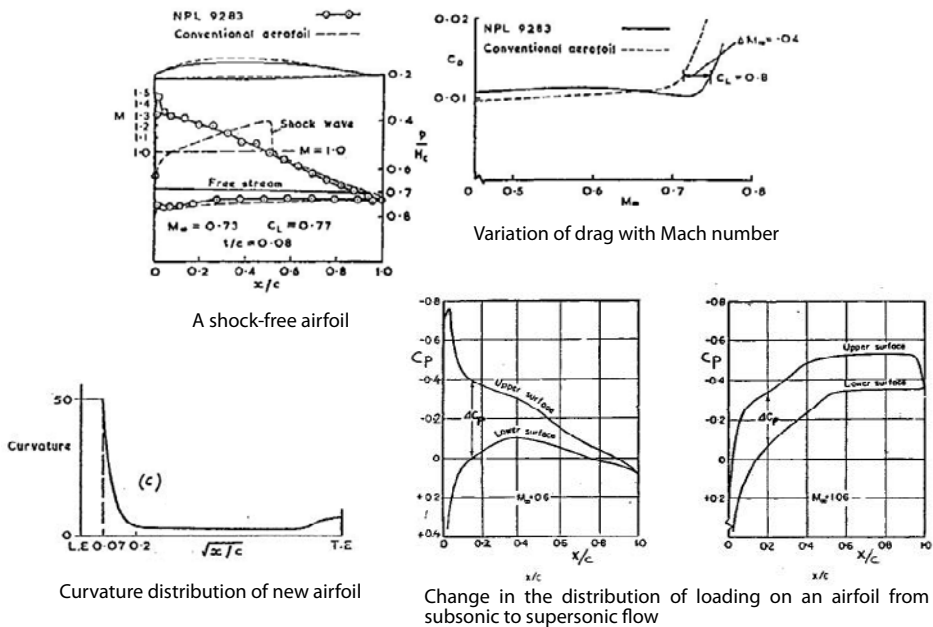

A shock-free airfoil

Variation of drag with Mach number

Curvature distribution of new airfoil

Change in the distribution of loading on an airfoil from subsonic to supersonic flow

Figure 15.25 - Illustration of effects of airfoil with large region of supersonic flow.
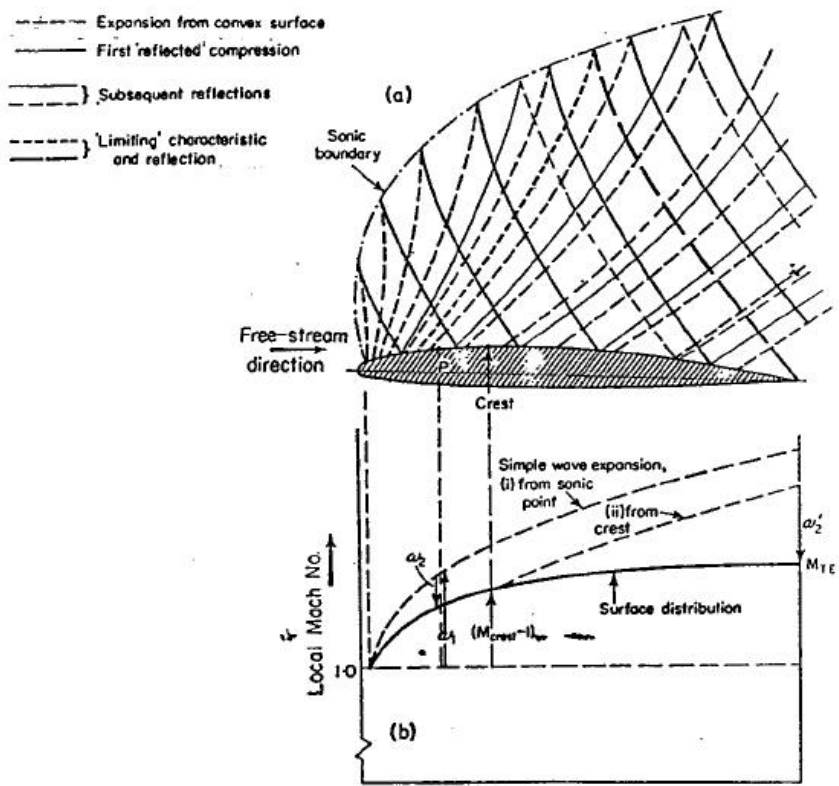*Source: Aeronautical Quarterly, november 1974, page 245, 246.*

Figure 15.26 - Sketch of Mach-wave pattern, (a), in a region of supersonic flow on an airfoil and the local Mach-number distribution, (b), resulting from the supersonic position of the first simple wave, ω_1, and the compressive effect, ω_2
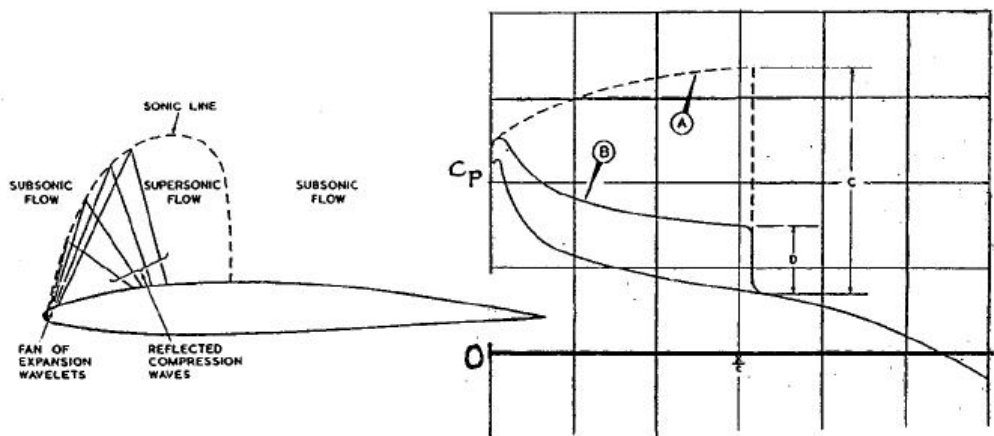

Figure 15.27 - 'Peaky' wing flow development. Source: Aircraft Engineering, June 1962

Figure 15.28 illustrates that if C_{Pmin} occurs further aft, attaining C_P^* immediately causes adverse transonic flow conditions as can be seen by the rapid drag rise around M = 0.6.

Analysing or performing computations on transonic flows is far more intricate than the analysis of subsonic flow. But with the use of numerical analysis methods this has become possible. A comparison between computations and test data is shown in figure 15.29.
With these techniques designing transonic airfoils has become possible. The figure shows however that contrary to the situation in subsonic flow in transonic flow incorporation of boundary layer effects is absolutely mandatory to obtain meaningful results.
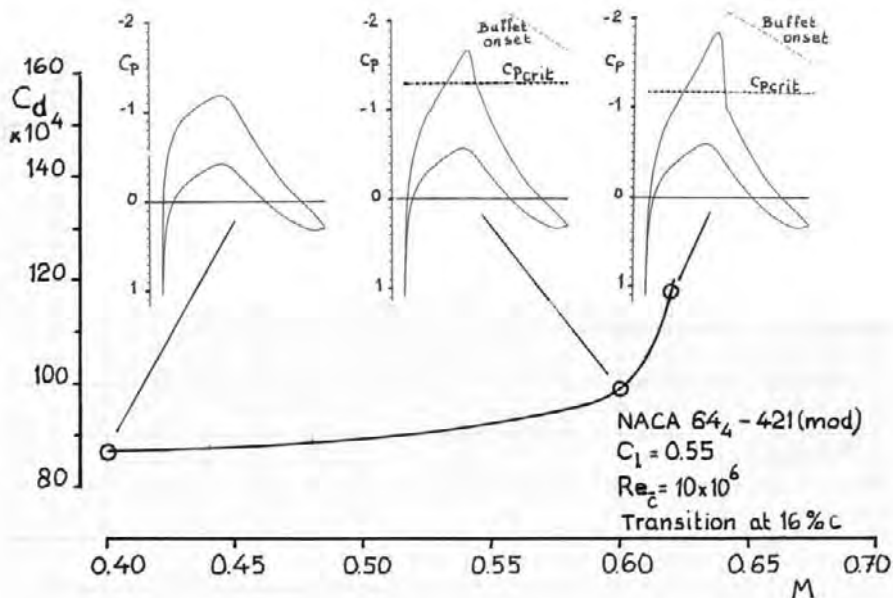

Figure 15.28 - Development of drag and pressure distribution with increasing Mach number on airfoil section NACA 64$_4$ - 421 (mod) (C$_l$ = 0.55). Source: Fokker Report L-27-204

Numerical methods allowed detailed analysis of the relation between geometry, transonic design pressure distribution and section characteristics. Examples are given in figures 15.30 to 15.32.
Figure 15.32 shows a study performed at Lockheed-Georgia illustrating the variety of possible transonic airfoil sections and the changes made to improve the characteristics.
Note that this study started with an analysis of the basic section of the C-5 wing which again had a family resemblance with the NACA Modified Four-Digit sections.
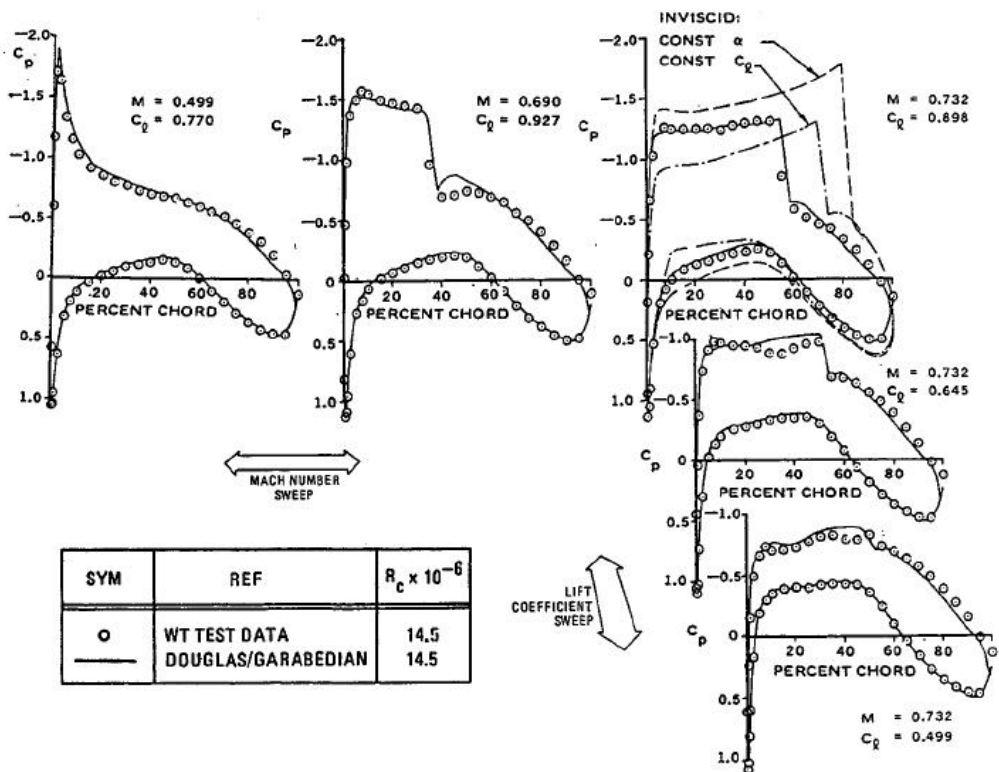
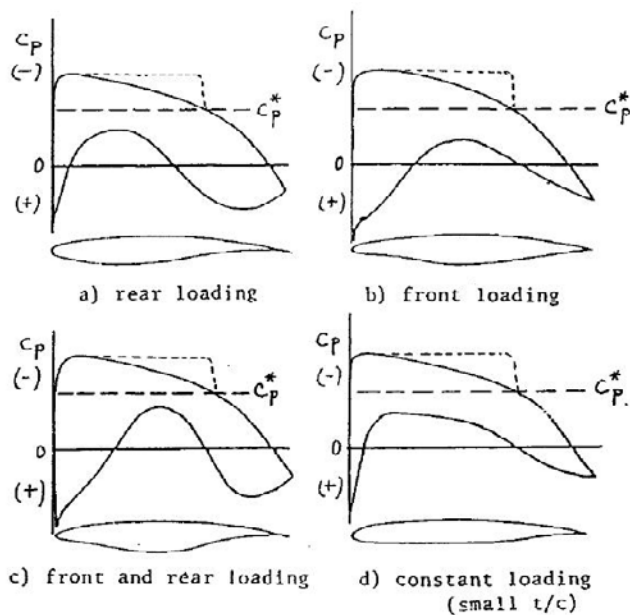*Figure 15.29 - Comparison of calculated and measured pressure distributions for supercritical airfoil DSMA 671*

a) rear loading

b) front loading

c) front and rear loading

d) constant loading (small t/c)

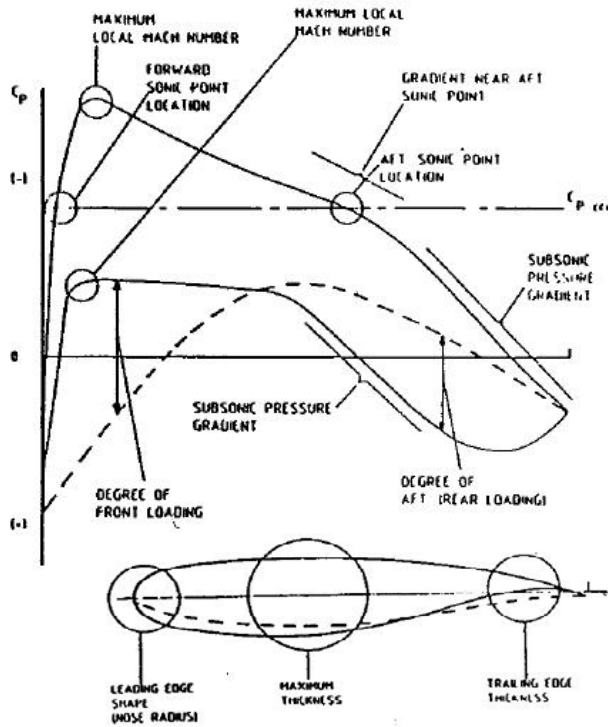*Figure 15.30 - Typical C_P - distributions of transonic airfoils*

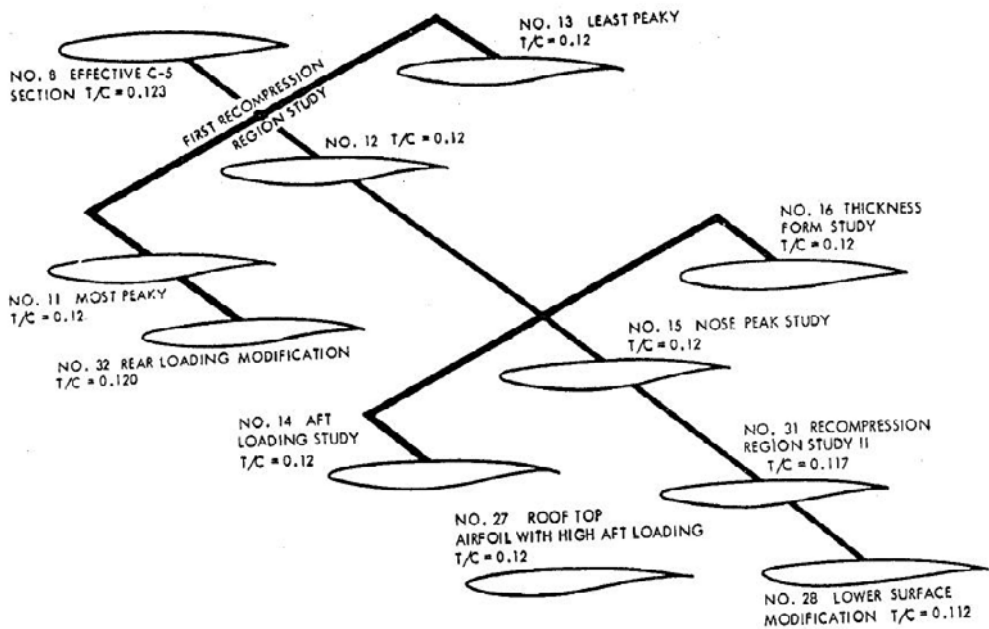*Figure 15.31 - Significant design pressure distribution parameters for off-design characteristics*

Figure 15.32 - Lockheed-Georgia design concept evaluation airfoil series. Source: AIAA paper 73-792

From figures 15.33 to 15.36 several relationships between airfoil shape, pressure distribution, lift coefficient and design (or drag divergence) Mach number, indicated by the symbol in the figures, can be extracted. When adding thickness to the airfoil at constant camber, higher local velocities will occur due to the stronger surface curvature. For a given lift coefficient this will lead to a lower design or drag divergence Mach number or for an increase in design Mach number will lead to a thinner section.

Adding thickness only to the lower part of the airfoil results in an increase in supervelocities on the lower surface. This may only marginally decrease the lift coefficient in the design condition but may appreciably lower the drag divergence Mach number at lower lift coefficients.

Decreasing aft loading by thickening the rear part of the airfoil results in a lower lift coefficient at the design Mach number. As a positive effect this modification leads to a less negative zero-lift pitching moment coefficient.
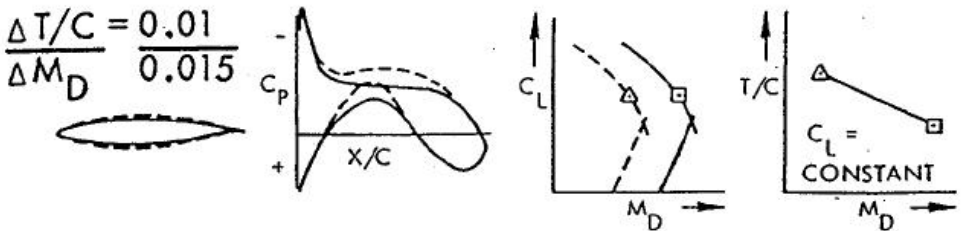

Figure 15.33 - Effect of thickness to chord ratio with camber held constant. Source: AIAA Paper No 73-792
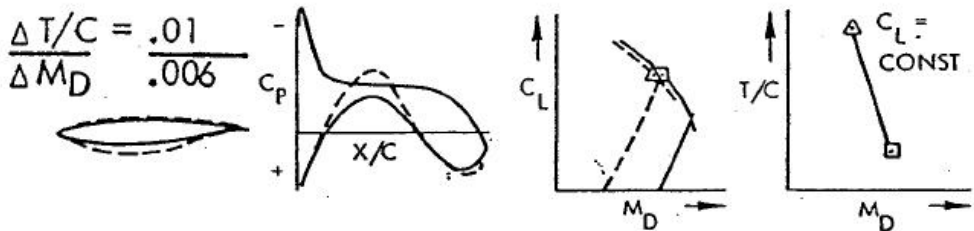

Figure 15.34 - Effect of thickness to chord ratio with $C_{P_{upper}}$ held constant. Source: AIAA Paper No 73-792
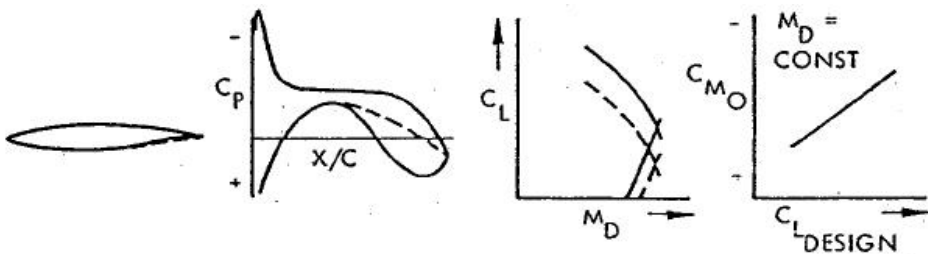

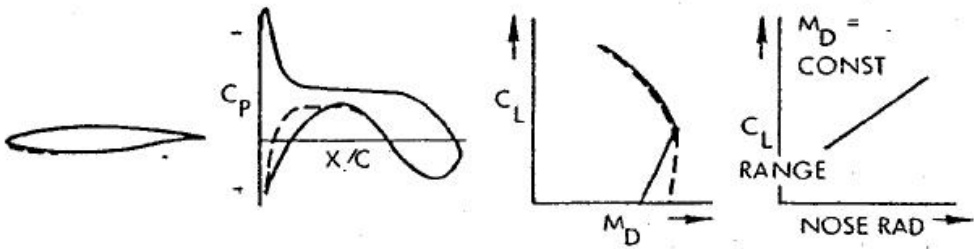Figure 15.35 - Effect of aft loading. Source: AIAA Paper No 73-792

Figure 15.36 - Effect of nose radius. Source: AIAA Paper No 73-792

More examples of pressure distributions are given in figures 15.37 to 15.46. They illustrate an airfoil design concept evaluation. In these figures the features that were explained earlier can be recognized again. Note in figure 15.46 that in transonic flow the pressure distribution on the lower surface can develop even stronger suction peaks than the pressure distribution on the upper surface in particular at low lift coefficients.
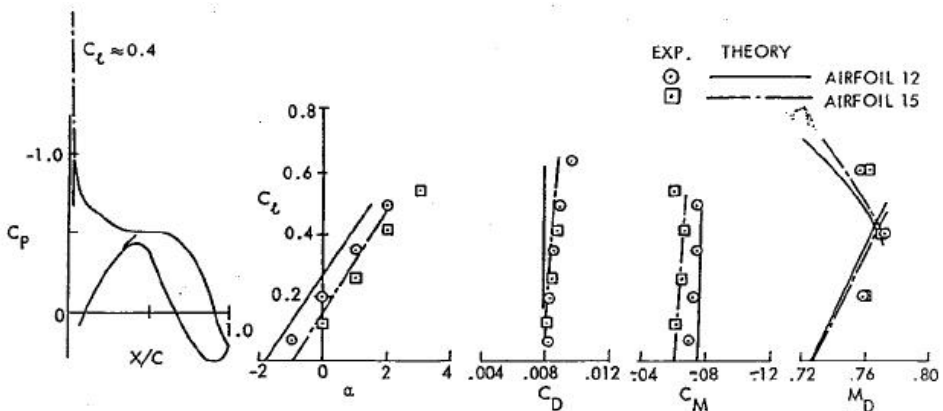
Figure 15.37 - Nose peak height study, subcritical conditions, M = 0.64. Source: AIAA Paper No 73-792
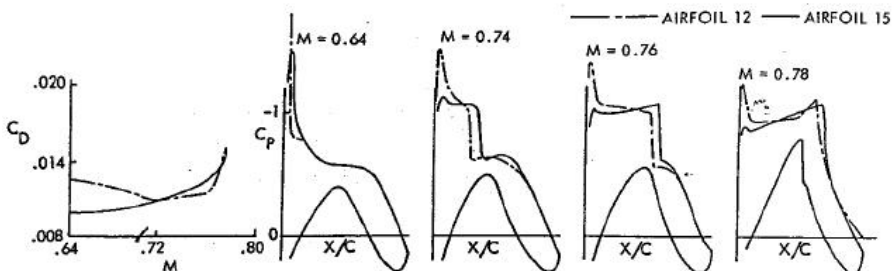
Figure 15.38 - Nose peak height study, transonic conditions, $C_l \approx 0.6$. Source: AIAA Paper No 73-792

Figure 15.39 - Recompression region study, subcritical design conditions, M = 0.64.
Source: AIAA Paper No 73-792
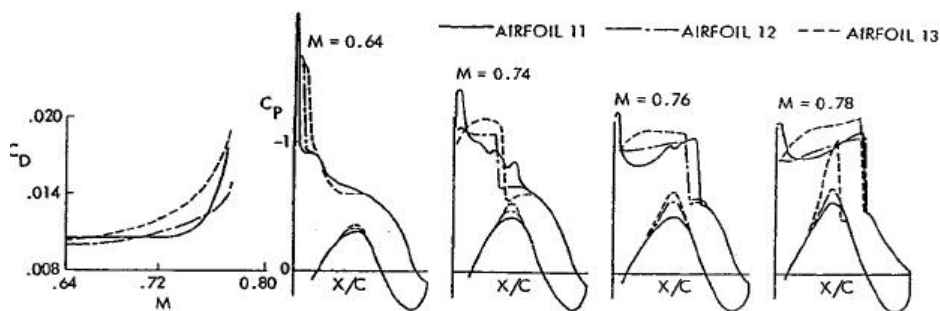
Figure 15.40 - Recompression region study, transonic design conditions, $C_l \approx 0.6$.
Source: AIAA Paper No 73-792
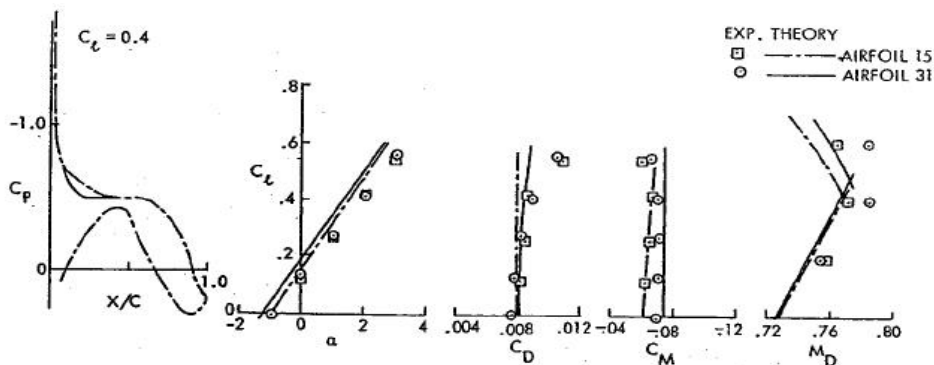
Figure 15.41 - Recompression region study, subcritical design conditions, M = 0.64.
Source: AIAA Paper No 73-792
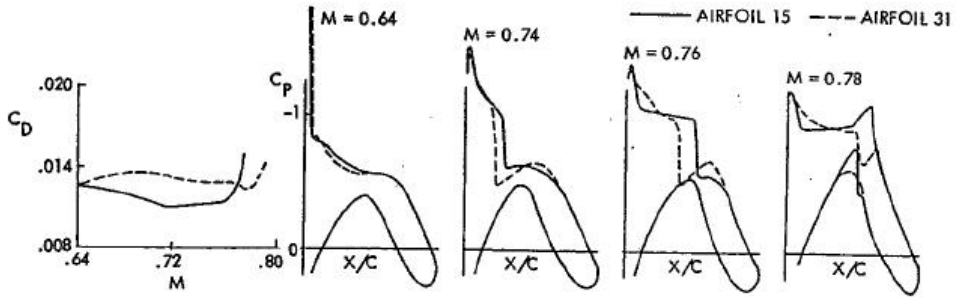
Figure 15.42 - Recompression region study, transonic characteristics, high speed comparison, $C_l \approx 0.6$.
Source: AIAA Paper No 73-792

Figure 15.43 - Aft loading study, subcritical design conditions, M = 0.64. Source: AIAA Paper No 73-792

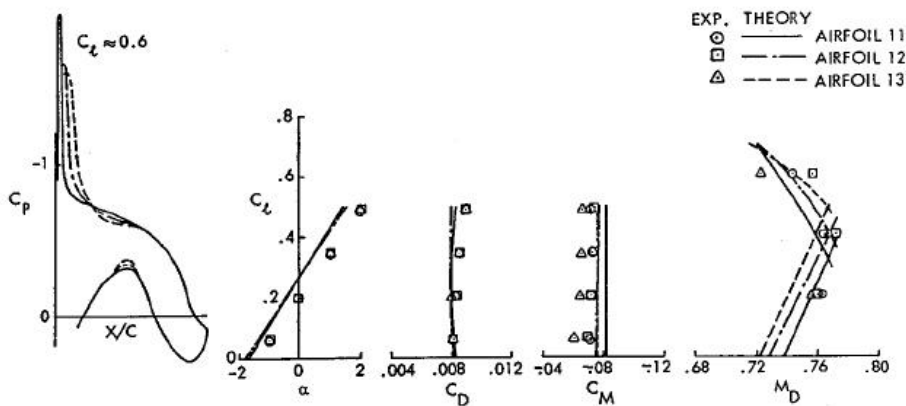Figure 15.44 - Aft loading study, transonic characteristics, $C_l \approx 0.6$. Source: AIAA Paper No 73-792

Figure 15.45 - Lower surface pressure distribution study, subcritical design conditions, M = 0.64.
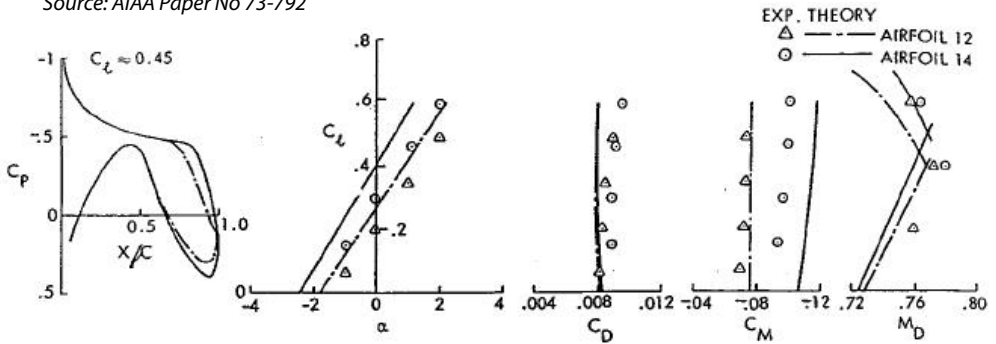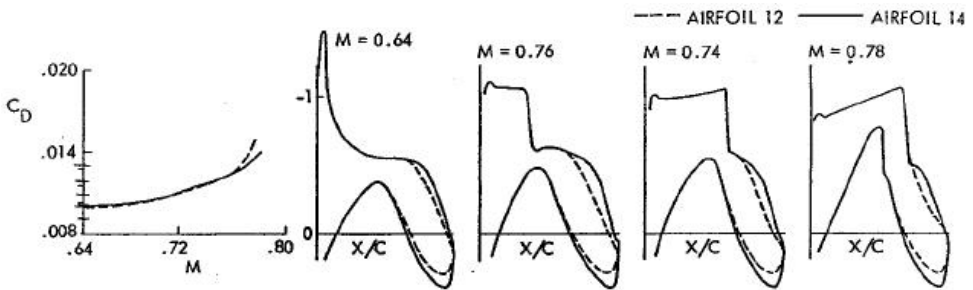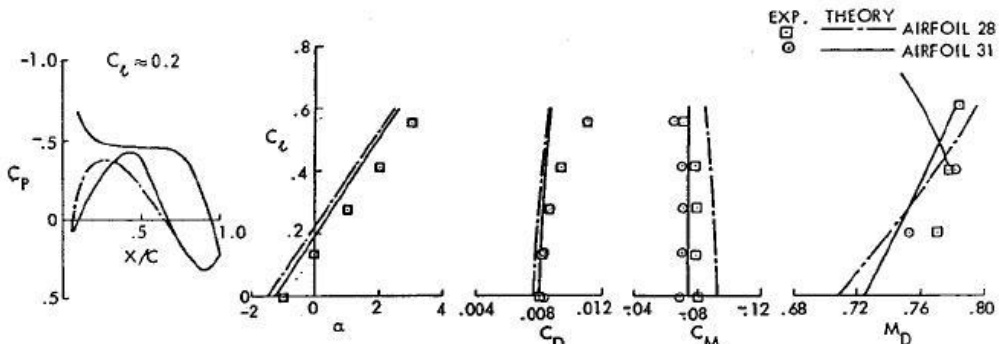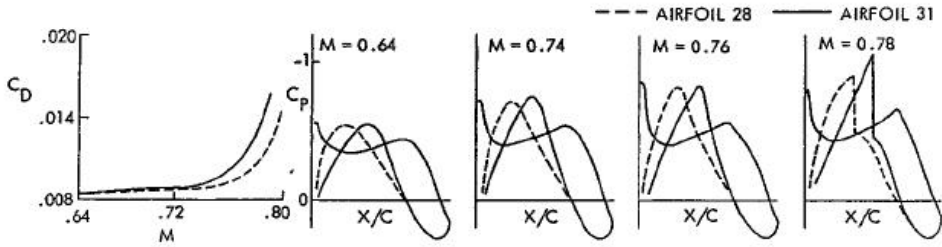Source: AIAA Paper No 73-792

Figure 15.46 - Lower surface pressure distribution study, transonic characteristics, $C_l \approx 0.2$.
Source: AIAA Paper No 73-792

The development of the transonic airfoil

In the development of transonic airfoil sections, i.e. airfoil sections which in their design condition exhibit a pressure distribution characteristic of a mixed supersonic-subsonic flow, four phases can be recognized. These are not consecutive phases and overlap to a large extent.

In the first phase an improvement in transonic characteristics was sought through systematic shape modifications of existing section families. These studies produced general relations between airfoil geometry and aerodynamic characteristics without really increasing the understanding of the underlying physics. The best known examples from this period are the NACA Modified Four-Digit series but also modifications of NACA 6-series sections were studied.

In the second phase a beginning was made by incorporating the physics of transonic flow in the airfoil section design procedure. Starting from the general observation that for a successful section design in subsonic flow conditions the pressure distribution should have a narrow suction peak at the leading-edge followed by a region of almost constant pressure section curvature modifications were studied in a mixed theoretical-experimental approach. The main tool was the hodograph method well known from supersonic aerodynamic theory. This development was started by Pearcey at NPL in the UK and later extended by others. However, the computational possibilities were limited in the early 60's and designing airfoil sections was much a matter of trial and error. This work led to the belief that in transonic airfoil design the effort should be aimed at realizing a complete isentropic recompression over the region of supersonic flow in the design condition. Small deviations from the design condition would then lead to only weak shock waves with a small increase in drag even when the peak Mach number was high. This was actually achieved in the wind tunnel (see figure 15.24). The problem with this approach was that the final result, when a particular section was tested in the wind tunnel, was to a certain degree

"unpredictable" and not in agreement with theory. This was partly due to the fact that the crucial role of the boundary layer was only just beginning to be understood, and thus as well that of the Reynolds number for this type of flow condition. Nevertheless, the basic wing sections for the DeHavilland DH-121 Trident and Vickers VC-10 were designed according to these principles. Both aircraft did not completely come up to their manufacturers' expectations but incorporating these sections into highly swept tapered wing must have been an extra challenge. This experience led Hawker-Siddeley to applying sections with a sonic rooftop upper surface pressure distribution with a small leading-edge pressure peak in the design of the Airbus A-300 wing. Experience with this type of sections had shown that if this type of pressure distribution was adopted for the initial design condition at higher lift coefficients (required to cater for weight growth) transonic flow would develop such that the region of supersonic flow would be terminated with a weak shock wave. This did occur on the aircraft.

In the late 60's Nieuwland and Spee at the National Aerospace Laboratory (NLR) in the Netherlands developed a series of transonic airfoil sections which exhibited in the design condition complete isentropic recompression over the supersonic region on the upper surface in full potential flow. Potential flow implies that viscous effects and entropy increases (i.e. boundary layer effects and the occurrence of shock waves) were not included.

The calculations were based on the hodograph method for finding exact analytical solutions of the full potential flow equations. Although the sections developed this way, in most cases showed a weak shock in the wind tunnel test data for the design condition, after learning how to correct for these deficiencies their characteristics in general were as expected.

One unexpected phenomenon which time and again frustrated section developers was that, even if in the design condition the wind tunnel test data showed only a weak shock, the drag started rising slowly at Mach numbers appreciably below the design Mach number, the so-called "drag creep", which differed from the steep "drag rise" which occurs at higher than the design Mach number. This drag creep was in particularly significant when in the theoretical design condition a high level of supervelocities in the supersonic region was prescribed. Theory suggested that as the recompression was fully isentropic no extra drag would result from that.

Figure 15.47 shows on the left the local Mach number distribution on the upper surface as prescribed by the calculation for two sections NLR 7101 and 7301. On the right, drag curves are presented for both sections as calculated with

modern CFD methods. Wind tunnel test data, albeit at lower Reynolds-numbers, showed comparable results. The difference in drag creep behaviour is evident. This investigation showed that if significant drag creep is to be avoided in the design condition the local Mach numbers in the supersonic region should remain below M = 1.2.

Although the analytical approach discussed above is now superseded by modern CFD design and analysis methods the analytical computational method to design shock-free transonic airfoil sections was an important milestone in the development of airfoil section aerodynamics.

In the late 60's the name "supercritical airfoil section" was introduced by Whitcomb of NASA for sections with upper surface pressure distributions as shown in figure 15.13 suggesting that this was a new development. Later it became clear that the development of practical transonic airfoil sections was an evolutionary process but the name came into general use.
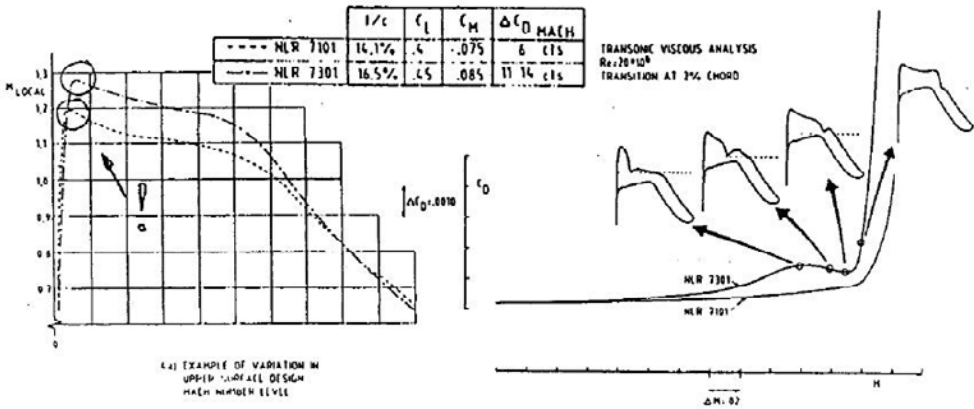
Figure 15.47 - Effect of upper surface local Mach number level on drag creep

The development of computer technology, both in terms of hardware and software, led in the 70's and 80's to the development of numerical computer programmes that allowed the analysis of weak shock waves embedded in transonic flow. Originally based on full potential flow theory, special mathematical measures were incorporated to handle the discrepancy between potential flow and the (small) entropy increase due to the weak shock wave. These early programmes in general were not accurate with respect to shock wave position. Well-known programs were early versions of the FLO-programmes developed by Bauer-Garabedian and Korn (BGK). At a later stage boundary layer effects were incorporated either artificially by modifying the Kutta-Joukowsky boundary condition or in a physically correct way by the previously mentioned researchers and Jameson. The programme FLO-22 is representative of this period.

Today, many programmes are available for analysis and design of transonic airfoil sections varying from programmes with a weak coupling between a full potential outer flow and a boundary layer programme up to programmes based on the complete time-averaged Navier-Stokes equations. Most programmes suitable for industrial applications are based on a coupling of Euler-equations for the outer flow and Navier-Stokes equations for the boundary layer.

In figures 15.48 and 15.49 the geometry and some calculated aerodynamic characteristics are presented for two fairly thick airfoil sections designed for $M = 0.707$ and $c_{l_{design}} = 0.5$ and 0.6. For this relatively low Mach number $C_p^* = 0.75$ according to figure 10.1. This high value of C_p^* limits the possibility of developing a region of supersonic flow over the forward part of the section because if the shock wave moves too far aft the resulting pressure gradient in the subsonic part of the pressure distribution would become too steep and the boundary layer would separate near the trailing edge. The figures clearly indicate that already in the design condition the boundary layers on both upper and lower surface are close to separation as near the trailing-edge the local friction coefficient c_f is close to zero.

From the above it will be clear that the so-called supercritical pressure distribution in the design condition is only applicable at sufficiently high Mach numbers. Figures 15.50 to 15.54 present some data on two sections one designed by Fokker, the other by Boeing according to the modern design principles discussed above and summarized in figure 15.55.

On most modern airfoil sections some degree of camber is applied on the rear part of the section to produce extra lift, the so-called rear-loading. This is not done in the classical way by maintaining the section thickness distribution and "bending" the section over the camberline but by modifying the lower surface without affecting the upper surface.

When initially high-speed airfoil sections were studied, relations were discovered between the geometry and the aerodynamic characteristics of different section families. It was soon concluded that on non-cambered (i.e. symmetrical) sections the transonic characteristics were better than on cambered sections. Furthermore, with increasing speeds but still using cables to operate control surfaces, phenomena such as aileron upfloat and aileron buzz were more difficult to control when rear camber was applied.

It was only with the advent of hydraulic control systems and the general use of provisions in the aircraft flight control system to compensate for transonic pitch-up or pitch-down tendencies that rear camber came in use again. It was first deliberately applied on the DH-121 Trident and Airbus A-300 and is now a standard element in modern design section principles.
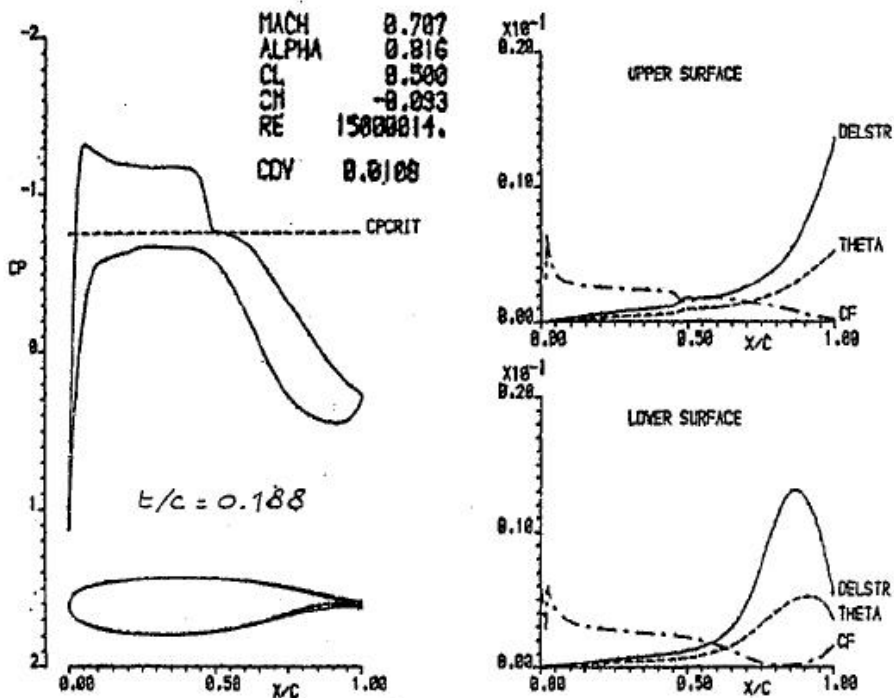
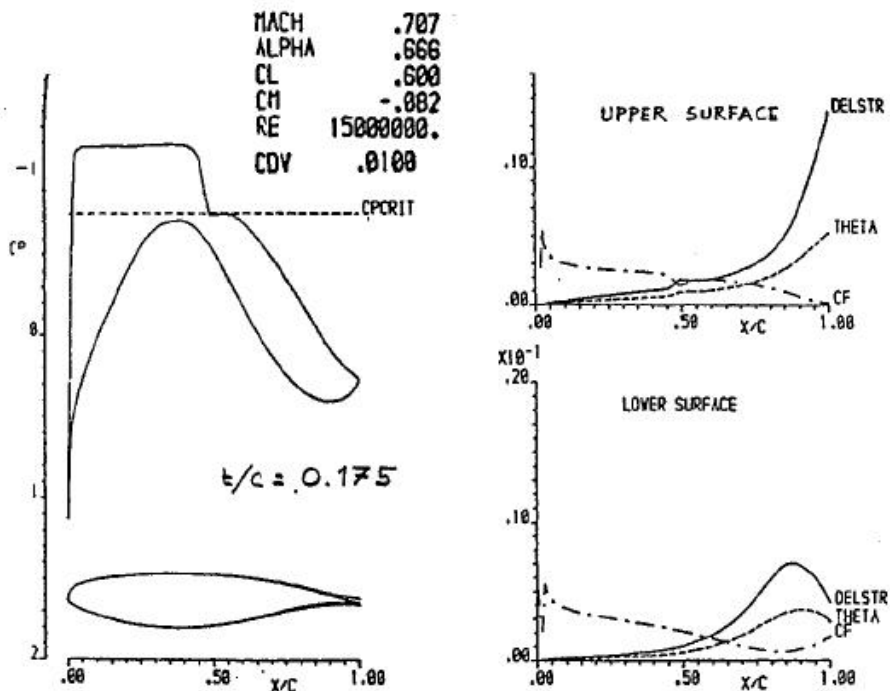*Figure 15.48 - Design pressure distribution and boundary layer characteristics*

Figure 15.49 - Computed pressure distribution at the drag divergence Mach number
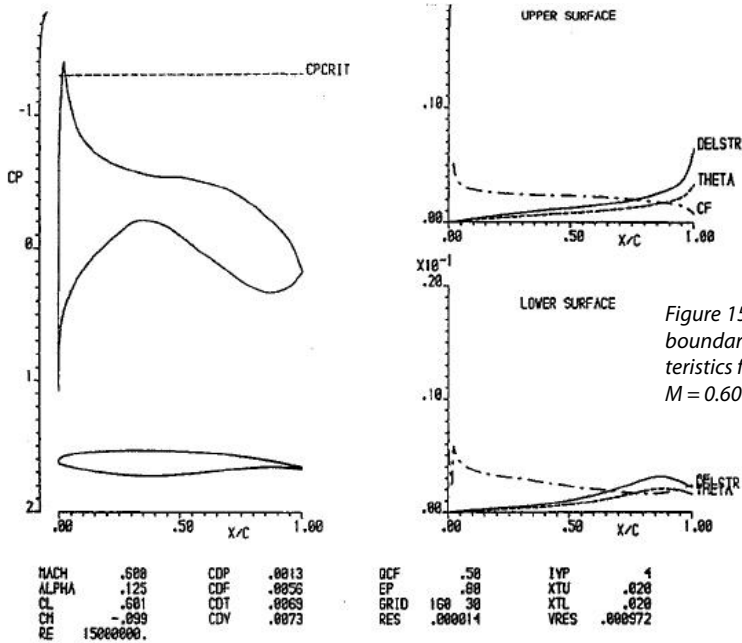
Figure 15.50 - Pressure distribution, boundary layer and drag charac-teristics for a high-speed airfoil. $M = 0.600$. $C_l = 0.601$

MACH	.600	CDP	.0013	QCF	.50	IVP	4
ALPHA	.125	CDF	.0056	EP	.00	XTU	.020
CL	.601	CDT	.0069	GRID	160 30	XTL	.020
CM	-.099	CDV	.0073	RES	.000014	VRES	.000972
RE	15000000.						
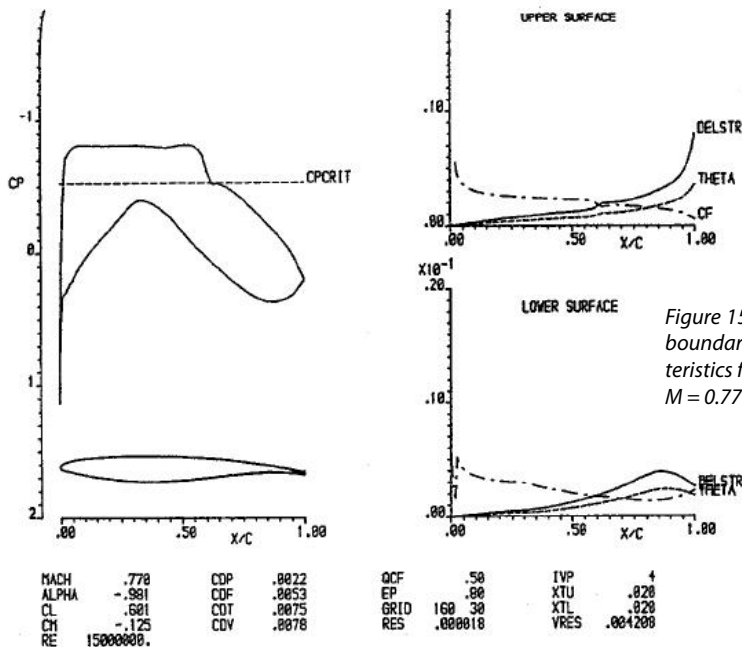
Figure 15.51 - Pressure distribution, boundary layer and drag charac-teristics for a high-speed airfoil. $M = 0.770$. $C_l = 0.601$

MACH	.770	CDP	.0022	QCF	.50	IVP	4
ALPHA	-.981	CDF	.0053	EP	.00	XTU	.020
CL	.601	CDT	.0075	GRID	160 30	XTL	.020
CM	-.125	CDV	.0078	RES	.000818	VRES	.004200
RE	15000000.						

Figure 15.52 - Drag creep for the high-speed airfoil

Figure 15.53 - Pressure distribution of super-critical airfoil, as given in Figure 15.54. Source: NASA TM 87600

Figure 15.54 - A modern airfoil section - Boeing BAC-1. Source: NASA TM 87600

Figure 15.55 - Typical supercritical airfoil. Source: Agard-FDP VKI Special Course
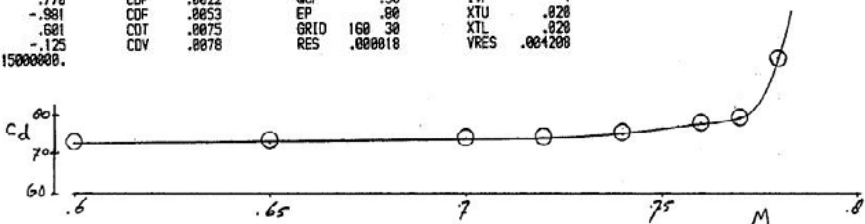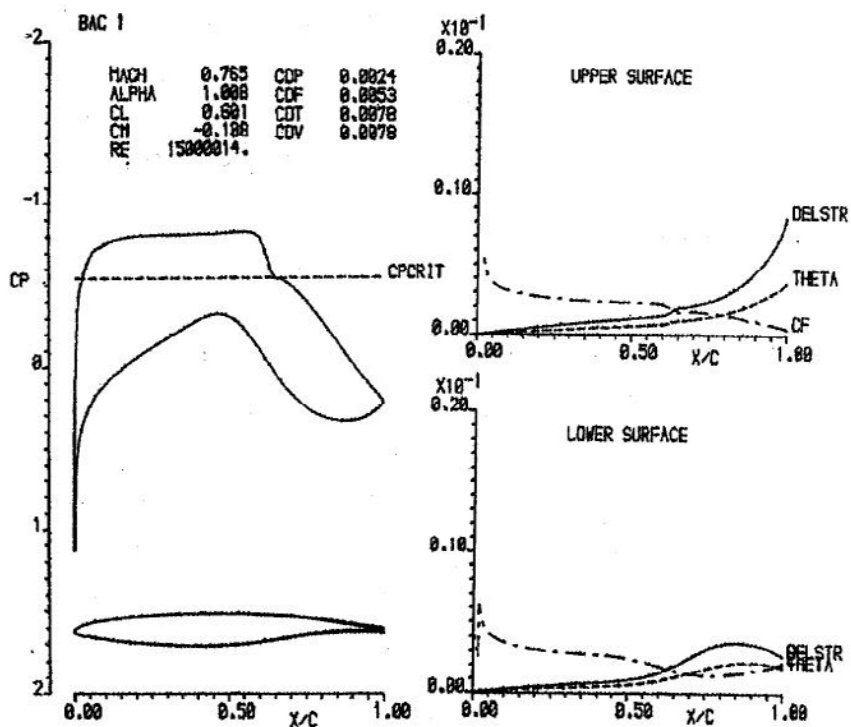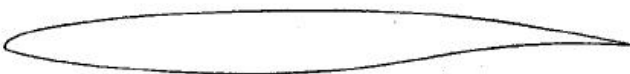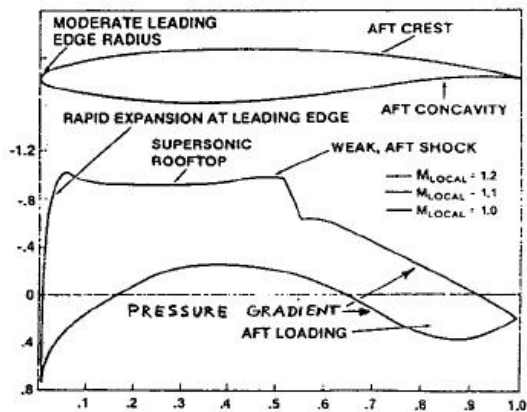on Subsonic/Transonic Aerodynamic Interference for Aircraft, May 2-6, 1983

16 The advantages of supercritical airfoil sections in comparison to sonic roof-top sections

From the foregoing it is clear that supercritical airfoil sections have the following advantages compared to sonic roof-top sections:

• A larger relative thickness
• A larger leading-edge radius leading to higher $c_{l_{max}}$ –values.

A comparison between two such sections is presented in figure 16.1 to 16.3. Both sections were designed for M = 0.72 with an identical lower surface pressure distribution. The sonic roof-top section has a lower design lift coefficient but a higher drag rise Mach number than the supercritical section. If the sonic roof-top section would have been designed for the same lift coefficient as the supercritical section its relative thickness would have been even lower than 11.0 percent. However, when the angle-of-attack of this section is increased so that the same lift coefficient is obtained, a small leading-edge suction peak will occur followed by a region of supersonic flow with a weak shock. Thus most probably the drag rise Mach number will be very comparable to that of the supercritical section but the lower thickness will remain. The conclusion must therefore be that sonic-roof-top sections were considered of practical significance in a period when sections with mixed supersonic-subsonic flow were considered erratic in their behaviour but should now be seen as part of history.

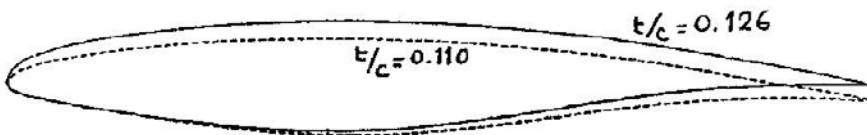

Figure 16.1 - Supercritical airfoil (t/c = 0.126) and sonic rooftop airfoil (t/c = 0.110)
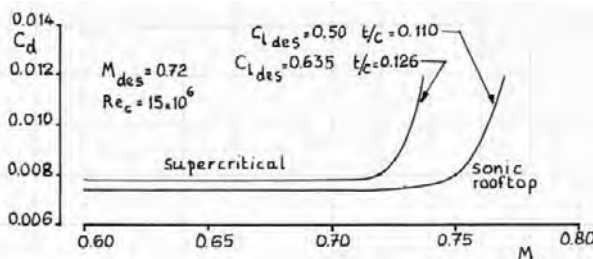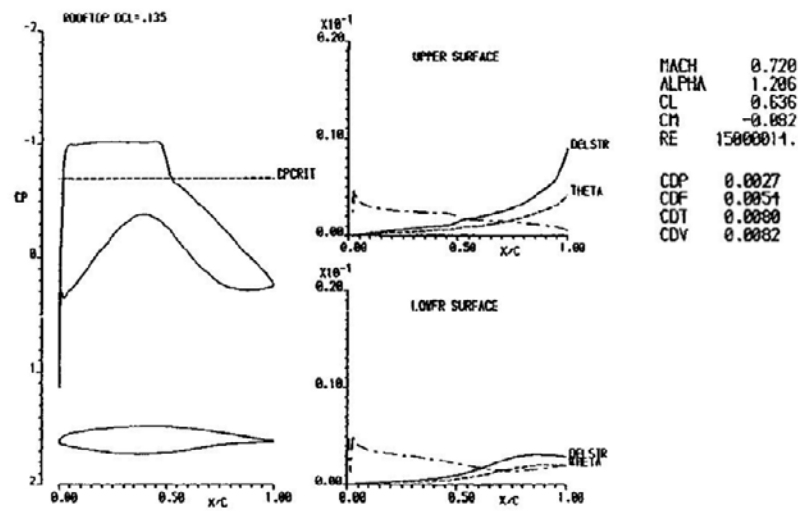

Figure 16.2 - Comparison between the pressure distribution on a sonic-roof-top and a supercritical section
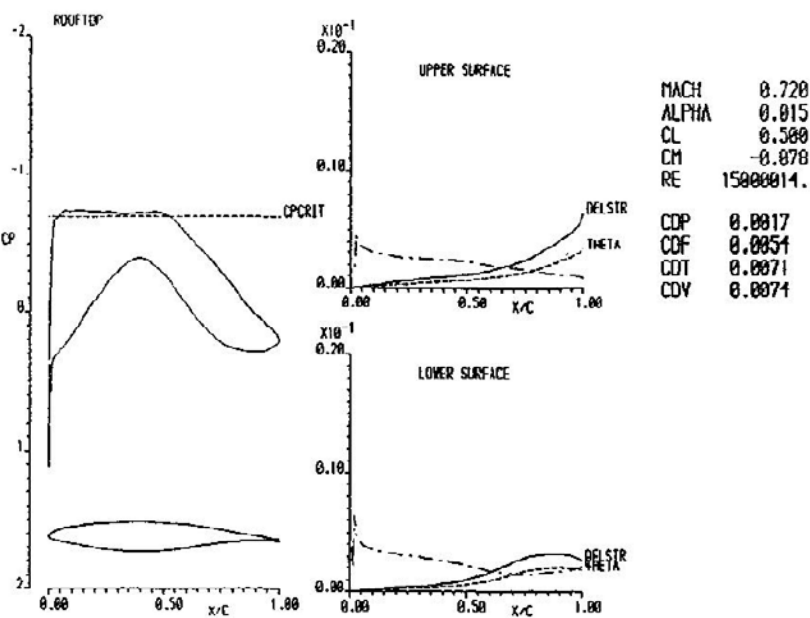
Supercritical

Sonic rooftop

Figure 16.3 - Comparison between the pressure distribution on supercritical and sonic rooftop airfoils

17 *The buffet onset boundary and beyond*

Buffet is a form of airframe vibration caused by pressure fluctuations in separated flow felt by the occupants in the cockpit and the cabin. This means that the vibrations have to surpass a certain level to be sensed by the occupants although this level is low. Buffet can be recorded with accelerometers. Buffet can appear in different forms and have different causes, for example:

- Low-speed buffet due to flow separation when approaching the low-speed stall, sometimes strengthened in severity by the wing wake hitting the horizontal tailplane.
- Buffet due to lift dumper or speedbrake extension.
- Buffet due to local flow separation caused by insufficient attention to geometry details in particular at the rear end of the aircraft.
- High-speed buffet due to flow separation caused by strong shock waves.

It is this latter phenomenon which is covered in the present chapter.

High–speed buffet occurs when a separation bubble, which starts at the foot of the shock wave and gradually increases rearwards, reaches the trailing edge or when the boundary layer separates near the trailing edge before the shock wave becomes strong enough to cause separation at its foot, see figure 17.1. The latter may be expected on such sections as shown in figures 15.48 and 15.49. Trailing-edge pressure divergence is used in wind tunnel tests as an indication of buffet onset on the real aircraft.
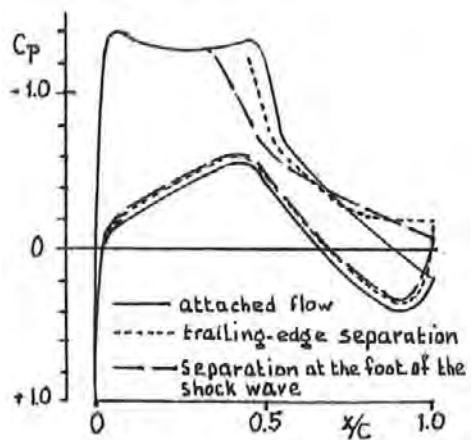

Figure 17.1 - Pressure distribution over an airfoil section with flow separation at the foot of the shockwave and near the trailing edge (see also figure 18.3)

High-speed buffet develops gradually, in particular with increasing angle of attack. If this flow regime is penetrated too far it may result in structural damage. High-speed buffet is annoying and sometimes frightening, particularly for unsuspecting passengers. Therefore airworthiness requirements state that in normal operating conditions a margin must exist between normal flight conditions and buffet onset both with regard to speed and to angle-of-attack as indicated in figure 17.2. This margin is required because the aircraft must be able to:

- manoeuvre in cruise flight (to turn or to pull-up up to n = 1.3g)
- deal with disturbances due to turbulence, be it in speed or in normal load factor
- deal with upsets due to aircraft system failures.
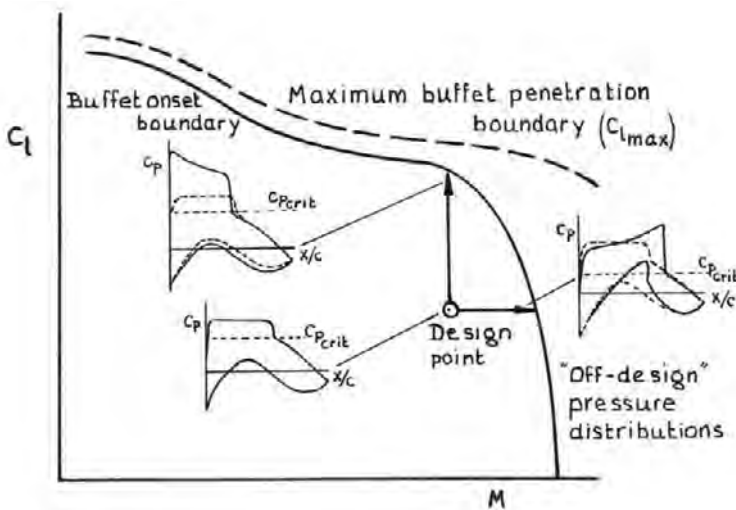
Figure 17.2 - The buffet onset and maximum buffet penetration boundaries

The occurrence of flow separation at the foot of the shockwave seems to be independent of the design pressure distribution. Separation and thus buffet occurs when the local Mach number in front of the shockwave reaches a given value (M_{local} = 1.35 - 1.50 depending on shockwave chordwise position and, to a lesser extent, on Reynolds number). The peak Mach number, which usually occurs at the leading-edge, can be higher, up to M_{local} = 1.7. This is illustrated in figures 17.3 to 17.5.

Figure 17.3 presents minimum pressure coefficients and maximum local Mach numbers as a function of free-stream Mach number for the section presented in figure 17.4. For the higher free-stream Mach numbers the maximum local Mach number varies between M_{local} =1.4 and 1.5.
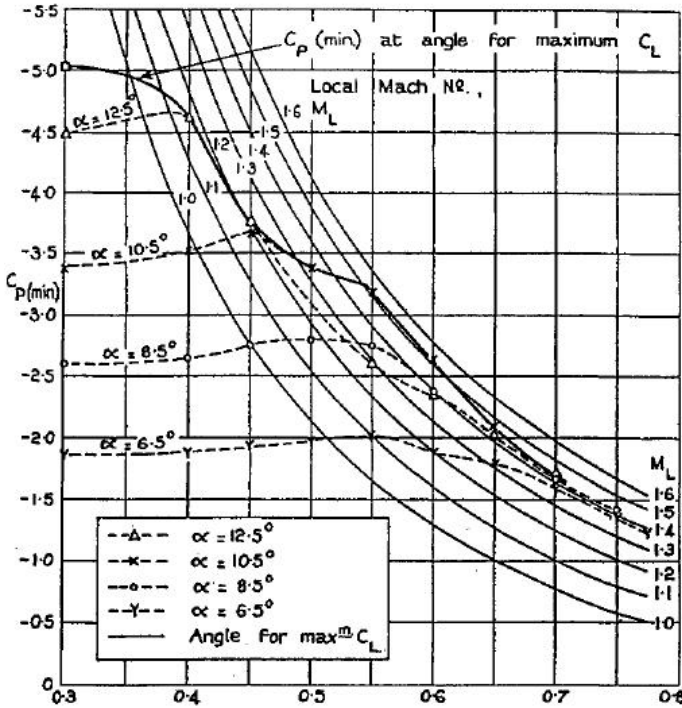
Figure 17.3 - Variation with Mach number of the minimum pressure coefficient on the upper surface for high incidences

Figure 17.4 - Goldstein rooftop airfoil 1442/1547. Source: ARC R&M 2849

Figure 17.5 shows the design upper surface pressure distribution and the pressure distribution at buffet onset for four different airfoil sections. Although the design pressure distributions show a considerable variation buffet onset occurs on all four section when the maximum local Mach number in front of the shock $M_{local} = 1.38$ with shock wave positions at 55 to 60 percent of the chord.

From these and other experimental data an empirical relation can be derived which shows the maximum local Mach number in front of the shock wave at buffet onset as a function of shock wave chord wise position. Such a correlation is presented in figure 17.6. With the aid of such correlations buffet onset can be estimated when pressure distributions are computed for successive angles-of-attack.

Figure 17.5 - Pressure distribution at buffet onset
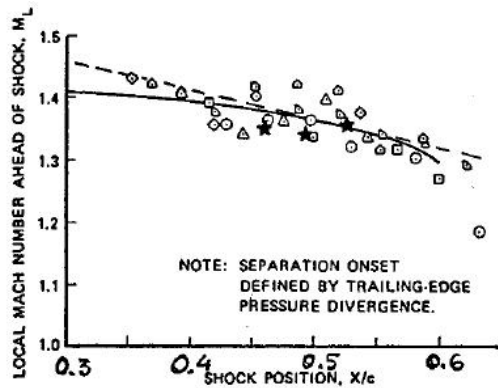
Figure 17.6 - Shockwave parameter correlation at buffet onset

Apart from trailing-edge pressure deviation flow separation and buffet onset can also be deduced from a sudden change in the lift curve slope as indicated in figure 17.7.
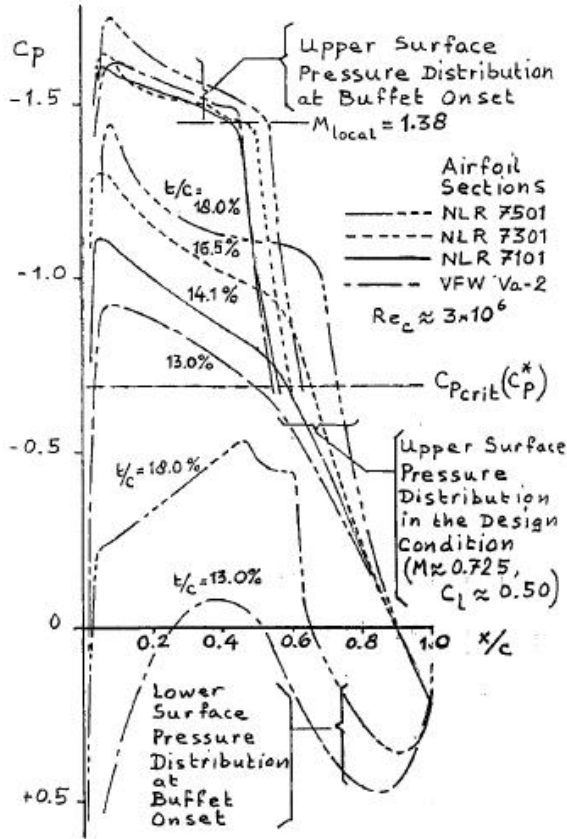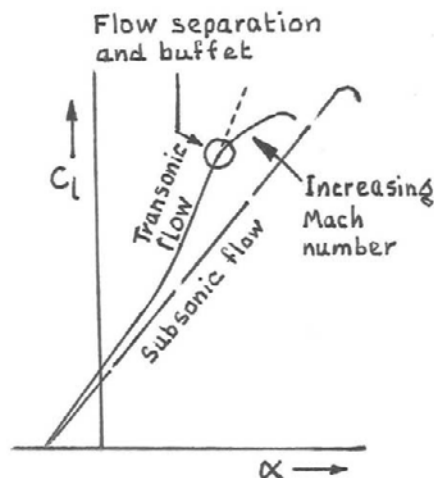
Figure 17.7 - Buffet onset as indicated by a change in the lift-curve slope

Contrary to the stall at low speed, flow separation at higher Mach numbers may produce an appreciable increase in lift at increasing angle-of-attack beyond buffet onset (see figure 17.7). Therefore, apart from the buffet-onset boundary the maximum buffet penetration boundary plays a role in aircraft design. Also the maximum dive Mach number (M_D) for an aircraft may be considerably greater than the Mach number for buffet onset.

Figures 17.8 and 17.9 show more empirical correlations of maximum local Mach numbers occurring on high-speed airfoil sections. Figure 17.9 shows maximum local Mach numbers, both in front of the shock wave and at the leading edge.

Figure 17.8 - $M_\infty^2 C_p$ values as a function of Mach number for four conditions. 0.7 vacuum corresponds to $M_\infty^2 C_p = -1$. Source: AIAA 74-939
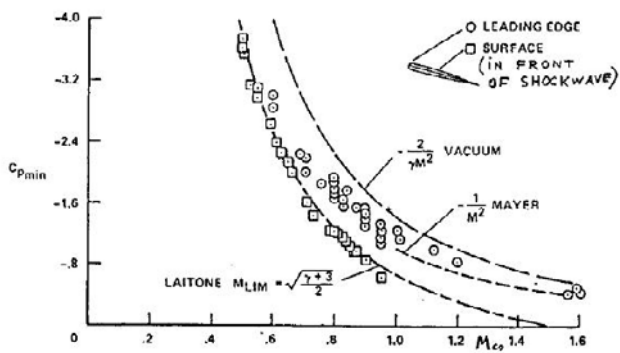
Figure 17.9 - Minimum pressure coefficients in transonic flow. Source: AIAA Paper No 75-996

18 *Reynolds number effects on section characteristics at high Mach numbers*

For supercritical airfoil sections operating near their design point the upper surface has a region of supersonic flow coupled with an almost constant static pressure. The Reynolds number effects are much stronger than for subsonic flow. This has two causes:

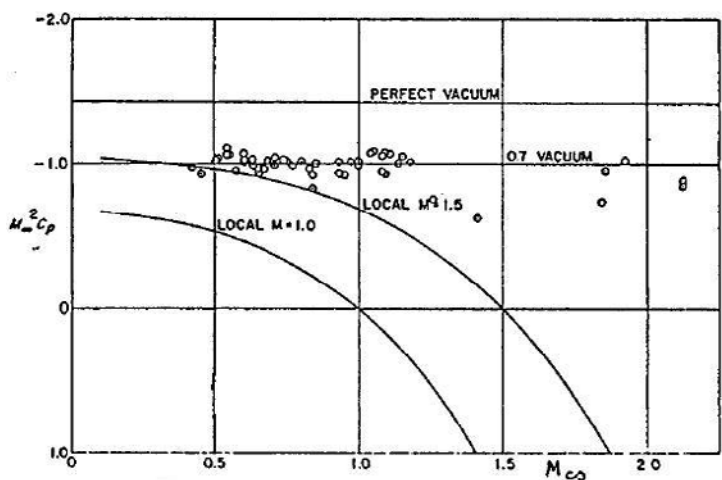- The boundary layer may be laminar up to the shock wave at low Reynolds numbers. The shock wave terminating the supersonic region will then be a lambda shock wave which the boundary layer can negotiate much easier than a straight shock wave associated with a turbulent boundary layer. With increasing Reynolds number transition will occur progressively further ahead of the shock wave.

- Increasing the Reynolds number when the boundary layer is turbulent will decrease the displacement thickness and therefore effectively increase the flow curvature near the section surface. This will produce a more aft shock wave position at constant Mach number and angle-of-attack. This again may cause an increase in shock wave strength and even a second shock wave.

These effects are very small or non-existent on classical airfoils as was shown in figure 15.27. In subsonic flow Reynolds number effects are only connected with the boundary layer condition and changes in the pressure distribution are second order effects.

Figure 18.1 (part 1) - Scale effects on shock-induced boundary layer separation.
Source: ICAS Conference 1978, B3-01

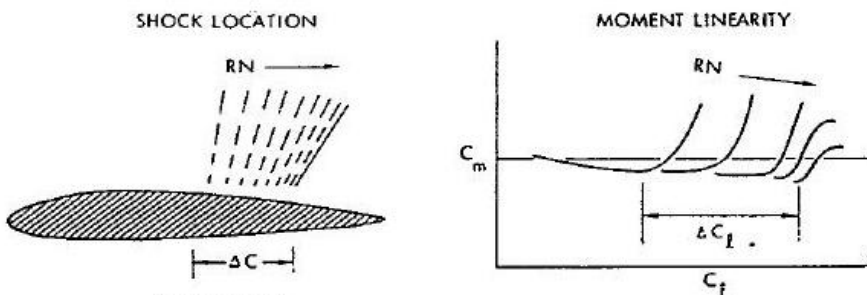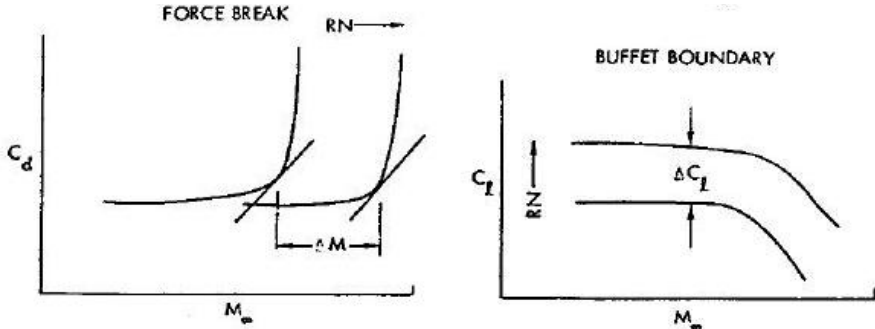*Figure 18.1 (part 2) - Scale effects on shock-induced boundary layer separation.*
Source: ICAS Conference 1978, B3-01

As illustrated in figure 18.1, an increase in Reynolds number has the following effects on an airfoil section with a turbulent boundary layer:

Shock location: The shock moves aft, leading to an increase in lift coefficient at constant α due to the larger area of supersonic flow.

Moment linearity: Before flow separation occurs the linear part of the pitching-moment-vs.- lift –coefficient curve increases with increasing Reynolds number due to the rear movement of the shock. At high lift coefficients this leads to a more negative pitching moment coefficient at high Reynolds numbers.

Force break: In general the drag rise Mach number increases with increasing Reynolds number.

Buffet boundary: Buffet is postponed with increasing Reynolds number.

On modern transonic airfoils the boundary layer is highly loaded in particular over the rear part of the airfoil due to high pressure gradients as indicated in figures 18.2 and 18.4. A locally high effective curvature near the trailing edge may lead to a secondary shock as illustrated in figure 18.5. This makes these airfoils sensitive to Reynolds number effects and requires wind tunnel tests at high Reynolds numbers in order to obtain useful results for design purposes. The two types of boundary layer separations which
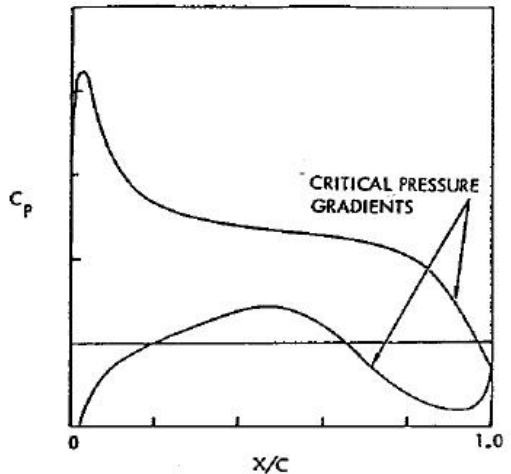
Figure 18.2 - Scale effect on pressure gradient induced boundary layer separation (subsonic). Source: ICAS Conference 1978, B3-01

may occur are shown in figure 18.3 (see also figure 17.1).
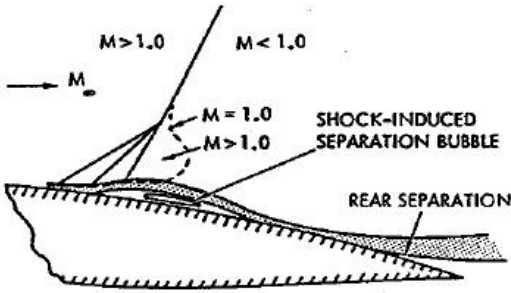
Figure 18.3 - Model of transonic shock / boundary layer interaction. Source: ICAS Conference 1978, B3-01 (see also Figure 17.1)

Figure 18.4 - Airfoil with Reynolds effects. Source: ICAS Conference 1978, B3-01

Figure 18.5 - Scale effects on boundary layer thickness (transonic). Source: ICAS Conference 1978, B3-01

Figure 18.6 shows for a very thick airfoil section (21% t/c) the large difference between the pressure distribution calculated for inviscid flow and obtained from wind tunnel tests at Re = 7.10^6 both at M = 0.68. Whereas the lift coefficient c_l = 1.27 in inviscid flow c_l = 0.60 was found in the wind tunnel.

Note that pressure distributions calculated for inviscid flow represent a limit case and are an indication of the pressure distributions at very high Re-numbers.

In figure 18.8 a comparison is shown of the rearward movement of the shock wave with increasing Re-number on a section used in the Lockheed C-141 wing and of a classical NACA 6-series section.

The large rearward shift on the C-141 was only noticed during the flight tests necessitating an extensive redesign of the wing. Since then also the civil airworthiness authorities require that on new aircraft designs the wing pressure distribution is determined in flight to check if this is in accordance with the data used as a basis for load calculations.
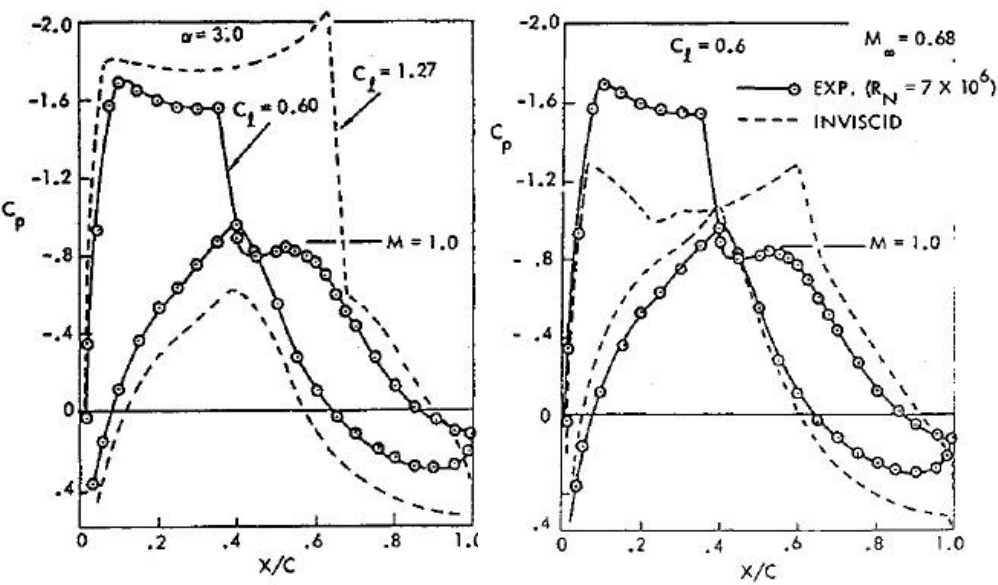
Figure 18.6 - Viscous effects on Lockheed 21% thick supercritical airfoil. Source: ICAS Conference 1978, B3-01
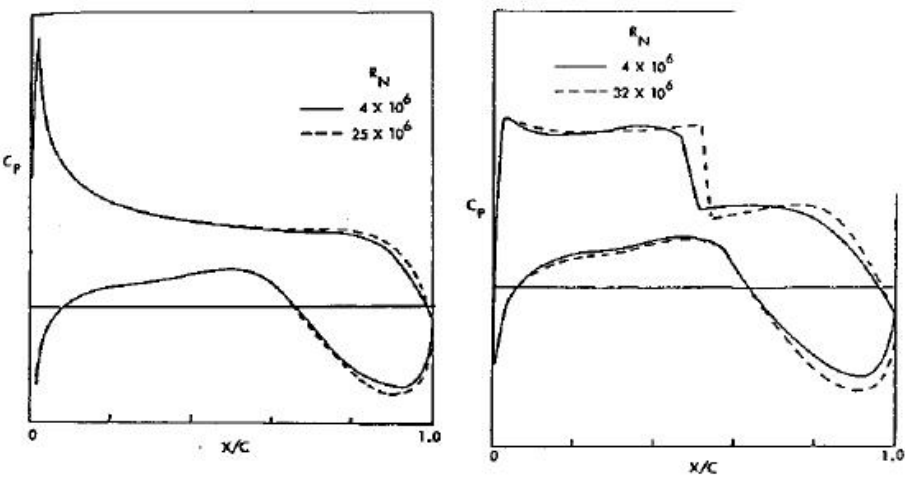
Figure 18.7 - Effect of Reynolds number on wing shock location. The airfoil section and test conditions are mentioned in the caption of figure 18.9. Source: ICAS Conference 1978, B3-01
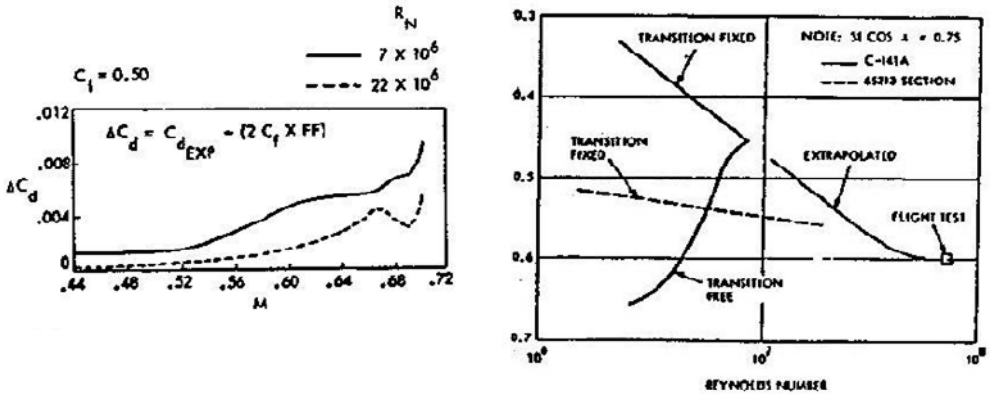
Figure 18.8 - Effect of Reynolds number on wing shock location. Source: Journal of Aircraft 1968, page 496

In figure 18.9 the effect is shown of an increase in Reynolds number on lift and pitching moment for two Mach numbers, M = 0.6 and M = 0.8. At the higher Mach number, the rearward shift of the shock wave causes a much larger increase in lift and in the negative pitching moment than at the lower Mach number where only the boundary layer is affected by an increase in Reynolds number. The same effect is shown in figures 18.7 and 18.10.

Figure 18.11 shows that above about Re = $10 \cdot 10^6$ natural boundary layer transition occurs close to the leading edge assuring a regular dependency of aerodynamic characteristics on Reynolds number. This agrees with the shock wave movement in figure 18.8.
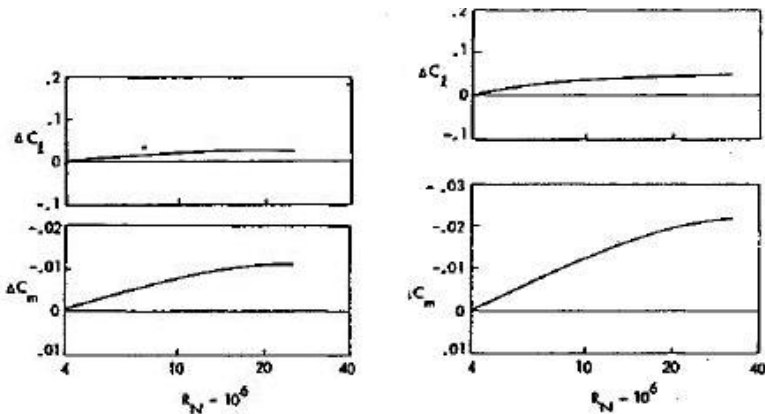
Figure 18.9 - Scale effect on lift and pitching moment data for NASA 10% thick supercritical airfoil, α = 1.5°, M = 0.60 (left), M = 0.80 (right). Source: ICAS Conference 1978, B3-01
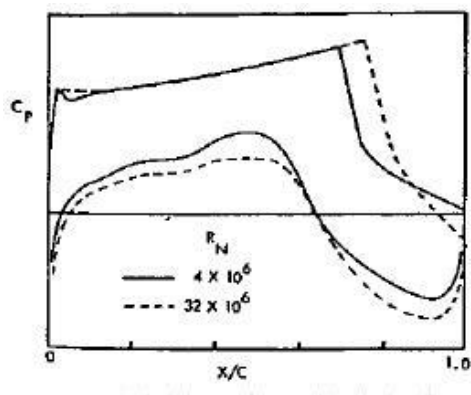
Figure 18.10 - Scale effect on pressure distributions for NASA 10% thick supercritical airfoil, $M_\infty = 0.84$, $\alpha = 1.5°$. Source: ICAS Conference 1978, B3-01
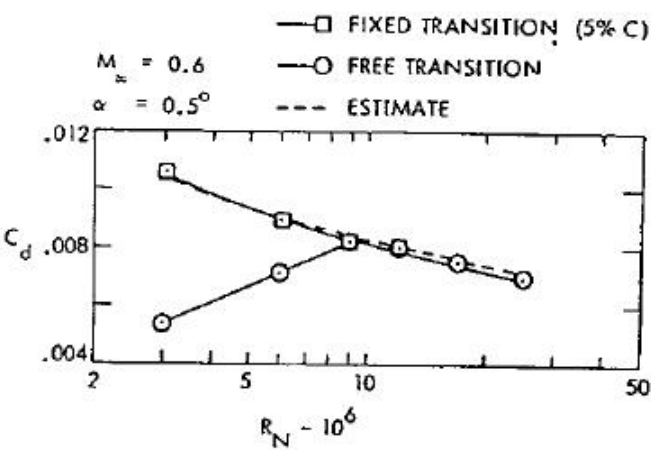
Figure 18.11 - Scale effect on drag for NASA 65_1-213 airfoil. Source: ICAS Conference 1978, B3-01

19 *Low-speed stalling characteristics of airfoil sections*

On airfoil sections the stall may take place according to three different patterns: trailing edge stall, leading edge stall and thin airfoil stall.

1. Trailing edge stall.

In this case boundary layer separation starts at the trailing edge and gradually spreads forward. This type of stall occurs on sections with a large leading edge radius and strong upper surface curvature.
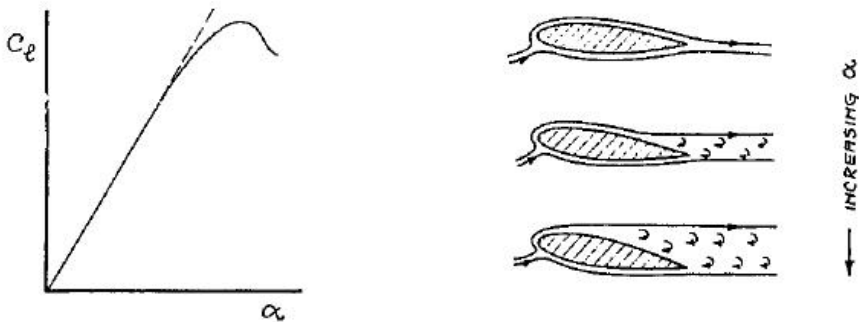
Figure 19.1 - Trailing edge stall (gradual). Source: NLR TR 69025

2. Leading edge stall

This type of stall is abrupt and causes flow separation over almost the entire section. The exact relation between the height of the leading edge suction peak, the adverse pressure gradient immediately following the suction peak and the flow conditions in the (short) transition bubble is as yet unclear. This type of stall occurs on sections with moderate leading edge radii and upper surface curvature distributions at moderate to high Reynolds numbers. The leading edge radius has a significant effect on the maximum lift coefficient. This type of stall is illustrated in figure 19.2.
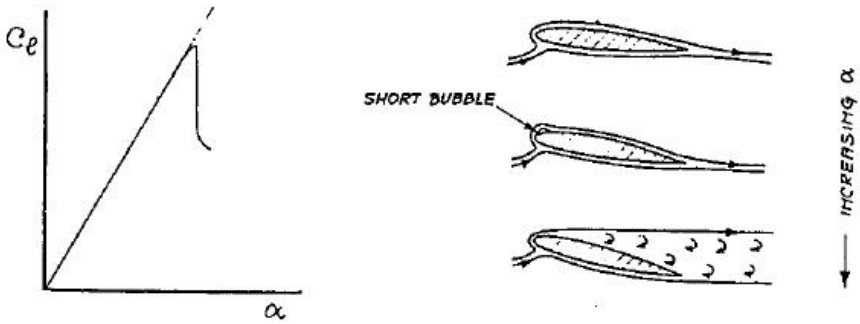
Figure 19.2 - Leading edge stall (abrupt). Source: NLR TR 69025

3. Thin airfoil stall

This occurs only on airfoils with very small leading edge radii (less than 0.7% chord) or on sections with thicker leading edges at low Reynolds numbers. The prime characteristic is the development of a long separation bubble. As can be seen in figure 19.3 the separation bubble increases with increasing angle of attack.
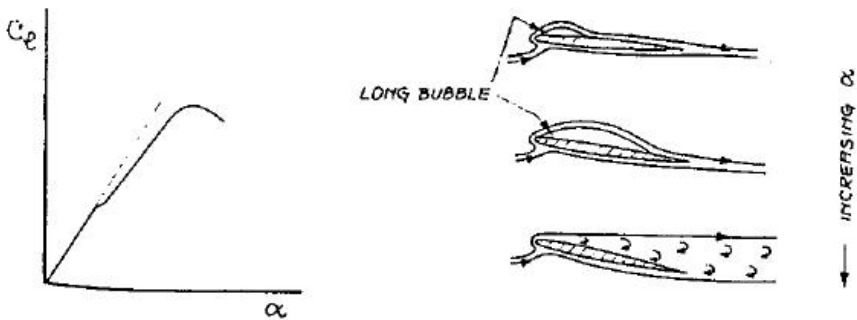
Figure 19.3 - Thin airfoil stall (gradual). Source: NLR TR 69025

In figure 19.4 the lift curves of an airfoil are shown for different Reynolds numbers. The figure illustrates how the maximum lift and the type of stall may change with Reynolds number.

The flow behaviour of a laminar separation bubble is shown in figure 19.5 and the effect of separation bubbles on the pressure distribution is illustrated in figure 19.6.
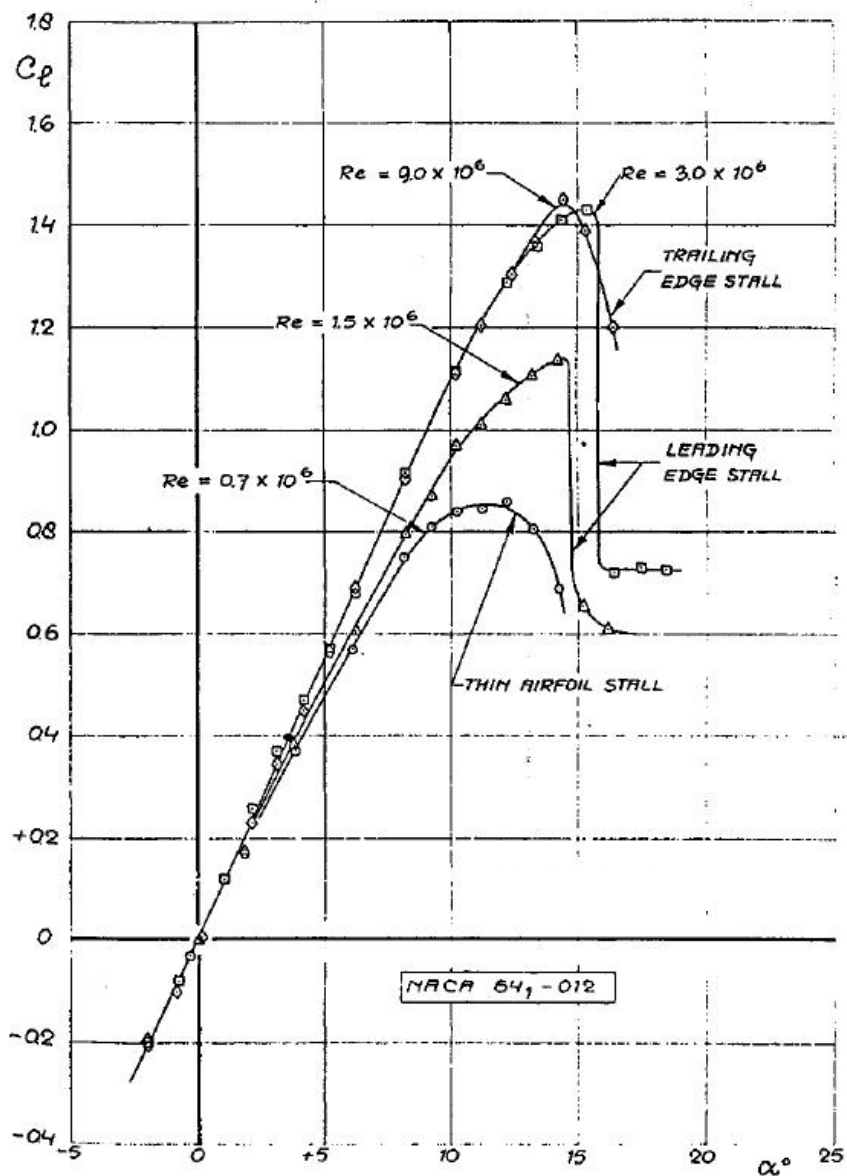
Figure 19.4 - Typical lift curves at various Reynolds numbers for a moderately thick airfoil.
Source: NLR TR 69025
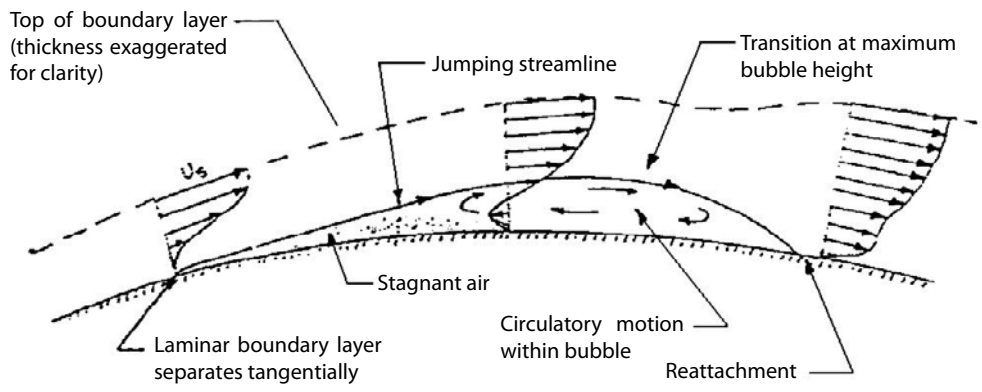
Figure 19.5 - Flow behaviour of laminar flow separation bubbles.
Source: Journal of the Royal Aeronautical Society, December 1963
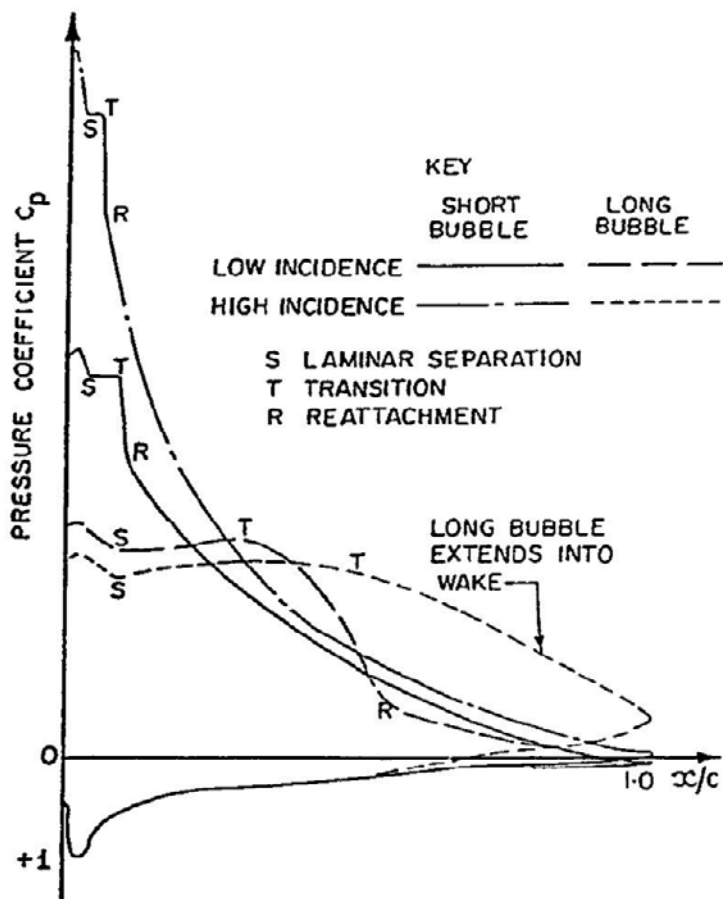
Figure 19.6 - The effect of long and short bubbles on the pressure distribution.
Source: Journal of the Royal Aeronautical Society, December 1963
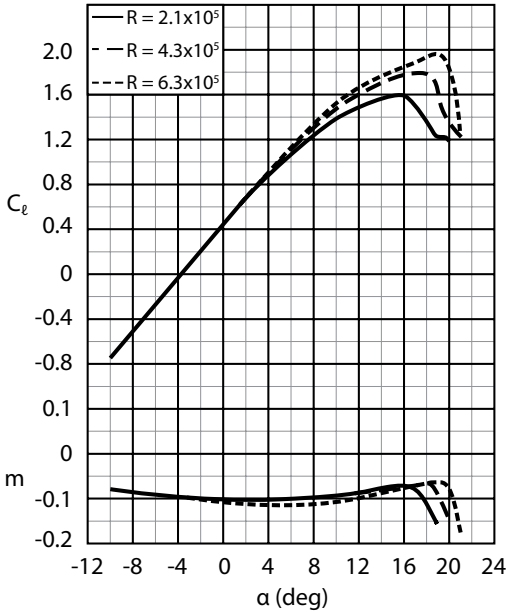
Figure 19.7 - Lift and moment curves at different Reynolds numbers. Airfoil section NASA GA(W)-1. Source: NASA TN D-7428

Figure 19.7 shows the lift curves for an airfoil at three different Reynolds numbers. For the Reynolds number Re = 6.3x10⁶ the pressure distributions have been plotted in figure 19.8 for three angles-of-attack. The first angle-of-attack is at maximum lift (19 deg) and the other two are beyond that point (20 and 21 deg). The negative pressure coefficient at the trailing edge of these pressure distributions indicates separated flow. Note that the point of separation moves forward with increasing angle of attack. Behind this point there is a plateau which points to fully separated flow that does not respond to the surface curvature any more.

Also note that the leading edge pressure coefficient is almost constant for these angles of attack. Here the Kutta-Joukowsky boundary condition does not apply.
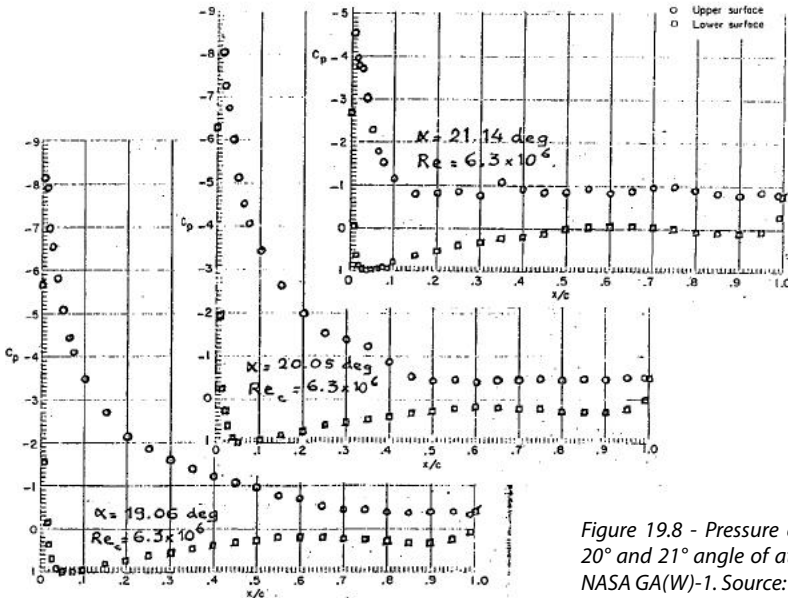
Figure 19.8 - Pressure distributions at 19°, 20° and 21° angle of attack. Airfoil section NASA GA(W)-1. Source: NASA TN D-7428

Maximum lift

This section discusses the influence of the Mach number and Reynolds number on maximum lift when the maximum lift is caused by a collapse of the leading-edge suction peak. Figure 19.9 shows the maximum lift coefficient as a function of Reynolds number at a constant Mach number M = 0.22. When the Reynolds number is increased, the boundary layer becomes thinner, tolerates larger unfavourable pressure gradients and the maximum lift increases.
From about Re = 10 million, increasing the Reynolds number does no longer benefit maximum lift.
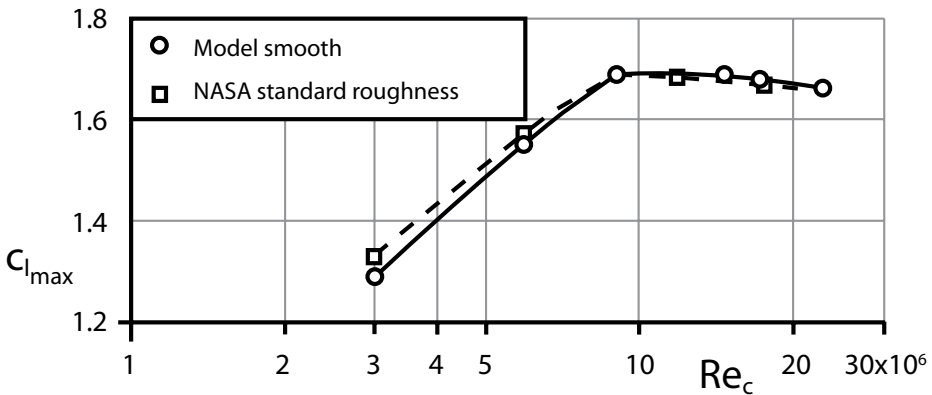
Figure 19.9 - Variation of maximum lift coefficient with Reynolds number at Mach 0.22. Source: NASA TMX-3160

In figure 19.10 the peak suction pressure coefficient at maximum lift is presented as a function of Reynolds number. Increasing the Reynolds number increases the minimum pressure coefficient until the critical value $c_{p,crit}$ is reached. A further increase in Reynolds number leads to supersonic flow and the formation of a shock wave with flow separation at higher angles-of-attack. Note that even at low Mach numbers such as in the present case at M = 0.22 local supersonic flow may occur.

Figures 19.11 and 19.12 show the effect on the maximum lift when the Mach number is increased at constant Reynolds number. The figures show that initially maximum lift is independent of Mach number for a given Reynolds number until the flow at the leading-edge reaches a local Mach number $M_{loc} = 1$ and $c_p = c_{p,crit}$.
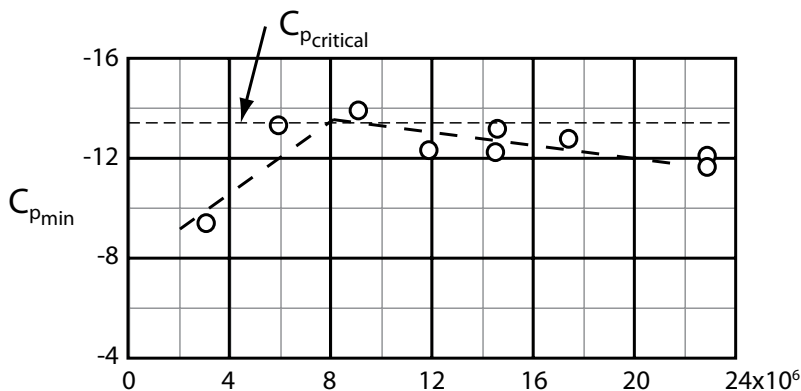
Figure 19.10 - Variation of airfoil minimum upper surface pressure coefficient with Reynolds numbers. M=0.22; transition fixed at x/c=0.05. Source: NASA TMX-3160

With increasing free-stream Mach-number the minimum pressure coefficient $c_{p,min}$ becomes less negative but not at the same rate as the critical pressure coefficient $c_{p,crit}$. So at higher Mach numbers the peak local Mach number becomes higher than $M_{loc} = 1$. In figure 19.12 at M = 0.36 $c_{p,min}$ = -6.2 whereas $c_{p,crit}$ = -0.46 and M_{loc} = 1.22. In this intermediate Mach number range (M = 0.30 to M = 0.50) the low-speed stall regime merges into the high-speed stall regime (buffet onset and maximum buffet penetration boundary) as discussed in chapter 17.
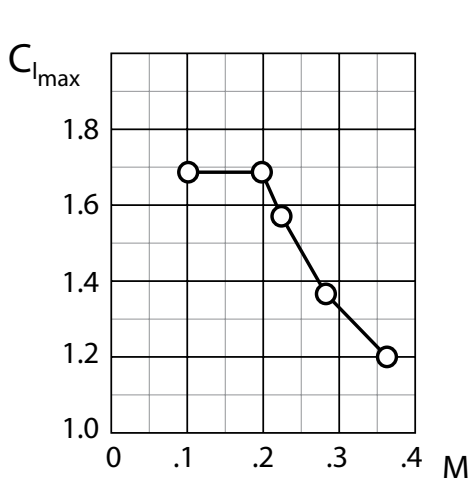
Figure 19.11 - Variation of maximum lift coefficient with Mach number. Re=5.9x10⁶; transition fixed at x/c=0.05. Source: NASA TMX-3160
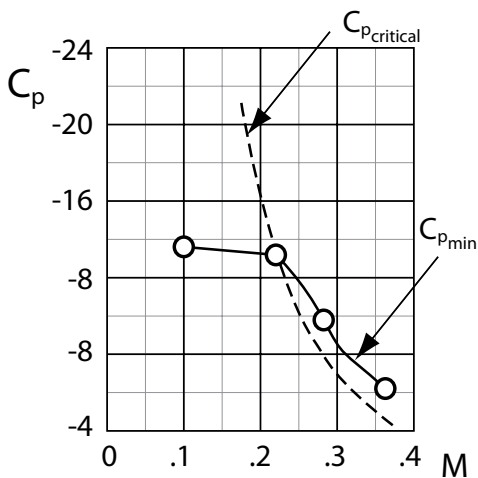
Figure 19.12 - Variation of airfoil minimum upper surface pressure coefficient with Mach number. Re=5.9x10⁶; transition fixed at x/c=0.05. Source: NASA TMX-3160

From the data presented in figures 19.9 and 19.11 the generalized graph as presented in figure 19.13 may be constructed. The graph indicates again that, at low free-stream Mach numbers, for Reynolds numbers above Re = 10x10^6 the maximum lift coefficient is independent of Mach mumber as long as the local Mach number M_{loc} < 1 at $c_{l,max}$. At higher free-stream Mach numbers the maximum lift coefficient decreases although the maximum local Mach number will increase to values above M_{loc} = 1.
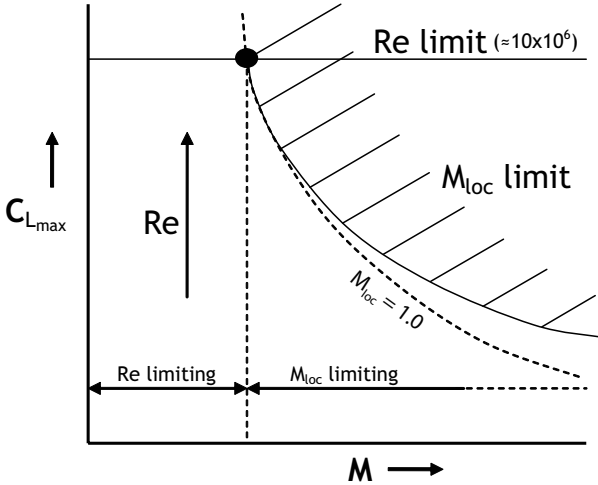
Figure 19.13 - Limitations of the maximum lift coefficient as a function of Mach number

Figure 19.14 shows the relation between leading-edge radius as a fraction of chord length and minimum pressure coefficient when leading-edge stall occurs as a function of Reynolds number. The graph is valid for leading-edge radii between 0.7 and 3 percent of the chord length.

Note that, as $c_{p,min}$ varies between $c_{p,min}$ = -8 and -16 the free stream Mach number at which M_{loc} = 1 is reached varies between M = 0.28 to M = 0.20.
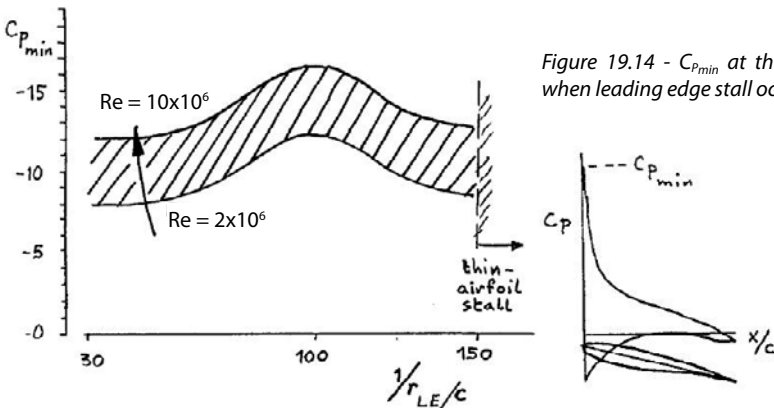
Figure 19.14 - C_{Pmin} at the stall when leading edge stall occurs
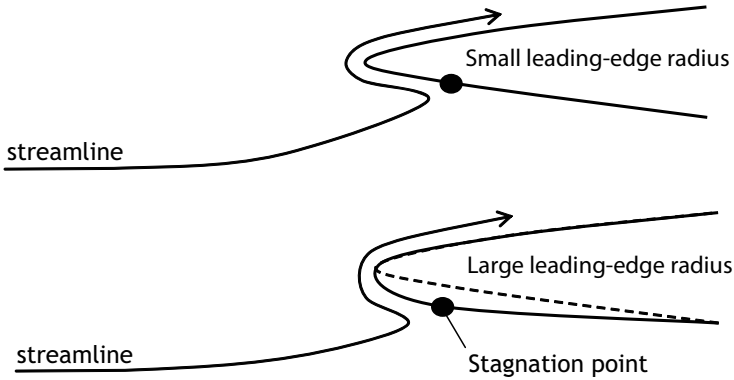
Figure 19.15 - Effect of leading-edge radius on airflow

When an airfoil section has a sharp leading-edge with a small leading edge radius the flow has, at large angles of attack, to deal with a strong curvature leading to high velocities, as illustrated in figure 19.15. When the leading-edge radius is increased without altering the upper surface curvature distribution the peak velocities can, at the same angle of attack, be lowered, due to less severe curvature, without affecting the high-speed characteristics. Consequently the angle of attack can be increased to higher values than the basic section before the suction peak collapses, leading to a higher maximum lift coefficient. This is illustrated in figures 15.16 and 15.17.

Figure 19.16 - Lift curve and profile of the original and the modified NACA 64A-010 airfoil. Source: NACA TN 3871
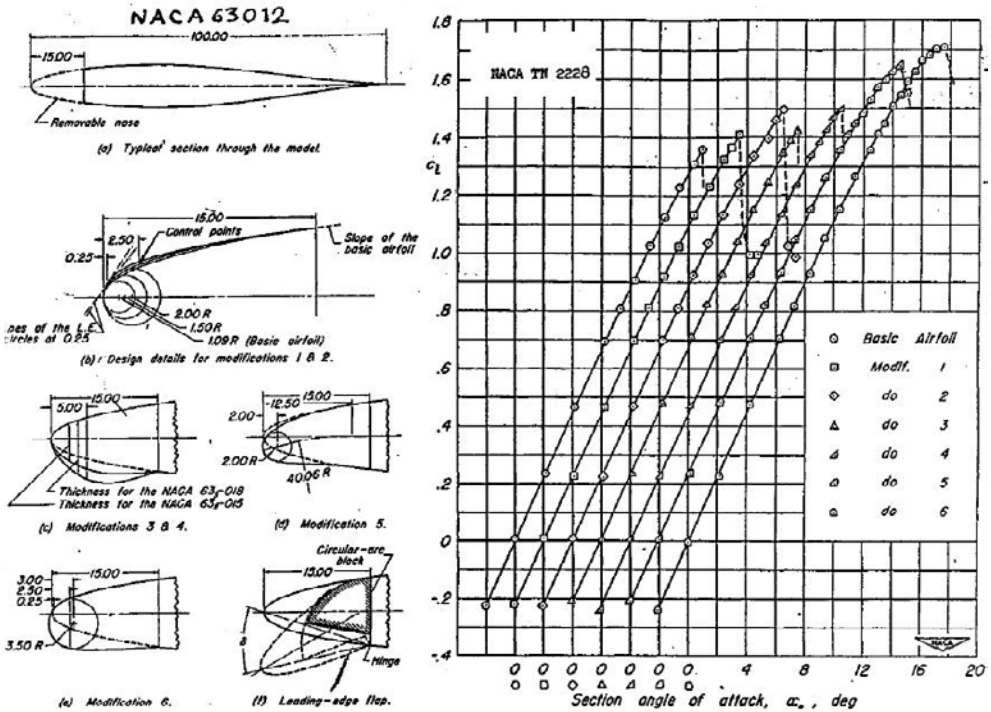
Figure 19.17 - Geometry of the model and the effect of various leading-edge modifications on the section lift characteristics. Source: NACA TN 2228

Note that the main parameter that affects the maximum lift coefficient while keeping the upper surface constant is the leading-edge radius. The shape of the lower surface of the section behind the leading-edge has no effect on the maximum lift coefficient. This is shown in figure 19.17 where modifications 1 and 3 show the same maximum lift coefficient as do modifications 2 and 4 although their lower surfaces are shaped differently.

A slight modification of the curvature distribution of the forward upper surface such that the change in curvature behind the region determined by the leading-edge radius becomes more gradual may increase the maximum lift coefficient. This is illustrated by comparing the test results from the modifications Airfoil 1 and Airfoil 2 in figure19.16 and modifications 2 and 5 in figure 19.17. Also figure 19.18 shows an improvement in maximum lift due to such a modification when compared with the basic section.

The latter figure shows again however that an increase in leading-edge radius is far more effective . The maximum lift coefficient can in this case be increased from $c_{l,max}$ = 1.1 to 1.5.

Modifying the upper surface curvature distribution should however not be considered for high-speed supercritical sections as this may lead to deterioration of high speed characteristics.
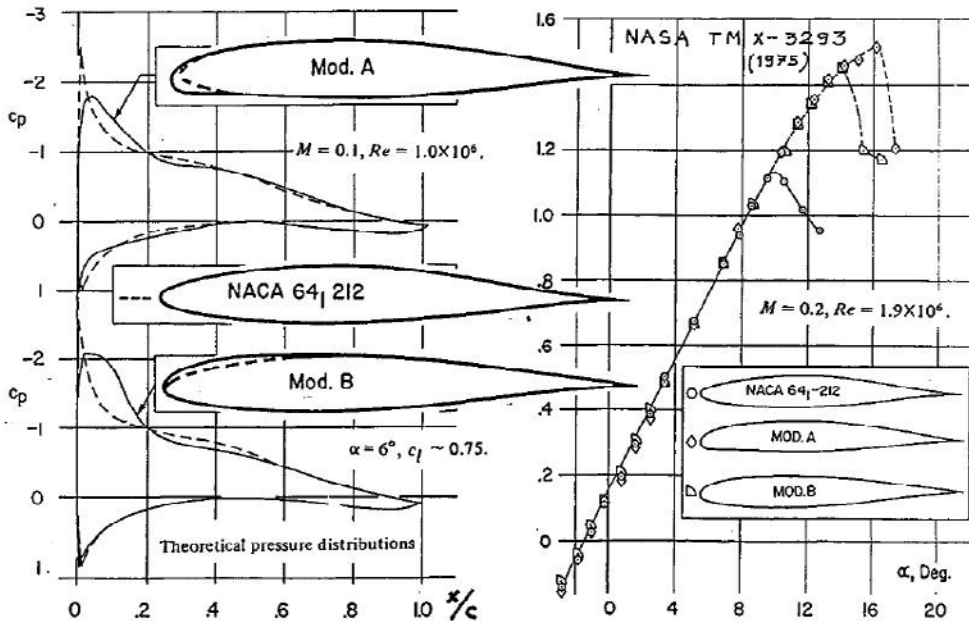
Figure 19.18 - Effect of airfoil modifications on pressure distribution and lift curve.
Source: NACA TMX-3293, 1975

The Fokker 100

 When the full-scale development of the Fokker 100 was started it was decided (based on earlier studies) that, in terms of geometry, the wing torsion box would be maintained and that modifications would be limited to leading-edge and trailing-edge regions and tip extensions, see figure 19.19. The leading-edge modifications were intended to achieve lower cruise drag and higher maximum lift coefficients.

In order to increase the maximum lift coefficient but also to assure good stalling characteristics the leading-edge radius in the outer wing in the first instance was chosen too large. This led to large suction peaks on the lower surface of the outer wing immediately behind the leading-edge (see figure 19.20) resulting in a large drag increase in cruise at low lift coefficients. A small decrease in leading-edge radius led to a considerable improvement in drag characteristics (see figure 19.21).

With the aid of the principles outlined in this chapter a trimmed low-speed maximum lift coefficient for the Fokker 100 with flaps retracted was achieved $C_{Lmax,1g} = 1.72$ compared to $C_{Lmax,1g} = 1.50$ for the Fokker F-28.
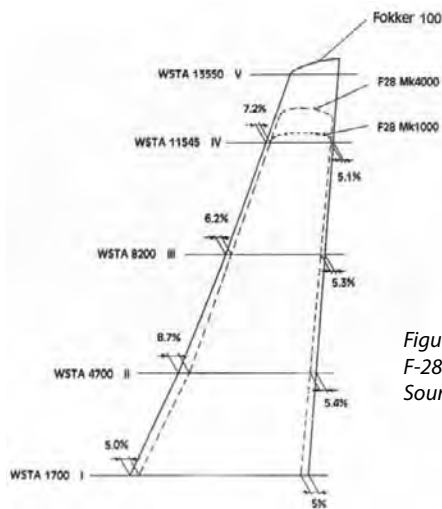
Figure 19.19 - Comparison between F-28 and Fokker 100 wing geometry. Source: ICAS-88-6.1.2.
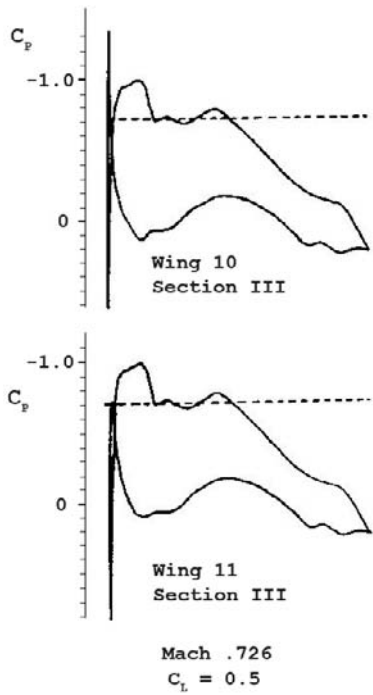
Figure 19.20 - Effect of blunt leading-edge on the lower-surface leading-edge suction peak. Source: ICAS-88-6.1.2.
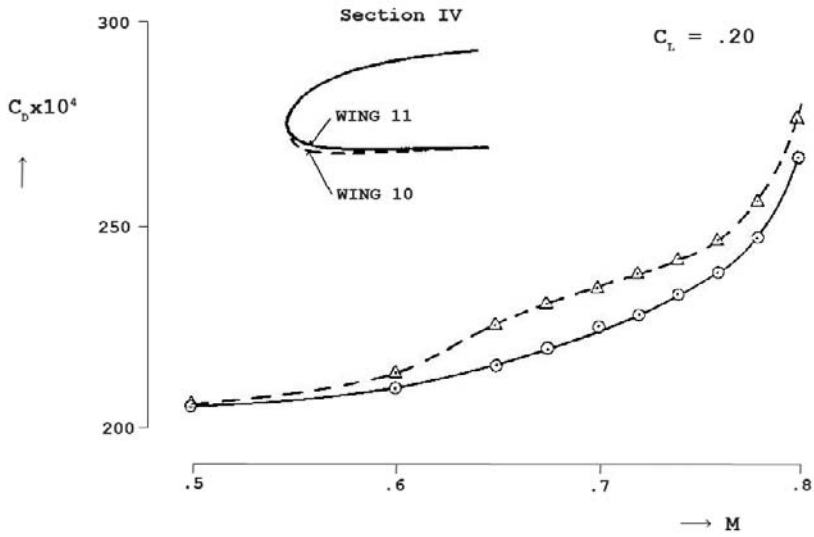
Figure 19.21 - Effect of blunt leading-edge on the Mach drag rise at low lift coefficient.
Source: ICAS-88-6.1.2.

PART 4

SWEPT WINGS

20 *The development of the swept-wing concept*

In the previous chapters two-dimensional lift- generating bodies have been dealt with. This chapter discusses three-dimensional lift-generation bodies: wings, and in particular the concept of swept wings, a concept introduced by German scientists.

Historical background

In 1935 at the Volta Conference in Rome entitled "High Velocities in Aviation" all Western countries that would be involved in the Second World War exchanged new ideas concerning high speed flight. Busemann, a German aerodynamicist, proposed the concept of the swept wing for supersonic flight. As the means of propulsion for supersonic flight were not yet available the qualities of the swept wing were not considered at that time, also because the means to verify the concept experimentally (sufficiently large wind tunnels) did not exist yet. The use of swept wings for high subsonic speeds was contemplated by Busemann but the first wind tunnel tests on a swept wing model were performed by Betz and Ludwieg in December 1939 in a new wind tunnel with a test section measuring 11 x 11 cm. This first swept wing model had a span b = 5.65 cm and the tests were performed at Re = 0.42x10^6. In 1941 a test section with a diameter d = 22 cm became available. Only in 1943 did sufficiently large high-speed wind tunnels come into use to produce credible data.
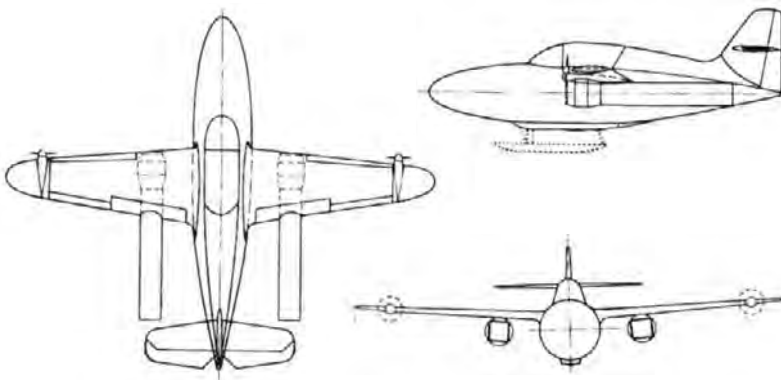
Figure 20.1 - Messerschmitt 328b

It took some time before the German designers applied sweep to their aircraft. This is illustrated by the many high speed airplanes with straight wings as can be seen in figures 20.1 to 20.5. It took even more time before swept wings were applied to aircraft in other countries: the Gloster Meteor, the Bell XP-59 Aircomet and the Lockheed XP-80 Shooting Star are examples of high-speed aircraft without swept wings, see figures 20.6 to 20.8. The preliminary design sketches of the De Havilland Comet in figure 20.9 show that the design started with a straight wing, but after the designers had received information from Germany after the war the wing was swept.
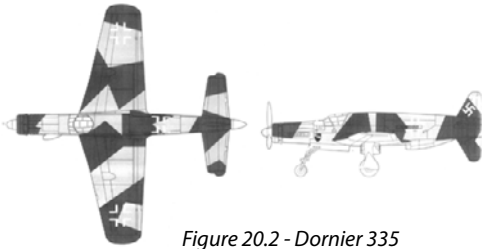
Figure 20.2 - Dornier 335

Figure 20.3 - Heinkel 178, the first jet-powered airplane in the world
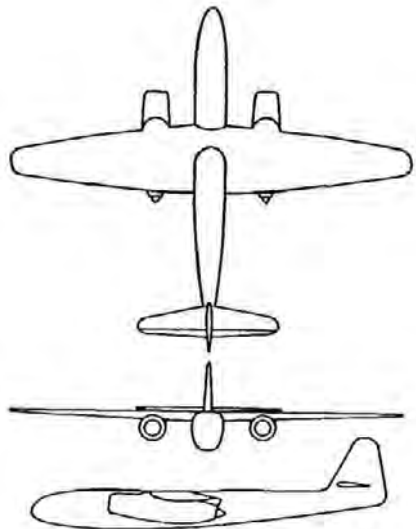
Arado Ar 234
Root aerofoil : 1.267 20 13 – 1.1 – 35
Tip aerofoil :   1.227 20 10 – 1.1 – 30

Figure 20.4 - Arado 234.
Source: Interavia January 1948

Figure 20.5 - Heinkel 162

Figure 20.6 - Gloster Meteor and DeHavilland Vampire

Figure 20.7 - Bell XP-59 Aircomet.
Source: Smithsonian Institution

Figure 20.8 - Lockheed XP-80 Shooting Star. Source: US Air Force
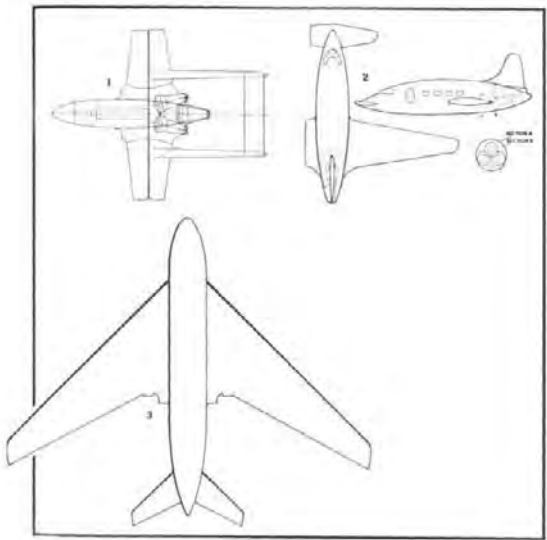
Figure 20.9 - DeHavilland Comet preliminary design

Messerschmitt Me 262
Root aerofoil : 0 00 12 – 0.625 – 40
Tip aerofoil :   0 00 12 – 0.625 – 40
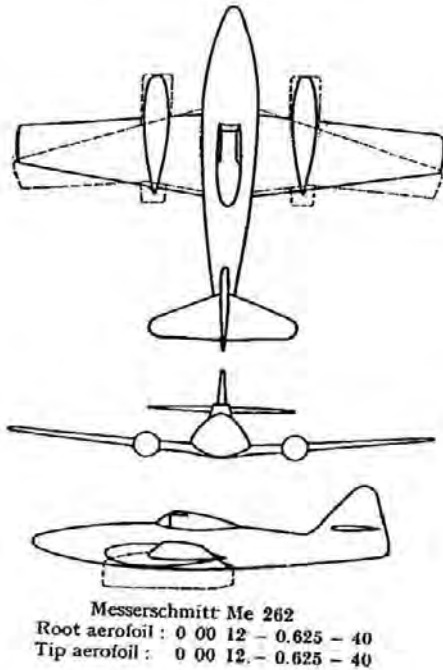
Figure 20.10 - Messerschmitt 262 with the original wing and the final wing. Source: Interavia January 1948
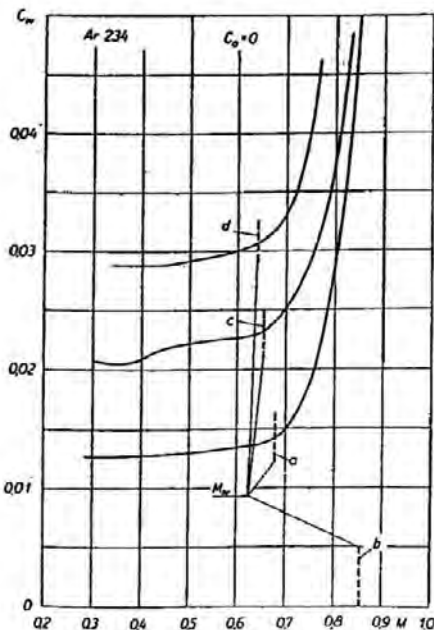
Figure 20.11 - Ar-234, drag coefficient versus Mach number for a) wing alone, c) entire model without nacelles, d) entire model. b) Critical Mach number of fuselage. Source: Interavia January 1948
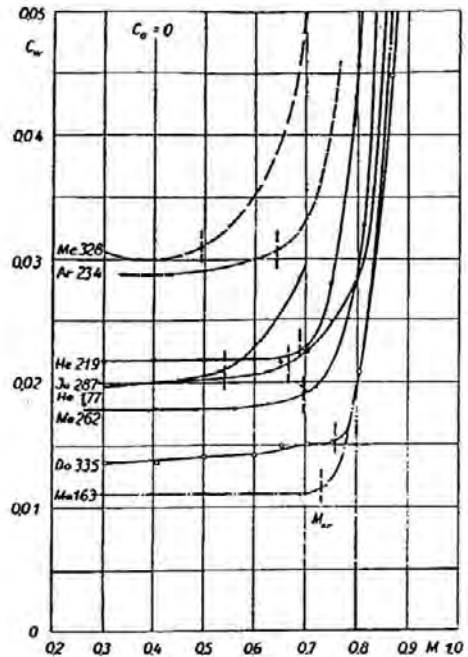
Figure 20.12 - Drag versus Mach number diagram for a number of German airplanes from 1942 to 1943. Source: Interavia January 1948

The first high-speed airplane with swept wings had wing sweep applied not to reduce drag. Due to a miscalculation of the centre-of-gravity position the position of the aerodynamic centre had to be redefined. In order to limit the required redesign work the wings were slightly swept backwards moving the centre-of-lift closer to the centre-of-gravity. This aircraft became the Messerschmitt Me 262 "Schwalbe" of figure 20.10.

Figure 20.12 shows that a number of German World War II aircraft were flying at speeds higher than M = 0.7 which is close to the airspeeds of most airliners today.

The principle of wing sweep

In this section the basic theoretical principle behind the concept of the swept wing is explained. It is a theoretical explanation, it holds only for an infinitely long, sheared wing without viscous or three-dimensional effects.
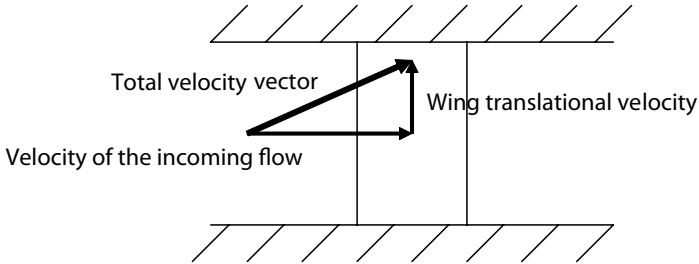
Figure 20.13 - Wing placed in a two-dimensional wind tunnel

Imagine an infinitely long wing placed in a wind tunnel and being translated with a certain speed perpendicular to the incoming flow. This results in a total free-stream velocity experienced by the wing as shown in figure 20.13. The pressure distribution however does not change due to the translation because the airflow only experiences the curvature of the wing surface in the direction of the incoming flow. The velocity component perpendicular to the wind tunnel walls does not experience any curvature and will therefore not contribute to the pressure distribution.

Now the same airfoil as used for the translating wing experiment is put in an oblique position in a wind tunnel, as sketched in figure 20.14. The total free-stream velocity of the translating wing can also be produced for the slanted wing. The only velocity vector that determines the pressure distribution over the airfoil is the component V_e perpendicular to the leading and trailing edges. The velocity component parallel to the oblique wing, V_{par}, does not experience any curvature. Note that the above only applies for airfoils with a sufficiently large span-to-chord ratio as close to the tunnel walls this simplified flow picture can not be maintained.
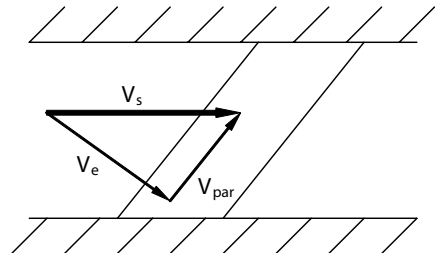
Figure 20.14 - Wing placed obliquely across a two-dimensional wind tunnel
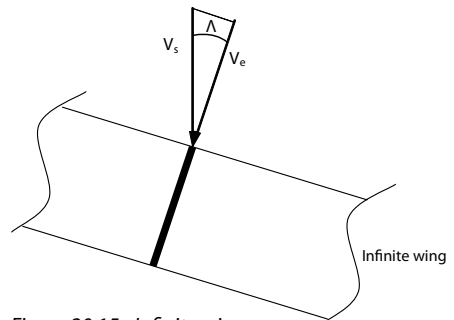
Figure 20.15 - Infinite wing

The same reasoning can be applied to an infinite sheared wing subject to a free-stream velocity V_s. To compute the aerodynamic forces on the section shown in figure 20.15 the velocity component perpendicular to the wing leading-edge must be considered.

The main reason for applying wing sweep is to increase the drag rise Mach number. But wing sweep also affects other aerodynamic parameters such as the lift curve slope.

In the foregoing the pressure distribution was considered in a plane perpendicular to the leading edge. However, the lift coefficient is usually defined in terms of the free-stream velocity. So the lift coefficient must be converted into a coefficient based on the free-stream velocity. This results in the following wing sweep relationships:

$$M_e = M_s \cos \Lambda \tag{20.1}$$

$$C_{P_e} = C_{P_s} / \cos^2 \Lambda \tag{20.2}$$

$$C_{L_e} = C_{L_s} / \cos^2 \Lambda \tag{20.3}$$

$$\alpha_e = \alpha_s / \cos \Lambda \tag{20.4}$$

$$\left(\frac{Z}{C} \right)_e = \left(\frac{Z}{C} \right)_s / \cos \Lambda \tag{20.5}$$

Where   e = effective

       S = streamwise, in the flight direction

       Λ = the sweep angle

From the relation between the effective and the streamwise lift coefficients (equation 20.3) it can be concluded that the lift coefficient based on the free-stream velocity will decrease if wing sweep is applied. This means that high-speed aircraft with highly swept wings require more attention to their performance in the low-speed regime than aircraft with straight wings because their maximum lift coefficient is lower. As a consequence a swept-wing aircraft will often require effective high-lift devices in order to show satisfactory take-off and landing performance.

Figure 20.16 shows the pressure distribution at the mid section of a wing that is placed obliquely at different sweep angles in a two-dimensional windtunnel such as given in figure 20.14. These pressure distributions have been converted with the sweep relations of equations 20.1 to 20.5. The converted pressure coefficients almost coincide which proves the principle of wing sweep described above.
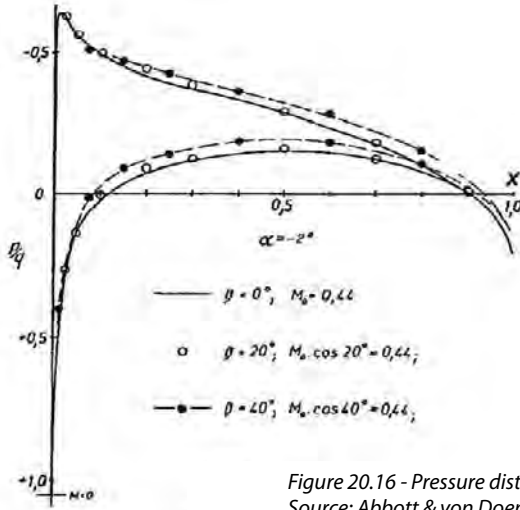
Figure 20.16 - Pressure distributions of obliquely placed wings.
Source: Abbott & von Doenhoff, Theory of Wing Sections

Wing taper

Figure 20.17 shows lines of constant chord percentage for a tapered, swept wing. To calculate the lift at each chord percentage the velocity component along the chord line should be defined and an integration should then be performed. This procedure, however, is unnecessarily complicated for most calculations. In practice the velocity component perpendicular to the quarter chord line with sweep angle Λ can be used. Only on highly-swept and highly–tapered wings this effect is noticible (see figure 20.18).
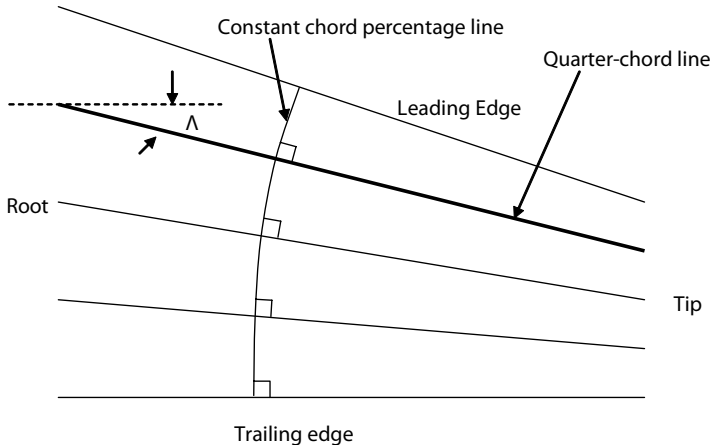
Figure 20.17 - Tapered swept wing, schematic
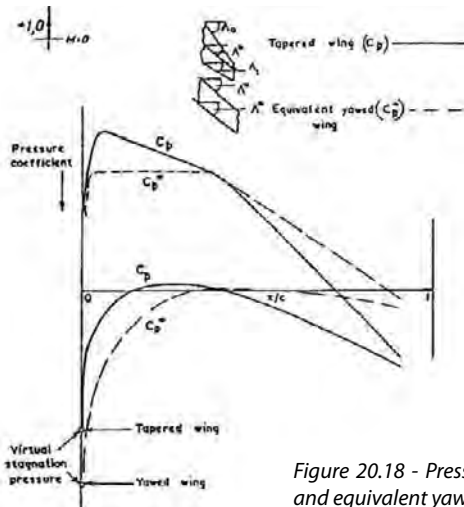
Figure 20.18 - Pressure distribution for a tapered wing and equivalent yawed wing. Source: ARC R&M 3346

Streamline curving

Consider a non-tapered swept wing in an undisturbed flow and the components of the velocity perpendicular V_e and parallel V_p to the leading edge as indicated in figure 20.19.

Because of the surface curvature and the angle-of attack, on the top surface of the wing the flow is accelerated and the velocity component V_e increases (middle of figure 20.19). This leads to curving inboard of the total local velocity vector. At the stagnation point there is only a velocity component parallel to the leading edge, the velocity component V_e is zero there. This causes a flow outboard.

Combining these two observations, the following can be stated: The flow from infinity will initially move outboard at the stagnation point. Following the contour along the top surface, the flow will experience an acceleration inboard which reduces along the chord. Figure 20.20 shows what the streamlines will look like on the top surface, outside the boundary layer.

A similar reasoning applies for the lower surface. Here the velocity vector V_e is decreased resulting in curving outboard of the streamlines. This is shown in figure 20.20 on the right side.

Note that this is valid for potential flow, without viscous effects, the boundary layer is not included. For a wing with forward sweep the situation is reversed, on the top surface streamlines will curve outboard and inboard on the lower surface.
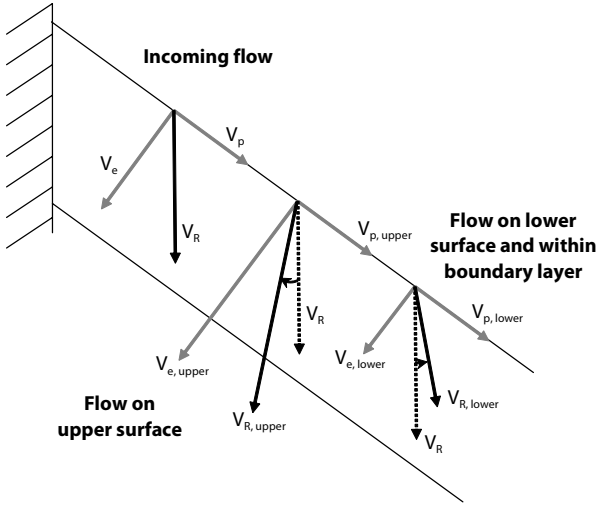
Figure 20.19 - Velocity components on the upper and lower surface of a swept wing
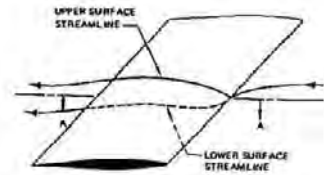
Figure 20.20 - Streamlines on a swept wing. Source: AGARD CP-285-27

Effect of a flat vertical surface

When a flat vertical surface is placed at the leading edge of a swept wing such as an engine pylon or a boundary layer fence a complicated flow condition arises. Free flow curvature is no longer possible and near the vertical surface the flow will follow the vertical surface wall. On the inboard side the flow situation will resemble the flow near the root of a swept-forward wing and on the outboard side the flow near the root of a swept-back wing. On the inboard side this will slightly increase the lift and on the outboard side the lift will slightly be decreased (see figure 20.21). This phenomenon is discussed more in detail at the end of this chapter and in chapter 22 .
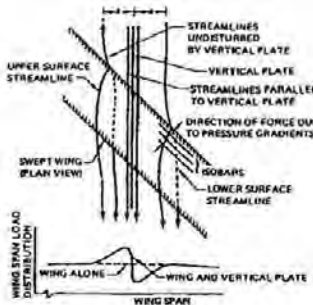
Figure 20.21 - Effect of a vertical plate on the flow field of a swept wing. Source: AGARD CP-285-27

The boundary layer

In the boundary layer the velocity component $V_e = 0$ at the wing surface. Consequently the velocity component V_p will force the boundary layer on a swept wing outboard as shown in figure 20.22. As a result of this outward flow the boundary layer on the inboard wing is thinner than on the comparable straight wing. On the outer wing near the tip concentration of boundary layer material occurs. Thus the boundary layer is thicker in this region than on the comparable straight wing. This phenomenon, together with the often observed low maximum lift coefficients combined with strong pitch-up tendencies on highly swept wings, may suggest that these unfavourable aerodynamic characteristics occur because the flow near the tip separates earlier than would be expected based on the airfoil section characteristics.

In the following the flow over two swept wings with sweep angle $\Lambda = 45$ deg is considered. One is a plain wing with the symmetrical section NACA 64A010 perpendicular to the quarter-chord line, the other one is twisted and uses the highly cambered airfoil section NACA 64A810 as shown in figure 20.24. Figure 20.23 shows the lift curves for both sections. Note that $c_{l,max} = 1.10$ and 1.68 respectively. Lift, drag and pitching moment coefficients for the two wings are presented in figure 20.25.

According to equation 20.3 the maximum lift coefficient of a wing section perpendicular to the quarter-chord line is converted into the streamwise maximum lift coefficient as follows:

$c_{l_{s,max}} = c_{l_{e,max}} \cdot \cos^2\Lambda_{1/4c}$. Table 20.1 presents an overview of the various maximum lift values.
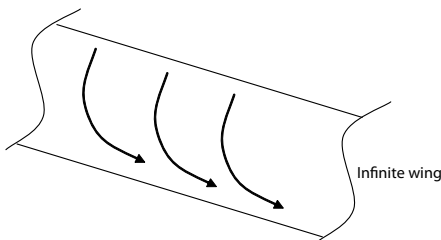
Figure 20.22 - Curving of the streamlines in the boundary layer on a swept wing
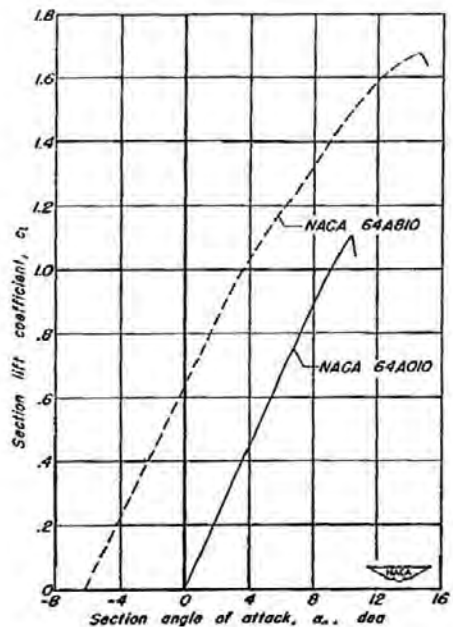
Figure 20.23 - Lift characteristics of two airfoil section models. Source: NACA RM A52A10

	2-D airfoil		3-D airfoil	
	$c_{l_{max}}$	$c_{l_{max}}.\cos^2\Lambda_{1/4c}$	$C_{L_{max}}$	Usable $C_{L_{max}}$
Plain wing	1.10	0.55	0.95	0.70
Cambered wing	1.68	0.84	1.10	0.95

Table 20.1 - 2-D and 3-D maximum lift coefficient
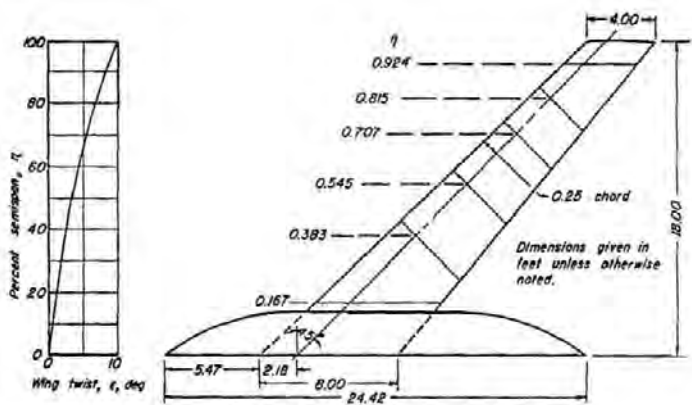
Figure 20.24 - Dimensions of the semispan wing-fuselage models including the orifice station locations and the twist distribution for the cambered, twisted wing. Source: NACA RM A52A10
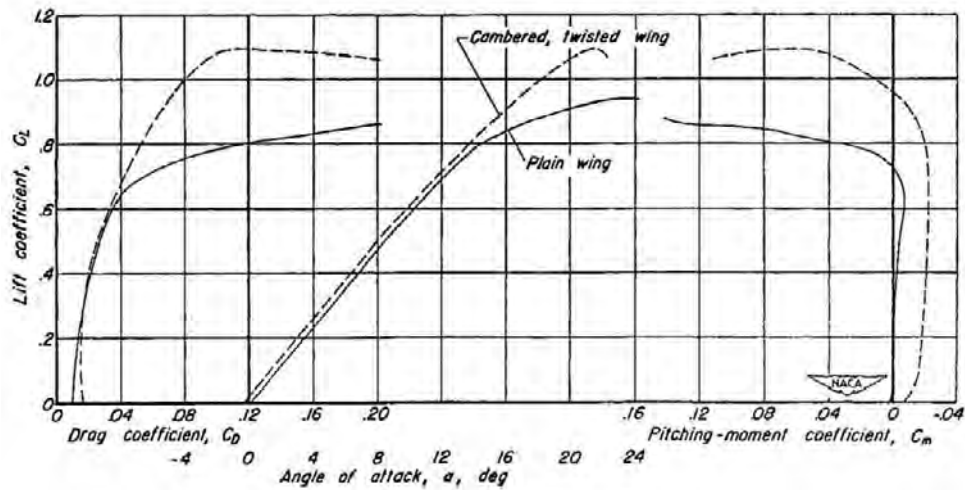
Figure 20.25 - Drag, lift and pitching moment characteristics of the two wing models. Source: NACA RM A52A10

Figure 20.26 shows the lift coefficient at the six wing stations of figure 20.24 for the plain wing. To the left in the figure the airfoil section lift curve of figure 20.23 is given but converted to the situation on an infinitely long wing with 45 deg sweepback.

Note that at the tip the local lift curve is almost identical to the converted section lift curve including the maximum lift coefficient. The identical lift curve gradients illustrate again the validity of the wing sweepback principle. The almost identical local maximum lift coefficients suggest that near the wing tip the thick boundary layer due to the cross flow has no noticible effect on flow separation.

Elementary swept-wing theory:

$$C_{l_\Lambda} = C_{l_{\Lambda=0}} \times \cos^2\Lambda$$
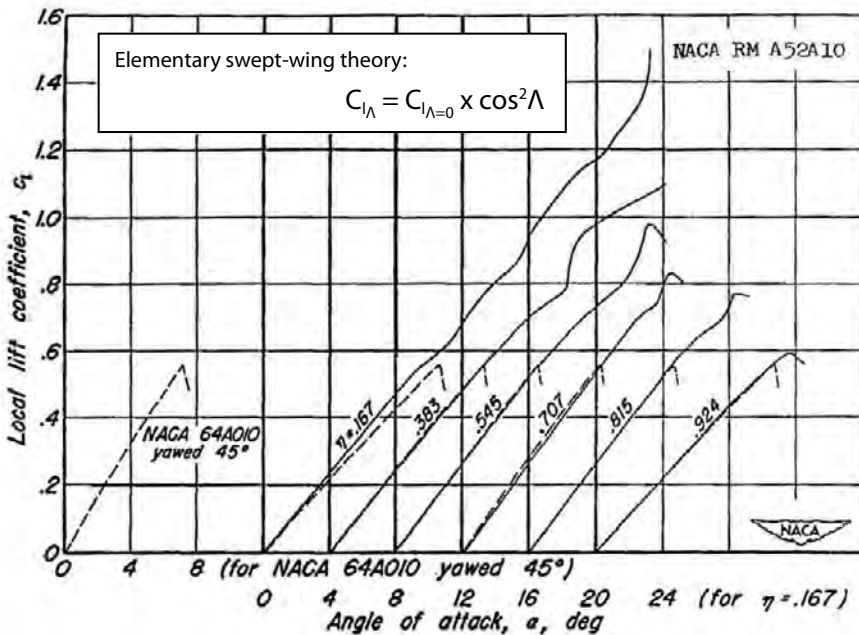
Figure 20.26 - Comparisons of local lift curves on the wing model with those derived from two-dimensional data for a plain wing. Source: NACA RM A52A10

On the inboard wing the boundary layer is thinner than would be found on a straight wing due to the cross flow. This leads to very high local maximum lift coefficients as shown in figure 20.26. No use can be made of this high-lift capability however because the flow separation near the wing tip ,which usually does not occur symmetrically, causes both pitch-up and a roll-off . The pitch-up tendency is clearly demonstrated by the sudden increase in the pitching moment coefficient at $C_L = 0.7$ in figure 20.25. Such characteristics are, unless very mild, unacceptable from a stability-and-control and certification point-of-view.

Figure 20.27 shows similar characteristics fot the cambered and twisted wing.

From the above it will be clear that the application of wing sweepback will in general lead to a decrease in the usable maximum lift coefficient compared to an equivalent straight wing as can also be concluded from the data presented in table 20.1.
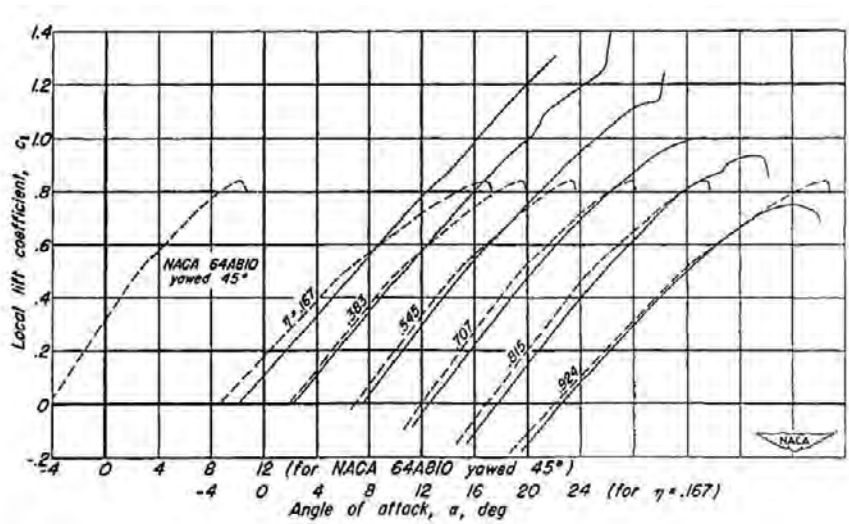
Figure 20.27 - Comparisons of local lift curves on the wing model with those derived from two-dimensional data for a cambered, twisted wing. Source: NACA RM A52A10
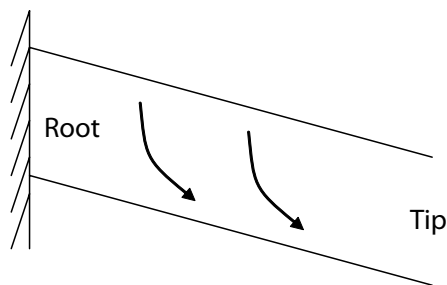
Figure 20.28 - The boundary layer moves outboard

In figures 20.29 and 20.30 the local maximum lift coefficient along the span is shown for both wings indicating again that the lifting capability of the outer wing near the tip resembles that of the infinitely long yawed wing.

The highly cambered wing shows trailing-edge flow separation well before the local maximum lift is reached. Near the wing tip this occurs again at lift coefficients comparable to the lift coefficient on the infinitely long yawed wing.

This investigation shows that the usable maximum lift of a swept wing is in accordance with the basic swept wing principles. However the boundary layer cross-flow produces unfavourable stability-and-control caracteristics.
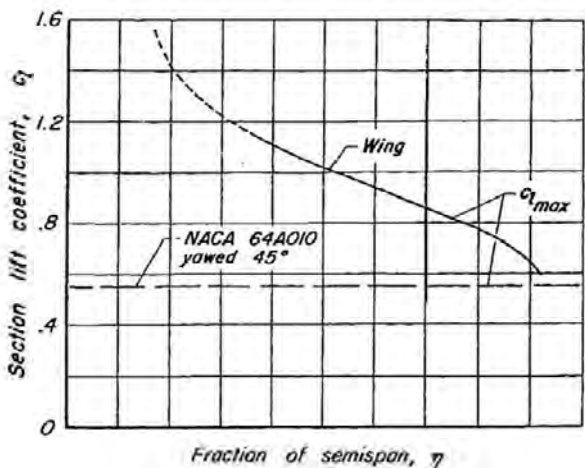
Figure 20.29 - Spanwise variation of the local lift coefficient for stall on the wing model with a plain wing. Source: NACA RM A52A10
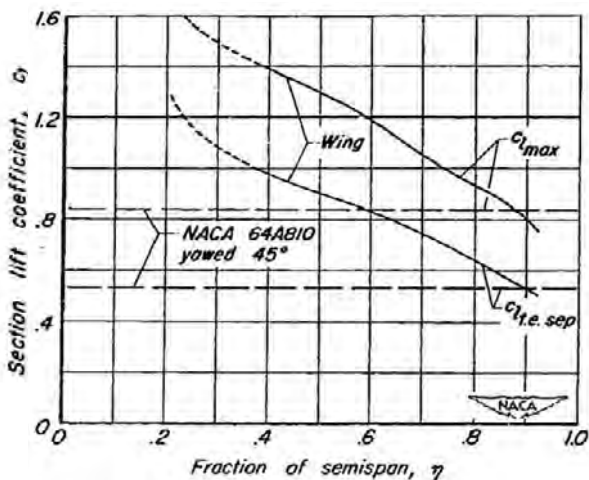
Figure 20.30 - Spanwise variation of the local lift coefficient for trailing-edge separation and for stall on the wing model with a cambered, twisted wing. Source: NACA RM A52A10

Transonic flow characteristics of swept wings

Figures 20.31 to 20.33 show airfoil section NACA 64A010 and lift and drag curves for this section. The drag rise occurs at $M = 0.80$ when $c_l = 0$ and at $M = 0.76$ when $c_l = 0.3$. In figure 20.34 estimated and measured drag curves are presented for two swept wings and two wing-fuselage combinations based on this wing section. The estimated drag curves were obtained with the equations 20.1 to 20.5. According to simple sweep theory the drag rise Mach number would increase to $M = 1.15$ and $M = 1.05$ for a wing sweep angle $\Lambda = 45$ deg and $C_L = 0$ and 0.3 respectively. The windtunnel test data however show an improvement only about half the difference between the estimated drag rise Mach number and the section drag rise Mach number.
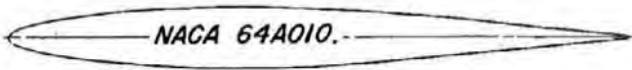
Figure 20.31 - NACA 64A010 airfoil.
Source: NACA RM A9E31
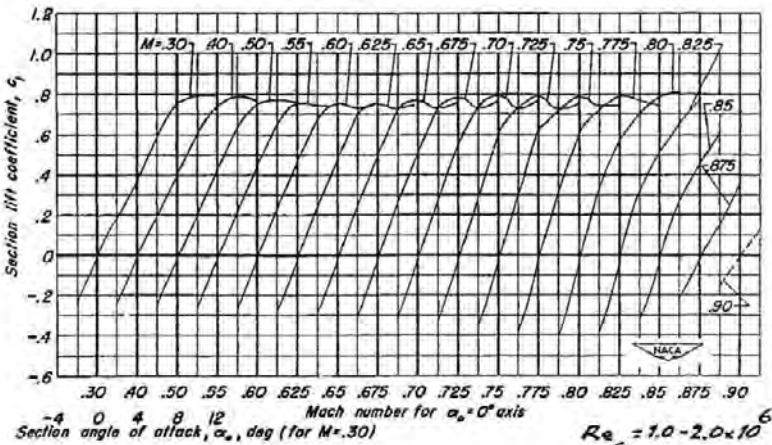
Figure 20.32 - The variation of section lift coefficient with angle of attack at various Mach numbers. Source: NACA RM A9E31
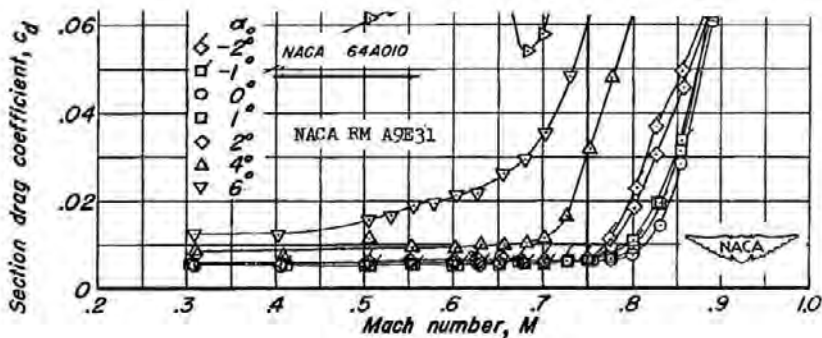
Figure 20.33 - The variation of section drag coefficient. Source: NACA RM A9E31

Figure 20.34 - Drag characteristics of swept wings. Section NACA 64A010 perpendicular to the quarter-chord line. Source: NACA RM A55C23

Figure 20.35 - Dimensions of the model and locations of the pressure orifices. Source: NACA RM A55C08

Figure 20.35 shows the geometry of the wing-fuselage combination with wing 24 mentioned in figure 20.24. In figures 20.36 to 20.38 chordwise pressure distributions for five wing stations and upper suface isobar patterns are presented for M = 0.70, 0.85 and 0.95 and C_N = 0.2. At M = 0.70 experimental data and data calculated with the simple sweep theory compare very well for the larger part of the wing. At the wing root however the pressures are higher over the forward part of the section and lower over the rear part. The reverse occurs at the wing tip. This causes a rearward curving of the upper surface isobars near the wing root and a forward curving at the wing tip. With increasing Mach number and/or angle-of-attack these effects become stronger.
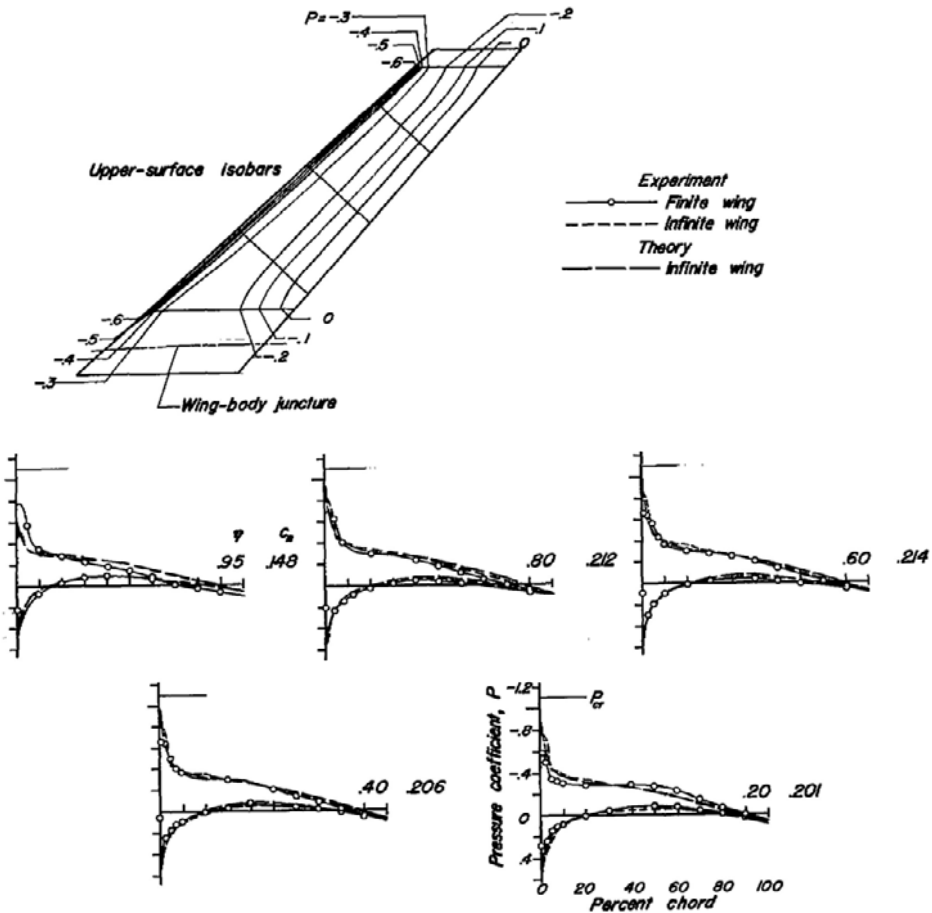
Figure 20.36 - Comparisons of experimental pressure distributions for five semispan stations with those for the NACA 64A010 section yawed 45° as derived from two-dimensional data and theory, plus experimental upper-surface isobars. M = 0.70, C_N = 0.203 and a = 3.26°.
Source: NACA RM A55C08
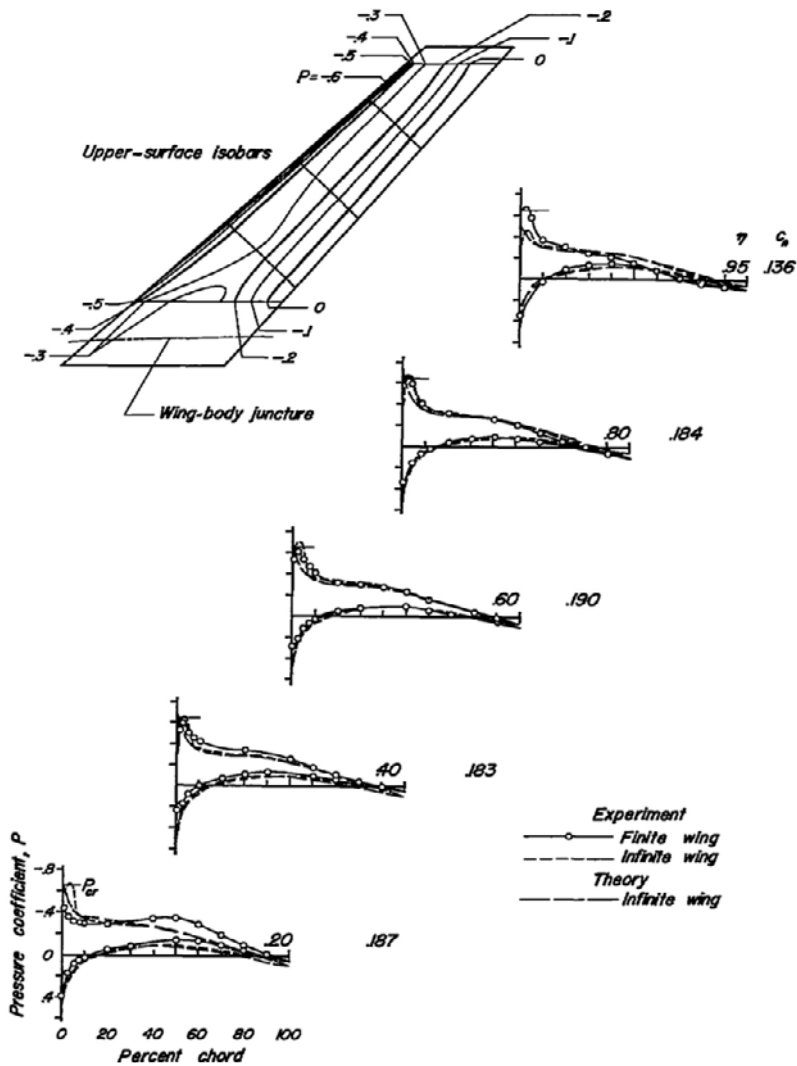
Figure 20.37 - Comparisons of experimental pressure distributions for five semispan stations with those for the NACA 64A010 section yawed 45° as derived from two-dimensional data and theory, plus experimental upper-surface isobars. M = 0.85, C_N = 0.184 and α = 2.29°. Source: NACA RM A55C08

In particular near the wing root the pressure distribution deviates increasingly from the prediction according to simple sweep theory. The increasing supervelocities over the aft part of the wing root region may lead to the formation of shock waves and flow separation. These may then spread further outboard (figure 20.39) and lead to a sharp drag rise much earlier than would be expected from simple sweep theory as shown in figure 20.34. A further illustration of root and tip effects on swept wings is presented in figure 20.40.
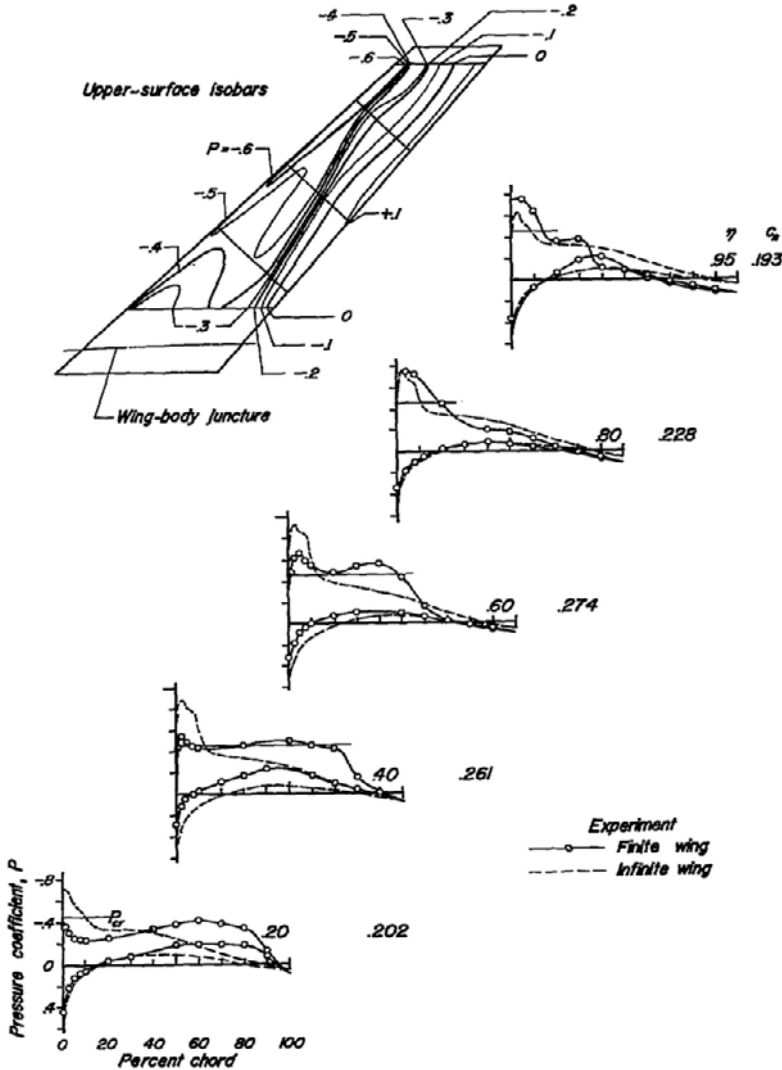
Figure 20.38 - Comparisons of experimental pressure distributions for five semispan stations with those for the NACA 64A010 section yawed 45° as derived from two-dimensional data and theory, plus upper-surface isobars. M = 0.95, C_N = 0.231 and α = 2.39°. Source: NACA RM A55C08

The flow development described previously occurs in particular on simple swept wings with constant or near-constant wing sections and constant fuselage cross sections. The latter prevents the curving of the streamlines as described in an earlier paragraph in this chapter. Root and tip effects on swept wings are discussed more in detail in chapter 22.
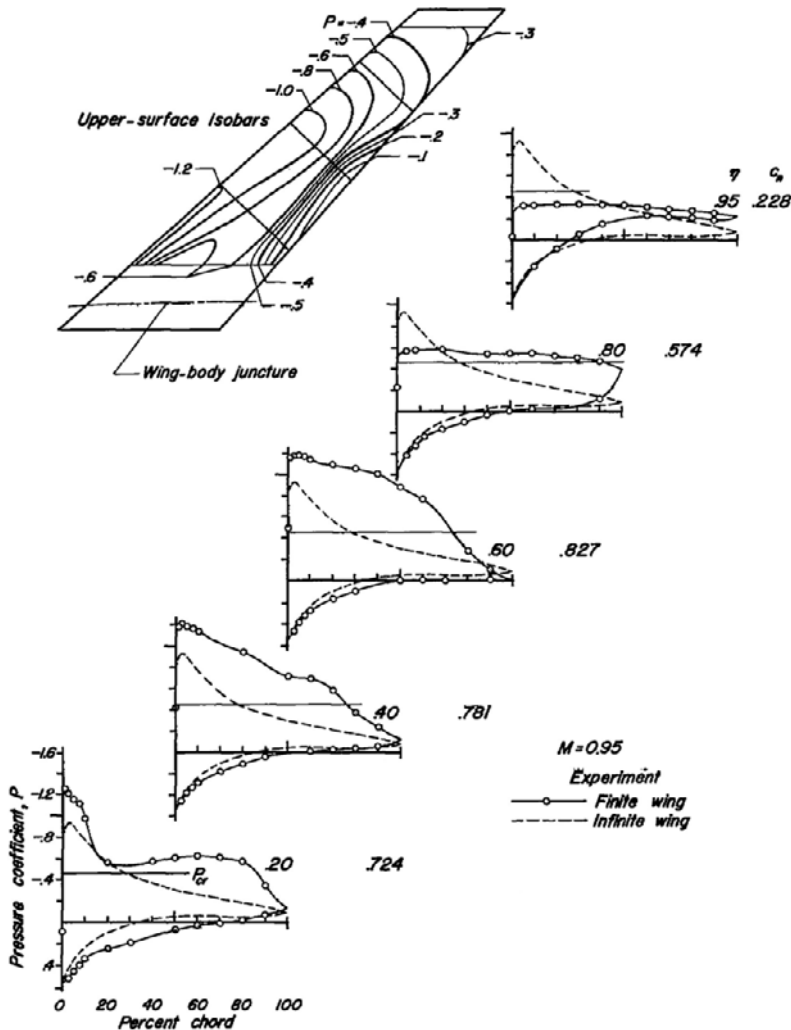
Figure 20.39 - Comparisons of experimental pressure distributions for five semispan stations with those for the NACA 64A010 section yawed 45° as derived from two-dimensional data and theory, plus upper-surface isobars. M = 0.95, C_N = 0.700 and α = 9.19°. Source: NACA RM A55C08
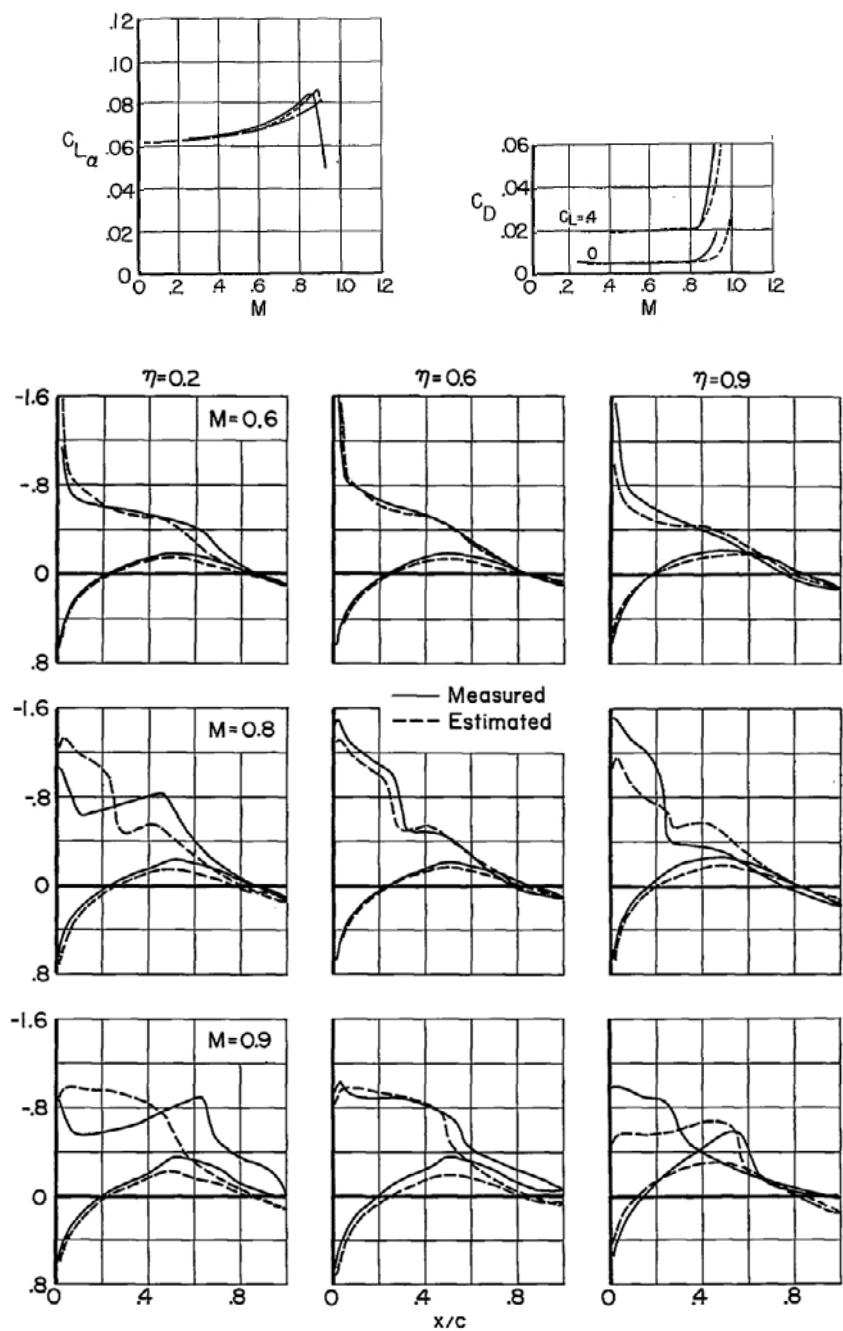
Figure 20.40 - Comparison of the estimated and measured pressure distributions for sections of a wing with a quarter-chord sweep of 35°. A = 5.1, λ = 0.71, α = 6°. NACA section definition: 65A012 II, used: 64A0(14.3). Source: NACA RM A55C23

For the same wing-fuselage combination, figure 20.41 shows that also at higher (but subcritical) Mach numbers the flow over the wing tip is in accordance with the simple wing sweep theory and the lifting capability of the inboard wing is much higher than theory predicts. At a Mach number (M = 0.95) where transonic flow conditions occur the section lift and pitching moment coefficients differ considerably from predictions based on simple sweep theory and this theory looses all meaning as shown in figure 20.42.
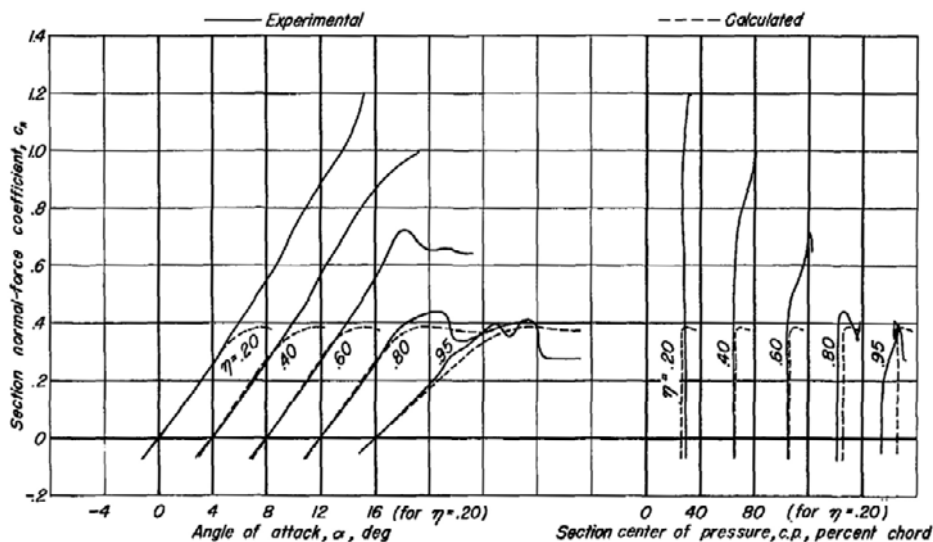
Figure 20.41 - Comparisons of the experimental section normal-force and center-of-pressure characteristics at Mach M = 0.70 with those calculated from two-dimensional data. Source: NACA RM A55C08
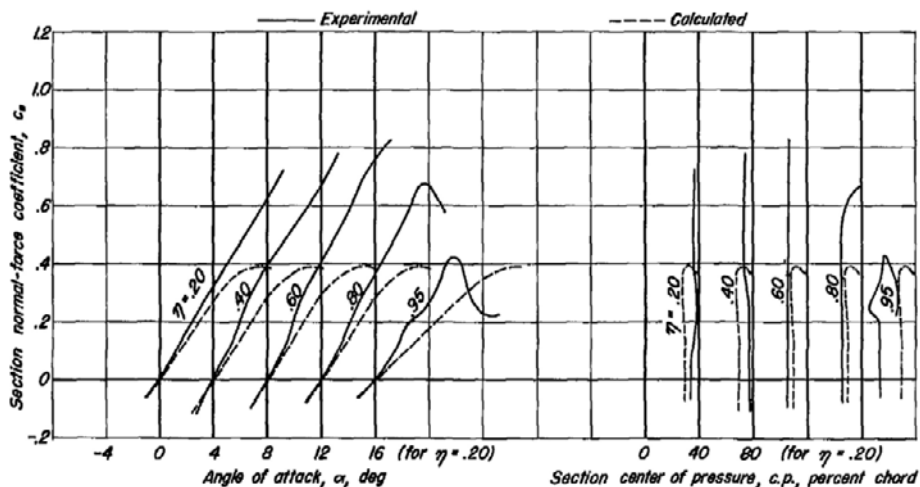
Figure 20.42 - Comparisons of the experimental section normal-force and center-of-pressure characteristics at Mach M = 0.95 with those calculated from two-dimensional data. Source: NACA RM A55C08

In chapter 19 it was explained that on low-cambered airfoil sections with small leading-edge radii boundary-layer transition takes place via a short transition bubble. On a highly-swept wing this transition bubble turns, for a certain range of Reynolds numbers at a given angle-of-attack into a leading-edge vortex, usually starting somewhere on the outer wing and slowly creeping inboard with increasing angle-of-attack. This vortex diminishes the leading-edge suction. The limiting case is a strong vortex completely eliminating the leading-edge suction force. The aerodynamic force on the wing will then be oriented perpendicular to the wing chord plane and the lift-dependent drag will be:

$$C_{D_i} = C_L \alpha = \frac{C_L^2}{C_{L_\alpha}} \tag{20.6}$$

as opposed to

$$C_{D_i} = \frac{C_L^2}{\pi A e} \tag{20.7}$$

as for wings with fully attached flow.

The drag curves in figure 20.43 show that on the wing considered the leading-edge vortex starts to develop at $C_L = 0.3$ and with increasing angle-of-attack grows in strength. Consequently above $C_L = 0.3$ the drag curve starts to deviate from the curve for fully attached flow and assumes the shape of the drag curve without leading-edge suction. This results in a large drag increase.

Although a leading-edge vortex usually also produces an increase in lift the higher lift curve gradient in figure 20.44 for the higher Mach numbers may also be caused by compressibility (Prandtl-Glauert) effects as shown in figure 20.40.
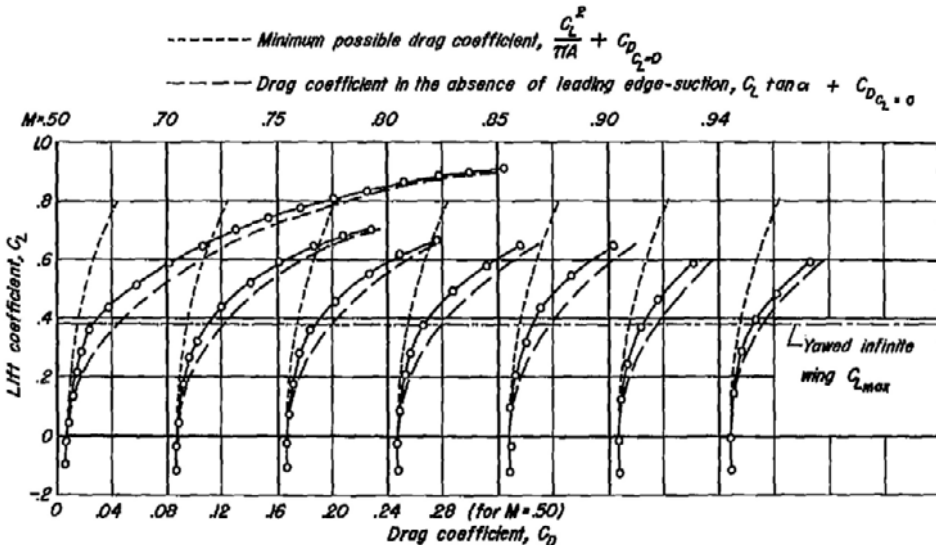
Figure 20.43 - Drag characteristics. Source: NACA RM A55C08

Figure 20.45 shows in combination with figures 20.41 and 20.42 that the angle-of-attack for tip stall and the resulting pitch-up also at high Mach numbers agrees with the prediction based on the simple wing sweep theory. Apparently the transition bubble burst coincides with the vortex burst. Although at the highest Mach numbers the large changes in pressure distribution cause an improvement in pitching characteristics roll-off due to tip stall will nevertheless occur at M = 0.95.

When the drag curves in figure 20.43 are compared with the drag curves in figure 20.25 it is evident that, although both figures refer to wings with the same sweep angle and use the same (symmetric sections), the latter indicates attached flow to much higher lift coefficients than figure 20.43. Apparently no leading-edge vortex was formed here. The explanation must be sought in the difference in test Reynolds numbers. The data in figure 20.24 were obtained at Re = 8.0 x 10^6 and in figure 20.43 at Re = 2.2 x 10^6.
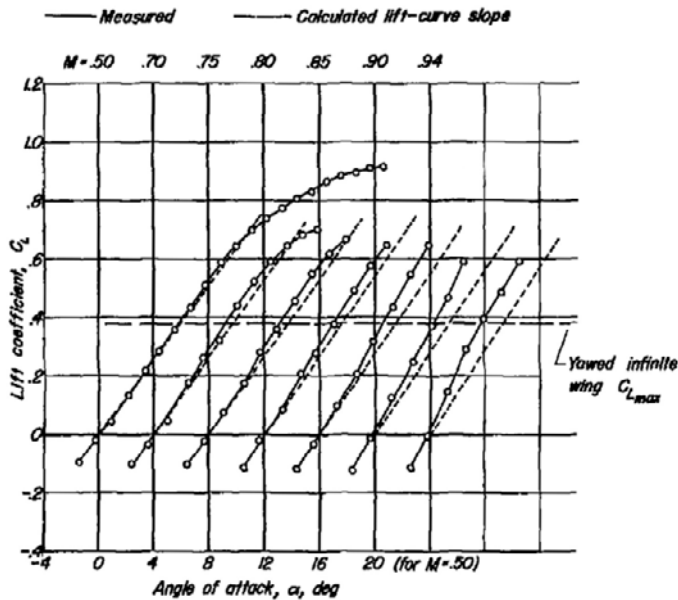
Figure 20.44 - Lift-curve slope of the wing-body combination from force-test measurements.
Source: NACA RM A55C08
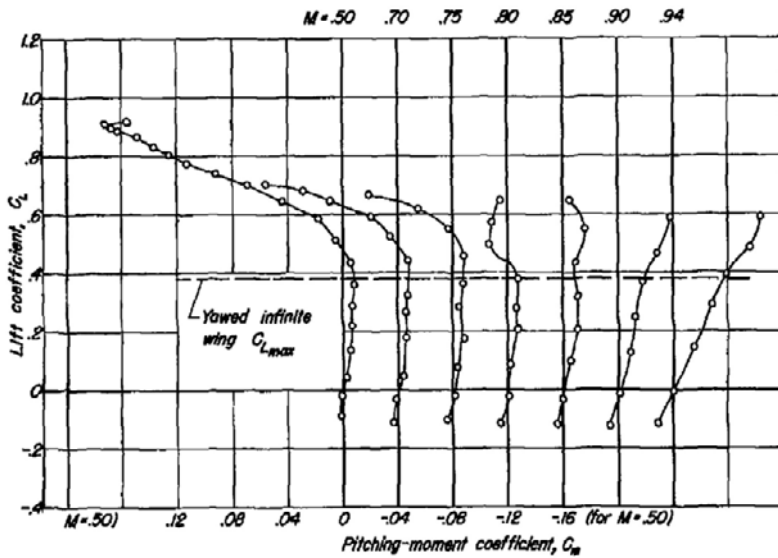
Figure 20.45 - Pitching moment coefficient versus lift coefficient of the wing-body combination from force-test measurements. Source: NACA RM A55C08

Fences

There are several ways of preventing tip stall on swept wings. Most measures, such as "shark" or "dog teeth" (local leading-edge extentions), "saw cuts" or leading-edge boundary layer fences create at high angles-of-attack a streamwise vortex such that the boundary-layer cross flow on the inboard wing is swept inboard thus relieving the boundary layer on the outer wing.

The oldest device for preventing tip stall is a vertical plate fitted on the wing upper surface in a streamwise direction thus forming a physical barrier for the boundary-layer crossflow, the full-chord fence.
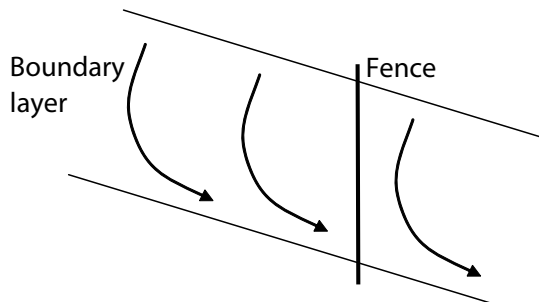
Figure 20.46 - Effect of a fence on the boundary layer
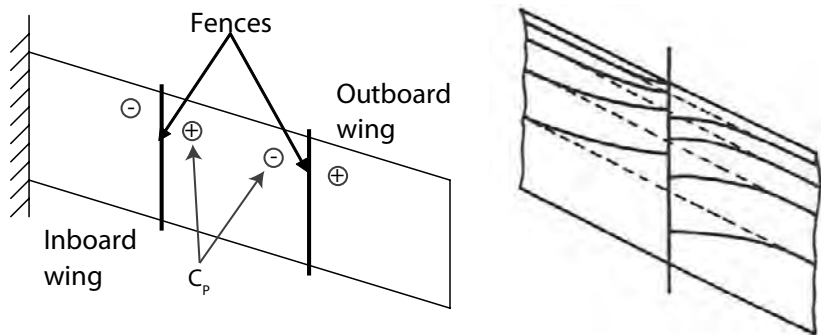
Figure 20.47 - Fences on a wing. Source: J. R. Ae. S. November 1953

Figure 20.46 shows a swept wing with the boundary layer flowing outboard. A fence placed on the wing creates on the upper surface near the leading-edge an increase in supervelocities inboard and a decrease outboard of the fence thus altering the shape of the isobars as illustrated on the right part of figure 20.47. The fence acts here as the fuselage wall on a swept-forward (on the inside) and a swept-back wing (on the outside) respectively (see chapter 22). The high inboard suction peak causes an early flow breakdown just inboard of the fence improving the flow over the outboard wing decreasing or eliminating the pitch-up and roll-off.

Optimizing the shape and spanwise position of a fence is done experimentally. No sufficiently accurate computational method exists. Sometimes more fences are required.
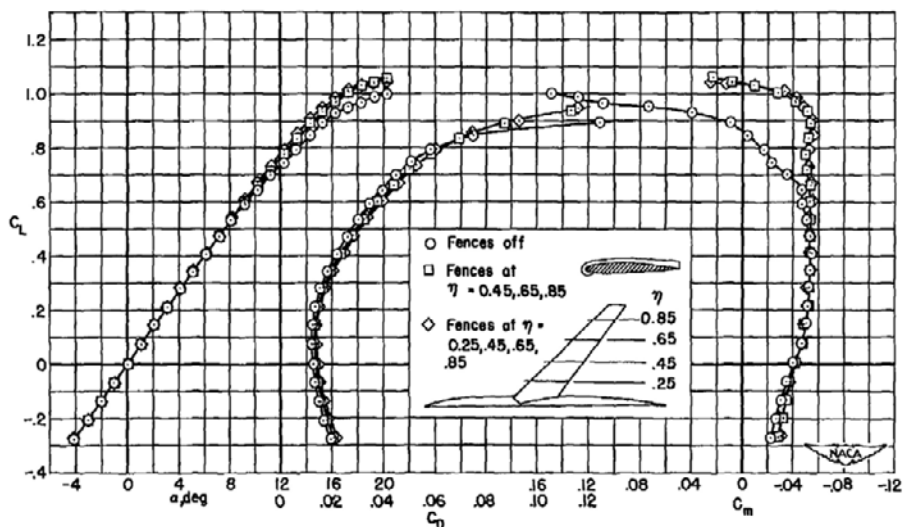
Figure 20.48 - The effect of three and four fences on the longitudinal characteristics of a wing-fuselage combination using a wing with 45° of sweepback and an aspect ratio of 6.03; M = 0.417; Re = 3,900,000. Source: NACA RM A54L08

Figures 20.48 to 20.50 present an example of the application of three and four fences on the wing-fuselage combination described in figure 20.51. Due to the fences the lift coefficient at which the pitch-up tendency starts and thus the maximum usable lift coefficient is increased considerably over the complete Mach number range investigated.

A disadvantage of wing fences is the increase in drag. Although their surface area may be small they may produce as much as 20 drag counts as in the configuration of figure 20.51. For this reason on modern aircraft wing fences are only applied when at a late stage in the development or during flight testing stalling characteristics are found to be unsatisfactory.
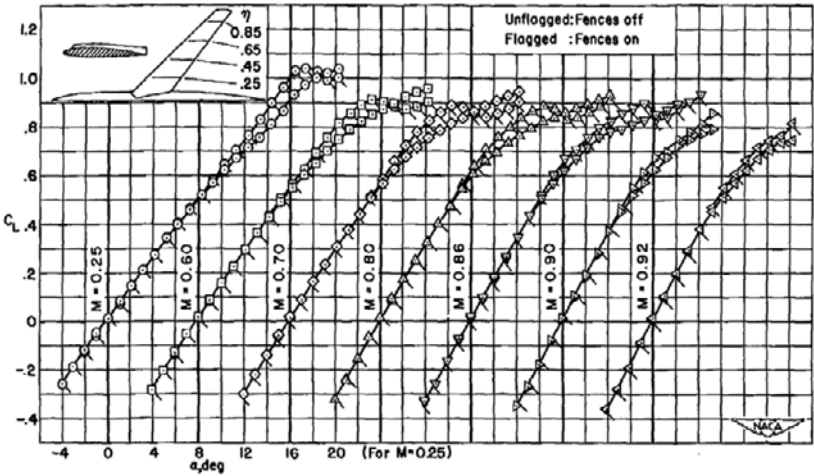
Figure 20.49 - The effect of wing fences at several Mach numbers on the lift characteristics of the wing-fuselage combination; Re = 2,000,000. Source: NACA RM A54L08
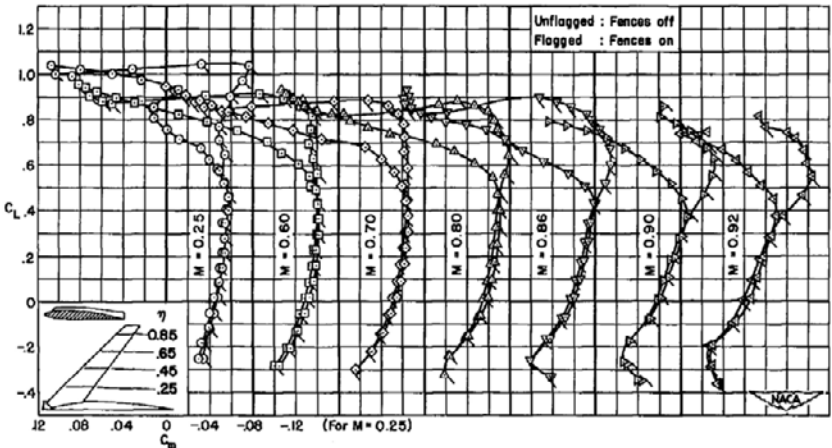
Figure 20.50 - The effect of wing fences at several Mach numbers on the pitching-moment characteristics of the wing-fuselage combination; Re = 2,000,000. Source: NACA RM A54L08

Wing sections perpendicular to the sweep axis have NACA 00XX thickness distributions combined with a NACA $a = 0.8$ (modified) mean line, $c_{li} = 0.4$.

Wing with 45° sweep has 4.7° twist (washout)

Root section: t/c = 0.14
Tip section: t/c = 0.11
(perpendicular to the quarter-chord line)
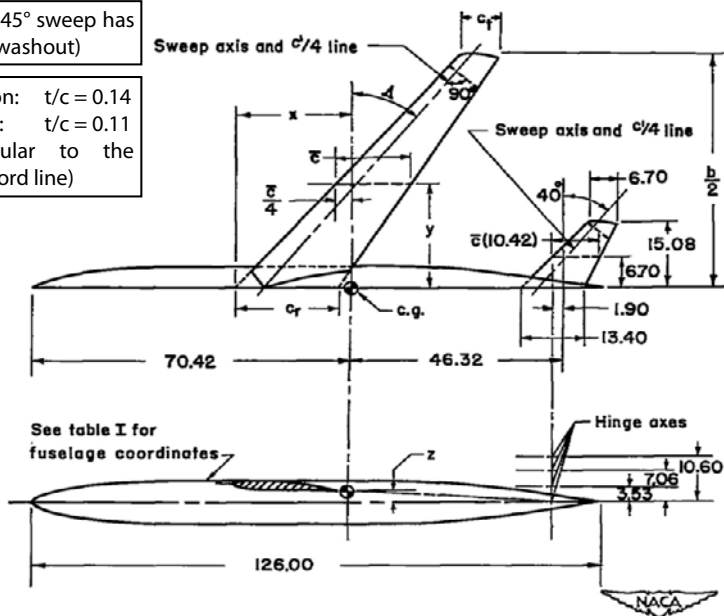
⋀	A	λ	b/2	c_r	c_t	$\bar{c}$	x	y	z	S	a_r for $a=0°$
40°	7.00	0.4	54.61	22.29	8.92	16.56	25.35	23.40	2.28	5.92	0°
45°	6.03	0.4	50.41	23.90	9.56	17.76	27.76	21.60	2.28	5.86	−.05°
50°	5.04	0.4	45.82	25.98	10.39	19.30	30.13	19.64	2.28	5.79	−.10°

Figure 20.51 - Geometry of the model used for investigating into the effect of wing fences. Source: NACA RM A54L08
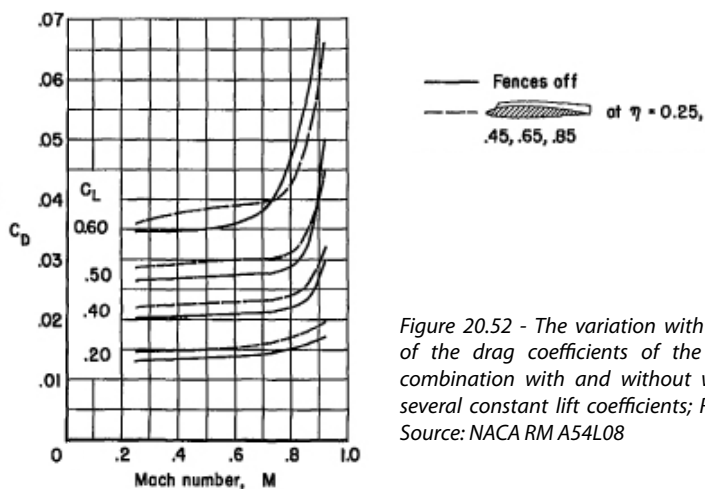
Figure 20.52 - The variation with Mach number of the drag coefficients of the wing-fuselage combination with and without wing fences at several constant lift coefficients; Re = 2,000,000. Source: NACA RM A54L08

The modern approach in tailoring stalling characteristics is to increase the leading-edge radius without modifying the upper surface curvature in order not to change the high-speed characteristic as described in chapter 19. Figures 20.53 to 20 56 show that in particular at high Reynolds numbers not only is the low-speed maximum lift coefficient increased but the sharp break in the lift curve at $C_{L,max}$ for $Re = 11 \times 10^6$ indicates sudden flow separation over a large part of the wing facilitating the efforts to obtain satisfactory stalling characteristics. This is contrary to the situation at lower Reynolds numbers where the flat top of the lift curve indicates early flow separation at the wing tip gradually spreading inboard. In actual wing design this large leading-edge radius would only be applied on the outer wing to guarantee that flow separation would start on the inboard wing.
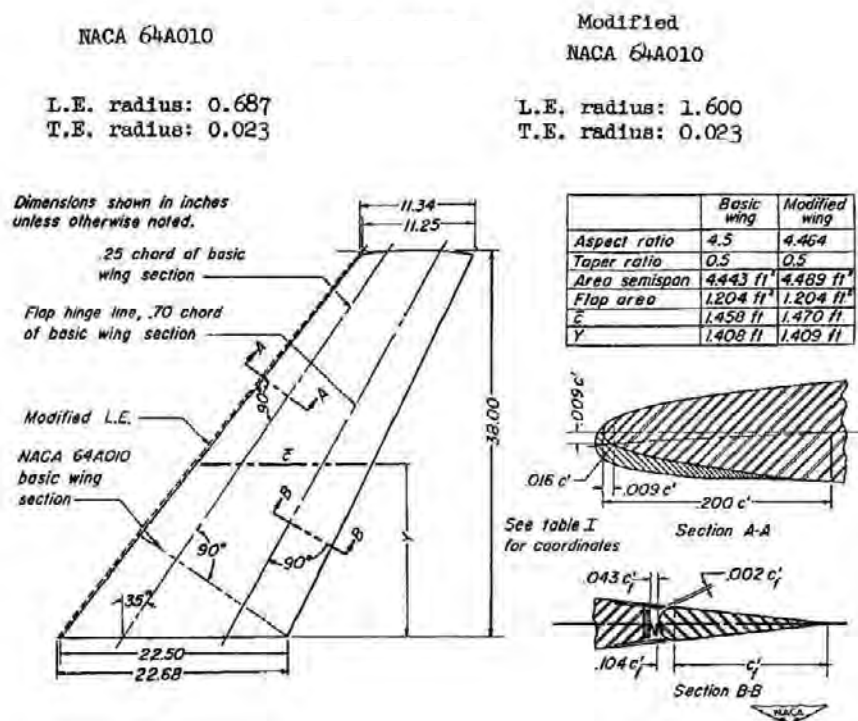
Figure 20.53 - Geometric characteristics of the model investigated in figure 20.52. Source: NACA RM A50K28a
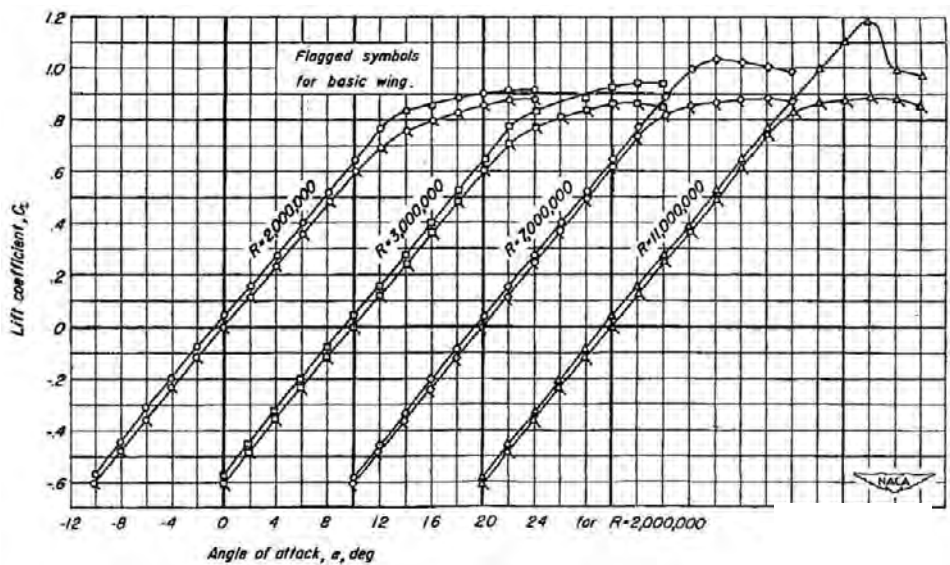
Figure 20.54 - The effect of Reynolds number on the low-speed aerodynamic characteristics. M = 0.21. Source: NACA RM A50K28a
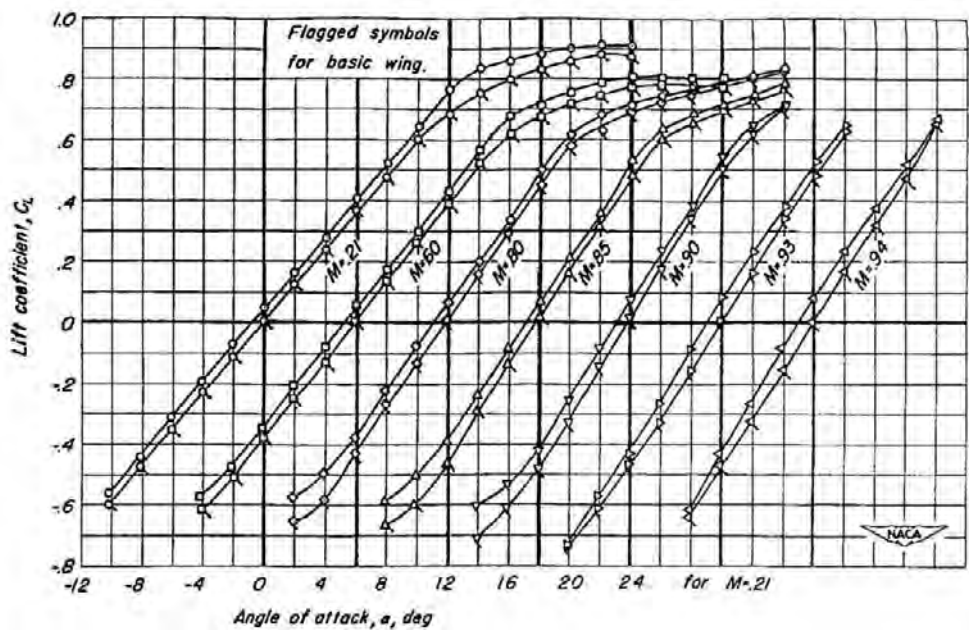
Figure 20.55 - The effect of Mach number on the lift versus angle of attack curve. Source: NACA RM A50K28a
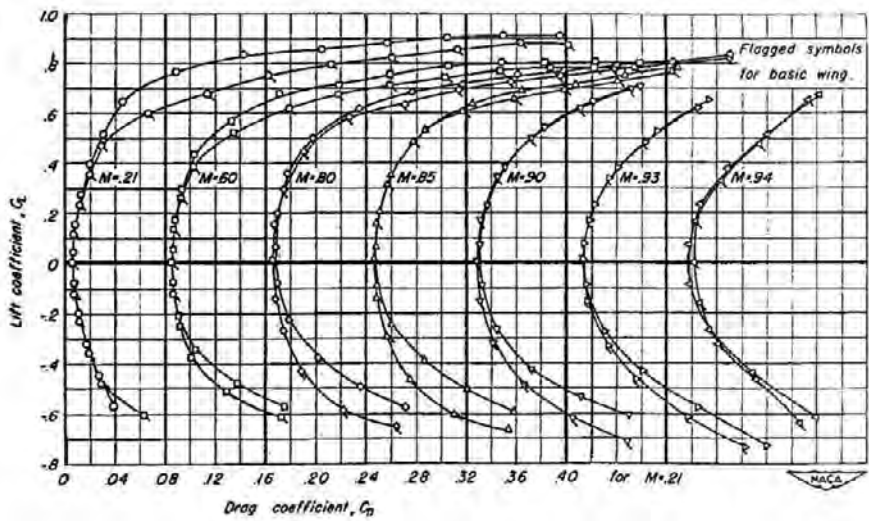
Figure 20.56 - The effect of Mach number on the lift versus drag curve. Source: NACA RM A50K28a

21 *The first generation of swept-wing aircraft*

In the previous chapter the principle of wing sweep was explained. This chapter discusses the first generation of aircraft with swept wings and the problems that were encountered.

The first swept wings were designed along the same principles as straight wings: root and tip sections were selected, the aspect ratio and taper ratio were chosen and the wing shape was determined by interpolation between the two profile sections.

The wings designed in this way exhibited unsatisfactory stalling characteristics. They showed pitch-up tendencies both at high and at low speeds due to the initial stall occurring on the outboard wing. This could also produce wing drop.

Examples of aircraft with wings that were designed along these principles and showed these unsatisfactory characteristics are the North-American F-86 Sabre and the Boeing B-47 Stratojet.

Figure 21.1 shows a top view of the F-86 and in figure 21.2 the wing shape of this aircraft is presented.

According to modern standards such flying characteristics would now be rejected but in the late 40's they were state-of-the-art. In the Korean War the F-86 built up a superior combat record over the Sovjet MiG-15 which was a formidable opponent but suffered from the same aerodynamic defects.
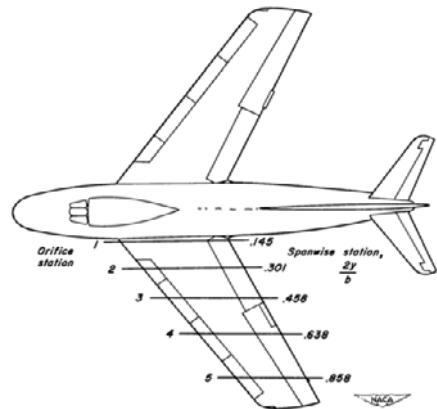
Figure 21.1 - North American F-86 'Sabre'. Source: NACA RM A52A31
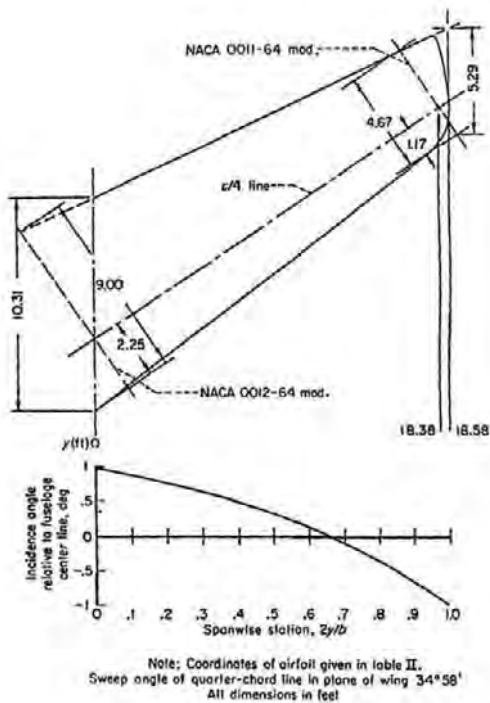
287.90 ft^2	Total wing area*
37.12 ft	Span
4.785	Aspect ratio
0.5131	Taper ratio
3'00'	Dihedral angle
97.03 in	Mean aerodynamic chord
35°13'31.4"	Sweepback of the 25% element
1°00'	Incidence of the root chord
-1°00'	Incidence of the tip chord
	*Includes flaps, slats and 49.92 ft^2 covered by fuselage

Table 21.1 - North American F-86 'Sabre' wing data.
Source: NACA RM A52A31

Figure 21.2 - North American F-86 'Sabre' wing geometry.
Source: NACA Report 1370

Figure 21.3 to 21.7 show the recordings of a turn with increasing bank angle or a gradual pull-up manoeuvre. The normal force coefficient, perpendicular to the body axis is given on the horizontal axis of figure 21.3. On the vertical axis various parameters are presented as a function of the normal force coefficient. The uppermost recording shows the elevator angle which increases as the pilot pulls back the control stick,but at an angle-of attack of about 5 degrees the elevator angle decreases as does the hinge moment and the elevator control force. This indicates that the pilot is reducing his input. However the angle-of-attack keeps increasing.

The explanation for this behaviour can be found in the shape of the tail-off pitching moment curve. At a normal force coefficient $C_N = 0.5$ the pitching moment changes rapidly in a nose-up sense due to flow separation on the outboard wing.
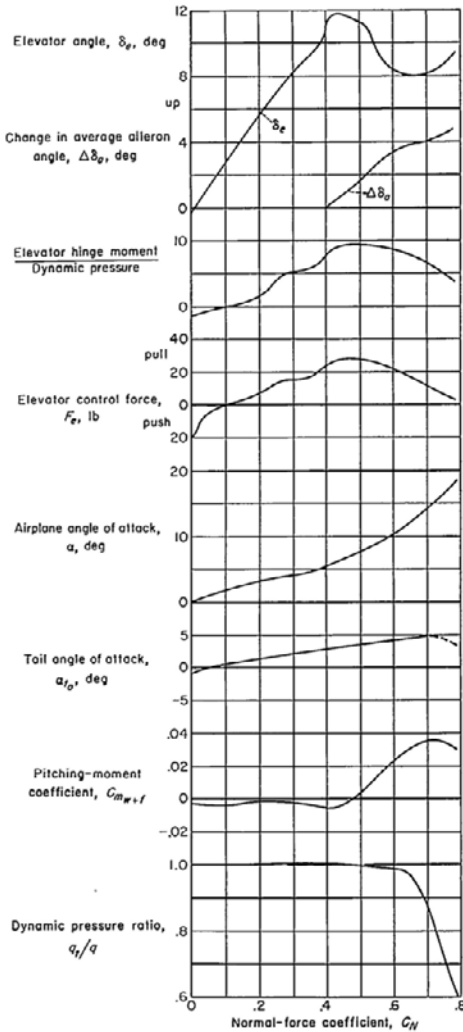
Figure 21.3 - Variation of the longitudinal control characteristics with normal force coefficient. M = 0.87.
Source: NACA RM A51I12 / Report 1237

The decreasing dynamic pressure ratio indicates that the tail is submerged in the wing wake leading to a diminishing contribution of the horizontal tail to stability and control.

Figure 21.4 shows the chordwise pressure distribution from the root to the tip of the wing. The steep pressure gradient at the tip pressure distributions indicates the presence of a shockwave. Moreover the trailing edge pressure coefficient is negative at the tip, which means the flow is separated there. Thus the outboard section is stalled. Note the angle of attack is 5 deg, so this is just before pitch up. The pressure distributions are higly irregular, not what one would design a wing for. This is because of the production quality of the aircraft of the 40's and 50's and deformations of the aircraft due to loading.
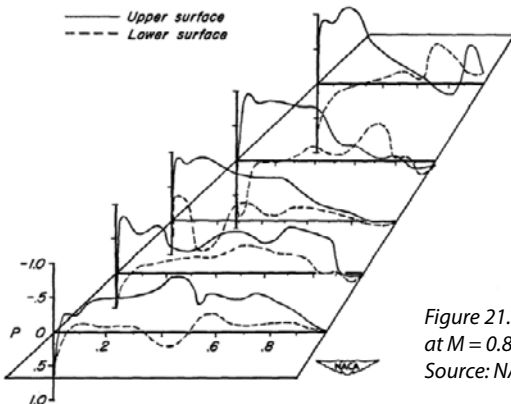
Figure 21.4 - Spanwise pressure distribution at M = 0.87, CNα = 0.39, α = 5.2°.
Source: NACA RM A52A31
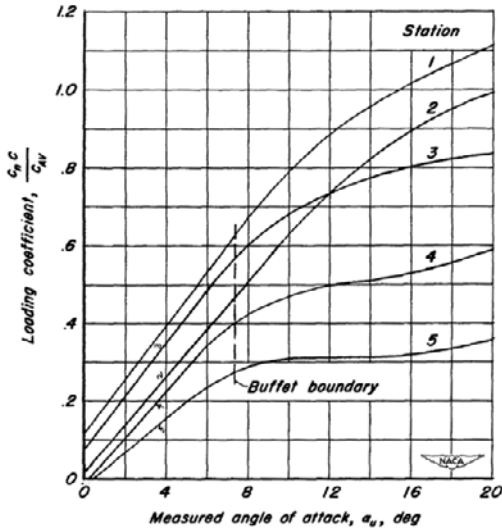
Figure 21.5 - Loading coefficient versus angle of attack at M = 0.87. Source: NACA RM A52A31

Figure 21.6 - Wing at M = 0.87 and C_{Na} = 0.49. Source: NACA RM A52A31

Figure 21.7 - Wing at M = 0.87 and C_{Na} = 0.74. Source: NACA RM A52A31

Figure 21.5 shows the loading coefficient as a function of the angle of attack for the 5 different wing stations. At station 4 for example separation has already occurred at an angle of attack of 8 deg.

Figures 21.6 and 21.7 are photographs taken during this flight test where tufts were attached to the wing upper surface in order to analyse the boundary layer condition. Some of the tufts are standing up or even pointing forward, which indicates separated flow. At a normal force coefficient C_N = 0.49 some separated flow already exists at the trailing edge as can be observed in figure 21.6. At a higher normal force coefficient as in figure 21.7 the tufts are all pointing in different directions, indicating separated flow over the complete outer wing.

Another example of a first generation swept wing aircraft is the Boeing B-47 bomber shown in figure 21.10. This airplane was a revolution in its time and represented a major breakthrough for Boeing. Table 21.2 gives some data on the wing design. The operational velocity of the B-47 was high: the maximum dive number was Mach 0.9 and the optimal cruise speed was Mach = 0.75.

In figures 21.8 and 21.9 some of the less desirable characteristics of the B-47 are described. Stalling the aircraft was not advised as it caused heavy buffet and a pitch-up tendency. Intentional spins were not allowed.

Span [ft]	116.0
Area [ft²]	1428.0
Aspect Ratio	9.43
Taper Ratio	0.42
Mean Aerodynamic Chord [in]	0.12
Sweep at 25% chord [deg]	155.9
Root chord [in]	35.0
Tip chord [in]	208.0
Airfoil Section	87.0
Incidence (root and tip) [deg]	BAC 145
Dihedral [deg]	0

*Table 21.2 - Boeing B-47 wing design data.
Source: Aeronautical Engineering Review,
November 1956*

I did not stall the aircraft myself, but learned that there is no trick about it. Plenty of warning buffet is given 10 to 12 kt above stalling speed and at the point of stall there is a slight nose-up trim change. Whether the vortex generator have affected the stall I do not know; they are primarily to postpone buffet at high speeds, which also causes a pitch-up tendency. Intentional spins are not permitted but the recovery is reported to be normal. When fully stalled, particularly with flap down, the buffeting is apparently severe and this is the main reason for avoiding it.

*Figure 21.8 - Boeing B-47 Pitch-up.
Source: Flight August 20, 1954*
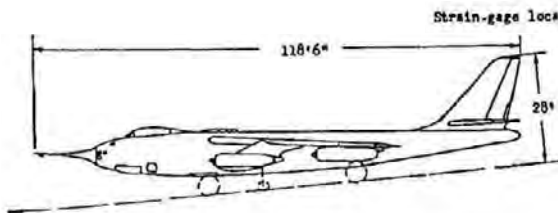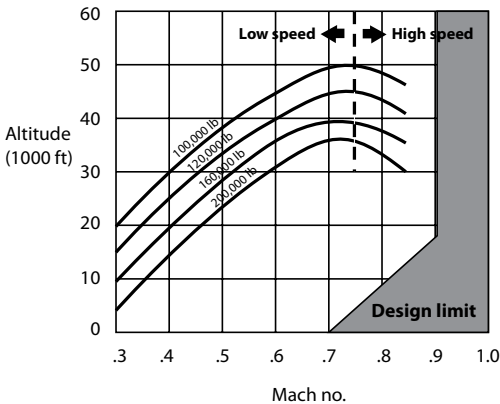
In the early days, "aileron reversal" was another expression to strike terror in the heart of the neophyte B-47 pilot. It seems that at certain speeds, when the wheel was rolled hard to one side, the airplane would roll in the opposite direction. This was understandably disturbing.

At high speeds, the aileron acted on the flexible wing much as a servotab acts on the elevator. The deflected aileron caused the trailing edge of the outboard section of the wing to twist in the opposite direction to the aileron. Thus the wing became a larger control surface than the aileron, neutralizing its effect at certain speeds and "reversing" it at higher speeds.

At one of the fire power demonstrations at Eglin AFB, a B-47 low-level, high-speed pass was included on the program. The B-47 was still new, and most of the viewers were anticipating, with some degree of excitement, their first look at a Stratocruiser. The pilot, anxious to please, had decided to give a convincing demonstration of the speed capability of the new bomber. As he came in at 200 ft., the reviewing stand loomed up ahead of him and a little to his right. A small adjustment in azimuth would position him for a perfect pass. He put in just the right amount of aileron, but nothing happened. He put in more - still no response. Then full right aileron - and then something happened. The airplane rolled *left* and streaked behind the reviewing stand!

*Figure 21.9 - Boeing B-47 aileron reversal.
Source: Aeronautical Engineering Review,
November 1956*
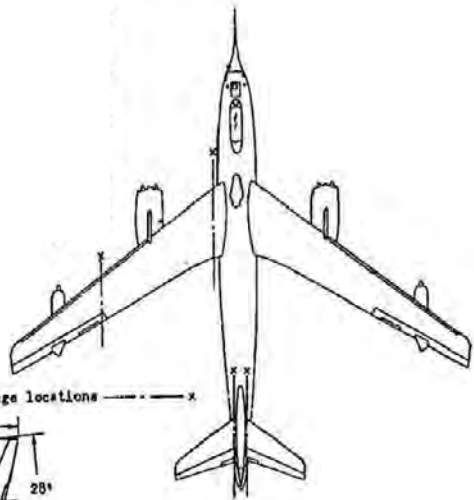
*Figure 21.10 - Boeing B-47.
Source: Aeronautical Engineering
Review, November 1956*

171

PROCEEDINGS
of the
Second European Aeronautical Congress
Scheveningen, September 25th - 29th, 1956

WING GEOMETRY

   The wing is free from alterations since all generating lines are straight and unbroken. Its geometrical definition is quite a simple one, it is a cone. The typical section is constant. We had to choose only one airfoil. As everybody else in the world, except opulent Americans, we could not afford to discover a new marvelous section, so we selected for the prototype the basic NACA 64.2.12 perpendicular to the 80 per cent chord line or theoretical flap hinge line.

   As the plane is built around a cruising Mach number of .75 (highest performance consistent with economy on shorthauls) the section parallel to the aircraft centre line has a 10 per cent thickness.

   The sweep back angle was fixed at 20 deg. at 25 per cent chord, this compromise being dictated by performance versus aeroelasticity, stability and structural weight.

   Further considerations on high angle of attack control and on stalling, gave a negative twist a bit over 2 deg. evenly distributed along the span.

   A positive static dihedral of 2 deg. 20 min. was fixed by the value of the ship's cross derivatives. This is due to the very low wing dictated by an unobstructed cabin. Of course, this angle increases in flight due to wing bending flexibility.

   Span is 112 ft 6 and total area 1580 sq. ft. Taper is 35 per cent, root and tip chords being respectively 248 & 88 inches. Wing loading is 57.5 p.s.f.

Figure 21.11 - Sud-Aviation SE 210 Caravelle wing geometry
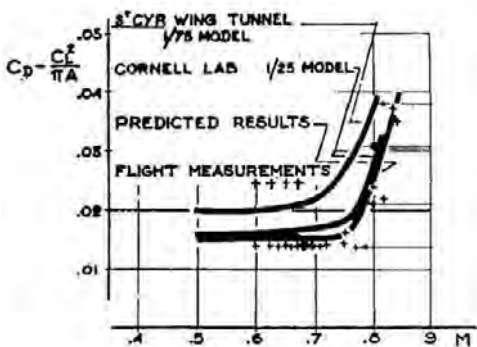
Figure 21.12 - Sud-Aviation SE 210 Caravelle Mach versus drag curve
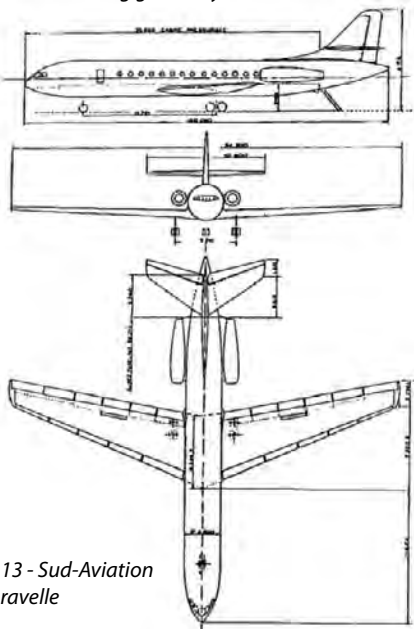
Figure 21.13 - Sud-Aviation SE 210 Caravelle

Figure 21.13 shows a third example of a first generation swept–wing aircraft, the Sud-Aviation SE-210 Caravelle. The wing used a constant NACA 64-212 laminar-flow airfoil section perpendicular to the 80%-chord line over the complete span. The wing sweep angle was limited to $\Lambda_{\frac{1}{4}c}$= 20 deg. Figure 21.11 presents some more geometric characteristics of this wing. In figures 21.12 and 21.14 drag curves are shown as a function of Mach number for low lift coefficients for two versions of the Caravelle as obtained from windtunnel and from flight tests.
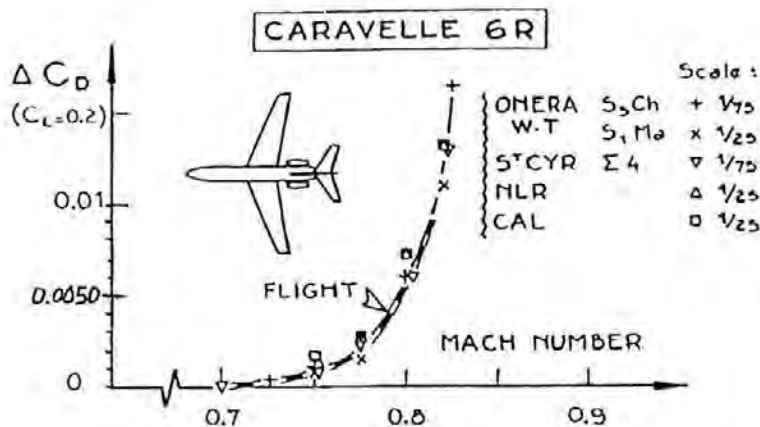
Figure 21.14 - Wind-tunnel/flight comparisons of the transonic drag rise for the Caravelle. Source: Journal of Aircraft May-June 1968

As $M_{MO} = 0.77$ the normal cruise Mach number was $M = 0.75$ and the extra drag due to compressibility effects was $C_D = 0.0010$ to 0.0015. Figure 21.15 presents the buffet boundary. It will be clear that due to the low sweep angle the drag characteristics of the wing were only marginally better than the drag characteristics of an unswept wing and the wing sweep angle will have been more beneficial to obtain satisfactory high-speed flying characteristics than to increase the drag rise Mach-number.
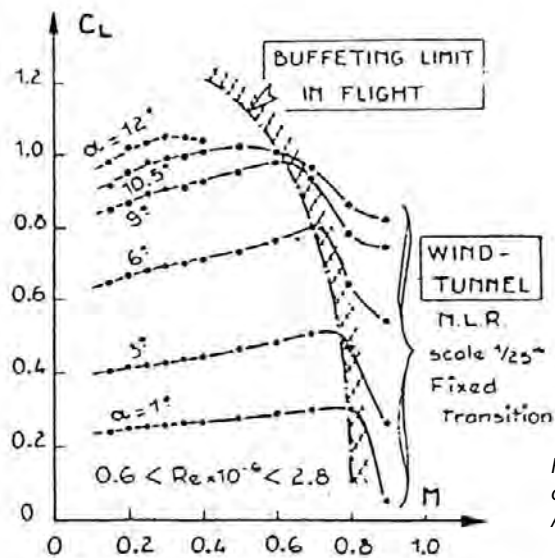
Figure 21.15 - The buffeting onset on the Caravelle. Source: Journal of Aircraft May-June 1968

Figure 21.16 shows test results from measurements on the Caravelle 10A performed both in the high-speed tunnel of NLR in the Netherlands and in flight. Because this model of the Caravelle had more powerful engines than earlier versions the maximum operating Mach number was raised from $M_{MO} = 0.77$ to $M_{MO} = 0.81$. Because of the higher weight of the engines the forward fuselage was lengthened by 1 m necessitating an increase in horizontal tailplane area. To improve the flow at the junction of the tail surfaces at these higher Mach numbers a bullet fairing was introduced. Finally the wing root chord was extended both at the leading and trailing edge. This latter modification was not intended to modify the high-speed characteristics. These modifications are indicated in figure 21.17. When on a tapered wing the spanwise lift distribution is elliptic the lift coefficient at the root is lower than at mid span in particular when at the root the leading edge sweep angle is increased
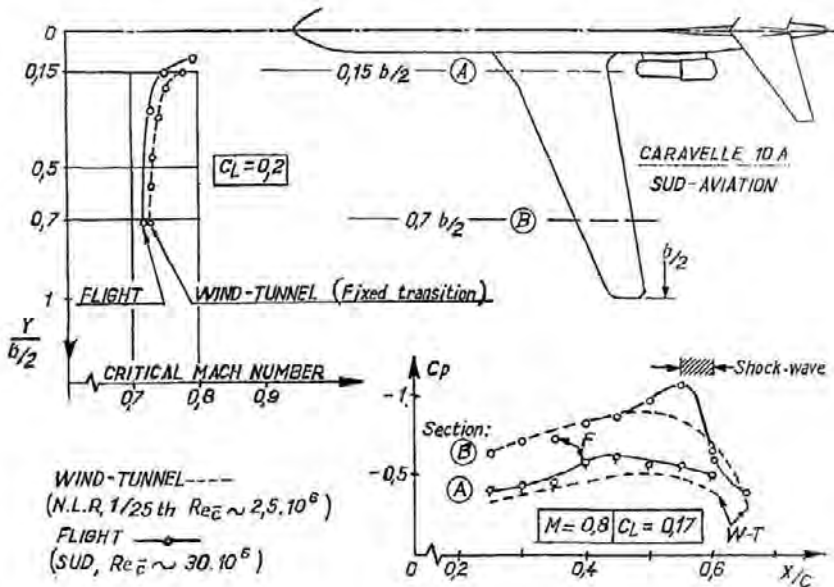
Figure 21.16 - Caravelle wind-tunnel results

As the wing on the Caravelle 10A has a constant section (and at the root has even a slightly lower relative thickness) supervelocities at the root are lower than at mid span and the local critical Mach number is higher. The transonic characteristics are entirely determined by the flow over the outer wing as illustrated in figure 21.16. If the higher M_{MO} of this model would permit higher cruising speeds these speeds would be accompanied by shock waves and high drag as shown in figure 21.16.

SUPER CARAVELLE

Major differences between the *Caravelle Super A* (2 × General Electric CJ 805-23 C) and the *Caravelle VIR* (2 × Rolls-Royce Avon 533 R), can be seen from this superimposition of the two profiles. The shaded areas indicate the modifications and enlargements in the newest version.
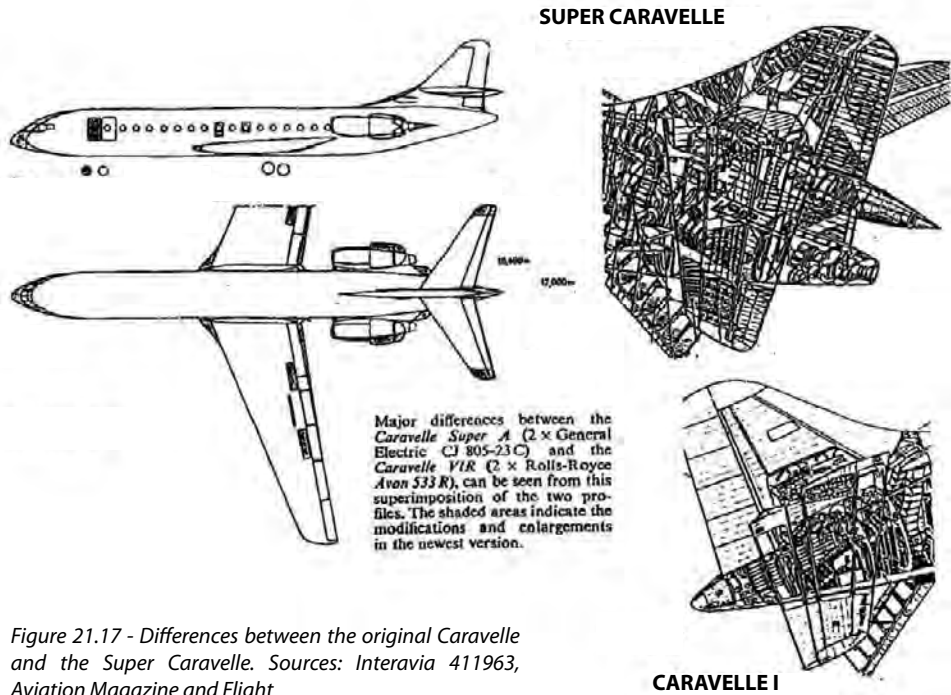
Figure 21.17 - Differences between the original Caravelle and the Super Caravelle. Sources: Interavia 411963, Aviation Magazine and Flight

CARAVELLE I

Aeroelastic deformation of high-aspect ratio wings

Consider a swept wing as depicted in figure 21.18. The main load-carrying component is the torsion box consisting of front and rear spar, ribs and upper and lower skin panels. In flight the lift forces will, partly counteracted by the weight of the wing itself, the fuel and the engines make the wing flex upward. As the deformation of the area A adjacent to the fuselage in the figure is only a secondary effect this bending takes mainly place in a plane perpendicular to the wing reference plane.

The lift usually applies close to the elastic axis and the torsional deformation about the aeroelastic axis is limited. Thus, corresponding points on front and rear spar, indicated as dots in the figure, are vertically displaced over the same distance. However this means that on each streamwise wing station the rear spar bends upward more than the front spar causing a progressive decrease in angle-of-attack towards the wing tip. The wing tip region is relieved and the aerodynamic centre moves forward. Note again that the effect described results in aerodynamic twist and not in structural twist.
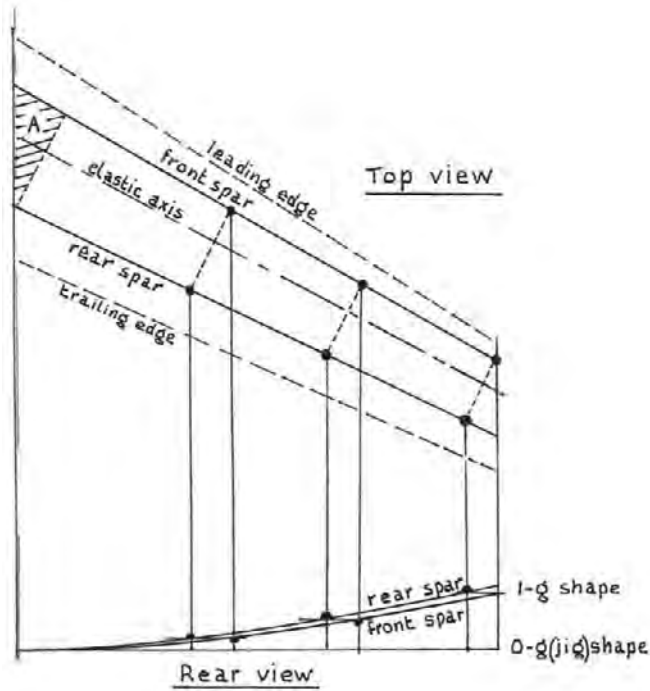
Figure 21.18 - Bending of a swept wing due to lift

When ailerons are deflected the extra lift applies behind the aeroelastic axis of the torsion box producing a torsion moment. A downward aileron deflection leads to a leading-edge-down torsion moment twisting the torsion box and producing a decrease in local angle-of-attack as shown in figure 21.19. The resulting change in lift on the outer wing counteracts the lift due to aileron deflection lowering the aileron efficiency. At high dynamic pressures the structural deformation may lead to aileron reversal. This occurred on the B-47, as discussed earlier.

Significant structural deformation may also occur when airfoil sections with high rear-loading are applied in the outer wing.
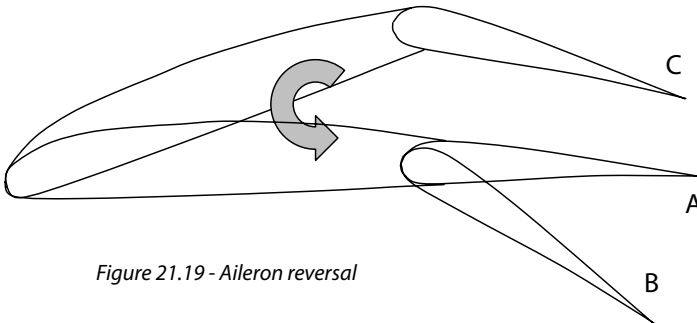
Figure 21.19 - Aileron reversal

22 *Root and tip effects on swept wings*

In the previous chapter it was shown that on a swept wing with constant airfoil section and a fuselage with a near-constant cross section at the wing-fuselage junction in subsonic flow the isobars tend to curve rearwards at the wing root and forwards at the wing tip. When the Mach number of the undisturbed flow is increased and a shock wave is formed this shock wave occurs further rearwards at the wing root than at the tip. This results in a lower drag rise Mach number than would be expected on the basis of simple sweep theory. In this chapter these root and tip effects will be considered more in detail together with possible measures to eliminate these effects.

In the first part of this chapter wings with symmetrical airfoil sections at zero lift will be considered.
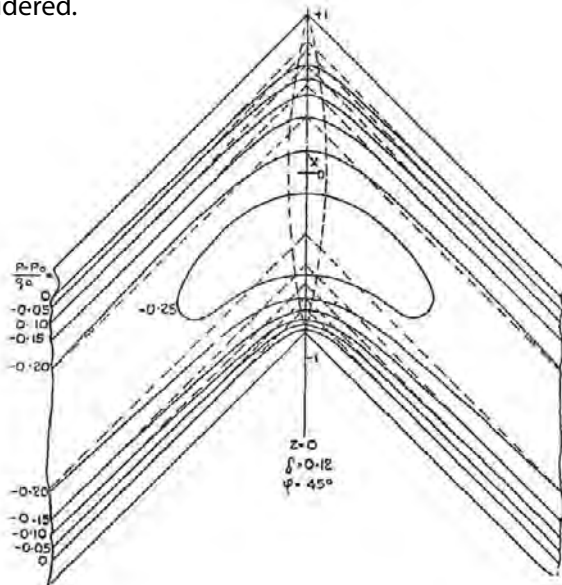
Figure 22.1 - Isobars on a wing with convex profile section. Source: RAE Report No Aero 2219

Figure 22.1 shows in top view the centre of an infinite wing swept-back 45 deg. with a biconvex profile. According to simple sweep theory at low speeds the isobars (lines of constant pressure) would be straight up to the plane of symmetry. The resulting discontinuity in flow conditions is physically impossible. The isobars curve and cross the plane of symmetry perpendicularly.
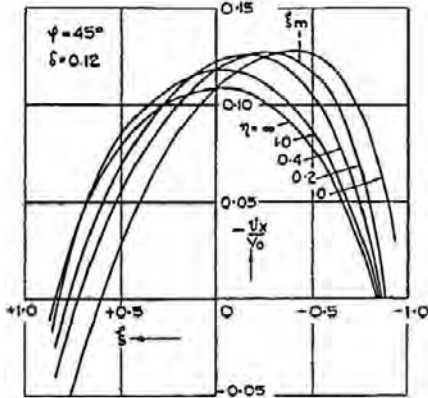
Figure 22.2 - Velocity distributions at various spanwise sections of wing with biconvex profile. Source: RAE Report No Aero 2219

This causes a decrease in supervelocities over the forward part of the centre wing and an increase over the rear part. Furthermore for this biconvex profile the peak velocity increases. Together these local changes in the velocity distribution result in an unfavourable pressure gradient over this part of the wing increasing the possibility of boundary layer separation. This is also shown in figure 22.2.

In figure 22.3 the isobar patterns are presented for two highly swept-back low-aspect-ratio wings. Figure 22.4 shows the velocity distribution at two streamwise sections for both wings both calculated and obtained from windtunnel tests.

At the wing centre the isobar patterns resemble the pattern of figure 22.1 with rearwards-curving isobars but at the tip the pattern is reversed as if the tip area forms half the centre part of a swept-forward wing.

On these wings the basic streamwise section is a conventional airfoil section with a fairly thick forward part (RAE 101) and, even at zero angle-of-attack, with the peak velocity near the leading edge. The curving of the isobars at the wing centre lowers the maximum velocity at the plane of symmetry of the wings below that of the sections further outboard.

Figure 22.3 - Isobars on two 53° swept-back wings of different aspect ratios (square-cut tips). Source: ARC R&M 2908, 1953
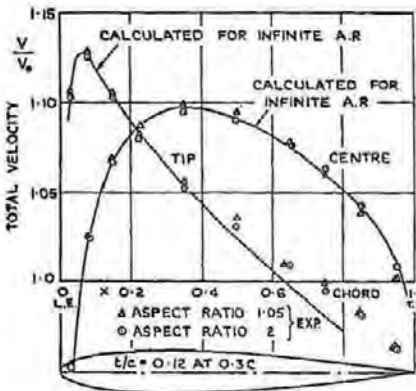
Figure 22.4 - Velocity distributions at centre and tip sections of two 53° swept back wings with constant chord (square-cut tips). Source: ARC R&M 2908, 1953

Spanwise drag distribution

On a body in a flow pressure acts perpendicular to the local surface. At each point on the surface the pressure force can be resolved into a component parallel to and a component perpendicular to the undisturbed flow.

On a straight wing (and according to simple wing sweep theory also on a swept wing) the flow characterisics of each wing section are to a large extent identical to that of a two-dimensional section and the sum of the pressure forces is also zero. On a swept wing however, due to the lower velocities over the forward part of the centre wing and the higher velocities over the rear part, the sum of the pressure force components in the direction of the undisturbed flow is not zero and is directed rearwards. The centre part of a swept wing with a constant airfoil section experiences a pressure drag in potential flow. Near the wing tips the situation is reversed and the tip regions show a negative pressure drag.
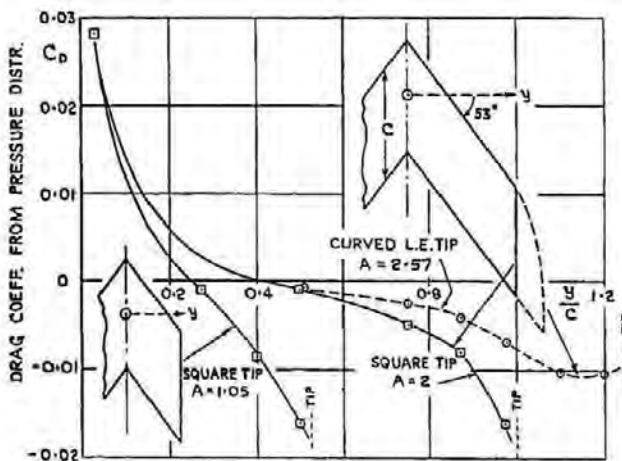
Figure 22.5 - Coefficient of local form drag along the span of some 53° swept-back wings with constant chord.
Source: ARC R&M 2908, 1953

Figure 22.5 shows the spanwise distribution of the pressure drag of the two wings given in the two previous figures derived from the pressure distributions at various wing stations. Figure 22.5 also shows a tip extension with a curved leading edge, known as a Küchemann tip. On this wing tip the isobars are curved backwards as shown in figure 22.6. From figure 22.5 the conclusion could be drawn that this tip shape is disadvantageous from a drag point-of-view because the suction forces on the outer wing are decreased. Their function is however to improve the high-speed characteristics of the wing by delaying the formation of shock waves and increasing the drag rise Mach number. This wing tip was applied to several aircraft designed in the 50's and 60' among them the Vickers VC-10.
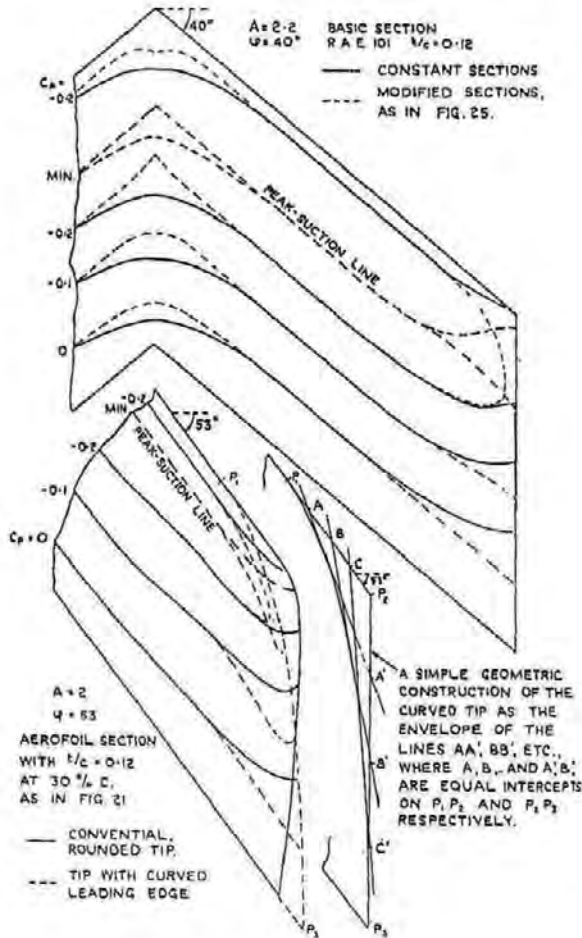
Figure 22.6 - Isobar patterns on two swept-back wings.
Above: Modification of the aerofoil section.
Below: Modification of the planform in tip region

The upper part of figure 22.6 is discussed in the paragraph related to figures 22.18 and 19.
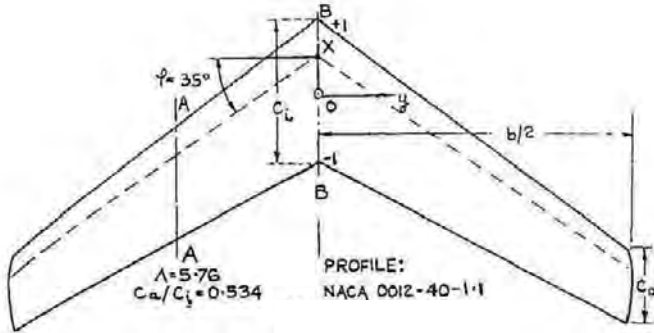
Figure 22.7 - Wing. Source: RAE Report Aero No 2219, 1947

Figures 22.7 to 22.9 present a further example of the root and tip effects on a swept-back wing with a constant airfoil section. Note that in figure 22.8 the spanwise drag distribution was obtained from experiments and incorporates friction drag.
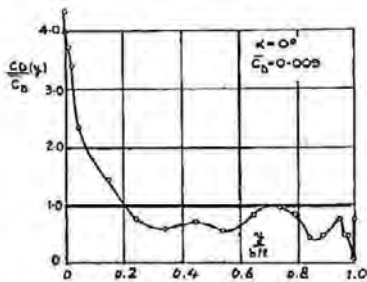
Figure 22.8 - Drag analysis.
Source: RAE Report Aero No 2219, 1947
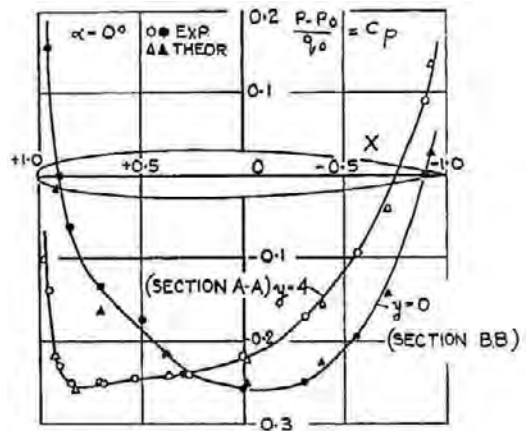
Figure 22.9 - Experimental and theoretical pressure distributions. Source: RAE Report Aero No 2219, 1947

Forward-swept wings

In figures 22.10 and 22.12 chordwise velocity distributions are shown , both at the centre section and at a section half-way the semi-span (termed "sheared wing" in the figures), for two sets of swept wings with different airfoil sections both calculated and from windtunnel tests. In each set a swept-back and a swept-forward wing is considered.

The two constant-chord wings mentioned in figure 22.10 with wing sweep angles Λ = +45 deg and Λ = -45 deg are based on airfoil section RAE 103. The comparable two wings in figure 22.12 are based on section RAE 101. The slight difference in velocity distributions can be ascribed to the different airfoil sections.

For the two swept-back wings the velocity distributions over the centre section and the section at mid-semi-span are comparable to the velocity distributions shown in earlier figures. On the centre section of the two swept-forward wings (Λ = - 45 deg) the isobars curve forwards and the leading edge shows a high suction peak similar to the situation near the tip of a swept-back wing.

Further on in this chapter it is shown that additional velocity distributions due to lift demonstrate the same changes, when moving from the mid-semi-span station to the wing root, as due to thickness. Also on a swept-forward wing there is a boundary layer inflow towards the wing root. These effects together will cause the wing root to stall first and produce a pitch-up unless special measures are taken. A severe wing drop is less likely to occur. If a swept-forward wing is applied on an otherwise conventional aircraft configuration the tailplane will be submerged in the separated wing wake in a stall. In particular with a T-tail a situation may develop where the aircraft can not be recovered from the stall.
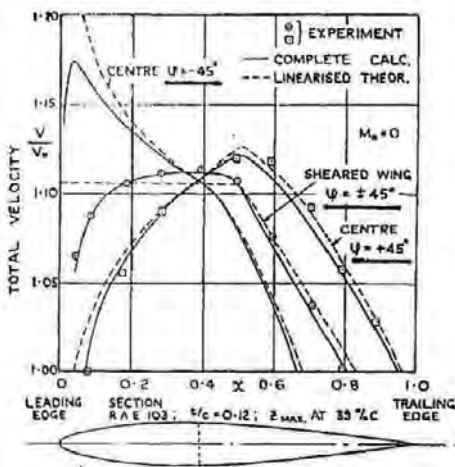
Figure 22.10 - Velocity distribution.
Source: ARC R&M 2908

The only Western aircraft built after World War II with swept-forward wings was the Hamburger Flugzeugbau HFB 320 Hansa Jet. During the flight tests the prototype entered a locked-in stall which developed into an unrecoverable flat spin with catastrophic results. The series aircraft were equipped with a short slat at the root and a stick-pusher which prevented the aircraft from reaching high angles-of-attack.

Figure 22.11 - Hamburger Flugzeugbau HFB 320 business jet. Source: R. Hesse
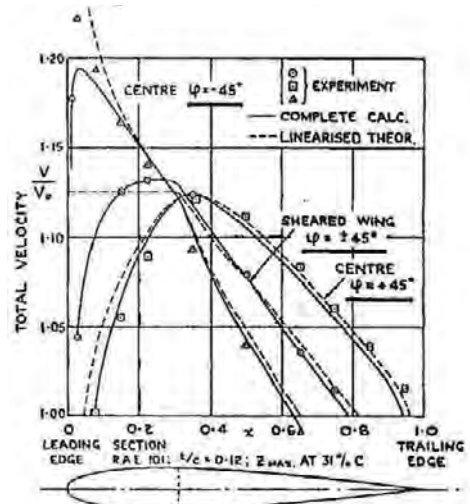
Figure 22.12 - Velocity distribution. Source: ARC R&M 2908

Effect of the fuselage on the isobar pattern

Figure 22.13 shows two low-speed windtunnel models with constant-chord swept-back wings with a sweep angle $\Lambda = 40$ deg. The first model, model 5, is a wing-fuselage combination with a contoured fuselage such that the streamlines over the wing adjacent to the fuselage are identical to those at mid-semi-span. At the wing tips Küchemann tips are applied. Root and tip effects are minimized in this way and velocity distribution at the mid-semi-span wing station should be identical to an infinite sheared wing according to simple sweep theory. Model 2 uses the same wing geometry but in combination with a flat-sided fuselage. In figure 22.14 a wing-alone model is shown fitted with one tip on the tunnel floor on a fairing to prevent a flow picture as over the root of a swept forward wing. In figure 22.15 the calculated and measured velocity distributions are shown for the section at mid-half-span (section f), at the wing root of model 2 (section j) and for the centre section of the wing-alone model. From this investigation it can be concluded that near a straight-sided fuselage wall the flow over a wing is similar to the flow over the centre part of a wing alone.
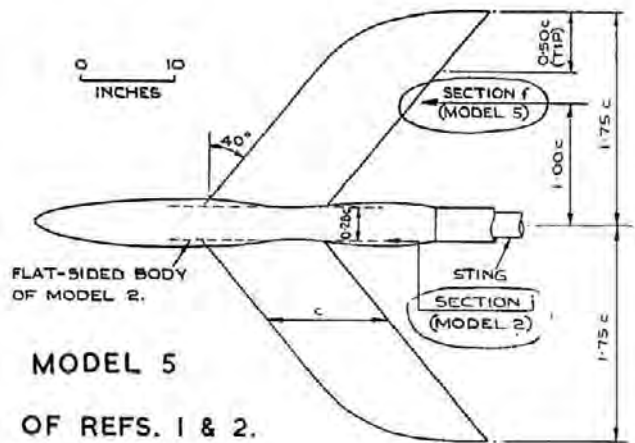
Figure 22.13 - Fuselage and wing test model. Source: RAE Report No Aero 2556
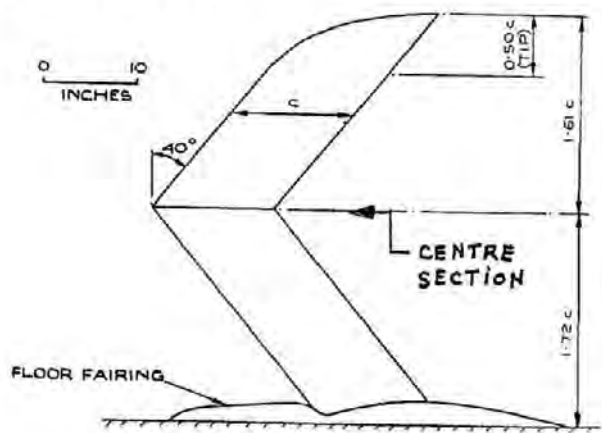
Figure 22.14 - Wing test model. Source: RAE Report No Aero 2556
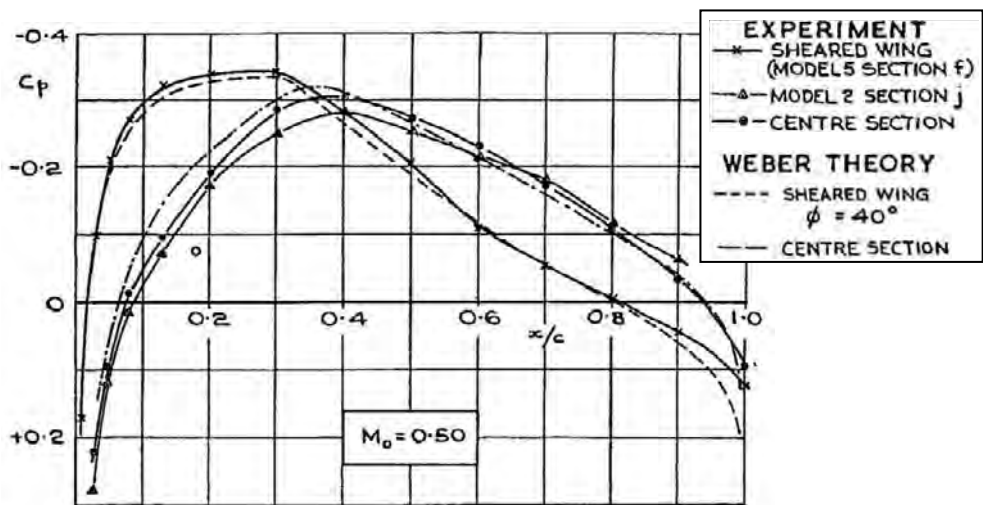
Figure 22.15 - Pressure distributions according to theory and tests. Source: RAE Report No Aero 2556

Supervelocities due to lift

In the previous sections of this chapter the wing root and tip effects on the velocity distributions on a wing due to thickness were discussed. Similar effects occur regarding the supervelocities due to lift. If a plane lifting wing is considered as a vortex plane the vortices will show a similar pattern near the wing root as the isobars on a non-lifting wing but not identical. The vortices tend to curve backwards and cross the plane-of-symmetry perpendicularly . Near the trailing-edge a part of the bound vortices turn into trailing vortices. This is illustrated in figure 22.16. This causes a decrease in lift at the wing root as shown in figure 22.17.
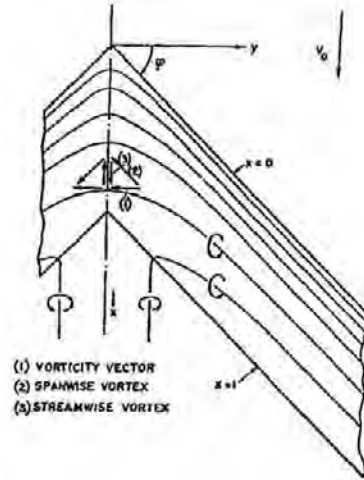
Figure 22.16 - Vortex pattern near the centre of a swept wing (schematic). Source: Aeronautical Quarterly, August 1953
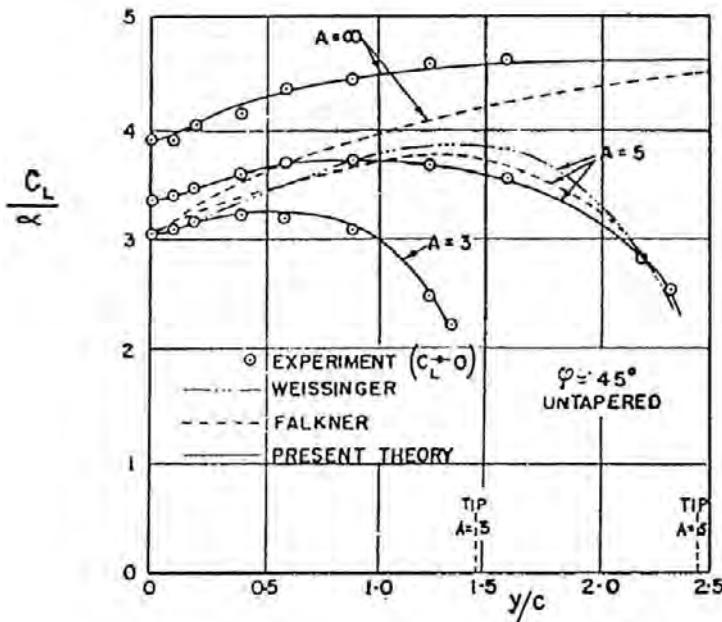
Figure 22.17 - Experimental and theoretical spanwise lift distributions. Source: Aeronautical Quarterly, August 1953

Minimizing root and tip effects on swept wings

It is extremely difficult to achieve a velocity distribution over a wing with straight isobars running right up to the fuselage in order to maximise the effect of wing sweep. It is possible however in particular at the wing root to improve the velocity distribution to such a level that most of the potential advantage of a swept wing can be realized. How this can be done is described in the following sections.

Improving the velocity distribution due to thickness at the root and tip of swept wings

As shown in the previous parts of this chapter on swept wings with constant symmetrical airfoil sections at zero lift the isobars tend to curve rearwards at the root and forwards at the tip. At the root the supervelocities over the forward part of the section are lower and over the rear part higher than at mid-semi-span. At the tip a reverse situation occurs.
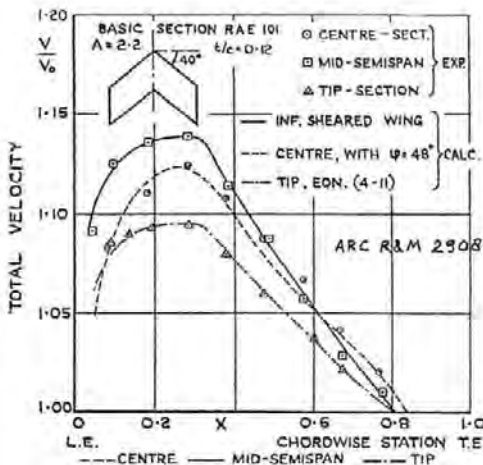
Figure 22.18 - Velocity distributions at three spanwise stations on a 40° swept-back wing of constant chord with modified section shapes. Source: ARC R&M 2908

Figure 22.19 - Airfoil sections corresponding to figure 22.18. Source: ARC R&M 2908

In chapter 11 the relation between geometry and pressure or velocity distribution was explained, in particular with respect to changes in these parameters. This means that if locally an increase in supervelocity is required the local curvature must be increased and to lower the supervelocity the local curvature must be decreased or even change sign. Thus to obtain a velocity distribution at the root equal or near-equal to that at mid-semi-span the forward part of the root section must be thickened and the rear part made thinner. The opposite applies to the tip. An example of such a modification is presented in figures 22.18 and 22.19.

If after applying this type of modification the velocity distributions on the various sections are similar but show different levels this can be corrected by modifying the thickness ratio of the different sections. In this way straight or near-straight swept isobars can be obtained.

Improving the velocity distribution due to lift at the root and tip of swept wings

In figure 22.20 the chordwise lift distribution is presented for a plane untapered wing with sweep angle $\Lambda = 45$ deg at $C_L = 0.3$ at both the centre line and near the mid-semi-span wing station. Lift distribution may also be read as an extra velocity distribution on top of the velocity distribution due to thickness.
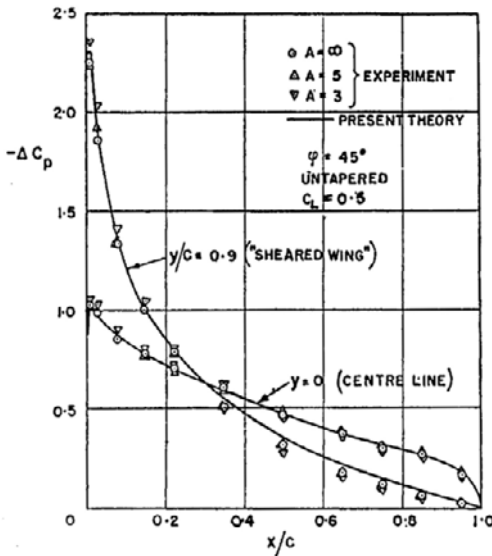
Figure 22.20 - Experimental and theoretical chordwise loadings. Source: Aeonautical Quarterly, August 1953
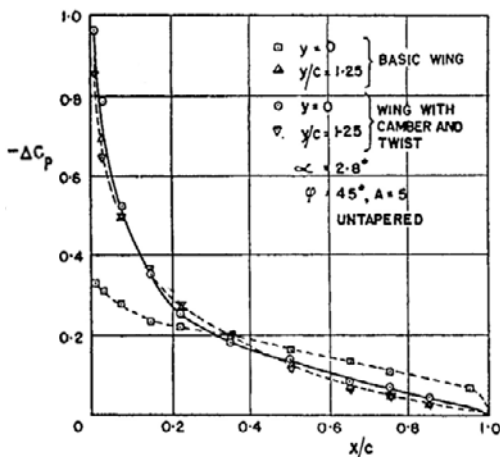
Figure 22.22 - Experimental chordwise loadings on a symmetrical wing and on a wing with camber and twist. Source: Aeronautical Quarterly, August 1953

This figure shows that due to the local rearward curvature of the lifting vortices such wings have less lift on the forward part of the wing root region and more on the rear part than on the corresponding parts of the mid-semi-span region.

This chordwise velocity distribution may be corrected by modifying the upper and lower curvature distribution such that effectively a negative camber line is constructed. The loss in lift as shown in figure 22.17 can be compensated for by an increase in incidence.
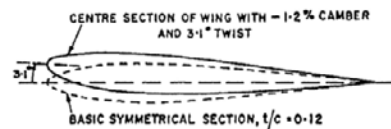
Figure 22.21 - Twist is applied to the wing centre section airfoil. Source: Aeronautical Quarterly, August 1953

Figure 22.21 shows the modified centre section of one of the wings mentioned above and figure 22.22 shows the result of this modification. Note that this modification was only applied to demonstrate that along the span a constant pattern of supervelocity due to lift can be achieved. In order to obtain straight swept isobars the changes in thickness described above have to be added to the modification.

The effect of wing taper and sweep on spanwise lift distribution

When a (straight or swept) tapered wing is designed such that in the design condition the spanwise lift distribution is elliptic or near-elliptic the local lift coefficients at the inboard wing are lower than at the outboard wing because the local lift is determined by the product of the local lift coefficient and the local wing chord (c_l x c).

If near the wing root a lower local lift coefficient is required than further outboard plus a constant chordwise velocity distribution on the wing upper surface, this to obtain constant percentage chord isobars, then this can only be achieved by increasing the supervelocities on the lower surface of the inboard wing. This leads to a stronger curvature and a larger thickness-to-chord ratio for the root section.

This has the additional advantages that a lighter inboard wing can be produced and that a larger fuel volume is available.

German notation:
η = relative spanwise position
λ = taper ratio
c_a = local lift coefficient
C_A = wing lift coefficient
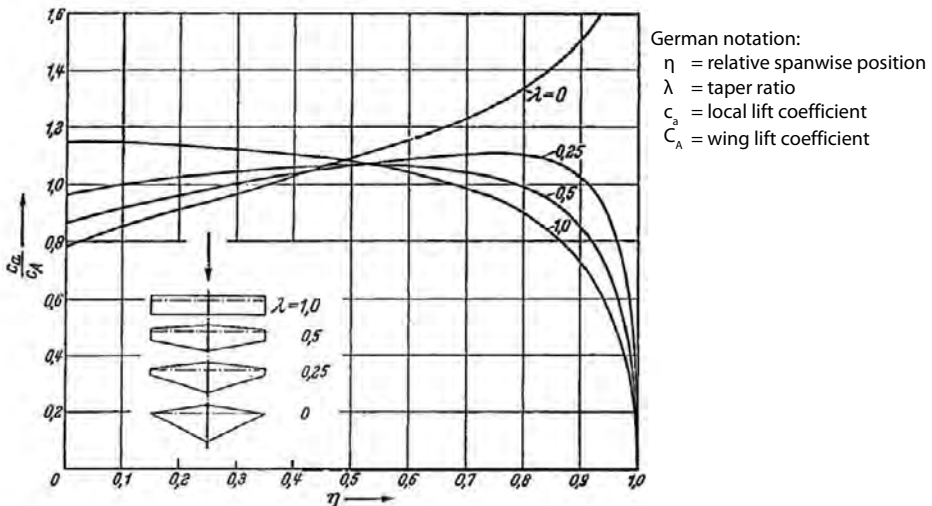
Figure 22.23 - Spanwise lift distribution for different taper ratios.
Source: Schlichting & Truckenbrodt, Aerodynamik des Flugzeuges

The above refers to the design condition. When the angle-of attack is increased to the much higher lift coefficients which can be reached at low speeds, the distribution of the additional spanwise lift coefficient along the span is presented in figure 22.23. In this figure the local lift coefficient divided by the wing lift coefficient is shown as a function of spanwise position for four plane wings with different taper ratios. With increasing taper the local lift coefficient on the inboard wing tends to decrease and on the outboard wing to increase.

The application of wing sweep has a similar effect as can be seen in figure 22.24.

The combination of wing sweep and taper leads to heavy demands on the high-lift characteristics of the airfoil sections in the outboard wing. It is clear that the combination of high-speed requirements with respect to straight swept isobars and low-speed requirements for high lift and good stalling characteristics are not incompatible but do require a careful analysis. This was also adressed in chapter 19.

A balance between the high-speed and the low-speed characteristics of the outer part of a tapered swept wing can be obtained by choosing the proper leading-edge radius without altering the upper surface curvature.
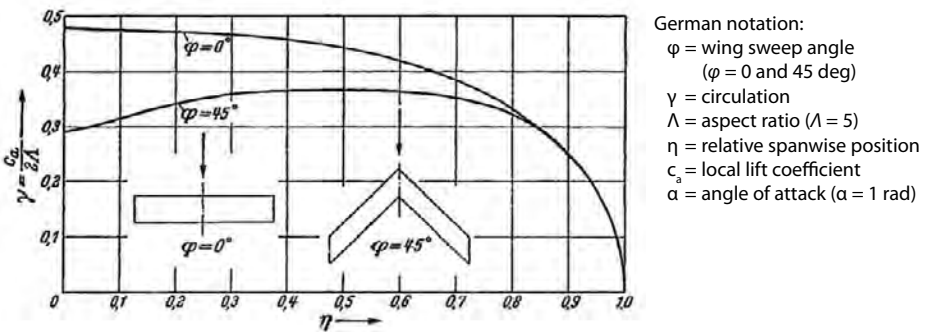
Figure 22.24 - Spanwise lift distribution for a straight wing and a swept wing.
Source: Schlichting & Truckenbrodt, Aerodynamik des Flugzeuges

German notation:
φ = wing sweep angle
  (φ = 0 and 45 deg)
γ = circulation
Λ = aspect ratio (Λ = 5)
η = relative spanwise position
c_a = local lift coefficient
α = angle of attack (α = 1 rad)

Minimising the pitching moment

The design requirement as discussed above is to produce a certain local lift coefficient at the root section. The chordwise velocity distribution is not prescribed however. Shaping the front part of the lower side of the root section such that this part gives maximum front loading is beneficial for minimizing the wing pitching moment and thus trim drag. Low rear loading leads to a thick rear part of the wing root region. This provides more room for flaps and the associated mechanisms and stowage of the main undercarriage legs.

Summary of modifications to be performed on a plane tapered swept wing with constant airfoil sections in order to obtain a wing with satisfactory high- and low-speed characteristics

These modifications are most pronounced at the wing root and should blend into the basic wing shape at 30 to 40 percent of the semi-span. In the tip region, the required modifications are usually of a secondary nature apart from adapting the lower part of the leading-edge area.

Mod. no	Modification	Reason
1	Increase the thickness of the forward part of the root section. Decrease the thickness of the rear part of the root section.	To obtain similar chordwise upper-surface velocity distributions due to thickness along the span.
2	Increase the thickness-chord ratio of the root section.	To obtain identical chordwise upper-surface velocity distributions due to thickness along the span.
3	Decrease the positive camber or apply negative camber on the root section.	To adapt the pattern of the chordwise upper-surface velocity distribution due to lift to that of the basic airfoil section.
4	Increase the incidence of the root section.	To obtain identical chordwise upper-surface velocity distributions along the span.
These four modifications together should lead to straight swept isobars over most of the wing upper surface in the design condition.		
5	Modify the wing lower surface along the span (mostly on the inner wing).	To obtain the desired spanwise distribution of the local lift coefficient.
6	Modify the lower surface velocity distribution on the root section regarding front and rear loading.	To minimise the wing pitching moment.
7	Modify the leading-edge region on the outer wing	To obtain satisfactory stalling characteristics

Table 22.1 - Summary of modifications to be performed on a plane tapered swept wing with constant airfoil sections in order to obtain a wing with satisfactory high- and low- speed characteristics

Some final remarks on the aerodynamic design of swept wings

In this chapter the modifications have been discussed which are required to turn a plane tapered swept wing with constant airfoil section into a design satisfying modern high- and low-speed requirements. This was illustrated with data from theoretical analyses and windtunnel tests at low speed so no compressibility effects were included. The basic section was symmetrical, so without camber. This allowed the use of a clearly visible step-by-step approach where the effects of successive steps could be added up.

For the design of a modern swept wing the starting point will be a supercritical airfoil section with transonic flow in the design condition. The design can only be accomplished with the aid of modern CFD methods which at least handle full potential flow with special provisions to take care of the trailing-edge boundary condition (such as the programme FLO 22) but preferably incorporate boundary layer and fuselage effects. Modern methods are mostly based on the use of a combination of Euler and time-averaged Navier-Stokes equations. But also with these modern methods many iterative steps are required along the lines indicated above before a satisfactory design is achieved. The design process is further complicated when engines and pylons under the wing have to be considered.

23 *Design considerations regarding the pressure distribution on finite wings*

As already mentioned in the previous chapters on airfoil sections in defining the design pressure distribution on modern wings for high-subsonic cruise Mach numbers the following boundary conditions should be adhered to:

1. The maximum local Mach number at each wing station.

In the supersonic region over the forward part of the upper surface of the wing the maximum local Mach number should not surpass $M_{loc} = 1.20$ to prevent an excessive drag creep above the subsonic drag level.
Boundary-layer separation behind the shock wave occurs when the local Mach number in front of the shock wave $M_{loc} = 1.35$ to 1.45 depending on Reynolds number and shock wave position. This condition determines the margin between cruise lift coefficient and buffet onset boundary. For swept wings these Mach numbers should be considered perpendicular to the isobars.

2. The pressure gradient in the subsonic part of the pressure distribution.

The adverse pressure gradient over the rear part of the wing, both on the upper and the lower surface, should not in any flight condition within the normal operating envelope of the aircraft cause trailing edge separation. This limits the most rearward position of the shock wave in the design condition or the amount of rear loading. It is therefore mandatory to perform the design computations including boundary-layer effects.

3. The spanwise distribution of the local lift coefficient.

With straight or near-straight swept isobars on the upper surface an elliptic or near-elliptic spanwise lift distribution should be obtained by tailoring the lower wing surface. As on a tapered wing the highest local lift coefficient is located at 60 to 70 percent of the semi-span, the choice of the section at that wing station should form the start of the design process.

4. The spanwise distribution of the local pitching moment coefficient.

Because of the required high lift coefficient the outboard wing sections will usually have positive camber and thus fairly large negative section pitching moment coefficients. Therefore the inboard wing sections should have an as low as possible section pitching moment coefficient. This means that as much as possible the required lift should be obtained through front loading.

A diagram of the wing design process is presented in figure 23.1 and the design objectives as discussed above are illustrated in figure 23.2.
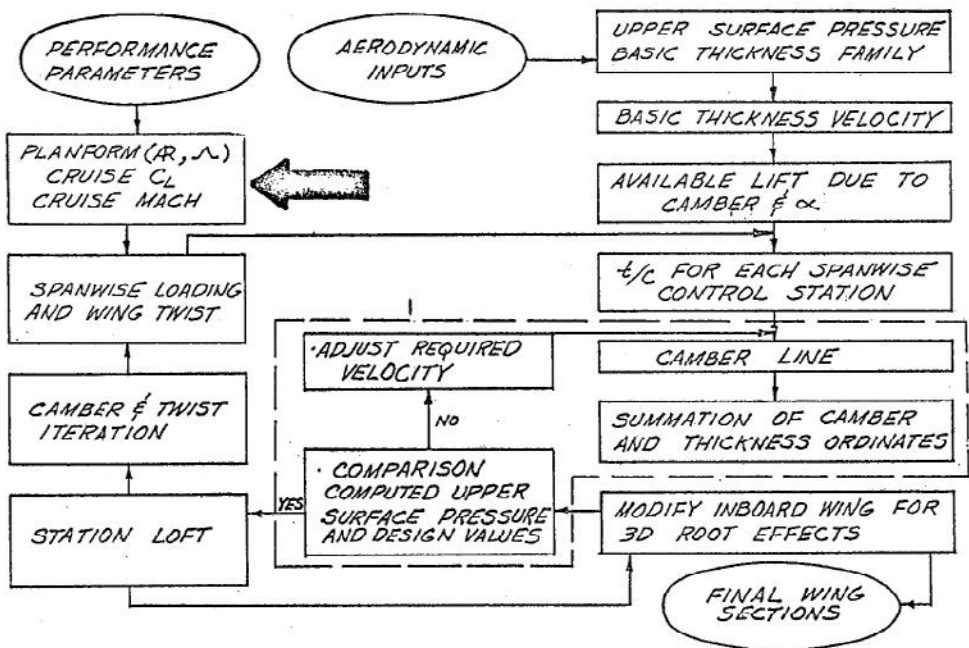
Figure 23.1 - The wing design process. Source: AGARD LS-37, paper no. 6
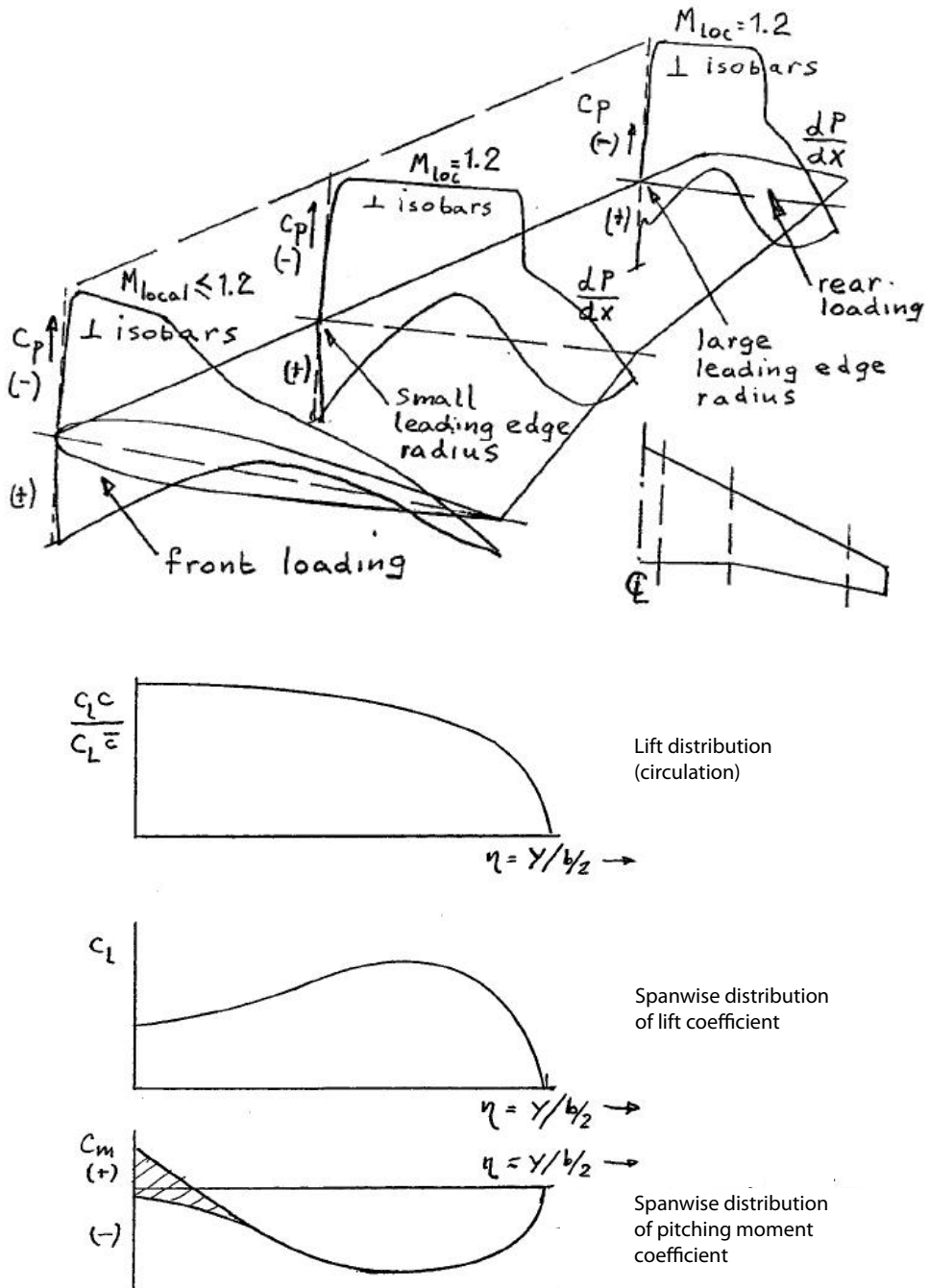
Figure 23.2 - Spanwise pressure, lift and pitching moment coefficient distributions (schematic)

24 *Examples of actual wing designs for high-speed transport aircraft*

In this chapter a number of examples are presented of actual transport aircraft wing designs. Most of them incorporate the characteristics as discussed in previous chapters but not all to the same degree. They also demonstrate the development over time of the understanding of transonic flow for complete aircraft configurations. Furthermore developments in production techniques have lessened the restrictions on certain geometry characteristics such as spanwise curvature of heavily-loaded wing skin panels. This again allowed practical wing shapes to approach more the ideal aerodynamic shapes.

In the last paragraph some general comments are given on the present state-of-the-art of transonic design and analysis methods and their possibilities and limitations. As has been mentioned before incorporation of boundary-layer effects greatly improves the validity of the computational results.

Canadair Bombardier 'Challenger' (first flight 1978)

The first example is the Canadair Bombardier 'Challenger' shown in figure 24.1. Chordwise pressure distributions at five wing stations at M = 0.82 and an angle-of-attack α = 1.5 deg are shown in figure 24.2. Data both from CFD computations and windtunnel tests are presented. Incorporating the fuselage in the computations clearly improves the comparison between theory and experiment although near the fuselage the discrepancies are not insignificant. The computer programme FLO 22 was developed for wings alone and the effect of the fuselage on the flow field has to be included through a mathematical dexterity. The design principles mentioned earlier can be recognized in the near-constant upper-surface pressure distribution along the span and the fading out of the rear loading when moving inboard.
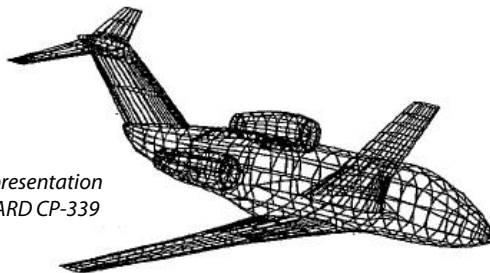
Figure 24.1 - WBAERO Panel representation of Challenger CL-600. Source: AGARD CP-339

The spanwise lift distribution is given in figure 24.3 for the complete aircraft and for the wing fuselage combination, both at M = 0.70 and C_N = 0.51. The effect of the compound wing taper on the distribution of the local lift coefficient on the inboard wing is evident. This allowed a relative thickness at the root t/c = 14%. Furthermore due to the vicinity of the engine nacelles the lift on the inboard wing is slightly suppressed.
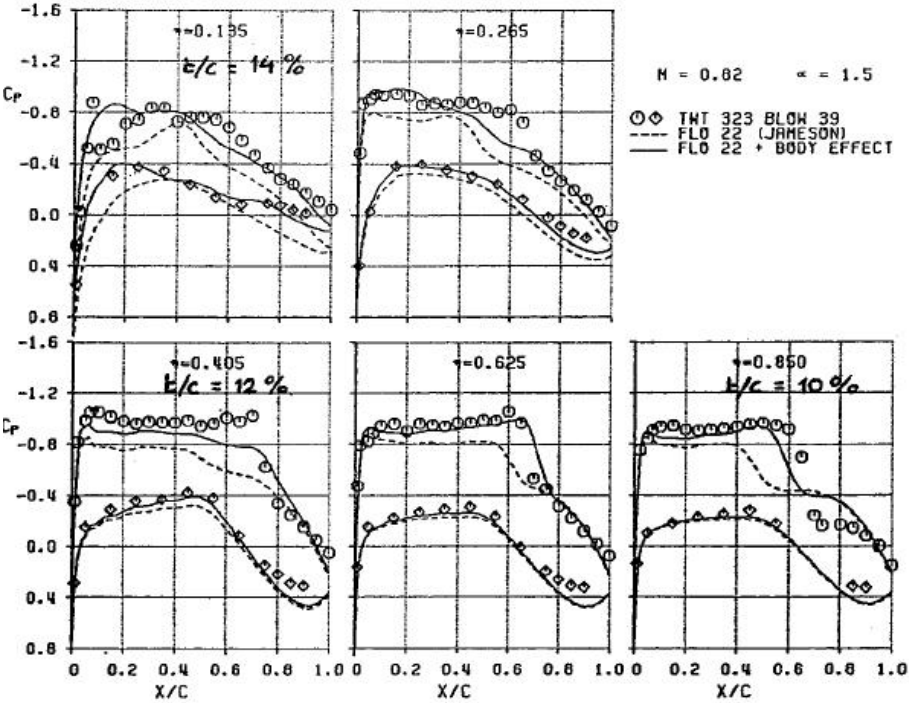
Figure 24.2 - Effect of body on wing pressure distribution theory (FLO 22) versus wind tunnel measurements. Source: AGARD CP-339
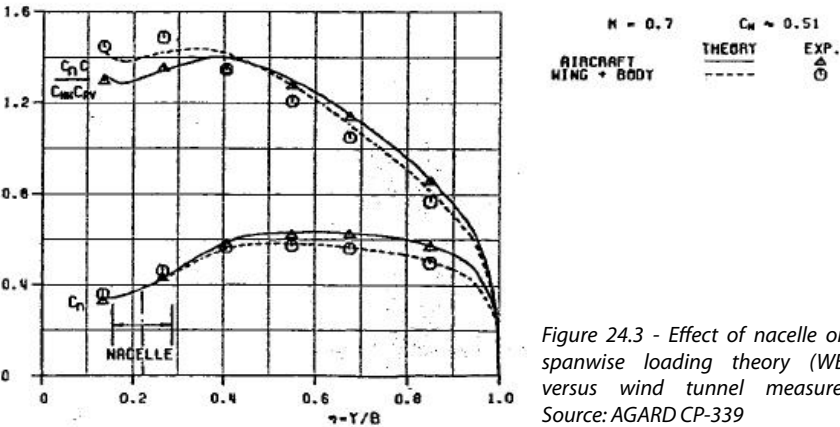
Figure 24.3 - Effect of nacelle on wing spanwise loading theory (WBAERO) versus wind tunnel measurements. Source: AGARD CP-339

Lockheed L-1011 Tristar (first flight 1970)

A competitor of the Boeing 747 and the DC-10 was the Lockheed L-1011 of which the wing sections are shown in figure 24.4. Again, the root section has all the characteristics required to counter the adverse root effects of swept wings: negative camber is applied and the position of the greatest thickness is fairly forward. The relative thickness is 12.6% instead of 9.9% (streamwise) in the outboard wing. The profile section in the outboard wing is shown perpendicular to the rear spar in order to show the wing structure in the plane of a wing rib.
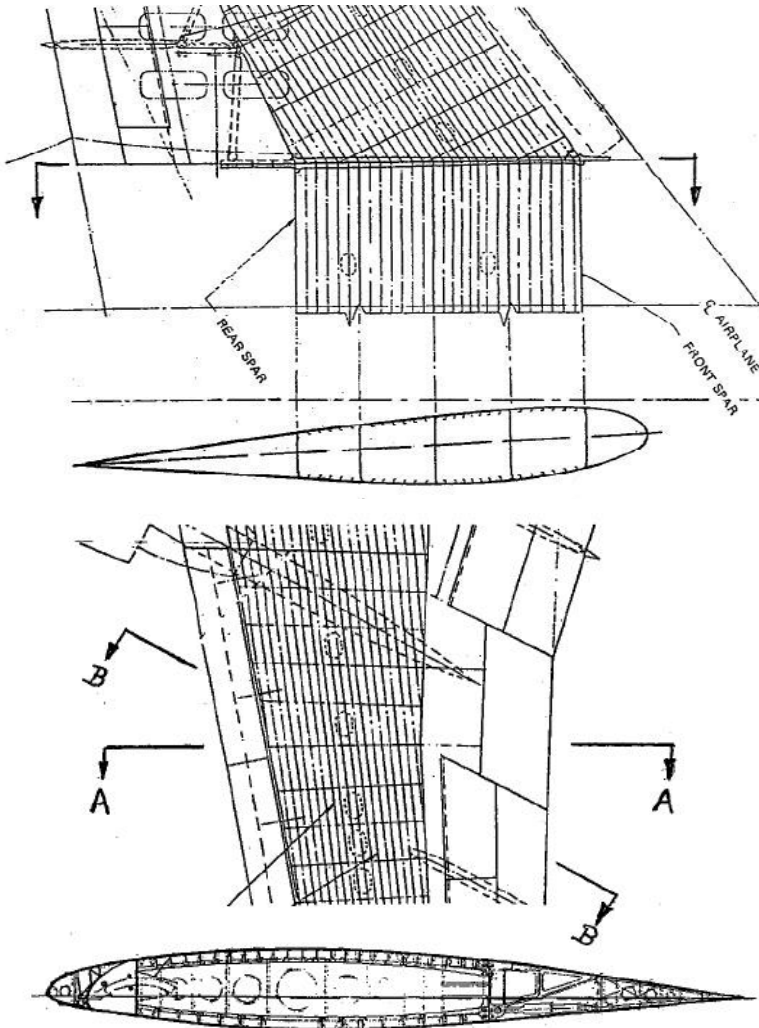
Figure 24.4 - Lockheed L-1011 wing

Douglas DC-8 (first flight 1958)

The DC-8 was the first civil jet airliner of the Douglas company. Figure 24.5 shows its wing design. The inboard section from the root to $y/(b/2) = 0.25$ has a constant section at an incidence $i = 3.9$ deg. The section with relative thickness $t/c = 12\%$ has negative camber and a somewhat forward position of maximum thickness. Further outboard the section changes into a 10 % thick section with positive camber and lower incidence. The sections are shown in figures 24.6 to 24.8 The negative wing twist continues up to the tip. The sections applied in the outboard wing were further developments of NACA Modified Four-Digit airfoil sections. The chosen root section shows the required chordwise pressure distribution for nearly straight isobars along the wing span. This section was maintained over the inner 25 % of the semi-span because the small leading-edge radius assured initial flow separation on the inboard wing in a stall.
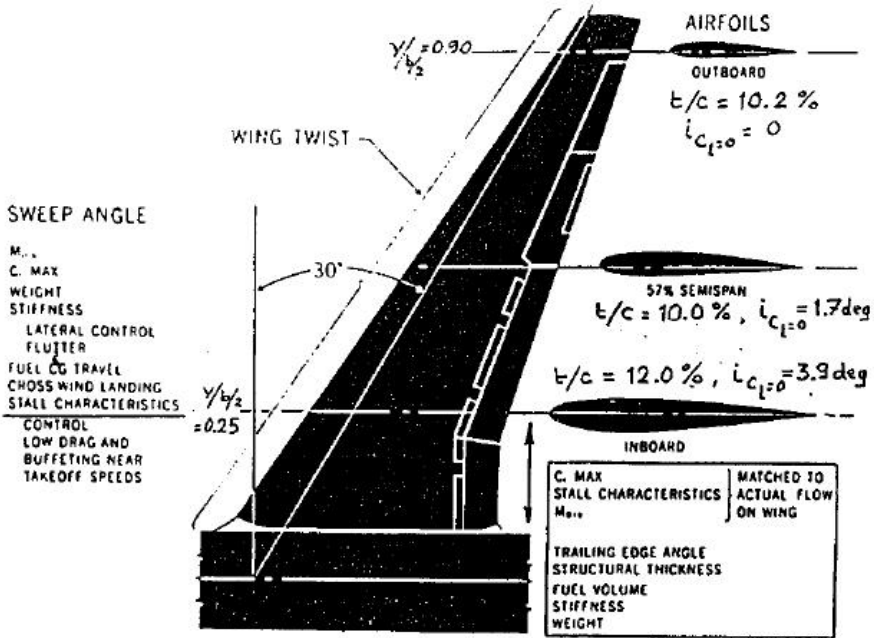
Figure 24.5 - DC-8 wing design criteria. Source: Canadian Aeronautical Journal, October 1960

Figure 24.9 shows the Mach drag rise characteristics as a function of Mach number from various windtunnel and flight tests. For the original production configuration two windtunnel models were tested, a 3.5 % scale complete model at $Re = 1.8 \times 10^6$ and a 7 % scale semi-span model at $Re = 6.5 \times 10^6$. The data from the half-model tests were mistrusted because of the half-model test technique. The complete-model data were used for the performance predictions. However

the flight test data agreed with the test results from the high-Reynolds-number tests. This was later substantiated by tests on a complete model at Re = 6x10^6 in the NACA Ames 11 ft pressurised transonic wind tunnel. The original production model of the DC-8 had disappointing drag rise characteristics.
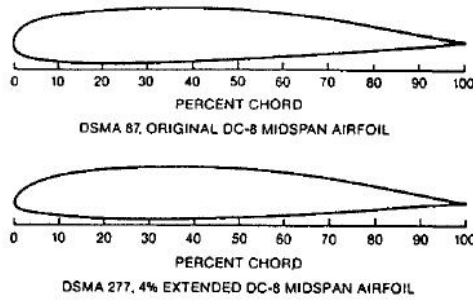
Figure 24.6 - Contours of original and 4% extended DC-8 airfoil. Source: AIAA paper No 85-4067
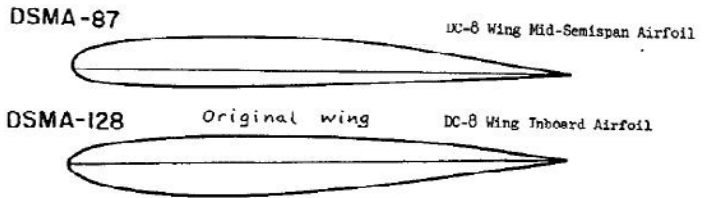
Figure 24.7 - DC-8 wing mid-semispan and inboard airfoils. Source: Canadian Aeronautical Journal, October 1960
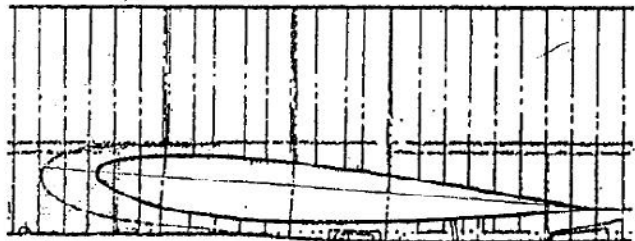
Figure 24.8 - The DC-8 wing incidence angle. Source: Canadian Aeronautical Journal, October 1960
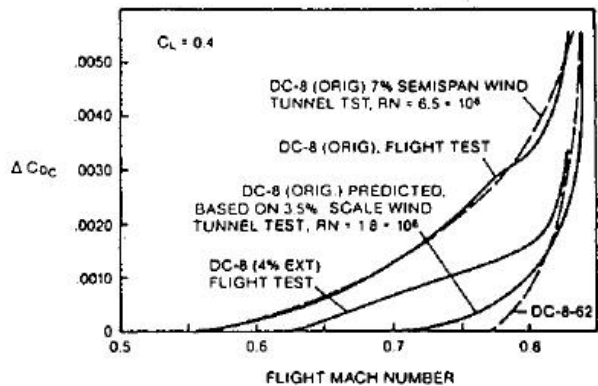
Figure 24.9 - DC-8 comparison of compressibility drag rise wind tunnel tests at low and high Reynolds number and flight test. Source: AIAA paper No 85-4067

In figure 24.10 a part of a paper presented by one of the leading aerodynamicists of the Douglas Aircraft company is shown to illustrate the rather limited means available to designers in the early 60's to optimise the characteristics of high-speed transport wings. This applies in particular to improvements on aircraft in production. On the DC-8 the allowable modifications to improve the drag rise characteristics had to be limited to the wing area ahead of the front spar. Analysis had shown that the high drag could also be attributed to excessive leading-edge supervelocities. A new leading edge was designed which increased the chord length by 4 percent ahead of the front spar with lower peak supervelocities. This considerably improved the cruise drag and was adopted on the production aircraft. During this period the work by Pearcey in England on peaky airfoil sections (see chapter 15) became known but had no effect on the modification on the DC-8. The knowledge was used however in the development of the DC-9.

We concluded that for some airfoils, and certainly with our peaky ones, the Reynolds number was important: exceed 6×10^6 Reynolds number or run a risk of getting the wrong drag rise answer. The problem was also attributed to an excessive nose peak. Therefore, a modified airfoil was designed to lower the nose peak pressure in the cruise condition. The modification was limited to the leading edge ahead of the front spar and increased the chord by 4%. This change eliminated about 70% of the problem, although a modest jump in the drag still occurred well below M_{DIV}.

Production was changed to the 4% extended leading edge and most of the early DC-8 aircraft were retrofitted with it.

During this period of agonizing reappraisal, we became aware of the theoretical airfoil work of Pearcey in England. From Pearcey's studies we decided that our real problem was that the incompressible airfoil pressure distribution did not have a sufficient sharp nose peak and that the slope of the pressure coefficient curve with distance along the airfoil had to become quite flat forward of the crest. This, in our opinion, was necessary to avoid excessive drag creep prior to M_{DIV}. Our ability to attain this on the modified DC-8 airfoil was limited by the existing structure, which could be changed only forward of the front spar, and the need to maintain the same stall speeds as originally achieved. Later, when the airfoil was further modified for the DC-9-30 series and subsequent versions of the DC-9 and fitted with a leading-edge extension of about 6% equipped with a leading-edge slat to handle the more stringent $C_{L_{max}}$ requirements, a sharper peak was achieved. We shall see, however, that the modified DC-8 airfoil was really quite good in itself. Much of the residual drag creep problem later turned out to be due to pylon interference.

Figure 24.10 - On the design and further development of the DC-8 wing. Source: AIAA paper No 85-4067
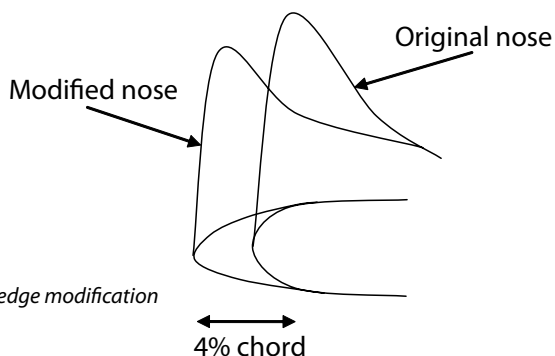
Figure 24.11 - DC-8 wing leading edge modification

Analysis of the wing upper surface pressure distribution showed that the engine pylons with leading edges running over the wing leading edge caused suction peaks just inboard of the pylons as shown in figure 24.13(a). This effect was discussed before in chapter 20 (see figures 20.21 and 20.47) and may be beneficial for low- speed stall control but may produce extra drag in cruise.
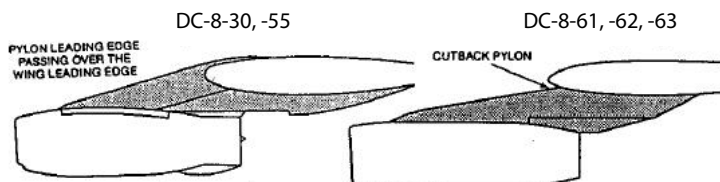
Figure 24.12 - Over-the-wing and cutback pylons for wing mounted jet or turbofan engines. Source: AIAA paper No 85-4067

For stall control their effect may be too strong if not shaped carefully. On the DC-8 prototype the maximum lift coefficients for all flap settings were lower than required. This necessitated the introduction of short leading-edge slots just inboard of the pylons to obtain the intended maximum lift coefficients.

In order to remove the suction peaks inboard of the pylon the pylon leading edges were cut back. The result is shown in figure 24.13(b). This modification was introduced on the DC-8 Series 61, 62 and 63.
The improvement in cruise drag is evident from figure 24.9. No loss in maximum lift occurred but the short leading-edge slots (which close in flight) were maintained. As the Series 60 received different engines the pylons had to be redesigned and the engine nacelles were placed in a lower position possibly decreasing the interference effects mentioned in chapter 11. Finally note in figure 24.13(b) the regular isobar pattern as mentioned in the beginning of this paragraph on the DC-8.
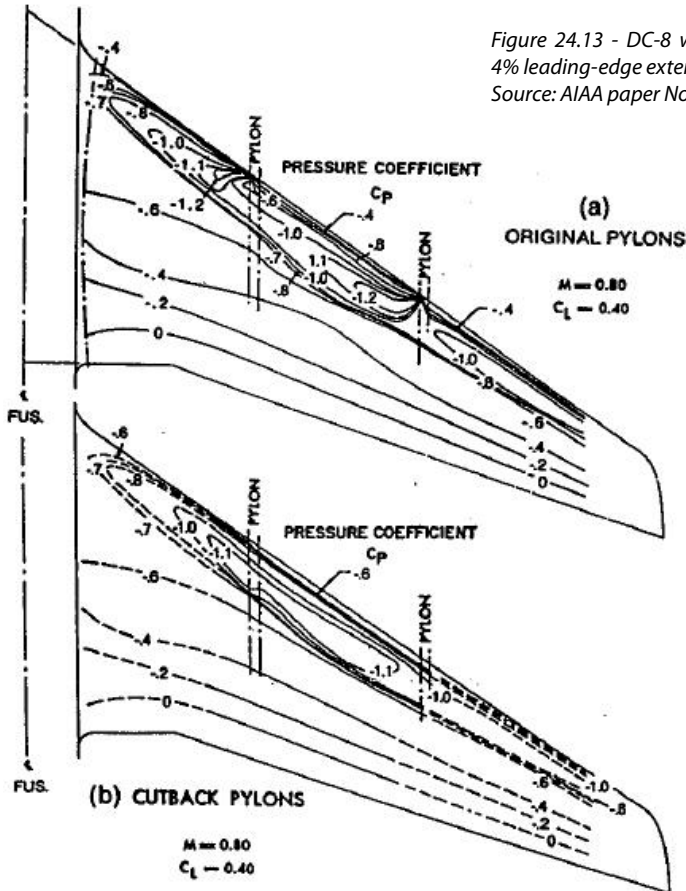
Figure 24.13 - DC-8 wing pressure distributions, 4% leading-edge extension / 7% semispan model. Source: AIAA paper No 85-4067

Douglas DC-9 (first flight 1965)

The DC-9 was designed for short and medium ranges and a cruise Mach-number M = 0.80. Consequently the wing sweep angle could be limited to $\Lambda_{1/4c}$ = 24 deg and the requirements concerning straight swept isobars in cruise and the stalling characteristics were less demanding than on the DC-8.

Figure 24.14 shows the spanwise thickness and twist distributions. The lower lift coefficients on the inboard wing allow a higher relative thickness while maintaining the required isobar pattern. The wing twist on the outboard wing is slightly larger than required for minimum induced drag in order to obtain satisfactory stalling characteristics. In figure 24.15 the airfoil sections that determine the wing shape of the DC-9 Series 10 are presented. Note the negative camber of the root section.
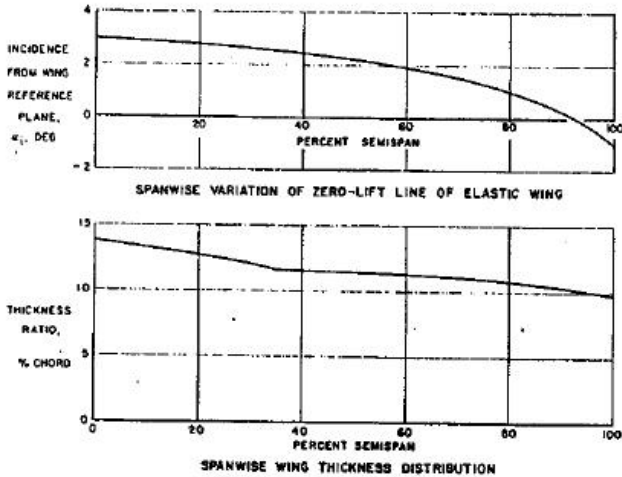
Figure 24.14 - Douglas DC-9 wing thickness and twist. Source: Journal of Aircraft, Nov-Dec 1966
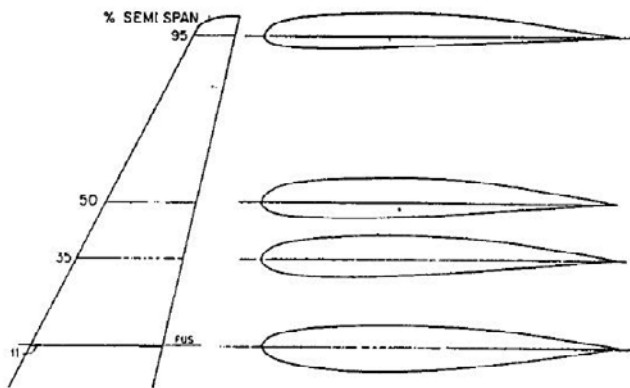
Figure 24.15 - Douglas DC-9 airfoils. Source: Journal of Aircraft, Nov-Dec 1966

As noted earlier in the early 60's the work by Pearcey in the U.K. on peaky airfoil sections became generally known. These sections were described in chapter 15.

The actual development of such sections was a tedious process because of the limited understanding of and the means to perform calculations on mixed subsonic-supersonic flow. A general idea was however that, in order to obtain the desired pressure distribution at the (transonic) design condition, for subsonic flow conditions the upper surface pressure distribution should exhibit a sharp suction peak at the leading edge followed by a region with a very low positive pressure gradient up to about mid-chord. Numerical values for these parameters could only be determined in the windtunnel so trial and error became a characteristic of the development process.

When the slatted version of the DC-9, the Series 30, was developed the wing chord was increased by 6 percent ahead of the front spar. This allowed the leading-edge shape and thus the pressure distribution to be modified.The resultant sharp suction peak in subsonic flow is shown in figure 24.16.

Figures 24.17 and 24.18 compare shock wave position in long-range cruise and M_{DIV} for the basic airfoil sections for both the original and the modified wing. Figure 24.19 shows that on the modified wing the drag creep was indeed lowered. At $C_L = 0.4$ the decrease in drag was 10 drag counts.
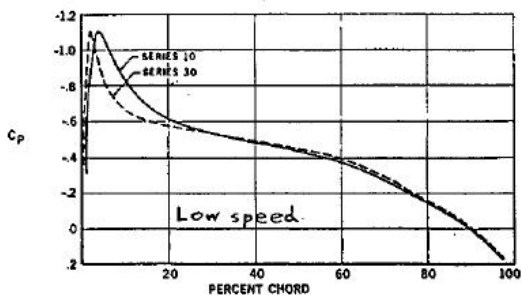
Figure 24.16 - Comparison of calculated two-dimensional pressure distributions for DC-9 series 10 and 30 airfoils.
Source: Journal of Aircraft Nov-Dec 1966
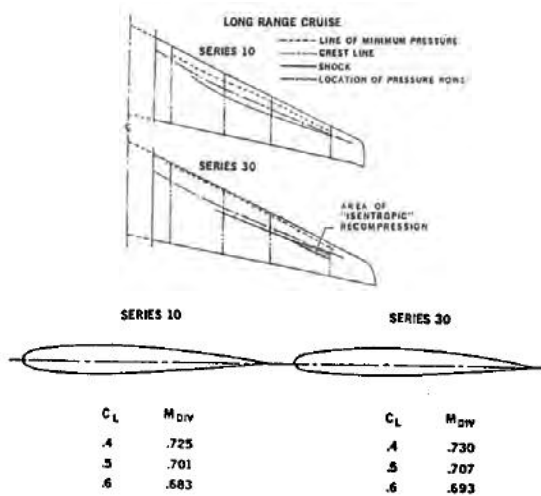
Figure 24.17 - Comparison of Series 10 and Series 30 shock wave position from wind tunnel tests.
Source: Journal of Aircraft Nov-Dec 1966
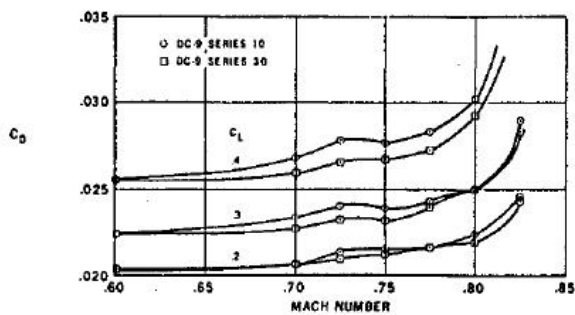
Figure 24.18 - Comparison of estimated unswept drag divergence Mach numbers.
Source: Journal of Aircraft Nov-Dec 1966

Figure 24.19 - Comparison of Series 10 and Series 30 drag rise characteristics from wind tunnel tests.
Source: Journal of Aircraft Nov-Dec 1966

Douglas DC-10 (first flight 1970)

The experience gained by the Douglas Aircraft Company in designing the wing of the DC-9 was incorporated in the wing design of the DC-10. Again peaky airfoil sections were employed. Figure 24.20 illustrates again the difference in the development of the upper surface pressure distribution when changing from a low to a high Mach number for NACA 6-series sections and for peaky sections.
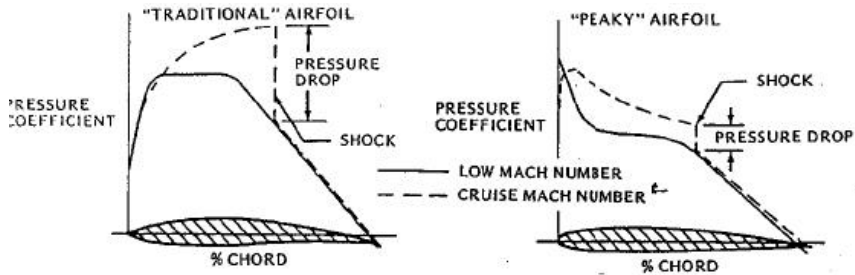
Figure 24.20 - Comparison of calculated pressure distributions. Source: Douglas Flight Approach, 1972

As the DC-10 is a long-range aircraft the wing was designed for a high cruise Mach number M = 0.85. This required a quarter-chord wing-sweep angle Λ = 35 deg. Figures 24.21 to 24.23 present the spanwise thickness and twist distribution for both the initial and the final wing and the basic wing airfoil section. In order to provide room for the main undercarriage legs between the rear wing spar and the inboard flaps the wing trailing edge shows a kink (sometimes called a Yehudi after the inventor at Boeing).

As this results in a large root chord the local design lift coefficient is low and the root section can have a 40 percent higher relative thickness than the sections in the outer wing. Figure 24.24 presents the drag rise characteristics of the aircraft at two lift coefficients. At M = 0.85 the increase in drag due to compressibility is only 15 drag counts both from windtunnel and from flight tests.
The basic airfoil section has very little rear loading. When the DC-10 was developed into the MD-11 some rear loading was applied in the flap and aileron area outside the trailing-edge kink. Together with the introduction of winglets this led to a significant drag improvement. Figure 24.25 presents the chordwise pressure distributions for both the DC-10-30 and the MD-11 at M = 0.825 and C_L = 0.53. The rear-loading is clearly exchanged for lower supervelocities over the upper front part of the wing.
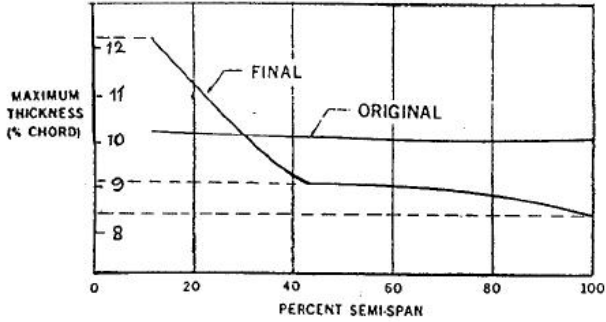
Figure 24.21 - Thickness distribution. Source: AIAA paper No 69-830
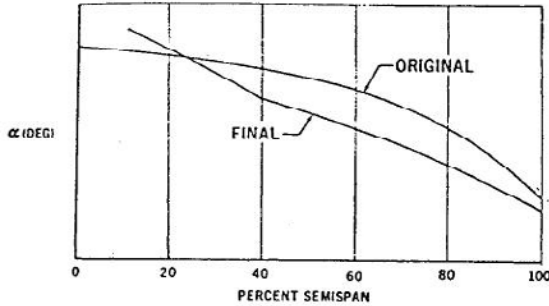
Figure 24.22 - Wing twist distribution. Source: AIAA paper No 69-830
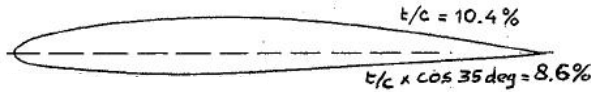
Figure 24.23 - Basic wing section. Source: AIAA paper No 69-830

In Figure 24.26 the high-speed drag curves are compared for the McDonnell-Douglas DC-10-30 and the MD-11. Note that at lower Mach numbers at $C_L = 0.50$ the extra drag due to the longer fuselage is compensated by the lower induced drag due to the winglets. At cruise Mach numbers the drag of the MD-11 is even 10 to 15 drag counts lower than of the DC-10-30.
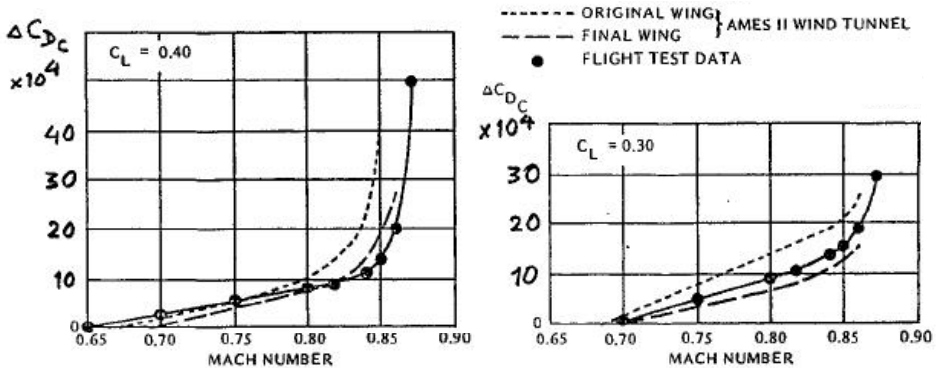
Figure 24.24 - DC-10 Series 10 compressibility drag rise. Source: Douglas Flight Approach, 1972
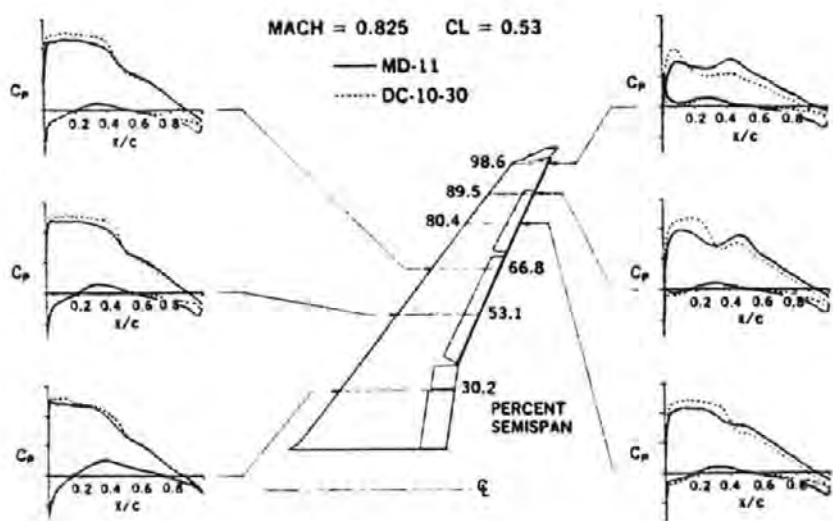
Figure 24.25 - Chordwise pressure distribution on the DC-10-30 and MD-11 wing.
Source: AIAA paper No 87-2928
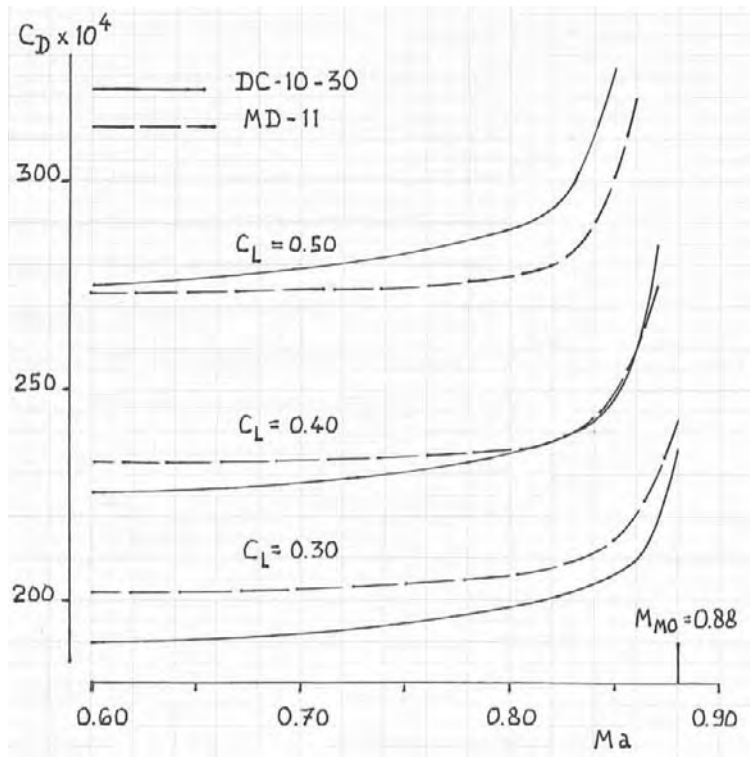
Figure 24.26 - Comparison of the high-speed drag of the DC-10-30 and the MD-11

De Havilland Trident (first flight 1962)

In the 1950's peaky airfoil sections were developed by Pearcey and his co-workers at the National Physical Laboratory. At the Royal Aircraft Establishment Küchemann and Weber performed extensive windtunnel investigations and developed a theory for the analysis and design of swept wings in compressible flow. One of the first civil transport aicraft where this new knowledge was used in designing the wing was the De Havilland DH-121 Trident.

In the design of the wing a balance was struck between the aerodynamic and the structural and production requirements. The wing was defined by four airfoil sections connected by straight generators so nowhere did the surface show double curvature. The break in the wing shape at the trailing edge kink was not chosen streamwise but perpendicular to the stringers as was the third governing section roughly halfway the outer wing. Figure 24.27 shows the position of the four sections.
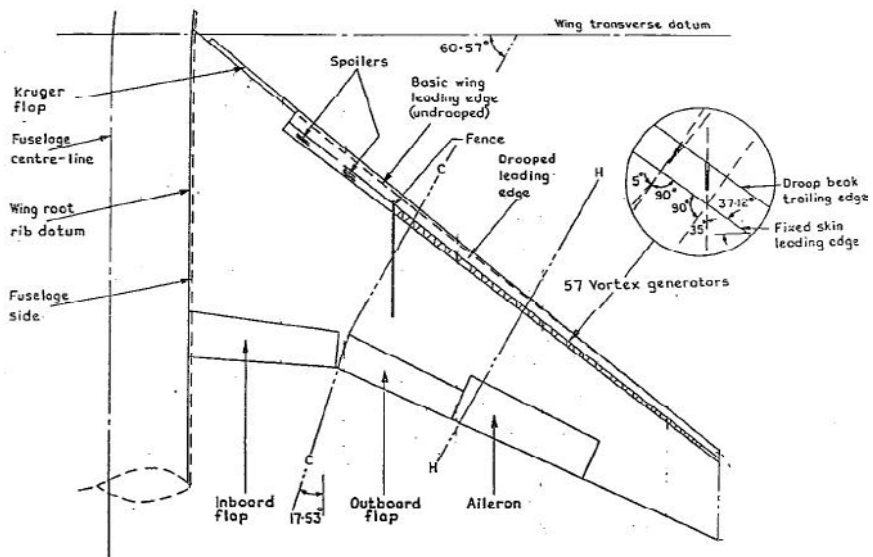
Figure 24.27 - De Havilland Trident 1c wing geometry. Source: RAE TR 68108

The aircraft had double-slotted flaps and a drooping leading edge with retractable vortex generators on the "knuckle" which extended when the leading edge was drooped.

In figure 24.28 the wing twist distribution is presented both for the wing in the production jig (zero-g twist) and in flight (1-g twist in the design condition). Figure 24.29 shows the position of the leading and trailing edge of the unloaded wing.
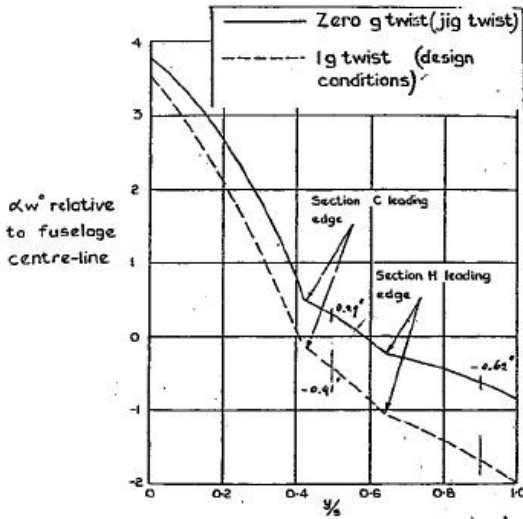
Figure 24.28 - Details of full scale wing twist. Source: RAE TR 68108
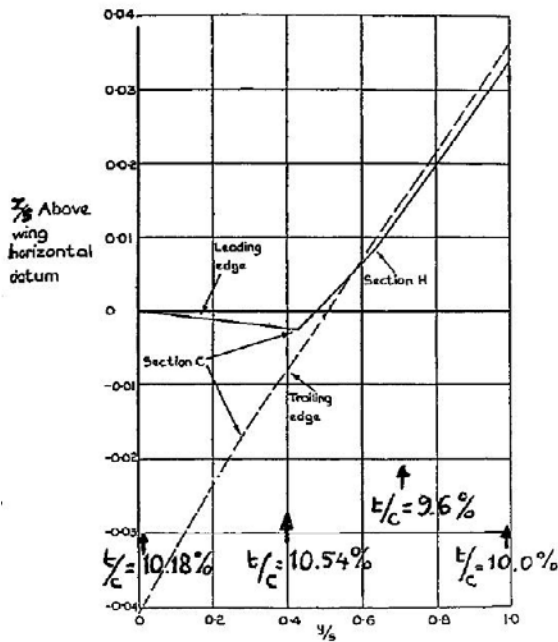
*Figure 24.29 - Full scale height location of unloaded wing leading and trailing edges (zero g shape).
Source: RAE TR 68108*
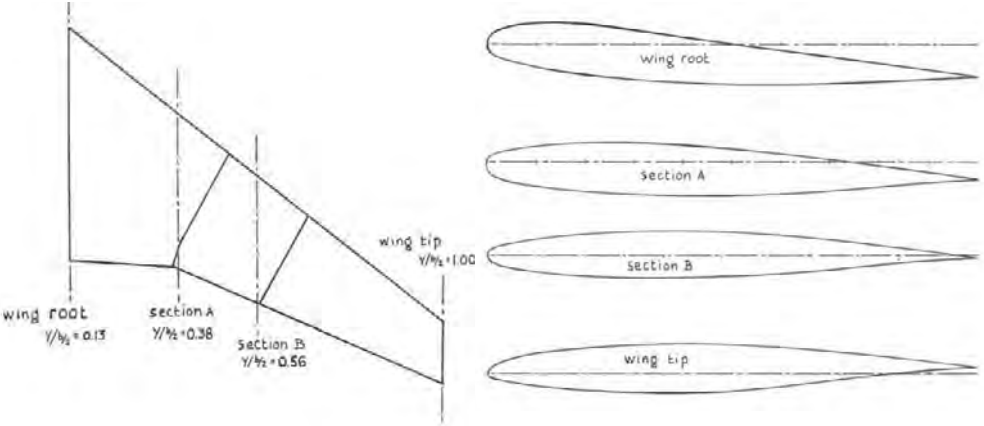
Figure 24.30 - Wing airfoil sections. Derived from data in RAE TR 68108, ARC R&M No 3608 and ARC C.P. No 1170

$C_{Lmax, landing}$	
Trident 1	1.95
Trident 2E	2.05
Trident 3B	2.07
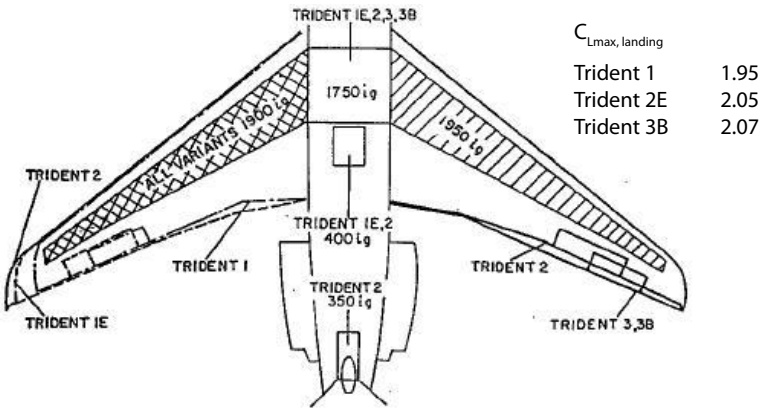
Figure 24.31 - Wing platform and fuel capacity.

In figure 24.30 four streamwise sections are given, the wing root and tip sections and two sections on both sides of the structural kink section. Note the progressive increase in incidence towards the root on the inner wing, the negative camber and the thick forward part of the root section in order to realise the required upper surface isobar pattern.

The Trident was designed for a high cruise Mach number ($M_{MO} = 0.88$). At low lift coefficients the drag rise characteristics in flight compared favourably with the windtunnel data as shown in figure 24.33. At higher lift coefficients the full-scale drag was somewhat disappointing. As during the development of successive versions the operating weights grew up to 40 percent the drag characteristics became a growing concern. Wing modifications were applied to leading and trailing edges together with span extensions but these served primarily to improve take-off and landing performance. Figures 24.31 and 24.32 show the successive modifications of the wing.

The experience with the Trident made designers aware that deliberately designing wings with significant regions of mixed subsonic–supersonic flow with little risk required a far better understanding of the physics of such flows and better mathematical tools than existed at the time.
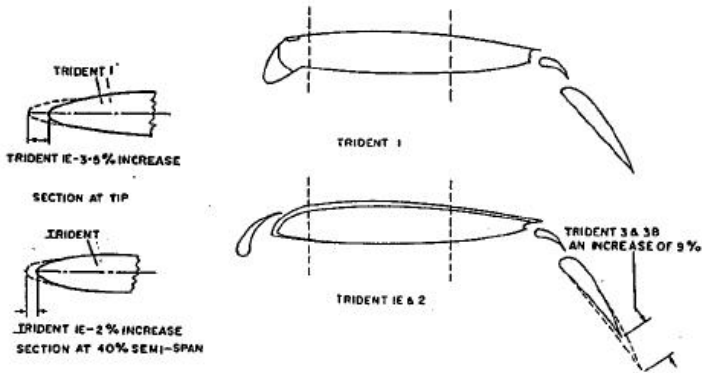
Figure 24.32 - Wing sections. Source: The Aeron. Journal of the R.A.e.S, November 1969
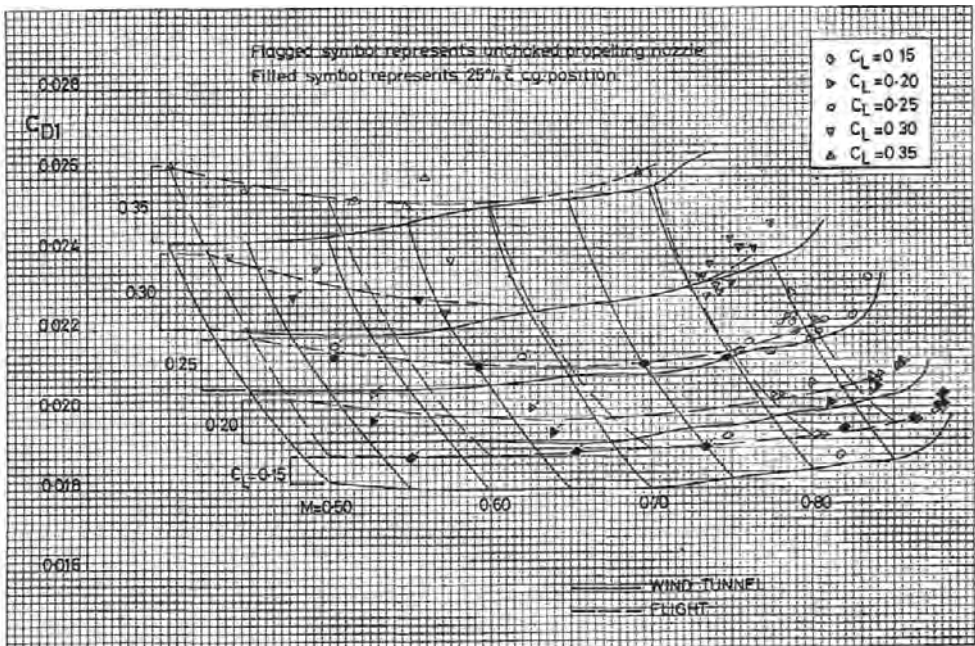
Figure 24.33 - De Havilland Trident 1. Comparison between drag data as found from wind tunnel and flight tests. Source: ARC CP 1170

British Aerospace Vickers VC-10 (first flight 1962)

In the same period that the medium-range de Havilland Trident was developed in the U.K. Vickers-Armstrongs developed the long-range and much larger VC-10. The wing design of that aircraft was also based on the work of Pearcey at NPL and Küchemann at RAE. However, on the inner wing double curvature was adopted in the upper and lower surface and Vickers-Armstrongs used the shot peening process in the production of the inner wing panels. The design condition for the VC-10 wing was M = 0.81 and C_L = 45.

The wing shape was determined by three sections in the inboard wing and four sections in the outer wing. As on the Trident, in a later version, the Super VC-10, the leading edge was modified by a 4% chord extension albeit over only 65% semi-span presumably to lessen the drag creep. Figure 24.34 shows the wing planform and the location of the governing airfoil sections. Root and outer wing sections are presented in figures 24.36 to 24.38. Note again the large incidence, the thick leading edge and the nagative camber of the root section.

In figure 24.35 the upper surface pressure distribution is presented for the basic section near the design condition and at a subsonic Mach number. Note again that, although the shock wave itself is fairly weak the high supervelocities at the leading edge lead (as was discovered in later years) to premature drag creep.

Figure 24.34 - BAe (Vickers) Super VC-10 wing. Source: ARC Current paper No 1125
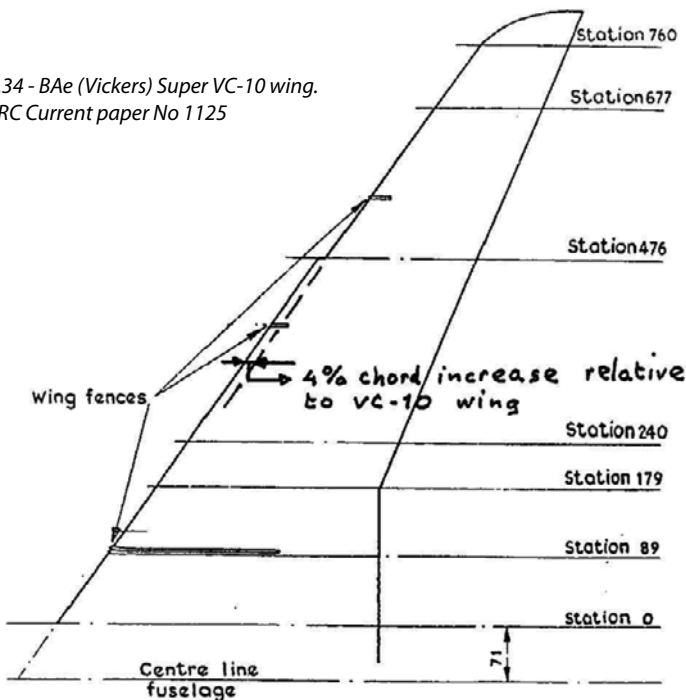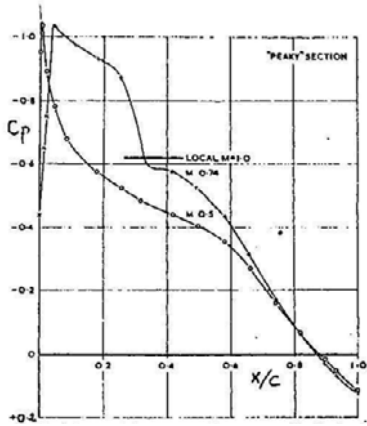
Figure 24.35 - 'Peaky' type of wing upper surface pressure distribution with and without the effects of compressibility.
Source: Aircraft Engineering, June 1962
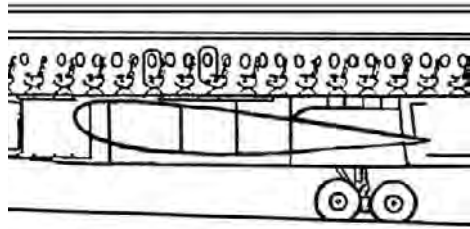
Figure 24.36 - Vickers VC-10 root airfoil section. t/c = 13.2%
Source: Flight International, April 1st 1965
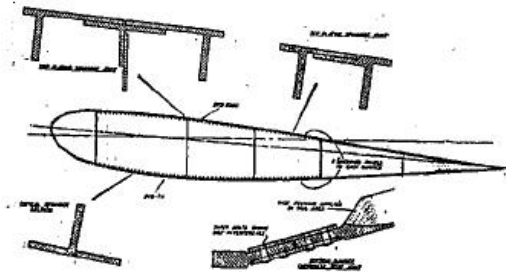
Figure 24.37 - Details of the VC-10 wing structural box. t/c = 13.2%. Source: Aircraft Engineering, June 1962
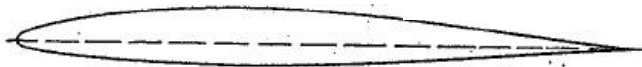
Figure 24.38 - Streamwise section of the VC-10 outer wing. t/c = 9.8%. Source: Aircraft Engineering, June 1962
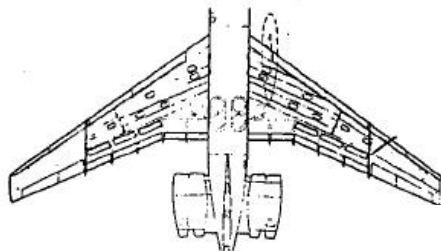
Figure 24.39 - Top view of the Vickers VC-10 wing. Source: Aircraft Engineering, June 1962

In figure 24.40 chordwise pressure distributions are shown for five wing sections and the spanwise distribution of the local lift coefficient at the design condition $M = 0.81$ and $C_L = 0.45$. Figure 24.41 shows chordwise pressure distributions at these wing sections together with upper surface pressure distribution on the wing for a flight condition slightly above the design condition, at $M = 0.84$ and $C_L = 0.45$. Both windtunnel and flight test data are given. In the design condition the high suction peaks at the leading edge caused certainly a premature drag creep.

Also flight test data are shown for $M = 0.694$. Note that at this lower Mach number where the flow is subsonic everywhere the isobar pattern is almost ideal. In the high-speed cruise flight condition however the isobar pattern is much more irregular. This illustrates again that the successful design of a transonic wing can only be achieved by the use of modern mathematical tools and the associated computers.
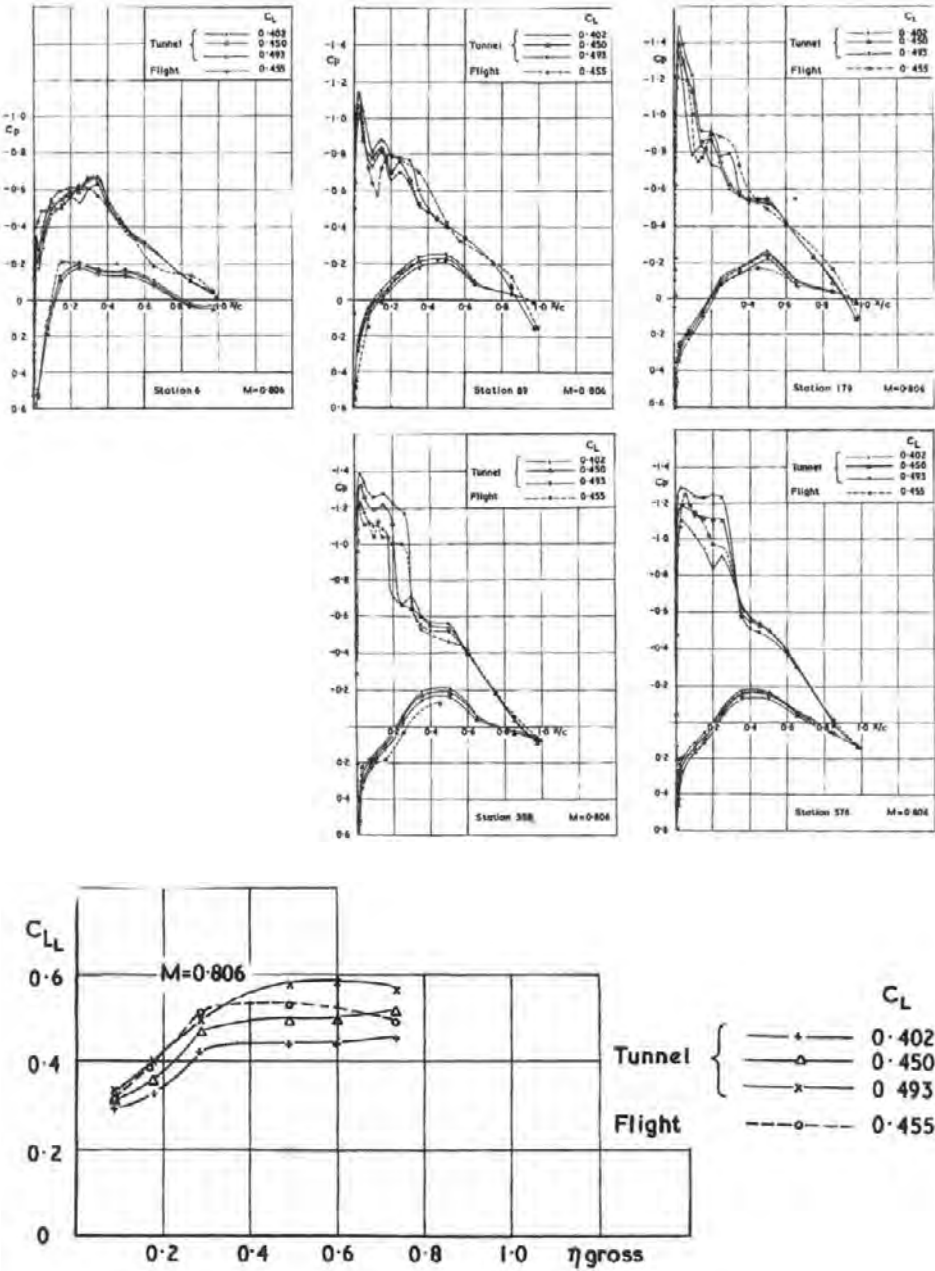
Figure 24.40 - A comparison of wing pressure distributions measured in flight and on a wind tunnel model of the Super VC-10 at M = 0.806. Source: Reports and Memoranda No. 3707
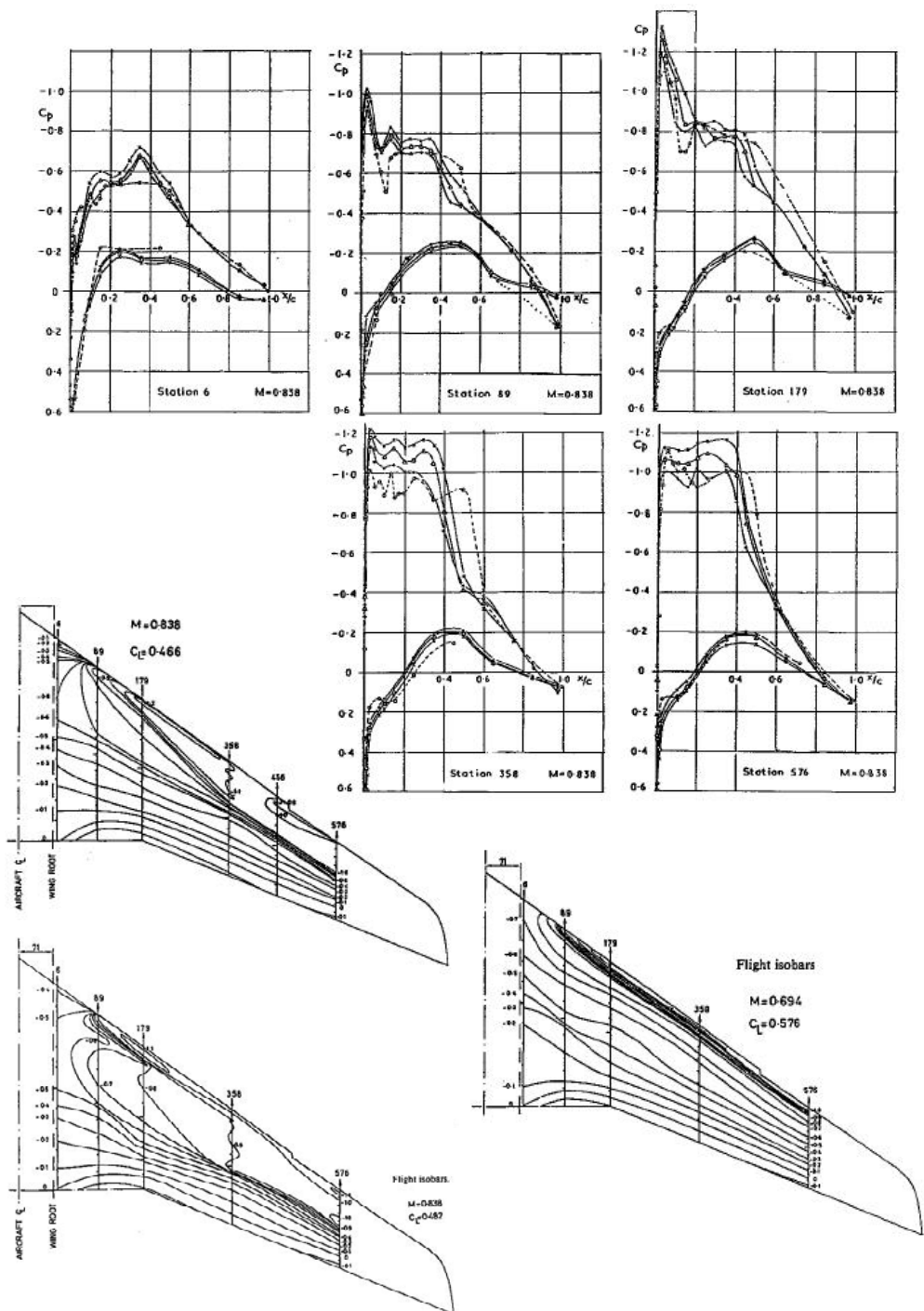
Figure 24.41 - A comparison of wing pressure distributions measured in flight and on a wind tunnel model of the Super VC-10 at M = 0.838. Source: Reports and Memoranda No. 3707

British Aircraft Corporation BAC-111 (first flight 1963)

The third British aircraft discussed in this chapter is the British Aircraft Corporation BAC-111. This was a short-to-medium range aircraft with a lower design Mach number ($M_{MO} = 0.78$). Contrary to the previous two aircraft the basic section has a sonic rooftop upper surface pressure distribution as illustrated in figure 24.42. In figures 24.43 and 24.44 the three wing sections that determine the wing shape and the wing planform are shown. Although less pronounced than on the previous aircraft because of the lower wing sweep the inner wing between the root and the section at the trailing edge kink shows a strong twist. The root section shows again a larger thickness than the sections in the outboard wing, negative camber and the maximum thickness is far forward.
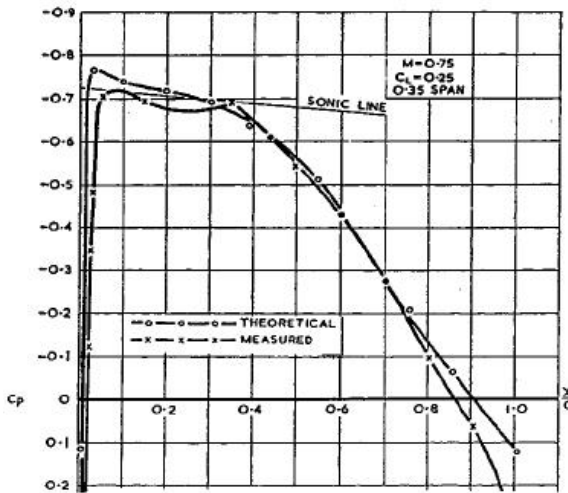
Figure 24.42 - Comparison of theoretical and measured chordwise pressure distribution on chosen wing section. Source: Aircraft Engineering, May 1963

WING ROOT SECTION   t/c = 12.3% $i_c = 2.5°$

SECTION AT 0·35 SPAN   t/c = 10.7% $i_c = -1.4°$

WING TIP SECTION   t/c = 10.7% $i_c = -1.6°$
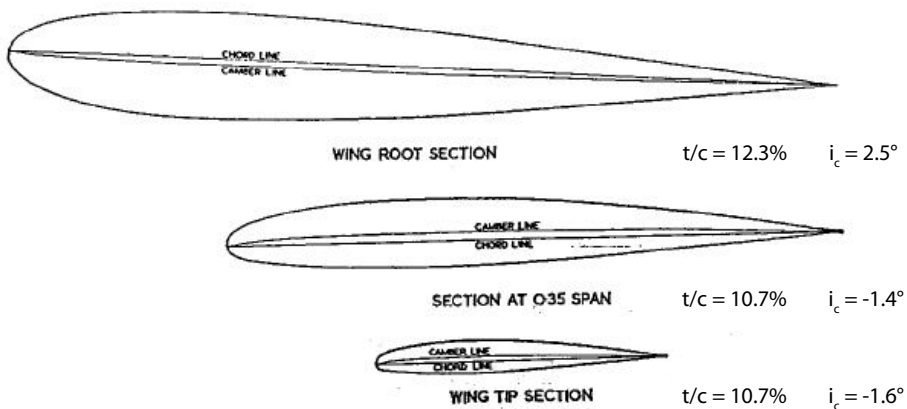
Figure 24.43 - Wing airfoil section shapes. Source: Aircraft Engineering, May 1963
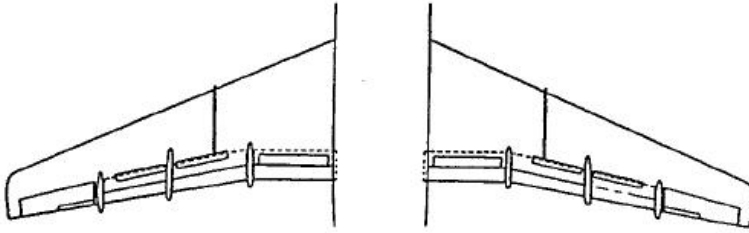
Figure 24.44 - BAC 1-11 wing. Source: Aircraft Engineering, May 1963

Boeing 707 (first flight 1957)

Although the first Boeing 707 flew in 1957 the wing design is identical to the wing of the Model 367-80 which served as the prototype of the KC-135 Stratotanker and flew for the first time in July 1954. Based on the experience gained in the design of the B-52 wing the 707 wing had a thick root (t/c = 15.1%) but no further refinements in order to obtain straight isobars in the root region are evident. The wing planform and outboard wing airfoil section are shown in figures 24.45 and 24.46.

In figures 24.47 and 24.48 chordwise pressure distributions are presented at four wing stations at M = 0.70 and C_L = 0.47 and at M = 0.78 and C_L = 0.49. No data is available for the isobar pattern inboard of 25% semi-span. Over the larger part of the wing a regular pressure pattern is shown but at the tip the isobars clearly curve forward. In figure 24.49 some high-speed drag data are shown.
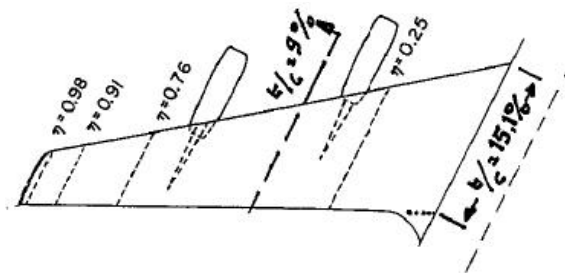
Figure 24.45 - Boeing 707 wing. Source: NASA TM 78786
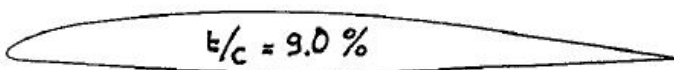
Figure 24.46 - Typical outboard wing airfoil section. Source: NASA TM 78786
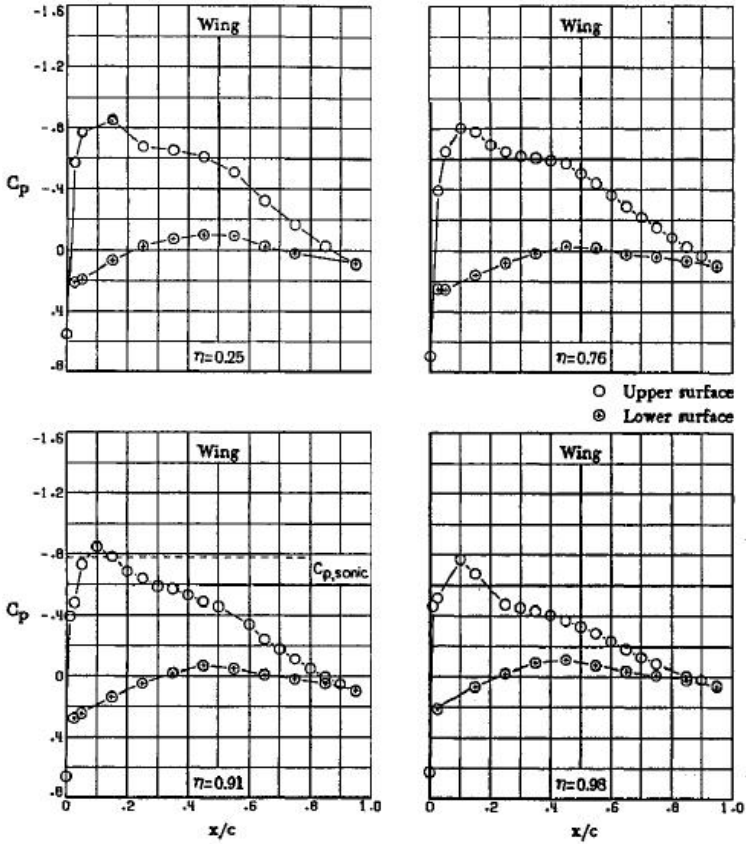
Figure 24.47 - Chordwise pressure distributions on the Boeing KC-135/707-100 wing. M = 0.70, α = 2.5°, C_L = 0.47. Source: NASA TM 78786
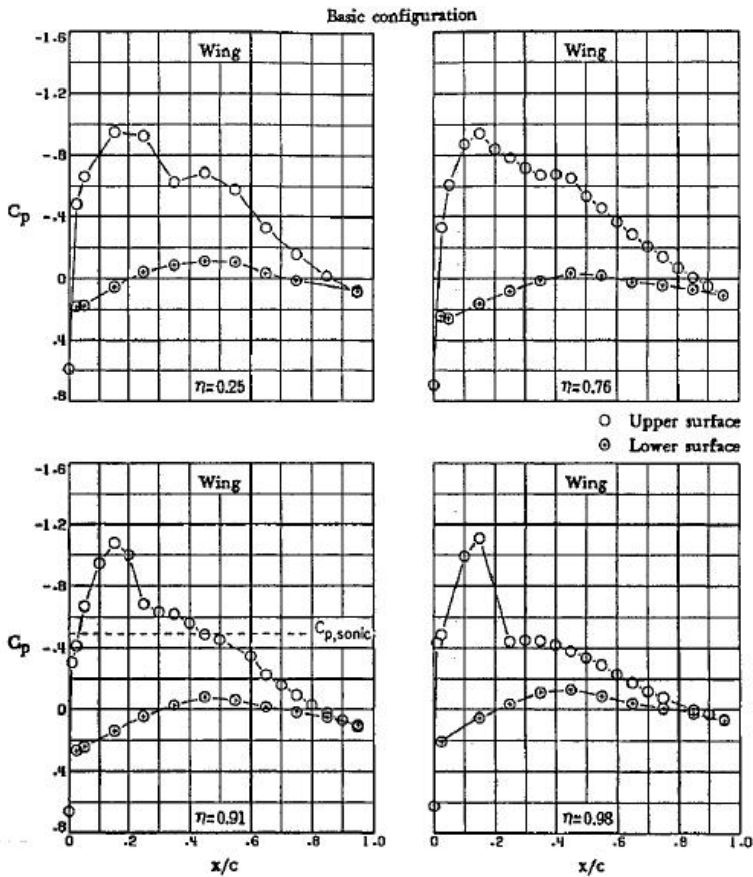
Figure 24.48 - Chordwise pressure distributions on the Boeing KC-135/707-100 wing. M = 0.78, α = 2.5°, C_L = 0.49. Source: NASA TM 78786
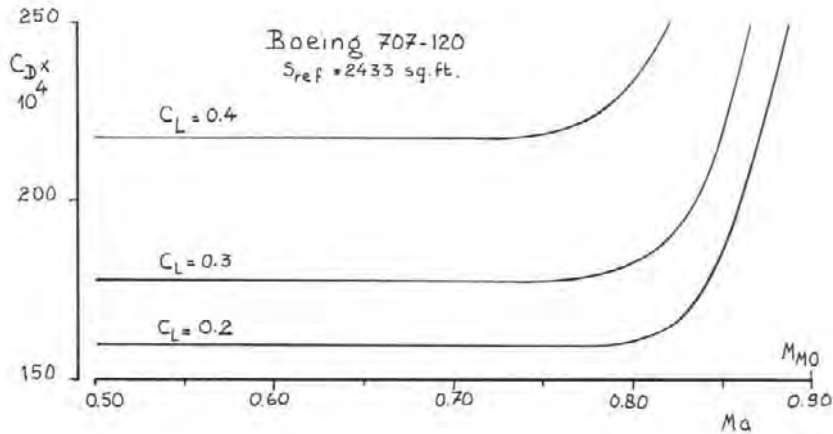
Figure 24.49 - Boeing 707-120 drag versus Mach diagram

Boeing 720 (first flight 1959)

The work by Küchemann and Weber on the root and tip effects on swept wings had been published in parts in various publications in the mid-50's and had certainly become known in the USA.

In November 1959 a smaller version of the Boeing 707, the Boeing 720 made its first flight. It had the same wing as the 707 but with a modified leading edge between the fuselage and the inner engine. The upper-right part of figure 24.50 illustrates the forward part of the root section in its original and in its modified form. The modification is entirely in line with the recommendations by Küchemann and Weber: a more forward location of the maximum thickness and a decrease in leading-edge camber. This modification increased the cruise Mach number from M = 0.78 to 0.79 to M = 0.82 (Flight, 19 August 1960).

This improvement and the illustration in the right part of figure 24.50 of the original root section of the 707 strengthens the suspicion that the upper surface isobar pattern in the root region was far from ideal. The lower part of figure 24.50 shows five sections of the 720 wing. A similar modification was later also adopted for the intercontinental version of the 707, the Boeing 707-320.
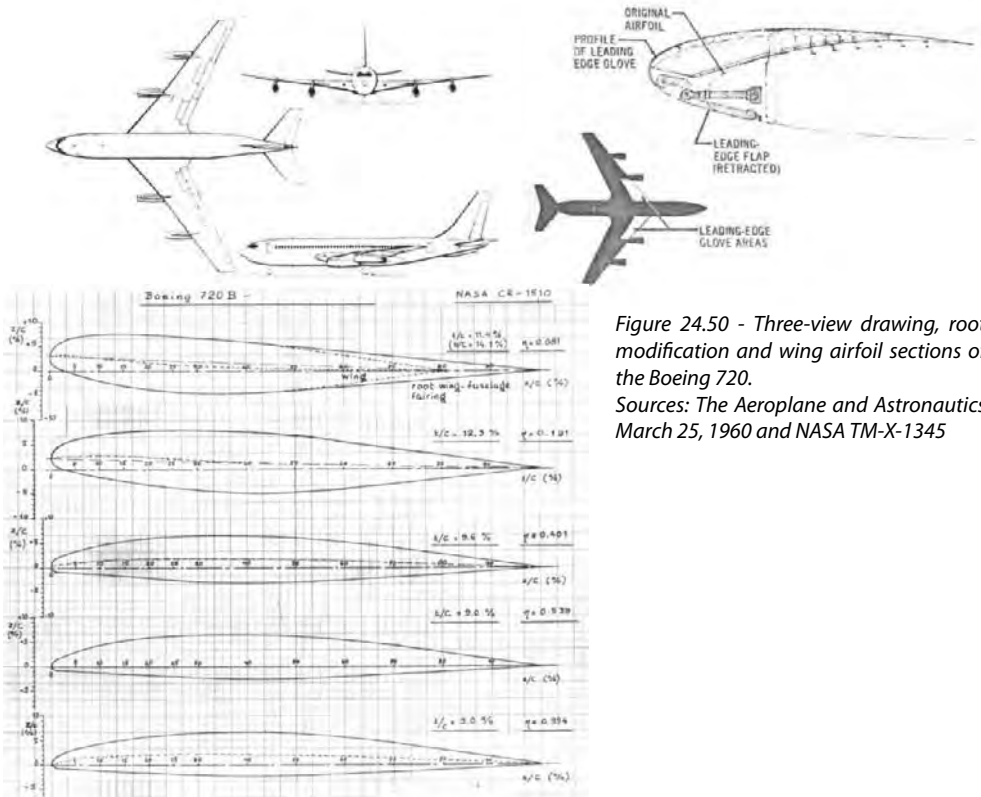
Figure 24.50 - Three-view drawing, root modification and wing airfoil sections of the Boeing 720.
Sources: The Aeroplane and Astronautics March 25, 1960 and NASA TM-X-1345

Boeing 727 (first flight 1963)

In designing the Boeing 727 wing as a starting point the wing of the Boeing 720 was taken. This wing, with a sweep angle $\Lambda_{1/4c}$ = 35 deg had a design cruise condition of M = 0.83 at C_L = 0.4. As the initial version, the 727-100, would be a short-to-medium range aircraft operating from relatively short runways the design cruise condition was fixed at M = 0.82 at C_L = 0.3.
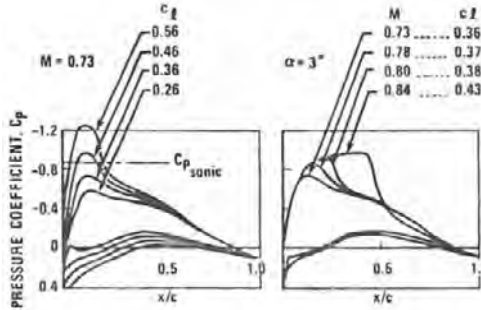
Figure 24.51 - Pressure distributions at 62% semispan.
The wing sweep angle chosen was $\Lambda_{1/4c}$ = 32½ deg.
Source: AIAA paper No. 71-289

This wing showed a marked family resemblance particular in the outboard wing. This is evident from a comparison of the pressure distribution at 62 % semi-span at M = 0.73 as given in figure 24.51 with the data in figure 24.47.

Furthermore the root and outboard wing section as shown in figures 24.54 and 24.55 are similar to the sections of the Boeing 720 wing in figure 24.50. In figure 24.56 the pressure distribution is presented at three wing stations at M = 0.80 and C_L = 0.44. Note the similarity between the pressure distribution at the root and at sections further outboard indicating that the particular shape of the root section does produce the required isobar pattern on the upper surface in the root region. Figure 24.53 shows the high-speed drag data.
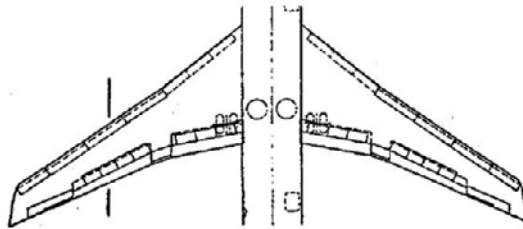
Figure 24.52 - Boeing 727 wing and thickness to chord ratios. Source: AIAA paper No. 71-289
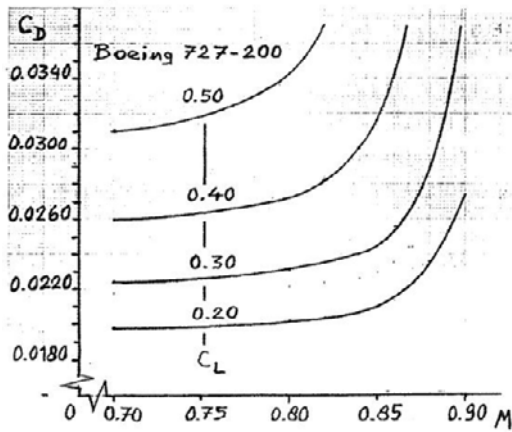
Figure 24.53 - Boeing 727 drag curve. Source: Case Study in Aircraft Design - The Boeing 727, 1978
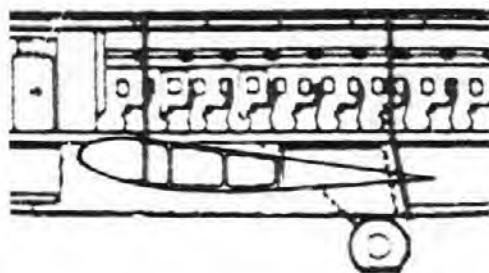
Figure 24.54 - Wing root section

Figure 24.55 - Outer wing section parallel to wing ribs.
Source: SAE Paper S408
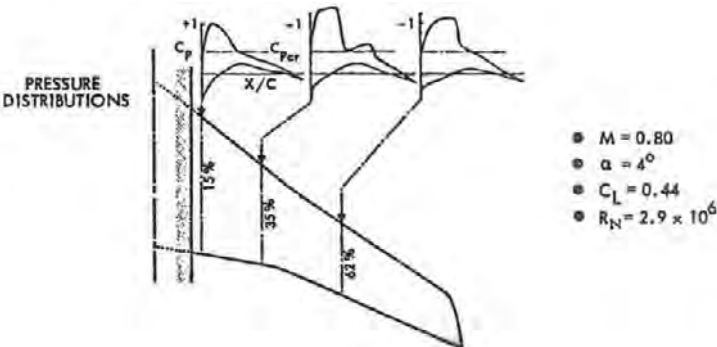
Figure 24.56 - Wing pressure distribution.
Source: AIAA Paper No. 71-289

In 1967 the Boeing 727-200 made its first flight. This version had a fuselage lengthened by 20 feet increasing the payload capability by about 40 percent. Subsequent development led to a significant increase in fuel capacity. The final version of the 727 showed a Maximum Take-Off Weight of 209,500 lb which was an increase of 37 percent over the MTOW of the intial version, see figure 24.57. This serves to illustrate that in defining the design cruise condition of a wing a considerable weight growth has to be anticipated during the lifetime of the programme.
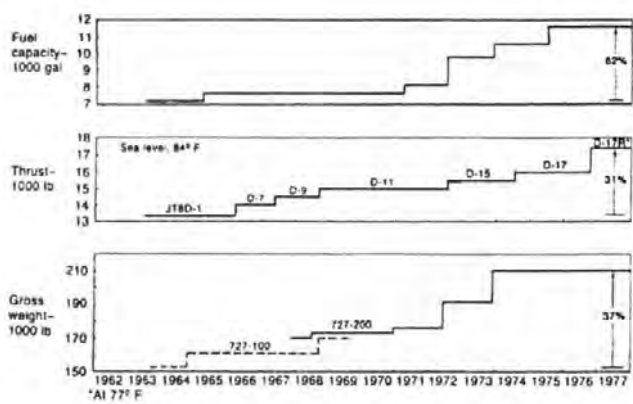
Figure 24.57 - Development history

Boeing 737 (first flight 1967)

The Boeing 737 programme started as a small short-to-medium range transport aircraft to complement the Boeing 727 for thinner routes. Two flight operating conditions were important in determining the aerodynamic design requirements for the wing:

      1. High-speed cruise (M = 0.78, C_L = 0.3)

      2. Long-range cruise (M = 0.74, C_L = 0.5)

The Maximum Operating Mach Number was fixed at M_{MO} = 0.82.

The slightly lower operating speeds than of the 727 allowed a wing sweep angle of $\Lambda_{1/4c}$ = 25 deg instead of $\Lambda_{1/4c}$ = 32½ deg and thicker airfoil sections as shown in figure 24.59. Note again the characteristic wing root section. The outboard section is clearly a further development of the section used on the Boeing 727. Computed pressure distributions on this section as shown in figure 24.58 show similarity with the data in figure 24.51.

The engine nacelles on the 737 were fitted under the wing with a minimal fairing. The original nacelles had thrust reversers in an unfavourable position which necessitated the lengthening of the nacelles rearwards by 45 inches.

M = 0.72
α = 0.35°
C_L = 0.32

M = 0.72
α = 1.4°
C_L = 0.61
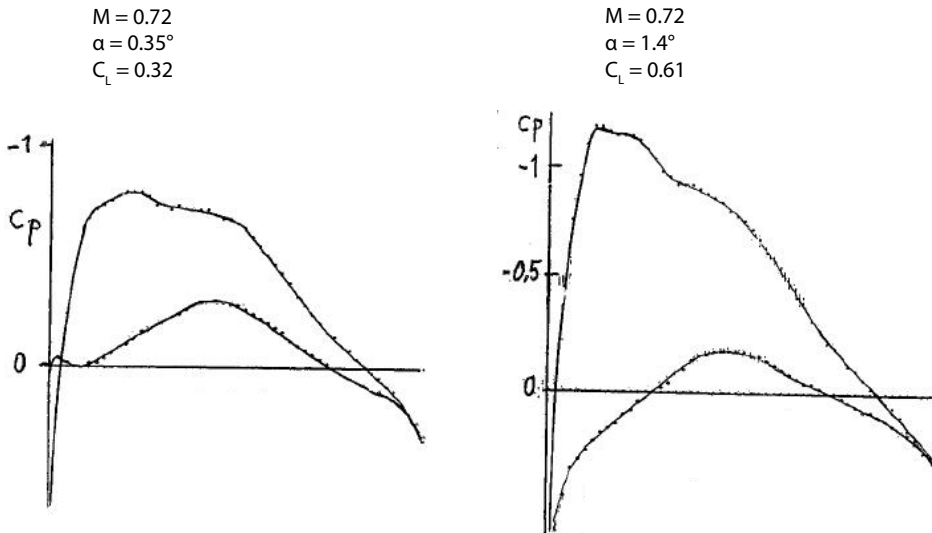
Figure 24.58 - Boeing 737-100, -200 pressure distributions on a section in the outboard wing. The calculation is performed without boundary layer

t/c = 15.4%

Root airfoil

t/c = 10.8%

Kink to tip
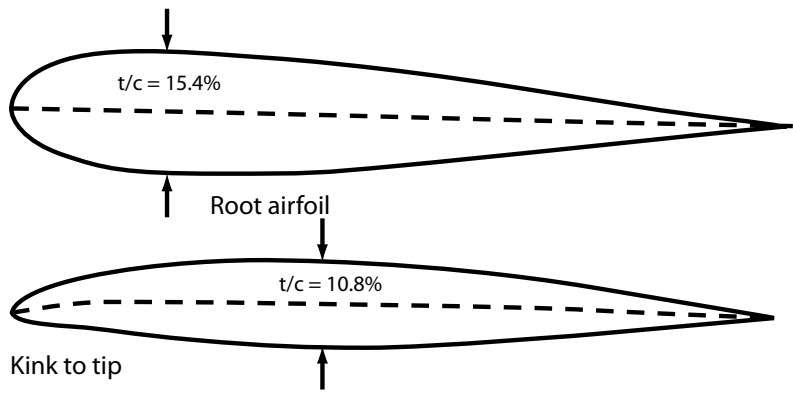
Figure 24.59 - Airfoil sections of the Boeing 737-100, -200. Source: NASA TN D-5971
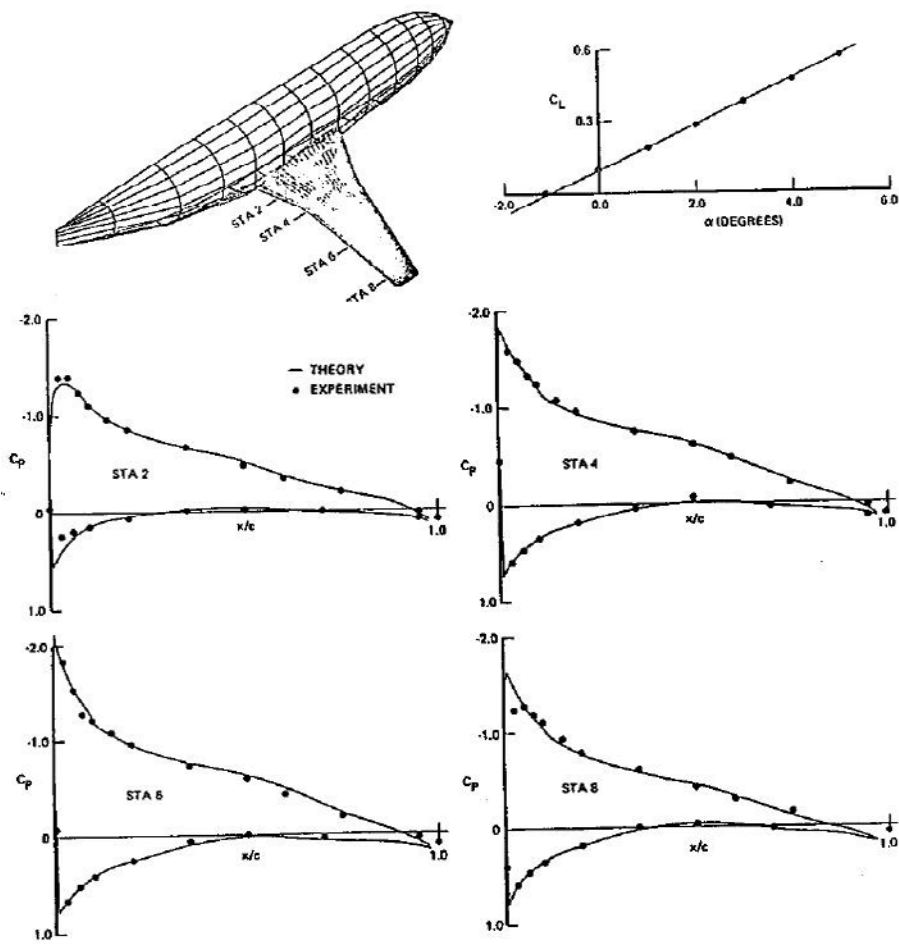
Figure 24.60 - Test/Theory comparison for a Boeing 737 wing-body model at low Mach number. Source: AIAA Paper No. 72-188

Figure 24.60 shows the chordwise pressure distributions at four wing stations at a low Mach number. Apart from the leading-edge region near the fuselage the pressure distributions are similar indicating a desired isobar pattern. However there is no guarantee that also at transonic flow conditions a satisfactory isobar pattern will occur. In figure 24.61 the effect of fitting the (lengthened) engine nacelles on the wing is shown. Near the wing leading edge the familiar (slight) increase in supervelocities on the inboard side and decrease on the outboard side is evident. On the lower inboard side fitting the nacelle increases the local velocities over the whole chord, but in general minimising the interference effects was successful.
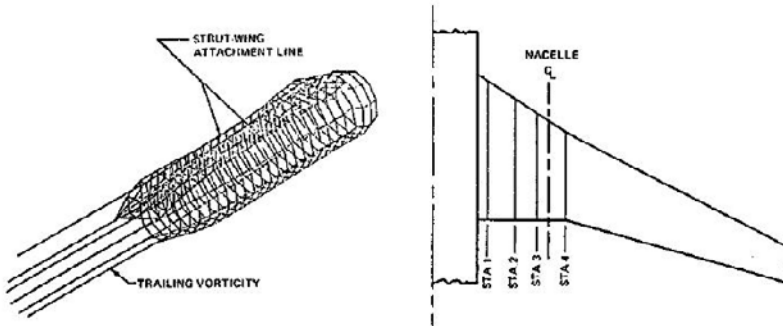
a) Nacelle and strut added to 737 wing-body model
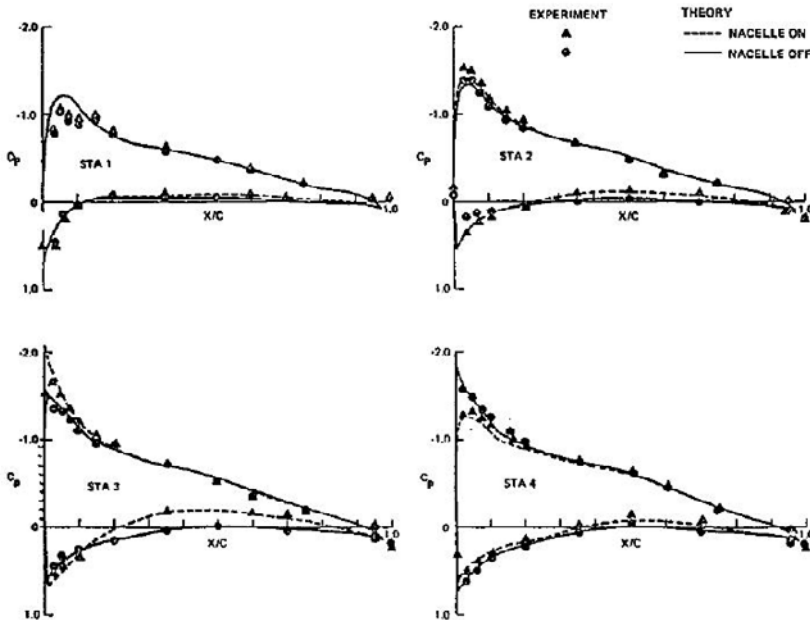
b) Wing surface pressure comparison at low Mach number

Figure 24.61 - Test/theory comparison showing influence of close-coupled nacelle installation on wing surface pressures, Boeing 737. Source: AIAA Paper No. 72-188
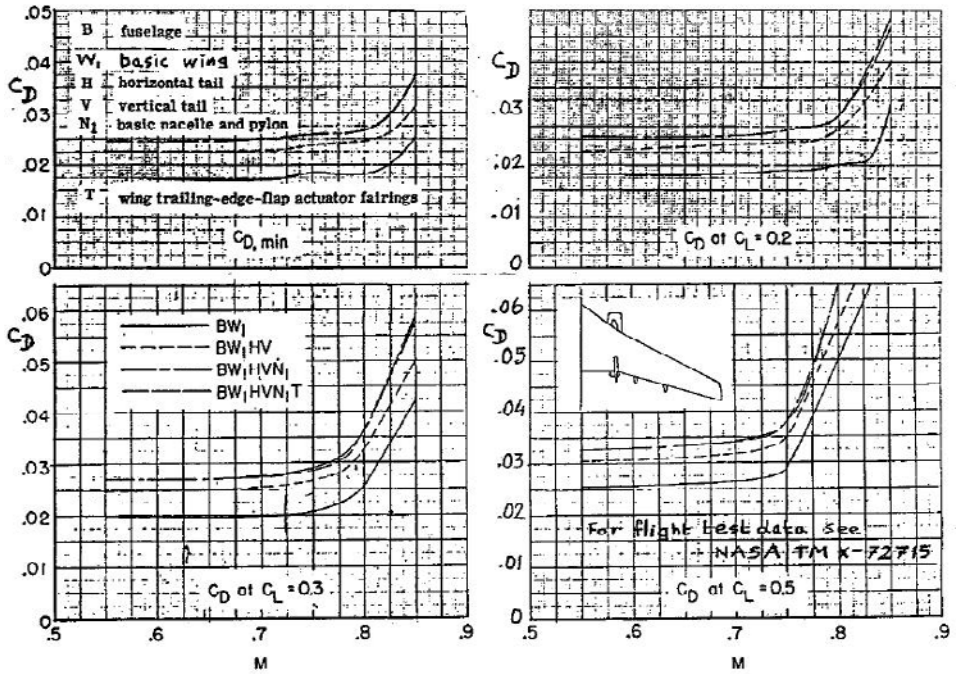
Figure 24.62 - Boeing 737-100 drag characteristics (Original configuration). Source: NASA TN D-5971

Figure 24.62 shows the drag characteristics of the Boeing 737-100 with the original engine nacelles as measured in the NASA Langley 16-foot transonic windtunnel. The drag rise characteristics of the wing-fuselage combination are in accordance with the design requirements. (In the design conditions at M = 0.78, C_L = 0.3 and M = 0.74, C_L = 0.5 the drag rise C_D = 0.0015 to 0.0020 relative to the drag at M = 0.60.) Fitting the nacelles and flap track fairings shows an almost constant drag increase over the whole cruise Mach number range. However, the addition of the tail surfaces increases the drag coefficient by C_D = 0.0050 at M = 0.60 and by C_D = 0.0070 at M = 0.75 to 0.78.
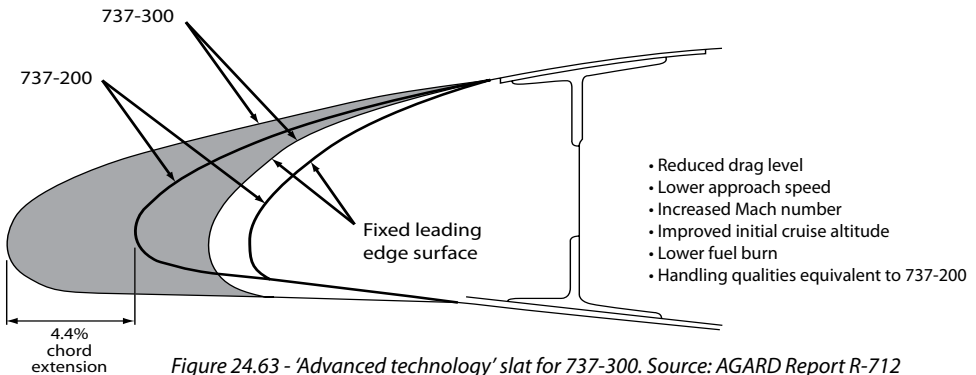
Figure 24.63 - 'Advanced technology' slat for 737-300. Source: AGARD Report R-712

This increase in drag at cruise Mach numbers was found to be caused by the interference between the flow fields of the fuselage and the horizontal and vertical tail surfaces leading to local flow separation on the rear fuselage. This led to the fitting of the, now for the 737 characteristic, vortex generators on the upper rear fuselage between the tail surfaces.

Of the Boeing 737-100 , with a Maximum Take-off Weight MTOW = 97,500 lb, only 30 examples were built. Four months after the 737-100 a second version, the 737-200 made its first flight. This aircraft had a 6-feet longer fuselage than the 737-100 but with an identical wing. When the production of the Boeing 737-200 was ended in 1988 after 1,114 aircraft had been produced the Maximum Take-Off Weight was 128,100 lb. So cruise lift coefficients had increased by more than 30 percent.

As this programme was so successful the development was continued. In February 1984 the first example of a new family of 737 models made its first flight, the prototype Boeing 737-300. The engines on this aircraft (and on all subsequent aircraft of this family) were high-by-pass-ratio CFM-56 engines, the fuselage was lengthened by 104 in. and the initial Maximum Take-Off Weight was raised to 135,000 lb. When the production of this model was ended in 1999 the MTOW was 139,400 lb.
In 1988 and 1989 the two other models of this family, the 737-400 and 737-500 made their first flights. On the 737-400 the fuselage was lengthened by 219 in compared to the 737-200 whereas the 737-500 had the same fuselage length as the 737-200. When the production of the 737-400 was ended in 2000 the MTOW was 150,000 lb. The MTOW was 138,000 lb when the production stopped of the 737-500 in 1999.

The wing on the 737-300, -400 and –500 was changed compared to the original wing on the -100 and –200. On the outboard wing the chord was increased by 4.4 % ahead of the front spar and the leading edge was modified as indicated in figure 24.63. Because the engines are mounted on pylons which are considerably narrower than the original engine fairings short flaps had to be added adjacent to the flaptrack behind the pylon. Finally the wing span was increased by 20 inches.

Figure 24.64 shows the effect of the leading-edge modification on the drag-rise boundary and the buffet-onset boundary. The effect of installing the pylon and the engine on the wing (see figure 24.65) on the pressure distribution on the wing lower surface at M = 0.80 is presented in figure 24.66. Over the complete inboard wing the local velocities on the forward part of the wing are increased by the presence of pylon and engine nacelle. A similar pressure pattern is shown in figure 24.67 for M = 0.74 and a fairly high lift coefficient. Note that both on the upper and on the lower surface the local velocities increase inboard of the nacelle and decrease outboard. Note furthermore in this figure that the leading-edge modification improved the chordwise pressure distribution by producing a high local velocity immediately behind the leading edge instead of the gradual increase in local velocity shown by earlier Boeing wings.
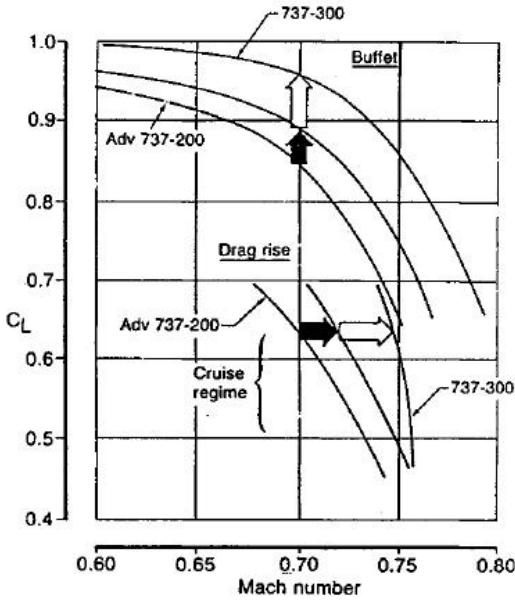
Figure 24.64 - Buffet and drag rise for the Boeing 737 series. Source: AGARD Report R-712
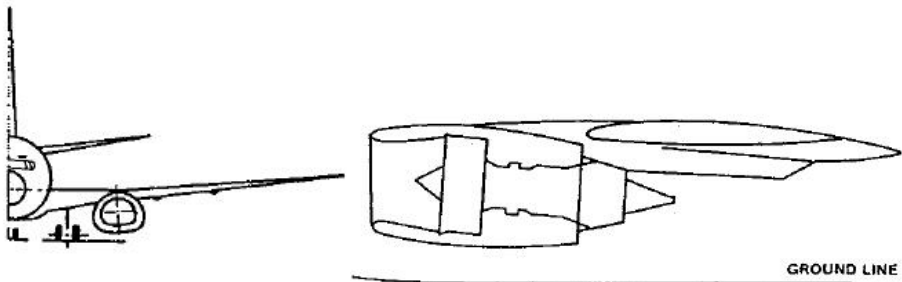
Figure 24.65 - 737-300 nacelle installation
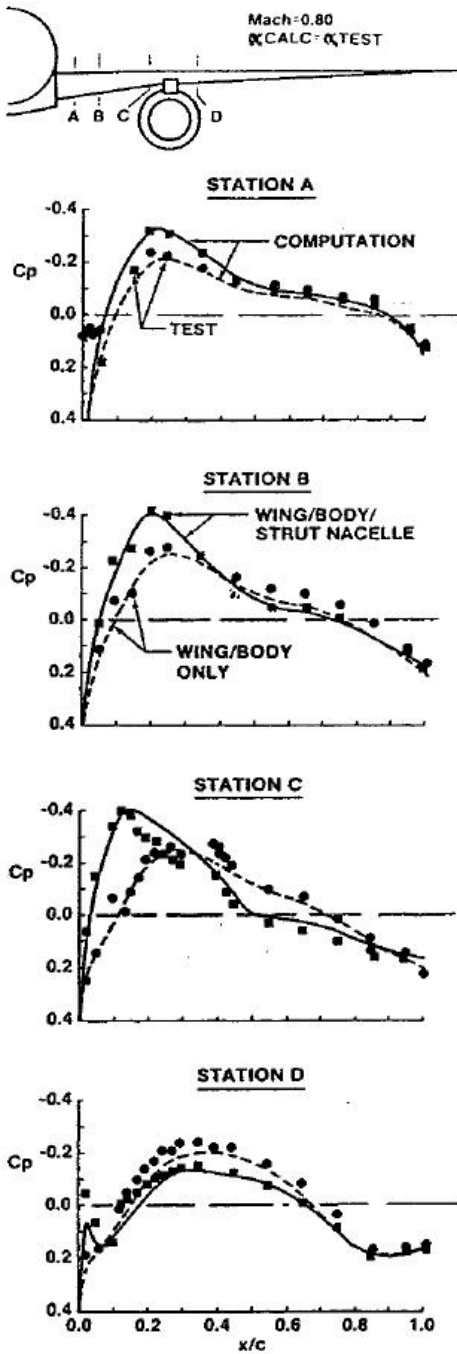
Figure 24.66 - Effect of strut and nacelle on wing lower surface pressure distribution.
Source: AIAA Paper No. 84-0381
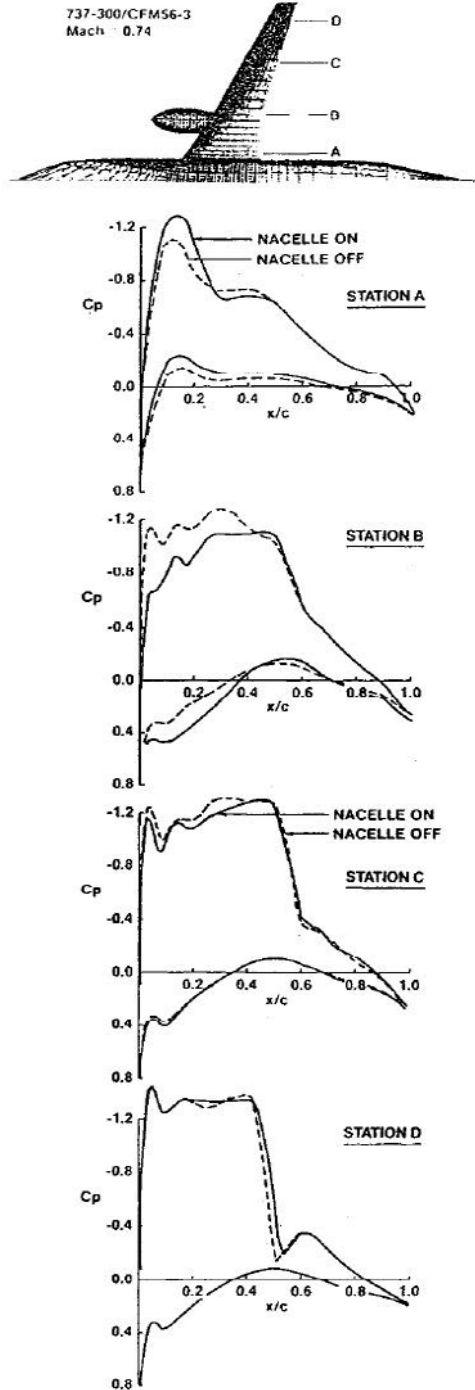
Figure 24.67 - Nacelle effect on wing pressure.
Source: AIAA Paper No. 84-0381

Figures 24.68 and 24.69 are presented to explain the at first sight large margin between design cruise condition(s) and Maximum Operating Mach number M_{MO}. When cruising at 35,000 ft at a weight of 135,000 lb for long-range cruise (minimum fuel consumption) the optimum Mach number is M = 0.745. This is almost the maximum cruise speed for an air temperature "standard day + 15°C". However when flying at 27,000 ft at a weight of 100,000 lb the maximum cruise speed is M = 0.82.

In 1997 the first prototype of the third generation of Boeing 737 models took to the air. Today four models are in production :

Model	MTOW (lb)	Increase in fuselage length relative to -200
737-600	143,400	13 in
737-700	170,000	104 in
737-800	174,000	336 in
737-900	174,000	439 in
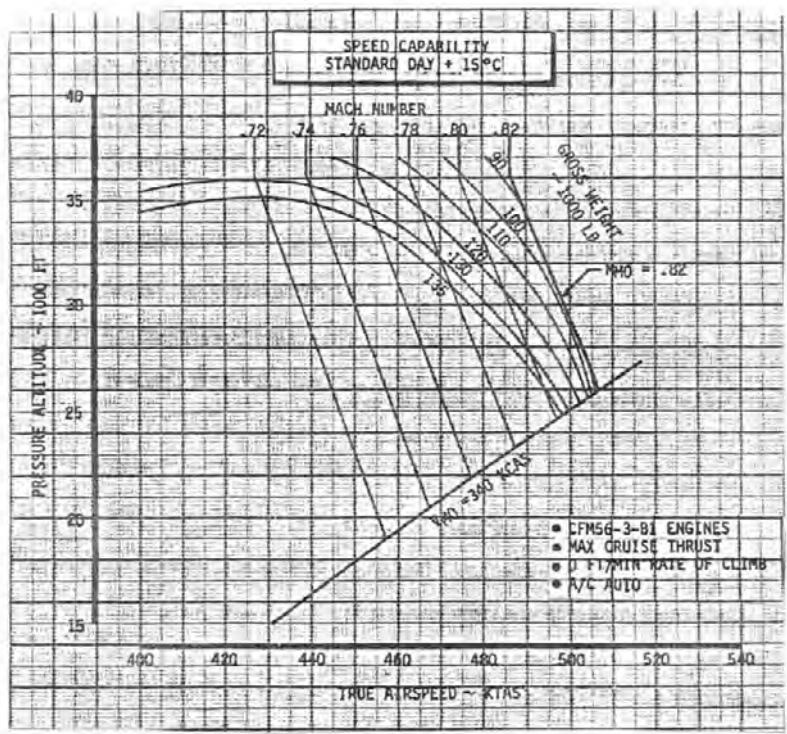
Figure 24.68 - Altitude versus airspeed diagram
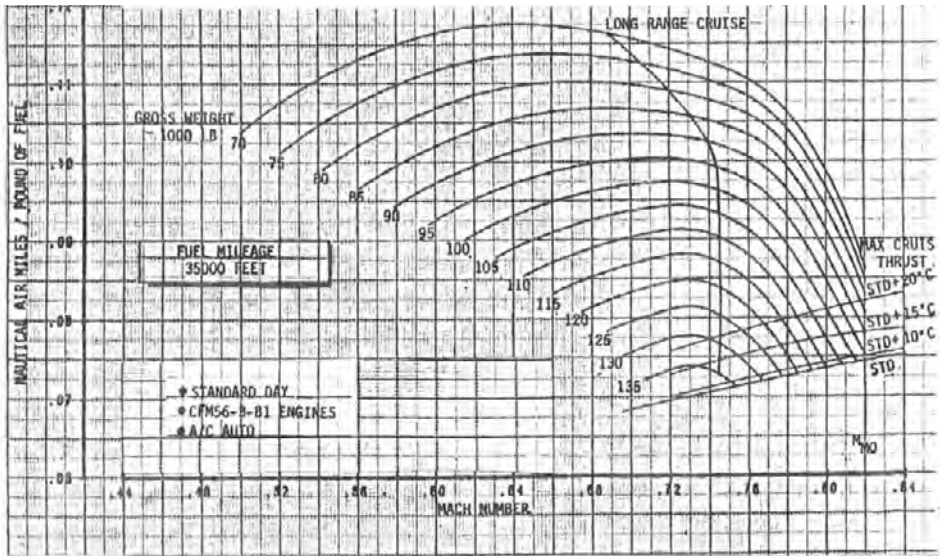
Figure 24.69 - Range per pound of fuel versus Mach number

The -600, -700, -800 and -900 made their first flight in1998, 1997, 1997 and 2000 respectively. For this new generation Boeing 737 models a new wing was designed with a wing area $S_{W,ref} = 125$ m^2. The planform is shown in figure 24.70 together with some information on the moving surfaces and some structural aspects. The root section is only slightly modified but the outer wing has a new supercritical airfoil section with rear loading as depicted in figure 24.71.
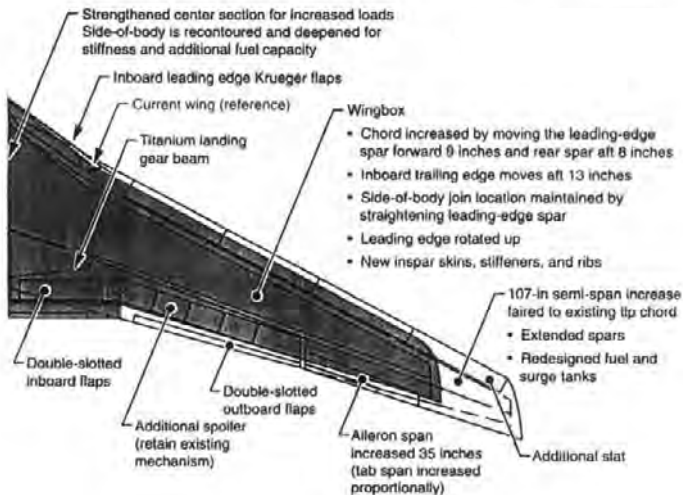
Figure 24.70 - Wing planform of the new generation Boeing 737 models. Source: Airliner Jan-March 1996

In figure 24.72 a comparison is presented between the high-speed drag curves of the Boeing 737-200 ADV, -300, and -800 at C_L = 0.2, 0.3 and 0.4. At higher lift coefficients the improvement in high-speed drag of the new wing is even more significant. The optimum Mach number for long-range cruise has been increased to M = 0.79. The maximum cruise altitude has been increased from 37,000 to 41,000 ft. Due to the larger wing the wing loading of the 737-800 and -900 has remained equal to the wing loading of the 737-200 ADV.

Boeing 737-600, -700, -800, -900

Boeing 737-300, -400, -500
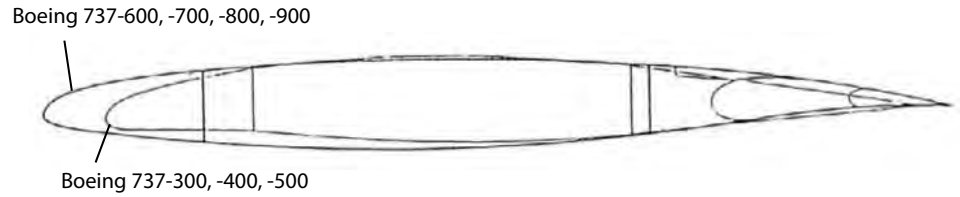
Figure 24.71 - Outer wing section of the Boeing 737-300, -400, -500 and -600, -700, -800, 900 models
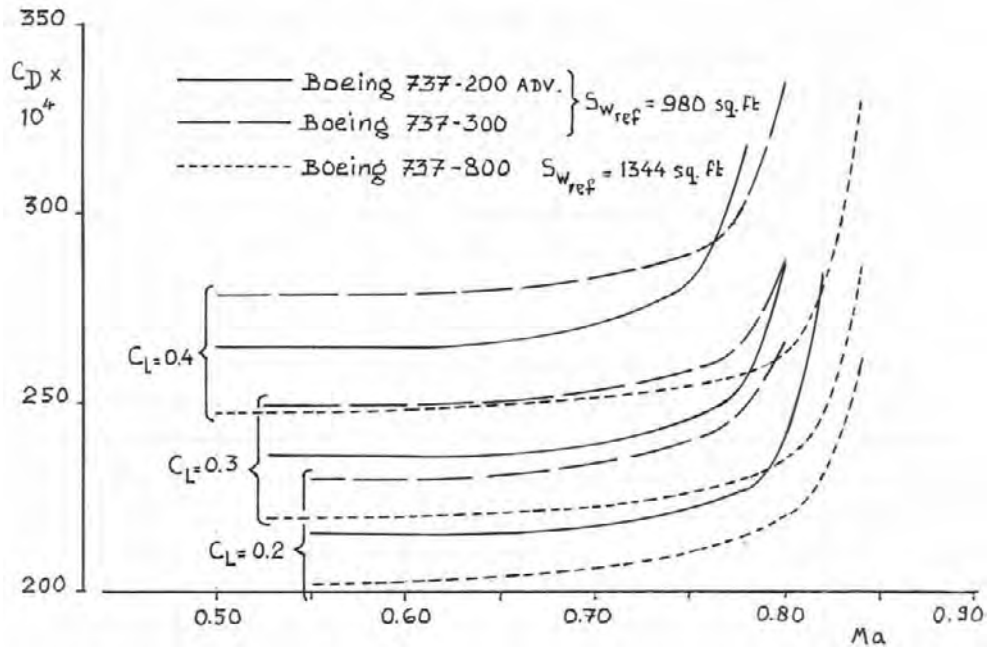
Figure 24.72 - Drag coefficient versus Mach number for the Boeing 737-200 ADV, -300 and -800

Boeing 747 (first flight 1969)

The Boeing 747 was designed and built in less than three years. Design work was started in January 1966, the roll-out was in September 1968 and the first flight was performed in February 1969. It was the first civil transport aircraft with high-bypass-ratio engines and twice the thrust of engines then in use on civil aircraft. Also in a number of other aspects such as weight and size this aircraft was a great leap forward. However, as a consequence the large extrapolation of design experience from previous programmes had its risks. The initial design specification was overly ambitious and had to be adjusted as shown in figure 24.73. But even the goals of this modified specification were not realised with the initial version.

	DESIGN OBJECTIVES Agreement of 22 Dec. 1965	**CONTRACT SPECIFICATIONS** Purchase Order No. 189, 13 Apr. 1966		**MODIFIED SPECIFICATIONS** 1968
Capacity	350-400 Passengers and their baggage. Excess space for air cargo implied as was the practice with 707s and 727s.	370 Passengers and their baggage. No additional cargo, specified.	Speed Take-Off	Mach .89 plus or minus 2% 541 knots plus or minus 2% 11,750 feet plus or minus 750 feet
Range	5,100 Nautical Miles	At least 4,462 Nautical miles	Approach Speed	135 knots maximum
Cruise Speed	Mach .90	Mach .877	Initial Cruise Altitude	
Take-Off	8,000 feet	9,900 feet		31,600 feet plus or 1,500 feet at speed of 0.84 M
Initial Altitude	35,000 feet (above 707s and DC8s)	33,000 feet (along with 707s and DC8s)	Take-Off Noise	
Noise Levels	Not specified	13-117 PNDB	Approach Noise	115 PNdb plus or minus 3 PNdb
Weight	Take-Off Gross Weight TOGW - 550,000 lbs. approximate	TOGW not specified, but expected to be 655,000 lbs.		109 PNdb plus or minus 3 PNdb
	Manufacturer's Empty Weight MEW - 240,000 lbs. approx.	MEW - 274,094 exact		
Power	Boeing's option - estimated	Boeing chose Pratt & Whitney JT9D engine		
	41,000 lbs. initial take-off thrust	41,000 lbs. initially		
		44,000 lbs. in 3 years		
		47,000 lbs. in 6 years		

Figure 24.73 - Boeing 747 - The development of performance guarantees.
Source: The Great Gamble: The Boeing 747, L.S. Kuter, 1973

M = 0.80
α = 3.75°
Re = 3.4x10⁶
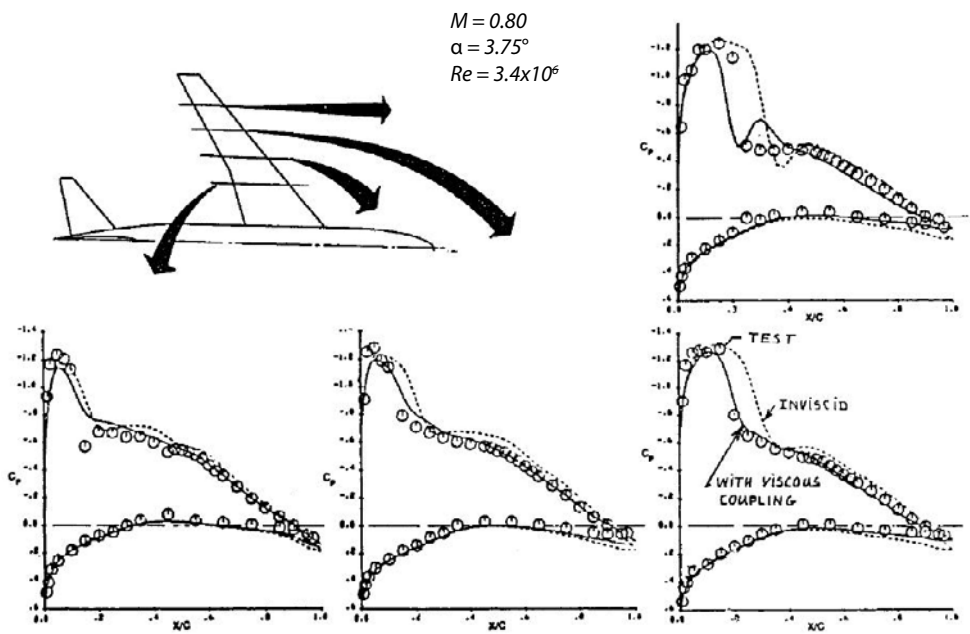
Figure 24.74 - Wing pressure distribution Boeing 747-200 at Mach 0.80. Source: Tinoco (Boeing) 1985

M = 0.88
α = 1.7°
Re = 3.4x10⁶
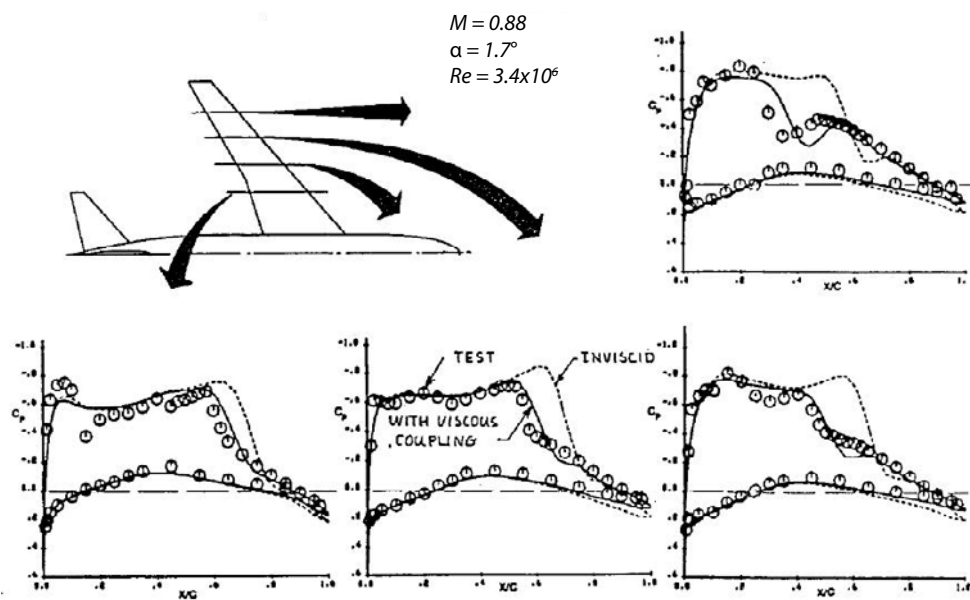
Figure 24.75 - Wing pressure distribution Boeing 747-200 at Mach 0.88. Source: Tinoco (Boeing) 1985

The maximum take-off weight came out at 710,000 lb instead of 655,000 lb and the cruise Mach number was M = 0.84 instead of M = 0.877. The high speed (M = 0.89 plus or minus 2%) mentioned in the specification of 1968 does not refer to a specific weight or altitude. Figure 24.76 shows that this speed can be reached at lower weights and altitudes.
The 747 SP was a short-body version for extreme long ranges.

In the end however most shortcomings were rectified and in particular later versions made the Boeing 747 one of the most successful civil aircraft programmes in history.

Although the original design targets were not realized on the early versions the wing design must be considered a great success given the fact that in an aerodynamic sense it remained largely unaltered for almost forty years. Chordwise pressure distributions at three high-speed flight conditions are shown in figures 24.74, 24.75 and 24.77. Contrary to on earlier Boeing wing designs the highest local velocities on the upper surface occur very close to the leading edge suggesting the influence of peaky airfoil sections. At high Mach numbers extensive regions of supersonic flow exist bordered by a weak shock.
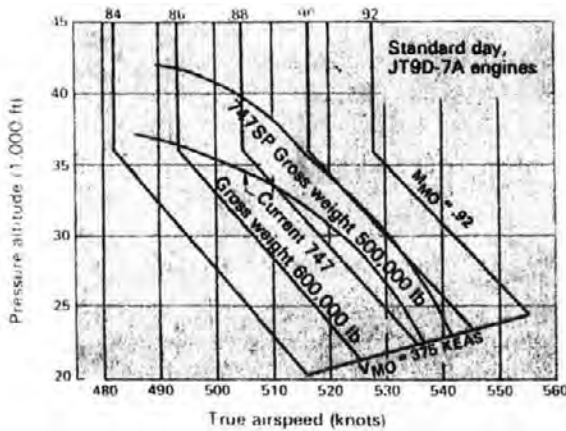
Figure 24.76 - Boeing 747 speed capability. Source: Interavia 7/1975
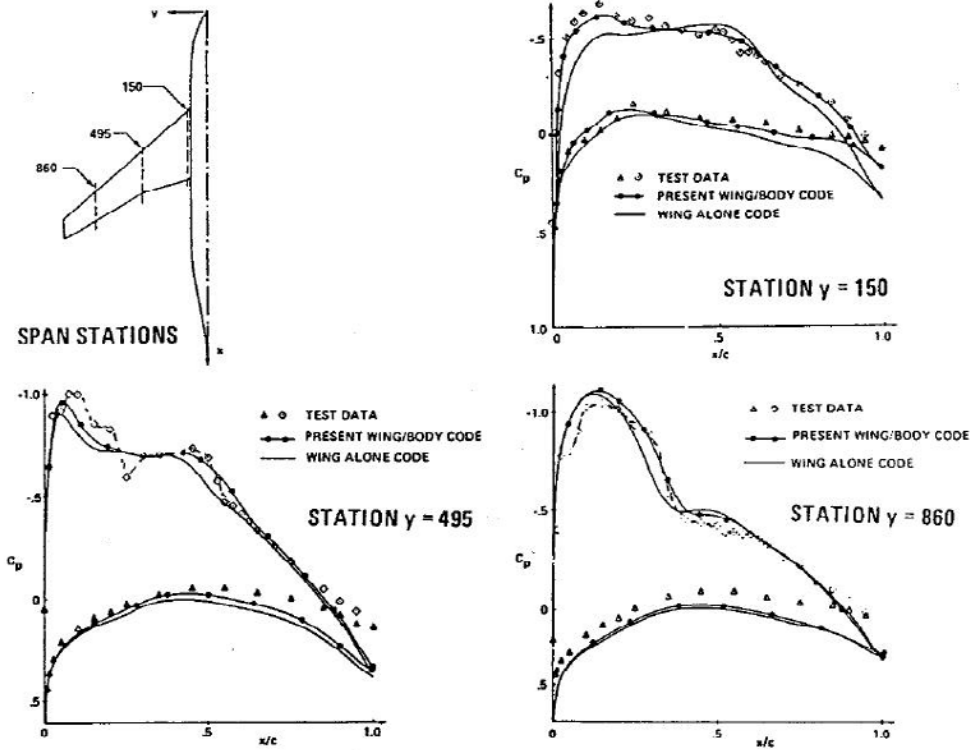
Figure 24.77 - Comparisons of wing surface pressures for a low wing transport configuration at M$_\infty$ = 0.84, α = 2.8°, C$_L$ = 0.42. Source: AIAA Paper No. 80-1391

In figure 24.78 the high-speed drag curves are presented for lift coefficients up to C$_L$ = 0.5. Contrary to earlier designs the 747 shows drag rise characteristics which do not worsen with increasing lift coefficient at least up to C$_L$ = 0.5. Even at M = 0.85 and C$_L$ = 0.5 the drag rise is only C$_D$ = 0.0020 relative to the drag at subsonic Mach numbers.

Figure 24.79 shows the design speeds at the high-speed side of the flight envelope where V$_{MO}$/M$_{MO}$ are the maximum operating speed and Mach number and V$_D$/M$_D$ are the dive speed and Mach number.

In figures 24.80 and 24.81 some comments are presented on the initial operating conditions of the 747-100 and some of the measures taken to rectify the shortcomings.

In figure 24.82 the airfoil sections defining the 747 wing are shown. The outboard wing is thinner than on any other transport aircraft because of the severe high-speed design requirements. The inboard wing thickens gradually towards the fuselage and the root sections has all the characteristics associated with straight swept isobars in the high-speed design condition.

$C_D \times 10^4$
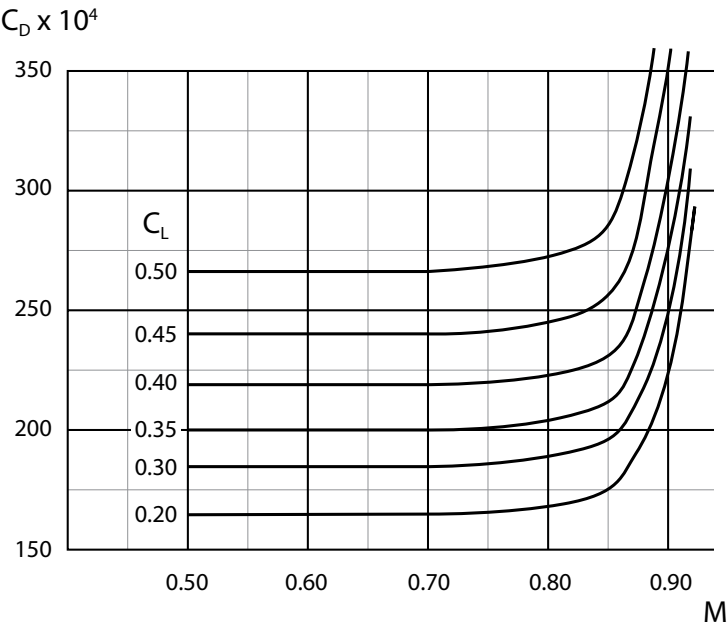
Figure 24.78 - Boeing 747-100 high-speed drag characteristics. Source: NASA CR-1756
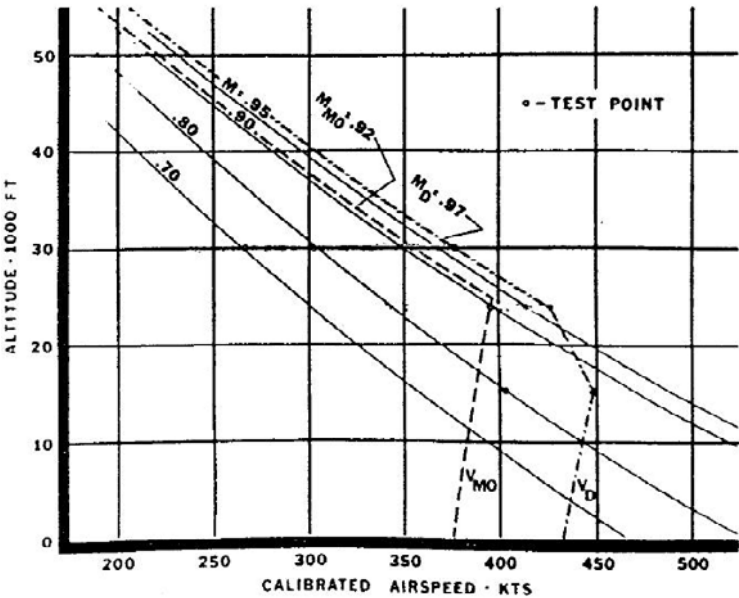
Figure 24.79 - Boeing 747 design speeds. Source: SAE Paper No. 700828

Cruise Speed, Altitude Below Predictions

Operational cruise altitude and cruise Mach number of the Boeing 747 over the North Atlantic are lower than the pre-delivery predictions. The airplane is cruising at Mach 0.84, not Mach 0.90, and at 32,000-33,000 ft, not over 35,000 ft.

Objective of the cruise altitude goal was to take the 747 above the heavily travelled Boeing 707/McDonnell Douglas DC-8 tracks where air traffic control separation requirements would have prevented the airplane from using its higher cruise speed. The Mach 0.84 cruise is slightly higher than the 707's Mach 0.82.

Basis of the cruise altitude and speed projections was what one airline official said was over-optimism that the manufacturer would meet empty weight targets, something he now says history should have warned against. When the empty weight rose, gross weight also rose from 655,000 lb. to 710,000 lb. to preserve payload weight fraction.

While the increase meant a sacrifice of performance, it also preserved the structural ruggedness that was amply demonstrated in the Pan American World Airways accident on take-off at San Francisco last summer (AW&ST Aug. 9, 1971, p. 26).

Time to climb remains a problem. Nevertheless the Pratt & Whitney JT9D-3A cruise thrust is within the performance band for meeting guarantees. Most of the thrust increase in the JT9D-7 goes into take-off power, not climb or cruise. Airplanes with the later powerplant version will not hit early cruise altitude goals either.

As it stands now, the 707-320B can cruise at a slightly higher altitude than the 747 on a similar route, but at a lower cruise Mach number. Structural limits of the 707 are lower -42,000 ft- than those of the 747, which is good to 45,000 ft. "The day will come when the 747 will get there," the airline official said, "but it will take more than the JT9D-7".

Figure 24.80 - Cruise speed, altitude below predictions.
Source: Aviation Week and Space Technology February 28, 1972

Airframe

The most irritating early operating problem with the airframe appeared to be with the passenger entry doors which mistakenly powered open a number of times, thus deploying the escape slides. Personnel training and hardware simplifications eliminated the problem. In the first year, particularly, the multiplexed passenger audio systems and cabin lights malfunctioned in harmony before fixes were found. The most important operating area, besides engine performance, falling below guarantees, was in airframe drag being about four percent higher than predicted in cruise. Boeing made commitments to a drag reduction programme, amounting to a 2.8 percent average improvement, of which rerigging the elevator and wing trailing edge compromised 1.7 percent. Where the aircraft was off in meeting guarantees, Boeing has paid for the improvements. In the course of static structural test at Everett, it was found that the wing flap tracks would not meet guaranteed life. Boeing accordingly retrofitted modified tracks on the 9 aircraft that had already been delivered to that time and introduced the modification in the factory on all later aircraft.

Figure 24.81 - Airframe. Source: Interavia, May 1972

2y/b = 0.109   t/c = 13.5 %

2y/b = 0.206   t/c = 10.4 %

2y/b = 0.303   t/c = 8.9 %

2y/b = 0.400   t/c = 8.0 %

2y/b = 0.500   t/c = 8.0 %
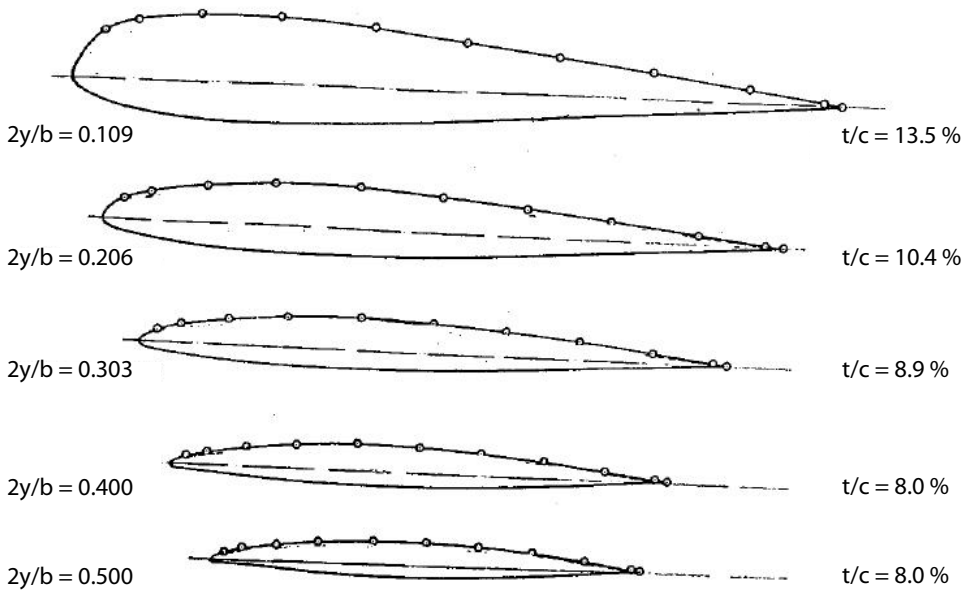
Figure 24.82 - Boeing 747 wing geometry. Source: NASA SP-347
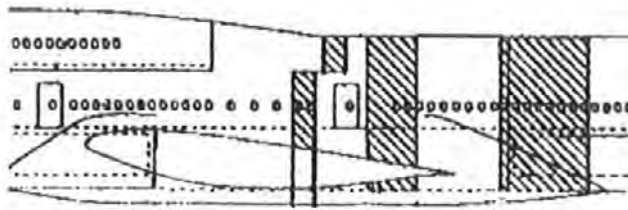
Figure 24.83 - Boeing 747-8 development, wing root.
Source: Aviation Week & Space Technology February 5, 1996

In November 2005 Boeing announced the development of a new verion of the 747, the Boeing 747-8. Boeing had been studying possible further developments of the 747 after the -400 for a number of years. In figures 24.83 and 24.84 a wing planform and wing root and outer wing airfoil sections are shown according to the development status of 1996 to 2001. Note that the outer wing section is a true supercritical section with considerable rear loading. To compensate for the large negative pitching moment of this section the root section has considerable front loading.

Although these figures will not depict the final wing design they should give a good impression of modern philosophy of wing design.
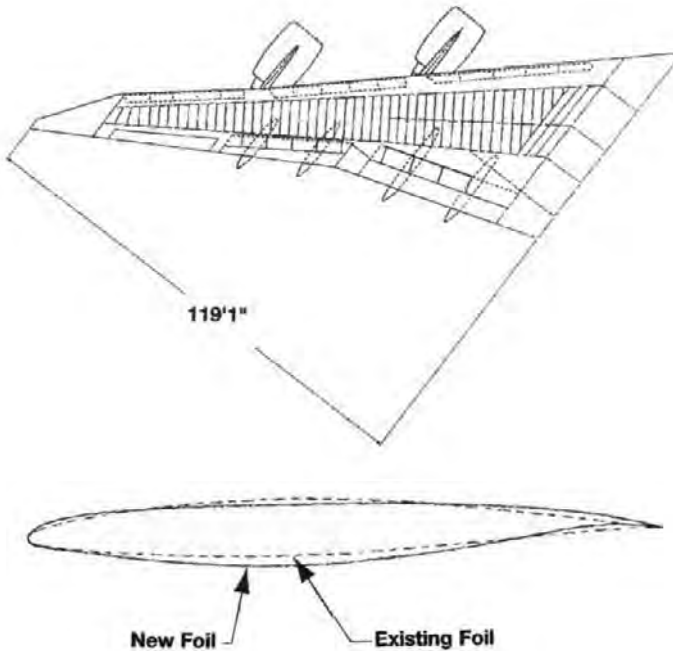
Figure 24.84 - Boeing 747-8 development, wing planform and outer wing airfoil sections.
Source: Aviation Week & Space Technology March 12, 2001

Boeing 757 (first flight 1982)

The Boeing 757 and 767 were developed almost simultaneously. The dates of the first flights were only 5 months apart. As the development of the previous entirely new civil Boeing programme, the 747, had taken place about 15 years before, in the design of the 757 and 767 the computer played a much greater role than in previous programmes. Also supercritical airfoil technology and rear loading were introduced. An example of a comparison between computed and measured pressure distributions on the wing of the Boeing 757 for a flight condition where over the whole wing the flow is just subsonic is given in figure 24.85. Note also the effect of the engine pylon and nacelle on the pressure distribution near the leading edge at adjacent wing stations. On the outer wing the characteristics of supercritical sections at subcritical speeds are evident:

A sharp suction peak at the leading edge followed by a slightly sloping plateau and a region with a fairly high adverse pressure gradient. The wing planform with high-lift devices, root and outer wing sections, the spanwise local lift and circulation distribution and high-speed drag curves are presented in figures 24.86 to 24.90.
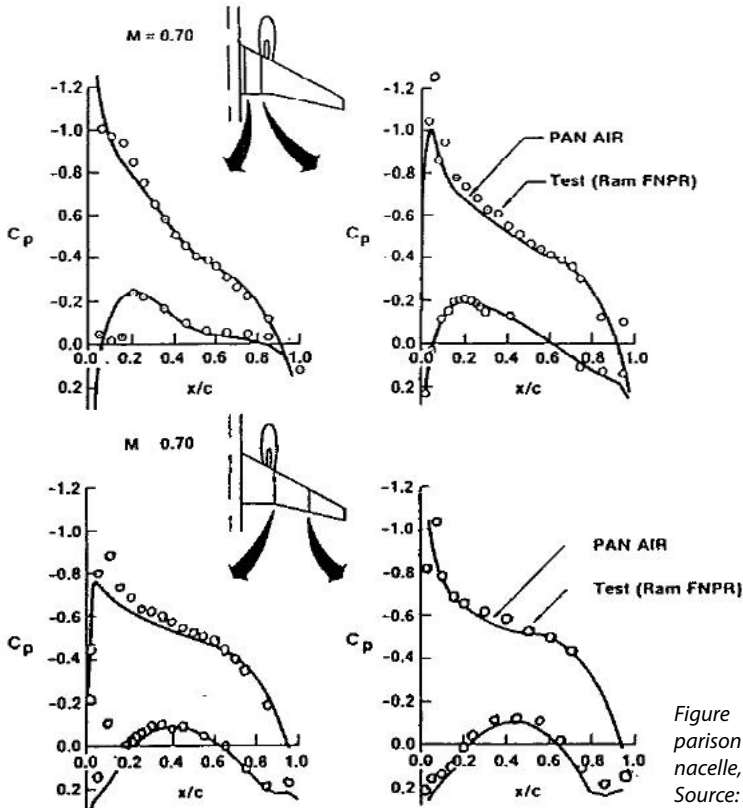
Figure 24.85 - Test/theory comparison for wing-body. Strut, blown nacelle, M = 0.70.
Source: AIAA Paper No. 83-1368
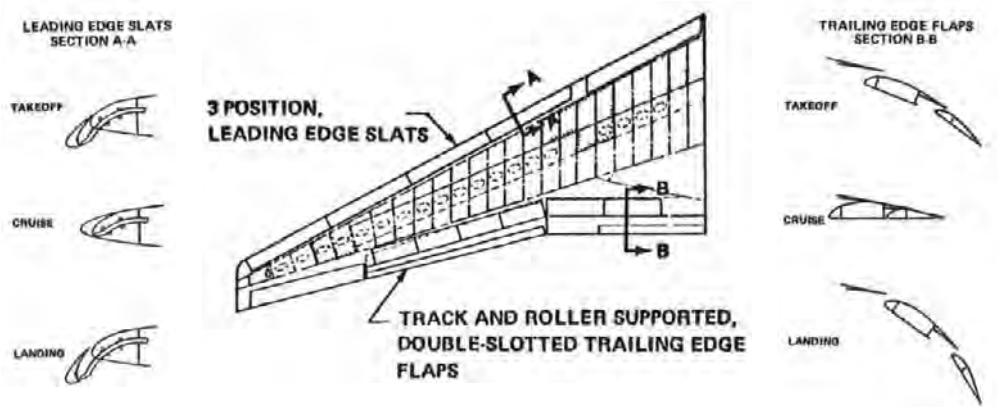
Figure 24.86 - Boeing 757 high lift devices

Root t/c = 13%   Outer wing t/c = 9.7%
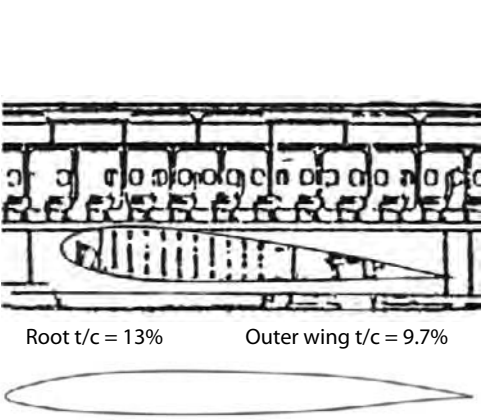
Figure 24.87 - Boeing 757 root and outer wing sections
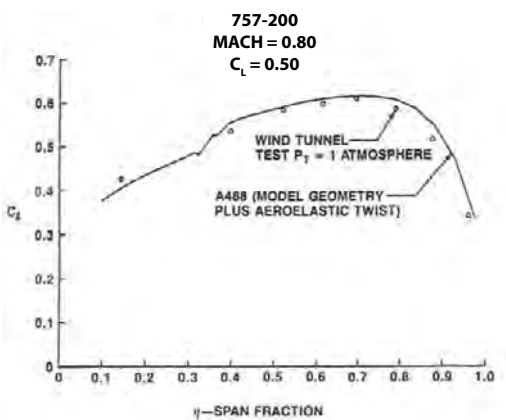
Figure 24.88 - Boeing 757-200 spanwise local lift. Source: NASA CP-3020 - Vol. 1
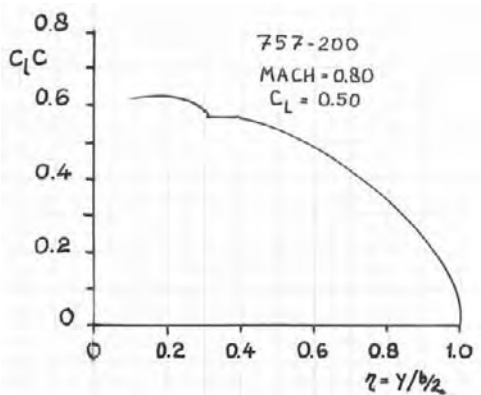
Figure 24.89 - Boeing 757-200 circulation distribution
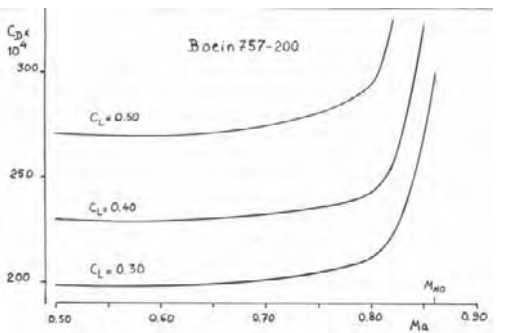
Figure 24.90 - Boeing 757 high speed drag curves

Boeing 767 (first flight 1981)

As the Boeing 757 and 767 were developed by different design teams it is interesting to see how, although the design conditions for cruise were the same (M = 0.82, C_L = 0.4), the two teams came up with different wing designs.

On the 757 the wing sweep $\Lambda_{1/4c}$ = 25 deg and the relative section thickness is t/c = 13% at the root and 9.7 % at the tip.

On the 767 the wing sweep $\Lambda_{1/4c}$ = 31.5 deg and the relative section thickness is t/c = 15.1 % at the root and 10.3 % at the tip.

The aspect ratio (based on the Boeing definition of wing reference area) were A = 7.95 and A = 7.88 respectively.
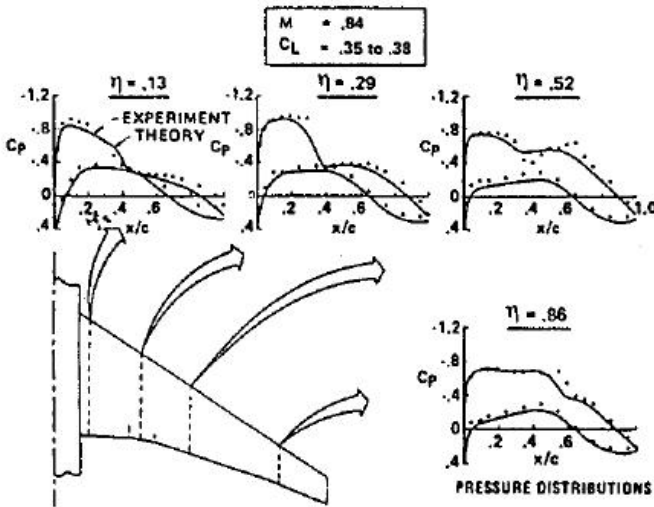
Figure 24.91 - Boeing design studies. Comparison of experimental and theoretical pressure distributions. Source: ICAS 1978 paper B2-01
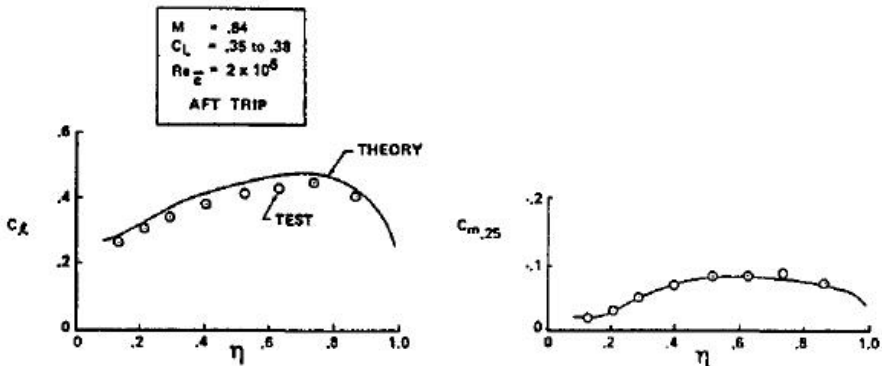
Figure 24.92 - Boeing wing design studies. Section lift and moment test-theory comparison, M = 0.84. Source: ICAS 1978 paper B2-01

Figures 24.91, 24.92 and 24.93 show the results of a Boeing 767 study. The pressure distributions at four spanwise stations are shown in figure 24.91. The lift and pitching moment coefficient distribution along the span are presented in figure 24.92.

The pressure coefficient on the forward part of the upper surface is almost constant indicating near-parallel isobars. There is less rear loading on the inboard than on the outboard wing. The lift coefficient distribution along the span shows the outboard wing region to be more loaded than the inboard part in order to obtain an elliptical lift distribution. The pitching moment coefficient distribution along the span decreases towards the wing root because of the diminishing rear loading resulting in less trim drag.

In figure 24.93 the results are shown of an analysis with the aid of total pressure rakes of the spanwise profile and wave drag distribution at $M = 0.84$ and $C_L = 0.4$. Note that at this flight condition the wave drag is only 8 to 10 drag counts.
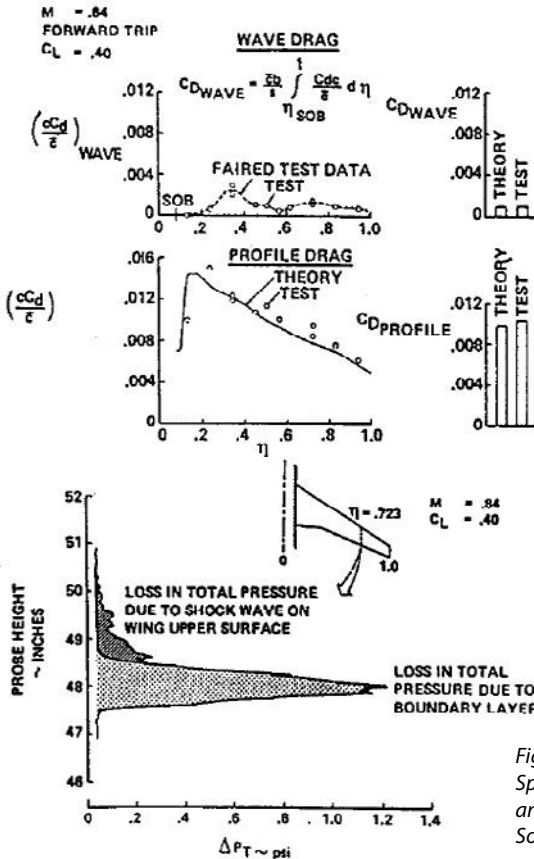
Figure 24.93 - Boeing 767 wing design studies. Spanwise profile and wave drag distributions and wake profile measurements, M = 0.84. Source: ICAS 1978 paper B2-01

The Boeing 767 was initially certified for a maximum take-off weight MTOW = 335,000 lb. When in 1988 the 767-300ER was certified the maximum take-off weight had risen to MTOW = 412,000 lb, an increase of 23 %. It was felt that for further development and weight growth for new versions of the 767 family the wing span had to be increased. For the Boeing 767-400ER which in the end was certified at MTOW = 450,000 lb this was done by the application of raked wing tips which increased the wing span by 4.30 m. Figure 24.94 shows the planforms of both the basic and the extended wing.

In figure 24.95 the wing root section is shown and in figure 24.96 the high-speed drag curves are given for the the 767-300.
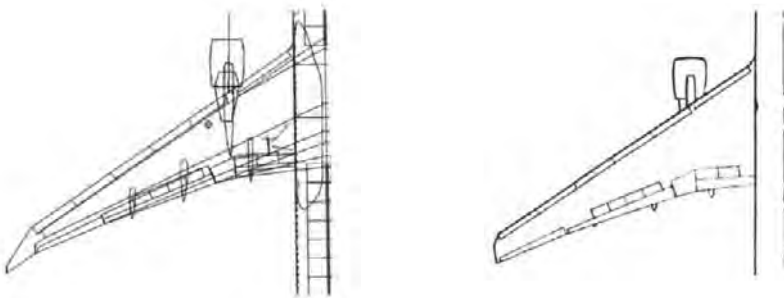
Figure 24.94 - Basic and extended Boeing 767 wing planforms
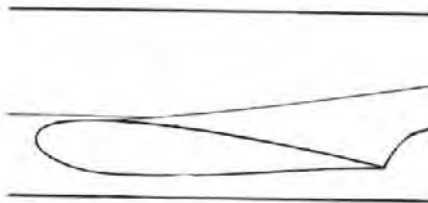
Figure 24.95 - Boeing 767 wing root section
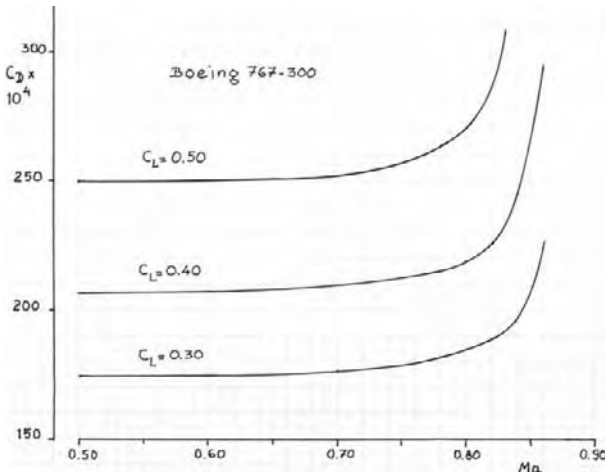
Figure 24.96 - Boeing 767-300 high-speed drag curves

Boeing 777 (first flight 1994)

The development of the Boeing 777 built on the experience with the 757 and 767. Also the 777 went through a number of development stages which up to now has resulted in a family of aircraft consisting of the 777-200, -200ER, -300, -200LR and –300ER. On the latter two the wing span was increased by raked wing tips similar to those on the 767-400ER. Figure 24.97 shows the wing planform for both the basic and the extended wing. In figure 24.98 the wing root section is shown. Clearly more front loading is applied than in earlier models but less than in the wing design for the 747-8 as shown in figure 24.83.

Figure 24.99 presents the high-speed drag curves of the 777-200. Although the wing sweep and the relative thickness at the root are almost equal to that of the 767 ($\Lambda_{1/4c}$ = 31.6 deg and t/c$_{root}$ = ± 14.5 %) and the wing aspect ratio A = 9.49, so the outer wing will not be much thinner than on the 767, the design Mach number was M = 0.83. On the aircraft the optimum cruise Mach number turned out to be M = 0.84 indicating another step forward in the quality of wing design and wing-pylon-nacelle integration.
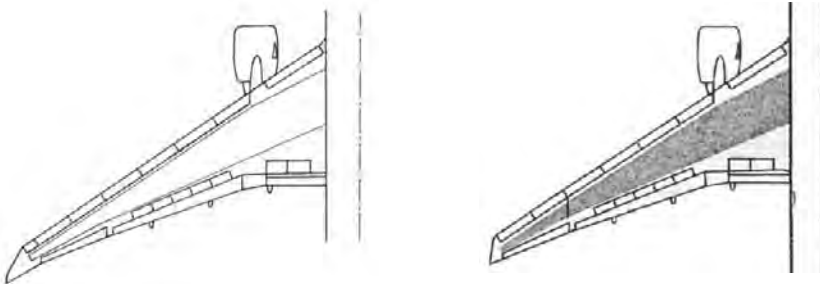
Figure 24.97 - Boeing 777 basic and extended wing planforms
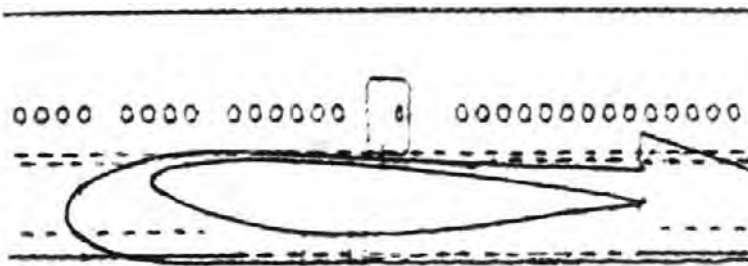
Figure 24.98 - Boeing 777 wing root section
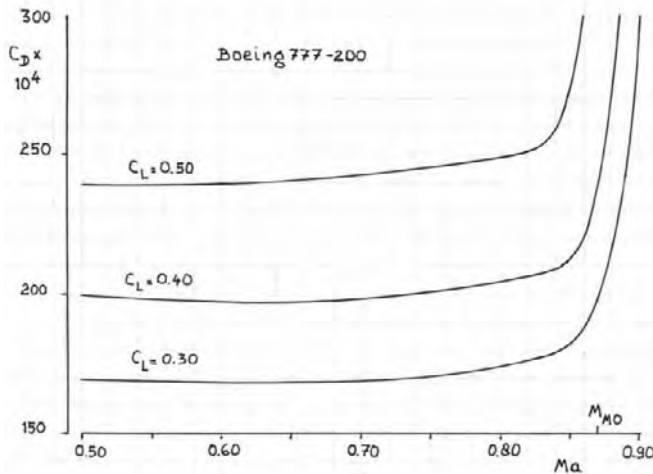
Figure 24.99 - Boeing 777-200 high-speed drag curves

Airbus A300 (first flight 1972)

Figures 24.100 and 24.101 present the view of the Airbus Company (i.e. Hawker Siddeley Hatfield) on swept-wing design at the time of the A300 development. In view of the experience with the Trident, Airbus developed as the basic section for the A300 wing a sonic rooftop profile with a small leading-edge suction peak in the design condition. The pressure distribution is compared with that of a conventional airfoil in figure 24.102. The airfoil section had much more rear loading than was usual at the time for high-speed sections, as indicated in figure 24.103, producing a large negative pitching moment. Figure 24.104 shows the correlation between experiment and theory and figure 24.105 shows the almost parallel isobars on the A300 wing.

Airbus aerodynamics

The British contribution to the A-300B, which has now been ordered by Air France and Iberia, with Lufthansa close to a decision, is not inconsiderable. Some 22 per cent of the research and development effort is being channelled through Hawker Siddeley, which has responsibility for the wing. This incorporates an advanced "roof-top" rear-loading section to a greater degree than on any other jet transport, although the concept has been under development for eight of nine years at Hatfield and was partially exploited on the Trident.

Development of considerably more lift over the rear portion of the aerofoil enables a higher lift coefficient to be carried by a wing of given sweepback and thickness before shock separations occur. Alternatively, it allows the design coefficient of lift to be achieved with a less-swept or a thicker wing for the same drag as a conventional section.

On the A-300B, this roof-top section had been combined with a "peaky" leading edge, which reduces the pressure coefficient in this region, thus delaying shock-wave formation aft of the crest of the aerofoil.

The aerodynamic development of the A-300B wing was described by D.M. McRae of Hawker Siddeley in a Royal Aeronautical Society lecture at Hatfield on February 8; a report follows.

Historically, basic A-300B design parameters were for a turbofan-powered aircraft competitive in speed with the best of the short- or medium-range aircraft in service or projected, and having the best possible economics when operated on stage lengths in the 350- to 500-mile bracket, which were obviously very much shorter than the maximum stage length required.

The field performance was aimed at being suitable for the routes on which major European operators were already providing services. A limitation was also placed on approach speed, as there was considerable anxiety about the high values used by other projects of the time, and indeed by some aircraft then in service.

Figure 24.100a - Airbus Aerodynamics (continued on next page). Source: Flight International February 10th, 1972

It was decided at an early stage that the wing design would be marched to performance at a temperature of not less then ISA+10°C, and that comparisons with the speed of competitive aircraft would be considered with this in mind.

The second consideration was that the provision of any unnecessary margin between actual cruise speed or Mach number and maximum permitted cruise speed or Mach number was an expensive luxury, since it implied an unnecessarily thin and heavy wing.

Thus the requirement was for a wing capable of an M_{MO} of 0.84 and with a drag-rise Mach number of not less than 0.83. Project-optimisation studies showed that the aircraft should have two engines and an aspect ratio of 7.72. The chosen sweep, combined with the necessary thickness, or rather thinness, has led to a wing close to the structural optimum combination and, as it is thicker than most at 10.5 per cent, Hawker Siddeley thinks it to be nearer the optimum combination than that of most competitive aircraft.

The emphasis on economy over short ranges meant that very high cruising altitudes were not required and hence, so far as cruising requirements were considered, a high wing loading would be used. The combination of this with the approach-speed requirements meant that within the likely range of landing $C_{L_{max}}$ values, the higher wing loading the better. There were two additional requirements, however. These were that high-risk technology should be avoided, and that the high-lift system should not have any adverse effect on take-off/climb drag or on high-Mach number characteristics.

The avoidance of high-risk technology ruled out any attempt at all-spoiler lateral control. The use of dropped outboard airliners was also ruled out since the reduced effectiveness and increased adverse yaw of such schemes generally results in drooped ailerons being so much larger in span than conventional ones that no increase in $C_{L_{max}}$ results. With a combined spoiler and aileron power and spoiler power, it was possible to reduce the outboard-aileron span until the outboard end of the flaps was at 84 per cent semi-span. At the chosen aspect ratio an outboard aileron would have too low a reversal speed for high-speed flight, and an inboard aileron fits conveniently into the cut-out in the flaps required to pass the engine efflux.

Spoiler-type control surfaces on the wing were also required as airbrakes and as lift dumpers to improve wheel-brake effectiveness.

Much work had been done at Hawker Siddeley on normalised sections of about 14 per cent thickness with a demand for very high lift coefficients at cruise at moderately high Mach number for Vtol transports such as the DH 129, HS 681 and

a Dornier Do31 development. Their very thickness was a disadvantage in achieving high lift coefficient at cruise.

Some dozen section were wind tunnel tested, incorporating varying amounts of trailing edge loading as a means of increasing the sonic roof-top design lift coefficient which would be achieved at given Mach numbers and thickness/chord ratio.

It was immediately obvious that any such improvement could, if desired, be utilised as an improvement in design Mach number rather than C_L, except perhaps at very low lift coefficients.

Wing-section design work for the Airbus started early at Hatfield with the HBN 100 airbus project and continued in the interval between the HBN 100 and the A-300 with two-dimensional models.

General considerations for such swept-wing designs include modifications to section shape or fuselage waisting, or both, to avoid premature shock waves, of low sweep, at the root of swept wings. The point is made that it is obviously desirable where possible to avoid fuselage waisting and to confine the "root treatment" to the wing. This commonly involves thickening the forward part of the aerofoil, making the rear part thinner, reducing the camber and increasing the incidence at the root compared with the outer part of the wing. Reducing the thickness of the rear of the aerofoil is not very practical, however, since an undercarriage leg has to be accommodated. Furthermore, wing-bending stresses tend to be concentrated near the rear spar at the root of a swept wing, and the rear of the outboard section is already rather thin.

In the early days aerodynamic design proceeded ahead of the availability of other design data – this was fed in later.

The tail-load calculations based on one test wing, for instance, showed that the design tail down-load in the clean configuration was greater than that in the flaps-out cases. A considerable saving of 120kg in tail weight and obviating fuel to overcome trim drag could be effected by making these two cases of equal severity. At the same time estimates of wing torsional and bending stiffness became available, and calculations showed rather large difference between jig-shape and flying-shape twists. It was decided therefore to explore the reduction of C_{MO} to make the two tail-load cases equal. This was done by increasing the washout and by slightly reducing the rear loading.

The final wing design evolved had an improvement in drag-rise Mach number of 0.01 and a substantially reduced zero-lift pitching moment at the expense of a slight reduction to the lift coefficient for buffet onset.

Figure 24.100b - Airbus Aerodynamics (continued). Source: Flight International February 10th, 1972

Wing design

Wing design has built upon that used on the Trident and HS.681, in combining an upper surface roof top pressure distribution at cruise conditions with a significant amount of rear loading obtained by aft camber. A dropped leading edge more favourable to low speed high lift characteristics has been developed which has little effect on the roof top pressure distribution at cruise or on the peaky type section pressure distribution development for higher lift coefficients. Typical pressure distibutions are shown in figure 6. This combination has made it possible to use sections 1.5 per cent thicker than with the Trident standard of technology, for the same combination of Mach number and C_L.

Based on this outer wing section, the complete wing has been developed by continuous wind tunnel testing in H.S.A. high speed tunnels, together with some checks at higher Reynolds number at RAE and ARA, against a theoretical framework to obtain uniformmupper surface pressure distribution at cruise conditions, while meeting the usual practical requirements of undercarriage stowage, wrappable skins, etc. The success of the design process is shown in figure 7, which shows the pressure distribution achieved on a model in the course of development. 90 per cent of the full cos effect has been obtained in going from the two-dimensional results to the complete wing.

Figure 24.101 - Wing design. Source: Aircraft Engineering, October 1969
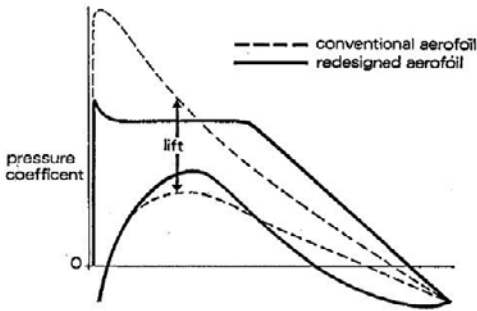
Figure 24.102 - A comparison of the pressure distribution for conventional and advanced section aerofoils. Source: Aircraft Engineering, March 1969
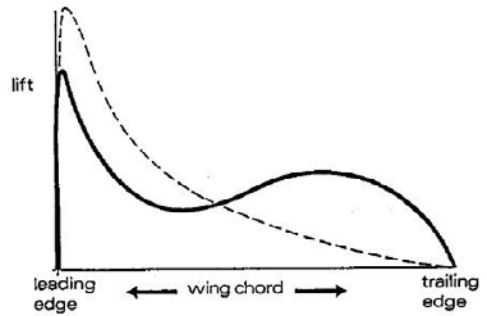
Figure 24.103 - The lift distribution for conventional and advanced section aerofoils compared. Source: Aircraft Engineering, March 1969
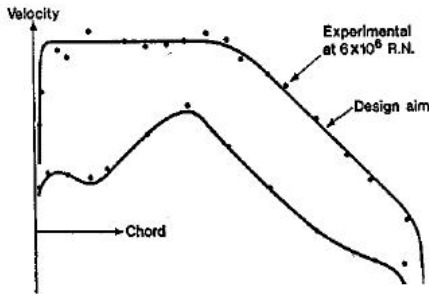
Figure 24.104 - Typical pressure distribution for the aerofoils at cruise condition. Source: Aircraft Engineering, October 1969
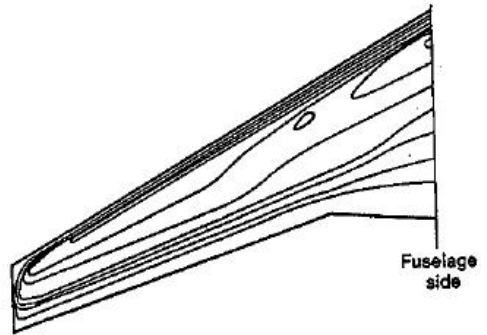
Figure 24.105 - A300 wing experimental isobar pattern at a cruise condition and Reynolds number of 1.47×10^6. Source: Aircraft Engineering, October 1969
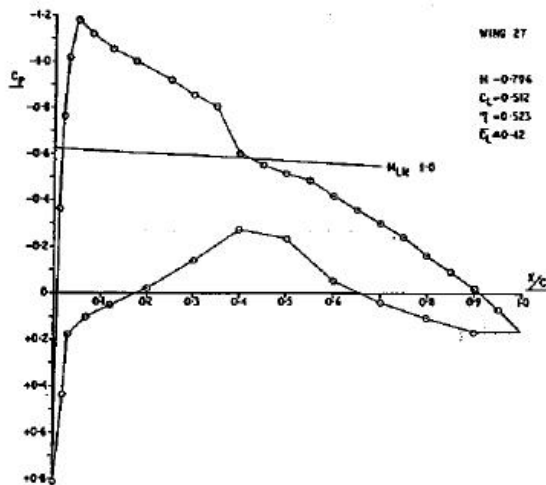
Figure 24.106 - Pressure distribution. Source: Aeronautical Journal, July 1973

Figure 24.106 shows the pressure distribution on the wing station at 52.3% semi-span at M = 0.796 and $C_L = 0.42$. In this condition supersonic flow occurs with a shock wave at 40% of the chord length. The region of supersonic flow exhibits a fair degree of isentropic recompression and the shock wave is very weak with little wave drag as can be concluded from figure 24.107. This illustrates that the concept of a sonic rooftop pressure distribution, with a small leading-edge suction peak in the design condition, produces a satisfactory "supercritical" type of pressure distribution at a slightly higher C_L than the design lift coefficient without the excessively high leading-edge supervelocities and associated high drag creep of the earlier "peaky" airfoil sections. But calling a particular combination of lift coefficient and Mach number the "design condition" is more related to the mathematical design tool used (or available) than to the aircraft's main operating condition.
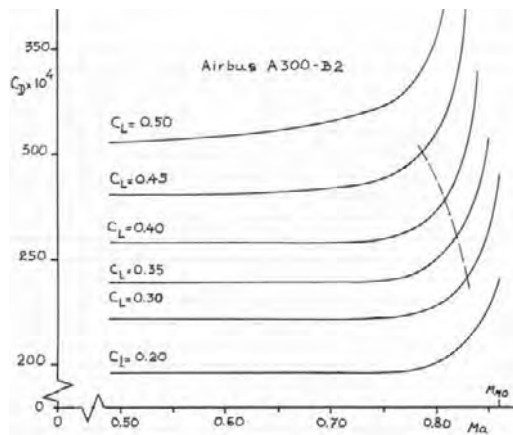
Figure 24.107 - Airbus A300-B2 high speed drag characteristics
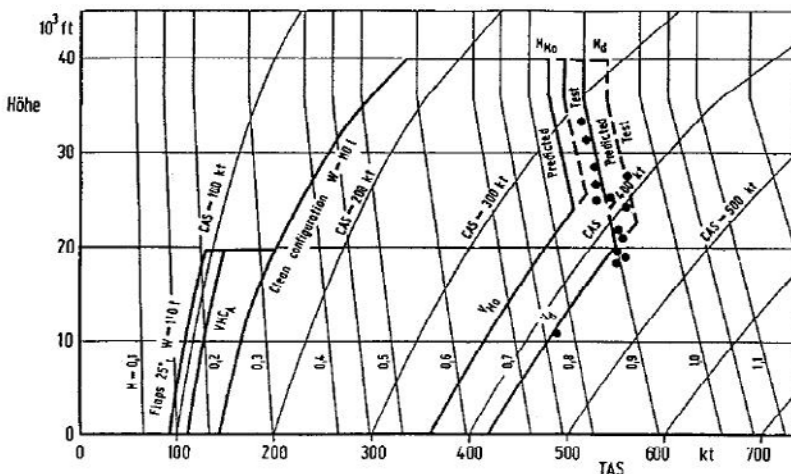
Figure 24.108 - Airbus A300 flight envelope. Source: Jahrbuch 1973 der DGLR

The A300 was designed for high-speed cruise at M = 0.82/0.83 and for long-range cruise at M = 0.78. Figure 24.107 shows that over the range C_L = 0.30 to 0.45 the drag rise Mach number (M for C_D = 0.0020 above the low-speed drag level) varies between M = 0.825 and 0.785 which is in line with the design requirements. In figure 24.108 the A300 flight envelope is presented. Note that for certification M_{MO} was increased from M_{MO} = 0.84 to 0.87.

Figures 24.109 to 24.111 present the four sections that determine the wing shape, the wing surface definition and the wing twist both as constructed and in flight. Note that, as on the Trident, the wing surface is described with straight generators. This had as a consequence that the root section relative thickness is 10.5% which is less than aerodynamically would have been possible. This was because Hawker Siddeley at that time had no equipment available to produce wing skin panels with double curvature. This equipment came only available for the production of the A310.
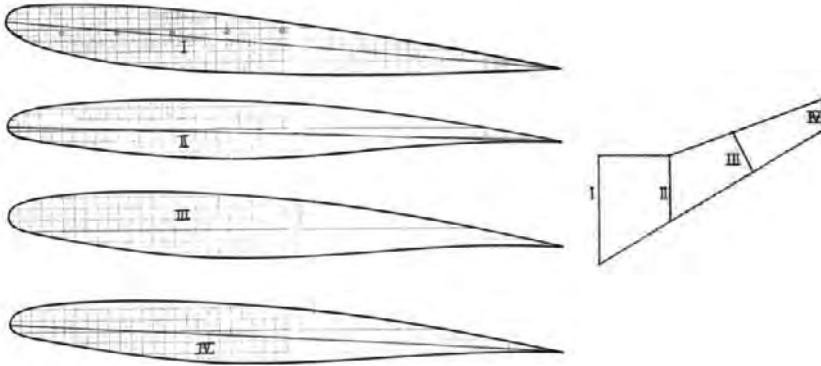
Figure 24.109 - Wing airfoil sections
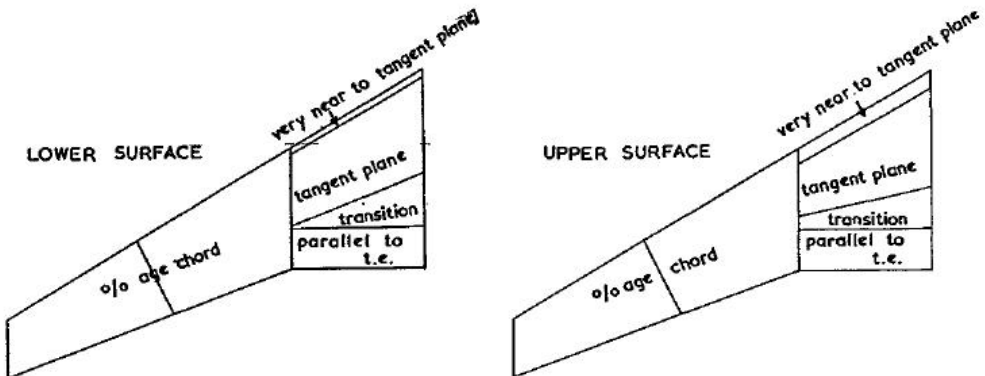
Figure 24.110 - A300 B wing. Source: Aeronautical Journal, July 1973
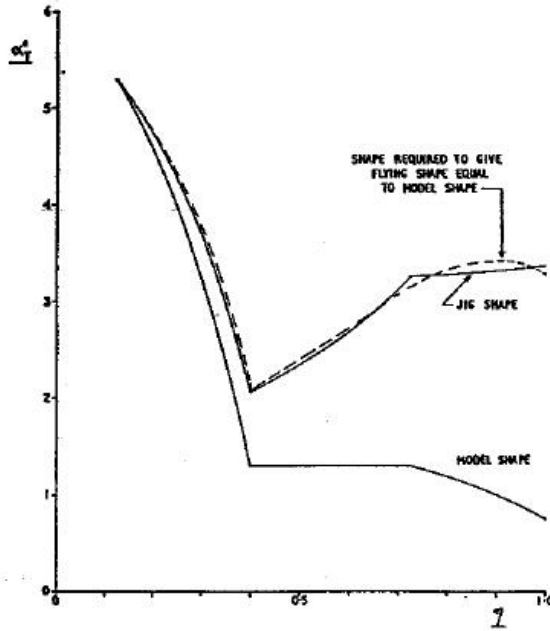
Figure 24.111 - Wing twist distribution. Source: Aeronautical Journal, July 1973
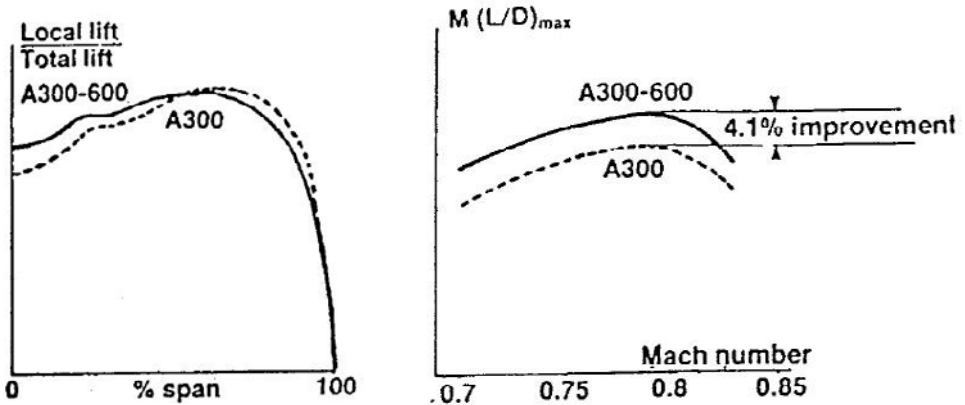
Figure 24.112 - Improvement in lift distribution of the A300-600 compared to the original A300. Source: Air & Cosmos September 10, 1983

Figure 24.113 - Increase of the product of Mach number and lift to drag ratio of the A300-600 compared to the original A300. Source: Air & Cosmos September 10, 1983

The spanwise lift distribution for the original A300 and the A300-600 are given in figure 24.112. In order to allow an increase in maximum take-off weight for the A300-600 the rear loading on the inboard part of the wing was increased and the lift was shifted inboard. This resulted in an increase in the lift-drag ratio as shown in figure 24.113 and an improvement in the buffet onset boundary as presented in figure 24.114.
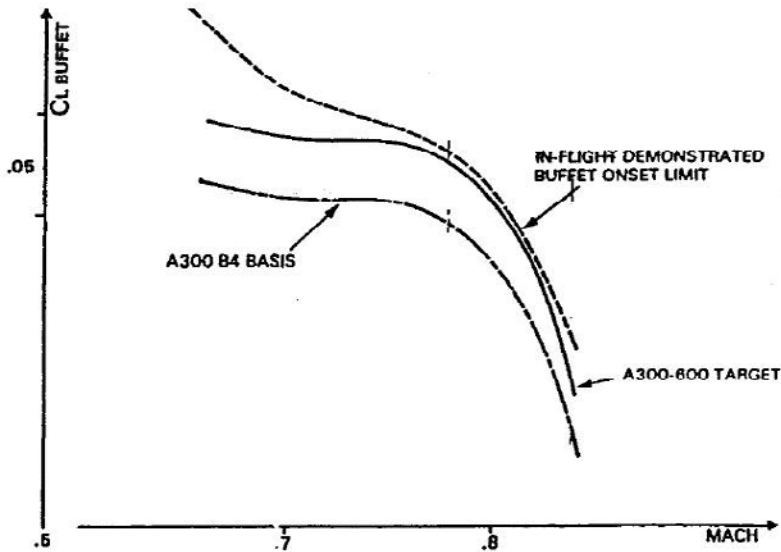
Figure 24.114 - Lift coefficient limit due to buffet as function of Mach number. The test flight results allow the A300-600 to fly at higher lift coefficients. Source: Air & Cosmos March 24, 1984

Airbus A310 (first flight 1982)

For the A310 a new wing was designed with double curvature on the inner wing panels allowing a much thicker root section. Figures 24.115 and 24.116 show the spanwise thickness distribution and the planforms of both wings.

	A300	A310
Surface Voilure (m²)	260	219
Envergure	44,84	43,90
Allongement	7,7	8,8
Flèche 25%	28°	28°
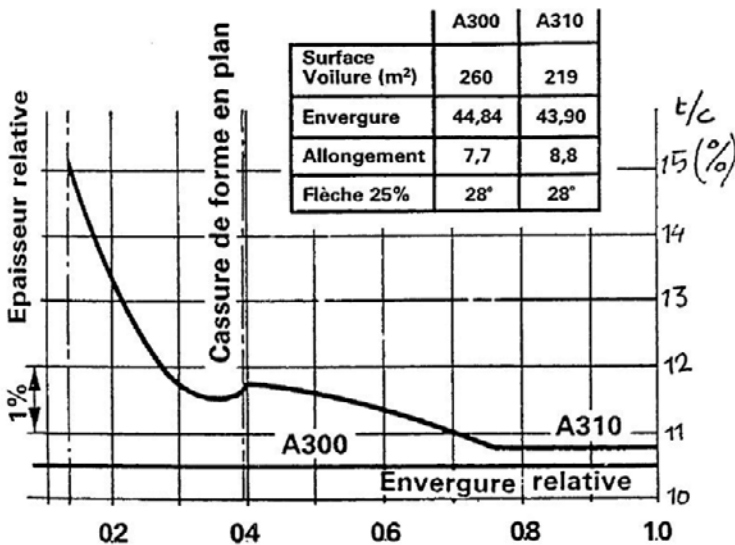
Figure 24.115 - Comparison of the A300 and A310 wing thickness and other dimensions. Source: AGARD CP-348 lecture 22
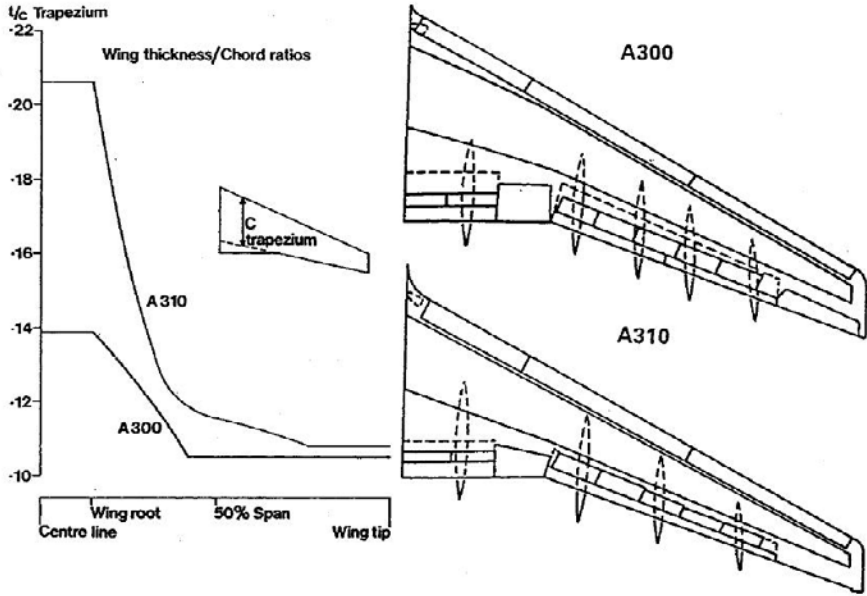
Figure 24.116 - Comparison between the A300 and A310 wing geometry. Source: AGARD CP-285 lecture 11

In figure 24.117 the airfoil sections at different spanwise positions are shown. The root treatment to obtain straight isobars in the design condition is evident. Moving inboard the incidence increases, the thickness increases, the thickest point moves forward, the leading edge becomes blunter and the rear loading disappears.
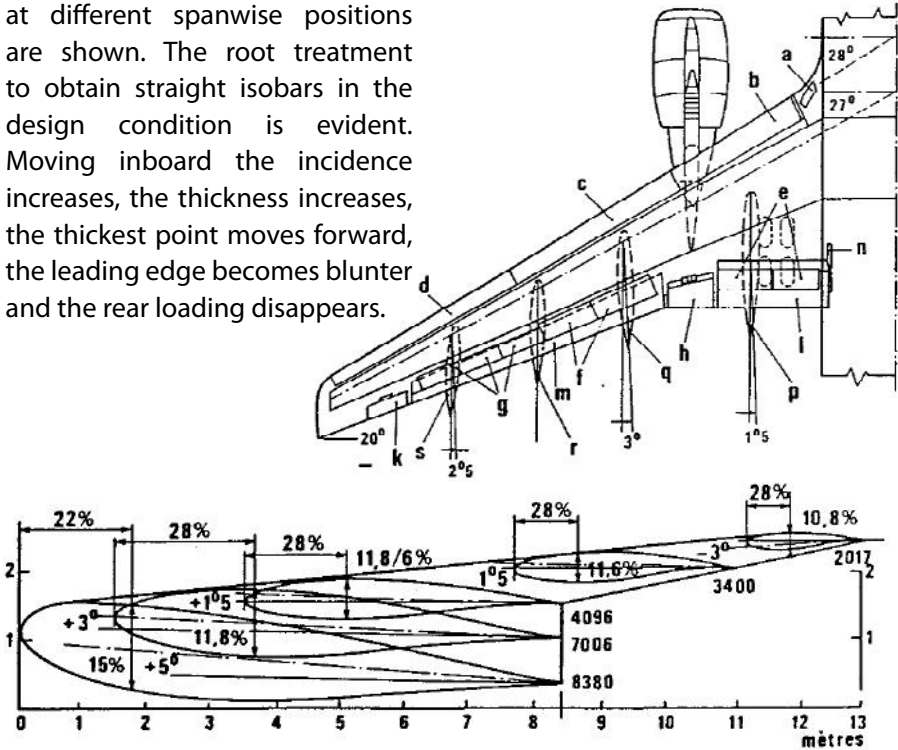
Figure 24.117 - The A310 wing. Source: L'Aéronautique et l'Astronautique, June 1981

Airbus A320 (first flight 1987)

As the A320 was designed for slightly lower operating speeds than the A300 and A310 (M_{MO} = 0.82 and the cruise speed is M = 0.79 - 0.80) the wing sweep is only $\Lambda_{1/4c}$= 25 deg.
In the design of the basic section much efford was put in minimising the rear loading and maximising the front loading as illustrated in figure 24.118. This allowed for lighter wing flaps and also helped to lower the trim drag.
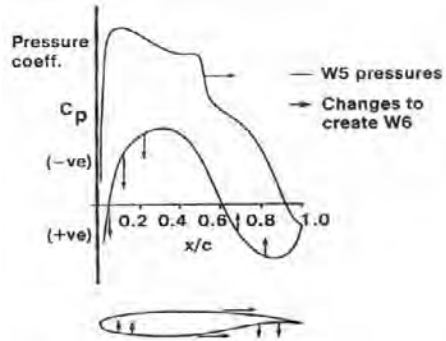
Figure 24.118 - Comparison of principal features of Wing W6 with those of W5. Source: Aerospace January 1986
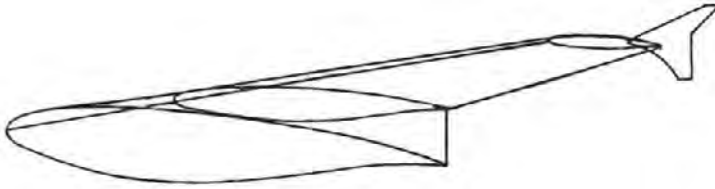
Figure 24.119 - Airbus A320 root, kink and tip sections
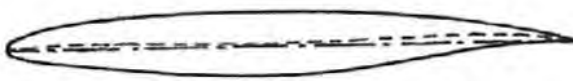
Figure 24.120 - Airbus A320 outer wing section

Figure 24.119 shows the root, kink and tip section whereas in figure 24.120 a section in the outer wing is illustrated at a larger scale. The thinner leading edge and thicker trailing-edge region are evident. Also the root section suggests more front loading than on the A310. In figures 24.121 and 24.122 the spanwise thickness distribution and wing twist are shown.
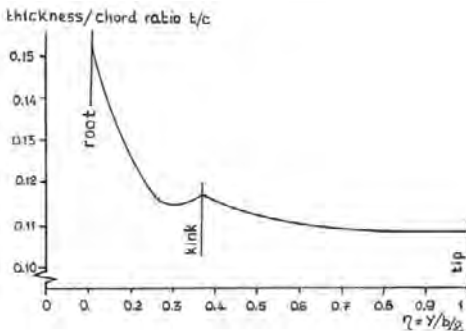
Figure 24.121 - Airbus A320 spanwise thickness distribution
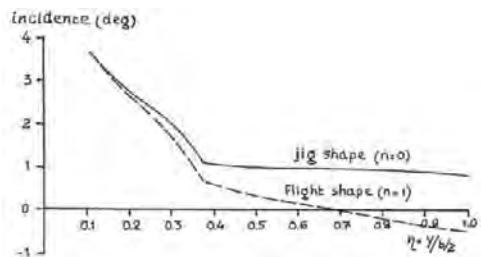
Figure 24.122 - Airbus A320 wing twist

The high-speed drag characteristics are presented in figure 24.123. In this figure also the drag curve is shown of the Boeing 737-800 for $C_L = 0.50$. This curve was not included for a direct comparison between the Airbus A320-200 and the Boeing 737-800 but to indicate the high degree of similarity. The aircraft have almost the same wing reference area (albeit based on different definitions) and fuselage length. (The estimated wetted area are $S_{wet} = 774.8$ m^2 and 790.3 m^2). But on the other hand the outboard wing of the 737 is about 10 percent thinner than of the A320 and in principle heavier. Furthermore there are differences in empty weight and engine performance. All this should make clear that a small difference in drag at a particular flight condition is no indication of the commercial potential of both aircraft but the fact that the difference is small indicates the high quality of both designs .
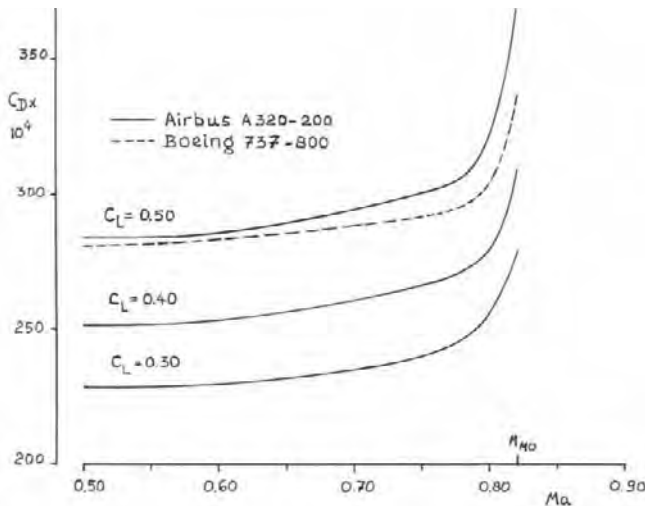
Figure 24.123 - High-speed drag characteristics of the Airbus A320-200 and Boeing 737-800
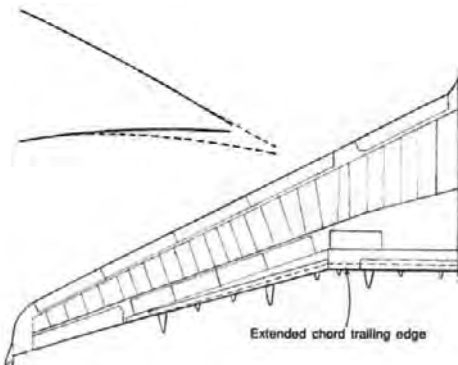
Figure 24.124 - Modified wing plan with double-slotted inner flap on the A321. Source: Flight International March 17-23 , 1993

In 1993 a lengthened and much heavier version of the A320, the A321 started its flight test programme. To prevent a deterioration of high- and low-speed performance the trailing edge was extended in the flap region and some camber was added at the flap trailing edge as shown in figure 24.124. This restored the performance to the level of the A320.

Airbus A340 (first flight 1991)

The Airbus A340 and A330 were the first true long-range aircraft developed by Airbus. This development took place simultaneously with the first A330 flying five months after the A340.

Originally the 4-engined A340 and the 2-engined A330 would have (nearly) identical wings with an aspect ratio A = 9.3 and a sweep angle $\Lambda_{1/4c}$ = 30 deg. A higher cruise Mach number range (M = 0.82-0.83) was specified than for the A310 and M_{MO} = 0.86.

Figure 24.127 shows the wing airfoil sections along the span with a separate view of the root and outboard wing sections in figures 24.125 and 24.126. Note the thin and high-loaded aft part of the basic section and the relatively thick forward part of the wing up to the wing root, all presumably to maximise the available fuel volume in the wing torsion box.
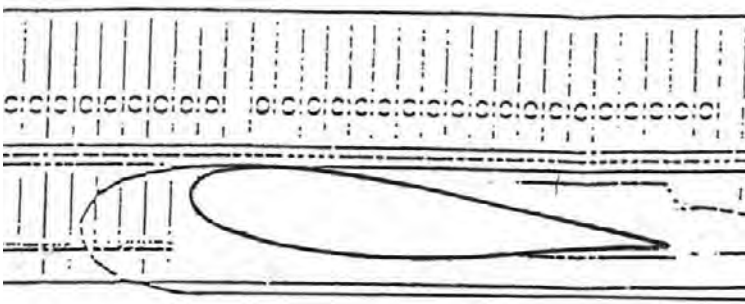
Figure 24.125 - Airbus A340 wing root section
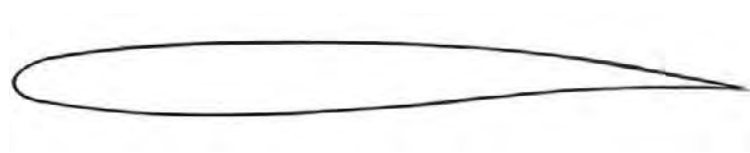
Figure 24.126 - Airbus A340 outboard wing section

Figure 24.127 - Airbus A340 wing airfoil sections
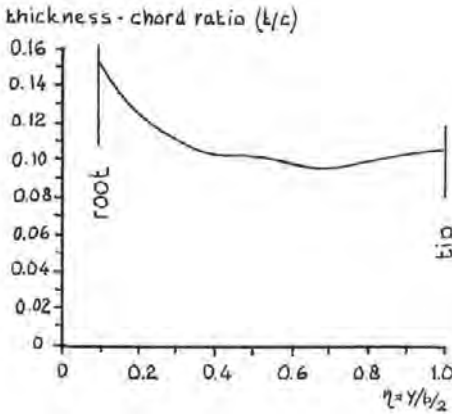
Figure 24.128 - Airbus A340 wing spanwise thickness distribution
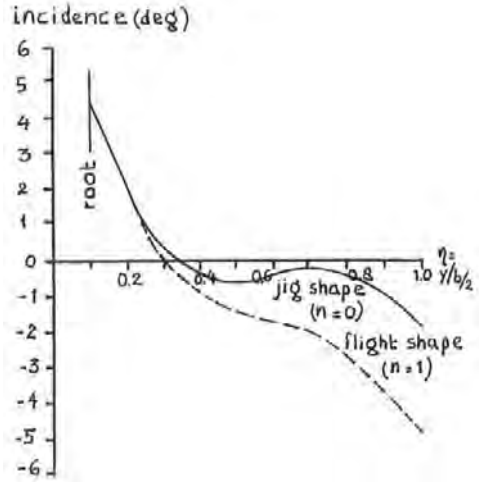
Figure 24.129 - Airbus A340 wing spanwise twist distribution

In figures 24.128 and 24.129 the spanwise thickness and twist distribution are presented.

Figure 24.130 shows the spanwise pressure distribution near the design condition. The high rear loading in the outboard wing is evident. In figure 24.131 the pre-flight estimate of the high-speed drag is presented. Note how small the drag creep is at M = 0.82 even at such a high lift coefficient as $C_L = 0.5$.
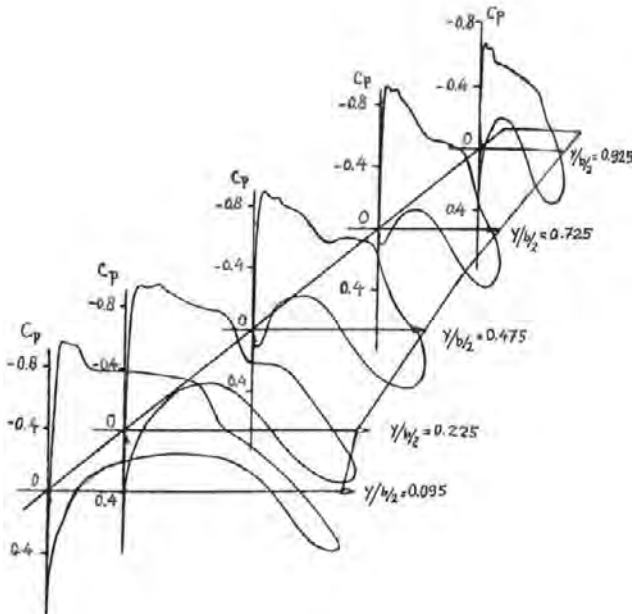
Figure 24.130 - Airbus A340 spanwise pressure distribution near the design condition.
Source: AGARD CP-547, Paper No. 11
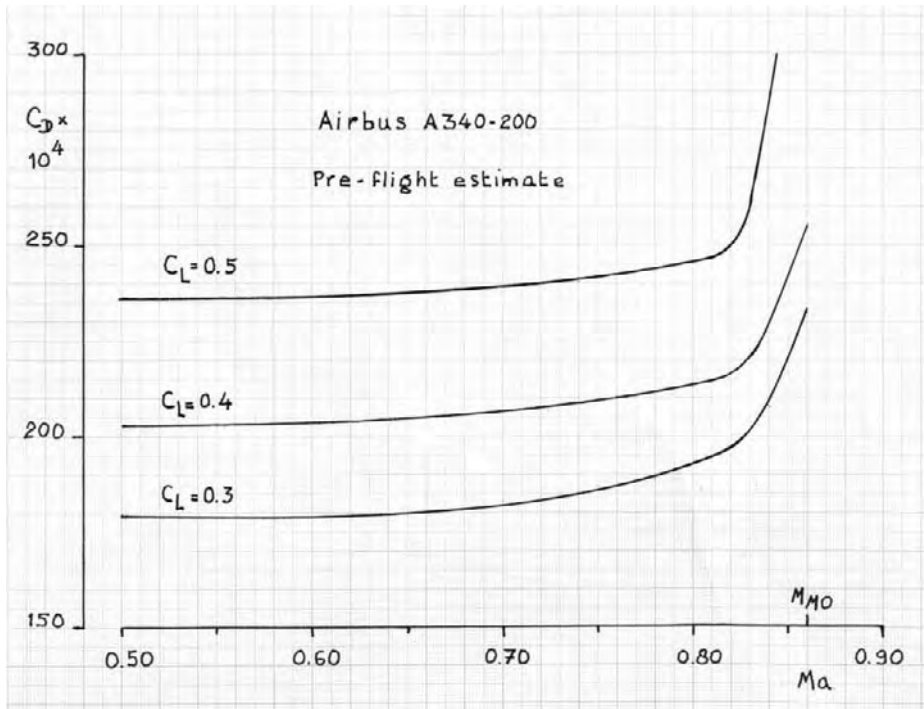
Figure 24.131 - Airbus A340-200 high speed drag characteristics

During the flight test programme of the A340 it was found that at low weight and altitude the dive Mach number $M_D = 0.93$ could not be attained safely because of excessive buffeting. This prevented flutter and stability and control tests up to M_D required for certification. Analysis indicated that the strong buffet originated from an area of separated flow on the inboard side of the outboard engine pylon. This occurred only at low lift coefficients but was aggravated by an underestimated extra torsional wing deformation due to the outer engine weight and the rear loading at the high dynamic pressures at low altitudes.
On the first production aircraft the flow at the pylon was rectified by a fairing on the lower wing surface adjacent to the engine pylon but the definitive solution lay in a modification to the spanwise twist distribution.

In the 1990's the need arose for variants with higher payload capacity and longer range. Two variants were developed, the A340-500 and A340-600. The latter one made its first flight in 2001 followed by the A340-500 in 2002. Both had a wing with a full-span insert between the front spar and the leading edge as illustrated in figure 132. This increased the basic fuel capacity by 38 percent. Also the wing span was increased by 3.20 m.

The Airbus A330/A340 now exists of the following basic models:

A330-200   MTOW = 230 tonnes
A330-300   MTOW = 230 tonnes
A340-200   MTOW = 275 tonnes
A340-300   MTOW = 275 tonnes
A340-500   MTOW = 372 tonnes
A340-600   MTOW = 368 tonnes
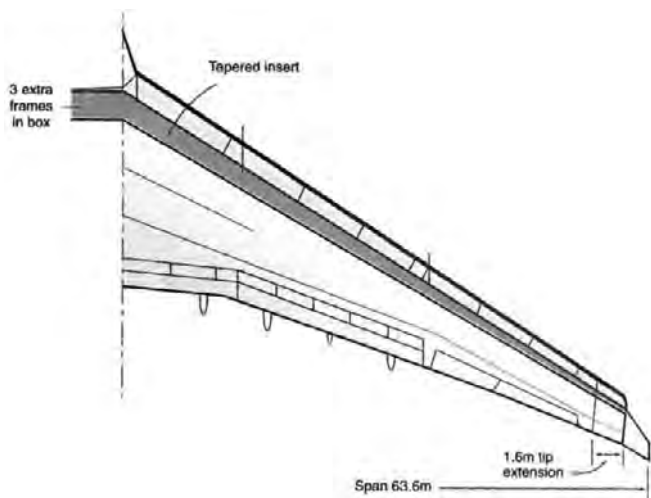
Figure 24.132 - A340-500/600 wing. Source: Flight International 2-8 September 1998

Airbus A380 (first flight 2005)

The Airbus A380 has the following design characteristics (A380-800):

MTOW	=	560 tonnes (1,235,000 lb)
Maximum cruise altitude	=	43,000 ft
Wing reference area S_W	=	845 m^2
Maximum operating Mach no. M_{MO}	=	0.89
Cruise Mach number M	=	0.85

These very demanding design requirements produced a wing with the following characteristics :

Wing sweep angle $\Lambda_{1/4c}$	=	33.5 deg
Aspect ratio A	=	7.67 (Airbus definition)
Relative root thickness t/c	=	0.132
Relative outer wing thickness t/c	=	0.087

Wing planform, root and outer wing sections are shown in figures 24.133 to 24.135. Note the thin trailing-edge region in the outer wing. In figures 24.136 and 24.137 the spanwise thickness and wing twist distribution are presented.
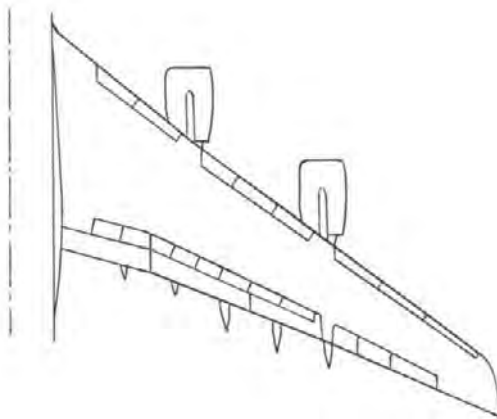
Figure 24.133 - Airbus A380 wing planform
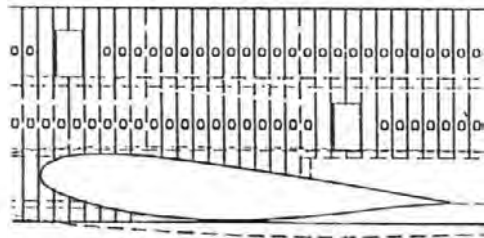
Figure 24.134 - Airbus A380 wing root section

Figure 24.135 - Airbus A380 outer wing section
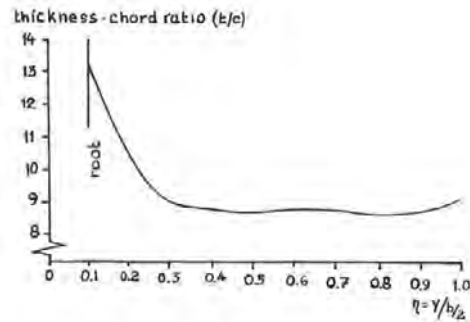
Figure 24.136 - Airbus A380 wing spanwise thickness distribution
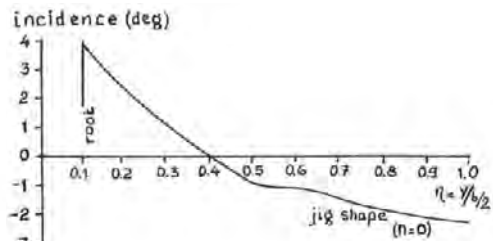
Figure 24.137 - Airbus A380 wing spanwise twist distribution

Fokker F-28 / Fokker 100 (first flight 1967 / 1986)

The design requirements for the F-28 wing contained an unusual element when compared to other first- or second-generation civil jet transport aircraft. Through the sales success of the F-27 Fokker obtained a detailed insight in the operating standards of many smaller companies, in particular in developing countries. Also a number of accidents had happened worldwide in the conversion from older propeller-driven aircraft to jet transports with their different operating characteristics.

This led to the decision that in the design of the Fokker F-28 achievement of benign flight handling characteristics across the complete flight envelope coupled with a minimum of system complexity would be accorded over growth and development potential.

Much attention was paid to the flight characteristics at transonic speeds. A requirement was that the aircraft should have positive longitudinal stability (no pitch-up or tuck-under) up to the dive Mach number without the use of a Mach trim compensator. To this end the thickest airfoil section was not placed at the wing root but at 40% semi-span. At transonic speeds flow separation behind the shockwave and a resultant lift loss would start in this region. The resulting redistribution of the downwash at the tail would then change the tail load compensating the change in tail-off pitching moment. The F-28 has positive longitudinal stability up to M_D without the use of a Mach-trim compensator.

The initial design condition for the F-28 was: MTOW = 54,000 lb, cruise altitude 25,000 ft and $M_{MO} = 0.75$ leading to $C_{L_{des}} = 0.23$ at M = 0.73. At this condition the drag creep was acceptable.

During subsequent development both take-off weight and cruise altitude increased. At these higher lift coefficients the drag characteristics were less than optimal as shown in figure 24.142.

When in 1982 the need arose to embark on a new programme the F-28 was taken as a starting point. The fuselage was lengthened, new engines became available and the wing was heavily modified. The external geometry of the wing torsion box was maintained as was the flap suspension and drive mechanism. The wing span was increased, the wing leading edge was modified, camber was applied in the increased flaps and new ailerons were down-rigged a few degrees.

The new wing geometry is presented in figures 24.138 and 24.139 compared with the F-28 wing geometry.
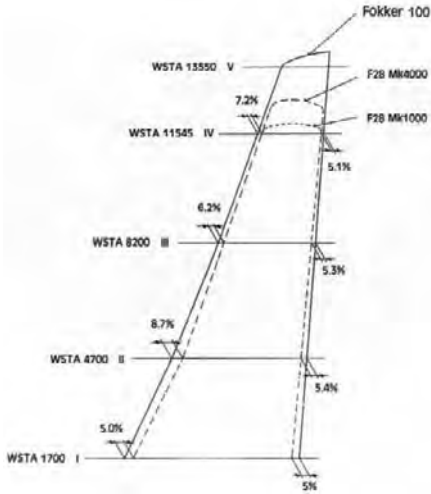
Figure 24.138 - Wing planform of the Fokker F-28 and Fokker 100. Source: ICAS-88, Paper 6.1.2
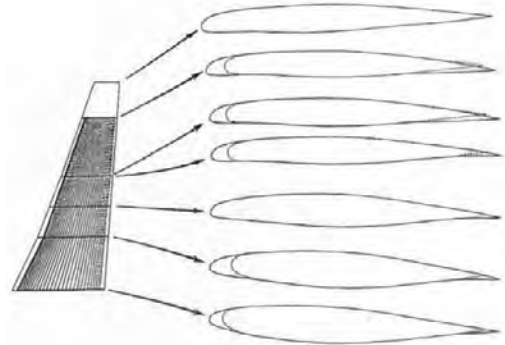
Figure 24.139 - Wing airfoil sections of the Fokker F-28 and Fokker 100. Source: ICAS-88, Paper 6.1.2

The resultant wing was a large improvement over the F-28 wing as illustrated in figures 24.140 and 24.141. The lower leading-edge suction peaks and the rear loading produced much more favourable drag characteristics as shown in figure 24.143. This improvement could only be achieved by the use of Computational Fluid Dynamics, CFD, in particular the programme XFLO22NLR, an NLR development of Jameson's FLO22 based on full potential flow theory.
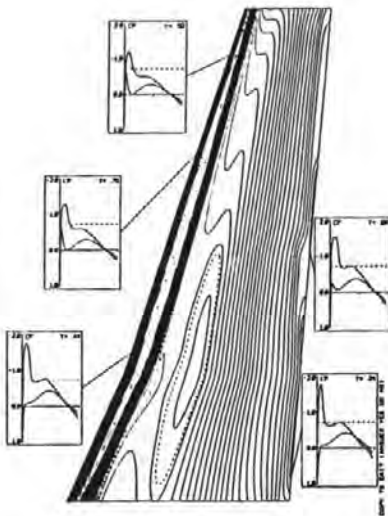
Figure 24.140 - Fokker F-28 Mk 1000 Wing pressure distribution at M = 0.72, C_L = 0.30. Source: Fokker Rep. L-28-316
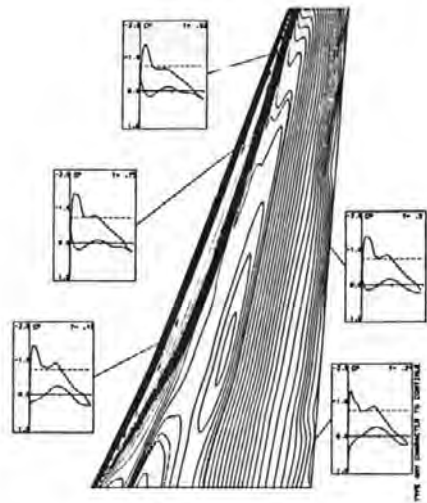
Figure 24.141 - Fokker 100 Wing pressure distribution at M = 0.72, C_L = 0.55. Source: Fokker Rep. L-28-341
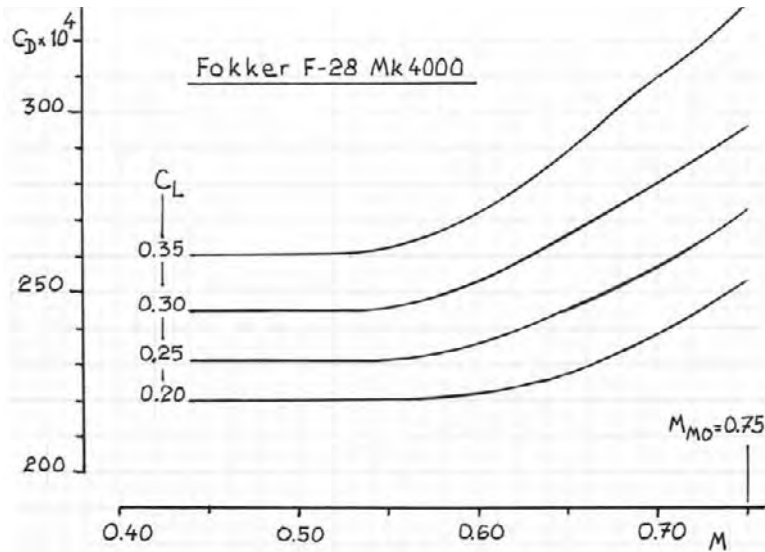
Figure 24.142 - Fokker F-28 Mk 1000 high speed drag characteristics.
Source: Fokker Report H-28.40-20.005
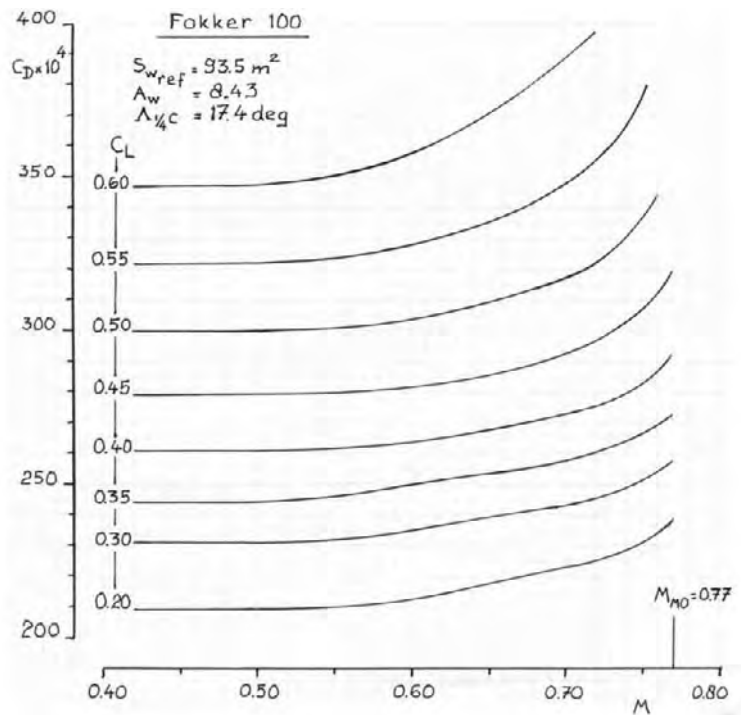
Figure 24.143 - Fokker 100 high speed drag characteristics.
Source: Fokker Report HX-28-S89-001

Definitions of wing reference area.

Three ways of defining the wing reference area are used by various manufacturers:

1. Leading and trailing edge of the basic (outer) wing are extended up to the fuselage centre line. Leading- and trailing-edge kinks are neglected. This definition was used by Fokker and is used by many U.S. manufacturers.

2. Leading and trailing edge of the root sections are connected and the area of this rectangle is added to the area of the wing halves outside the fuselage as illustrated in figure 24.144. This definition is used by British manufacturers and by Airbus.

3. The Boeing company uses the following definition :

$$S_{W_{ref}} = 2\left(A + B + F + D + H + \frac{X}{Z}E + \frac{Y}{Z}C + \frac{V}{Z}G \right)$$

The meaning of the various term are indicated in figure 24.145.
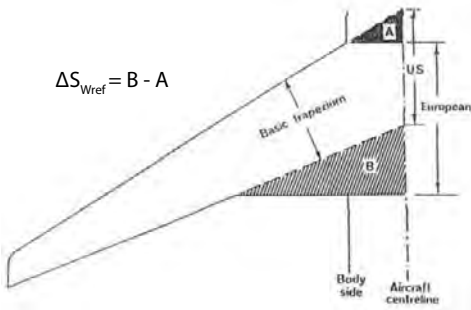
Figure 24.144 - Definition of wing reference area: Airbus
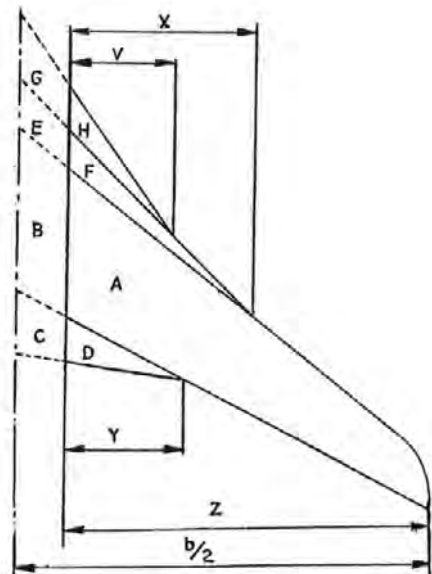
Figure 24.145 - Definition of wing reference area: Boeing

Some final remarks on modern high-speed wing design.

Today the most important tools used in the aerodynamic design of high-speed wings are the various CFD (Computational Fluid Dynamics) methods. A wide range of computer programmes has been developed. Some programmes are commercially available but most manufacturers, sometimes in cooperation with research institutes, prefer to either develop their own programmes or at least adapt them to their specific needs.
Possessing such programmes is no guarantee for success however as experience is required to handle these complex programmes and to understand their possibilities and limitations.

Programmes for analyzing flow conditions on aerodynamic configurations usually contain four components:

1. **Flow solvers**. Currently many flow solvers are available and/or in development. Their basis are the Navier-Stokes equations formulated more than one hundred years ago. For many aerodynamic design applications, the flow equations have to be simplified in order to make them amenable to solution. Neglecting viscosity leads to full potential equations, such as the Euler equations. Potential flow solutions can adequately simulate shock waves as long as they are relatively weak, which is normally the case for commercial transport configurations in cruise. Usually under many flight conditions the viscous effects are small and can be simulated by addition of boundary layer equations, a much simplified form of the Reynolds-averaged Navier-Stokes equations. Further simplification eliminates the nonlinear terms in the potential flow equations. This results in the Prantl-Glauert equation for linear compressible flows. The capability of modern computers to handle huge amounts of numerical data at great speed has allowed the use of large numbers of finely spaced control points where the flow equations apply, not only on the surface of the object under study but also in the space surrounding the object.

2. **Grid generators**. This is perhaps the most critical module because it is time-consuming in its manipulation. Grid-generation programmes are required to determine the control points where the flow equations apply. Many different types of computation grids are in use divided in two families, structured and unstructured grids.

3. **Pre- and post-processors** which help to make the CFD process run smoothly. Pre-processing provides a link between the aerodynamic surface definition (the loft), the grid and the CFD code. Examples are **surface interpolation and smoothing programmes** to accurately describe the shape of the object under study. Other pre-processors combine numerical parameters of the defined grid with the required flow parameters to generate the input deck for the flow solver and automatically start the CFD analysis, often for dozens of flow cases. **Graphic post-processors** allow the huge amount of numerical data resulting from the computations to be visualised as pressure distributions or as volumes indicating the location and/or strength of shock waves or vorticities in the flow field. These post-processors are essential for the designer in judging the end result of the computation.

4. **Optimization**. This is a separate category closely linked to flow solvers. There are several options available to an aerodynamicist to obtain the best possible solution for a design problem. One is the obvious trial-and-error process which is very time consuming, but is often the only option. Another possibility is to use inverse design techniques where a specific "ideal" wing pressure field is prescribed as a target. This approach requires much experience and currently   is used only in final stages of a design to smooth some unwanted pressures. Mostly used nowadays is optimization where transpiration is used to simulate surface movement and where multiple flow conditions are imposed to avoid unacceptable off-design characteristics. Optimization usually includes imposing multidisciplinary constraints such as requirements for thickness and curvature, wing root bending moment constraints, etc. A relatively new type of optimization, enabled by vastly increased computational capacities, launches dozens or hundreds of cases where certain geometric design parameters are varied within specified ranges and where optimization scripts are used to determine favourable directions for the next series of follow-up cases.

During the last few decades developments in computing technologies, flow solvers and especially pre- and post-processing software have made it possible to analyze multiple flow conditions for complete configurations practically overnight. CFD analysis for wing, fuselage, empennage, nacelle/strut combinations including flap support fairings, with boundary layers on most components can be done on a routine basis and solutions from 'lofts to plots' can be available in less than 12 hours.

One of the design objectives of modern high-speed wing design is the integration of a wing with engine nacelles fitted on pylons under the wing with minimal interference effects.

In figures 24.146 to 24.153 the results of such an exercise are presented . In figure 146 the configuration considered is shown. The wing was designed for M = 0.78 and C_L = 0.57 and had the following characteristics: A_w = 10.67 and $\Lambda_{1/4c}$ =26.5 deg. Note the large size of a modern high-bypass-ratio engine relative to the local wing chord. In figure 24.147 the development of the wing-pylon intersection is shown. Figures 24.148 and 24.149 show how through a series of pylon shape modifications the pressure distribution on the lower wing surface adjacent to the pylon ,in particular on the inside, was gradually improved until an acceptable flow field was obtained. But it took sixteen steps of computations with a computer programme based on Euler equations where for each step the computation grid had to be modified. The complete configuration with the finally adopted pylon shape was then analysed with the computer programme version based on the time-averaged Navier-Stokes equations to incorporate boundary-layer effects.

The optimisation was performed with the Euler programme because of the difference in complexity between computations on the basis of Euler and Navier-Stokes equations.

Figures 24.150 and 24.151 show the pressure distributions on both sides of the pylon as obtained with the Navier-Stokes programme. The difference with the data in the previous figures is small indicating that in this case boundary layer effects were of secondary importance.
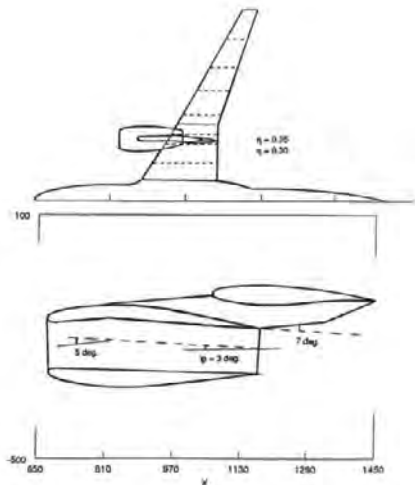
Figure 24.146 - Model VTP-4. Plan view and wing, pylon and nacelle side view and cross-section. Source: Fokker Report WT-P-159
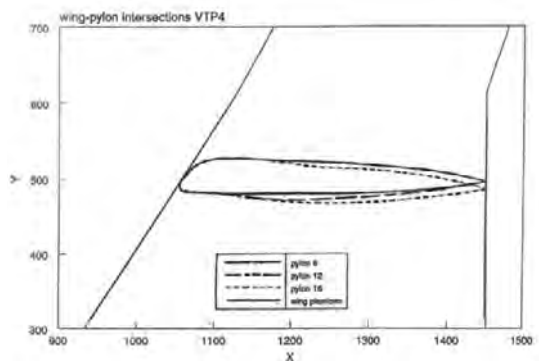
Figure 24.147 - Wing-pylon intersection. Source: Fokker Report WT-P-159

Figure 24.152 shows the small effect of fitting the pylons and engines onto the wing on the spanwise circulation distribution. Figure 24.153 illustrate the small increase in transonic drag creep due to the addition of the engines as found in the wind tunnel tests on this configuration. But this result could only be obtained with the aid of modern CFD.
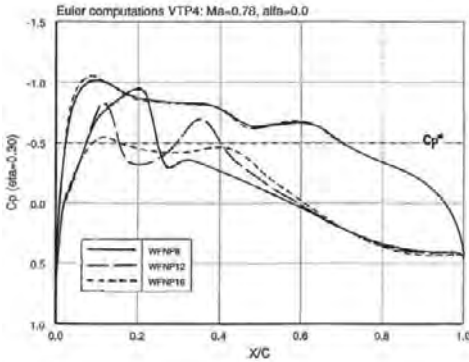
Figure 24.148 - Wing pressure distribution just inboard of the engine pylon (Euler programme). Source: Fokker Reports WT-P-159 and WT-P-160, February 1996
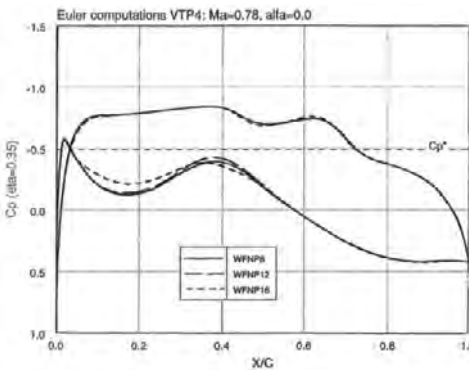
Figure 24.149 - Wing pressure distribution just outboard of the engine pylon (Euler programme). Source: Fokker Reports WT-P-159 and WT-P-160, February 1996
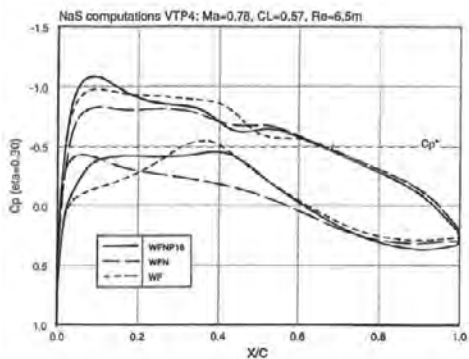
Figure 24.150 - Wing pressure distribution just inboard of the engine pylon (Navier-Stokes programme). Source: Fokker Reports WT-P-159 and WT-P-160, February 1996
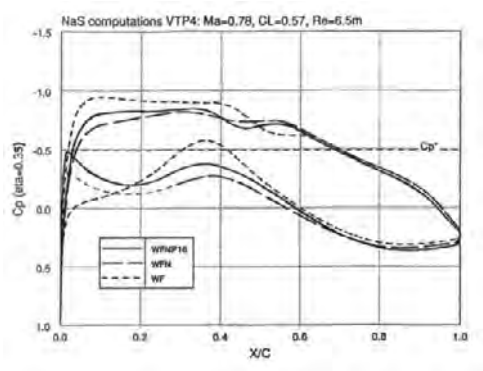
Figure 24.151 - Wing pressure distribution just outboard of the engine pylon (Navier-Stokes programme). Source: Fokker Reports WT-P-159 and WT-P-160, February 1996
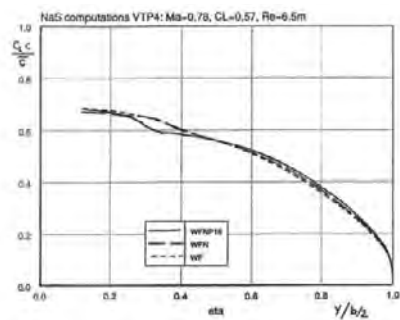
Figure 24.152 - Spanwise circulation distribution. Source: Fokker Report WT-P-159.
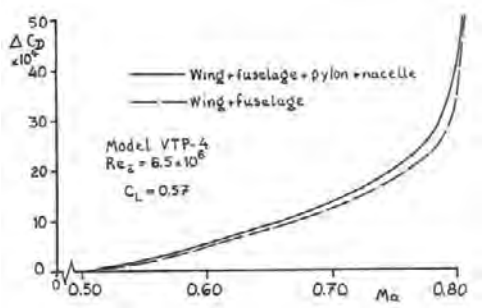
Figure 24.153 - Effect of pylon and engine nacelle on transonic drag rise characteristics

PART 5

LOW-SPEED AERODYNAMIC LIMITS

25

The maximum lift coefficient of airfoil sections equipped with high-lift devices

High-lift devices are employed to increase the maximum lift coefficient of a wing during take-off and landing. This allows the sizing of the wing to be primarily determined by climb and cruise drag and fuel volume considerations. Trailing-edge devices were already used during the First world War and slats since the early 20's, but their functioning in an aerodynamic sense was not understood well until 1972 when A.M.O. Smith published a paper on high-lift aerodynamics.

High-lift basics

There are three effects that determine the increase in maximum lift by the use of high-lift devices:

1. An increase in camber
It is well known that cambered airfoil sections have a higher maximum lift coefficient than symmetrical sections. But airfoil camber also produces (at excessive camber excessive) drag. This is why, already in an early stage of aviation history, variable camber was employed in the form of split or plain flaps.

If the trailing-edge of an airfoil is deflected downwards the effective camber is increased. This results in more circulation due to a change in the Kutta-Joukowsky boundary condition at the trailing edge and thus in more lift at constant angle-of-attack whereby the **angle-of-attack remains the angle between the chord line of the basic section and the direction of the undisturbed flow**. This is why the lift curve shifts upwards in figure 25.1 when the flaps are deflected. A leading-edge device or slat on the other hand decreases lift usually by a change in effective leading edge camber because the extension of leading-edge devices usually produces a leading-edge droop. At constant low angle-of-attack (according to the same definition) this produces a small downward shift of the lift curve as also shown in figure 25.1.
Flap deflection produces the higher maximum lift at nearly the same or slightly lower maximum angle-of-attack as the basic section whereas a slat or drooped leading edge produces the higher maximum lift at a higher angle-of-attack.
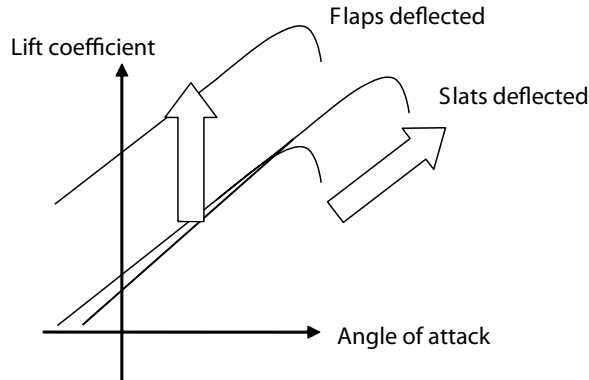
Figure 25.1 - Effect of flaps and slats on the lift curve

2. An increase in effective chord.

Deflection of a high-lift device can increase the effective chord length if there is a chord extension. A fixed-hinge flap with the hinge close to the chord line for example does not change the chord length, but a Fowler flap moves aft and does increase the effective chord. The same holds for a slat that usually moves down and forwards thereby increasing the effective chord length. Chord extension increases the lift curve slope because the wing reference area usually remains unaltered.

3. The mutual interaction effect.

The lift on an airfoil section can be analysed by replacing the actual section by a series of vortices on the section camber line. This series of vortices may vary between a continuous vortex sheet which allows the analysis of the chordwise lift distribution and a single vortex at the quarter chord position producing the total lift when the angle-of-attack is increased relative to the angle-of-attack for zero-lift, the zero-lift line.

By means of Joukowsky conformal transformations exact solutions **without linearization** can be obtained for the lift on **a flat plate or a circle segment at any angle-of-attack**. Note that on a section formed by a circle segment the zero-lift line passes through the middle of the circle segment and the trailing edge as indicated in figure 25.2.

The camber line of an airfoil section with a large drooping leading edge and a double-hinged plain flap with hinges on the camber line resembles a circle segment and will have the same lift coefficient at a given angle-of-attack if the same angle-of-attack definition is used.

CFD methods such as VLM allow the computation of the chordwise lift distribution on such an airfoil without conformal mapping by using a number of discrete vortices. For the analysis of the lift it makes no difference if this

airfoil is a single oddly-shaped section or a compound section with movable components. The mutual interaction of the vortices in the analysis remains the same.
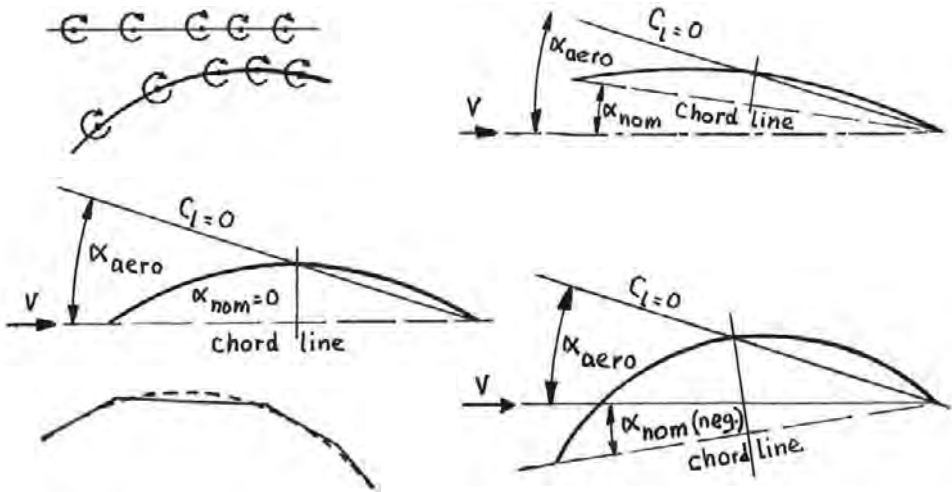
Figure 25.2 - The representation of a lifting flat plate and a circle segment by a series of discrete vortices, the zero-lift line and the aerodynamic angle-of-attack of circle segments and the approximation of a section with a hinged leading-edge and a double-hinged trailing-edge flap by a circle segment

Note that with increasing flap deflection the angle-of-attack for zero lift decreases because the nominal angle-of-attack is measured relative to the chord line of the clean section.

If the angle-of-attack would be measured relative to the zero-lift line the lift curves for the different flap angles would collapse and the angle-of-attack for maximum lift would increase with increasing flap angle in the same way as with a drooped nose. This is because **at a given lift coefficient deflecting either leading- or trailing-edge devices produces a decrease in the leading-edge suction peak allowing a larger increase in angle-of-attack before flow separation occurs**.

Up to now only the effect of (strong) curvature of the effective **continuous** camber line on lift has been discussed. If now the situation is considered that **the various components of the airfoil section are decoupled and over a very short distance moved away from each other** the situation changes. On a continuous camber line the camber line is a discontinuity with different velocities and pressures on opposite sides of the camber line. If the camber

line consists of several parts divided by small gaps this discontinuity can not exist in the gaps and the lift at the leading and trailing edge of each part will be zero. This means that the lift of such a combination of components will always be lower than when they are connected without leakage. However **the mutual interaction of the vortices will remain and the total chordwise lift distribution over the compound airfoil section will be similar to that on a single (highly-curved) section**.

This is illustrated in figure 25.3 from a paper read by A.M.O. Smith in 1974 which shows computed pressure distributions in non-viscous flow on three cambered airfoil sections positioned closely together. The dashed curves indicate the pressure distribution on the section individually, the drawn curves show the pressure distribution with the sections in the positions in the figure. At an angle-of-attack α = 10 deg the lift coefficient for the sections individually c_l = 1.69, for the three sections combined and based on the total chord length the lower value c_l = 1.54 was found. The total chordwise lift distribution is very similar to the lift distribution on a single section with little camber as can be seen from a comparison with the calculated lift distribution on a flat plate at α = 10 deg in figure 25.4. The difference is mainly due to the high camber of the three identical sections themselves.
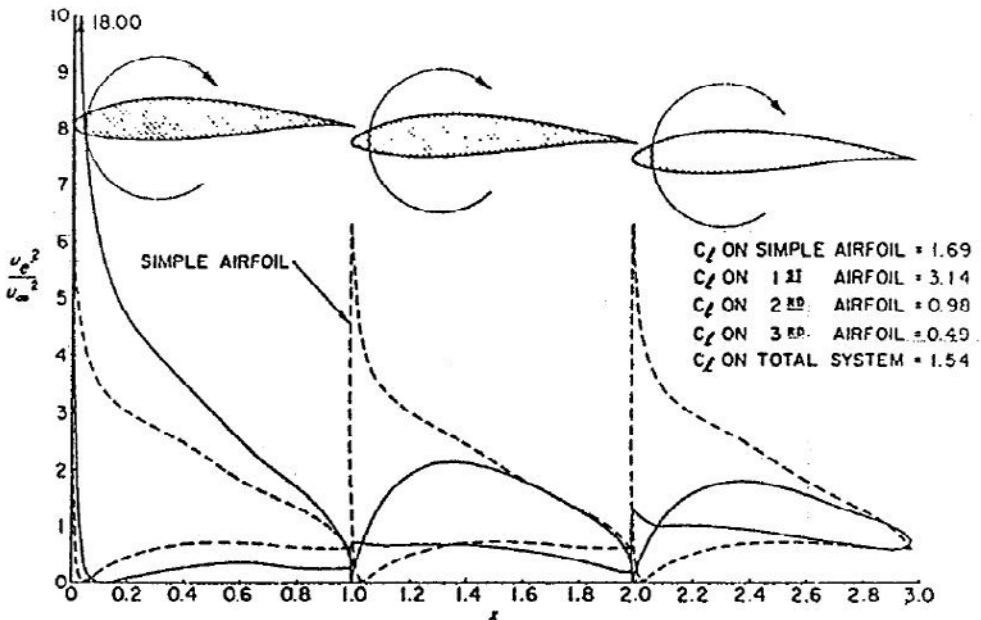
Figure 25.3 - Pressure distribution on a three-element airfoil formed by NACA 63₂-615 sections arranged as shown, all three at α = 10 deg. Also shown is the pressure distribution on the basic single section. The slat gaps are 1% of the basic section chord. Source: AIAA Paper No. 74-939 High-lift Aerodynamics, A.M.O. Smith.
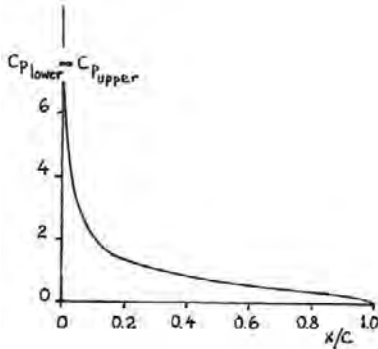
Figure 25.4 - Chordwise lift distribution on a flat-plate section at α = 10 deg

A very convincing example of the above is shown in figures 25.5 and 25.6. Handley-Page published in 1921 the results of an investigation whereby wings with aspect ratio A = 6 were tested, both with a single, somewhat modified, RAF 19 airfoil section and different numbers of combined sections within the modified RAF 19 section contour. Although the tests were done at Re = 250,000 the lift curves lie closely together with a constant slope and are only shifted slightly because of the increasing lift loss at constant angle-of-attack due to the increasing number of slots. The maximum lift however increases with each additional slot except with the last one.
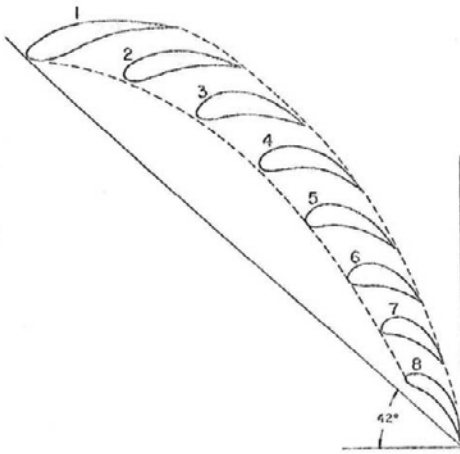
Figure 25.5 - A multi-component airfoil section within the contour of a modified RAF 19 airfoil section. Source: AIAA Paper No. 74-939
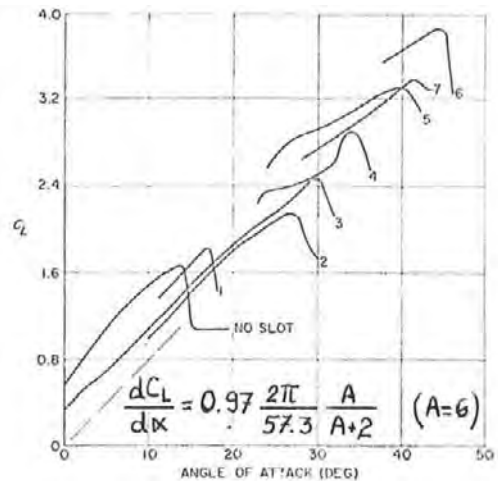
Figure 25.6 - Lift curves of the section of figure 25.5 with a successively increasing number of gaps between the components. Source: AIAA Paper No. 74-939

In the foregoing compound two-dimensional airfoils were treated as an entity. In the next part of this paragraph the flow about the individual components with small gaps between them will be considered.

Starting from a representation of a section with leading- and trailing-edge high-lift devices by discrete vortices (a single vortex for each component) each vortex is in turn replaced by the actual component which then experiences the influence of the remaining vortices in terms of upwash and downwash.

The main body (the centre wing) experiences the downwash of the preceding vortex (the slat) and the upwash of the succeeding vortices (the flap components). This leads to a lowering of the lift on the forward part of the main body, in particular to a decrease of the leading-edge suction peak, and to an increase of the lift on the rear part.

The leading-edge device, usually a slat or slotted Kruger flap is placed in the upwash of all succeeding vortices and experiences a large increase in effective angle-of-attack and thus a very high lift, even in the usual drooped position.

The last trailing-edge device experiences the downwash of all preceding vortices and has a small effective angle-of-attack and thus carries little lift notwithstanding a large nominal flap angle. If the trailing-edge flap is a compound flap, a double- or triple-slotted flap, the first or first and second component experience the influence of the adjacent vortices in the same way as the main body.

Note that, although trailing-edge flaps themselves may carry little lift, their influence on the preceding components is very large.

In the above circulation and lift have been discussed without any particular attention to the boundary layer.

On high-lift devices with fixed hinges close to the camber line the boundary layer flows, in particular on the top surface of the airfoil, from the leading edge to the trailing edge meanwhile having to negotiate the suction peaks and the following steep adverse pressure gradients at the kinks in the surface as shown in figure 25.7. At a given angle-of-attack this leads to flow separation near the trailing edge or behind one of the "knuckles".
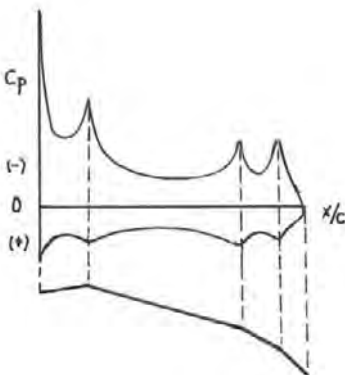
Figure 25.7 - The pressure distribution on a flat plate airfoil section with hinged leading-edge and double-hinged trailing-edge flap at a large angle-of-attack.

By separating the different components of a compound airfoil section each component will form its own boundary layer on upper and lower surface resulting in a wake.

Because each component has a considerably smaller chord length than the basic section the flow particles will have to cover a shorter distance before reaching the trailing edge and the energy loss of the boundary layer will be less than on the full chord basic section for a given pressure distribution.

On the rearmost component the trailing-edge pressure coefficient will be, just as on a single airfoil, $c_{P_{te}} = 0.15 - 0.25$ when no separation occurs. On the other components the trailing- edge pressure coefficient will be heavily influenced by the leading-edge pressure coefficient of the succeeding component and in most cases be lower (more negative) than on a single airfoil section. This trailing-edge velocity which, under the influence of the velocity at the leading edge of the succeeding component, is higher than on a single airfoil section, was termed by A.M.O. Smith the "dumping velocity".

The combined effects on each component of being placed in a flow field with upwash or downwash, the smaller chord length and the dumping velocity make that compound airfoil sections can reach much higher maximum lift coefficients than single airfoil sections.

The mutual positioning of the trailing edge of the preceding component and the leading edge of the succeeding component is very critical for an optimum fulfilment of the design requirements. The slot between each two components is usually defined by the gap width and the overhang as illustrated in figure 25.8.
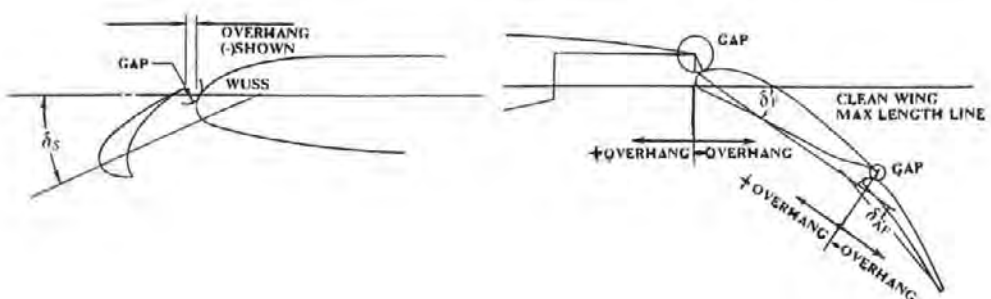
Figure 25.8 - Definition of gaps and overlaps between the components of compound airfoil sections. Source: AIAA Paper No. 93-3140

The highest maximum lift coefficient is obtained when the wake of the preceding component and the boundary layer of the succeeding component do not merge. This is illustrated in figure 25.9 which presents the flow field above a single-, a double- and a triple-slotted flap on an airfoil section with a slat. This flow condition, which requires a gap width of 2-3 percent and an overlap of +1 / -1 percent of the basic chord, depending on the Reynolds number and on the leading-edge shapes, produces however also the highest drag in normal operating conditions.

For take-off and go-around not only the maximum lift is important but also the lift-drag ratio. Therefore for these flight conditions smaller gaps are chosen so that wakes and boundary layers merge (confluent wakes and boundary layers). This produces improved lift-drag ratios albeit at lower maximum lift. This is illustrated in figure 25.9.
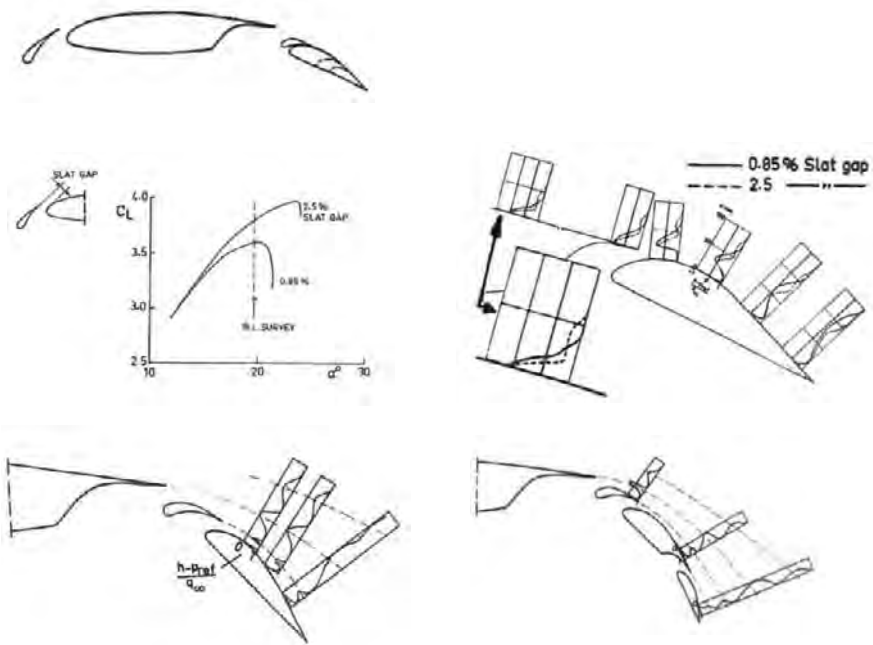
Figure 25.9 – Wake profiles on an airfoil section with a slat and a single-,double- and triple- slotted flap with confluent and non-confluent wakes and boundary layers. Source: AGARD CP-143, Paper 13

For the highest lift-drag ratios slat and flap positions may be adopted for take-off configurations without gaps such as shown in figure 25.10 for the Boeing 737.
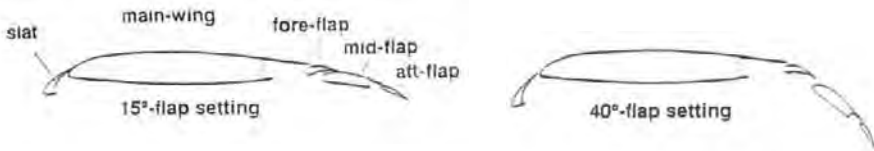
Figure 25.10 – Slat and flap positions at mid-semi-span for take-off and landing of the Boeing 737. Source: AIAA Paper No. 93-3140

An analysis of the flow around an airfoil with high-lift devices.

Figure 25.11 shows a slat in three different positions with respect to the wing. It may seem that the slat has a negative angle-of-attack but being placed in the upwash of the wing the effective angle-of-attack is only slightly negative or positive. The corresponding pressure distributions are presented in figure 25.12. For position 1 the lift on the slat is slightly negative but if the slat is moved closer to the main wing the pressure distribution changes: the local upwash increases closer to the wing and as a result the slat generates more lift. Because of the increased lift on the slat, which produces more downwash, the suction peak on the main wing drops and the wing loses some lift. But at high angles-of- attack the boundary layer will remain attached and a higher maximum lift can be achieved.

Figure 25.11 - Changing slat position to improve the pressure distribution on an airfoil section with a slat and a flap at α = 15 deg and δ_f =10 deg. Re = 3.8x10^6. Source: NASA TM 78566
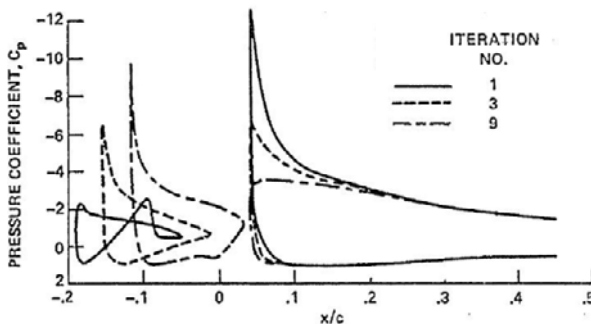
Figure 25.12 - Pressure distribution on the slat and the leading-edge region of the main airfoil for the three slat positions at α = 15 deg and δ_f = 10 deg. Re = 3.8x10^6. Source: NASA TM 78566

This is illustrated in figure 25.13. This figure shows the pressure distribution on the same airfoil with a slat and a flap as considered in the two previous figures for different angles-of-attack. The angle-of-attack is increased from 13 to 24 deg while the total lift coefficient increases by 43%. The increase in lift coefficient of the forward element is higher, 74% and for the middle and final elements the increases in lift coefficient are 38% and 22% respectively. At the low flap angle of $\delta_f = 10$ deg the lift on the flap increases slightly with increasing angle-of-attack. For higher flap angles the lift on the flap may even decrease with increasing angle-of-attack. This is discussed further later in this chapter.
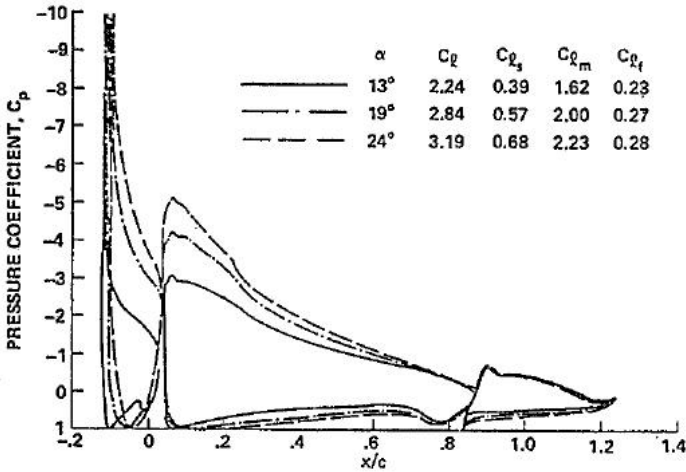
Figure 25.13 - Pressure distribution on a slat-wing-flap combination at different angles-of-attack. Source: NASA TM 78566

Types of flow separation

Figure 25.14 to 25.16 show the mechanics of flow separation at maximum lift for a wing with a flap.

1. Flow separation may occur at the trailing edge of the flap at small angles-of-attack and large flap deflections. This determines the maximum flap angle that can be used for a landing configuration. (Figure 25.14)

2. Trailing-edge separation may occur on the main wing just in front of the flap. Because of the effective de-cambering of the trailing-edge region of the main wing due to the separated flow the velocities on the main wing upper surface are lower over the full chord and once flow separation occurs the supervelocities change only slightly with increasing angle-of-attack.
Under the influence of the wake from the main wing flowing over the flap the lift on the flap is also lower. (Figure 25.15)

3. The flow may also separate at the leading-edge. In this case the stall will be abrupt and the lift loss will be large. Because of the loss in lift the downwash from the main wing is smaller and the effective flap angle-of-attack increases which is why the flap generates slightly more lift when leading-edge stall occurs. (Figure 25.16)
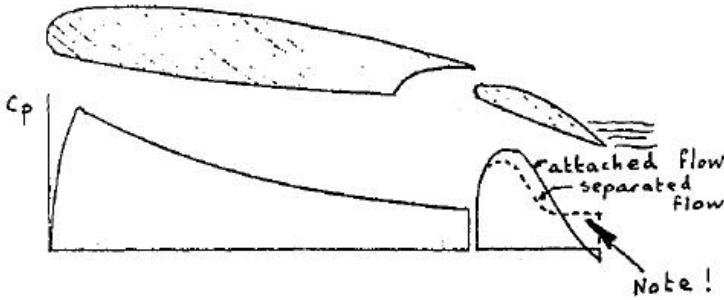
Figure 25.14 - Trailing edge stall on the flap for a section without a slat
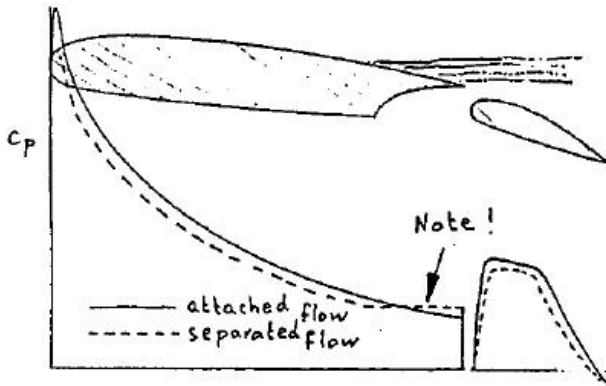
Figure 25.15 – Trailing edge stall on the main component for a section without a slat
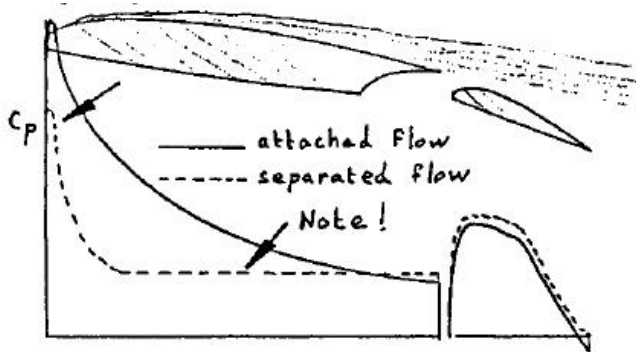
Figure 25.16 – Leading-edge stall on the main component for a section without a slat.

Figures 25.17 to 25.19 show the different types of flow separation which may occur when a slat is added to the main wing and flap combination.

1. Stall may occur on the slat. This results in a collapse of the leading-edge suction peak on the slat. This occurs usually at small slat deflection angles.

2. Trailing-edge separation on the main wing occurs in a similar way as explained for figure 25.15. This happens when the slat deflection is larger than in the case mentioned above.

3. When the slat is deflected even further separation may occur at the leading edge of the main wing. Two different types of flow separation are possible. The flow may separate right at the leading edge resulting in a collapse of the leading-edge suction peak. If the slat trailing-edge angle is larger than average (because of stiffness considerations) resulting in a kink in the main wing upper surface or because of a step in the upper surface to minimise the drag with the slat retracted (see figure 25.20) separation may occur at the kink or step.
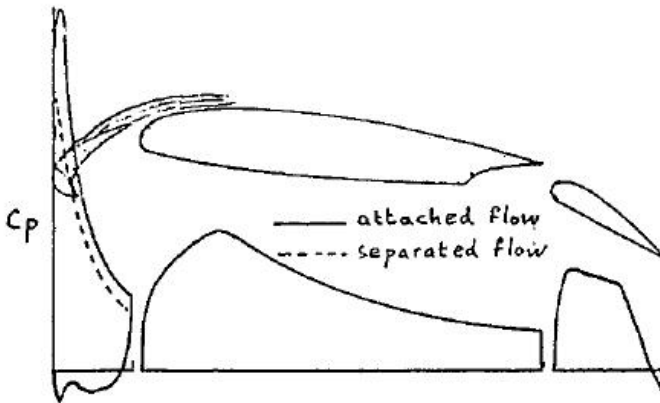
Figure 25.17 - Stall on the slat
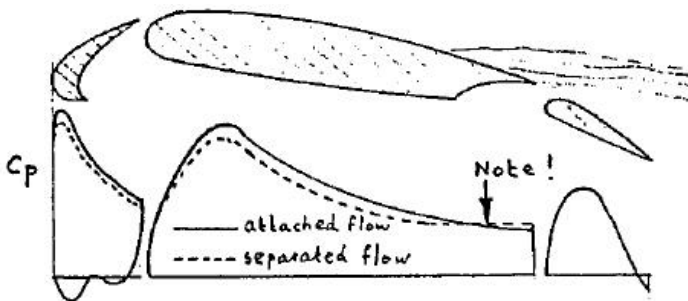
Figure 25.18 - Trailing-edge stall on the main component for a section with a slat
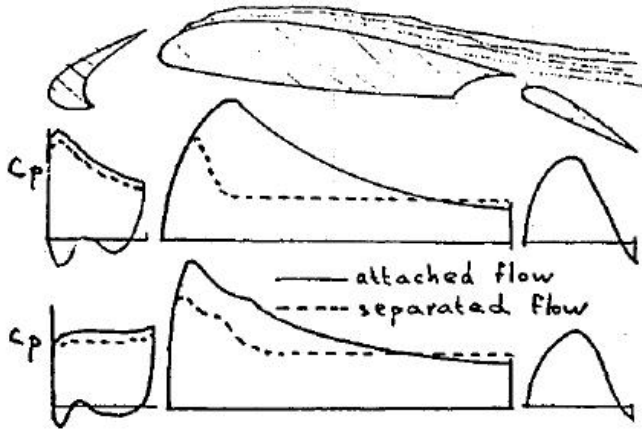
Figure 25.19 - Leading-edge stall on the main component for a section with a slat
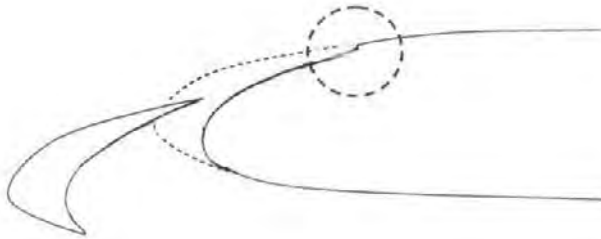
Figure 25.20 - Slat housing

In principle the optimum high-lift configuration is the one where separation is reached on all components simultaneously. On an aircraft this may produce unacceptable flying characteristics.

Examples of high-lift systems

A high-lift system was investigated in a wind tunnel test carried out by the Dutch NLR during the development of the Fokker F-28 "Fellowship". Figure 25.21 shows the wing section at mid semi-span of the F-28 with a slat and a double-slotted flap. A movable vane was fitted which is only deployed at flap deflections of more than 18 deg. During take-off from hot-and-high airfields flap deflections are limited to 18 deg to minimise drag. For take-offs from low-altitude airfields or at high thrust-to-weight ratios and for landing flap deflections of 25 or 42 deg are applied, in which case the vane is deployed.

The lift characteristics of the airfoil section applied on the F-28 are shown in figure 25.22. The dashed lines represent the configurations without a slat and the solid lines the configurations with the slat extended. Note that at low angles-of-attack slat deflection causes a slight decrease in lift as has been discussed at the beginning of this chapter. The slat increases the two-dimensional maximum lift coefficient by $c_{l_{max}} = 0.6$ with the flap retracted rising to $c_{l_{max}} = 0.9$ with the flap deflected to 42 deg. Deploying the flap alone raises the maximum lift coefficient from $c_{l_{max}} = 1.6$ to $c_{l_{max}} = 3.6$. Deployment of the flaps also decreases the angle-of-attack for maximum lift from 17 deg to 10 deg. This is because the deflected flap generates upwash which increases the effective angle of attack of the main component. Due to the definition of the geometric angle-of-attack the maximum angle at which separation occurs will then decrease.

The chordwise pressure distribution on the Fokker F-28 wing section is shown in figure 5.23 for zero angle-of-attack and $M = 0.19$. At the bottom of figure 25.23 the pressure distribution is presented for the configuration with slat and flap retracted. Moving up in the figure, the flap is deflected at an increasing angle and at a flap deflection angle of 25 deg the vane is also deployed. Note that the pressure distributions on the vane and the main flap have been shifted to the right for clarity. The total lift increases with increasing flap deflection but most of the lift due to flap deflection is not on the flap and vane themselves but on the main wing. This is in line with what has been discussed at the beginning of this chapter concerning the effect of strong mean line curvature and the changing Kutta-Joukowsky trailing-edge boundary condition and the chordwise pressure distributions resemble the pressure distribution shown in figure 25.7.

Figure 25.24 shows pressure distributions at maximum lift for different flap settings. The minimum pressure coefficient increases from $c_{p_{min}} = -9.5$ in the clean configuration to $c_{p_{min}} = -17$ with fully deployed flaps. As the dumping velocity, the velocity at the trailing edge of the main wing, also increases, the average pressure gradient remains about the same and the onset of flow separation is delayed. For the highest flap settings a small increase in free-stream Mach number may lead to supersonic velocities at the leading edge with shock waves which then determine the maximum lift even at these low speed conditions.
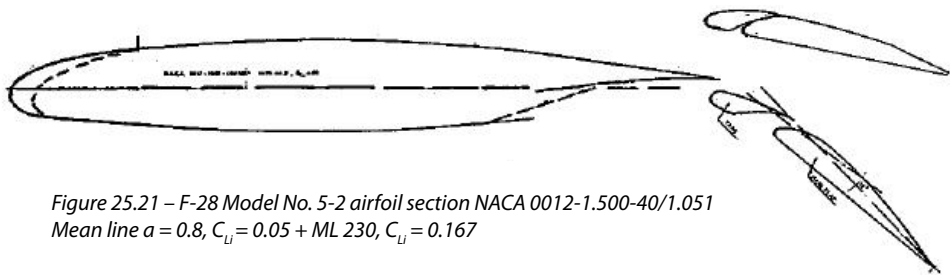
Figure 25.21 – F-28 Model No. 5-2 airfoil section NACA 0012-1.500-40/1.051
Mean line a = 0.8, C_{Li} = 0.05 + ML 230, C_{Li} = 0.167
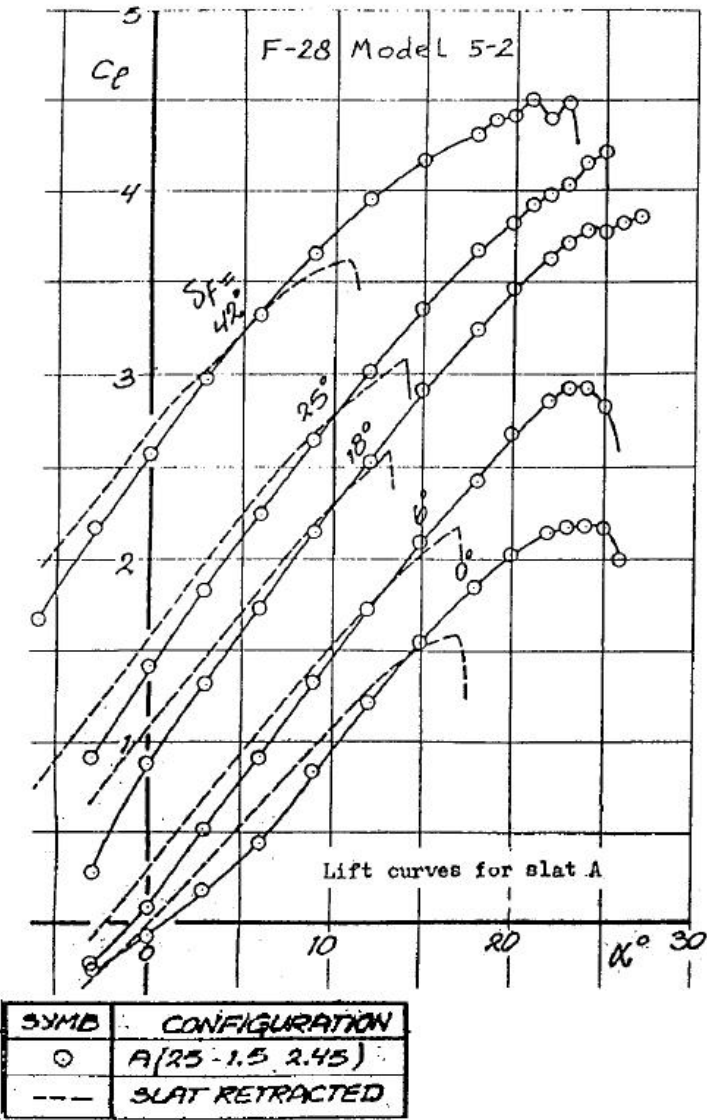
Figure 25.22 - Section lift curves with extended high-lift devices for F-28 Model 5-2. Source: NLR TR 70084C
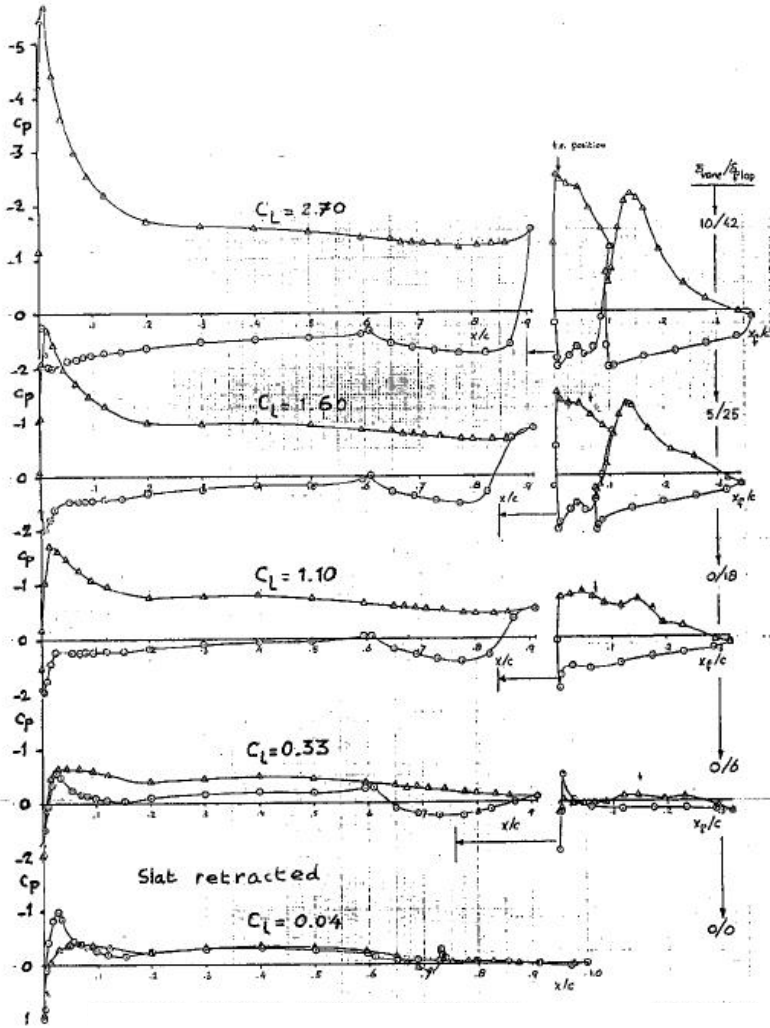
Figure 25.23 - Effect of flap angle on pressure distribution. F-28 Model 5-2. M = 0.19, α = 0°, Re = 2.8x10⁶

The pressure distributions on the F-28 model prior to and after the stall for a flap setting of 18 deg are shown in figure 25.25. Prior to the stall the minimum pressure coefficient is $c_{p_{min}}$ = -12 and it drops to $c_{p_{min}}$ = -7.5 after the stall. At about 10% chord the flow separates.

Note the small increase in lift on the flap due to the decrease in downwash from the main wing.

In figure 25.26 the minimum pressure coefficient and the pressure coefficient at the trailing edge are presented of the main wing, the vane and the main flap of
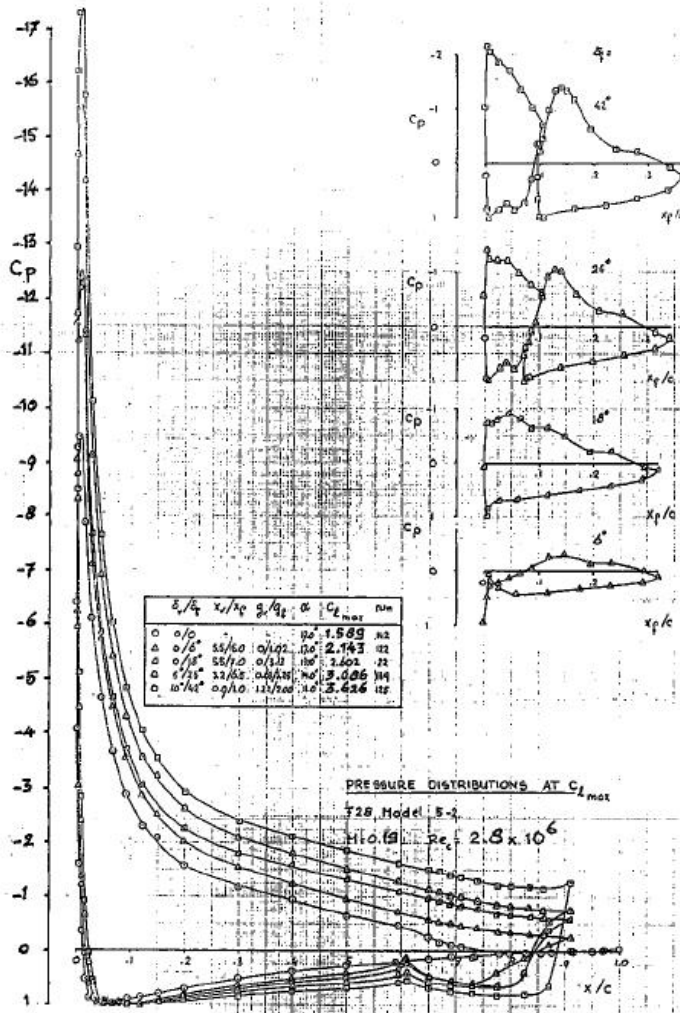
Figure 25.24 - Pressure distribution at $c_{l_{max}}$ F-28 model 5-2.

the F-28 model as a function of angle-of-attack. The graph on the left represents the clean configuration and towards the right the flap deflection increases. With increasing flap deflection the minimum pressure coefficient is increasing (in a negative sense). At separation the suction peak at the leading edge of the main wing drops. For flap deflections of 6 deg and 18 deg the minimum pressure coefficient of the flap increases when the flow on the main airfoil separates.

But when the flap angle is 42 deg the minimum pressure coefficient and the supervelocities on the flap in general drop. This is explained in the following.
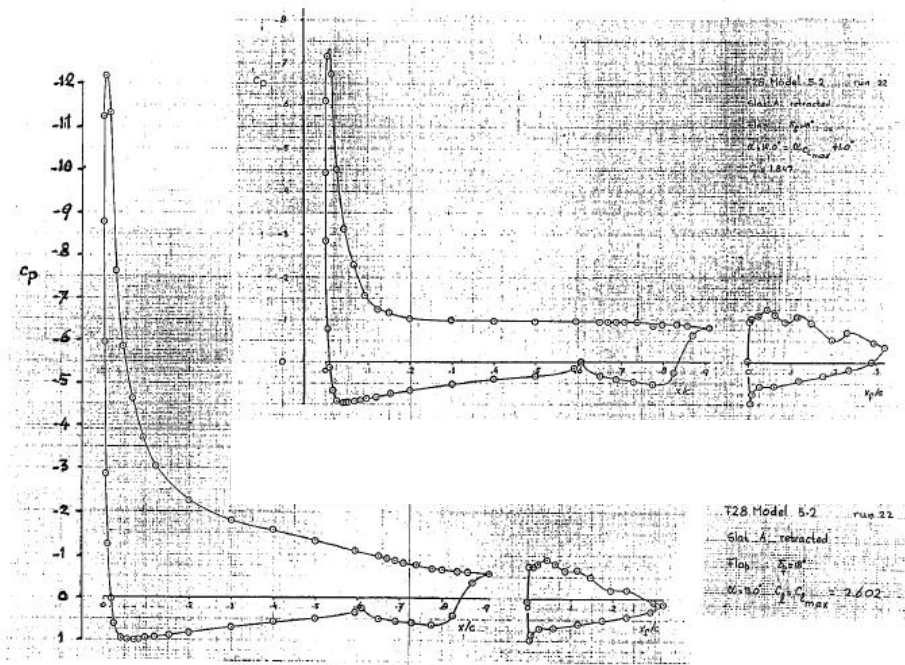
Figure 25.25 - Pressure distribution prior to and after stall
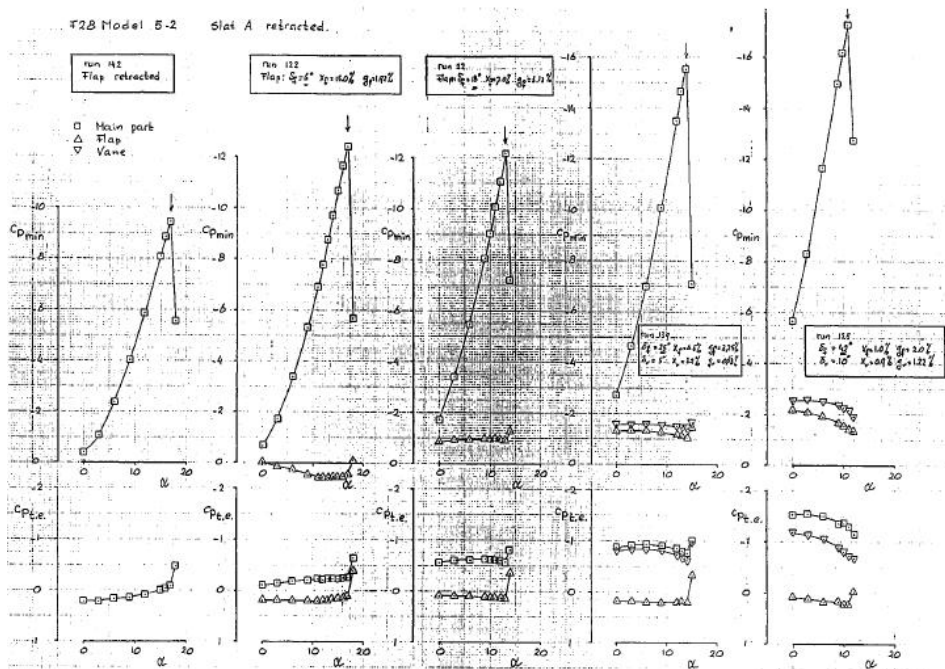
Figure 25.26 - Minimum- and trailing-edge pressure as a function of α and δ$_{flap}$. Source: NLR TR 70084C

Figures 25.27–25.33 show the results of a theoretical and experimental analysis of the behaviour of wakes in a flow field with strong adverse pressure gradients in particular of the wake from the main body of a multi-component airfoil section flowing over a trailing-edge flap at a large flap angle. Figures 25.27–25.31 refer to an investigation on airfoil section NLR 7301 with a single-slotted flap and figure 25.32 and 35.33 to an investigation on the Fokker F-28 section with the double slotted flap in the landing position ($\delta_f = 42$ deg).

Figure 25.27 shows the lift curves for airfoil section NLR 7301 with a single-slotted flap deflected to $\delta_f = 30$ deg. Three curves are shown: the theoretical curves for inviscid flow and for viscous flow and the curve derived from experimental data. The latter two are almost identical indicating the high quality of the calculation method.
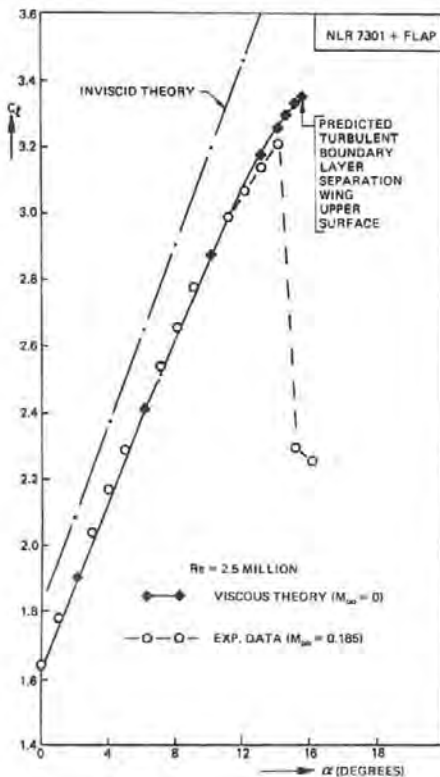
Figure 25.27 - Theoretical and experimental lift curves for airfoil section NLR 7301 with a single-slotted flap at $\delta_f = 30$ deg. Source: AGARD CP – 365, Paper No. 3

In figure 25.28 the growth of the wing-wake displacement body with increasing angle-of-attack according to the calculation procedure is presented. Figure 25.29 shows the rise in static pressure at the wing-wake centreline when moving towards the flap trailing edge. (This is the adverse pressure gradient mentioned above).

Figure 25.30 presents the chordwise pressure distribution on the flap as calculated both for inviscid flow and for viscous flow including the wing wake representation. The latter is compared with experimental data in figure 25.31. Note again the good agreement strengthening the credibility of the theoretical model.

This analysis and the good comparison between theory and experiment clearly proves that the decrease in lift with increasing angle-of-attack on a flap at a large deflection angle is caused by the influence of the growing wake from the main airfoil.
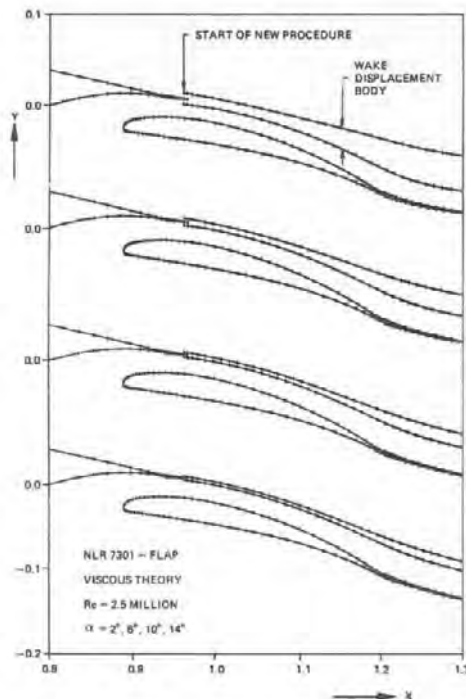
Figure 25.28 - Growth in wing-wake displacement body with increasing angle-of-attack in theoretical viscous flow. Source: AGARD CP – 365, Paper No.3
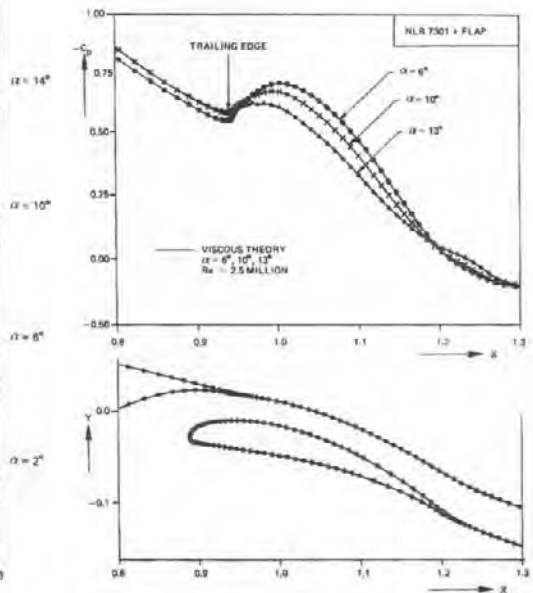
Figure 25.29 - Static pressure at the wing-wake centre line from viscous theory.
Source: AGARD CP – 365, Paper No.3
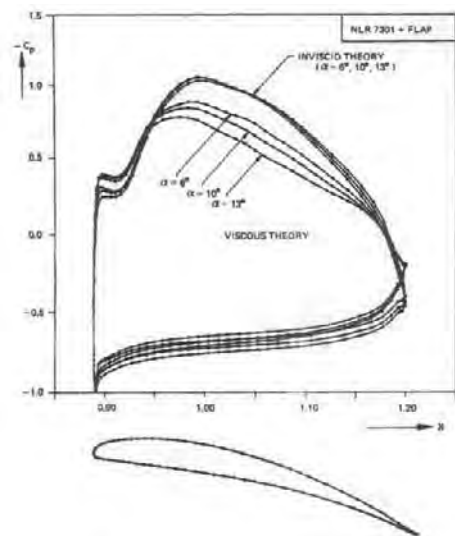
Figure 25.30 - Theoretical pressure distribution on the flap in inviscid and in viscous flow for α = 6, 10 and 13 deg. Source: AGARD CP–365, Paper No. 3.
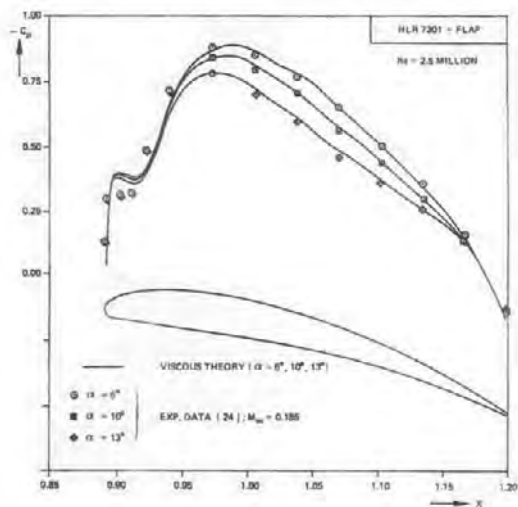
Figure 25.31 - Theoretical and experimental upper surface pressure distribution on the flap.
Source: AGARD CP–365, Paper No. 3.

A similar analysis was performed on the Fokker F-28 airfoil section with the flap set at δ_f = 42 deg. In figure 25.32 three lift curves are shown: the curve for inviscid flow, the theoretical curve for viscous flow and the curve based on wind tunnel test data. The difference between the latter two is caused by flow separation over the last 10 percent of the flap chord causing effectively a de-cambering effect on the flap.
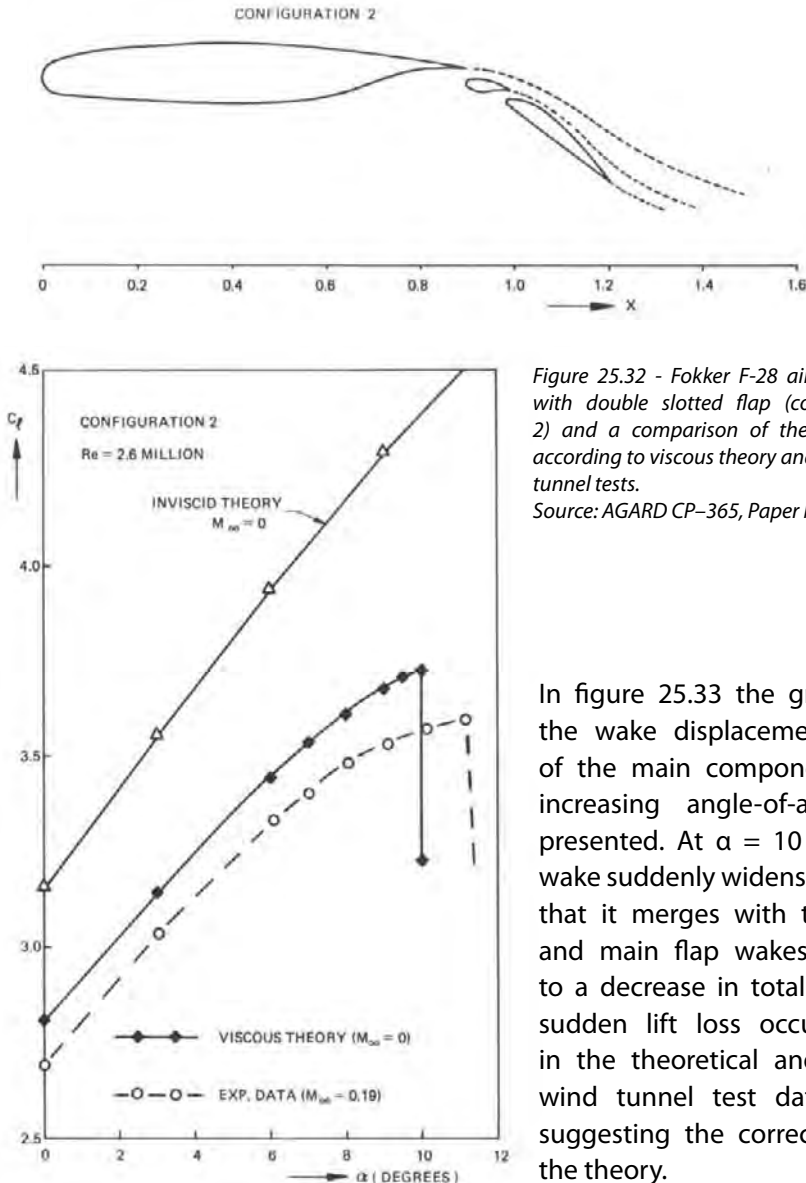
CONFIGURATION 2

Figure 25.32 - Fokker F-28 airfoil section with double slotted flap (configuration 2) and a comparison of the lift curves according to viscous theory and from wind tunnel tests.
Source: AGARD CP–365, Paper No. 3

In figure 25.33 the growth of the wake displacement body of the main component with increasing angle-of-attack is presented. At α = 10 deg the wake suddenly widens so much that it merges with the vane and main flap wakes leading to a decrease in total lift. This sudden lift loss occurs both in the theoretical and in the wind tunnel test data again suggesting the correctness of the theory.

CONFIGURATION 2
VISCOUS THEORY

ALPHA 10.00
REY 2600000.
ITERATION 15

ALPHA 9.50
REY 2600000.
ITERATION 9

ALPHA 6.00
REY 2600000.
ITERATION 8

ALPHA 0.00
REY 2600000.
ITERATION 8

—·— WAKE CENTERLINE

WAKE DISPLACEMENT THICKNESS

80   85   90   95   100   105   110   115   120   125

X (PERCENT CHORD)
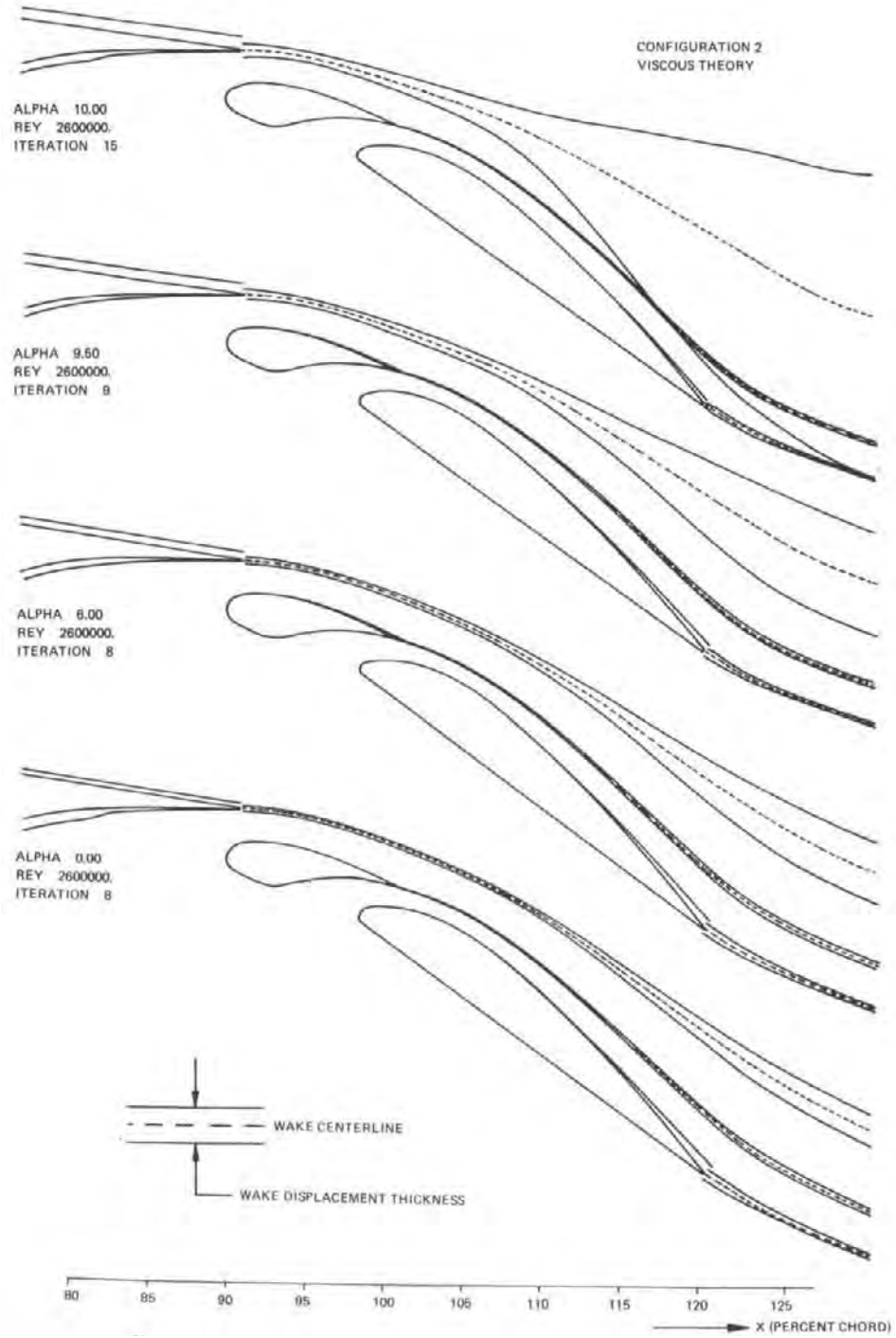
Figure 25.33 - Development of wake displacement bodies as a function of angle-of-attack for the F-28 airfoil section. Source: AGARD CP-365, Paper No. 3

Figure 25.34 shows a second airfoil section, NLR 7703 MOD, equipped with a slat and a double-slotted flap, a compound flap with equal-chord front and rear parts. This flap type allows the forward part, which is the most highly-loaded part of the flap, to be directly fitted to the flap support mechanism minimizing the flap load paths. The rear part may then be fitted to the front part with simple hinges.
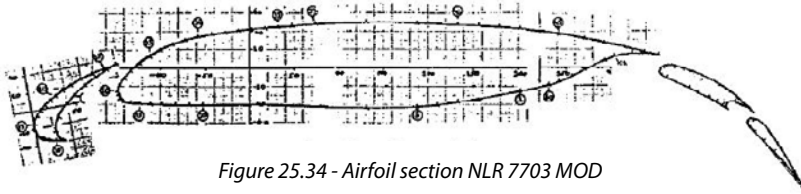
Figure 25.34 - Airfoil section NLR 7703 MOD
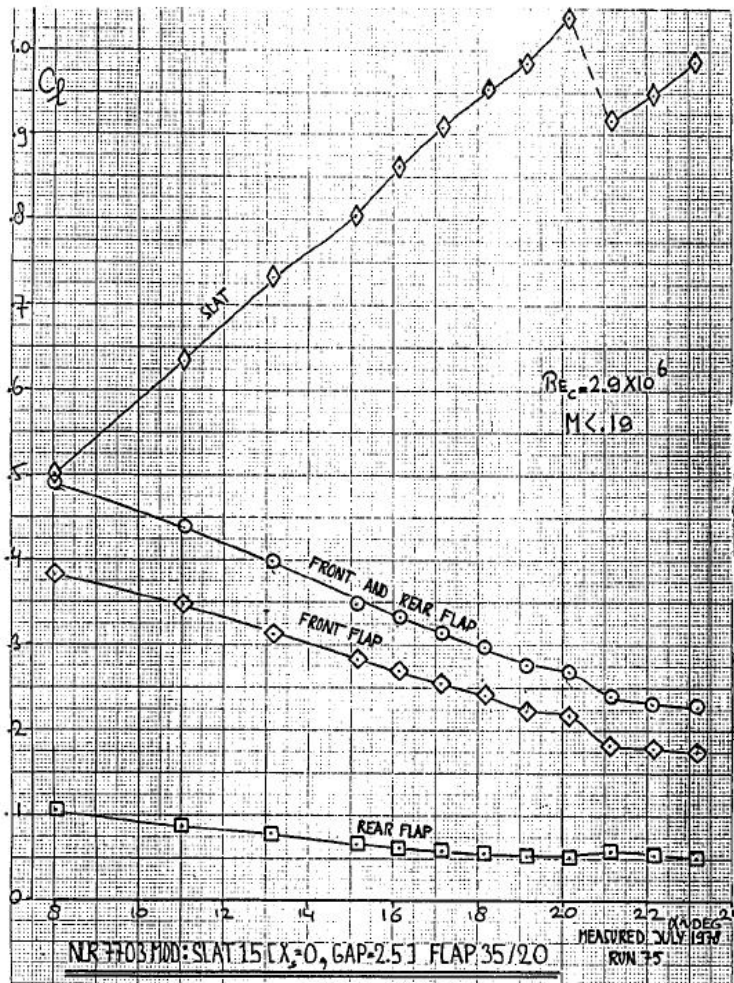
Figure 25.35 - Lift on slat and flaps for the NLR 7703 MOD airfoil section. Source: NLR TR 82044C

In figures 25.35 and 25.36 the lift on the slat, on the front and rear flap and on the main part is shown together with the total lift as a function of angle-of-attack for a slat setting $\delta_s = 15$ deg and a flap setting $\delta_f = 35 / 20$ deg. The flow over the main component becomes unsteady for this configuration above $\alpha = 13$ deg. which leads to an irregular shape of the upper part of the total-lift curve. However the change in lift with increasing angle-of-attack on the other components is regular up to the angle-of-attack for maximum lift, $\alpha = 20$ deg. Also on this configuration the lift on the flap decreases with increasing angle-of-attack under the influence of the wake from the main component.
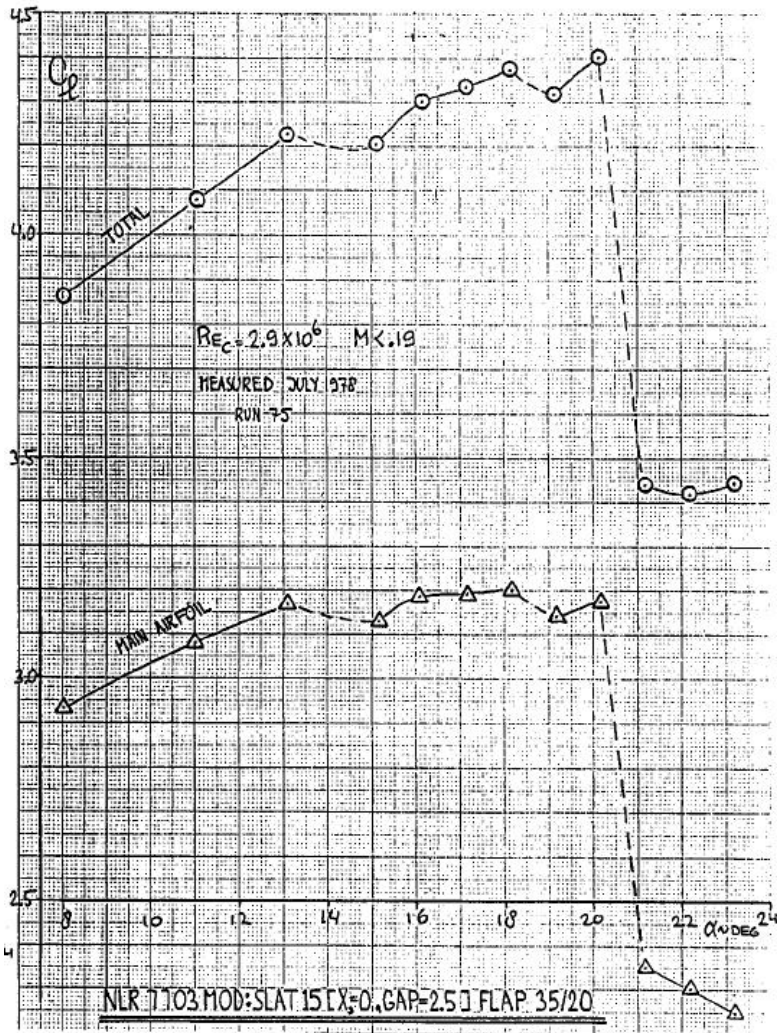
Figure 25.36 - Lift on main airfoil and total lift for the NLR 7703 MOD airfoil section. Source: NLR TR 82044C

Figure 25.37 and 25.38 show the pressure distributions on the complete airfoil section for slat angles $\delta_s = 15$ deg and $\delta_s = 30$ deg for two angles-of-attack just below and just above the occurrence of significant separation, in both cases near the main component trailing edge .
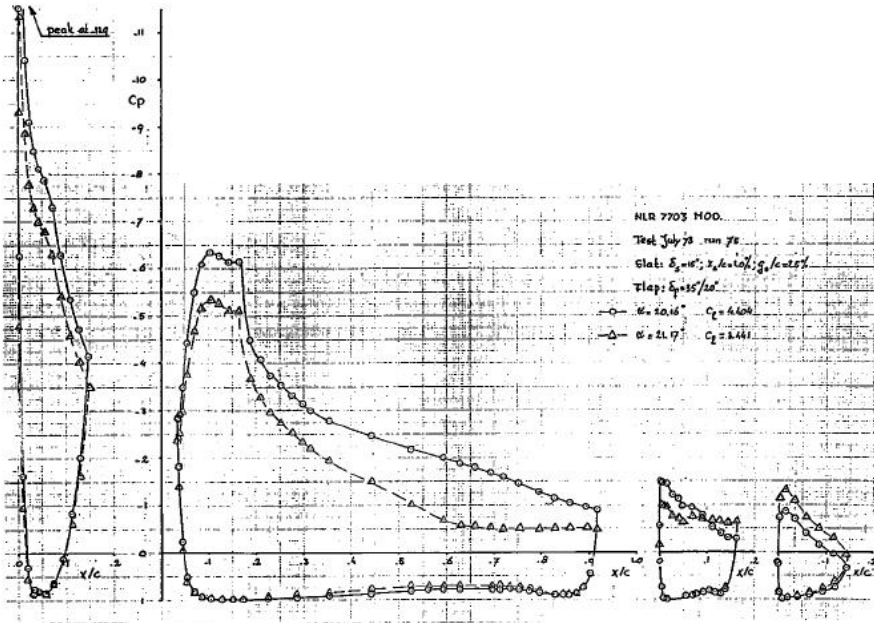
Figure 25.37 - Pressure distribution on the NLR 7703 MOD section at a slat angle $\delta_s = 15$ deg. Source: NLR TR 82050 C
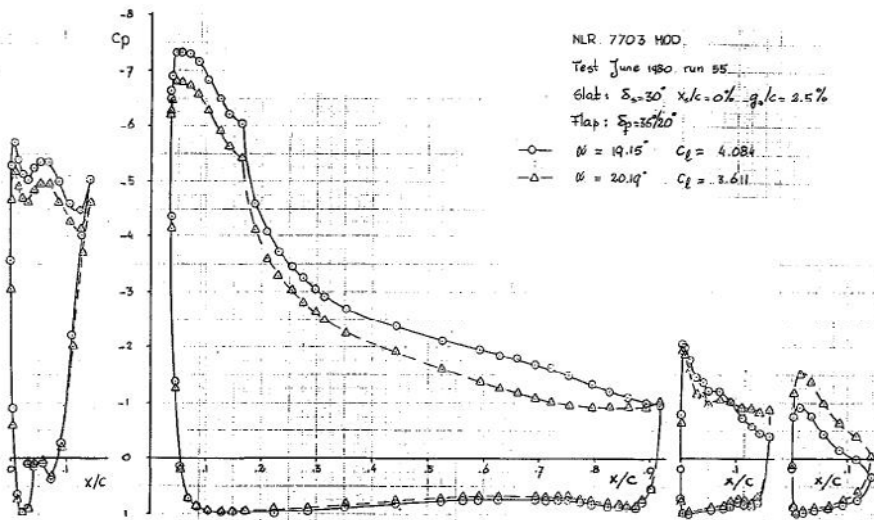
Figure 25.38 - Pressure distribution on the NLR 7703 MOD section at a slat angle $\delta_s = 30$ deg. Source: NLR TR 82050 C

For $\delta_s = 15$ deg the slat shows a high leading-edge suction peak and a high dumping velocity. When the slat angle is increased to $\delta_s = 30$ deg the lift on the slat is much lower than at $\delta_s = 15$ deg and even near maximum lift low maximum supervelocities occur. As a consequence the lower circulation and associated downwash of the slat suppresses the leading-edge suction peak on the main component to a lesser degree and flow separation near the trailing edge occurs earlier leading to a lower maximum lift coefficient than with a slat setting $\delta_s = 15$ deg. ($c_{l,max} = 4.08$ vs. 4.40).

Note that in both cases also the upper surface boundary layer on the front flap separates whereas the lift on the rear flap increases.

In figure 25.39 the lift curves near maximum lift are shown for the configurations with flap setting $\delta_f = 35 / 20$ deg and slat angles varying between $\delta_s = 5$ deg and $\delta_s = 35$ deg. The highest maximum lift is found with $\delta_s = 10$ deg but the differences in the range between $\delta_s = 5$ deg and $\delta_s = 25$ deg are small but not negligible. For slat angles $\delta_s = 30$ deg and higher the loss in maximum lift becomes appreciable and at $\delta_s = 35$ deg slat extension produces even a lift loss relative to the configuration without slat. ($c_{l_{max}} = 3.59$ vs. 3.67 see the table in figure 25.42.) In this case the slat shows a large wake over the complete angle-of-attack range partly flowing through the gap disturbing the flow over the main component. The slat functions more as a classical dive brake than as a high-lift device. At lower slat angles a dead water region will occur in the cove immediately above the slat hook on the lower surface facilitating the main flow to negotiate the sharp hook. This is illustrated in the upper part of figure 25.39.
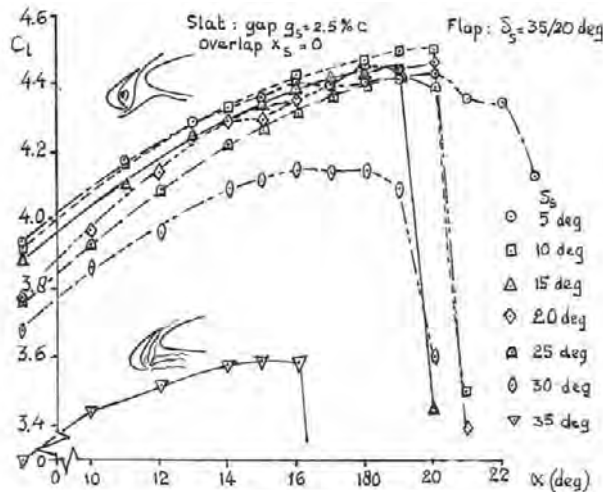
Figure 25.39 – Lift curves of airfoil section NLR 7703 MOD with flap setting $\delta_f = 35 / 20$ deg and slat angles varying between $\delta_s = 5$ deg and $\delta_s = 35$ deg.
Source: Fokker Rep. L-307-39 / NLR TR 82050C and Fokker Rep. L-307-98 / NLR TR 82050C
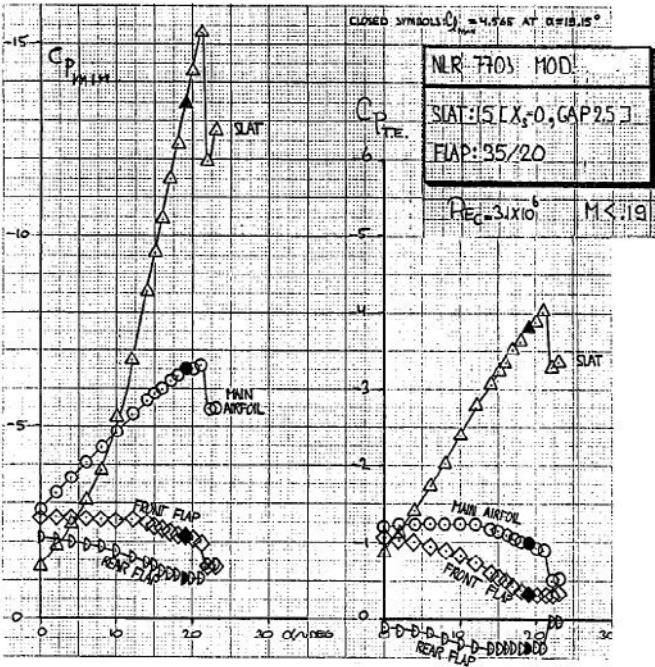
Figure 25.40 – Minimum and trailing-edge pressure coefficient versus angle-of attack for the NLR 7703 MOD section with a slat angle δ_s = 15 deg. Source: NLR TR 82050 C
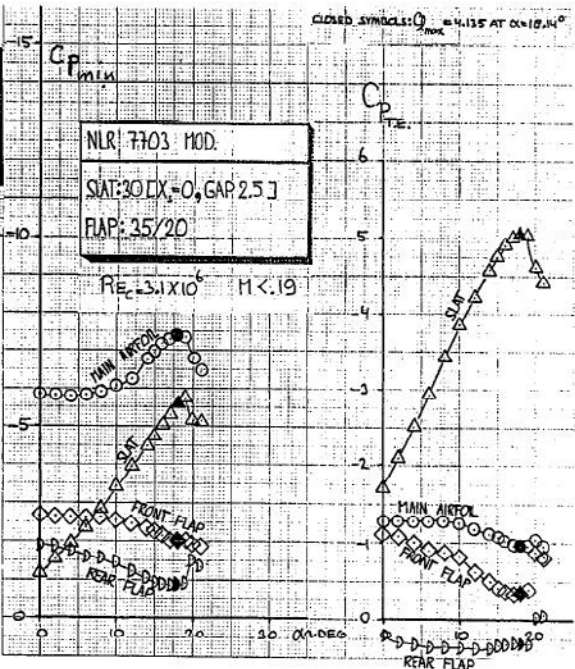
Figure 25.41 – Minimum and trailing-edge pressure coefficient versus angle-of-attack for the NLR 7703 MOD airfoil section with a slat angle δ_s = 30 deg. Source: NLR TR 82050 C

The data in figures 25.35 to 25.43 were obtained in two test series. Some configurations were tested twice and some, nominally identical, configurations showed small differences in gap or overlap. Both caused small variations in maximum lift coefficient in the various figures but these have no effect on the overall conclusions.

Figure 25.40 and 25.41 show a comparison between the development of the minimum pressure coefficient $c_{p,min}$ and the trailing-edge pressure coefficient $c_{p,te}$ with increasing angle-of-attack for the different components of the two configurations in figures 25.37 and 25.38.

NLR 7703 MOD run 56, 73, 63, 75, 54, 55 and 59. Slat: gap = 2.5, X_s = 0. Flap: 35/20

$Re_C \approx 3 \times 10^6$ M<1.9

Slat: IN	$C_{l,max}$	= 3.669 at α = 10.08°
Slat: 5	$C_{l,max}$	= 4.430 at α = 20.16°
Slat: 10	$C_{l,max}$	= 4.507 at α = 20.16°
Slat: 15	$C_{l,max}$	= 4.374 at α = 18.14°
Slat: 20	$C_{l,max}$	= 4.456 at α = 18.14°
Slat: 25	$C_{l,max}$	= 4.423 at α = 19.15°
Slat: 30	$C_{l,max}$	= 4.135 at α = 18.14°
Slat: 35	$C_{l,max}$	= 3.594 at α = 15.12°
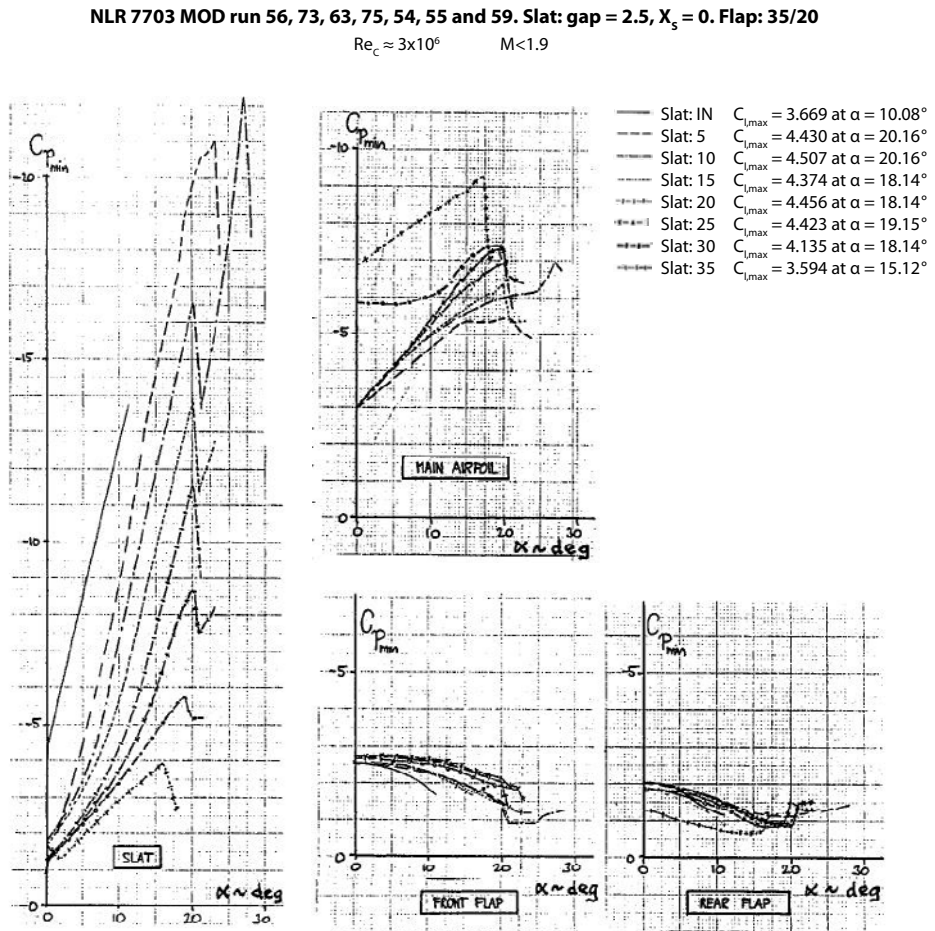
Figure 25.42 – Minimum and trailing–edge pressure coefficients versus angle-of-attack for the NLR 7703 MOD airfoil section at flap setting δ_f =35 / 20 deg and different slat deflections. Source: NLR TR 82050 C

NLR 7703 MOD run 01, 02, 03, 04, 40 and 63. Slat: 10 [$X_s = 0$, gap = 2.5]
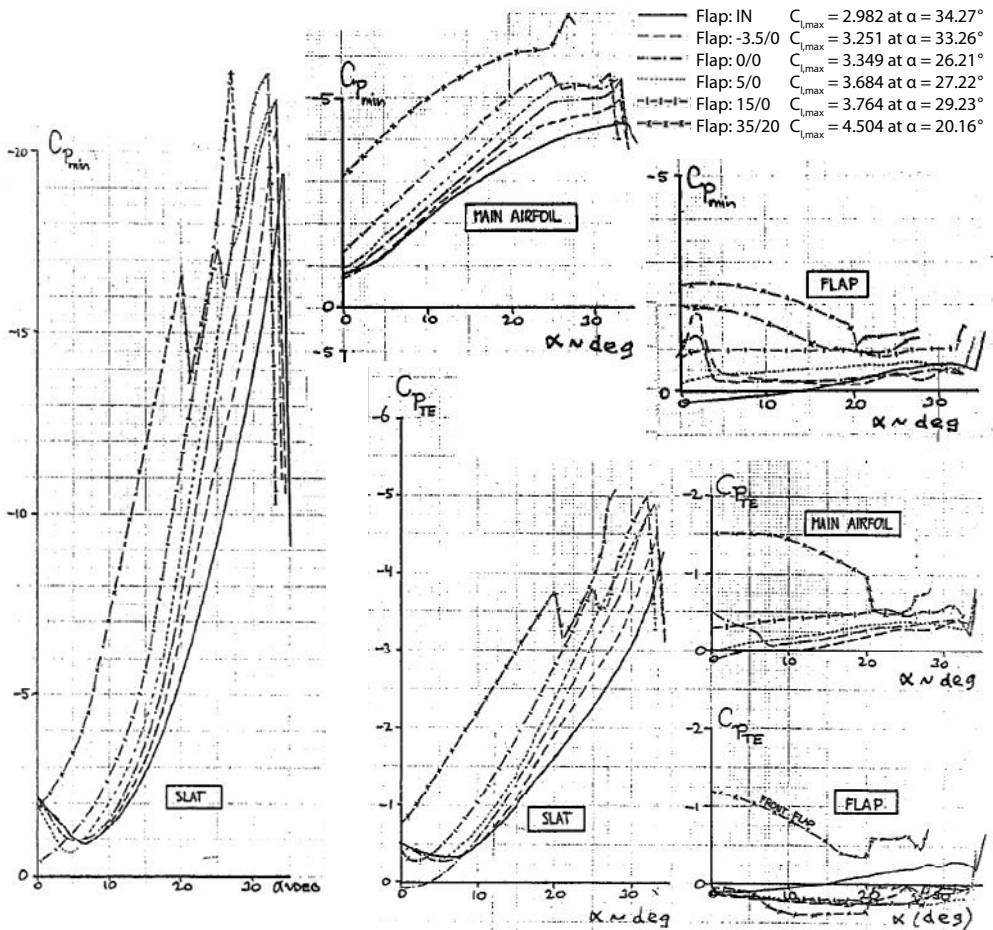
Figure 25.43 – Minimum and trailing-edge pressure coefficient versus angle-of-attack for the NLR 7703 MOD airfoil section at slat angle $\delta_s = 10$ deg and different flap deflections. Source: NLR TR 82050 C

In figure 25.42 the same data are presented for the configurations with flap setting $\delta_f = 35/20$ deg and slat angles from $\delta_s = 5$ deg to 35 deg. For $\delta_s = 5$ deg the maximum lift is reached at α = 20 deg (see figure 25.39) but at α = 20 deg the lift loss is still small compared to the configurations with larger slat angles. But the suction peak on the slat collapses suggesting that the stall is mainly determined by flow separation on the slat.

At larger slat angles a large lift loss occurs at α = 20 deg due to trailing-edge separation on the main component. However the flow over the slat remains attached and the lift on the slat increases with increasing angle of attack after an initial lift loss (and corresponding increase in $c_{p,min}$) due to the sudden decrease in upwash in front of the main component at α = 20 deg.

Figure 25.43 shows similar variations in the significant pressure coefficients when, with a slat angle $\delta_S = 10$ deg, the flap angle is progressively increased. With the flap retracted or set at a small angle the stall is determined by flow separation on the slat at a very high angle of attack. At higher flap settings the stall is determined by trailing-edge separation on the main component.

This investigation shows that to find the highest maximum lift the largest flap setting should be selected without or only limited flow separation on the flap at low angles-of-attack. The slat however should be set at such an angle that trailing-edge separation occurs near the trailing edge on the main component just prior to flow separation on the slat.

The effect of Mach number on the low-speed maximum lift coefficient.

In 1982 a wind tunnel test programme was performed by Fokker/NLR on a two-dimensional model, F-29 Model 12-1, equipped with high-lift devices to investigate the effect of the free-stream Mach number on the low-speed maximum lift coefficient at high Reynolds numbers.

The airfoil section is shown, both in the clean and in the high-lift configurations, in figure 25.44. In figure 25.45 and 25.46 the maximum lift coefficient and the minimum pressure coefficient at the leading-edge suction peak are presented for the different configurations as a function of Reynolds number at M = 0.19. Both parameters increase with increasing Reynolds numbers at this Mach number.
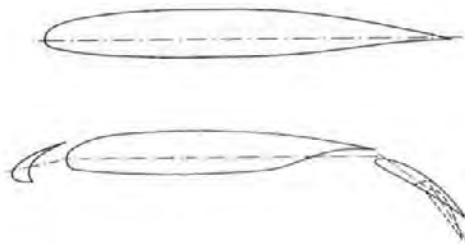
Figure 25.44 – Airfoil section on F-29 Model 12-1. Clean configuration and high-lift configuration. Source: Fokker Rep. L-29-196 / NLR TR 83059 C
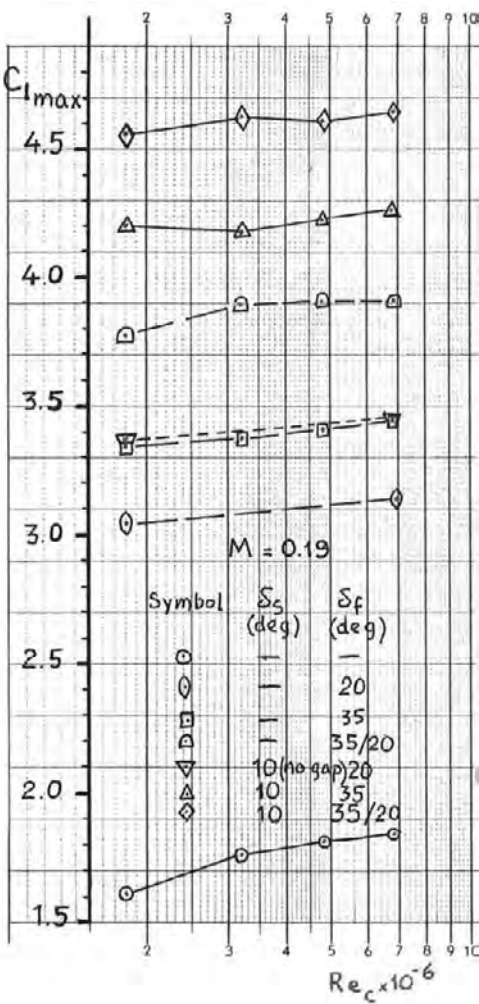
Figure 25.45 – The maximum lift coefficient as a function of Reynolds-number.
Source: Fokker Report L-29-196
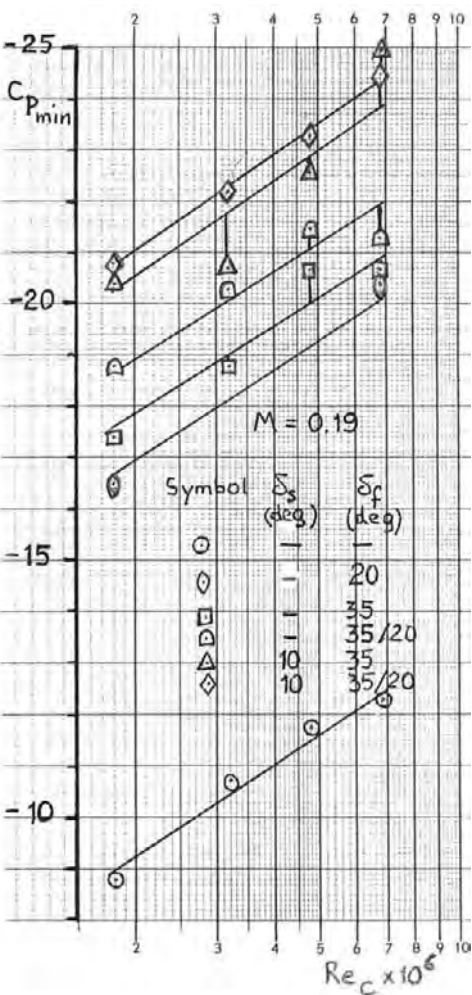
Figure 25.46 – Minimum suction pressure coefficient as a function of Reynolds number.
Source: Fokker Report L-29-196

If at a high Reynolds number the free-stream Mach number at low speed is increased the maximum lift coefficient hardly changes until a Mach number is reached after which the maximum lift coefficient decreases. This particular Mach number is the lower the more effective the high-lift devices are as is illustrated in figure 25.47.
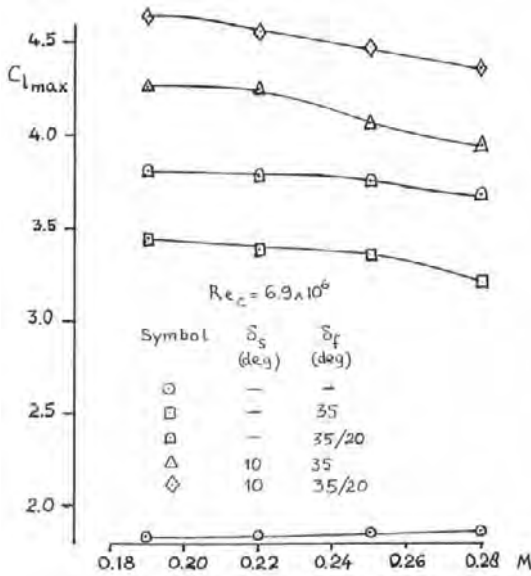
Figure 25.47 – The maximum lift coefficient as a function of Mach number at Re_c =6.9 x 10⁶. Source: Fokker Report L-29-196
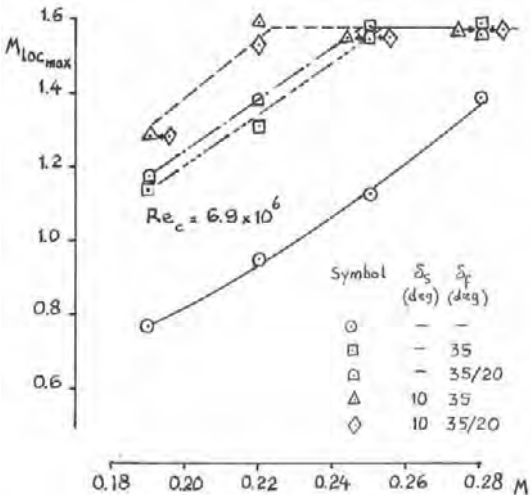
Figure 25.48 – The local peak Mach number at the maximum lift coefficient as a function of the free-stream Mach number at Re_c = 6.9 x 10⁶. Source: Fokker Report L-29-196

In the past this was thought to occur as soon as near the leading edge a local Mach number M_{loc} = 1.0 was reached as suggested in figure 19.12. However in the latter case the model had a transition strip near the leading edge which adversely affected the maximum lift coefficient. Figure 25.48 shows that the local Mach number may appreciably exceed M_{loc} = 1.0 but that the maximum Mach number reached is close to M_{loc} = 1.60 and does not surpass this value.

In figure 17.8 it is shown that for higher free-stream Mach numbers the minimum pressure coefficients that have been observed on airfoil sections in wind tunnel tests can be described with the equation:

$$M_\infty^2 c_p = -1.0$$

As $c_p = \dfrac{p - p_\infty}{\frac{1}{2}\gamma p_\infty M_\infty^2}$,

in perfect vacuum (p = 0)

$$c_p M_\infty^{\,2} = \frac{1}{\frac{1}{2}\gamma} = \frac{1}{0.7} = 1.43$$

Or, $M_\infty^2 c_p = -1.0$

is 0.7 vacuum

In figure 25.49 the minimum pressure coefficient at the leading-edge suction peak at the maximum lift coefficient at Re = 6.9 x 10^{6} is presented as a function of the free-stream Mach number for the different configurations investigated. The figure shows that the curve for $M_\infty^2 c_p = -1.0$ lies close to the curve for $M_{loc} = 1.58$.

In a theoretical treatise on transonic flow (Symposium Transsonicum 1964) E.V. Laitone stated that the maximum Mach number that may occur in transonic flow is

$$M = 4\sqrt{3 - \gamma}$$

or M = 1.581. The data in figure 25.49 agree with this theory.

From figures 25.48 and 25.49 it can be concluded that at high Reynolds numbers on modern airfoil sections with effective high-lift devices this limiting peak Mach number occurs at low free-stream Mach numbers which lie in the range of Mach numbers where on actual aircraft the maximum lift coefficient is determined. The maximum lift coefficient becomes then a function of aircraft weight and flight altitude. This is discussed in the next chapter.
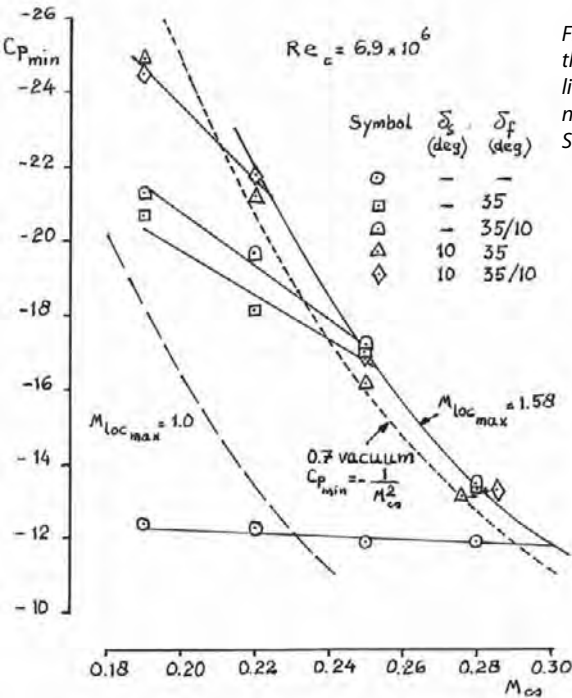
Figure 25.49 – Minimum pressure coefficient at the leading –edge suction peak at the maximum lift coefficient as a function of free-stream Mach number at $Re_c = 6.9x10^6$.
Source: Fokker Rep. L -29 -196 / NLR TR 83059 C

In the late 1960's and the 1970's many investigations were performed to improve the understanding of the functioning of high-lift devices, both on airfoil sections and on three-dimensional configurations. One important conclusion that was reached was that on swept wings, unless the sweep angle is extreme, the behaviour of the outboard wing largely agrees with the characteristics of the airfoil sections which determine the outer wing's shape if the basic swept wing relations are taken into account as was discovered before for clean wings. An illustration of these findings is presented here below.
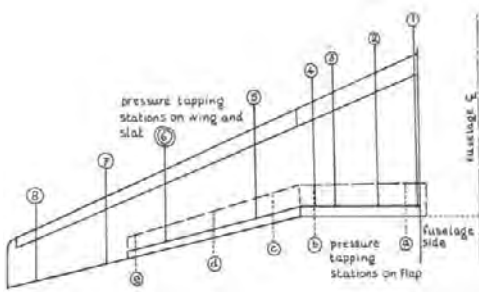
Figure 25.50 – Plan view F-29 Model 10-7. Source: Fokker Report L-29-202 / NLR TR 84010 C
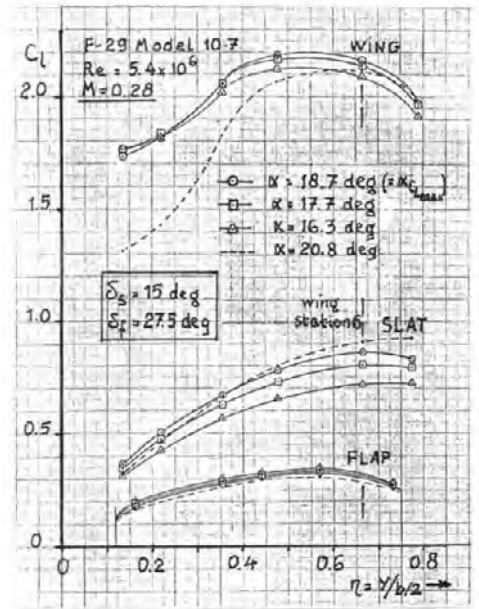
Figure 25.51 – The spanwise distribution of the local lift coefficient of slat, wing and flap at high angles-of-attack. F-29 Model 10-7. Fokker Report L-29-202

As a continuation of the analysis of sections with high-lift devices Fokker / NLR investigated a large half-model equipped with a slat and a flap and provided with pressure tappings at a number of slat, wing and flap stations as illustrated in figure 25.50. This model, F-29 Model 10-7 had an outer wing of which the upper surface strongly resembled the upper surface of the section of the two-dimensional airfoil model F-29 Model 12-1 if corrected for sweep effects.

The spanwise distribution of the local lift coefficient for each component at high angles-of-attack is presented in figure 25.51 for M = 0.28 and Re = 5.4x10^6. (The reference length with which the dimensionless coefficients were obtained was for each wing station the local chord of the clean wing).

This data was also available for lower Mach numbers and Reynolds numbers.

By adding the individual contributions of slat, wing and flap the total local lift coefficient at wing station 6 was obtained for M = 0.19 and M = 0.28 as shown in figure 25.52 With the relations from elementary swept-wing theory :

$$M_{2-D} = M_{3-D} \cos \Lambda_{1/4c}$$

$$\alpha_{2-D} = \alpha_{3-D} / \cos \Lambda_{1/4c}$$

$$c_{l_{2-D}} = c_{l_{3-D}} / \cos^2 \Lambda_{1/4c}$$

and by applying an elementary correction for the induced angle-of-attack the lift curves from figure 25.52 were converted to the equivalent two-dimensional lift curves . These are compared with estimated two-dimensional lift curves derived from an interpolation of the test data from F-29 Model 12-1 as presented in figure 25.53. **Note in particular the good agreement in the maximum lift coefficient.** The shift in the lift curve for M = 0.19 near α =16 deg is caused by flow separation on the inboard wing which affects the spanwise induced angle-of-attack distribution. But with increasing angle-of-attack the lift on the outboard wing keeps growing. The flow separation pattern is discussed more in detail in the next chapter.

Estimated two-dimensional lift curves from an interpolation of F-29 Model 12-1 data.

Local lift curves of wing station 6 on F-29 Model 10-7 converted to two-dimensional flow conditions
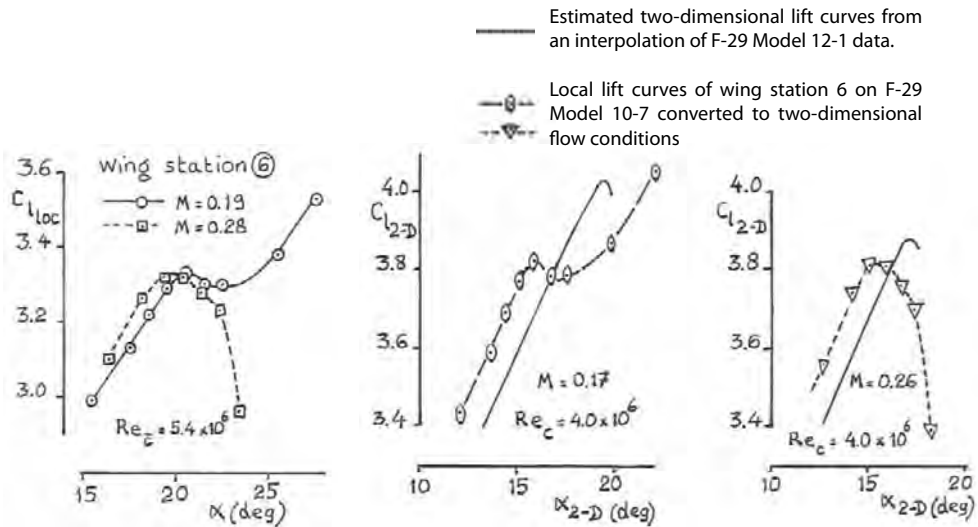
Figure 25.52 - Local lift curves at wing station 6

Figure 25-53 - Local lift curves at wing station 6 converted into two-dimensional lift curves and compared with data from F-29 Model 12-1

The detailed pressure measurements also allowed an analysis of the (negative) peak pressure coefficient at the slat leading-edge at wing station 6. Converting these local pressure coefficients into their equivalent values in two-dimensional flow and calculating the corresponding local Mach numbers with the equation (see chapter 10):

$$M_{loc} = \sqrt{5\left[\frac{1 + 0.2 M_\infty^2}{\left(c_{p\min} \times 0.7 + 1 \right)^{\frac{\gamma-1}{\gamma}}} - 1 \right]}$$

where $\qquad M_{2-D} = M_{3-D} \cos \Lambda_{LE}$

and $\qquad c_{p_{min,2-D}} = c_{p_{min,3-D}} / \cos^2 \Lambda_{LE}$

with Λ_{LE} = 24.4 deg

produced the figures 25.54 and 25.55. Comparing these two figures with figures 25.48 and 25.49 clearly illustrates that on moderately-swept wings with high-lift devices two-dimensional airfoil- section characteristics can be reproduced in the wing characteristics.
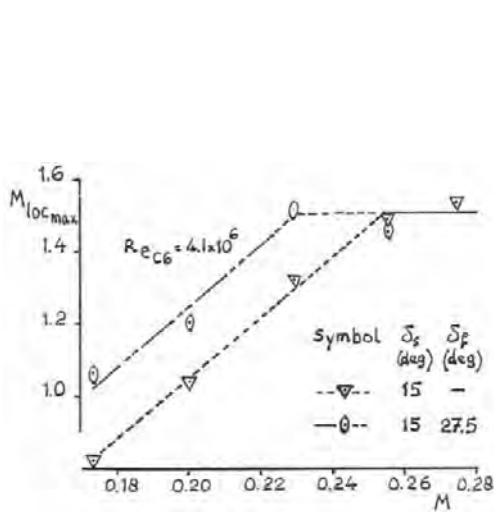
Figure 25.54 – Maximum local Mach number on the slat at wing station 6 as a function of free-stream Mach number
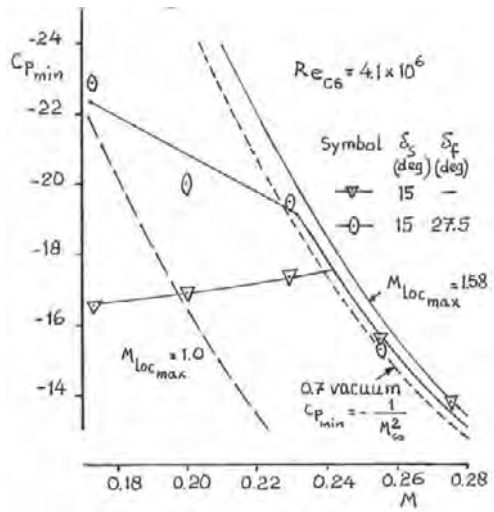
Figure 25.55 – $C_{p,min}$ on the slat vs. Mach number
Source: Fokker Rep. L-29-202 / NLR TR 84010 C

The maximum lift coefficient of a compound airfoil section is attained when the flow separates near the trailing edge of the main component, or when the wake bursts in a strong adverse pressure gradient or when the leading-edge suction peak collapses on the slat or the main component. Maximum lift occurring by the first two causes can today be predicted with reasonable accuracy by modern CFD methods. To determine maximum lift when a leading-edge suction peak collapses the present state-of-the-art does not yet allow reliance on a purely theoretical approach and some degree of empiricism is required.
Almost 200 model configurations of airfoil sections with flaps and slats on which maximum lift was signalled in wind tunnel tests by collapse of a leading-edge suction peak were analysed.
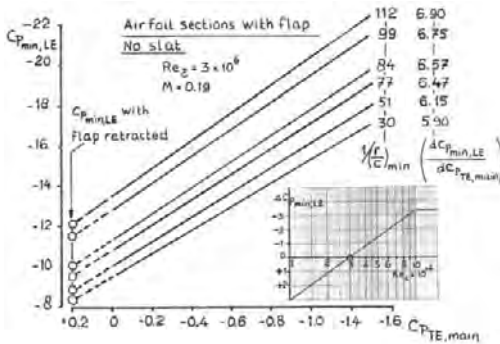
Figure 25.56 – Maximum peak suction coefficient vs. trailing-edge pressure coefficient on the main component. Source: Fokker Report A - 158
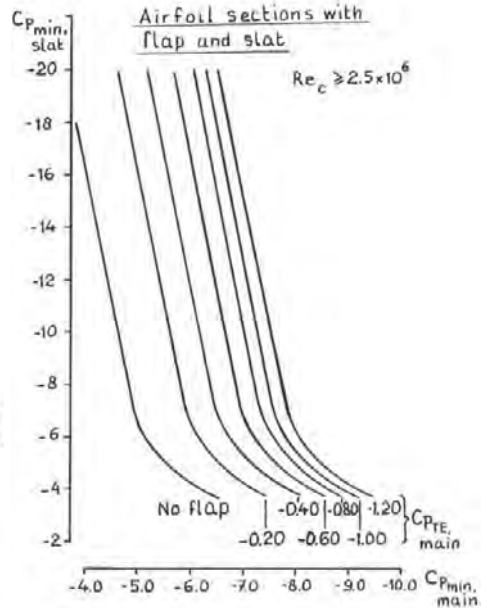
Figure 25.57 - Maximum slat peak suction coefficient vs. main component peak suction and trailing-edge pressure coefficient. Source: Fokker Report A - 158
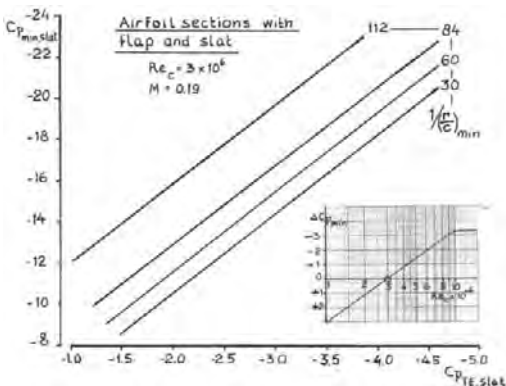
Figure 25.58 – Maximum peak suction coefficient vs. trailing-edge pressure coefficient on the slat. Source: Fokker Report A - 158
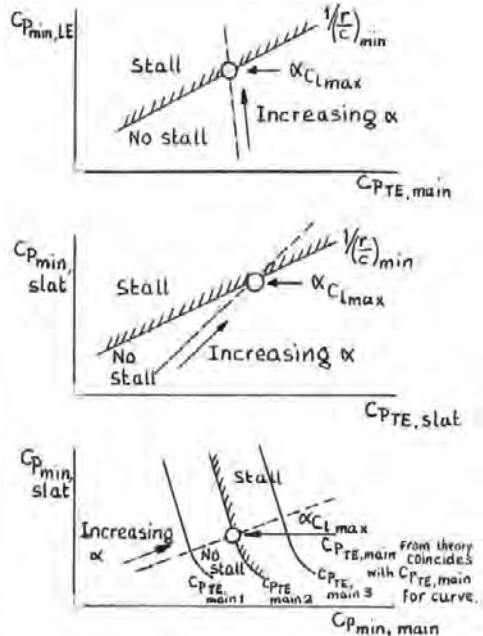
Figure 25.59 – Procedure to determine the maximum lift coefficient due to collapse of the leading-edge suction peak. Source: Fokker Report A - 158

313

Based on these data relations were produced between the minimum pressure coefficient at the leading edge of the slat or the main component, the trailing-edge pressure coefficient and the leading edge radius. These relations are presented in figures 25.56 to 25.58.

Figure 25.60 - Airfoil section NLR 7301 with slat and double slotted flap
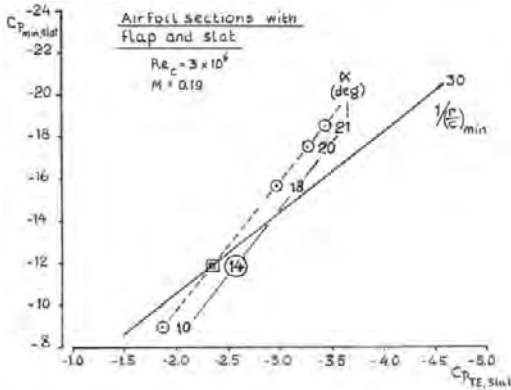
Figure 25.61 - Determination of flow break-down on the slat. Source: Fokker Report A-158
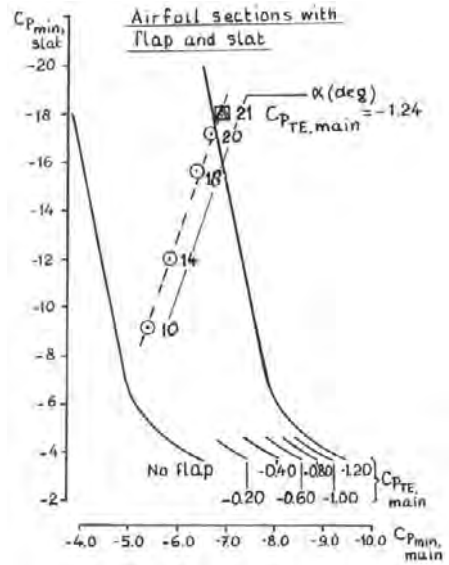
Figure 25.62 - Determination of flow breakdown on main component. Source: Fokker Report A - 158

Figure 25.63 - Estimation of maximum lift coefficient on section NLR 7301 with slat and double-slotted flap. Source: Fokker Report A-158

If with a modern CFD method which includes viscosity the pressure distribution on an airfoil section is calculated at successive angles-of-attack the data in figures 25.56 to 25.58 allow an estimate of the maximum lift coefficient according to the procedure indicated in figure 25 58. Mach number effects can be deduced from figures 25.48, 25.49, 25.54 and 25.55.

An example of this procedure is presented in figures 25.60 to 25.63. note that each form of flow separation has to be checked and the first limit reached determines the maximum lift.

26 The maximum lift coefficient and the stalling characteristics of full-scale aircraft

The maximum lift coefficient

To determine the maximum lift coefficient of a full-scale aircraft, three different definitions of $C_{L_{max}}$ are used:

1. The maximum lift coefficient of the aircraft in steady, rectilinear flight:

$$C_{L_{max_{1-G}}} = \frac{nW}{\frac{1}{2}\rho V^2 S_W} \tag{26.1}$$

This value will vary slightly over the centre-of-gravity range considered because of the varying tail load required for trim. This value is the true maximum lift coefficient in the physical sense and determines the minimum steady flight speed at a given aircraft weight. Usually $C_{L_{max_{1-g}}}$ is considered at zero thrust ($T_C = 0$).

$C_{L_{max_{1-g}}}$ may either be determined in full-stall tests or fixed by an angle-of-attack limiter. The more elementary angle-of-attack limiter is the stick pusher used in earlier generations of transport aircraft. Modern aircraft with fly-by-wire control systems just keep the aircraft flying at the maximum safe angle-of-attack also when the pilot tries to reach a higher angle-of- attack.

2. The maximum lift coefficient of the aircraft without tailplane in steady flight, $C_{L_{max_{T-O}}}$ (where T-O stands for tail-off). This condition can not be determined directly from flight tests but must be determined from $C_{L_{max_{1-g}}}$ by subtracting the tail contribution.
This $C_{L_{max_{T-O}}}$ -value is significant for judging the value of low-Reynolds-number windtunnel tests and associated estimation and extrapolation methods for pre-flight-test estimates of $C_{L_{max_{1-g}}}$.

3. The maximum lift coefficient based on the minimum speed measured in a stall manoeuvre precisely prescribed in previous editions of the airworthiness requirements FAR 25 and JAR 25.

$$C_{L_{max_{V_{min}}}} = \frac{W}{\frac{1}{2}\rho V^2 S_W} \tag{26.2}$$

(Note that at V_{min} n < 1 is not taken into consideration.)

Furthermore JAR 25 stated explicitly and the FAA (FAR 25) tended to adopt it as a policy, that:

$$C_{L_{max_{V_{min}}}} < (1.06)^2 \ C_{L_{max_{1-g}}}$$

For certification purposes both values should be determined from test data obtained at the most forward C.G. position, which is the least favourable C.G. position.

An example of the time-history obtained from a certification stall manoeuvre for a Boeing 747 is shown in figure 26.1. The different definitions of $C_{L_{max}}$ lead to different moments of stall at different airspeeds and different lift coefficient values.

In 2002 the FAA and the newly established European Aviation Safety Agency, EASA, harmonised the rules for establishing stall speeds for large transport aircraft. Both agencies now use the term Reference Stall Speed V_{SR} which is based on $C_{L_{max_{1-g}}}$:

The same kind of data for the determination of the maximum lift coefficient as shown for the Boeing 747 in figure 26.1 is presented in figure 26.2 for the Fokker F-28.

Figure 26.1 - Flight record of a stall manoeuvre of a Boeing 747
Source: AGARD CP-102, Paper No. 21
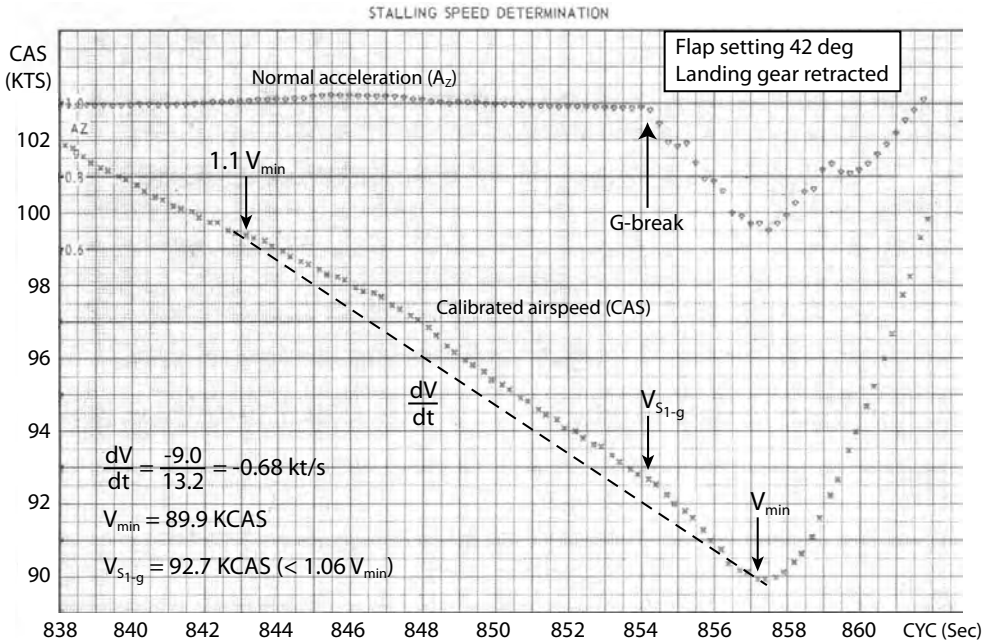
Figure 26.2 - Stall speed determination of a Fokker F-28 Mk 4000.
Source: Fokker Report H-28.40-27.001

$C_{L_{max}}$ is reached because at some part on the wing upper surface the flow in the boundary layer can no longer negotiate the large adverse pressure gradients and separates. This results in a change in the distribution of forces over the wing and a consequent change in downwash characteristics. As a consequence, the aircraft develops apart from the lift loss a tendency towards abrupt attitude changes.

In-flight determination of $C_{L_{max}}$ is difficult because of the abruptness of the motion. To determine $C_{L_{max}}$ as accurately as possible, the stall should be approached in a steady motion. To do so, the speed decay (dV/dt) should be low, to obtain a steady manoeuvre. Certification regulations restrict this to dV/dt = -1kt/s between 1.10 V_{min} and V_{min}.

In figure 26.3 the maximum lift coefficient is presented versus the deceleration (dV/dt) and the figure shows that with increasing decelerations $C_{L_{max_{Vmin}}}$ increases whereas $C_{L_{max_{1-g}}}$ remains constant.
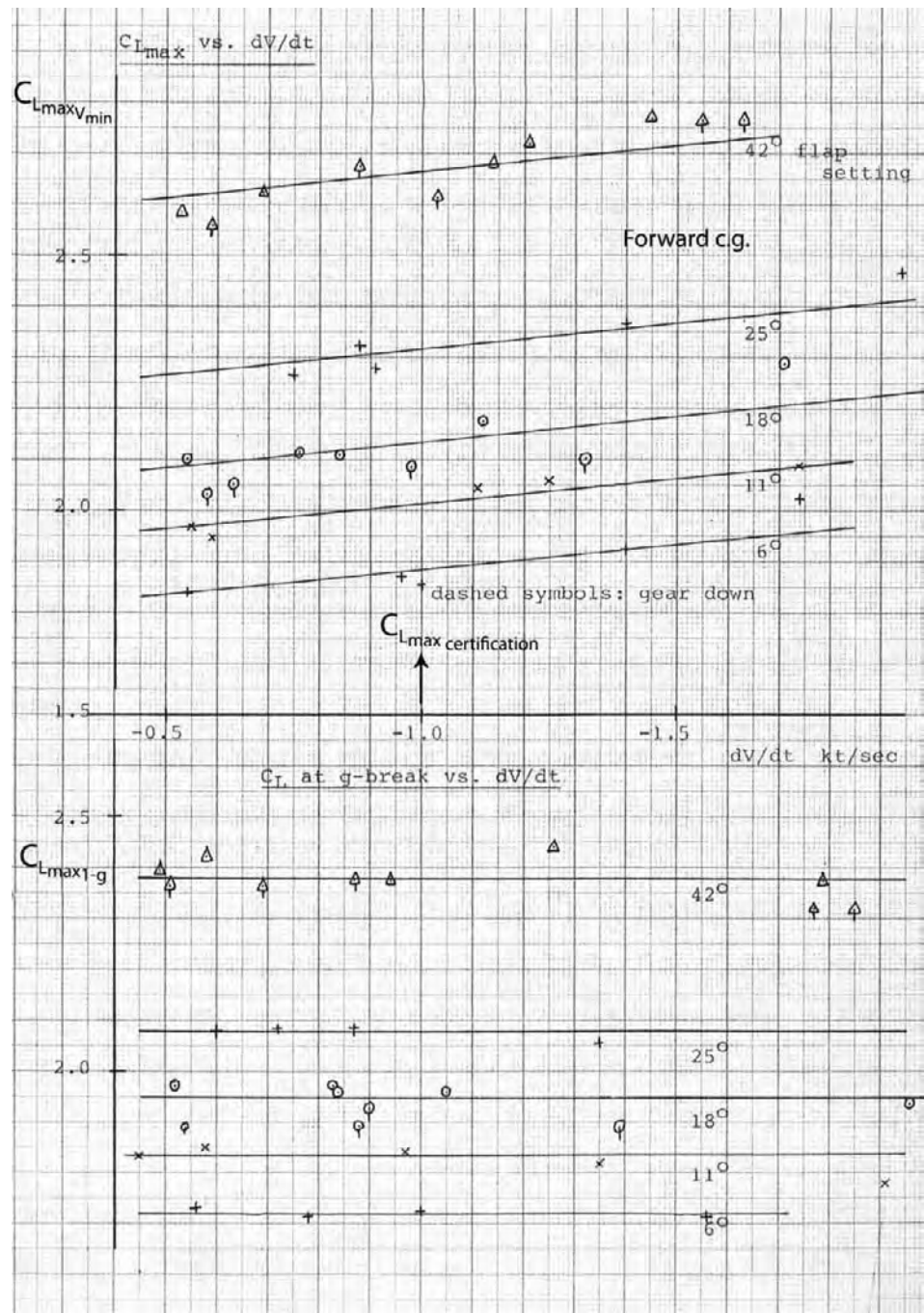
Figure 26.3 - Certificated $C_{L_{max}}$ values of the F-28 Mk 4000.
Source: Fokker Report H-28.40-27.001
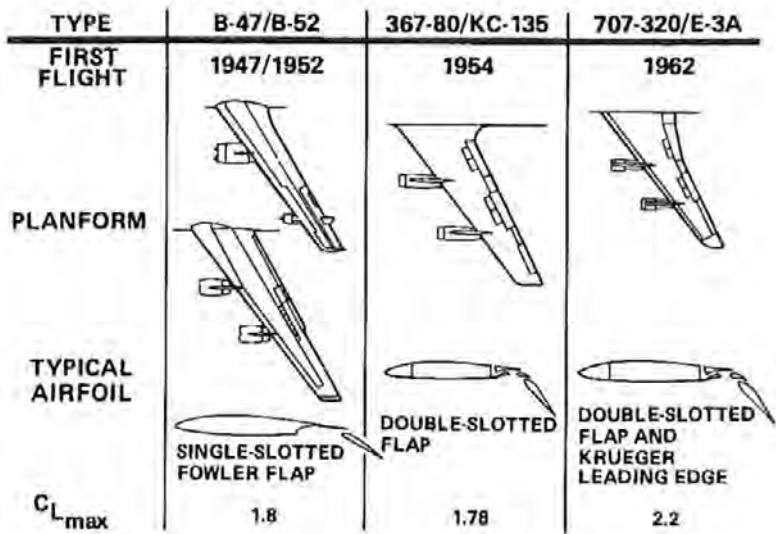
Figure 26.4 - Trends in Boeing transport high-lift development.
Source: AGARD CP-365, paper no. 9

Figures 26.4 and 26.5 show how high-lift devices were developed and used by Boeing over the past decades. It shows an initial increase in maximum lift coefficient with increasing number and complexity of high-lift system components. On later models however $C_{L_{max}}$ has stabilised as indicated for the Boeing 747 and 767. Today the emphasis is on minimising system complexity and maintenance costs.
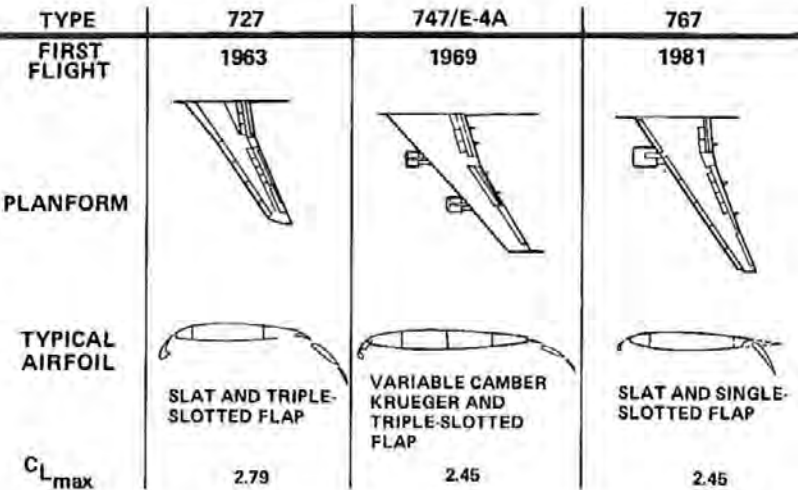
Figure 26.5 - Trends in Boeing transport high-lift development - continued
Source: AGARD CP-365, paper no. 9

Figure 26.6 shows another example of the various definitions of the maximum lift coefficient. Also, it shows the difference between estimated and measured values. These differences illustrate that predicting the maximum lift coefficient accurately is still a challenge notwithstanding the developments in CFD and wind tunnel test techniques. Accuracy is affected by complicated flow separation patterns in viscous flow, Reynolds number effects on full-scale aircraft, details in the flap and slat suspension mechanisms and the flight handling characteristics of the full-scale aircraft in the stall. To obtain a Certificate of Airworthiness each new type of transport aircraft is required to perform an extensive flight test program to determine the stall speeds and the stall characteristics for each aircraft configuration. The difference between tests results and design values may be as high as $\Delta C_{L_{max}} = 0.1$, also illustrated in figure 26.6.

Figure 26.7 shows all high-lift devices installed on the Airbus A300 to achieve the lift characteristics as presented in figure 26.6.

Vorflügel =
  Slats
Schwerpunktslage =
  c.g. position
Klappenausschlag =
  Flap deflection
Eingefahren =
  Retracted
Ausgefahren =
  Deployed

- - - Design $C_{L_{max_{1-g}}}$
——— $(1.06)^2$ $C_{L_{max_{1-g}}}$, estimate based on windtunnel tests
— · — $(1.06)^2$ $C_{L_{max_{1-g}}}$, as obtained from flight test data
— · · — $C_{L_{max_{V_{min}}}}$, as obtained from flight test data
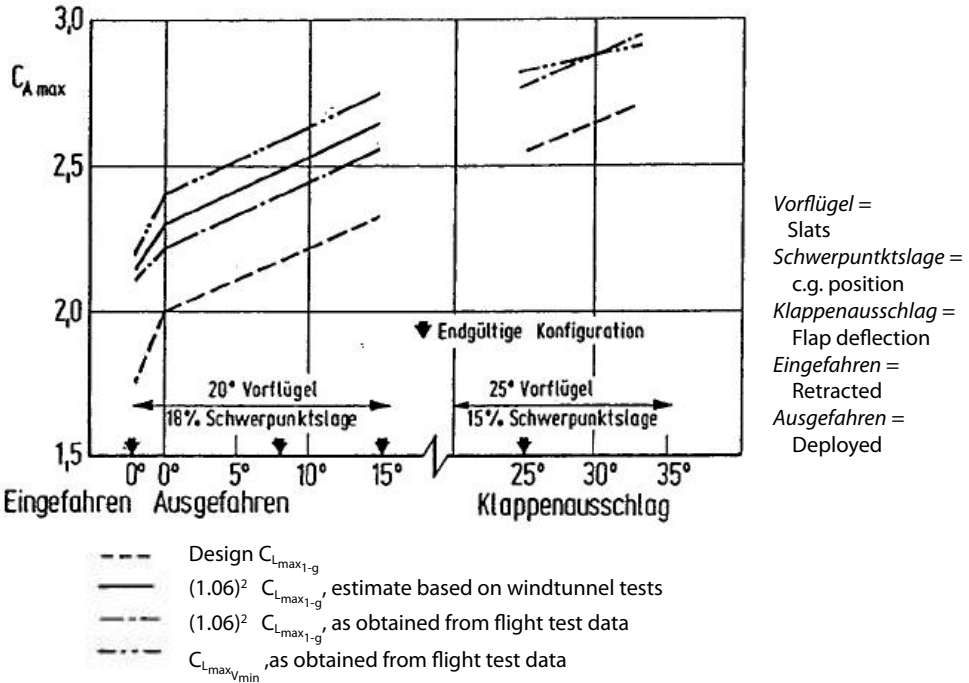
Figure 26.6 - The maximum lift coefficient of the Airbus A300-B
Source: Jahrbuch 1973 der DGLR

Vorflügelspalt-
abdeckklappe =
    Slat gap cover plate
Allgeschwindig-
keitsquerruder =
    All-speed aileron
Grenzschichtzaun =
    Boundary-layer fence
Hochauftriebshilfen =
    High-lift devices
Luftbremsen =
    Airbrakes
Querruder =
    Aileron
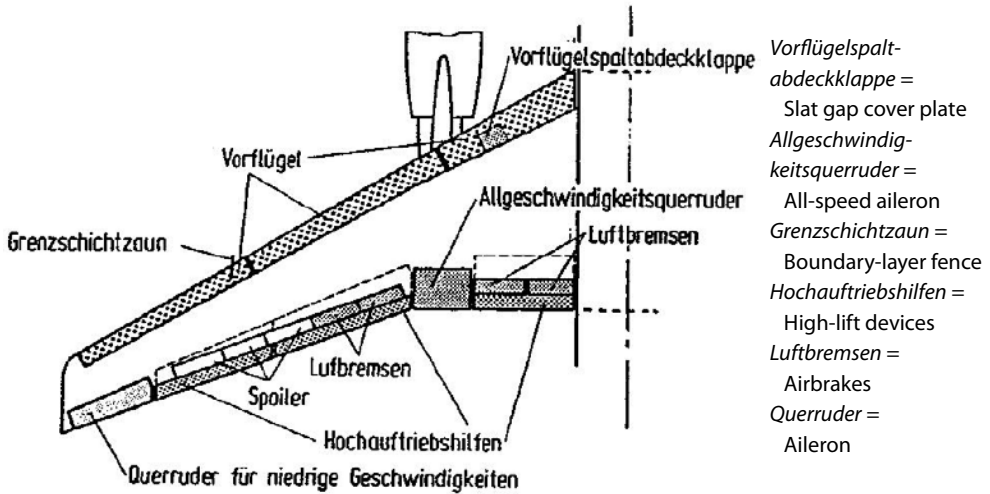
Figure 26.7 - Wing of the Airbus A300. Source: Jahrbuch 1973 der DGLR

In figure 26.8 an overview is given of $C_{L_{max}}$ based on V_{min} for all civil jet transport aircraft the Hawker-Siddeley company in the UK has been involved in. In figure 26.10 a turboprop aircraft has been added.

first flight	aircraft	configuration	wing sweep	M_{mo}	leading-edge device	trailing-edge device	landing $C_{L_{max}}$
1962	T.1	trijet; rear engines	35°	0.87	droop	double slotted	1.95
1962	125	twin; rear engines	20°	0.73	none	double slotted	2.16
1964	T1E	trijet; rear engines	35°	0.87	slat	double slotted	2.05
1967	T2E	trijet; rear engines	35°	0.87	slat	double slotted	2.04
1969	T3	trijet and booster rear engines	35°	0.87	slat	double slotted	2.11
1971	126-600	twin; rear engines;	20°	0.78	none	double slotted	2.05
1972	A300-B2	twin; underwing engines	28°	0.84	slat	tabbed Fowler	2.83
1974	A300-B4	twin; underwing engines	28°	0.82	slat plus Kruger	tabbed Fowler	2.80
1981	146-100	underwing, four engines	15°	0.7	none	tabbed Fowler	3.45
1982	A310-200	twin; underwing engines	28°	0.84	slat	single slotted	3.10
1982	146-200	underwing; four engines	15°	0.7	none	tabbed Fowler	3.45
1983	A300-600	twin; underwing engines	28°	0.84	slat	single slotted	3.00
1983	125-800	twin; rear engine	20°	0.80	none	double slotted	1.87
1985	310-360	twin; underwing engine	28°	0.84	slat	single slotted	3.01

Figure 26.8 - Comparison of $C_{L_{max}}$ based on V_{min} for various aircraft.
Source: Proc. R. Soc. Lond. A 416, 43-62 (1988)

Figure 26.9 presents the maximum lift coefficient for two medium-speed turboprop transport aircraft developed by De Havilland Canada.

Medium-speed aircraft with straight or moderately-swept wings and thick leading edges may, even without leading-edge devices, reach maximum lift coefficients of around $C_{L_{max_{1-g}}} = 3.0$ as exemplified by the DeHavilland DHC-7 and DHC-8 and the Hawker-Siddeley HS-146.
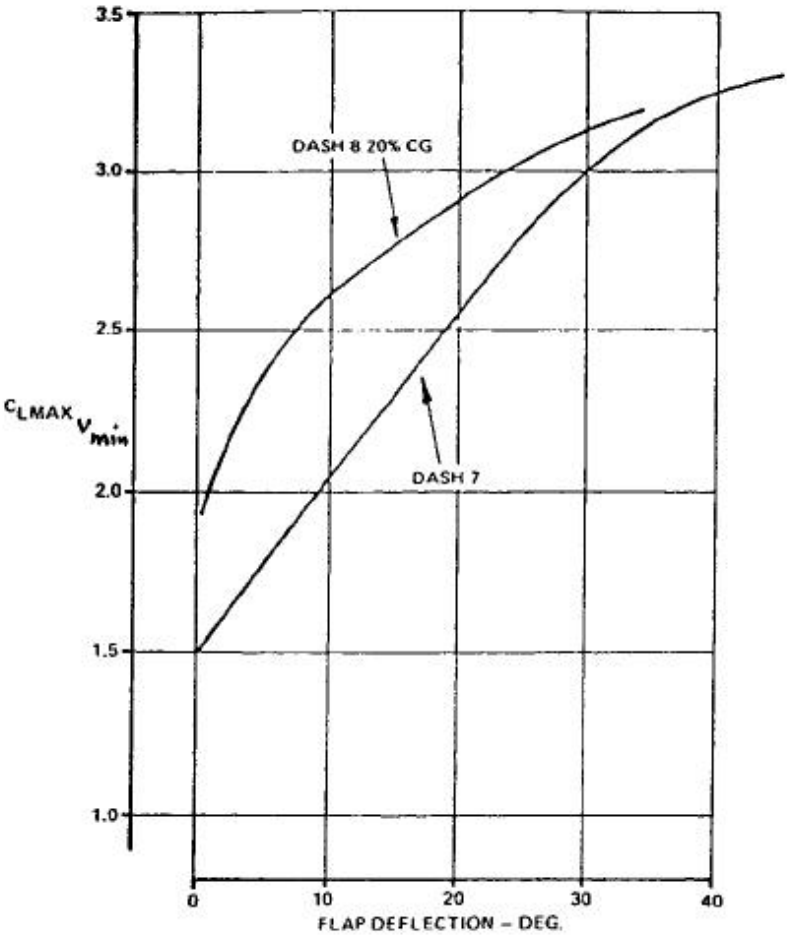
Figure 26.9 - De Havilland Canada DHC-7 (Dash 7) and DHC-8 (Dash 8) $C_{L_{max}}$ comparison. Source: Canadian Aeronautics and Space Journal, September 1984
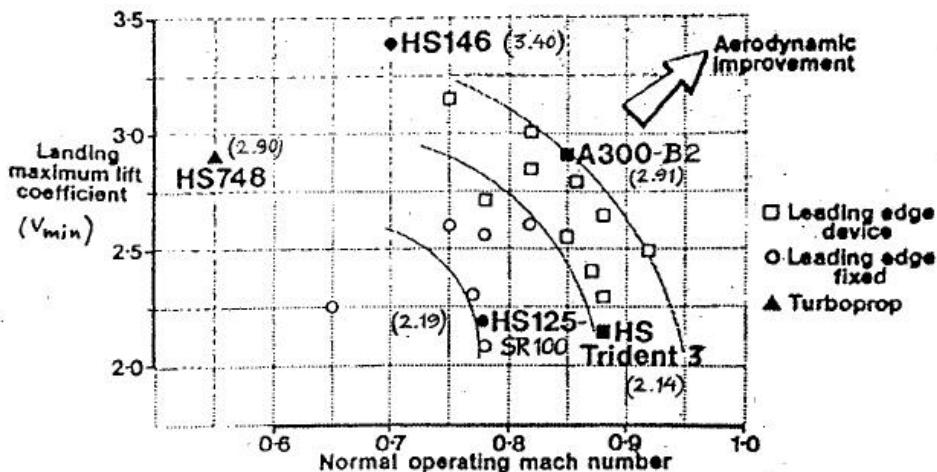
Figure 26.10 - Aircraft performance comparison. Source: Aerospace Journal (RAeS) June/July 198?.

Figure 26.11 shows the leading-edge shapes of three Boeing transport aircraft, the 737-300, the 757 and the 767.

In combination with the increase in wing sweep angle ($\Lambda_{1/4c}$ = 25° on the B737 and B757 and $\Lambda_{1/4c}$ = 31.5° on the B767) the thinner leading edges lead to the $C_{L_{max_{1-g}}}$ for landing decreasing from $C_{L_{max_{1-g}}}$ = 3.0 via 2.60 to 2.15, although the simplification in the flap configuration also has played its role (see figure 26.12).

For the latest generation of large transport aircraft, represented by the Boeing 737-800 and 777-200 and the Airbus A320-200 and A330-200, $C_{L_{max_{1-g}}}$ is shown as a function of flap setting in figures 26.12 to 26.16. $C_{L_{max_{1-g}}}$ = 2.5 to 2.6 for the landing configuration apparently suffices to comply with the performance design requirements.

Note again that the various manufacturers use different definitions for reference wing area and aspect ratio.
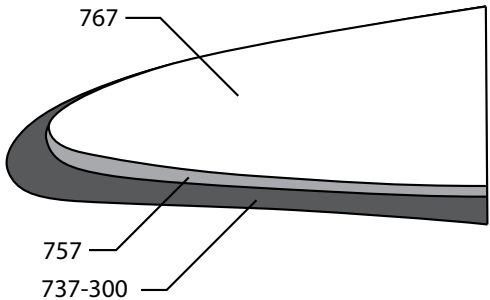
Figure 26.11 - Outboard wing LE of Boeing airliners
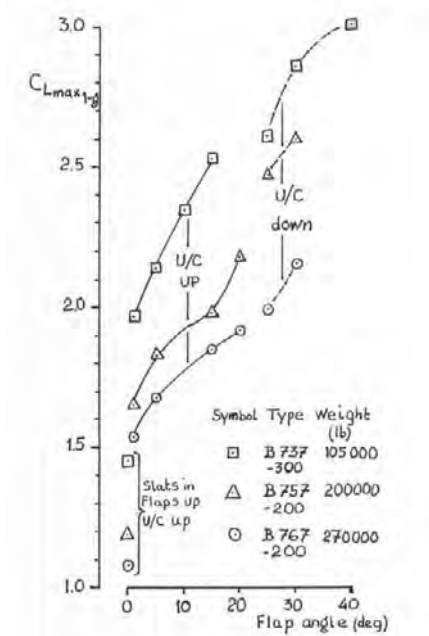
Figure 26.12 - $C_{L_{max_{1-g}}}$ for the Boeing 737-700, 757-200 and 767-200
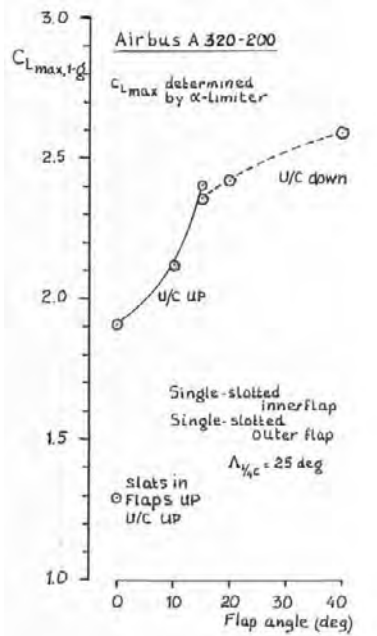
Figure 26.13 - $C_{L_{max_{1-g}}}$ for the Airbus A320-200
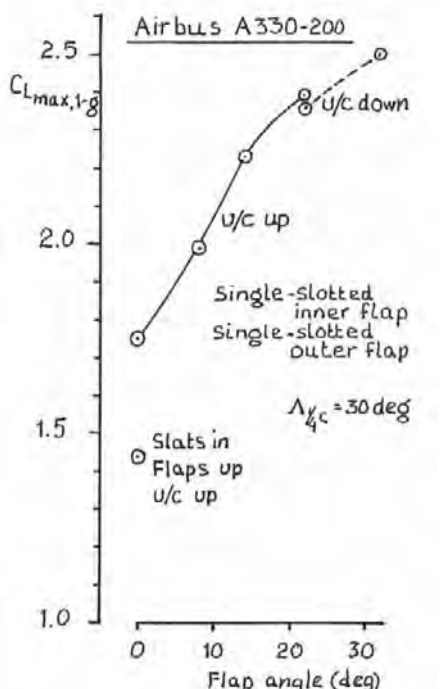
Figure 26.14 - $C_{L_{max_{1-g}}}$ for the Airbus A330-200
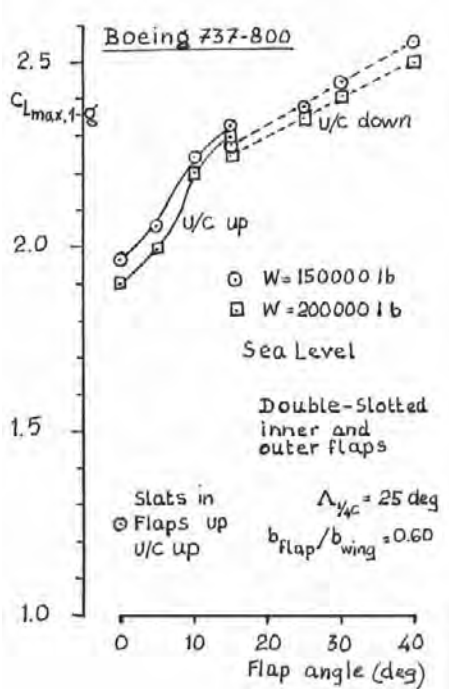
Figure 26.15 - $C_{L_{max_{1-g}}}$ for the Boeing 737-800
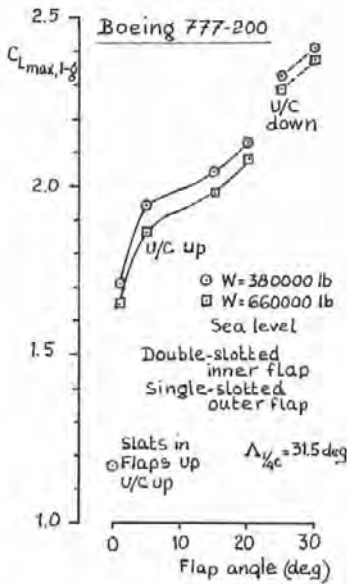
Figure 26.16 - $C_{L_{max_{1-g}}}$ for the Boeing 777-200
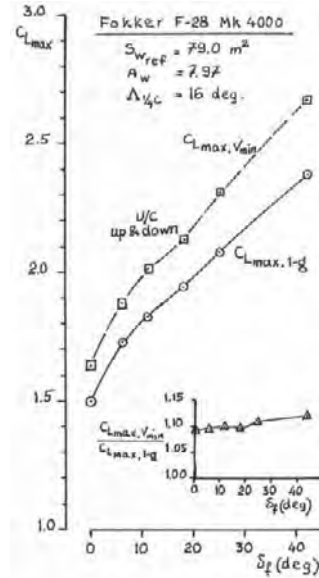
Figure 26.17 - $C_{L_{max}}$ for the Fokker F-28 Mk 4000. Source: Fokker Report H-28.40-27.001

Maximum lift data for the Fokker F-28 and Fokker 100 are presented in figures 26.17 to 26.20.

The F-28 Mk 4000 did not require a stick pusher and consequently a $C_{L_{max_{V_{min}}}}$ higher than $C_{L_{max_{1-g}}}$ could be certified which was advantageous as the alternative definitions of V_2 (=1.13 V_s) and V_{appr} (= 1.23 Vs) were not in use yet.

The F-28 Mk 6000 was provided with a stick pusher and the maximum lift coefficient for performance certification was determined by the stick pusher setting as indicated in figure 26.19. In careful flight tests $C_{L_{max_{1-g}}}$ was determined. Note that $C_{L_{max_{1-g}}} = 3.18$ is the highest $C_{L_{max_{1-g}}}$ ever certified for any civil jet transport aircraft. Unfortunately the associated high induced drag during take-off and landing, combined with the limited engine development, did not turn this F-28 version into a commercial success. Comparing the flight test data in figure 26.18, which presents lift curves corrected for stabiliser setting and elevator deflection, with figure 26.19 shows that longitudinal trim at forward C.G. causes a lift loss $C_{L_{max_{1-g}}} = $ -0.15 to -0.20.

$C_{L_{max}}$ for the Fokker 100 is presented in figure 26.20. Because $C_{L_{max_{V_{min}}}} = 1.84$ with the flaps retracted the F-100 is the only jet transport aircraft certified for take-offs without extended high-lift devices.

The increase in $C_{L_{max}}$ due to flap deflection is less than on the F-28 due to the lower relative flap span. (b_f / b = 0.57 vs. 0.64)
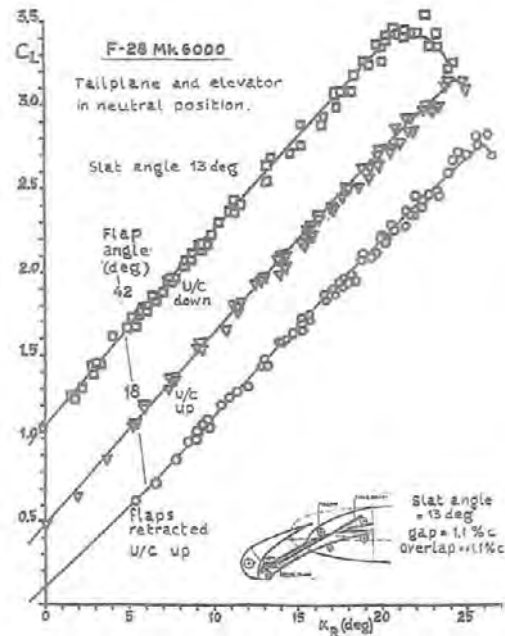
Figure 26.18 - Fokker F-28 Mk 6000 lift curves derived from flight test data. Source: AGARD CP-515, Paper No. 27
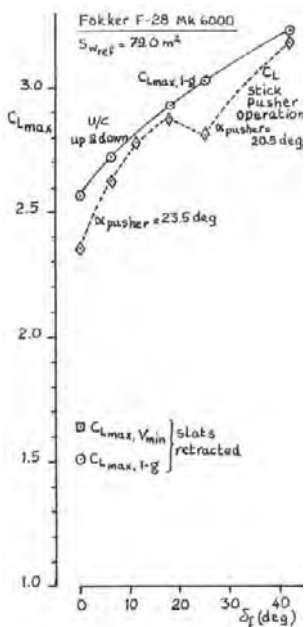
Figure 26.19 - $C_{L_{max}}$ for the Fokker F-28 Mk 6000. Source: Fokker Report H-28.60-27.001
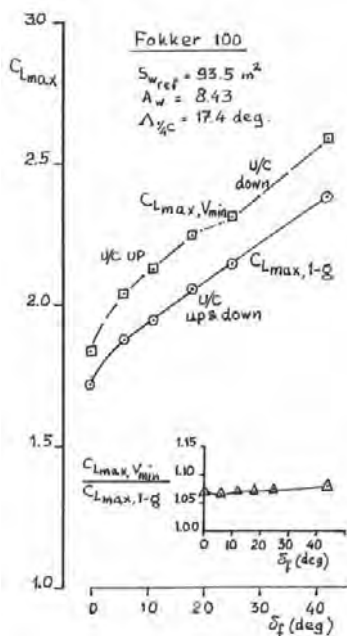
Figure 26.20 - $C_{L_{max}}$ for the Fokker 100. Source: Fokker Report V-28-87

An increase in maximum lift coefficient in general requires an increase in system complexity. The experience in the past has shown that, for practical applications, on airfoil sections using more high-lift components than a slat and three flap elements does not produce a worthwhile gain in maximum lift. The highest section maximum lift coefficient that can be obtained is about $c_{l_{max}} = 5.0$ depending heavily on leading edge bluntness.

Wing geometry is to a large extent determined by the design Mach number, altitude and range (and thus fuel volume). From these wing sweep, relative thickness, (and thus leading edge shape), aspect ratio, taper ratio and overall size are derived. The first two parameters, together with roll control requirements, which strongly influence the relative flap span, and requirements on stalling characteristics determine the maximum achievable maximum lift coefficient of the aircraft.

As a result the maximum lift coefficient on high-speed production aircraft, when no recourse is taken to boundary layer control , lies between
$C_{L_{max}} = 2.0$ and 3.0.

The effect of design Mach number (and thus of wing sweep angle) on the maximum lift coefficient for landing is clearly demonstrated with the data in figures 26.21 and 26.22.

Stalling Characteristics

The stalling characteristics of an aircraft determine the response of the full-scale aircraft to the occurrence of significant flow separation on the wing. Satisfactory stalling characteristics means that the response to flow separation should be either favourable (such as a strong nose-down pitch tendency which restores a condition of attached wing flow) or should be easily controlled by the pilot (such as a roll-off which the pilot can limit to roll angles less than 20°, a FAR 25 or CS 25 requirement). Under no circumstances shall flow separation cause an abrupt pitch-up or yaw movement which may lead to autorotation in a spin. A vivid description of what happens in such a case is given in figure 26.23. This should always be prevented in a transport aircraft, because neither are the characteristics of the aircraft predictable in this condition nor is the aircraft stressed for such load cases.
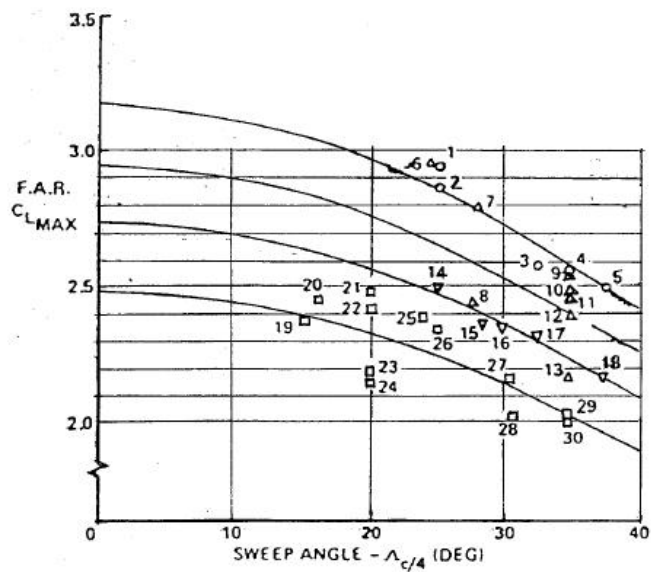
Figure 26.21 - Maximum lift coefficient comparison for various aircraft.
Source: ICAS 1980, paper 12.2

SYMBOL	LEADING EDGE DEVICE	TRAILING EDGE SLOTS	K	SYMBOL NUMBER	AIRPLANE
O	Yes	3	3.17	1.	B737-200
				2.	B737-100
				3.	B727-200
				4.	TU-154
				5.	B747-100
△	Yes	2	2.95	6.	DC-9-30
				7.	A300 B4
				8.	FALCON 10
				9.	DC-10-10
				10.	L-1011-1
				11.	DC-10-30
				12.	TRIDENT 3B
				13.	B707-320B
▽	Yes	1	2.74	14.	C5A
				15.	SABRE-LINER
				16.	FALCON 20F
				17.	VC-10
				18.	B747 SP
□	No	1 or 2	2.49	19.	VFW 614
				20.	FOKKER F28
				21.	BAC 111-500
				22.	BAC 111-400
				23.	HS 125
				24.	CARAVELLE
				25.	DC-9-10
				26.	C141
				27.	DC-8-63
				28.	DC-8-50
				29.	TRIDENT 1C
				30.	B707-120B

FITTED CURVES: $C_{L_{max}} = K \cos \Lambda_{c/4}$

Figure 26.22 - Aircraft types and their high-lift devices mentioned in figure 26.21.
Source: ICAS 1980, paper 12.2

The flight day begins. Chuck meets me in the air on take-off, glues himself to my wing. "Morning, Commander. What've you got today?"

Item Number 1 on my knee pad calls for 20,000 feet; low-speed runs, three to four minutes each. The first run is at 200 miles per hour. She is nose up, dressed at a high angle of attack, and she's hard to manipulate. The controls are mushy. Three minutes. Back again on the same path, slower this time, 180 miles per hour for another three minutes. I continue the series of runs, decreasing the speed until she buffets. Until this flight the complete stall has been unprobed. Today Carder wants a thorough investigation. In previous flights I have been allowed to bring the Skyrocket up to the edge of the stall, backing off at the last second. Today I will go all the way into it.

I remember Gene May's repeated advice, "Treat her with respect; if you don't, she won't forgive you." It has been established that the Skyrocket will not withstand a "spin"; according to the aerodynamicists she will not recover from such treatment. Another instance where the must be handled respectfully. Today we are going to push her a shade more than we ever have before.

One hundred forty miles per hour, on the edge. Nose up, flaps down, gear down… data switch on. I ease a fraction of an inch back on the stick to 139, 138… she protests, rolling laterally, and she shudders along the road I hold her on. She doesn't like it… a little more… a little more… easy… she becomes wilder… I walk the rudder to the stall. That's it! She stalls.

We drop flat through the sky, at 2000 feet a minute. She rolls and pitches violently all the way.

"Got a mind of her own, hasn't she?" Yeager's voice floats calmly into my helmet. "You exciting any of that stuff… you trying to damp that out?"

"I'm attempting to, Captain." She'll take it. A half an inch more and I'll really have it. They can't ask for any better than this, this should impress Carder. I press back on the control column – and immediately I know the movement is too sudden.

The stick hits against its socket.

Holy God… here we go! A wild lunge and she pitches up, rolls to the right, then points her nose toward the ground. She is in a spin. I swallow a gulp of air – a fist in my stomach – and hand on as she cuts loose from me. She's on her way down, corkscrewing crazily through the sky with a whip-lash motion, building up speed terrifically and the earth revolves rythmically below me. This time I've pushed her too far; she didn't take it. A spin! According to Carder, the book, the men who built her, a spin will destroy her. According to their careful estimation she won't recover. With both hands I grab the gear and the flap handles and clear her up. It's all automatic movement now, all feel, no theory. Apply full opposite rudder, neutralize the stick. There's no pressure on the rudder, no response, it is as if the ship had no rudder. The solitary thought I have is this: will the corrective action take effect fast enough, is the rate of "rudder-pressure" return greater than the speed at which the ground is coming up? Come on, answer me, will you! A little pressure against my foot now, a little more, she's coming around. I can feel the pressure building on the rudder. The rolling and twisting motion stops and the Skyrocket straightens out into a steep dive. Once more I've got an airplane under me. She recovered. They were wrong, only this time the error in prognostics was in my favour. She has lost 7000 feet in ten seconds as I start the long pull out and my breath returns heavily.

"Oops!" It's Yeager's voice and on my left wing there he is – a big orange helmet with a big kid's grin. He had been right with me all the way to the bottom. When the Skyrocket is straight and level, as if the last two or three minutes hadn't happened, Yeager asks, nonchalantly, for the benefit of the engineers on the ground listening attentively to the radio, "How are the stalls progressing?"

"They're finished. I'm going in. Fuel to 40 gallons."

In a reflective tone the chase pilot sagely replies, "I would say they were finished…"

Figure 26.23 - Text about stall resulting in a spin. Source: 'The lonely sky' by W. Bridgeman, 1955.

There are some general rules to prevent undesirable stalling characteristics:

1. Flow separation should start on the inboard wing so that spoilers and ailerons for roll control remain effective in the stall. This can for example be achieved by making sure that peak $C_{p_{min}}$ - values at the leading edge (either on the wing or on the slat) occur on the inboard wing.

2. When the stall occurs the tailplane and elevator shall not lose effectiveness due to becoming immersed in the wake of the separated flow on the wing.

Wing under slat surface (WUSS)
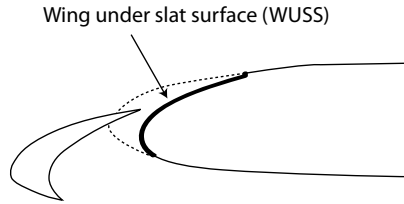
Figure 26.24 - Definition of Wing Under Slat Surface (WUSS)
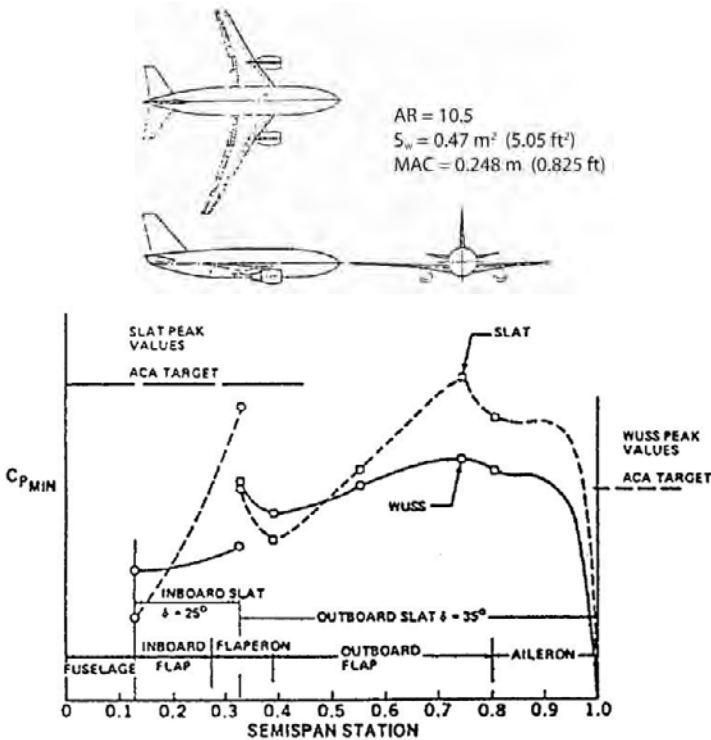
Figure 26.25 - Theoretical spanwise variation of slat and WUSS (see figure 26.24) minimum pressures for the ACA low-speed wind tunnel model (landing flaps $C_L = 3.4$). Source: J.G. Callaghan, W.G. Oliver, Douglas Aircraft Co.

Figure 26.25 illustrates that the minimum pressure coefficient $C_{P_{min}}$ on slat and main wing may vary considerably along the span. For good stalling characteristics the spanwise distribution should be such that initial stall inboard of the engine nacelle is ensured. The WUSS is defined in figure 26.24. ACA is a project name.

If inboard wing stall cannot be ensured through variation along the span of effective twist, camber and leading-edge radius this may be achieved artificially through breaker strips (alternatively termed leading-edge stall strips or leading-edge spoilers), wing fences, vortices stemming from fences on engine nacelle, etc. A drawback is that these will invariably lower the maximum lift coefficients. Examples are given in figure 26.26. A blocked slat gap reduces lift of the inboard side of the wing relative to the outboard side and thus triggers to first stall inboard. This system is used on the De Havilland 121-1E, A300 and A310. Humps (or bulges) on the leading edge flap knuckle of the De Havilland 121-1 also trigger initial separation on the inboard wing.

More explanatory pictures are given in figures 26.27 to 26.29. Notice the significant maximum lift coefficient decrease that is caused by the stall strips in figure 26.27.
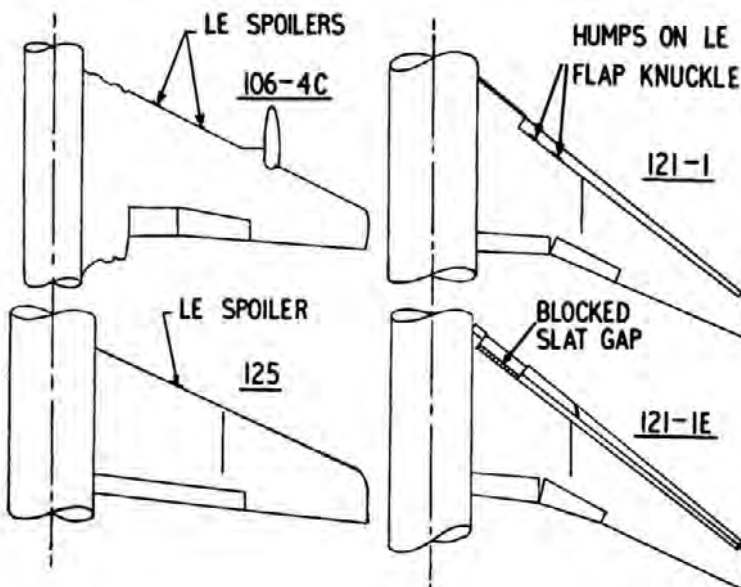
Figure 26.26 - Stall control devices (DeHavilland aircraft).
Source: AGARD LS-43, D.M. McRae, 1971
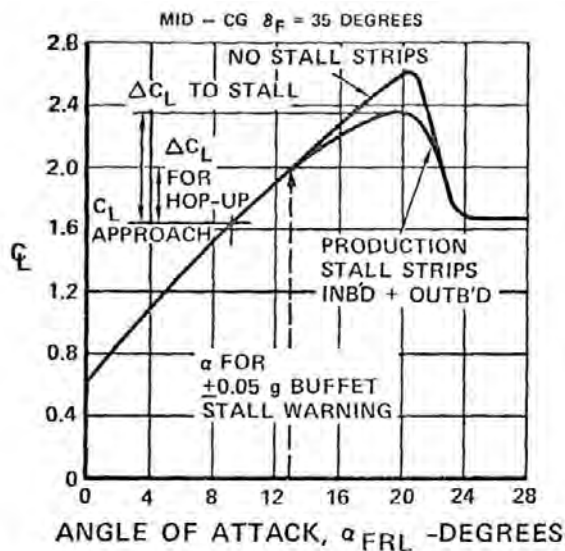
Figure 26.27 - "Tailoring" the stall characteristics.
Source: AIAA Paper No 73-778

1. SUFFICIENT DETACHMENT IN THIS AREA TO PROVIDE ±0.05 g AT 13 DEGREES ANGLE OF ATTACK. HORIZONTAL TAIL PICKS UP THIS TURBULENCE.

2. PROGRESSIVE SEPARATION IN THIS AREA TO PROVIDE SYMMETRIC WING FLOW AT 16-17 DEGREES ANGLE OF ATTACK
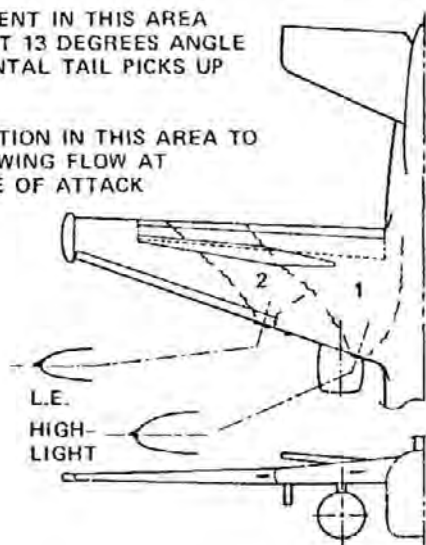
Figure 26.28 - Flow separation growth. Source: AIAA Paper No 73-778
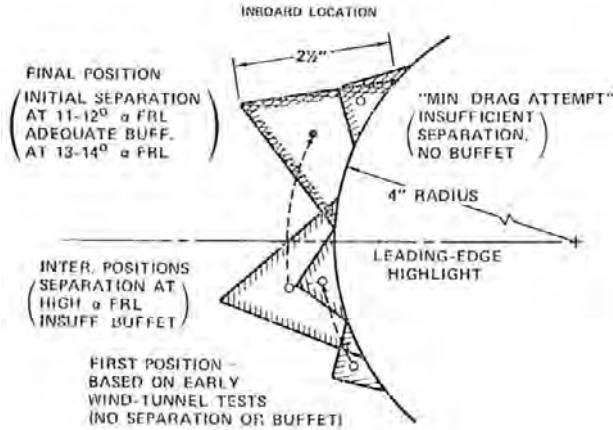
Figure 26.29 - Stall strip progression. Source: AIAA Paper No 73-778

In the previous chapter a wind tunnel investigation was mentioned on F-29 Model 10-7. The wing plan form is shown in figure 25.50 and figure 25.51 shows the spanwise local lift distribution at high angles-of-attack .

This investigation demonstrated the complexities of the flow separation pattern on a tapered swept wing with high-lift devices. The model was tested at Re-numbers between Re = 1.6 x 10^6 and Re = 5.4 x 10^6 but only the latter will be discussed here.

In figure 26.30 the lift curve of this model at high angles-of-attack is shown at M = 0.19 and M = 0.28 for the configuration with a slat angle δ_s =15° and the single-slotted flap set at δ_f = 27.5°.
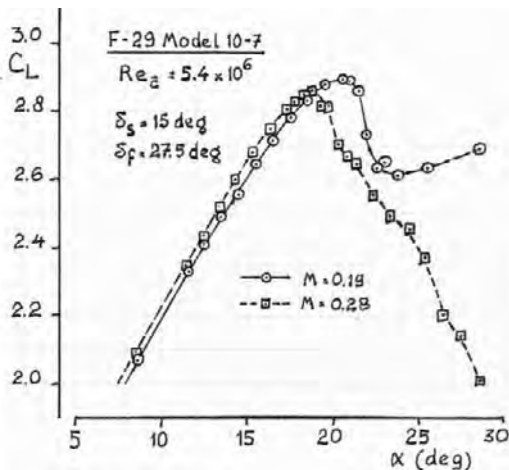
Figure 26.30 - Lift curves at high angles-of-attack at M = 0.19 and M = 0.28, F-29 Model 10-7 Source: Fokker Rep. L-29-202 / NLR TR 84010 C

At M = 0.19 it is clear that at reaching maximum lift only limited separation occurs as after the initial stall the lift increases on a large part of the wing at further increasing the angle-of-attack. This is also shown in figure 25.31 where the local lift keeps increasing up to α = 28.5°.
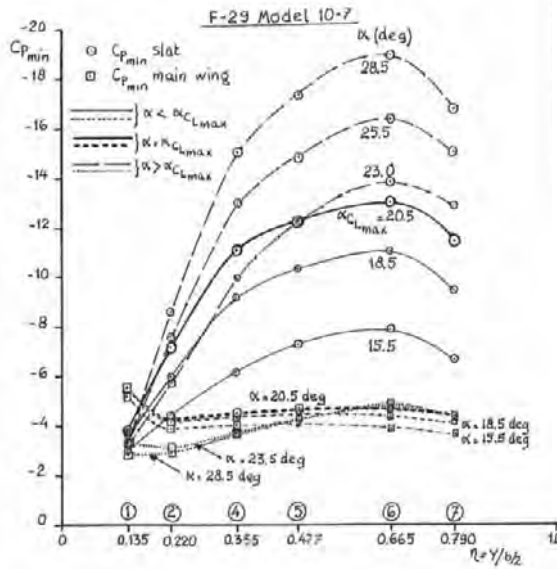
Figure 26.31 - Spanwise suction peak distribution at
M = 0.19 at various angles-of-attack.
Source: Fokker Rep. L-29-202 / NLR TR 84010 C

Figure 26. 31 shows the s**panwise distribution of the peak suction coefficient on the slat as a measure of the local lift coefficient for various angles-of-attack**. The low $C_{p_{min}}$ near the root is due to the low local lift coefficient as a consequence of the strong tapering of the inboard wing. Maximum lift is reached at α = 20.5°. Above this angle-of-attack $C_{p_{min}}$ decreases on the inboard wing at wing stations 1,2 and 4 (station 3 was deleted from the tests). This indicates some loss in circulation due to flow separation but at α = 23.0° the lift starts to increase again. The explanation is shown in figure 26.32. At wing station 1 the slat is lightly loaded and at the wing leading-edge there is a strong suction peak. This situation improves further outboard. Above α = 20.5° the flow separates at the flap shroud, separation being strongest at the root.
This is accentuated by the strongest drop in the main wing suction peak at station 1 as shown in figure 26.32.

On the outboard wing the circulation distribution between slat, main wing and flap is clearly better in balance as the lift at wing stations 5, 6 and 7 shows a steady increase in local lift with increasing α up to α = 28.5 deg, the highest angle-of attack that could be reached in the wind tunnel tests. As was shown in the previous chapter (figures 25.54 and 25.55) at wing station 6 the leading edge suction peak on the slat rises at M = 0.19 to an equivalent local Mach number M_{loc} = 1.06 in two-dimensional flow.
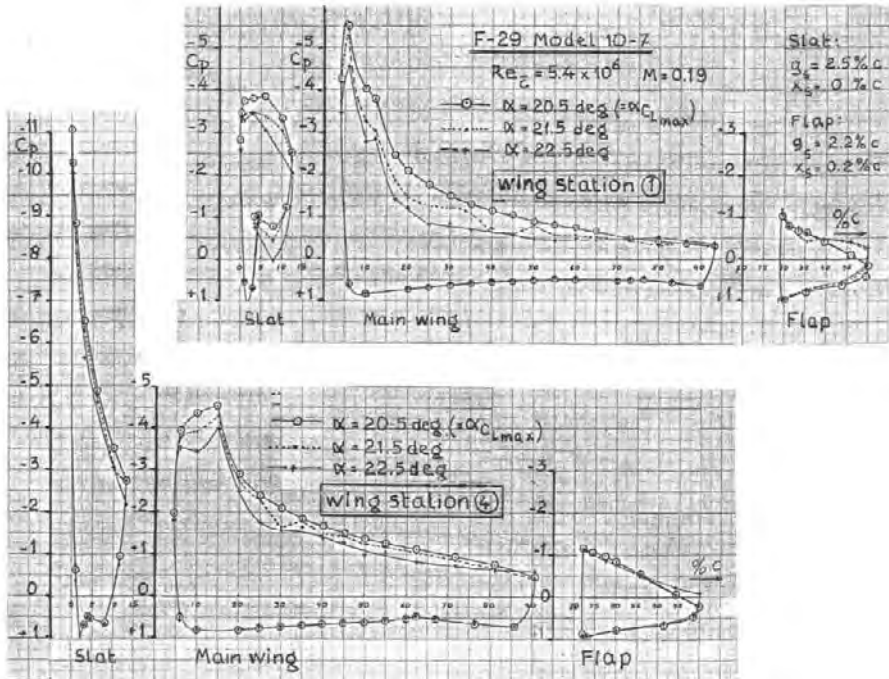
Figure 26.32 – F-29 Model 10-7 – Chordwise pressure distribution at high angles-of-attack on wing stations 1 and 4 at M = 0.19. Source : Fokker Rep.I-29-202 / NLR TR 84010 C

At M = 0.19 the maximum lift coefficient of the wing may possibly be increased by decreasing the deflection of the inboard slat between wing root and trailing-edge kink to δ_s =10° or even less and still maintain favourable stalling characteristics.

At M = 0.28 initial separation also occurs on the inboard wing as is evident from figure 26.33 but also in this case after an initial small lift loss the lift on the slat increases with increasing angle-off-attack. On the outboard wing the lift on the slat increases slightly up to α = 23.5° after which strong separation occurs. The maximum peak suction coefficient, $C_{p_{min}}$ = -12.8, at wing station 6 has been converted to equivalent two-dimensional flow condition in figures 25.54 and 25.55. The local Mach number in equivalent two-dimensional flow M_{loc} = 1.50 indicating that the maximum achievable lift on the slat has been realised.

The difference in stalling characteristics between inboard and outboard wing is so small that it is unlikely that a change in inboard slat setting will produce an improvement in maximum lift without deteriorating the flight characteristics in the stall.
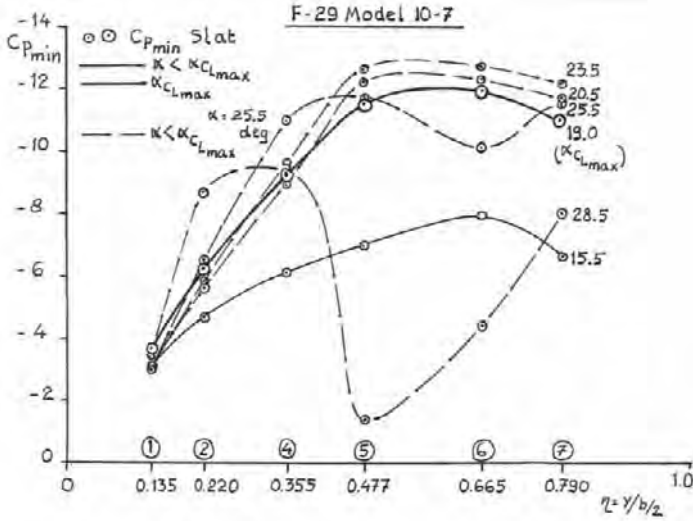
Figure 26.33 - Spanwise suction peak distribution at
M = 0.28 at various angles-of-attack.
Source: Fokker Rep. L-29-202 / NLR TR 84010 C

The main difference between aircraft with a low-set tailplane and a T-tail is their response to flow separation on the main wing. Therefore aircraft with T-tails require special attention for their stalling characteristics.

On a T-tail, the flow over the horizontal tail plane is initially largely undisturbed after the flow over the wing separates. Flow separation on the wing decreases the wing lift, so that the vertical balance of forces changes, making the aircraft lose altitude and increase the angle-of-attack. A strong nose-down pitching moment at large angles-of-attack is required to compensate the tendency to pitch-up at an increasing rate. But if this large-enough nose-down pitching moment is not produced the angle-of-attack will keep increasing until the tail plane becomes immersed in the wake of the wing as illustrated in figure 26.34. This and following figures refer to wind tunnel investigations performed during the development of the Douglas DC-9 Series 10 and reported in AIAA Paper No. 65-738.
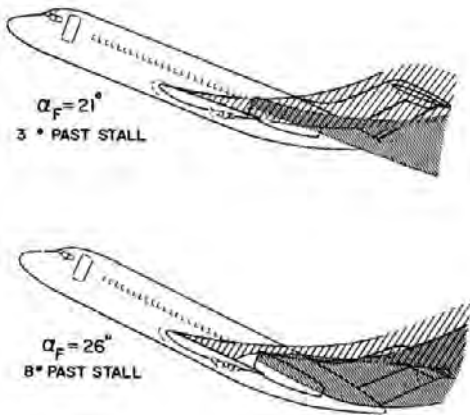
Figure 26.34 - Wake location beyond stall, $\alpha_F = 21°$,
$\alpha_F = 26°$, flaps up, low Reynolds number.
Source : AIAA Paper No. 65-738

If the tailplane is immersed in the wake of the separated flow of the main wing, the aircraft will loose its longitudinal stability. It will remain unstable and pitch-up until a new equilibrium is found at a very high angle-of-attack. This may result in a "locked-in stall" or "deep stall", from which recovery may be extremely difficult. The principle of deep stall will be explained with the aid of figure 26.35.
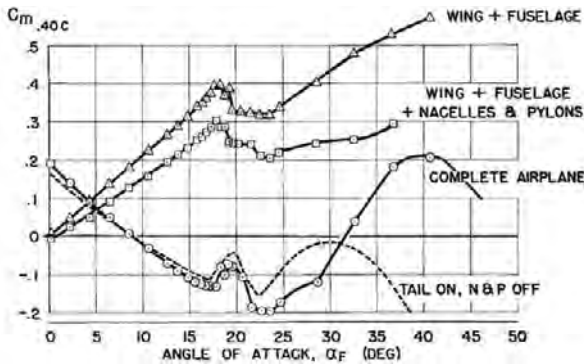
Figure 26.35 - Pitching moment buildup, flaps up, typical model with deep stall problems. Source : AIAA Paper No. 65-738
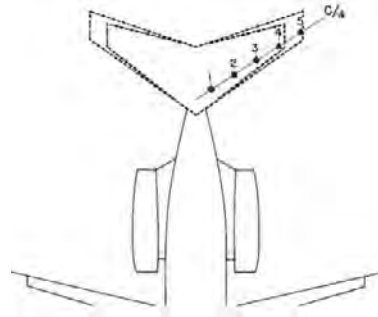
Figure 26.36 - Wind tunnel model probe locations. Source : AIAA Paper No. 65-738

Here, the pitching moment coefficient is plotted (for a fixed stabiliser and elevator position) against the angle-of-attack. The curve of the complete aircraft shows that stall occurs at α = 18°. When further increasing alpha, a more negative pitching moment can be obtained, having its minimum at α = 23°. Continuing the increase in angle-of-attack a positive pitching moment gradient is found, meaning the aircraft is unstable. Although the pitching moment is negative up to α = 32° (for this particular stabiliser and elevator position). the dynamics of the manoeuvre due to the decreasing lift will cause the aircraft to surpass this angle of attack if no immediate pilot action is taken.

Above α = 32° the aircraft will search for a new equilibrium position, for which C_{m_α} is again negative. This is found at an angle-of-attack at about 50 degrees. Now, the aircraft is in a stable deep stall situation in longitudinal trim, from which it will be almost impossible to recover.

Note in figure 26.35 that fitting engines on the rear fuselage considerably strengthens any deep stall tendency.

The DC-9 wind tunnel model was tested with five pitot-static probes at the location of the horizontal tail surface of the T-tail. Figure 26.36 shows the position of the probes.

In figures 26.37 and 26.38 the effect of increasing the size of the horizontal tail surface to improve aircraft controllability is presented. Figure 26.37 shows the ratio between the local and the wind tunnel dynamic pressure for the five probes as a function of angle-of-attack. The four inner probes, which cover a span equal to the span of the original stabiliser show that dynamic pressure drops dramatically above $\alpha = 20°$ indicating a large loss in stabiliser effectiveness at high angles-of-attack.

With an extended tail surface (probe 5 added) the outer parts of the tailplane are now outside the wake of the separated flow from the nacelles, improving the tail surface effectiveness sufficiently to enable recovery from an initial stall. In figure 26.38 the local angle-of-attack at the five probe positions is given.
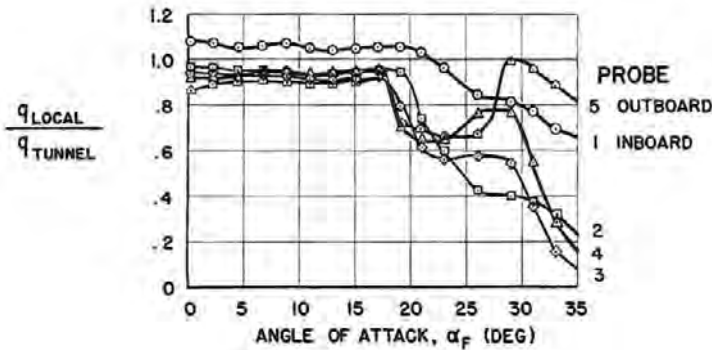
Figure 26.37 - Dynamic pressure ratio at the tail, flaps up.
Source : AIAA Paper No. 65-738.
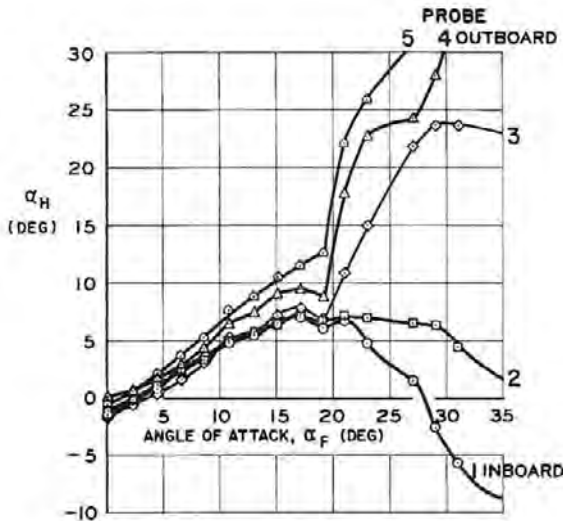
Figure 26.38 - Angle-of-attack at the tail, flaps up.
Source : AIAA Paper No. 65-738.
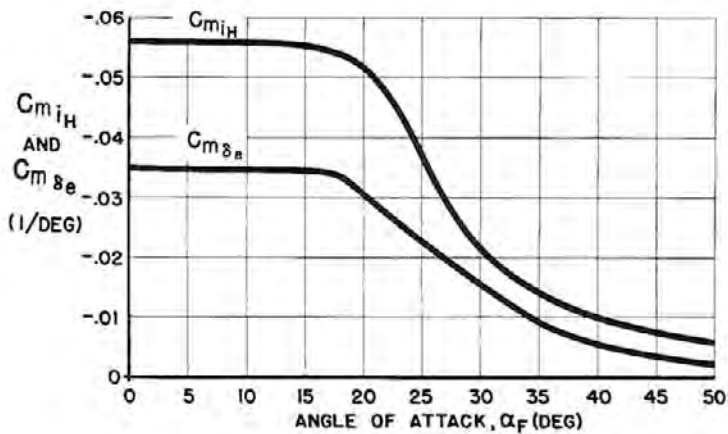
Figure 26.39 - Stabilizer and elevator effectiveness .
Source : AIAA Paper No. 65-738.

Contrary to the flow at the two inner probe positions the flow direction further outboard is almost equal to that of the undisturbed flow. The large spanwise variation in local angle-of attack points to the presence of strong vortices springing from the upper front fuselage.

As mentioned before, when the horizontal tail surface is immersed in the wake from wing and engine nacelles the effectiveness of the tail surface and thus its contribution to the pitching moment diminishes. Figure 26.39 shows for the DC-9 Series 10 the decrease in stabiliser and elevator effectiveness at higher angles-of-attack.

Figure 26.40 presents a further illustration of the longitudinal behaviour of T-tail aircraft. The middle curve is basically a repeat of the pitching moment curve from figure 26.35. The upper fully drawn curve indicates the pitching moment versus α for full upward elevator deflection. The intermediate broken curves show how with increasing upward elevator deflection stable trimmed conditions are found at increasing angles- of-attack up to $α_{crit}$ when the aircraft becomes unstable. The lower curve shows the pitching moment versus angle-of-attack at the same stabiliser angle but with full downward elevator deflection. Depending on the particular aircraft configuration this may just produce sufficient nose-down pitching moment to prevent a deep stall.
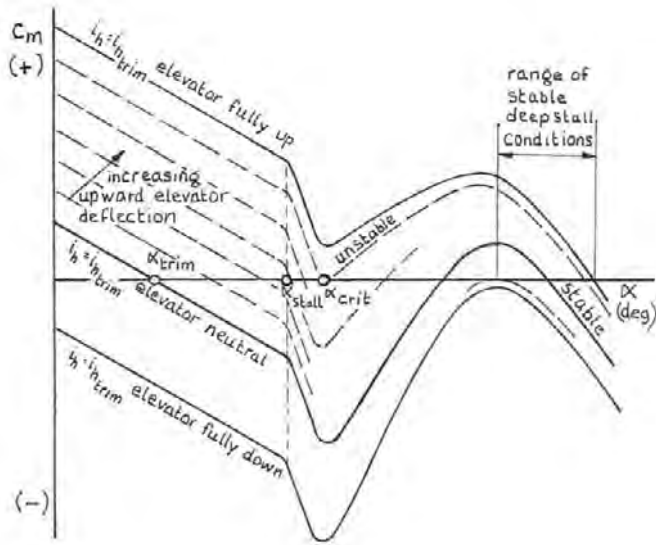
Figure 26.40 - Stability and controllability on an aircraft with a T-tail

This may however have only a theoretical meaning. The unpredictability of the lateral and directional characteristics of the full-scale aircraft in the post-stall regime makes it preferable to tailor the stalling characteristics such that high angles-of-attack can not or only by deliberate abuse be reached.

Apart from the danger of creating a deep-stall condition due to flow separation on the wing of an aircraft with a T-tail, also the elevator will lose its effectiveness as shown in figure 26.39. The separated flow over the complete wing span will eliminate most of the aileron-effectiveness as well. A roll-off will most likely result in a spin, which at these high angles-of-attack will be a flat spin, from which recovery is extremely difficult.

Reaching these very high angles shall therefore under all circumstances be prevented, if necessary by means of an mechanical angle-of-attack limiter (a "stick-pusher").

Certification authorities demand that at least the wind tunnel data show that at reaching high angles-of-attack sufficient elevator capacity is available to pitch the aircraft down to normal flight conditions again. Therefore, during the DC-9 development the stabiliser span was extended and vortilons were fitted. The vortilon is a vortex generator based on the experience with the pylons on the DC-8. It is used to make the inboard wing stall first and then to limit the region of separated flow to the inboard wing. Since the point of application of the lift on this section is in front of the aerodynamic centre of the complete wing, the use of vortilons improves the stalling characteristics by increasing the tendency
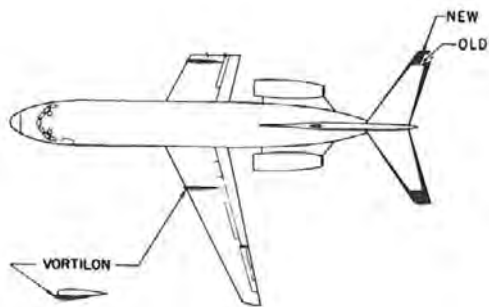
Figure 26.41 - DC-9 modified horizontal tail and vortilon. Source: AIAA Paper No. 65-738

of the aircraft to pitch the nose down in particular in the α-range between $\alpha_{C_{L_{max}}}$ and the angle-of-attack where the tailplane becomes immersed in the wing wake. The modifications and the resulting pitch characteristics are shown in figures 26.41 and 26.42.

Notwithstanding these characteristics the DC-9 is equipped with a system incorporating a hydraulic ram which forces the elevator fully down if the aircraft does not react normally to pilot control inputs.
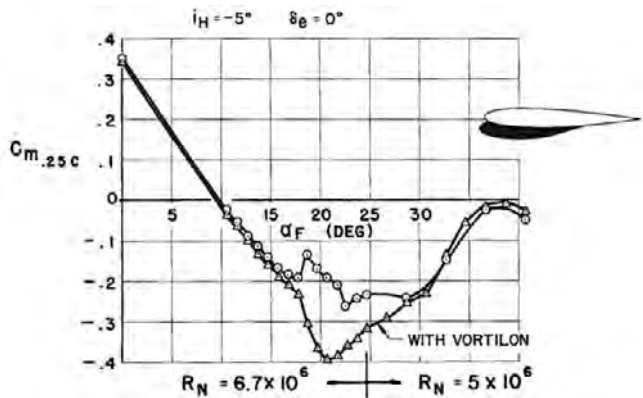
Figure 26.42 - Effect of vortilon on pitching moments, flaps up, high Reynolds number. Source: AIAA Paper No. 65-738
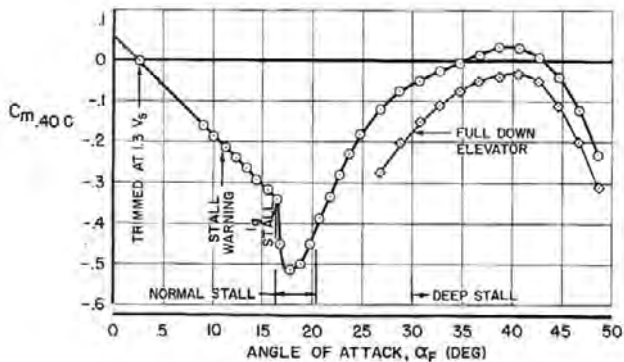
Figure 26.43 - Pitching moment coefficients for DC-9-10 configuration, flaps 50° . Source: AIAA Paper No. 65-738
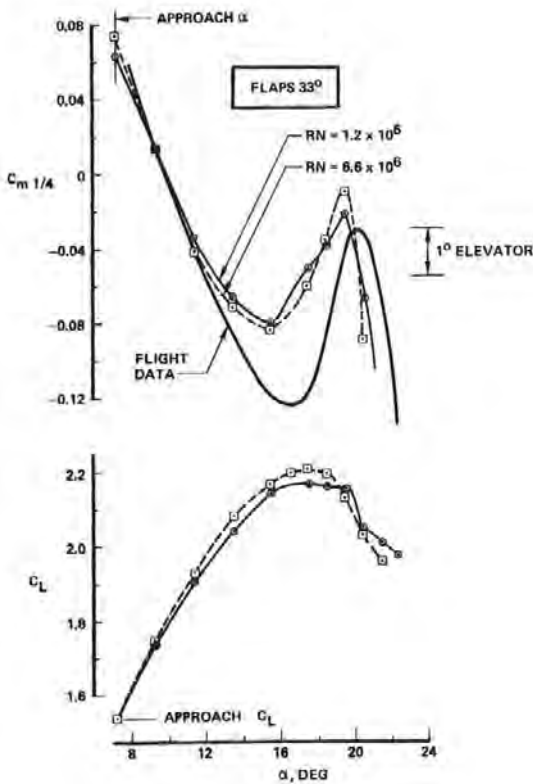
Figure 26.44 - Stall characteristics of a Boeing 747. Source: AGARD CP-102, Paper No. 21
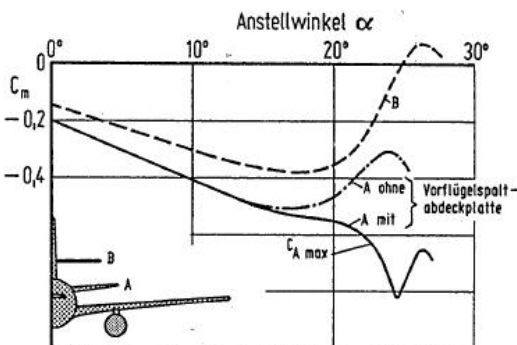
Figure 26.45 - Stability with and without blocked slat gap for the Airbus A300. Source: Jahrbuch 1973 der DGLR

Not only T-tailed aircraft may suffer from undesirable pitch characteristics. Also aircraft with a low-set tail need to investigate this and less favourable characteristics may have to be remedied. An example is the Boeing 747 which in the landing configuration does not exhibit the formally required pitch-down tendency at the stall (figure 26.44). However, due to the small α-range where this instability occurs this characteristic was accepted by the authorities.

For the Airbus A300 low-speed pitching moment curves are shown in figure 26.45 for three configurations. The provision on the inner wing whereby the slat gap is partially blocked does not only produce satisfactory lateral characteristics in the stall (see figure 26.7) but also gives satisfactory longitudinal characteristics.

Deep stall is a phenomenon that has to be studied carefully in the design of an aircraft, in particular on T-tail configurations. T-tail aircraft are as safe as low-tail aircraft if their characteristics are understood and respected, in particular during flight testing. Several T-tailed aircraft have suffered serious accidents during stall tests, among them: BAC-111, De Havilland Trident 1, Lockheed C-141, HFB-320 and Canadair Challenger.

27 *The lift-drag ratio in take-off and landing*

The use of high-lift devices during take-off and landing increases the maximum lift coefficient and thus decreases take-off and landing field length, approach speed and decreases the wing area as required for optimum cruise performance. This is illustrated in figures 27.1 and 27.2.
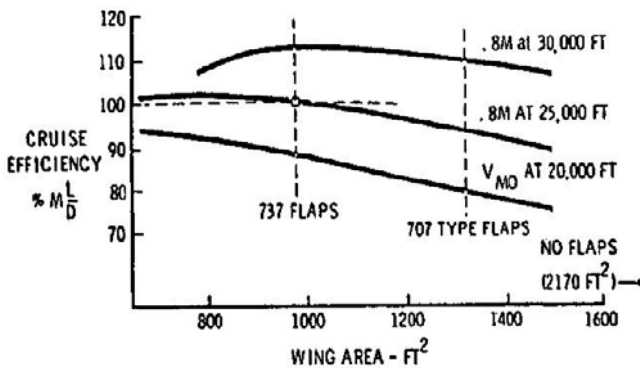
Figure 27.1 - Cruise efficiency. Source: Shell Aviation News nos. 343, 344 / AIAA Paper No 65-739
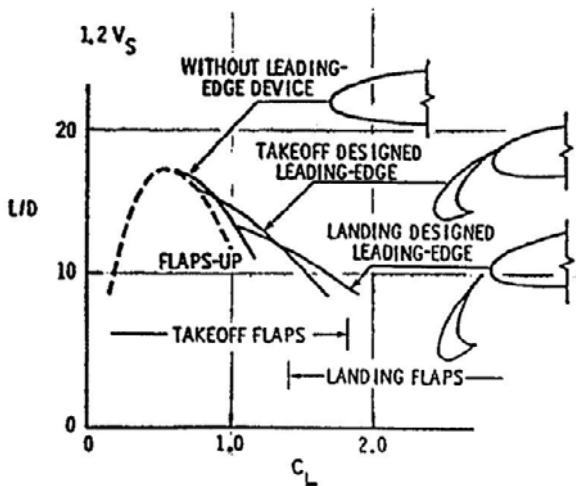
Figure 27.2 - Polar envelopes, effect of leading edge, 737 trailing-edge flaps. Source: Shell Aviation News nos. 343, 344 / AIAA Paper No 65-739

Figure 27.1 illustrates how the range parameter of the Breguet formula is related to the wing area. Improvements on the slats and flaps to obtain a higher lift coefficient during take-off and landing will concurrently lead to a smaller required wing area, and higher cruise efficiency. In recent years however, the ever-present pressure on maximum range and the associated requirement concerning maximum fuel volume has limited the possibility of minimising the wing area by the use of sophisticated high-lift devices. Therefore the interest has shifted to simpler systems with more emphasis on costs and reliability and maintainability.

Figure 27.2 shows the effect of applying slats on the L/D ratio, as well as on the maximum lift coefficient.

Besides increasing lift, high-lift devices also increase drag at the lift coefficients of interest. Therefore, the L/D ratio decreases at increasing flap setting and maximum lift coefficient. Flap and slat design as well as the wing aspect ratio affect the relation $(L/D)_{V_2}$ versus $C_{L_{V_2}}$.

With a superior design, this relation can be improved, thus increasing the maximum take-off weight for a given airport, as illustrated in Figure 27.3.
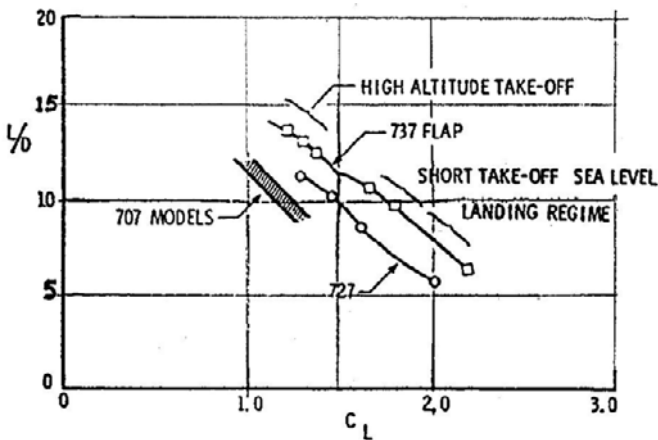
Figure 27.3 - Polar envelopes, airplane comparison.
Source: Shell Aviation News nos. 343, 344 / AIAA Paper No 65-739

Another illustration of the decrease in lift-drag ratio by the use of high-lift devices is presented by figure 27.4 for the original Boeing 737. A clean configuration gives, if it would not be limited by $C_{L_{max}}$, the highest L/D ratio although it would diminish with increasing C_L. As the $C_{L_{max}}$ of a clean wing is rather low, $C_{L_{max}}$ is increased by fitting high-lift devices. These increase the drag due to their own
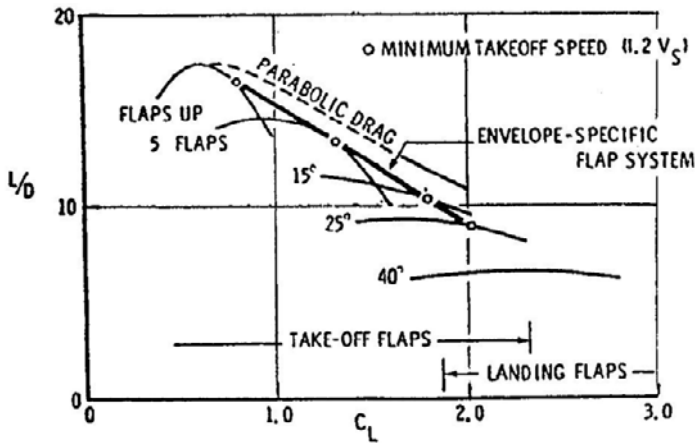
Figure 27.4 - Take-off aerodynamics, polar envelope.
Source: Shell Aviation News nos. 343, 344 / AIAA Paper No 65-739

form drag and suspension mechanisms and a less favourable spanwise lift distribution.

Although design of airfoil sections with extended high-lift devices can be performed to a fair degree with computer codes as was shown before (in chapter 25), final optimization in the wind tunnel is still advisable.

For designing three-dimensional transport aircraft configurations with high-lift devices CFD has had up to now only limited applicability. The complicated shapes with three-dimensional boundary layers put such a heavy demand on both the software and the hardware that at present both accuracy and turn-around times limit the usefulness of CFD for design purposes. Details in the flow can be studied effectively but the shortcomings refer to the integration process so that overall characteristics can not be determined accurately and within acceptable turn-around times.

Theory can be used for three-dimensional configurations however for certain particular applications:

1. Analysing the spanwise lift distribution and the induced drag. Simplified non-planar lifting-surface theories with empirical corrections produce the most reliable answers.

2. Analysing chordwise pressure distributions and for smoothing irregularities in the pressure distribution. Note that incorporation of boundary layers is still not possible on a routine basis so overall forces may be grossly overpredicted.

Figures 27.5 to 27.7 show several comparisons between computations and test data of aircraft with deflected high-lift devices. It shows that it is possible to obtain reasonably accurate predictions on the spanwise lift distribution. Calculations with panel methods, thus excluding viscous effects give a good impression of chordwise pressure distributions along the span.
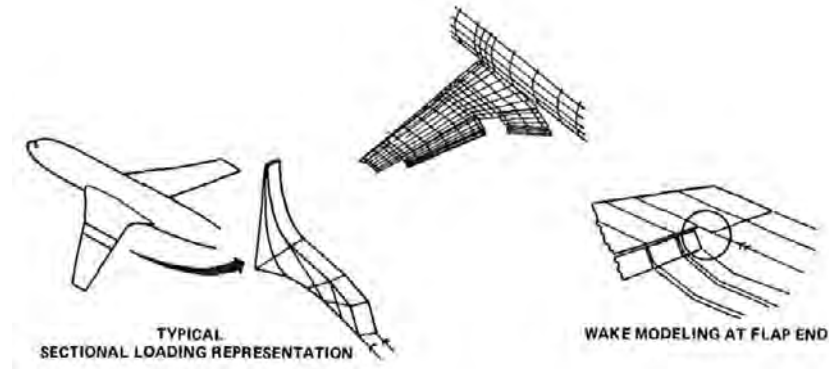
Figure 27.5 - DVM Lifting surface analysis for high-lift configurations.
Source: AIAA Paper No. 83-1845
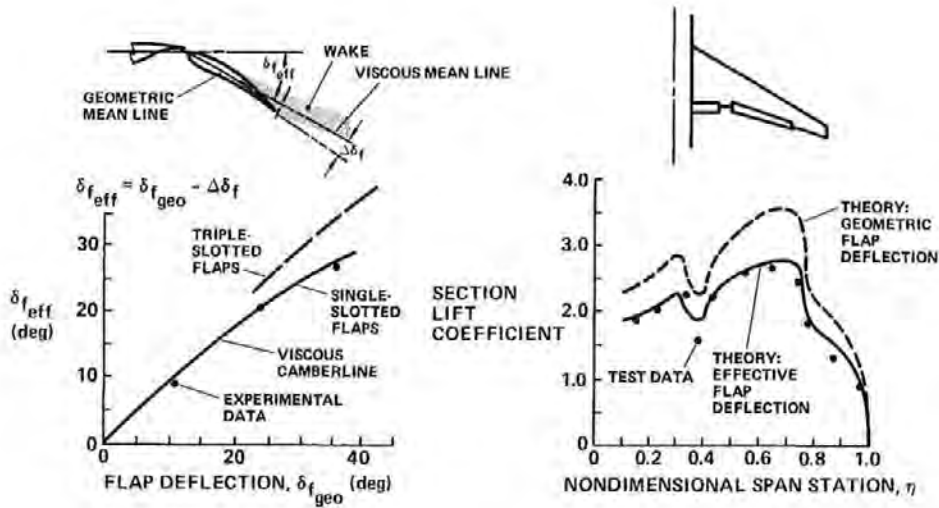
Figure 27.6 - Effective flap deflection - influence on span loading.
Source: AIAA Paper No. 83-1845
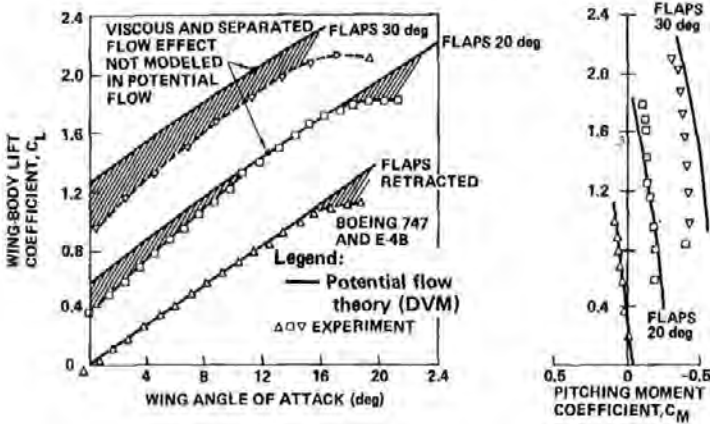
Figure 27.7 - Typical distributed vorticity method (DVM) results.
Source: AIAA Paper No. 83-1845

The boundary layer and some partial flow separation on the flap upper surface has a de-cambering effect on the flap causing the effective flap angle to be smaller than the nominal flap angle as shown in figure 27.6. If this effective flap angle is included in calculations based on lifting surface theory, good agreement between theory and experiment can be obtained in particular with small flap angles. At higher flap angles the agreement may be less good, particularly at low angles of attack as can be noticed in figure 27.7. This is due to the rear fuselage being placed in a strong downwash resulting in vortices or flow separation on the lower fuselage and, with rear-engine configurations, on the lower surface of nacelles and pylons. For higher angles-of-attack the rear fuselage is better aligned with the local flow direction. This is illustrated in figure 27.8.

α small: highly 3D flow with vortices

α larger: mean line of aft fuselage better aligned with local airflow including downwash
$\alpha_{effective}$ decreases as α increases
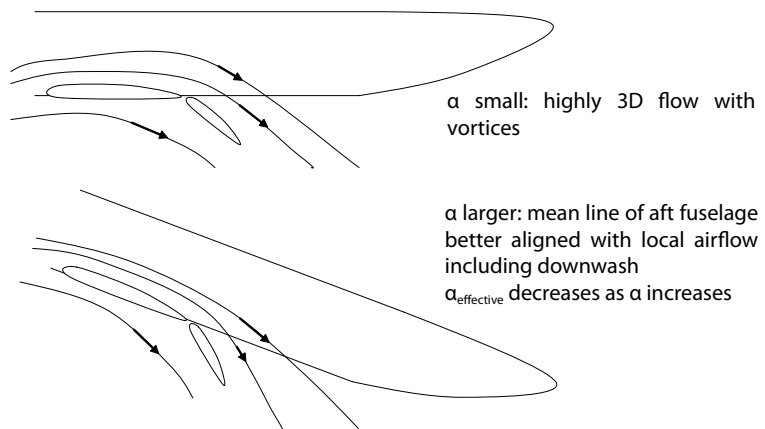
Figure 27.8 - Variation in local flow direction with increasing angle-of-attack

Non-planar lifting surface theory, combined with empirical data can be used to estimate **lift-drag ratios** for take-off and landing configurations when no wind tunnel date are available. This is discussed in the next part of this chapter.

Classical lifting surface theories, which due to the limited computing capabilities then available, could only handle small perturbations in the flow. Thus planar vortex sheets had to be considered and only configurations with small flap angles could be analysed. Modern CFD methods have removed these limitations. Figures 27.5 to 27.7 show lift and pitching moment data for configurations with large flap angles computed with non-planar trailing vortex sheets.

In the 1980's a non-planar lifting surface programme, NPLS, was developed at the Fokker Company based on an earlier subsonic panel method developed by the Dutch aerospace research institute NLR. This programme allowed the analysis of complete aircraft configurations described by a limited number of panels with lifting surfaces of zero-thickness.

Figure 27.9 shows the panel and the vortex distribution used for the analysis of the Fokker 100. The trailing vortices along the edge of each panel follow the effective flap angle and continue some distance further down the flap before continuing rearwards and the vortex distribution continues in the fuselage.
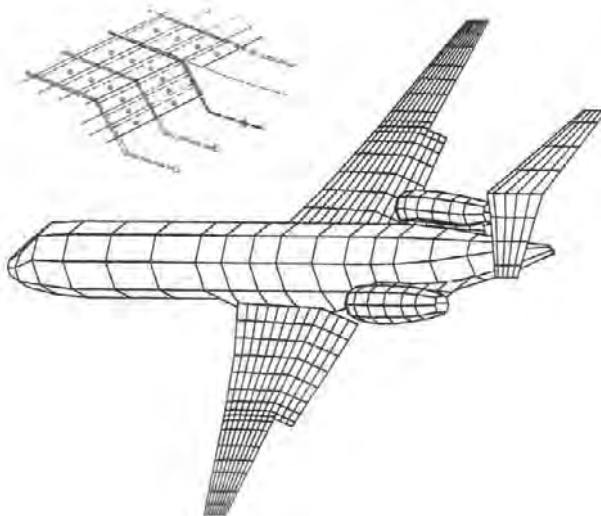
Figure 27.9 - NPLS panel distribution for the Fokker 100.
Source: Fokker Rep. A – 173.
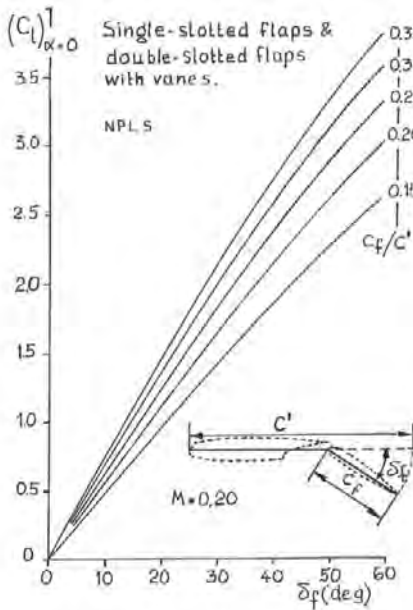
Figure 27.10 - Lift due to single-flap deflection. Source: Fokker Rep. A – 173.
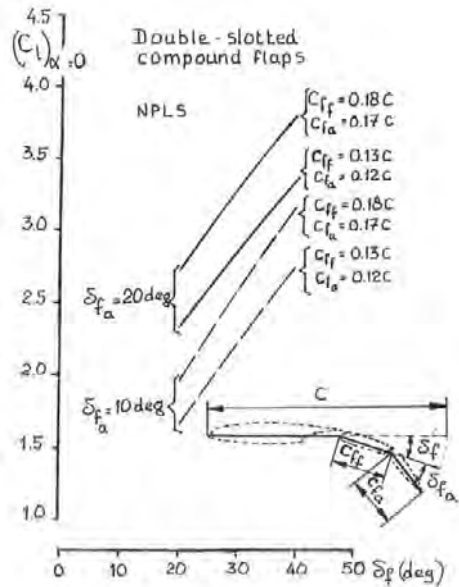
Figure 27.11 - Lift due to double-flap deflection. Source: Fokker Rep. A – 173.

In figures 27.10 and 27.11 the lift coefficient at zero angle-of-attack is given of a two-dimensional flat plate with single and double plane flaps as a function of flap angle and relative flap chord as calculated with the programme NPLS.

A large amount of wind tunnel test data on two-dimensional airfoil sections with high-lift devices were compared with these theoretical data. This comparison produced the relations between nominal and effective flap angle shown in figures 27.12 and 27.13. Figure 27.6 shows similar results.

Having established the effective flap angles for the nominal flap angles $\delta_f = 20$ deg and $\delta_f = 42$ deg the tail-off lift curves for the configurations flaps retracted, $\delta_f = 20$ deg and $\delta_f = 42$ deg could be obtained with NPLS. These curves are presented in figure 27.14.
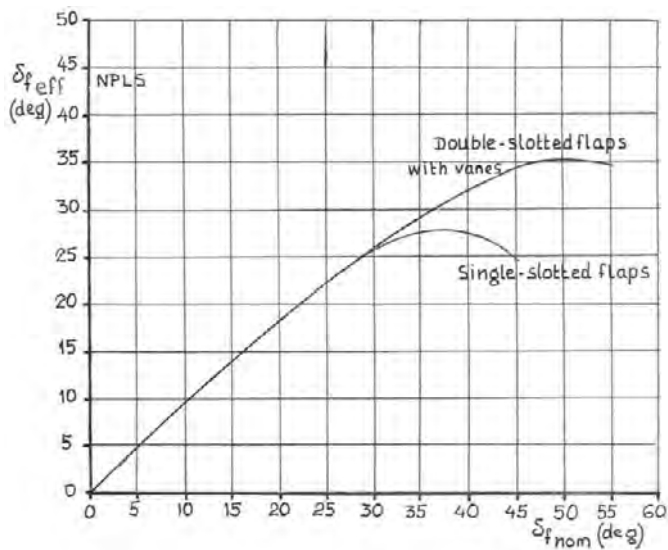
Figure 27.12 - Nominal versus effective flap angle for single- slotted flaps and double-slotted flaps with vane.
Source: Fokker Rep. A - 166 and A - 173.
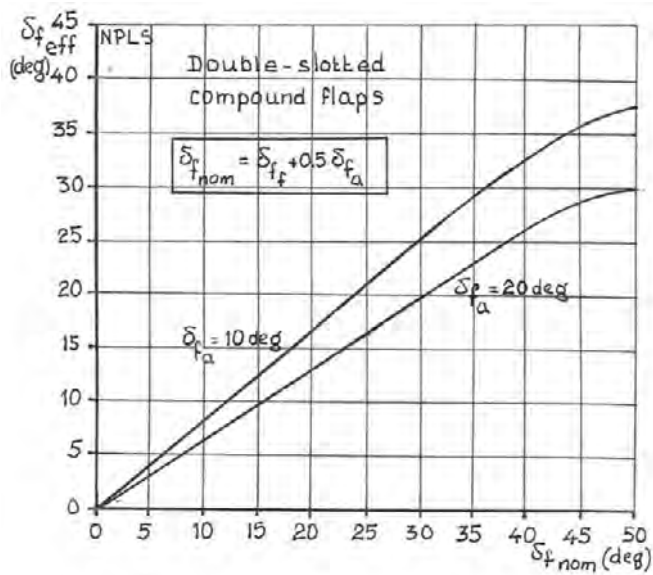
Figure 27.13 - Nominal versus effective flap angle for double-slotted compound flaps. Source: Fokker Rep. A - 166 and A - 173.
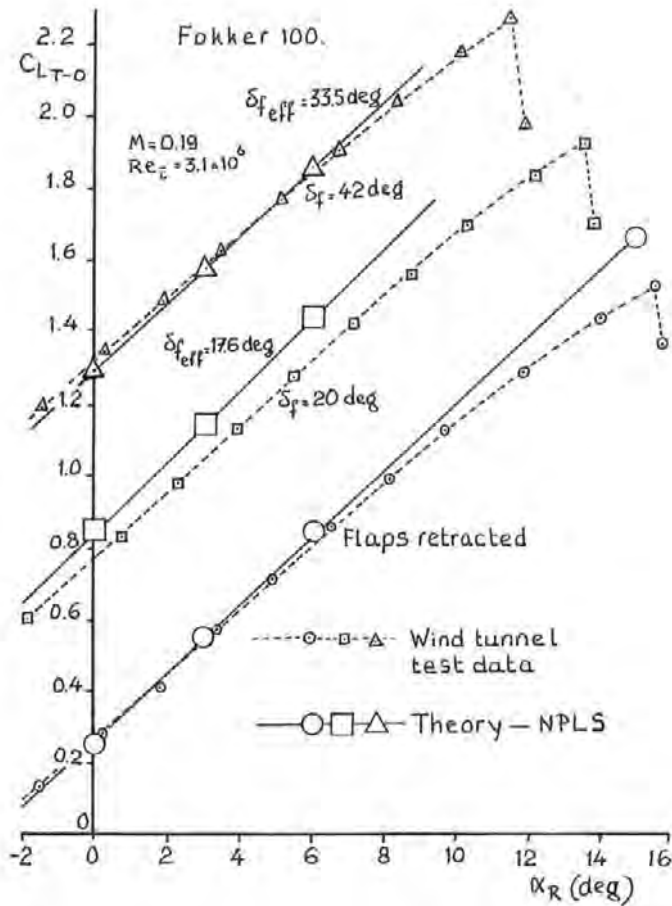
Figure 27.14 - Tail-off lift curves for the Fokker 100.
Source: Fokker Rep. A - 166 and A - 173.

In figures 27.15 to 27.17 the spanwise distribution of the local lift coefficient for the three configurations is presented.

To estimate the form drag of the wing with extended flaps the local lift coefficient has to be converted to local angle-of-attack. Assuming that each local wing section has the same characteristics as the equivalent two-dimensional section it only requires the determination of section lift curves. Airfoil section lift curves for different effective flap angles for single-slotted and double slotted flaps with vanes were calculated with the NPLS programme and are shown in figure 27.18. For double slotted compound flaps the same lift curve slopes may be used.
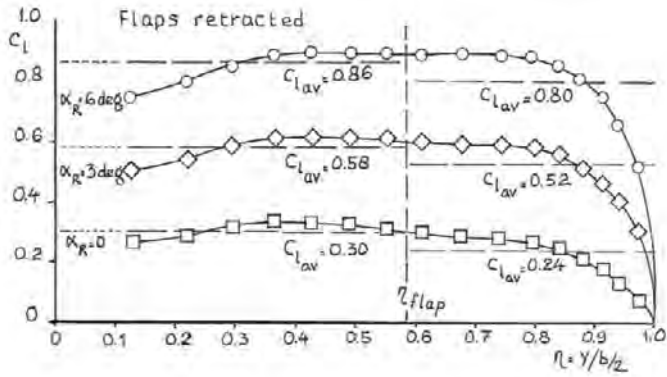
Figure 27.15 - Spanwise lift distribution with flaps retracted
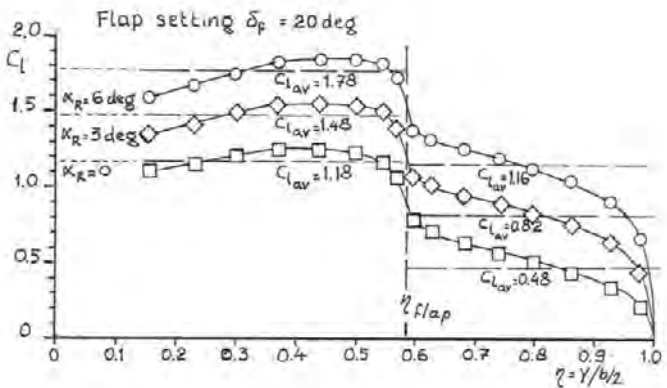
Figure 27.16 - Spanwise lift distribution with flap setting δ_f = 20 deg
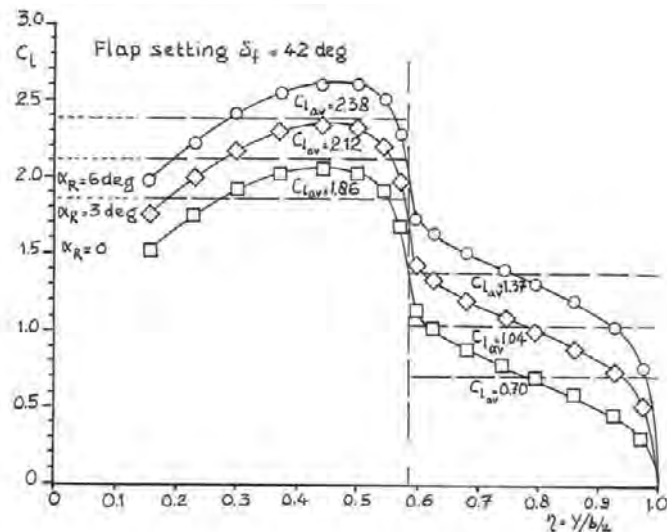
Figure 27.17 - Spanwise lift distribution with flap setting δ_f = 42 deg
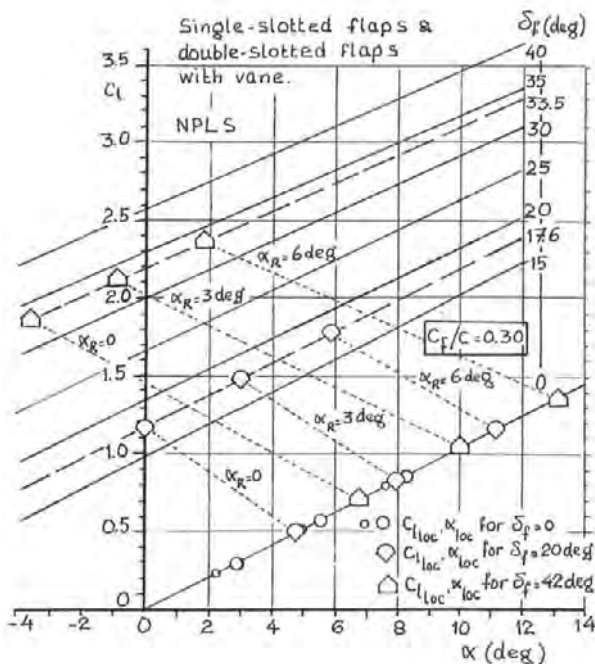
Figure 27.18 - Airfoil section lift curves for different effective flap angles. Source: Fokker Rep. A - 166 and A - 173.
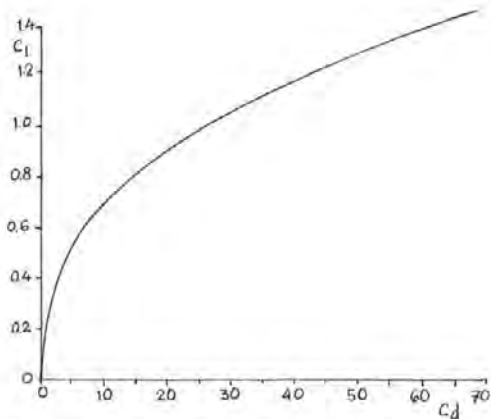
Figure 27.19 - Average lift-dependent drag of single airfoil sections. Source: Fokker Rep. A - 166 and A - 173.

A large amount of wind tunnel test data on two-dimensional airfoils with trailing-edge flaps have been analysed. Based on the combined drag data for three types of flap generalised curves were produced for the drag due to flap deflection as a function of angle-of-attack. These curves for single-slotted-flaps, for double-slotted flaps with a vane and for double-slotted compound flaps are presented in figures 27.20, 27.21 and 27.22.
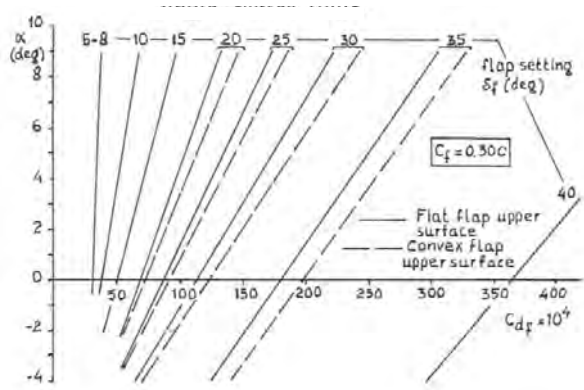
Figure 27.20 - Drag due to flap deflection, single-slotted flaps.
Source: Fokker Rep. A - 166 and A - 173.
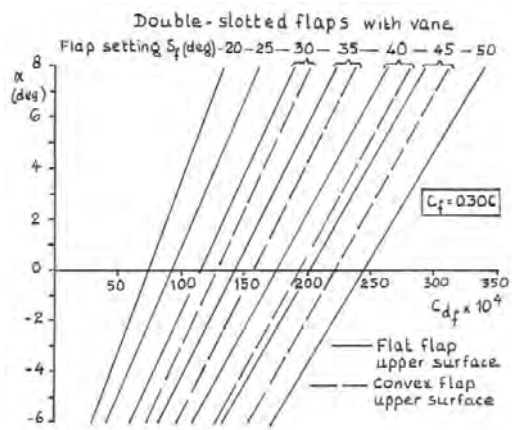
Figure 27.21 - Drag due to flap deflection, double-slotted flaps with vane.
Source: Fokker Rep. A - 166 and A - 173.
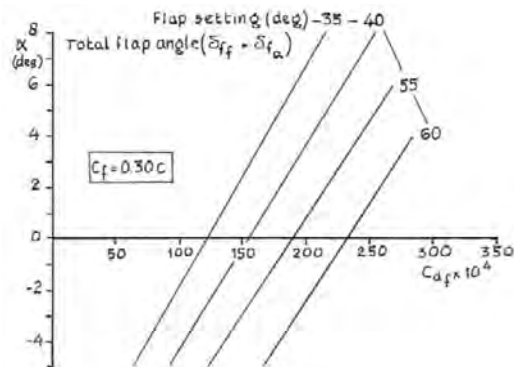
Figure 27.22 - Drag due to flap deflection, double-slotted compound flaps.
Source: Fokker Rep. A - 166 and A - 173.
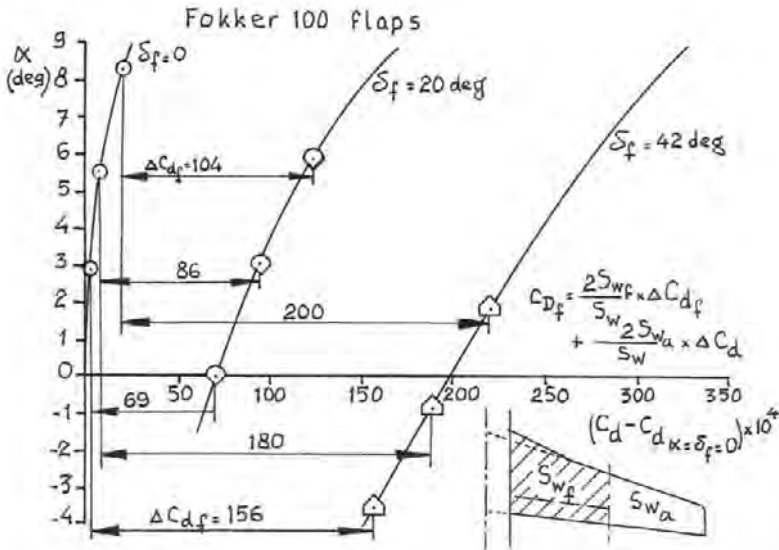
Figure 27.23 - Drag due to flap deflection at three angles-of-attack, Fokker 100.
Source: Fokker Rep. A - 166 and A - 173.

Figures 27.19 to 27.22 show airfoil section data. In figures 27.15 to 27.17 the **average local lift coefficient** is indicated for the inner wing part covered by the wing flaps and for the outer wing part where the aileron is situated at three aircraft angles-of-attack for the three Fokker 100 configurations under study. Assuming again that each wing section has the same characteristics as the equivalent two-dimensional section the **average local angle-of-attack** for inboard and outboard wing can be determined for the three aircraft angles-of-attack and aircraft configurations with the aid of figure 27.18.

With the appropriate curves from figure 27.19 to 27.21, figure 27.23 is constructed and the average drag coefficient due to flap deflection for the inner wing can be read off the figure for the nine conditions under consideration. The increase in drag of the outer wing due to flap deflection is determined via figure 27.19.

As indicated in figure 27.23 the total increase in wing profile drag due to flap deflection is then:

$$C_{D_f} = \frac{2S_{W_f}}{S_W} \times \Delta c_{d_f} + \frac{2S_{W_a}}{S_W} \times \Delta c_d \qquad (27.1)$$

The induced drag, as calculated with NPLS for the Fokker 100 with flaps retracted, and flap settings $\delta_f = 20$ deg and $\delta_f = 42$ deg is presented in figure 27.24.
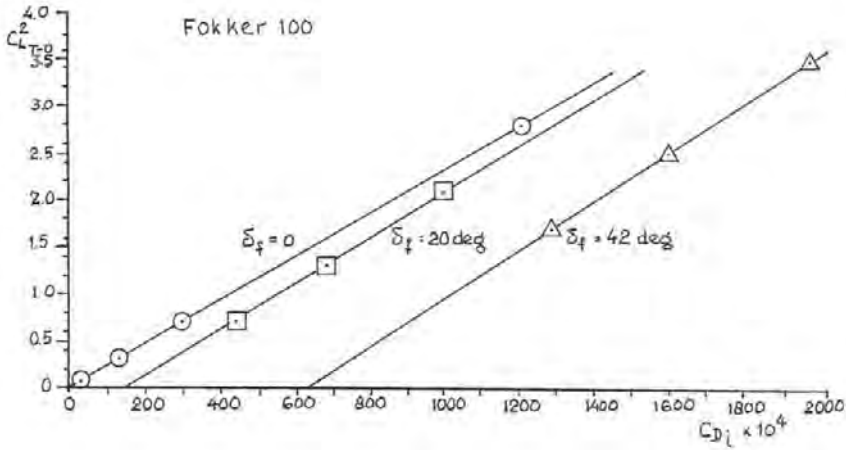
Figure 27.24 - Induced drag of the Fokker 100.

To find the trim drag the tail-off pitching moment coefficient curves are calculated. These are compared with wind tunnel data in figure 27.25 for a centre-of-gravity position $x_{C.G.}$ = 30 %. As the lift-drag ratio is of interest at the forward C.G. position, the pitching moment curves are shown in figure 27.26 for $x_{C.G.}$ = 7 %. The downwash angles as calculated and as found in wind tunnel tests are presented in figure 27.27. The stabiliser lift curve slope is calculated as $C_{L_{\alpha_h}}$ = 0.067 / deg compared to $C_{L_{\alpha_h}}$ = 0.065 / deg from wind tunnel tests. With these data the trim drag is obtained as

$$C_{D_{trim}} = \frac{1}{\pi A_W e}\left(C_{L_{T-O}}{}^2 - C_{L_{trim}}{}^2\right) + \frac{1}{\pi A_h e}C_{L_h}{}^2\frac{S_h}{S_w} + C_{L_h}\sin\varepsilon\frac{S_h}{S_W} \qquad (27.2)$$

where

$$C_{L_{trim}} = C_{L_{T-O}} + C_{L_h}\frac{S_h}{S_W} \qquad (27.3)$$

and

$$C_{L_h} = \frac{C_{M_{T-o,7}}}{\overline{V}_{h,7}} \qquad (27.4)$$

In equation (27.4), $\overline{V}_{h,7}$ is the stabiliser volume coefficient.

The trim drag is presented in figure 27.28. This figure also contains some generalised drag data on the drag of the flap track fairings for different flap positions.
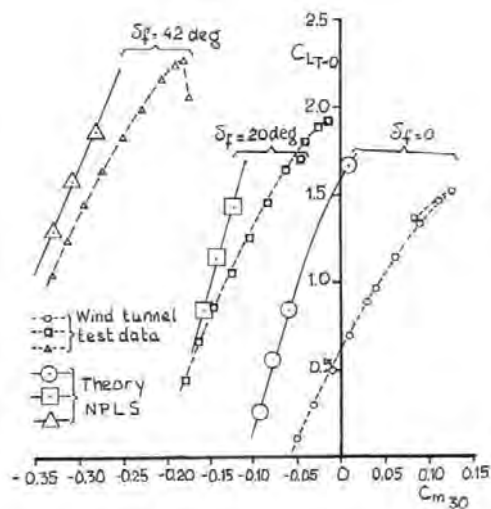
Figure 27.25 - Tail-off pitching moment curves. C.G. at 30% m.a.c.
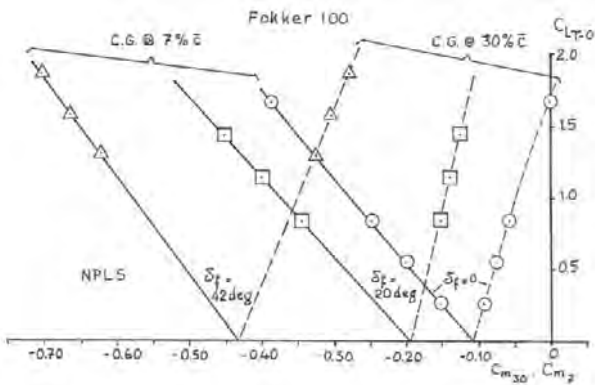
Figure 27.26 - Tail-off pitching moment curves. C.G. at 7% m.a.c.
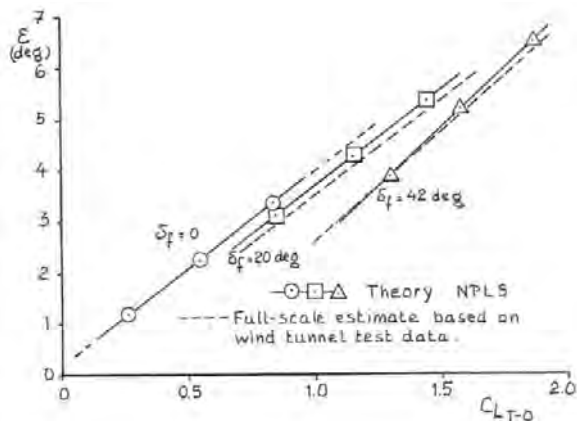
Figure 27.27 - Average downwash at the stabiliser position
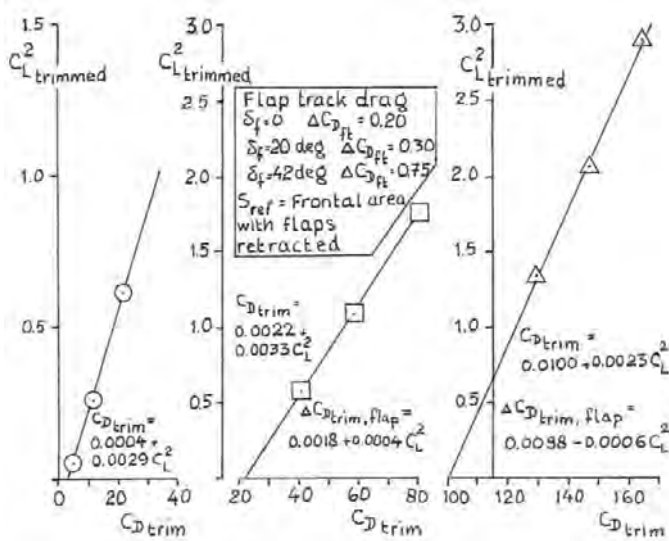
Figure 27.28 - Fokker 100 trim drag

The calculated increase in induced drag, wing profile drag and flap track fairing drag are shown in figure 27.29 in comparison to wind tunnel test data. At the medium flap angle the agreement is satisfactory but at the maximum flap angle a higher drag was found in the wind tunnel than in the theoretical analysis in particular at low angles-of-attack. As mentioned before this is due to the unfavourable flow around the rear fuselage and stub wings and nacelles leading to partial flow separation not considered in the theory.

Adding these drag increases, in combination with the extra trim drag given in figure 27.28 to the drag polar of the clean aircraft (obtained separately) produces the polars for the Fokker 100 presented in figure 27.30.
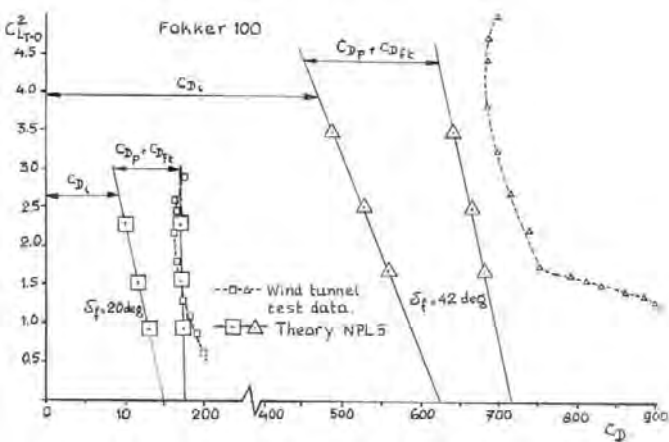
Figure 27.29 - Tail-off drag due to flap extension

The lift-drag ratio for the three Fokker 100 configurations analysed as obtained from theory, from wind tunnel tests and from flight tests are shown in figure 27.31.

A similar analysis was performed for the Fokker 50. The results are shown in figure 27.32.
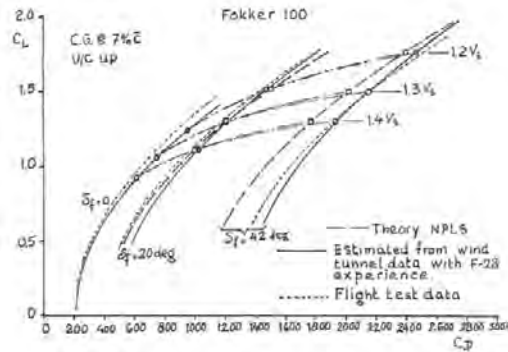
Figure 27.30 - Fokker 100 low-speed drag polars. Source: Fokker Reports A-166 and A-173
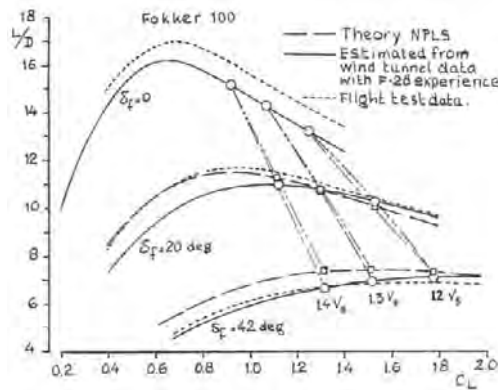
Figure 27.31 - Fokker 100 lift-drag ratios. Source: Fokker Reports A-166 and A-173
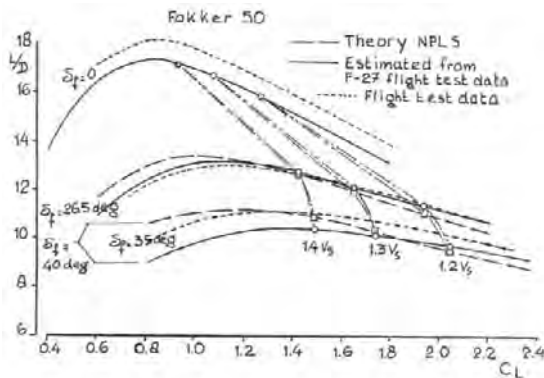
Figure 27.32 - Fokker 50 lift-drag ratios. Source: Fokker Reports A-166 and A-173
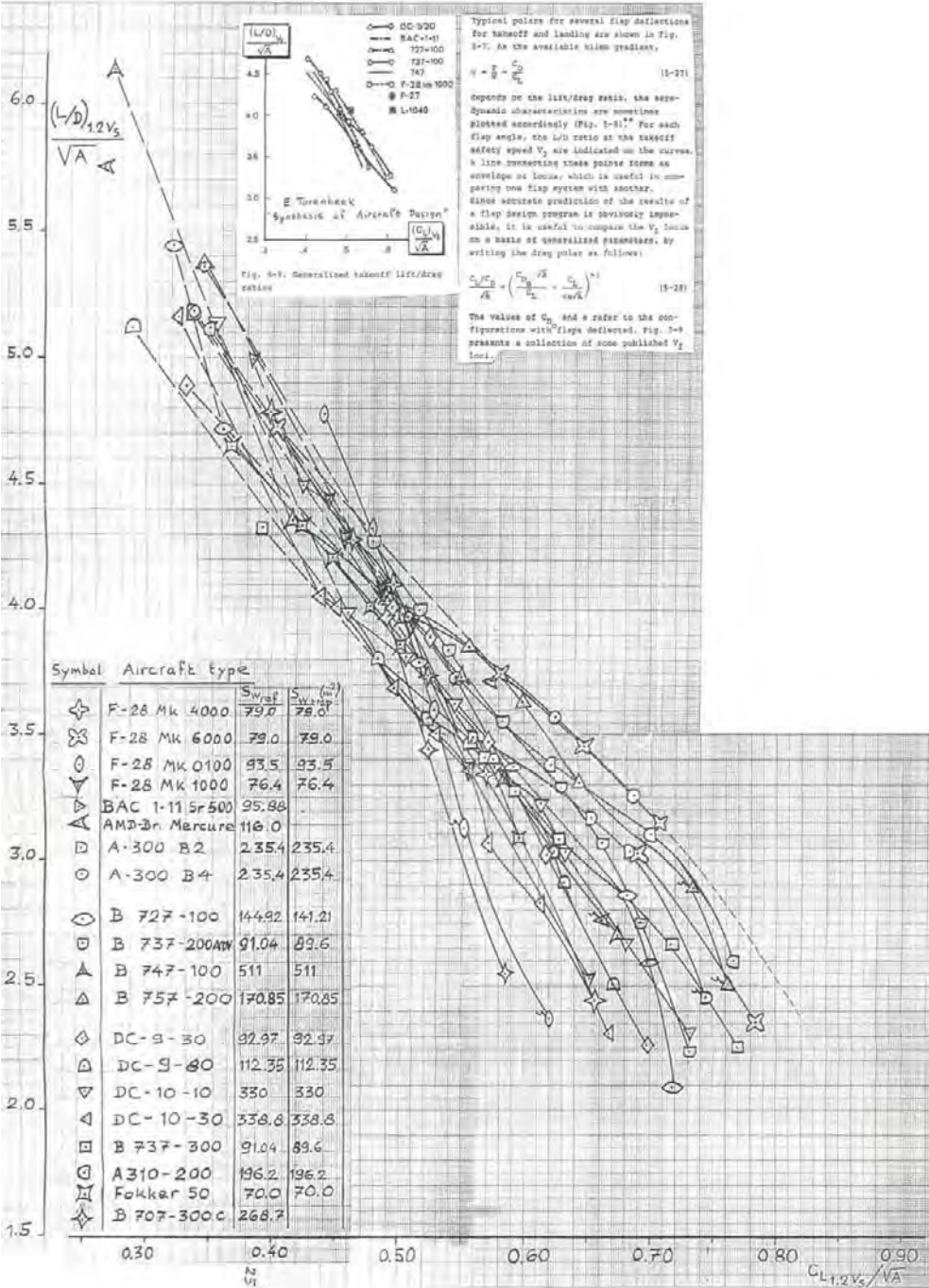
Figure 27.33 - Lift-drag ratios 1

Figures 27.31 and 27.32 demonstrate that the method described for estimating drag polars for high-lift configurations is useful for preliminary design purposes.

In figures 27.33 and 27.34 the lift-drag ratios as a function of $(C_L)_{1.2V_s}$ or $(C_L)_{1.13V_s}$ are collected for a number of civil jet transport aircraft. By dividing both the lift-drag ratio and the lift coefficient by $\sqrt{A}$ all data fall into a narrow band particularly for the newest aircraft.

Figure 27.34 - Lift-drag ratios 2
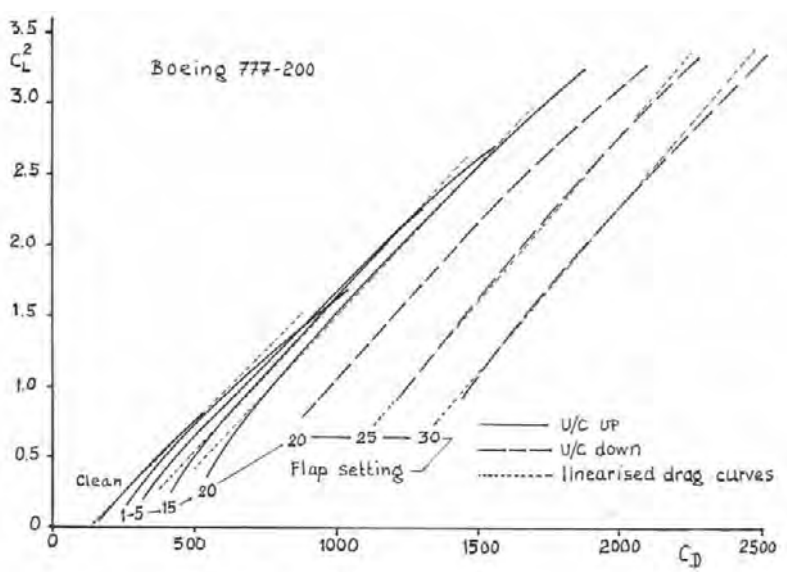
Figure 27.35 - Boeing 777-200 low-speed drag polars

This simplifies a first estimate of achievable lift-drag ratios for a new design. As the data refer to all flap settings, both for take-off and landing, additional information is required to determine the lift-drag ratios for landing at speeds 30 to 40 percent above V_S.

The low-speed drag polars for the Boeing 777 in figure 27.35 show that the slope of the C_L^2 –vs. – C_D curve decreases with increasing flap angle. This applies to most aircraft, the effect being stronger for rear-engined aircraft.
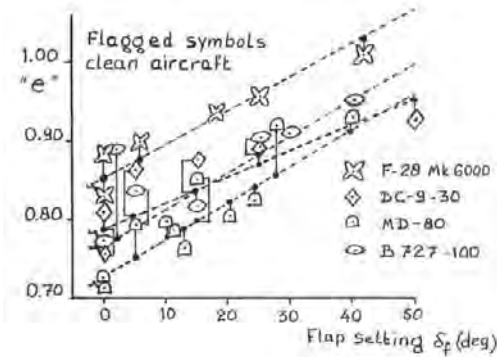
Figure 27.36 - Increase in "Oswald efficiency factor" due to flap deflection. Engines on the rear fuselage.
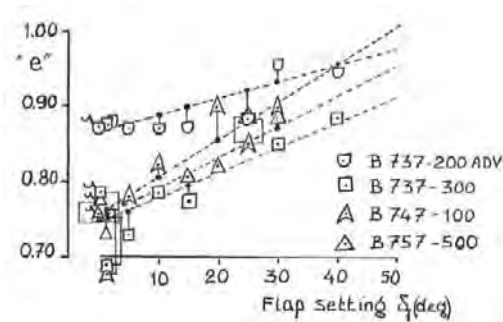
Figure 27.37 - Increase in "Oswald efficiency factor" due to flap deflection. Engines on the wing.

Figures 27.36 to 27.39 present some specific and also average increases in "Oswald efficiency factor" due to flap deflection. When the slope of the linearised C_L^2 – vs. – C_D curve for the clean aircraft configuration is known the average increase in "e" mentioned in figures 27.38 and 27.39 allow the estimation of the drag polar for speeds between $1.2V_S$ and $1.4V_S$ for every flap angle.

The estimation of the drag due to slat deflection is less straightforward. On many aircraft slats have different positions coupled to different flap settings for take-off or landing to minimise drag. On some aircraft, as on the Boeing 777, the slat gap is closed for the smaller take-off flap settings in the normal operating conditions but is opened automatically at angles-of attack close to the stall.

When the slat is fully deflected with a maximum slat gap $C_D = 0.0040$ to 0.0080 at angles-of-attack near V_2.

The first true application of CFD for design purposes started in the mid 1960's when panel methods, producing pressure distributions about arbitrary bodies in inviscid, incompressible flow became sufficiently developed to produce reliable results. At first only simple bodies or wing-fuselage combinations were analysed but gradually, with further developments both in hardware and in software the
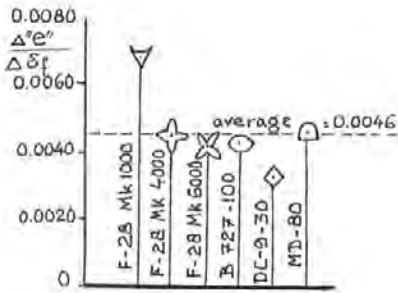
Figure 27.38 - Increase in "Oswald efficiency factor" due to flap deflection. Engines on the rear fuselage 2.
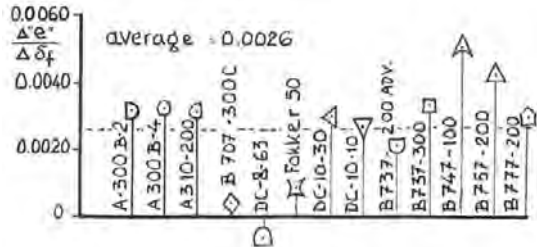
Figure 27.39 - Increase in "Oswald efficiency factor" due to flap deflection. Engines on the wing 2.

capabilities of panel methods were expanded. One of the first panel methods used by an aircraft manufacturer for design purposes was PAN AIR, developed at Boeing. Figures 27.40 to 27.46 show some results of CFD computations on high-lift configurations performed in he development of the Boeing 737 - 300 in the early 1980's. Many details in the geometry were modelled as accurately as possible at that time requiring the for those days large number of up to 2900 panels for the Flaps 15 configuration.
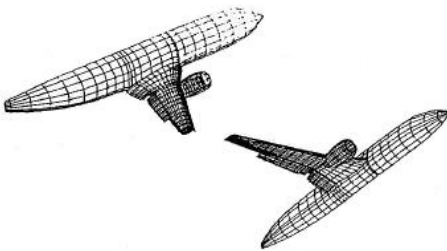
Figure 27.40 - Paneling - flaps 15 configuration
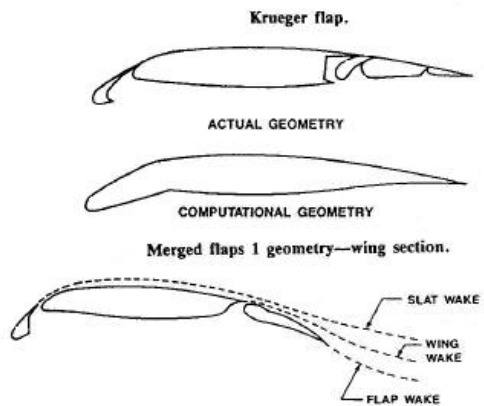
Figure 27.42 - Flaps 15 geometry and wakes. Source: AIAA Paper No. 86-1811
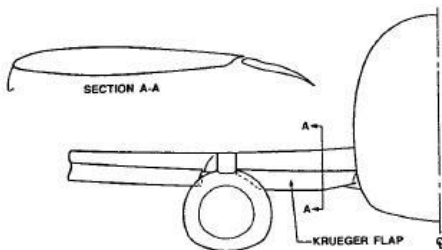
Figure 27.41 - Krueger flap. Source: AIAA Paper No. 86-1811

Although panel methods apply in principle only to incompressible flow an elementary compressibility correction, the Prandtl-Glauert correction, is often applied. This allows the analysis of pressure distributions with locally high-subsonic velocities as occur near leading edges.

Figures 27.43 and 27.44 show the chordwise pressure distributions at four wing stations for the two take-off configurations Flaps 1 and Flaps 15 both as calculated with PAN AIR and as obtained in the wind tunnel tests.
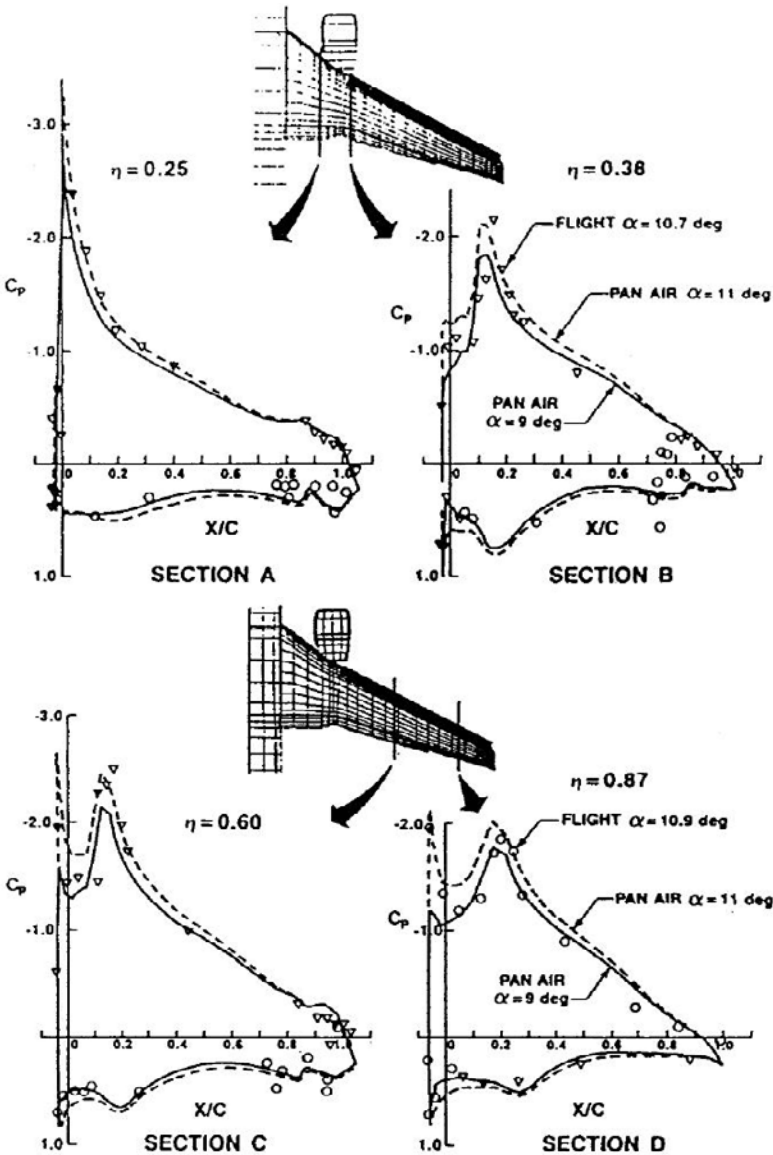
Figure 27.43 - Flaps 1 wing pressure distribution of a Boeing 737-300. Source: AIAA Paper No 86-1811
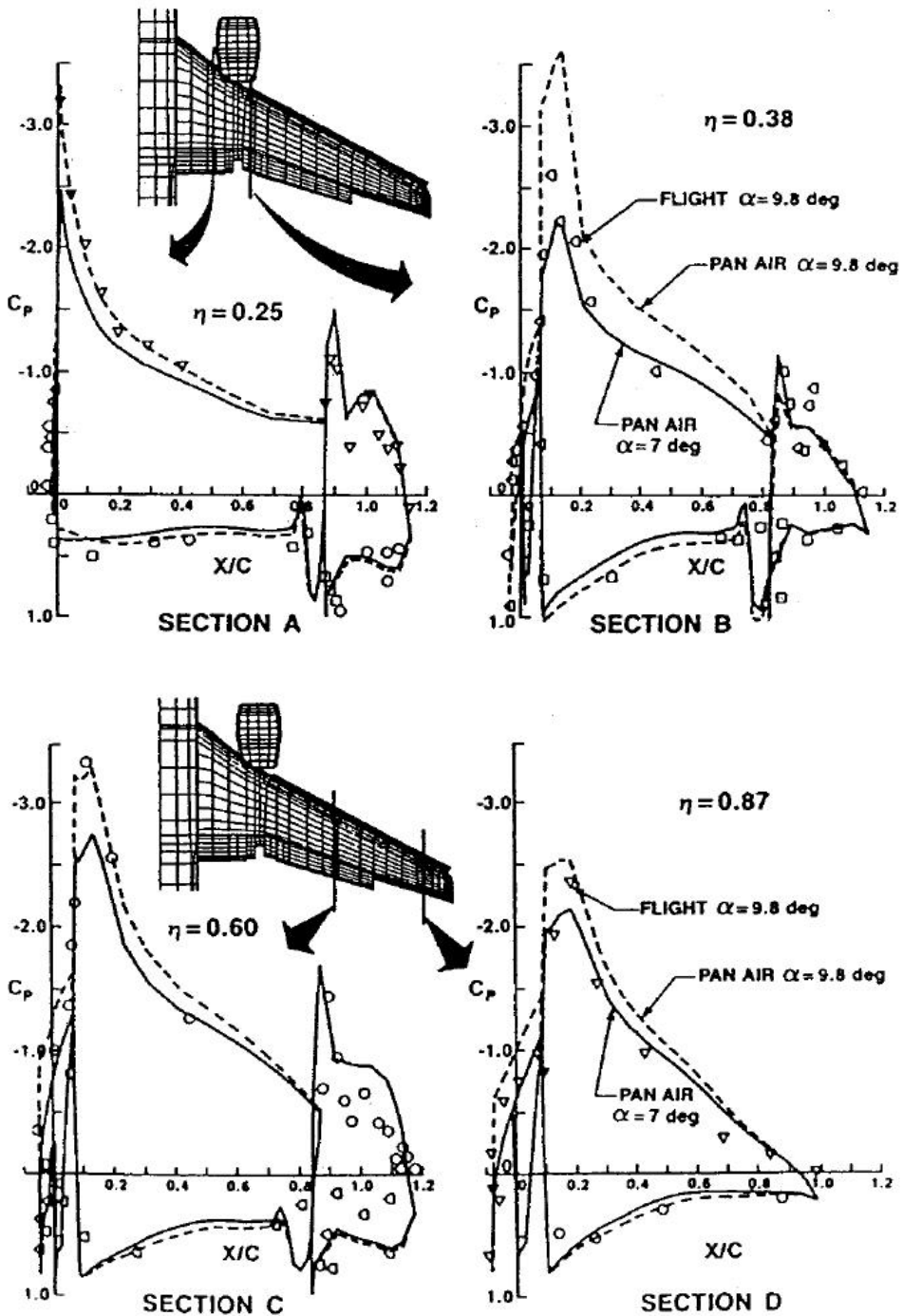
Figure 27.44 - Flaps 15 wing pressure distribution of a Boeing 737-300. Source: AIAA Paper No 86-1811

In panel methods the boundary conditions are formulated on the body surface. When no special measures are taken boundary-layer effects are not incorporated. This leads in the calculations to higher supervelocities than in real flow. This is clearly demonstrated in the chordwise pressure distributions and in the local lift curves. One way of reducing this shortcoming is to compare theory and experiment not at the same angle-of-attack but at the same lift coefficient. This leads to a satisfactory comparison of the chordwise pressure distribution and the spanwise distribution of the local lift coefficient particularly when also aero-elastic deformation is taken into account as shown in figure 27.45.

The main value of panel methods for the analysis of high-lift configurations lies in the ability to study the effect of geometry details on the local flow (if sufficiently fine panelling is used) coupled with short turn-around times. For accurate overall numerical data, in particular drag, even the far more sophisticated CFD methods are not yet entirely satisfactory and the final answer still has to come from the wind tunnel.
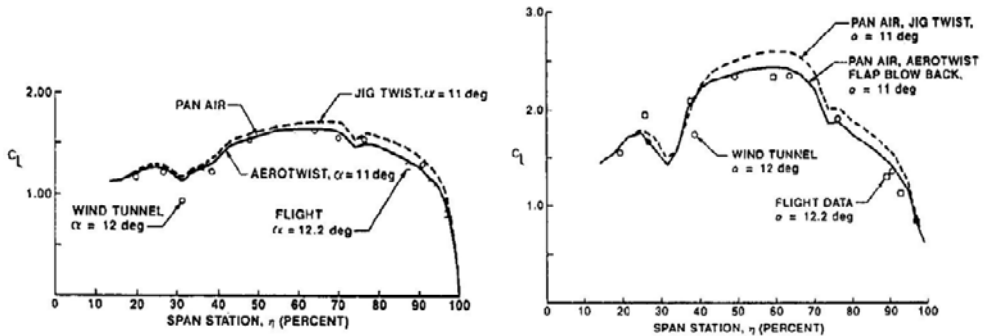
Figure 27.45 - Boeing 737-300 flaps 1 (left) and 15 (right) wing spanload. Source: AIAA Paper No 86-1811
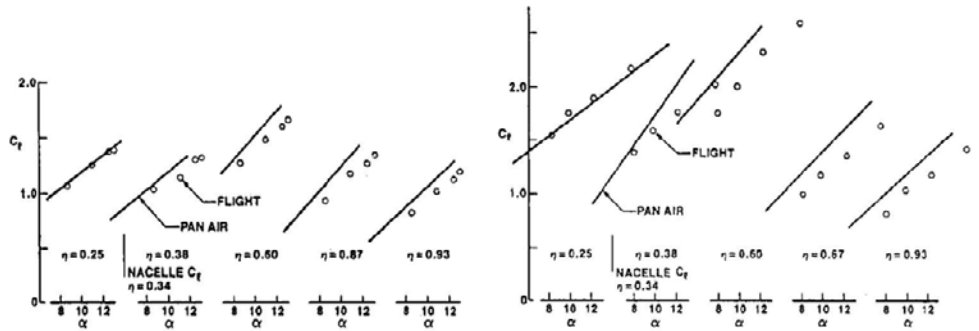
Figure 27.46 - Boeing 737-300 flaps 1 (left) and 15 (right) section lift. Source: AIAA Paper No 86-1811

PART 6

HIGH-SPEED AERODYNAMIC LIMITS

28 *The buffet onset boundary*

Whereas in chapter 17 the basic principles were explained of transonic flow separation and high-speed buffet in two-dimensional flow, in the present chapter the three-dimensional buffet onset boundary of actual aircraft will be discussed.

Just as the low-speed stall **the buffet onset boundary forms a limitation of the aircraft flight envelope**. That buffet indeed introduces a limitation is vividly explained in figure 28.2 by W. Bridgeman, test pilot of the Douglas Skyrocket - the first plane to reach Mach 2. The Skyrocket is shown in figure 28.1, although the text in figure 28.2 deals with a flight test of the Lockheed F-80 (figure 20.8).

As was described in chapter 19 a low-speed stall is characterised either by trailing edge flow separation or by the collapse of the leading-edge suction peak where in the latter case local Mach numbers as high as M = 1.5 may occur. Therefore the distinction between the low-speed stall and the buffet onset boundary is an artificial one because physically there is a gradual change from a flow condition where flow separation starts near the leading edge at M = 0.25 - 0.30 to a condition where flow separation starts further aft and an increase in angle-of-attack still produces some extra lift albeit with very strong buffet in particular on high-aspect-ratio wings.

Figure 28.1 - Douglas D-558-2 Skyrocket. Source: NASA

… stomach forcing against my chest, trying to suck in enough oxygen, I feel the fantastic speed she is gathering and I'm transfixed. I forget the Machmeter. What a way to commit suicide this would be. The earth remains a long way below. *This is too good to stop just yet, there is lots of time.*

A little more speed, a little faster. The jet dives powerfully, pushing the air out of her way as she plummets straight down. Accelerating as she plunges, churning up the air in her wake.

Then a sudden violent, hammering vibration jolts through the plane - a machine gun in rapidfire. I freeze. I'm stripped of ego, reduced to a startled child. She can't take the speed I've forced on her, she's hit the wall all right and she shakes on the edge of the destruction that surely lies ahead. The Sky God has caught us in his teeth and below me the earth quakes convulsively. She'll pull to pieces with this God-awful hammering… instinctively I want to slow down, to alter this wild dive to

an easy flight altitude… power off… dive brakes out. The hammering beating is growing stronger. It is as if my body were afflicted with uncontrollable convulsions. How can it stay together, how can it? Hang on! Treat her gently, very gently. Get the damned nose up. I pull hard at first… God, that makes it even worse, the jolting is more violent. Keep your head; hold what you've got. There can be no increase in the angle of the dive. The wings will snap off for sure.

What can I do to slow her down? Think. What did they say Ed did wrong when he "dug a hole" last month? What did they say in the hangar about it? Remember the answer from somewhere in all the hangar talk. Remember a hundred things. What one of those hundred answers have I neglected to recall? One is surely the answer. The buffet is a continuous bolt of electricity buzzing through me. We're picking up speed all the way down.

For God's sake, try something! Pull a little and ease a little - that's it - she takes it. A little more, ease up, not too far! Leave enough room so you can back out quick if you're wrong. Anything to change the radical dive angle to something reasonable. That's it. Pull back, take the hard jolt that bounces the airplane, ease up. Got the nose

up ten per cent that time; again, pull back… oh God, that hammering… now ease. Once more pull… ease up. The diving, buffeting plane that carries me in its pod tears wildly through several thousand feet more and the indicated air speed moves continuously up, the bottom of the ride is coming up closer.

The spring is being wound too tight; something is bound to give momentarily. Ways to save the plane are clouded now with thoughts of escape. How long can I wait before I get out, how many things can I try before I open the canopy and let her go? When is the proper moment of surrender to this thing? Just a little bit longer. Instinctively I feel I am handling the plane properly, but the ground is coming closer. I had better be right. If I decide to give her up I will open the hatch, kick the stick forward with my body-the negative G's enforced by this maneuver will hurtle me out into the air free of the tail section. Optimism! Chances of getting out are slim at this speed.

I wait. I lift the nose a little. The awful shaking is dying out! A little bit more… hold it! Suddenly it is quiet. Why? As abruptly as it began the buffeting stops. The ride is over; the wings stayed on. My head rolls forward on my chest; I can hear myself breathing deeply from the oxygen mask. Before my eyes close, I see the Machmeter needle slipping back .78, .77, .76, .75 - there's the answer to the giant hand that shook the dive into a nightmare. The F-80 hums evenly now as if the 30 seconds never happened. I remember Roth's last warning: "The limiting Mach number on the ship is .8." The ship will buffet on the tender edge of the speed of sound. Inadvertently I have driven into an aerodynamic fact, a truth I was aware of but never bothered to investigate. If I had understood it more thoroughly, the compressibility phenomenon would not have occurred. I am a fool. This time an intuitive feeling of the plane's reactions got us through, and as she reached lower altitudes, although curiously, she picked up speed, she ran away from the critical Mach number. Of course, at altitude you hit the high Mach numbers with less true air speed than in the denser warmer air closer to the ground!

Figure 28.2 - Experiencing loss of control and surpassing the buffet-onset boundary in the Lockheed F-80 Shooting Star. Source: 'The lonely sky' by W. Bridgeman, 1955.

Airworthiness regulations require that in normal operation of civil transport aircraft the buffet onset boundary is not surpassed.

Buffet may not intrude the normal operating envelope of the aircraft. Buffet can thus only appear during a pull-up or turn manoeuvre. **The certification regulations require the lift coefficient in operational cruise conditions to be limited such that a load factor of n = 1.3 can be reached without encountering buffet.**
Figures 28.3, 28.4 and 28.5 illustrate this by showing the margin in lift coefficient between normal flight conditions and the buffet onset boundary.
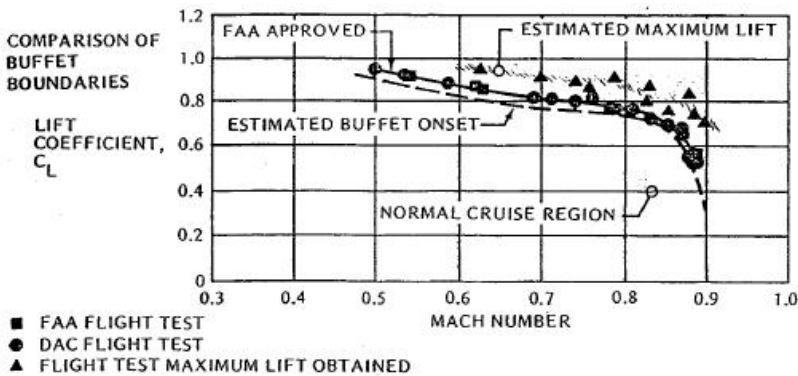
Figure 28.3 - Comparison of buffet boundaries for the Douglas DC-10.
Source: Douglas Flight Approach, 1972
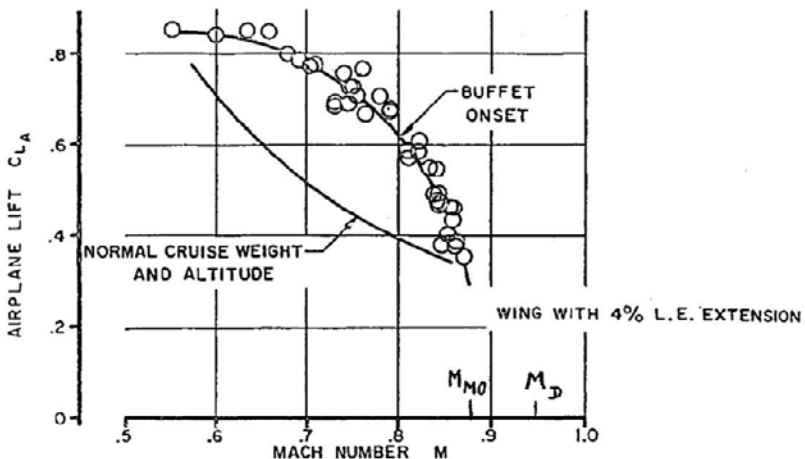
Figure 28.4 - DC-8 High speed buffet boundary with revised wing leading edge.
Source: SAE Paper No. 237-A, 1960
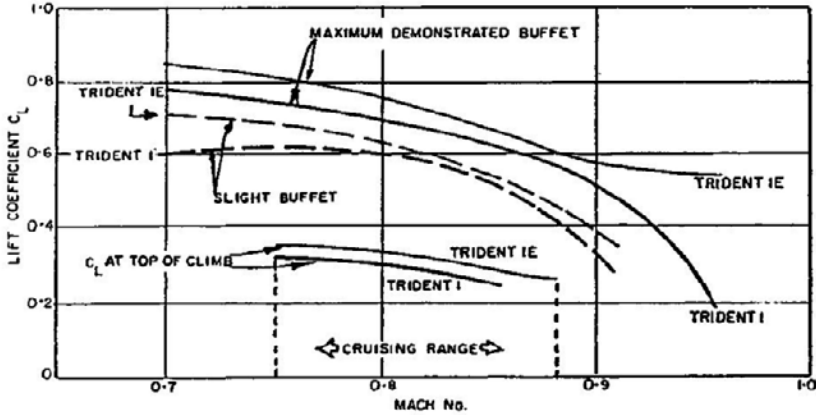
Figure 28.5 - Hawker-Siddeley Trident buffet boundary. Source: Aeron. Journal, Nov. 1969

Due to the ever-present pressure on payload-range and cruise altitude capability, improvement of the buffet onset boundary is often one of the prime requirements in the development of a new member in a family of aircraft as demonstrated in figures 28.5 for the HS Trident, 24.64 for the Boeing 737 and 24.114 for the A300.
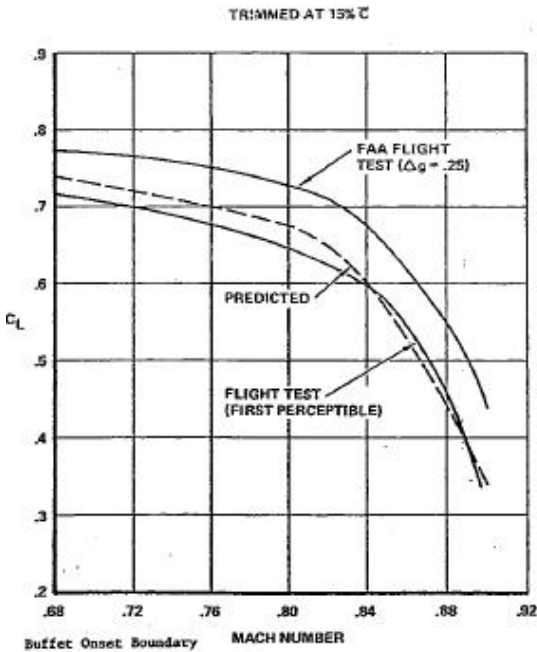
Figure 28.6 - Buffet onset boundary for the Lockheed L-1011-1. Source: AGARD CP-242, Paper No. 21

The buffet onset boundary is not a uniquely defined physical phenomenon. Flow separation leads to vibration and it is the latter which is recorded either by a human or by an accelerometer. This means that the intensity of the buffet as perceived by a human or recorded by test equipment depends on their position relative to the nodes and loops of the vibrating structure. Certification authorities accept buffet onset boundaries based on accelerometer recordings at the pilot's seat position with peak-to-peak amplitudes n = 0.25g as shown in figure 28.6.

With modern CFD methods buffet onset boundaries can be predicted with reasonable accuracy .

Even a basically full-potential programme as XFLO-22 produces reliable pressure distributions on a wing with peak local Mach numbers as high as $M = 1.50$ perpendicular to the shock wave. With an empirical correlation between the Mach number at which flow separation occurs and the chordwise shock wave position as determined from
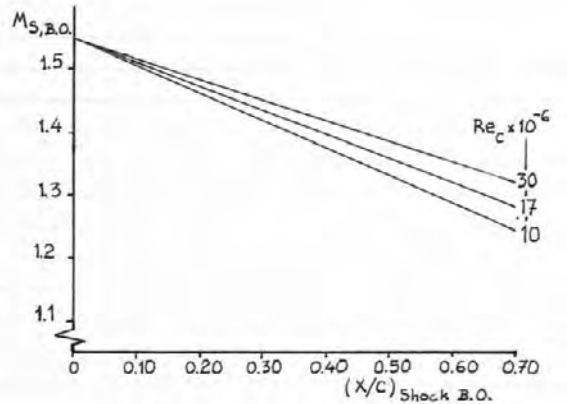
Figure 28.7 - Empirical relation between shock wave position and peak Mach number just in front of the shock wave in two-dimensional flow. – See also figure 17.7.
Source: Fokker Rep. A – 143

numerous tests on two- and three-dimensional models and presented in figure 28.7 the buffet onset boundary can be determined. Alternatively, buffet onset may be determined with three-dimensional boundary-layer programmes with a suitable flow separation criterion. For the Fokker 100 the buffet onset boundary has been determined according to the latter method and is shown in figure 28.8, together with wind tunnel and flight test data and, based on the wind tunnel tests, the full-scale pre-flight prediction.
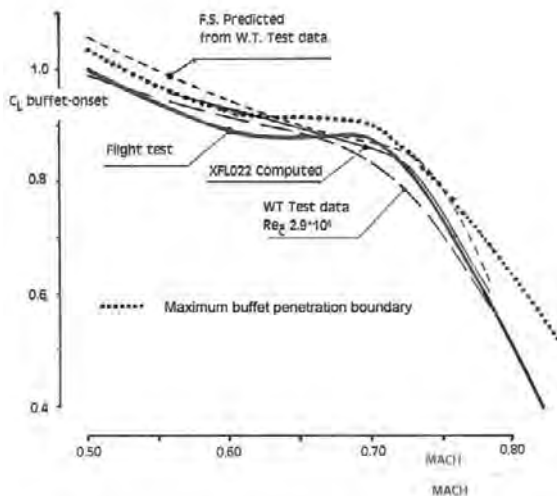
Figure 28.8 - Fokker 100 buffet onset boundary.
Source: Fokker Rep. L-28-448

In the wind tunnel the buffet onset boundary may be determined from a number of characteristics as shown in figure 28.9:

1. Breaks in C_L-α, C_M-α or C_X-α curves.
2. Trailing-edge pressure divergence on the outboard wing.
3. Divergence of dynamic wing root strain-gauge recordings.

As other aerodynamic phenomena where the boundary layer is involved the onset of buffet depends on the Reynolds number. For full-scale predictions wind tunnel test data have to be extrapolated to full-scale Reynolds numbers.
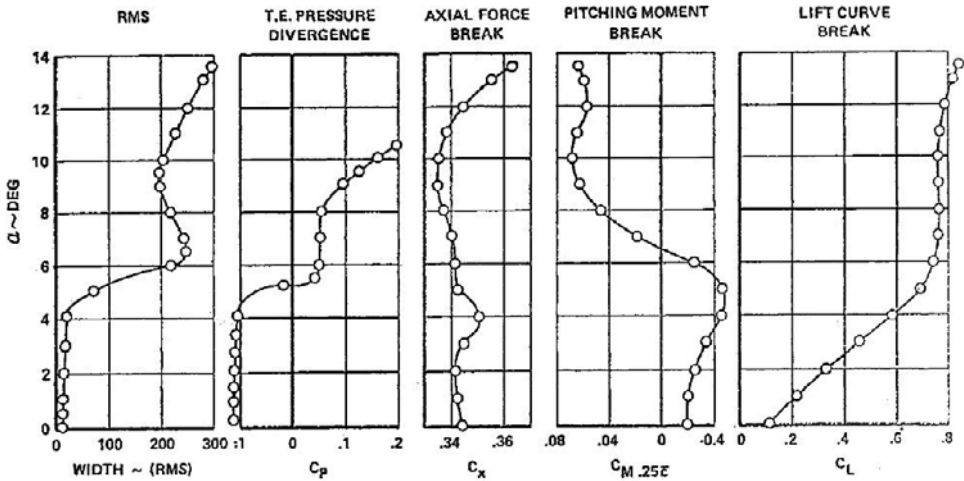
Figure 28.9 - Buffet onset prediction technique. Wind tunnel data at $R_N = 3.5 \times 10^6$/ft, Mach = 0.84. Source: AGARD CP-242, No. 21

On modern supercritical airfoils particular attention must be paid to the boundary layer condition ahead of the shock wave at buffet onset as depending on boundary-layer thickness and condition the shock wave will have a different strength and position. In particular when the boundary-layer ahead of the shock wave is laminar erratic conclusions may be drawn. Therefore wind tunnel tests are performed with different positions of boundary-layer transition strips in order to obtain insight in the effect of turbulent boundary layer thickness at the foot of the shock wave on the buffet onset boundary.

Although the structural characteristics of wind tunnel models and full-scale aircraft differ widely fortuitously the relation between the frequencies of the pressure fluctuations in the separated flow and the natural frequencies of the structure of wind tunnel models and full-scale aircraft are comparable. Therefore strain-gauge recordings of the root bending moment on a wind tunnel model are a reliable indication of buffet onset.

The airworthiness requirements demand that if the buffet regime is penetrated this should be in fully controlled flight. Flow separation on a swept wing should therefore start not too far outboard, to prevent strong roll or pitch-up tendencies. For certification the buffet regime is deliberately penetrated in flight to demonstrate acceptable flight handling characteristics and the maximum buffet penetration boundary or maximum demonstrated lift boundary has to be recorded as indicated in figures 28.3. and 28.8.

Supercritical airfoil technology has not only allowed higher design lift coefficients but has also led to improved buffet onset boundaries compared to earlier generations of transport aircraft as shown in figures 28.10 to 28.13.
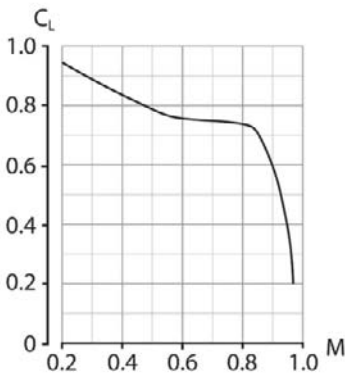
Figure 28.10 - Boeing 747-400 buffet onset boundary
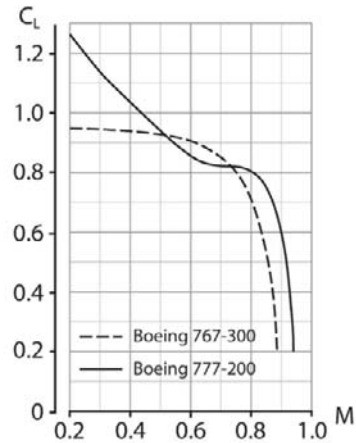
Figure 28.11 - Boeing 767-300 and Boeing 777-200 buffet onset boundary
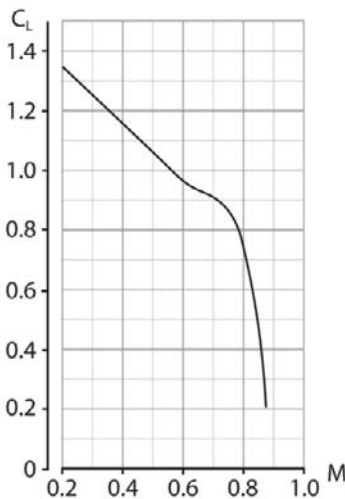
Figure 28.12 - Boeing 737-800 buffet onset boundary
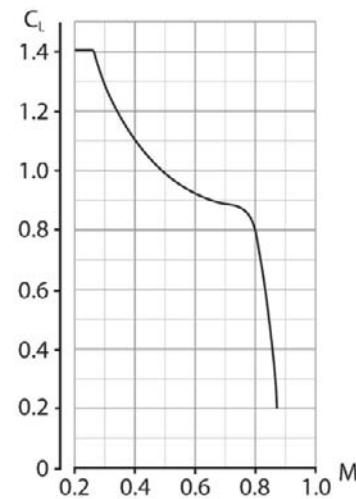
Figure 28.13 - Airbus A320 buffet onset boundary

29 *Flight characteristics between M$_{MO}$ and M$_D$*

Although civil transport aircraft normally do not exceed the Maximum Operating Mach Number (M$_{MO}$) in day-to-day operation these aircraft are still required to comply with certain minimum requirements on flying characteristics above M$_{MO}$.

From time to time system failures or severe atmospheric upsets cause the aircraft to pitch down and to exceed M$_{MO}$ in a dive. Examples of this are given in figure 29.1 and 29.3.

Airbus Industrie officials currently are reviewing crew training procedures following a recent incident involving an Air France Airbus en route from Paris to Tel Aviv. Trim system for the fully trimmable horizontal stabilizer slowly trimmed the stabilizer to a nose-down position while the aircraft was cruising with the autopilot engaged. When the trim force reached the limits of the autopilot's authority, the autopilot automatically disengaged, and the aircraft entered a steep dive due to the position of the horizontal stabilizer.

Airbus Industrie officials said a fix had been adopted for the autopilot system to avoid this type of incident, but the fix had not been installed on this particular aircraft. The pilot pullen 1.6 to 1.7g to recover the aircraft from the dive, and a landing was made at Marseilles. Other than the fix to the autopilot, no other service was needed on the aircraft to put it back into operation.

But Airbus officials said that the difficulties of the crew in coping with the incident suggested that not enough emphasis during crew training had been put on manual backup systems available to the aircraft in the event of failure of the automatic systems, and a solution to this is now being studied.

Figure 29.1 - Why acceptable flight handling characteristics are required above M$_{MO}$.
Source: Aviation week and space technology, October 20, 1975

Therefore the civil airworthiness requirements (for large aircraft with W > 5,700 kg FAR 25 or CS 25, formerly JAR 25) require that the aircraft demonstrates acceptable flight characteristics up to the design Dive Mach Number M$_D$ (M$_D$ = M$_{MO}$ + 0.05 to 0.09). Furthermore, it is common practise to design the wing such that the design Mach number M$_{design}$ = M$_{MO}$ - 0.03 to 0.05.
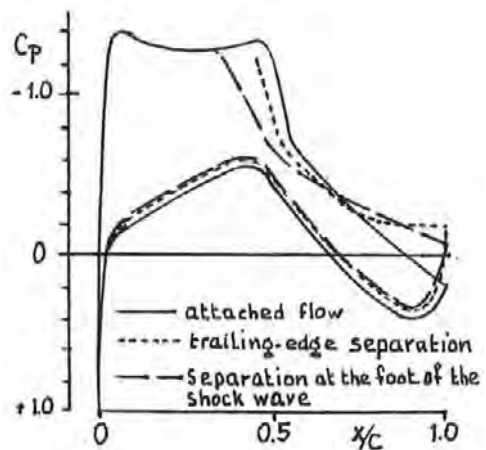
Figure 29.2 - Change in pressure distribution when increasing the speed above the design speed

When a jet transport aircraft is flying at or near its design condition and the flight speed is increased the pressure distribution on the wing changes rapidly.

Initially the shock wave moves rearwards over a part of the wing and the pattern of the wing upper surface pressure distribution changes as shown in figure 29.2. When the speed is further increased the boundary layer will separate behind the shock wave and the suction forces over the front part of the wing will decrease further. On the lower surface the supervelocities increase in a regular pattern until, in particular at low lift coefficients, locally sonic speed is reached behind which point the flow will further accelerate until a shock wave appears. This is illustrated in figure 17.2. This different development of upper and lower surface pressure distribution causes, in particular on swept wings, that the development of the tail-off

PanAm 707 Dives 29,000 ft

Aircraft N712PA was at 35,000 ft. flying from London to Gander, Newfoundland, positioned at 52.5 deg. N., 40.5 deg. W., when the dive occurred at approximately 2200 Greenwich Mean Time. At cruise, outside air temperature was -55C, cruise speed was Mach .82, gross weight was between 190-195,000 lb. The 707 was pulled out at 6,000 ft., following which it was flown manually and landed at Gander.

Capt. Lynch said the plane experienced some buffeting and may have reached Mach .94 in the dive. Company spokesman said a portion of non-structural material tore loose, but had no effect on flight characteristics.

Pilots and members of PanAm's egnineering staff last week met with technicians from Bendix-Eclipse Pioneer division, which manufacturers the PB-20D autopilot used on all 707s. Unit includes an approach coupler, yaw damper and Mach trim.

Boeing says the 707 can be operated safely without Mach trim but closer pilot attention is needed. Mach trim is automatically shut off when the autopilot is operating because static longitudinal stability is guaranteed by the autopilot.

In its official statement, Boeing reported that the autopilot disconnected in the Atlantic incident and lack of Mach trim combined with crew inattentiveness resulted in the near-sonic dive.

Figure 29.3 - Upset due to autopilot disconnect. Source: Aviation week, Feb. 9 and March 23, 1959

pitching moment at different angles-of-attack or lift coefficients with varying Mach number may show large variations for different wing geometries.

Due to this rapidly changing wing pressure distribution not only the tail-off pitching moment changes over a small range of Mach numbers but also the tail-off lift curve, the downwash characteristics, and, above very high Maximum Operating Mach Numbers, also the stabiliser lift curve.

All these changing characteristics cause that the tail-on pitching moment shows considerable variations between different aircraft designs. On most aircraft this leads to an unstable longitudinal stability with a diving tendency known as "tuck under" but sometimes a slight pitch-up occurs. Minimising the

adverse effects of transonic wing pressure distributions is one of the challenges of modern aerodynamic design.

To illustrate the different transonic pitch characteristics that transport aircraft may exhibit some high-speed aerodynamic characteristics are presented for the Fokker F-28 and Fokker 100. Figures 29.4 through 29.15 show the tail-off and tail-on pitching moment curves and some additional aerodynamic characteristics for both aircraft.

As mentioned before, in the design of the F-28 much emphasis was placed on benign flight characteristics in the transonic regime without a Mach trim compensator. This was stimulated by occurrences such as described in figure 29.3. Figure 29.11 shows that the tail-off pitching moment shows relatively little variation over the critical Mach number range due to the chosen design wing pressure distribution shown in figure 29.16. Consequently the tail-on pitching moment behaviour is acceptable although the tail-off lift curve and the downwash show significant variations. The variation of the tail-off lift curve slope with speed deviates from the Prandtl-Glauert rule and the aerodynamic centre and neutral point positions vary slightly.
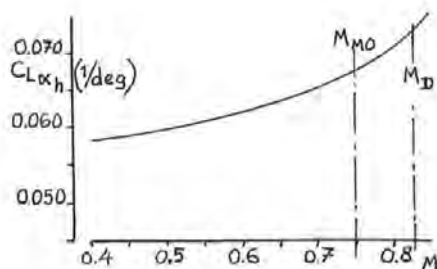
Figure 29.4 - Fokker F-28 stabiliser lift curve slope
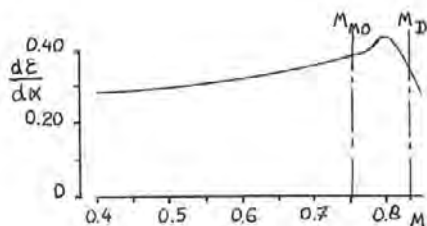
Figure 29.5 - Fokker F-28 downwash gradient
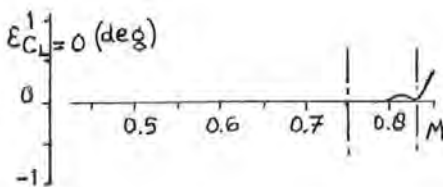
Figure 29.6 - Fokker F-28 downwash angle
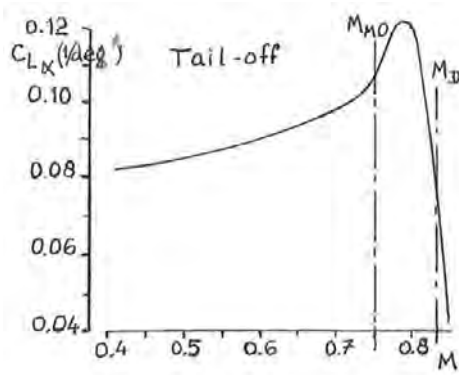
Figure 29.7 - Fokker F-28 tail-off lift curve slope
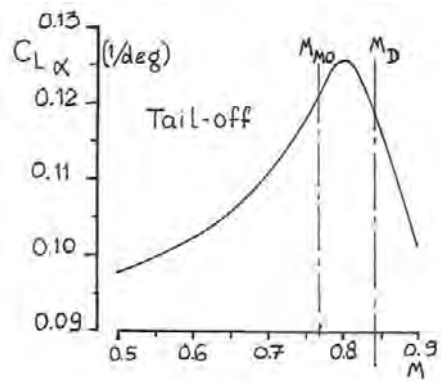
Figure 29.8 - Fokker 100 tail-off lift curve slope
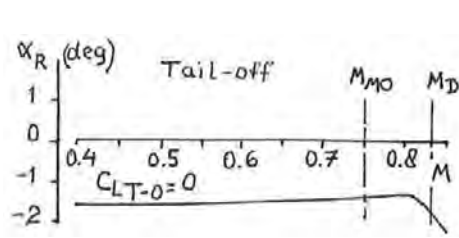
Figure 29.9 - Fokker F-28 tail-off angle-of-attack
for zero lift
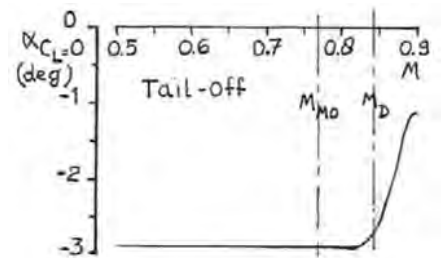
Figure 29.10 - Fokker 100 tail-off angle-of-attack
for zero lift

Figures 29.17 and 29.18 illustrate that the design goal was achieved and that although slight control force reversal occurs the airworthiness authorities agreed that the F-28 shows acceptable longitudinal characteristics between M_{MO} and M_D without a Mach trim compensator.

The situation is different on the Fokker 100. The highly-modified design wing pressure distribution which produced a considerable reduction in cruise drag also produced a more conventional pitch behaviour between M_{MO} and M_D. Figures 29.8, 29.10, 29.12 and 29.15 show the much more pronounced variations in the aerodynamic characteristics in the transonic speed range. To illustrate the consequence of this on the longitudinal stability two flight conditions are considered, a condition at a given aircraft weight and flight altitude at $M = 0.75$ and $C_L = 0.52$ and a condition reached after a shallow rectilinear dive at $M = 0.84$ and, due to the higher dynamic pressure, $C_L = 0.40$.
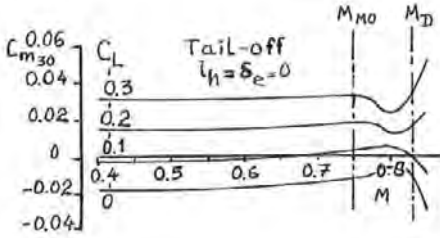
Figure 29.11 - Fokker F-28 tail-off pitching moment
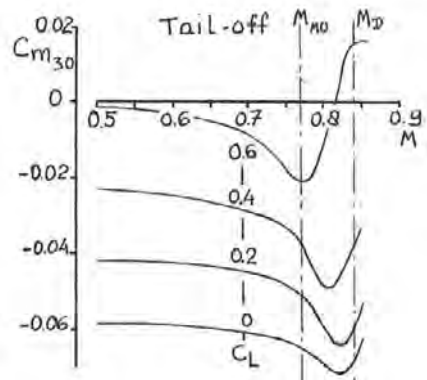
Figure 29.12 - Fokker 100 tail-off pitching moment
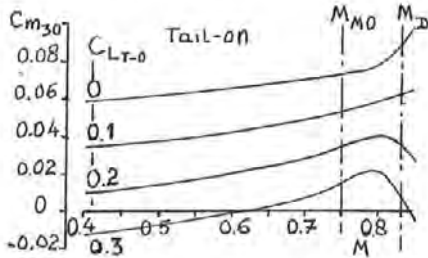
Figure 29.13 - Fokker F-28 tail-on pitching moment
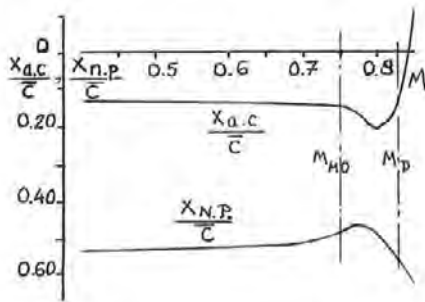
Figure 29.13 - Fokker F-28 aerodynamic centre and neutral point
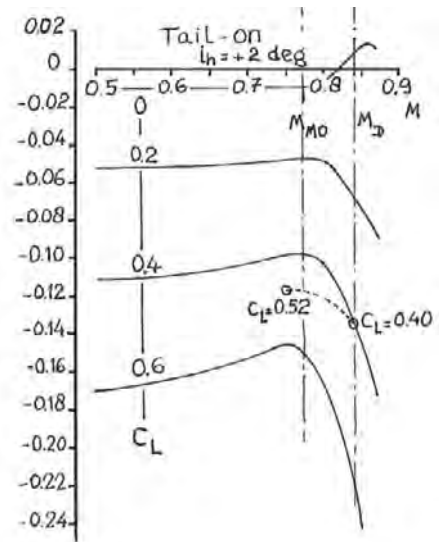
Figure 29.15 - Fokker 100 tail-on pitching moment

If the aircraft was in trim at M = 0.75 and C_L = 0.52 (with a stabiliser setting clearly more negative than i_h = +2 deg mentioned in figure 29.15) at M = 0.84 and C_L = 0.40 a change in pitching moment coefficient ΔC_m = -0.02 would have to be compensated by a further change in stabiliser setting, about Δi_h = -0.3 deg (stabiliser leading edge down) to be in trim again. If the change in stabiliser setting would be slightly larger some downward elevator deflection would be required to obtain a state of equilibrium again and the aircraft would have positive stick force stability over the complete speed range considered.
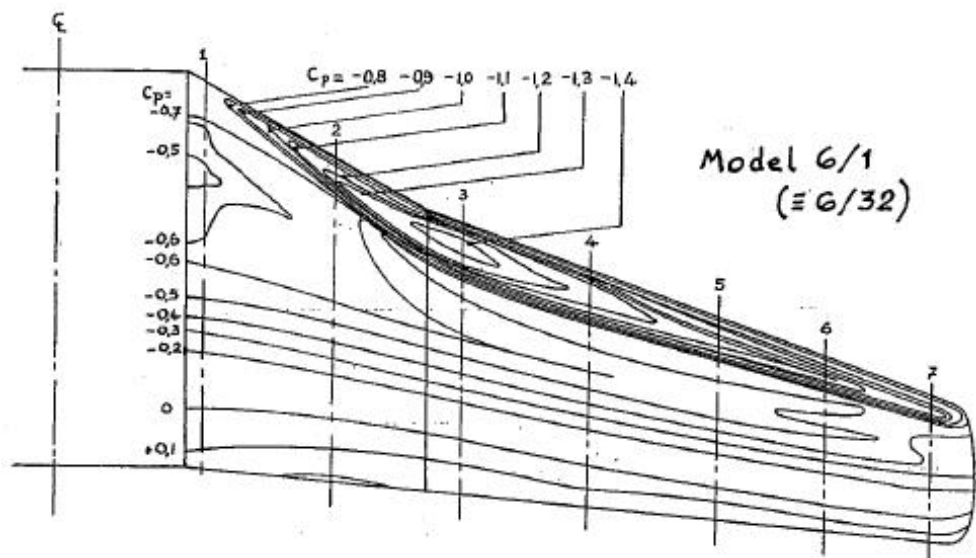
Figure 29.16 - Fokker 28, isobar pattern on wing upper surface, M = 0.745, C_L = 0.255
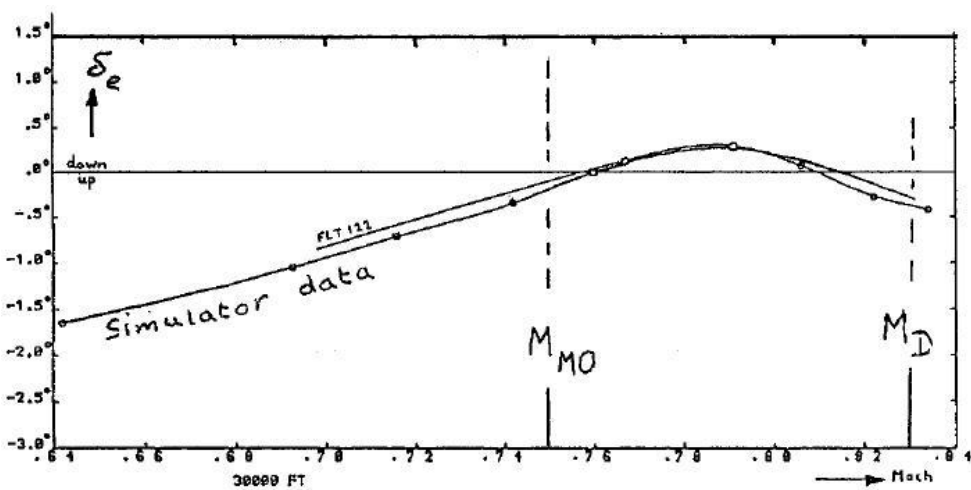
Figure 29.17 - Fokker 28 longitudinal characteristics between M_{MO} and M_D; δ_e vs Mach
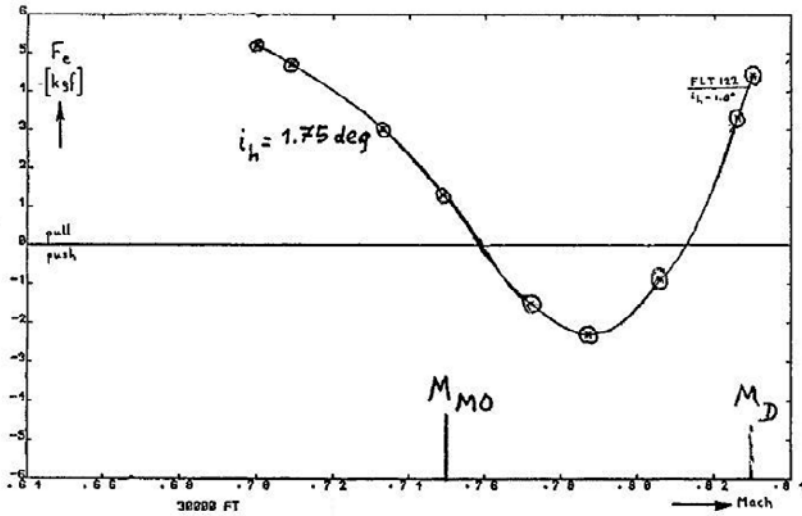
Figure 29.18 - Fokker 28 Longitudinal characteristics between M_{MO} and M_D; F_e vs Mach

The Mach trim compensator on the Fokker 100 functions exactly along these lines as illustrated in figure 29.19. Between M = 0.50 and M = 0.85 the Mach trim compensator changes the stabiliser setting automatically with varying Mach number according to a fixed programme independent of the pilot around the stabiliser setting for trim selected by the pilot.

Contrary to the situation on the F-28 a Mach trim compensator was not seen as a serious disadvantage, firstly because the reliability and design architecture of such devices had improved considerably in 20 years time and secondly because it was a relatively simple addition to the highly sophisticated Automatic Flight Control Augmentation System (AFCAS) used in the Fokker 100.

Most early or modern jet transport aircraft are equipped with Mach trim compensators. On many aircraft they already provide a significant input at the lowest cruise Mach numbers. On the Boeing 707 in cruise at high altitude at M = 0.82 the Mach trim compensator was already required when not on autopilot (see figure 29.3) although M_{MO} = 0.90.

Trimmed condition: 310 kCAS   24000 ft M.73
Configuration: $W_{\dot{e}}$ = 41500 kg c.g. 37,6% DF = 0
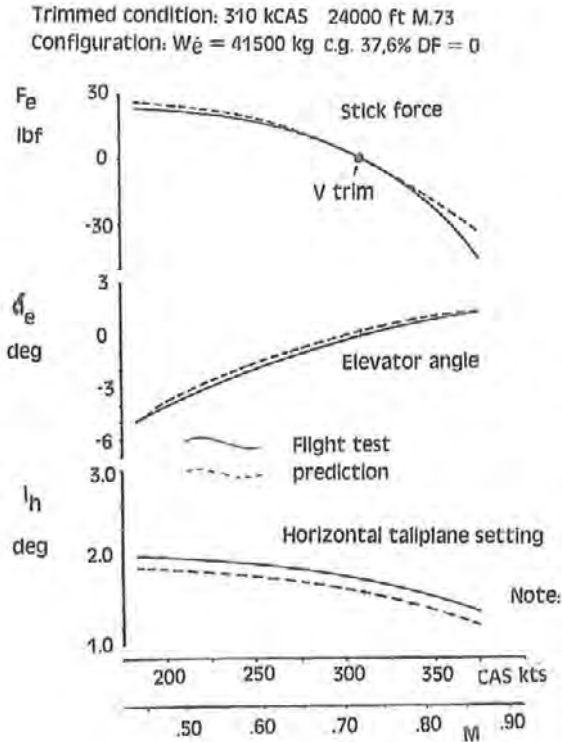
Figure 29.19 - Fokker 100 - High-speed stick-force stability. Mach trim compensator operative. Source: ICAS 1988, Paper 6.1.2.

The DC-8 also had control force reversal at normal operating Mach numbers below M_{MO}. To satisfy certification requirements a Mach trim compensator was installed to obtain satisfactory pitch characteristics. The effect is illustrated in figure 29.20.

When the DC-8 wing was modified and the 4% leading-edge extension was applied the tuck-under tendency was also reduced but a Mach trim compensator remained necessary as shown in figure 29.21.

(Note in figures 29.20 and 29.21 that the control force curves refer to different trim speeds.)
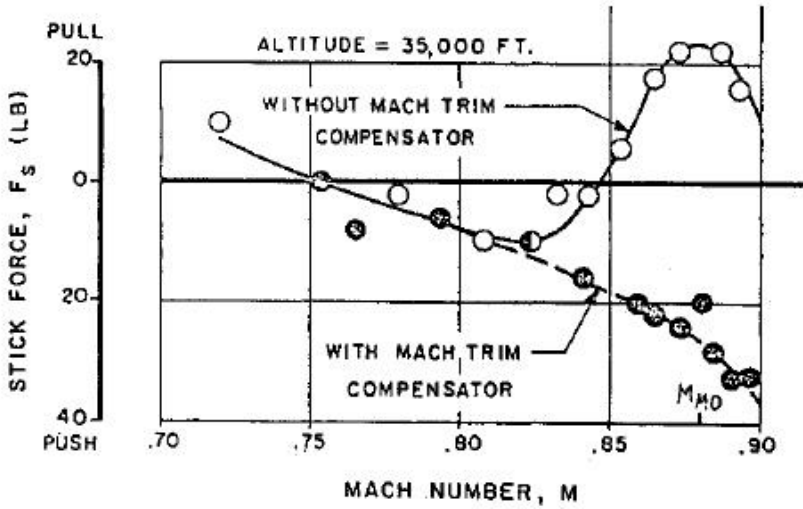
Figure 29.20 - Effect of DC-8 Mach trim compensator on pilot forces in the transonic tuck region.
Source: SAE meeting, O.R. Dunn, Oct. 10-14 1960
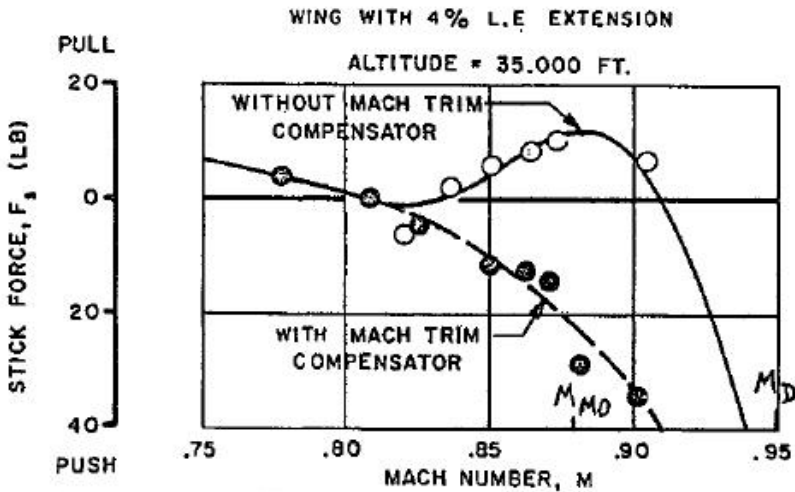
Figure 29.21 - DC-8 transonic tuck pilot force characteristics with revised wing.
Source: SAE meeting, O.R. Dunn, Oct. 10-14 1960

PART 7

STABILITY AND CONTROL

30 *Tail surface design*

Tail surfaces perform three functions:

1. They provide static and dynamic stability.
2. They enable aircraft control.
3. They provide a state of equilibrium in each flight condition.

The first and second items are covered in detail in textbooks and courses on Stability and Control.
The ability to maintain a state-of-equilibrium is often taken for granted, yet to cover extreme flight conditions it often sets design requirements for horizontal and vertical tail surfaces and their control surfaces.

Examples are minimum control speed with a failed engine (V_{MC}), extreme out-of-trim conditions or maximum cross-wind capability.

In general the following design requirements can be formulated for tail surfaces:

1. They shall provide a sufficiently large contribution to static and dynamic longitudinal, directional (and sometimes lateral) stability. This determines primarily their lift gradients

$$\frac{dC_{L_h}}{d\alpha_h} S_h \quad \text{and} \quad \frac{dC_{L_v}}{d\alpha_v} S_v \; .$$

This requires a maximum aspect ratio and for high aspect ratios minimum sweep.

2. They shall provide sufficient control capability, which again determines their lift slope. This also requires a maximum aspect ratio and for high aspect ratios minimum sweep.

3. Control shall be possible with acceptable control forces. This requires a maximum aspect ratio because control force

$$F = C_h \tfrac{1}{2}\rho V^2 S_c \bar{c}_c$$

where

C_h = hinge moment coefficient
$\tfrac{1}{2}\rho V^2$ = dynamic pressure
S_c = control surface area
$\bar{c}_c$ = control surface mean aerodynamic chord

4. The tail surfaces shall be able to cope with high tailplane angles-of-attack, both for the horizontal tail (in particular at higher speeds with flaps deflected) and for the vertical tail surface (high cross-winds). In this case a low aspect ratio is required and sweep is beneficial. The requirement to be able to cope with high tailplane and fin angles-of-attack is aggravated when flight in icing conditions is possible.

5. The tail surfaces shall be able to provide a maximum force sufficiently large to balance the total tail-off forces and moments so that static equilibrium is achieved in all flight conditions. This leads to specific requirements on tail surface areas and on the maximum lift coefficient for the tail surfaces with varying degree of control surface deflection, including the effect of ice roughness.

6. For high-speed aircraft the Mach-number at which serious flow separation occurs shall preferably lie above the design dive Mach-number M_D. Serious flow separation on the stabilizer will aggravate the effect of the changes in tail-off pitching moment due to changes in the wing flow (See pages 29.1-29.5). This applies in particular to aircraft with reversible control systems.

Therefore on stabilizers for high-speed aircraft the sweep angle is often about 5 deg higher than on the wing. Furthermore the section is often 1 or 2% (relative to the chord) thinner than on the outboard wing.

Note that flow break-down on the tail surfaces should preferably not occur below M_D also with deflected control surfaces required for small side slip corrections or pull-up manoeuvres with n = 1.5.

Furthermore the following shall be kept in mind:

1. A high aspect ratio has an adverse (although relatively small) effect on weight. Also, in particular for T-tails the flutter analysis requires extra care. A few degrees anhedral (negative dihedral) has a very beneficial effect.

2. Excessive taper ratio may lead to premature tip stall. This risk is higher when sweep is applied although the stall is then more gradual with less loss in lift. On the other hand tapering leads to lower weight.

31 *The horizontal tail surface*

General design requirements for the aerodynamic design of horizontal tail surfaces have been given on the previous pages. Specific requirements and some examples of applications will be discussed in the present chapter.

Figures 31.1 to 31.3 present the aerodynamic characteristics related to the general design requirements. Figures 31.1 and 31.3 show the effect of aspect ratio, sweep and taper on the lift- curve slope (indicated in figure 31.1 as C_{L_h}). When the aspect ratio decreases the quasi-two-dimensional flow pattern associated with high-aspect-ratio wings changes into a three-dimensional flow pattern where the tip vortices become more and more dominant and section characteristics become less and less recognisable. Lifting surfaces with aspect ratios below A = 1.5 are discussed in the next chapter.
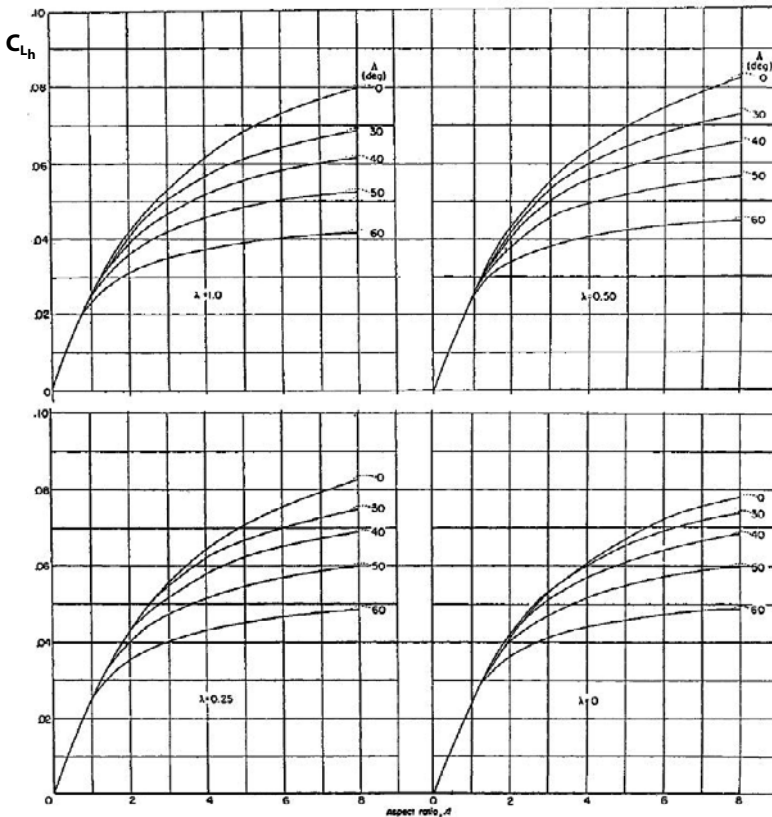
Figure 31.1 - Variation of lift-curve slope with aspect ratio, taper ratio, and sweepback for subsonic incompressible flow. Source: NACA Report 1098

Figure 31.2 shows that due to the increasing role of the tip vortices the maximum lift is almost independent of the aspect ratio for wings in the range of aspect-ratios considered but due to the large variation in lift curve slope the angle-of-attack for maximum lift may vary considerably.
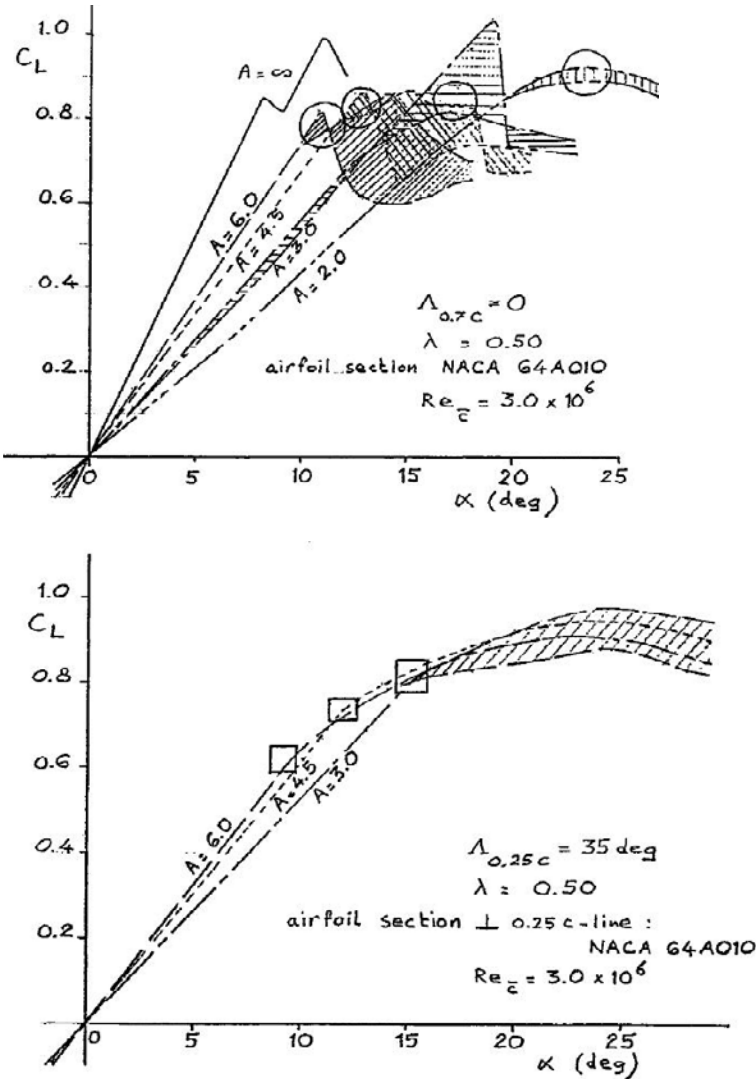
Figure 31.2 - Lift curves of low aspect-ratio airfoils. Source: NACA TN 3497
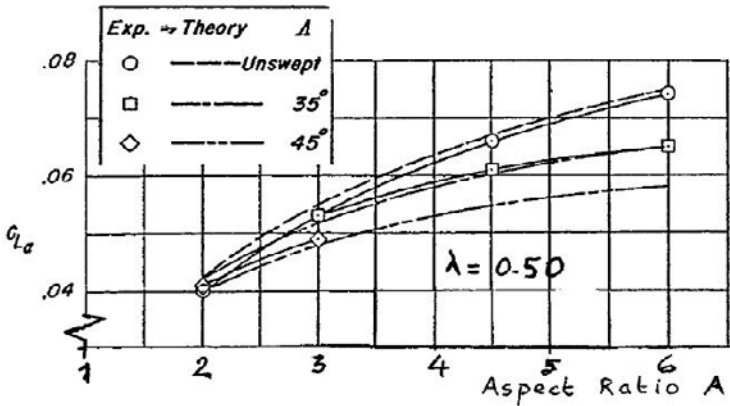
Figure 31.3 - Lift curve slope of low aspect-ratio airfoils. Source: NACA TN 3497

Figure 31.4 shows the effects of wing sweep and very low aspect ratio. For wings with nearly the same aspect ratio (A = 2.09 and A = 2.13) adding sweep (sweep angle Λ = 45 deg for A = 2.09) increases, due to the leading-edge vortices, both the stall angle of attack and the maximum lift coefficient. For an even lower aspect ratio (A = 1.13) and without applying sweep, the maximum lift coefficient is higher than on the straight wing with A = 2.13 and, due to the low lift gradient, the angle-of-attack at which stall initiates is postponed even further. This is because on such low-aspect-ratio wings the lift is mainly produced by the tip vortices which burst only at high angles-of-attack.
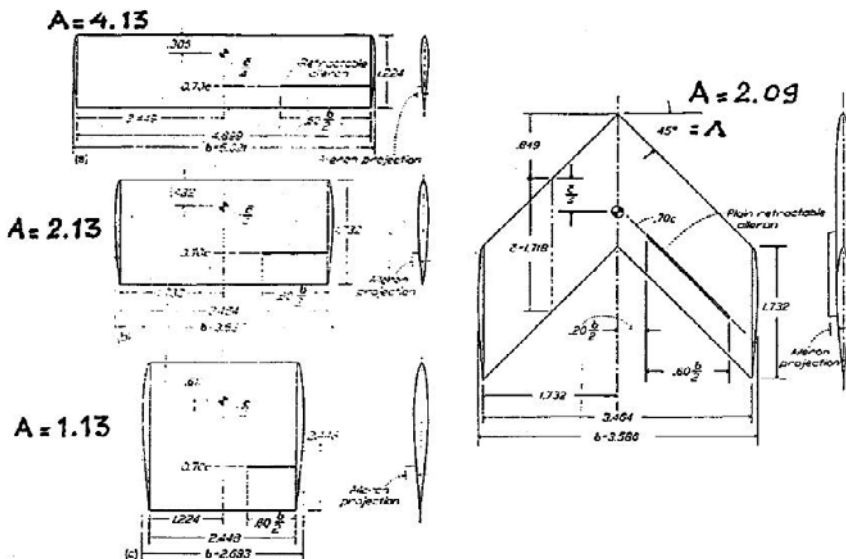
Figure 31.4 (part 1) - Lift curves of low-aspect ratio arifoils. Source: NACA Report 1091
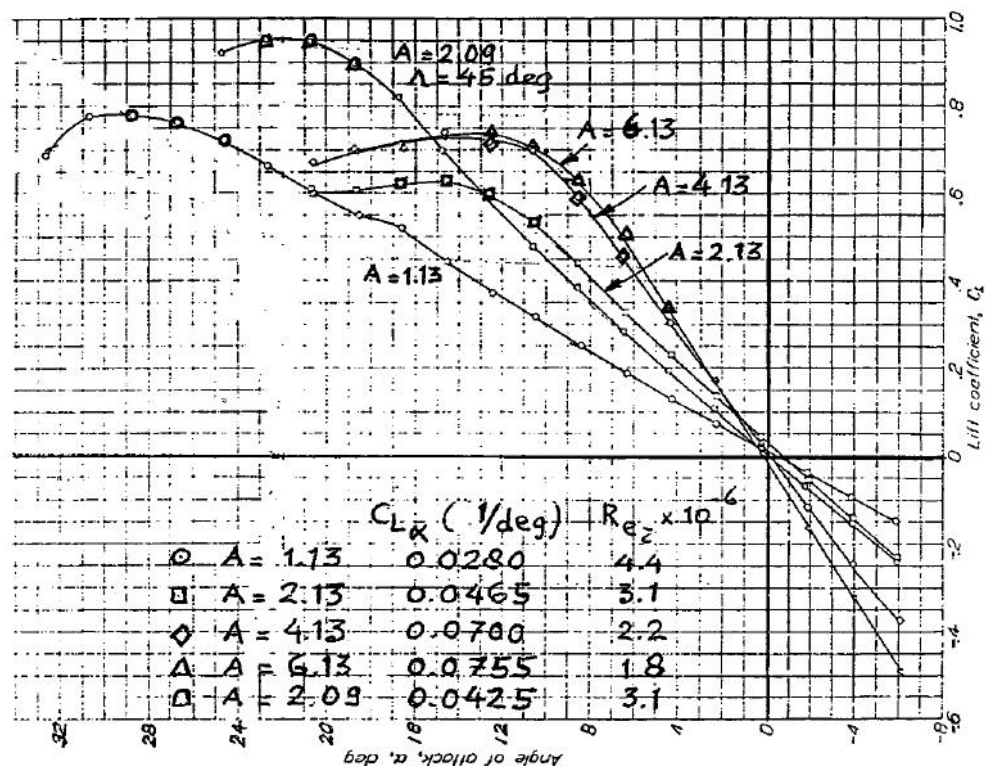
Figure 31.4 (part 2) - Lift curves of low-aspect ratio arifoils. Source: NACA Report 1091

Static aeroelastic deformation

Aeroelastic deformation has been a subject of concern since the dawn of aviation. Torsional divergence was a major source of accidents in the first two decades of powered flight. Later, understanding and preventing aileron flutter and wing bending-torsion flutter became a challenge for designers. Problems with static aeroelastic deformation arose during World War II when, with the high speeds (and high dynamic pressures) then achievable, control surfaces distorted in manoeuvres leading to erratic flight handling characteristics.

Since the advent of jet aircraft the static aeroelastic deformation under air loads of all major aircraft components in normal operation is being considered in the design process on a routine basis.

The first aircraft on which a detailed analysis was performed of the effect of static aeroelastic deformation on all major aerodynamic coefficients and thus on performance and flight handling was the Boeing B-47. This investigation was reported in NACA Report 1298.

The main types of deformation are:

1. Wing bending and torsion. These cause a re-distribution of spanwise and chordwise loading, a reduction in wing lift curve slope, a reduction in aileron effectiveness and, on swept wings, a forward shift of aerodynamic-centre position. In order to have the proper shape under average flight loads, the 1-g shape, the wings are built in a different shape, the jig shape.
   In the landing configuration flaps and flap attachment may be deformed leading to an effective reduction of the flap angle.
2. Fuselage bending and torsion. These cause a reduction in stabiliser and fin lift curve slope.
3. Stabiliser or horizontal tailplane bending and torsion. The torsional deformation occurs primarily when the elevator is deflected leading at high dynamic pressures to a considerable reduction in elevator effectiveness.
4. Fin or vertical tailplane bending and torsion. These lower the fin lift curve slope and reduce the rudder effectiveness.
5. Deformation of movable stabiliser attachment leading to a reduction in stabiliser lift curve slope.

The effect of wing, stabiliser and elevator deformation on the lift curve slope as a function of dynamic pressure is shown in figures 31.5 to 31.8. Elevator reversal as suggested by figure 31.7 does not occur in reality as at low altitude the Mach number at the design dive speed V_D is much lower than M = 0.85.
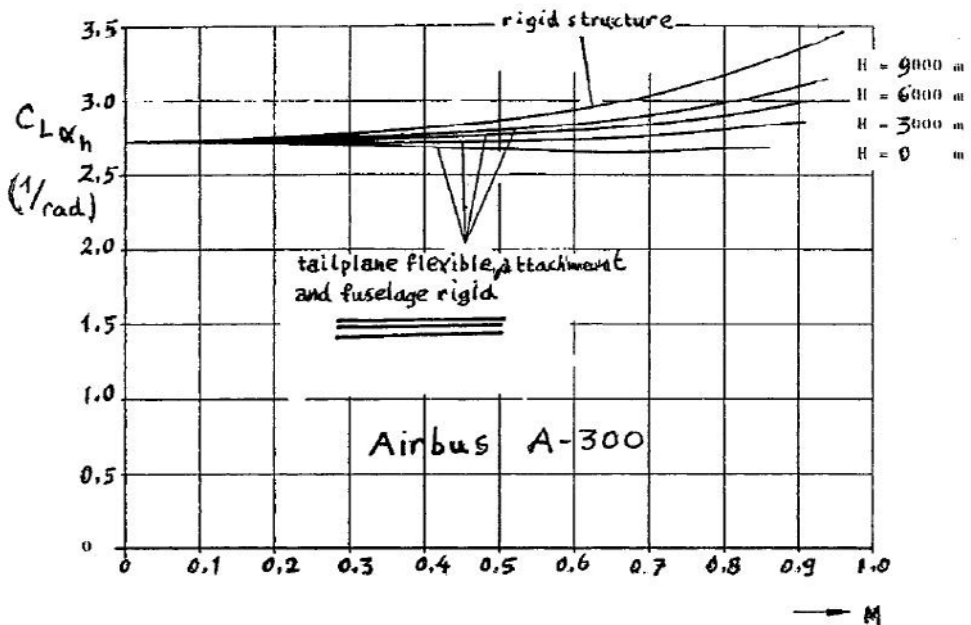
Figure 31.5 - Lift curve slope of the horizontal tailplane. Source: AGARD CP No 46, Paper No 17, 1969
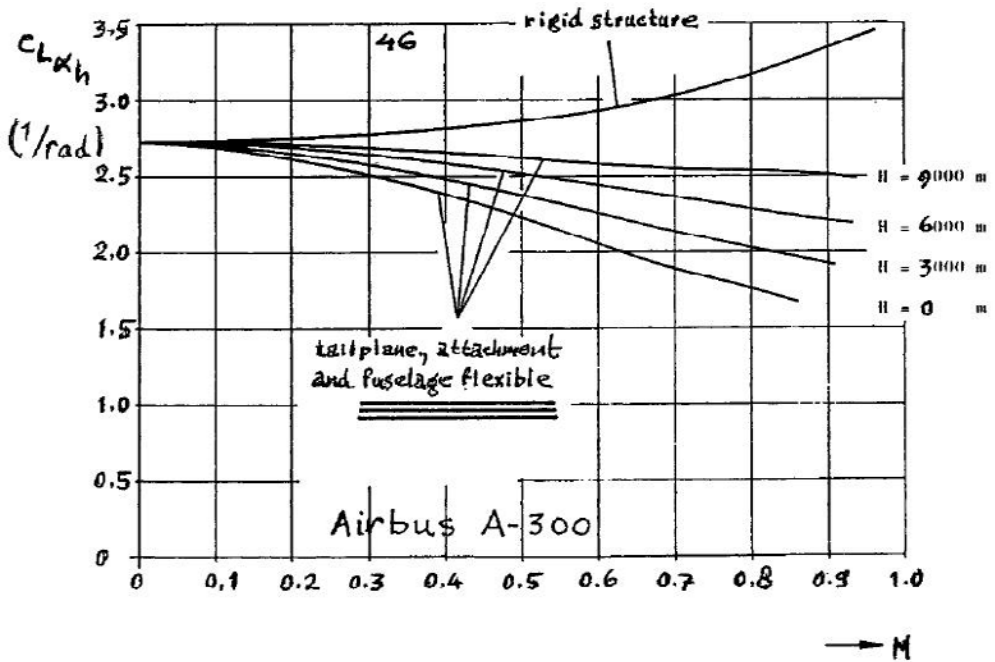
Figure 31.6 - Lift curve slope of the horizontal tailplane. Source: AGARD CP No 46, Paper No 17, 1969
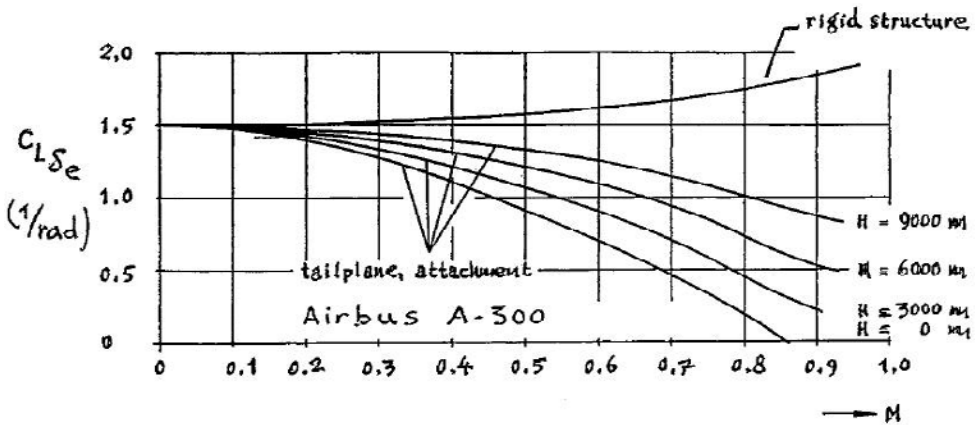
Figure 31.7 - Elevator effectiveness. Source: AGARD CP No 46, Paper No 17, 1969

To reduce the negative effects of fuselage bending, the elevator can be "down-rigged", as shown in figures 31.9 and 31.10. The resulting negative zero-lift pitching moment of the horizontal tailplane will, with increasing dynamic pressure, tend to bend the rear fuselage and tailplane attachment upwards thus increasing longitudinal stability.

The lower part of figure 31.9 does not belong to the present chapter but corresponds to the next one.
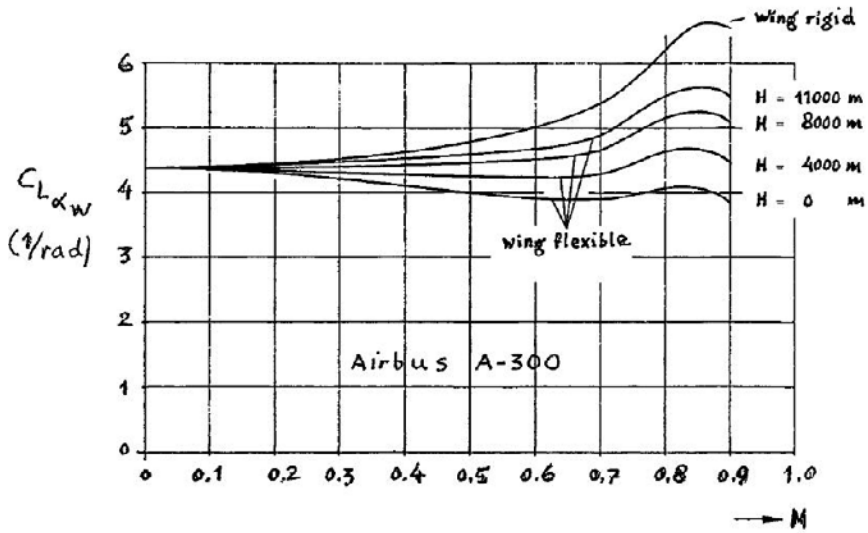
Figure 31.8 - Lift curve slope of the wing. Source: AGARD CP No 46, Paper No 17, 1969
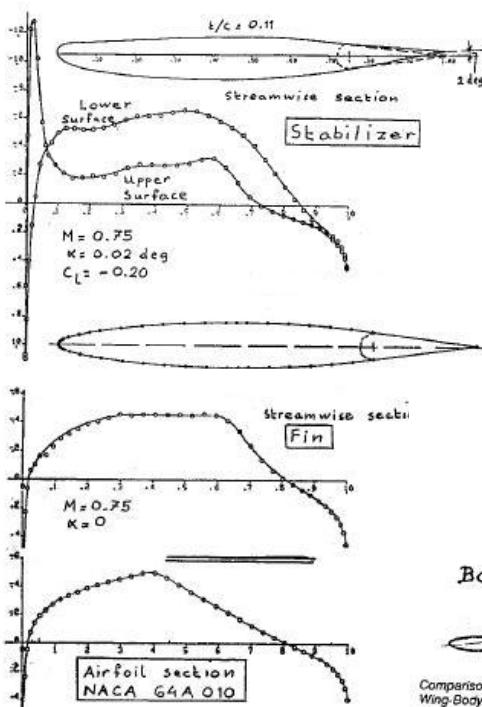
Figure 31.9 - Airfoil sections used on the tail surfaces of the Boeing 737 and a comparison with section NACA 64A010. Source: NASA TN D-5971
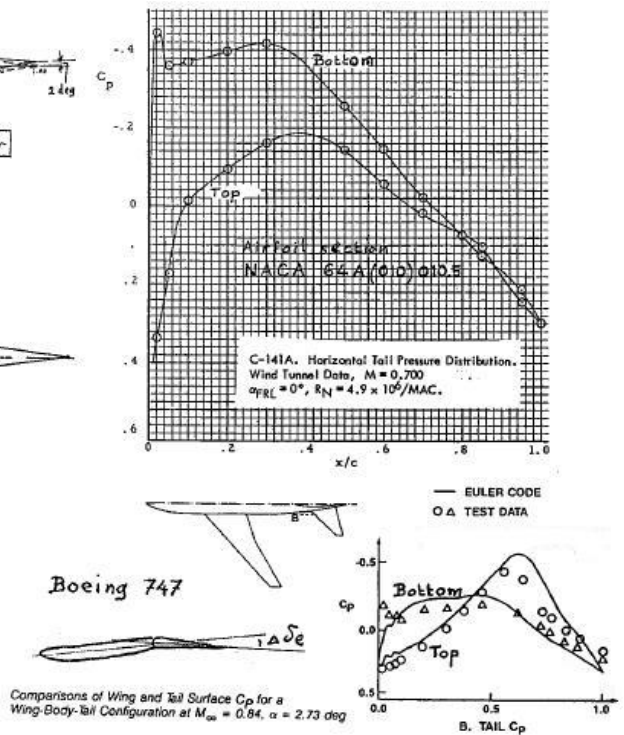
Figure 31.10 - Horizontal tailplane pressure distributions. Source: AIAA Paper No 87-0454

The general function of the horizontal tail surface is to enable controlled flight for a variety of aircraft and flight conditions, as mentioned in figure 31.11.
The various lines indicate the tail-off pitching moment coefficient $C_{m_{c.g.}}$ as a function of the tail-off lift coefficient $C_{L_{T=0}}$ for different configurations and centre of gravity positions.

The tail contribution to the aircraft pitching moment to obtain a state of equilibrium can be written as $\Delta C_{m_{c.g.}} = -C_{L_h} \bar{V}_h$ with $\bar{V}_h = \dfrac{S_h l_h}{S_w \bar{c}}$. Since the horizontal tailplane volume coefficient is assumed to be $V_h = 1.0$ in figure 31.11, the values of $C_{m_{c.g.}}$ and $C_{L_h} (= C_{L_{tail}})$ are equal and hence the identical double axes.

When the flaps are extended for take-off the zero-lift pitching moment becomes more negative. Extending the flaps to the landing position leads to another negative increase in zero-lift pitching moment, shifting the pitching moment curves further to the left.
The range of pitching moments for which the tail must be able to balance the aircraft is given by the difference in pitching moments of the first take-off flap setting at the aft centre of gravity position and the landing-flap setting at the forward C.G. position, both at maximum lift.
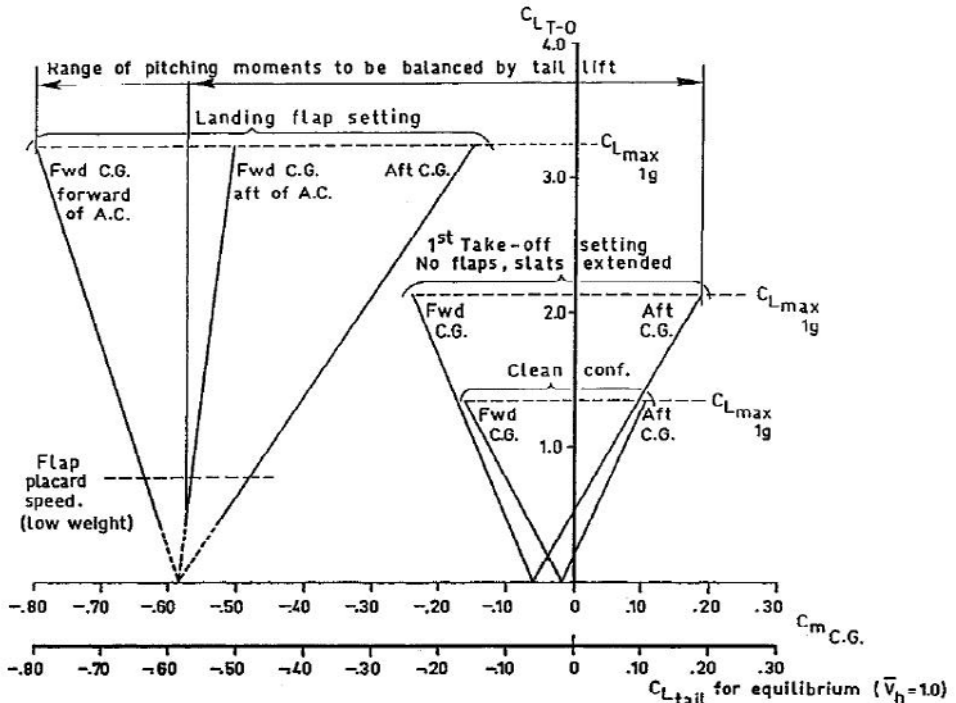
Figure 31.11 - Pitching moment, aircraft less tail. Source: AGARD CP-160, Paper No. 10
Flap placard speed = maximum speed at which aircraft is allowed to fly with flaps deployed

This requirement for a high (negative) tailplane lift capability for trimming is more severe for rear-engined aircraft than for aircraft with the engines on the wings because due to the long forward fuselage where a large part of the payload is situated the required centre-of-gravity range is larger.

Some centre-of-gravity diagrams are presented in figures 31.12 to 31.17.
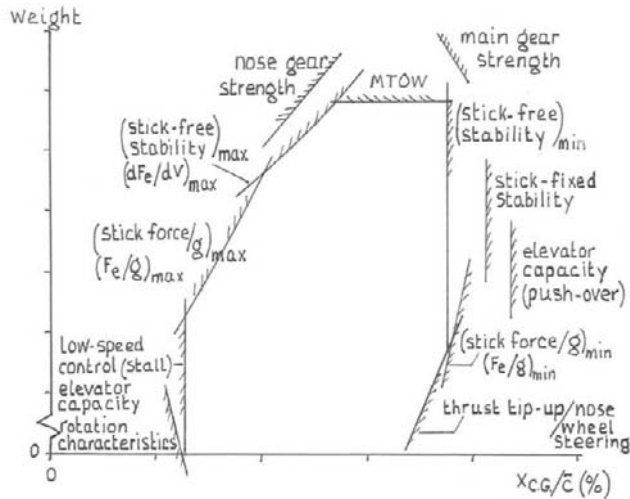
Figure 31.12 - Loading diagrams of some jet transport aircraft: Limits of the loading diagram.

Note that the centre-of-gravity range of the Caravelle III is only $x_{c.g.}/\bar{c} = 14\%$. Therefore this aircraft did not need a variable-incidence horizontal tailplane.
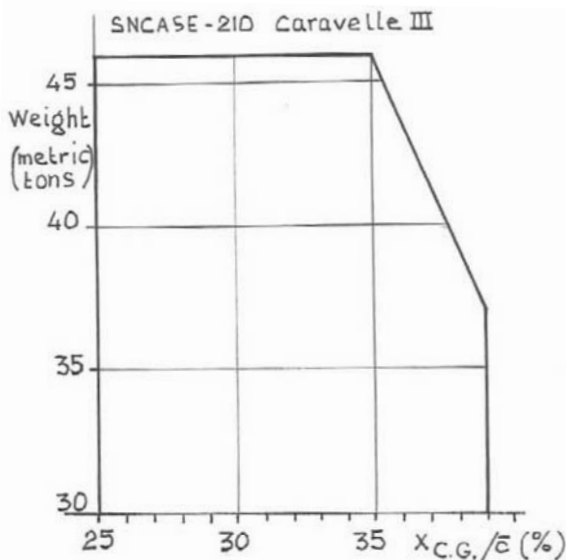
Figure 31.13 - Loading diagrams of some jet transport aircraft: Loading diagram of the SE-210 Caravelle III.

767-300ER Tri-Class. Notice the change in CG values with increasing fuel weight.
Airliner/Oct-Dec 1994
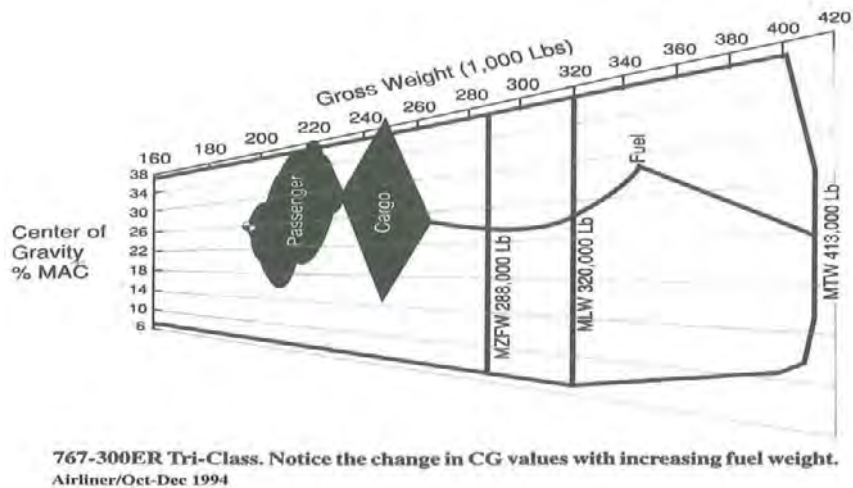
Figure 31.14 - Loading diagrams of some jet transport aircraft: Loading diagram of the Boeing 767-300ER.
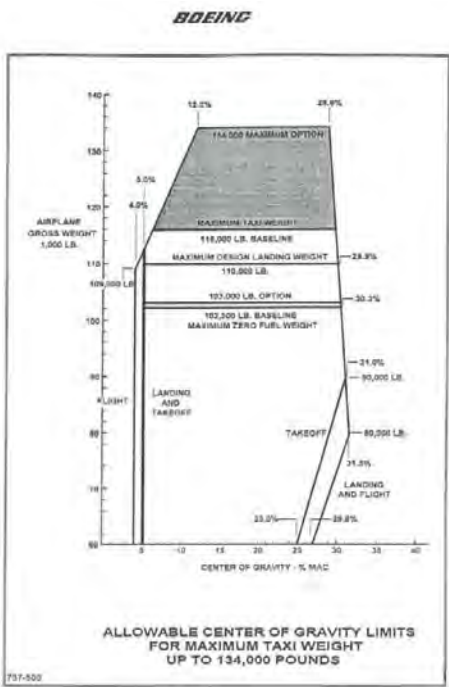
ALLOWABLE CENTER OF GRAVITY LIMITS FOR
MAXIMUM TAXI WEIGHT UP TO 138,000 POUNDS

Figure 31.15 - Loading diagrams of some jet transport aircraft: Loading diagram of the Boeing 737-500.
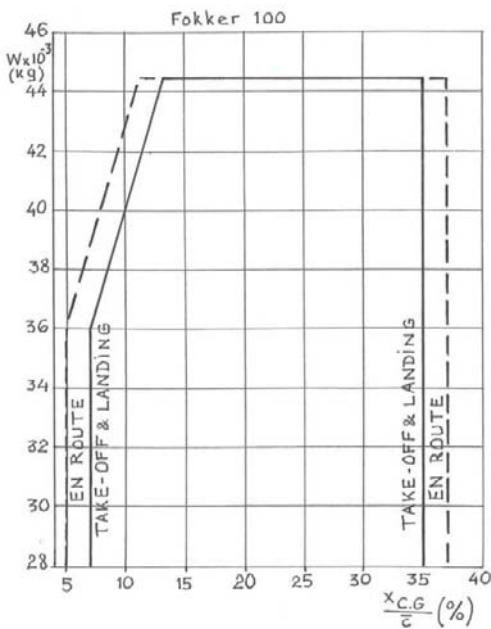
Figure 31.16 - Loading diagrams of some jet transport aircraft: Loading diagram of the Fokker 100.
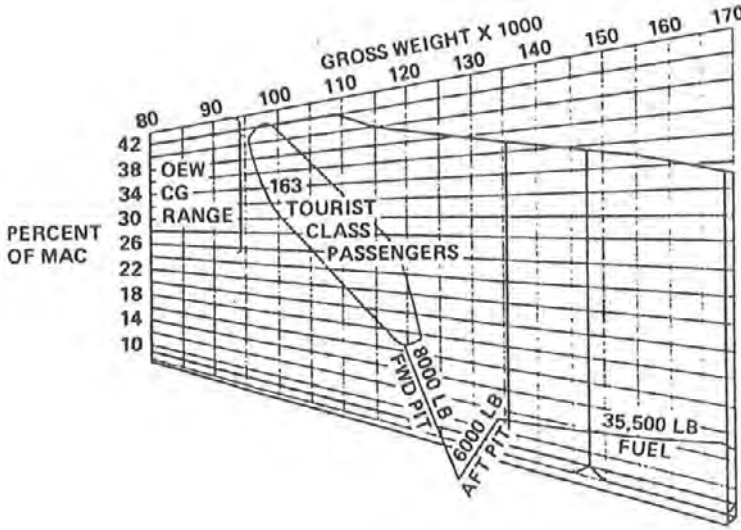
Loading Flexibility

Figure 31.17 - Loading diagrams of some jet transport aircraft: Loading diagram of the Boeing 727-200.

The contribution of the horizontal tail surface to the pitching moment equilibrium can be described with the following equations:

$$C_{m_{tail}} = -C_{m_{T-O}} = -(C_{L_{\alpha_h}} \cdot \alpha_h + C_{L_{\delta_e}} \cdot \delta_e) \frac{q_h}{q} \overline{V_h}$$ eq. (31.1)

$$\alpha_h = \alpha_R - \varepsilon + i_h + \Delta\alpha_{(q)} \qquad \left(\alpha_R - \varepsilon = \alpha_R \left(1 - \frac{d\varepsilon}{d\alpha}\right) - \varepsilon_0\right)$$ eq. (31.2)

$$C_{m_{tail}} = -C_{L_{\alpha_h}} \left(\alpha_R - \varepsilon + i_h + \Delta\alpha_{(q)} + \frac{C_{L_{\delta_e}}}{C_{L_{\alpha_h}}} \cdot \delta_e\right) \frac{q_h}{q} \overline{V_h}$$ eq. (31.3)

In figure 31.18 tail-off and tail-on pitching moment coefficient curves are presented for the Fokker F-28. Although the tail-off configurations show the large range of pitching moments as discussed above the tail-on pitching moment curves lie closely together for a certain C.G. position.

With increasing flap angle a given lift coefficient is reached at a lower angle-of-attack (see figure 25.1). With the horizontal tailplane and elevator in the neutral position the tailplane will therefore show a downward change in tail lift. This will to a large degree compensate the change in tail-off pitching moment and produce the narrow band of tail-on pitching moment curves. This is illustrated in figure 31.19. Nevertheless, it is necessary to be able to balance a wide range of pitching moment coefficients by changing the tailplane setting or elevator deflection.
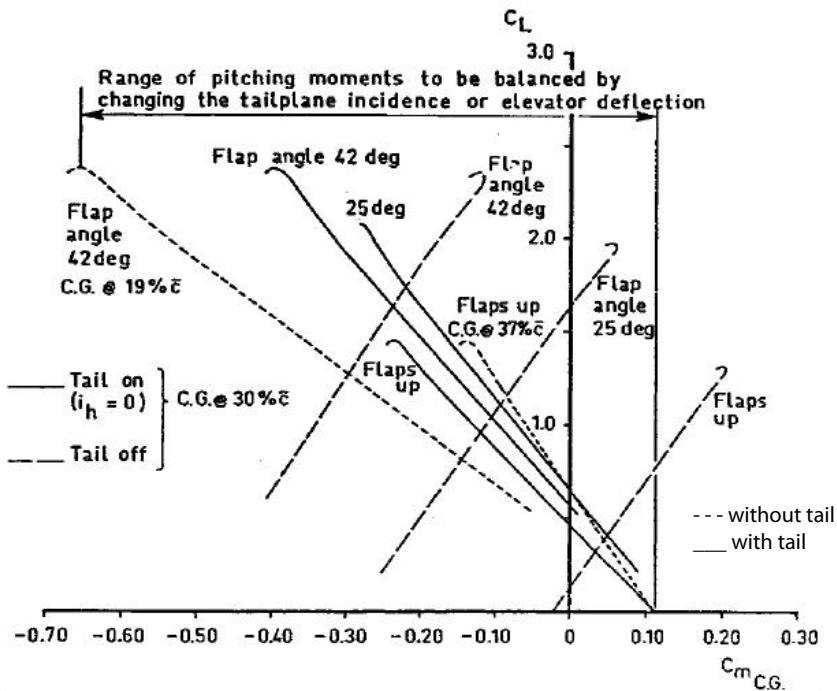
Figure 31.18 - Fokker 28 pitching moment curves. Source: AGARD CP-160, Paper No. 10
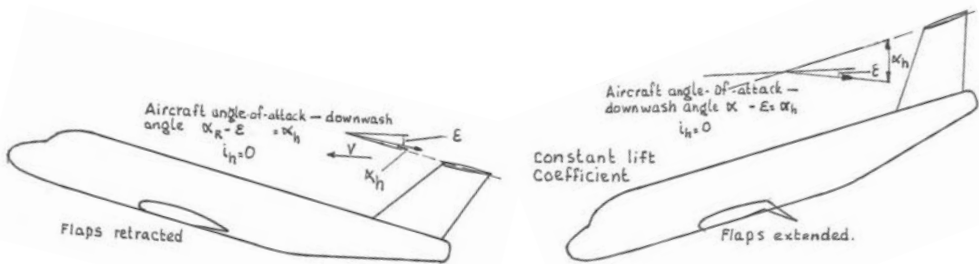
Figure 31.19 - Change in flow condition at the tail due to flap extension.

The tail surfaces have also to perform their functions in icing conditions. Different types of ice may be accumulated in flight depending on the meteorological conditions in the clouds. The three main types are rime ice, glaze ice with many mixed shapes and hoar-frost. This is illustrated in figures 31.20 and 31.21.

CASE	DATA SYMBOL	AIRSPEED, km/hr	TEMP., °C	LWC, g/m³	TIME, min
A	□	209	-8	L3	8
B	○	209	-2	L3	8
C	◇	209	-26	L3	8
D	◊	209	-8	L3	3
E	△	338	-8	L05	6.2
F	▲	209	-18	L3	8

21 INCH CHORD 0012 AIRFOIL AT 4 DEGREE ANGLE

Glaze ice

DROP SIZE, DVM, μm

- - - - 14
——— 20
——— 26
——— 36

Rime ice
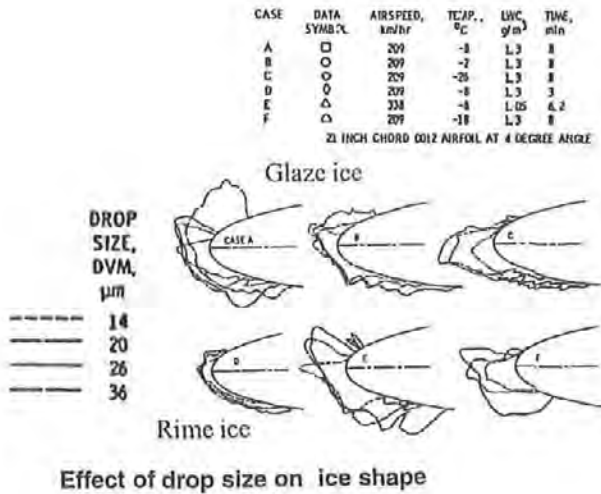
Effect of drop size on ice shape

Figure 31.20 - Ice Shapes I. Source: NASA TM 83556

CASE	AIRSPEED, km/hr	TEMP. °C	LWC, g/m³	DVM μm
A,B,C	209	-8	2.1	20
D,E,F	209	-26	1.0	12

21 INCH CHORD 0012 AIRFOIL

ACCRETION TIME, MINUTES
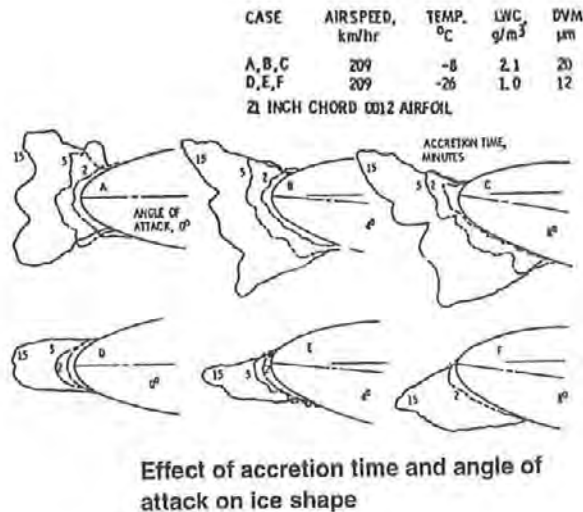
ANGLE OF ATTACK, 0°

Effect of accretion time and angle of attack on ice shape

Figure 31.121- Ice shape II. Source: NASA TM 83556

Ice accretion on aircraft parts, particularly on lifting surfaces, must be considered with the greatest care. Rime ice and glaze ice form in flight on leading edges if no anti-icing equipment is operative. Hoar-frost will form when warm air with some water vapour content comes in contact with cold aircraft parts for example during overnight stops. Hoar-frost will cover large parts of the aircraft. All forms of ice accretion lower the maximum lift capability of lifting surfaces and should be removed with de-icing fluids before take-off.

As shown in figure 31.11 the highest demand on the stabiliser trim capability is made with the aircraft in the landing configuration at forward centre of gravity. In that condition a high negative stabiliser lift coefficient is required ($C_{L_{tail}} = -0.8$ in the example of figure 31.11).

In figure 31.22 two groups of curves giving relations between the aircraft lift coefficient and the stabiliser angle-of attack are shown. One group (drawn curves) indicates the stabiliser angle-of-attack with the stabiliser setting for zero stick force (elevator neutral). The other group (the broken curves) indicates the change in stabiliser angle-of-attack when the aircraft speed is increased from a certain lower trim speed to the flap placard speed by increasing elevator deflection or by combining a speed increase with a n = 0.5 push-over. In this extreme manoeuvre the stabiliser angle-of attack approaches the maximum angle-of-attack of the stabiliser with leading edge ice accretion.

The Fokker F-28 stabiliser lift curves and elevator hinge moments with and without simulated ice roughness are shown in figures 31.23 and 31.24. With simulated ice roughness the angle-of-attack for maximum lift is reduced appreciably. When the maximum lift is reached and flow separation occurs the elevator hinge moment suddenly changes sign and becomes very high. The change in pressure distribution on tailplane and elevator is indicated in figure 31.25. This hinge moment reversal is also indicated as "elevator lock". This should be prevented to occur in flight as the aircraft will pitch down and it will be extremely difficult if not impossible for the pilot(s) to regain control as is described in figures 31.26 and 31.27.
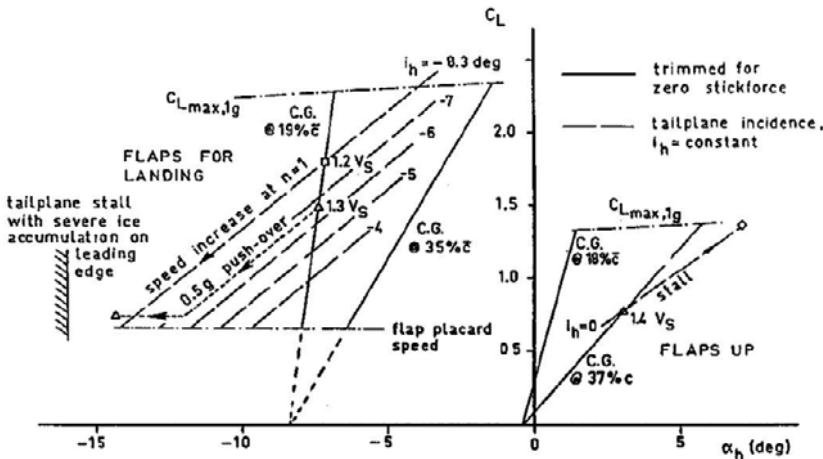
Figure 31.22 - Fokker 28 tailplane angle-of-attack. Source: AGARD CP-160, Paper No. 10
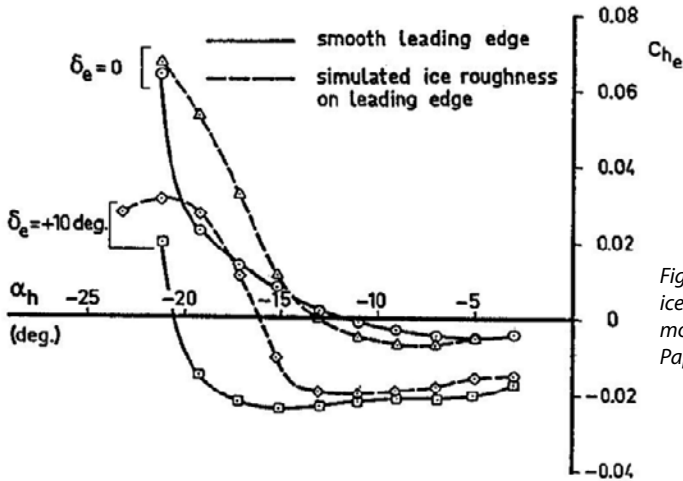
Figure 31.23 - Effect of simulated ice roughness on elevator hinge moments. Source: AGARD CP-160 Paper No. 10
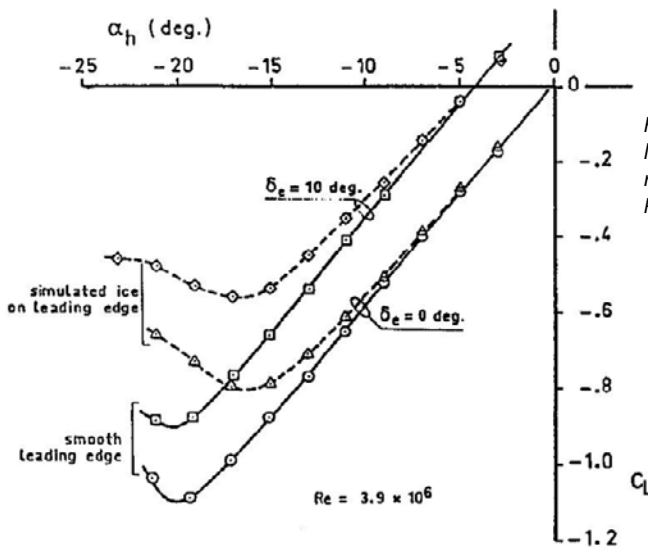
Figure 31.24 - Fokker 28 tailplane lift curves. Effect of simulated ice roughness. Source: AGARD CP-160 Paper No. 10
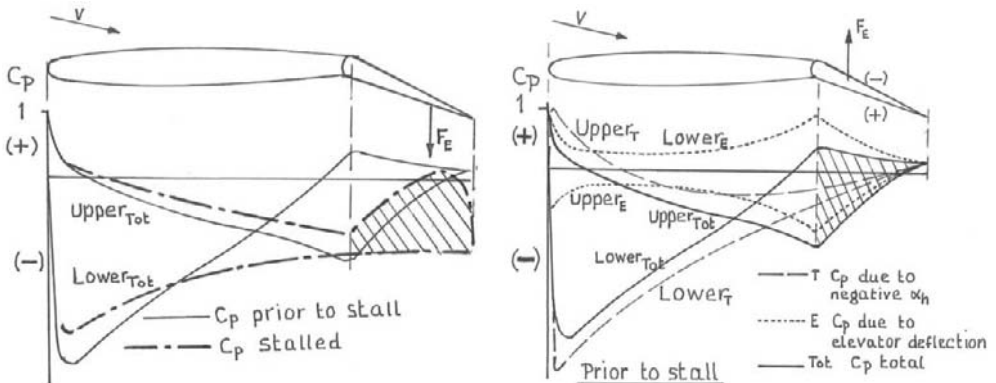
Figure 31.25 - Pressure distribution on the horizontal tailplane prior to and after the occurrence of elevator lock.

407

Aerospatiale's SN-600 Corvette prototype has determined that over-trimming of the aircraft's variable-incidence tailplane probably is what caused the twin turbofan business jet to pitch over into an uncontrollable dive.

Aerospatiale officials are convinced the final accident report will clear the basic Corvette design and are accelerating development of two production aircraft and two test specimens. Flight tests with the new models—embodying configuration changes resulting from early prototype flight tests—are scheduled to begin late next year.

The aircraft should be certified by the end of 1973, in time to guarantee production delivery in early 1974. Three crewmen from the French civilian test center (CEV) were killed in the crash of the prototype, which occurred as they were doing high-altitude stalls (AW&ST Apr. 12, p. 53). The aircraft pitched over about 20 kts above normal stalling speed and entered a steep dive.

The only transmission from the pilots was a terse report from one of them that together they were unable to pull the aircraft out of the dive.

After long study of data from flight test recorder tapes, the investigators have determined that the pilot, who was flying the Corvette for the first time, apparently trimmed the tailplane to an excessive negative incidence, nose-up attitude during preparations for the stall tests. No stops had been installed to limit tailplane travel, because that portion of the flight envelope had not been fully explored.

All aircraft with variable-incidence tailplanes could encounter the same problem which caused the Corvette crash, according to several officials. When setting up the aircraft for the stall series, the pilot apparently put it in a configuration which ultimately reversed the action of the tailplane and elevator controls, they said.

The large-span flaps were deployed, creating a relative downward (or nose-up) airflow over the tailplane. While trimming the tailplane, the pilot apparently released back pressure on the control yoke – as is general practice – and the elevator control surfaces moved to a nose-down position opposite that of the tailplane as they streamlined in the relative airflow, they said.

The resultant control surface configuration created a nose-down pitching moment before stall speed was reached, they said, and :the deflected airflow generated by the flaps created aerodynamic pressures on the elevator controls which the pilots could not overcome. The Corvette has straight mechanical linkages without servo-controls in its flight control system.

To recover from the dive, the pilots would have had to move against their automatic reactions and trim the tailplane for nose-down, according to one official. This probably would have re-established the aerodynamic balance of the tailplane, they said. Raising the flaps also might have helped correct the control imbalance, they added.

Aerospatiale test pilots were aware that without stops the tailplane could be over-trimmed, they operated within certain limits while exploring the aircraft's envelope. How the CEV test pilot managed to trim the aircraft past these limits probably will not be determined.

Program officials said production aircraft will be equipped with stops which will make it impossible to establish an imbalanced configuration.

The French accident investigating board has completed a study of the accident and has submitted its report to Aerospatiale and the French flight test center (CEV).

The official report said the cause of the accident was an "aerodynamic anomaly in the horizontal tail" and that the problem has been corrected on the new production design. The problem encountered basically was tailplane stall, according to one source, which was aggravated by a 45-deg. flap setting and high negative incidence setting of the horizontal tailplane. The aircraft pitched down about 20 kt. above normal stall speed.

The problem has been eliminated on production versions through a combination of previously planned lengthening of the fuselage – aimed primarily at improving aerodynamic drag – and smaller limits on movement of the three control surfaces involved.

Travel of the variable incidence tailplane has been reduced from +2 deg and -10 deg to +2 deg and -8 deg.

Elevator travel has been reduced from +25 deg and -15 deg to +20 deg and -10 deg. Flap deflection angle has been reduced from 45 deg. to 40 deg.
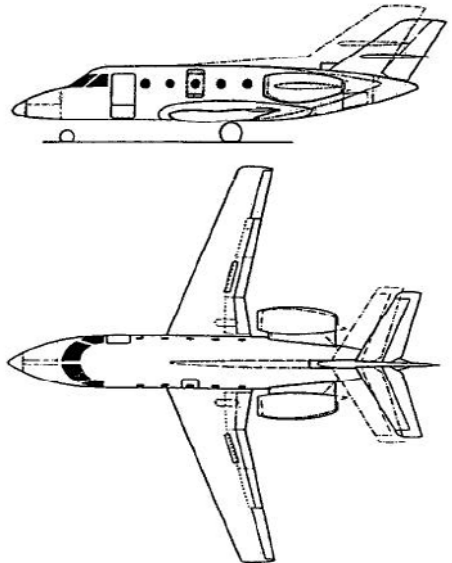
Figure 31.26 - Over-trimming cited in Corvette crash.
Source: Aviation Week and Space Technology, May 31 and October 18, 1971

Having trimmed the variable stabiliser to neutral, the CAA pilot then proceeded to the next step which was to trim fully nose down in stages, to see if that could be held by the manually operated elevator (there is no trim tab on the elevator, and a balance tab which was in the original design turned out to be unnecessary and has been deleted). It was at this point where things started to go wrong. The data recorder shows that the stabiliser went from 0 to 4.6˚ nose down in one run lasting 7 seconds. This needed an excessive stick force of 50 to 60 kg to hold the aircraft level, but Greer managed to apply this. The stabiliser then moved fully down to 5˚ and stick force rose to 70 kg, but the pilot still held the aircraft level by sheer muscle power. The recorder then shows that the stabiliser moved a further 0.5˚ (beyond its design limit). Then the elevator force lessened, the aircraft nose went down and the speed started to increase.

At this point the CAA pilot asked Beckham to help him in pull back the stick and the two pilots pulled a combined force of 150 kg (when the aircraft is operated normally stick force does not exceed 22 kg). The nose continued to go down and at 30˚ below horizontal the airspeed passed the V_{MD} of 250 kts (V_{MO} of the Dornier-228 is 200 kts). At 34˚ nose down the power was reduced by Beckman, but the stabiliser failed to respond to attempts to retrim. At a speed of 302 kts, a height of about 1,500 ft and with a negative g of -1.8, the aircraft started to break up. When it hit the ground in the middle of a forest, the pitch angle was 75˚ nose down and acceleration -3g.

Figure 31.27 - Stabilizer mistrim accident. Source: Interavia letter No 9977, April 13, 1982

For sizing studies on horizontal tail planes the tail-off zero-lift pitching moment coefficient is an important parameter. Handbook methods for preliminary design provide little information on the zero-lift pitching moment with deflected flaps. As an aid for preliminary design studies an average curve is presented in figure 31.28 showing the change in tail-off zero-lift pitching moment coefficient due to flap deflection as a function of the increase in lift coefficient due to flap deflection at zero angle-of-attack based on the data of some wind tunnel models and actual aircraft.

In figures 31.29 and 31.30 the horizontal tailplane geometry is presented for a number of jet and propeller transport aircraft. The sweep angle of the majority of the tailplanes on the jet aircraft is 5 to 10 degrees larger than on the wing, particularly on aircraft with reversible control systems, to prevent control problems between M_{MO} and M_D. Also for that reason the tail airfoil section is 1 to 2% t/c thinner than the airfoil section on the outer wing. On aircraft with irreversible control systems (and usually high M_{MO} and M_D), such as the Boeing 747 and the DC-10, transonic flow on the tailplane is accepted and the sweep angle is identical to the wing sweep angle.

409
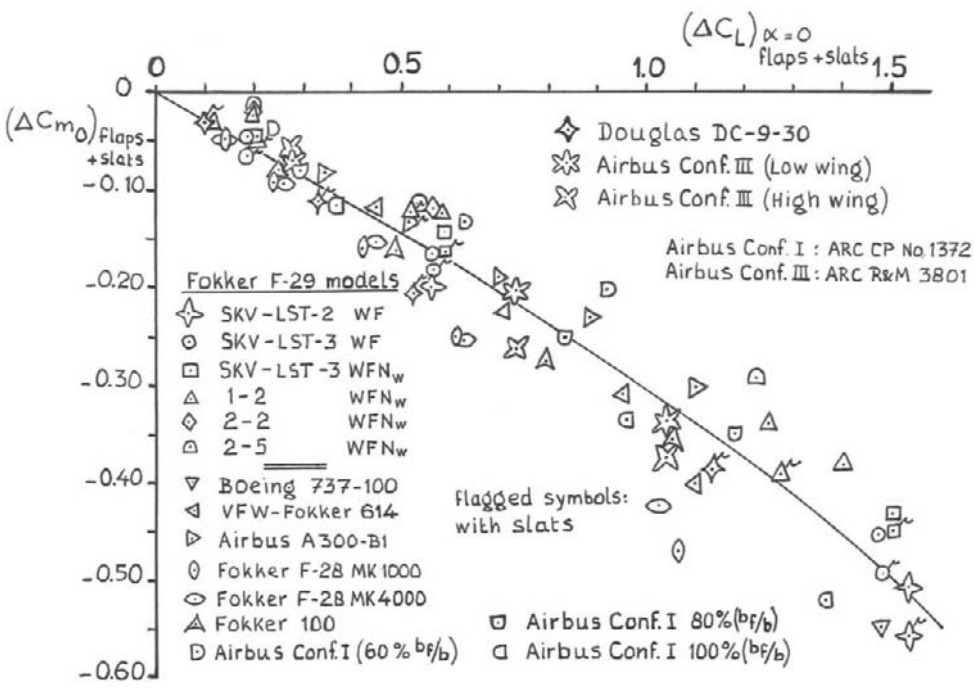
Figure 31.28 - Change in tail-off zero-lift pitching moment coefficient due to slat and flap deflection as a function of the increase in lift coefficient due to slat and flap deflection at zero angle-of-attack. Source: Fokker Report H-O-83
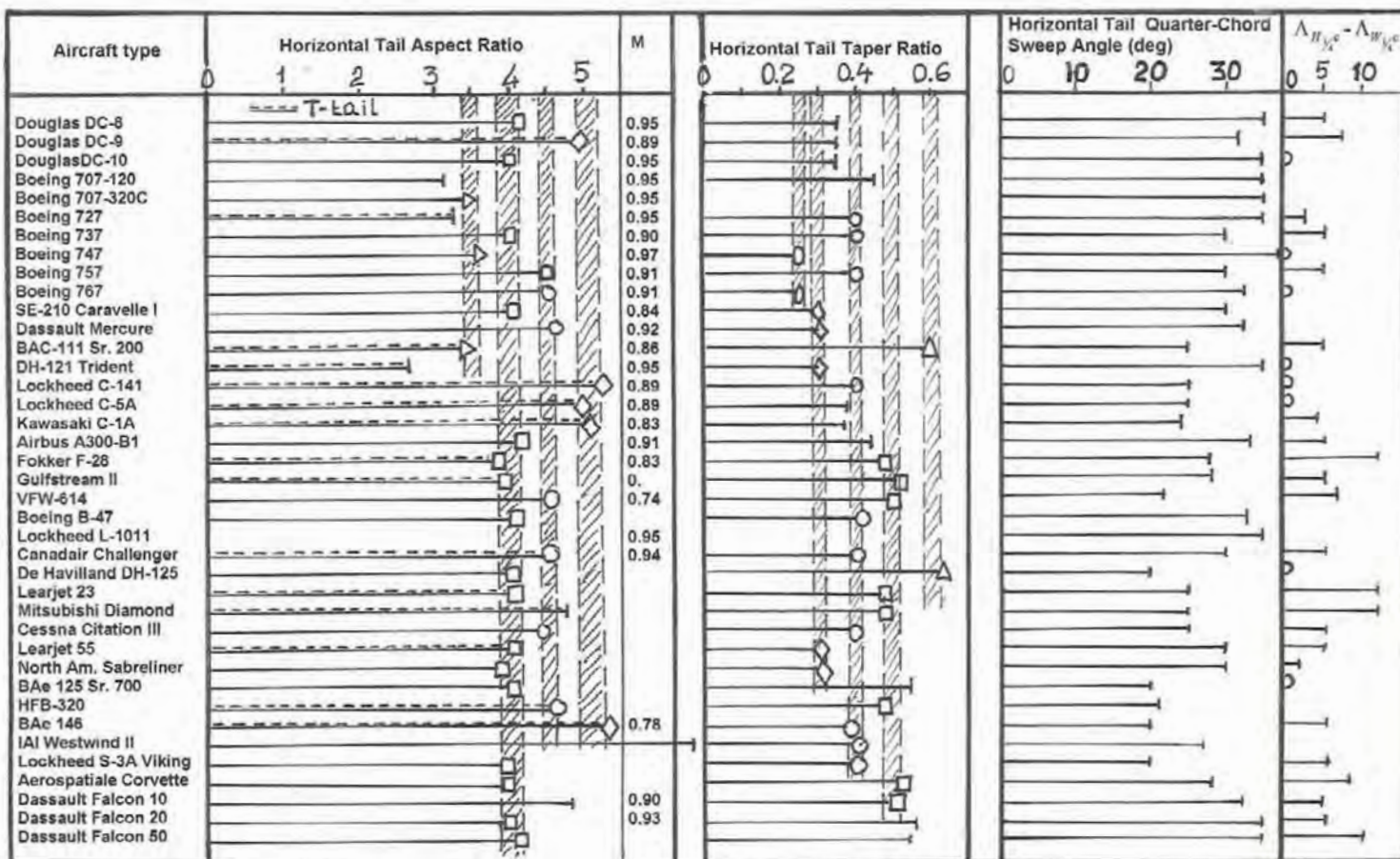
Figure 31.29 - Horizontal-tail data of several jet aircraft
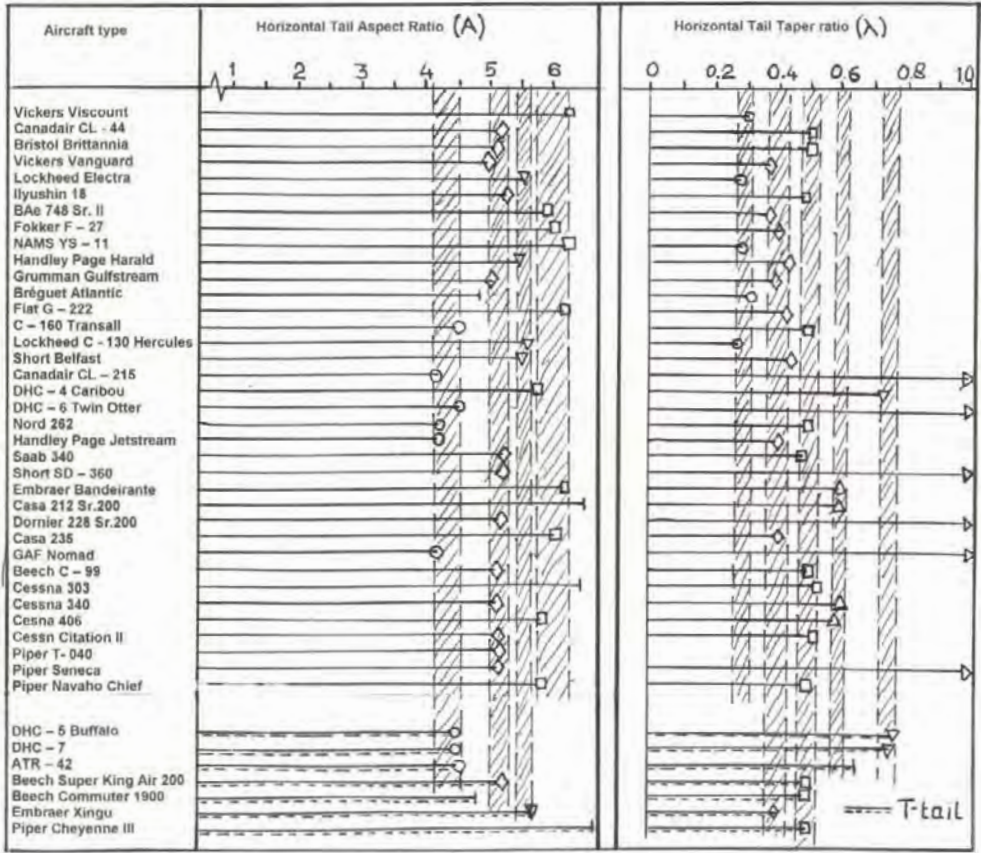
Figure 31.30 - Horizontal-tail data of several propellor aircraft

The maximum aspect ratios found are:

$A_H = 6$ for propeller aircraft
$A_H = 5$ for (faster) jet aircraft

32 *The vertical tail surface*

One of the most significant design requirements for vertical tail surfaces (or fins) is the ability to cope with very large side slip angles β, up to 25 deg. Therefore vertical tail surfaces have low aspect ratios, large leading edge sweep and/or dorsal fins. The effects of these features will be discussed in this chapter.

As can be seen in figure 32.1 (and earlier in figure 31.1) according to lifting surface theory the gradient of the lift coefficient vs. angle-of-attack curve is linear with aspect ratio for airfoils with low aspect ratio (up to about A = 1.5) and practically independent of planform as substantiated by figures 32.2 to 32.5. This leads to the following conclusion:

The aspect ratio is defined as $A = b^2/S$

(32.1)

For A < 1.5, the lift gradient equals (figure 32.1) $C_{L_\alpha} = \dfrac{\pi A}{2}$ (rad⁻¹) or

$C_{L_\alpha} = \dfrac{\pi A}{2 \times 57.3} = 0.0274A$ (deg⁻¹).

(32.2)

The lift force (or side force) on the vertical tailplane can be written as

$L = C_{L_{\alpha V}} \alpha \dfrac{1}{2} \rho V^2 S_V$

(32.3)

Combining the latter two equations produces $L = 0.0274 b_v^2 \alpha \dfrac{1}{2} \rho V^2$

(32.4)

At a given fin angle-of-attack the side force on a vertical tail surface is only dependent on the fin height and planform is of secondary importance.

This explains why from the early days of aviation vertical surfaces showed a large variation in shapes and nevertheless in most cases apparently had satisfactory characteristics.

In figure 32.6 various dorsal fins (forward extensions of the fin root area), investigated in the development of the Fokker F-27, are shown. The effects of these 11 modifications on the aircraft yawing moment (a measure for the effect on the fin lift curve) are presented in figures 32.7 and 32.8.

Up to 15 deg angle-of-sideslip, the dorsal fin does not affect the lift curve. From 15 deg on, whereas without dorsal fin the maximum lift is almost reached, the dorsal fin modifies the flow over the vertical tail due to the vortex springing

413
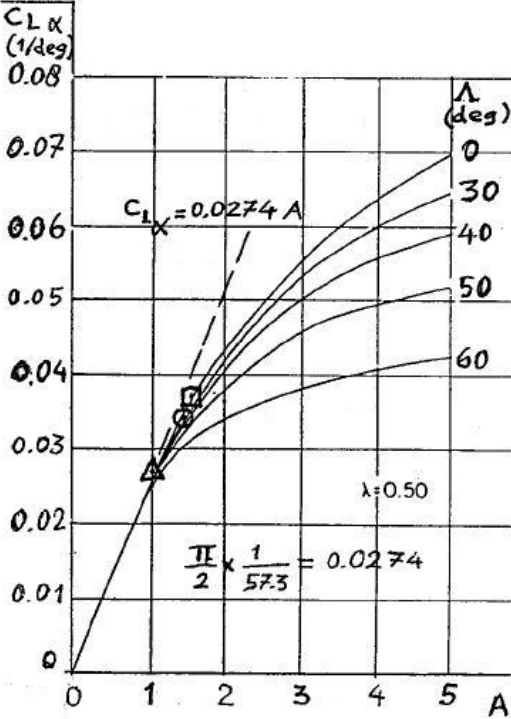
Figure 32.1 - Vertical tail plane lift curve slope.
Source: NACA TN 2010, Rep. 1098
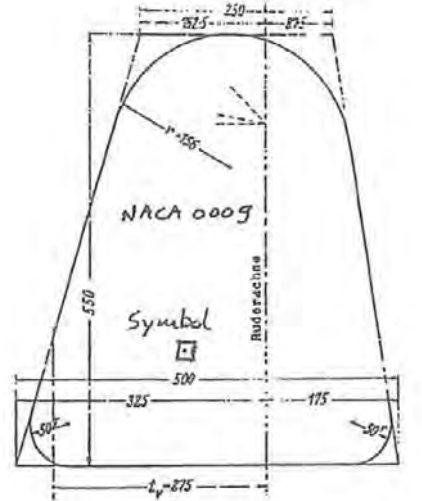
Figure 32.2 - Vertical tail lift curve slope (I).
Source: Forschungsbericht FB 1519 / 3

from its leading edge. This is controlled local flow separation which stabilises the flow further outboard postponing complete flow separation to a higher angle-of-sideslip. Thus a higher maximum lift and a higher stall angle are achieved. On the full-scale F-27 dorsal fin no.1 was selected. The reason is evident although fin no.6 could also have been a candidate.
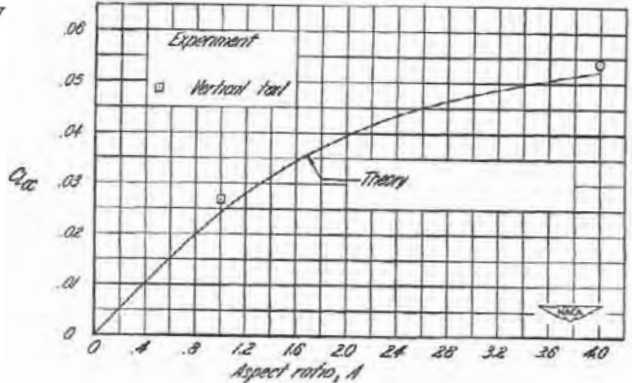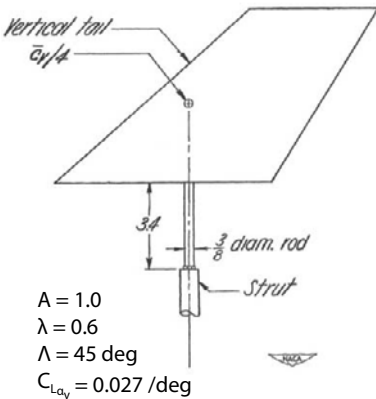
Figure 32.3 - Vertical tail lift curve slope (II). Source: NACA TN 2010

A_v = 1.45
$C_{L_{a_v}}$ = 0.034 /deg
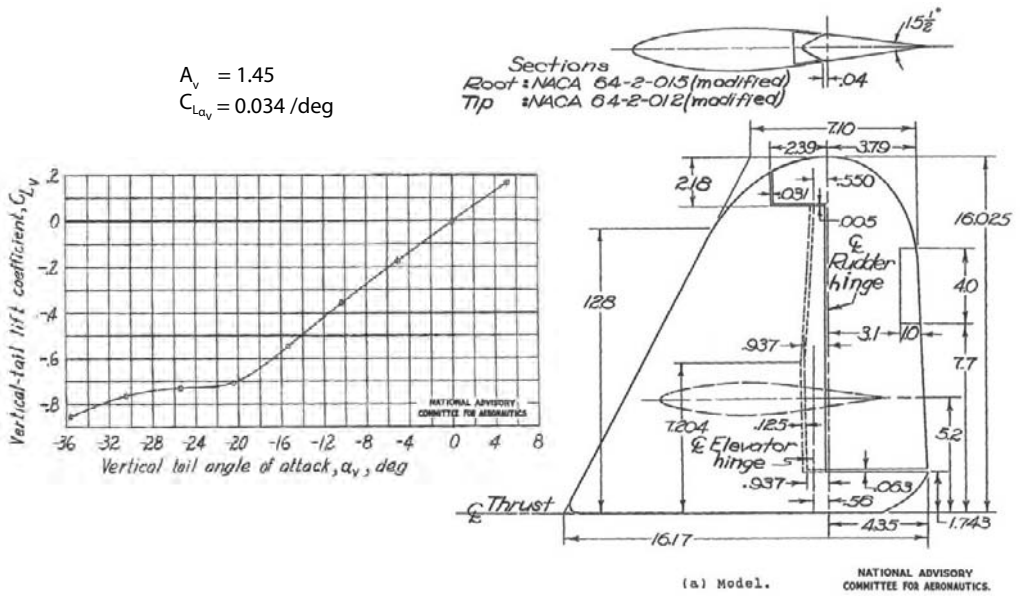
Figure 32.4 - Vertical tail lift curve slope (III) . Source: NACA TN 1146
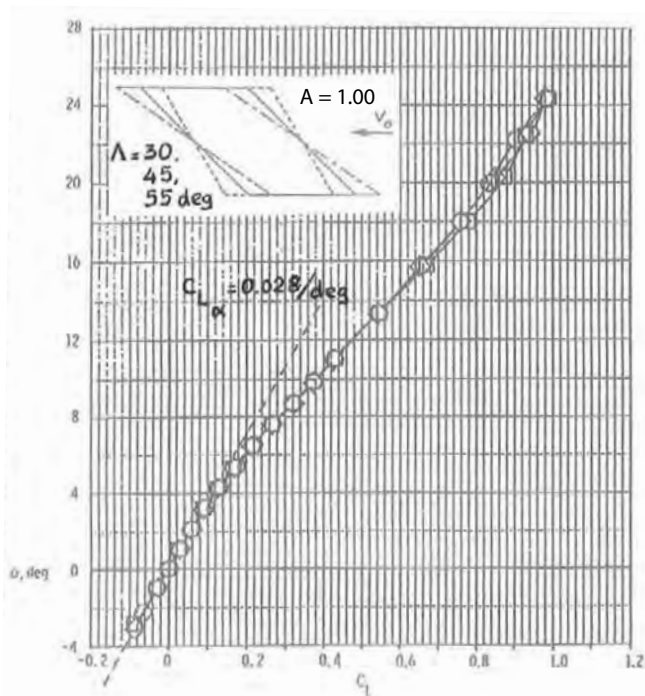
Figure 32.5 - Vertical tail lift curve slope (IV) . Source: NASA TN D-8512
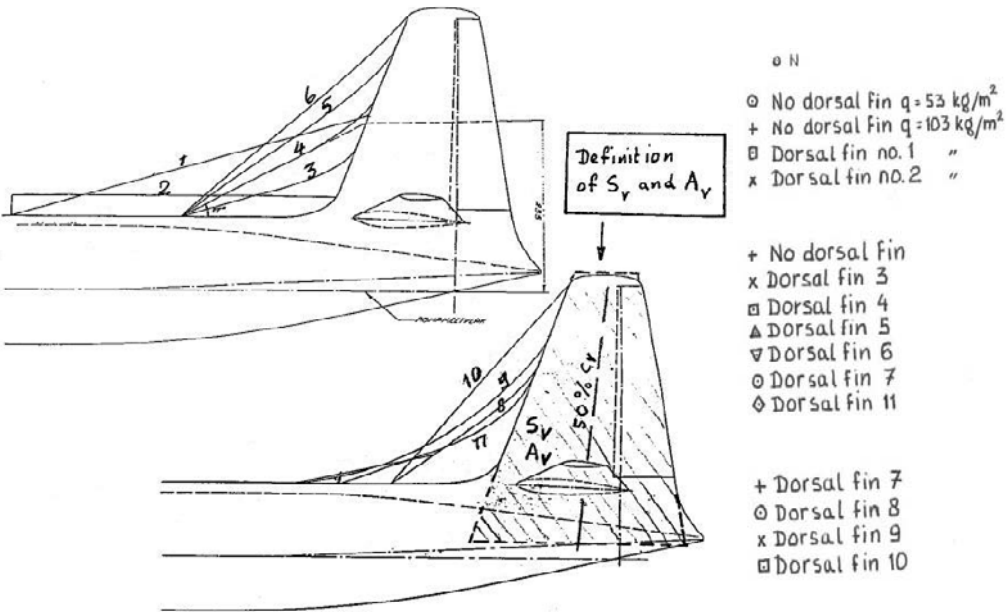
Figure 32.6 - Different dorsal fins. Source: NLL Report A-1374
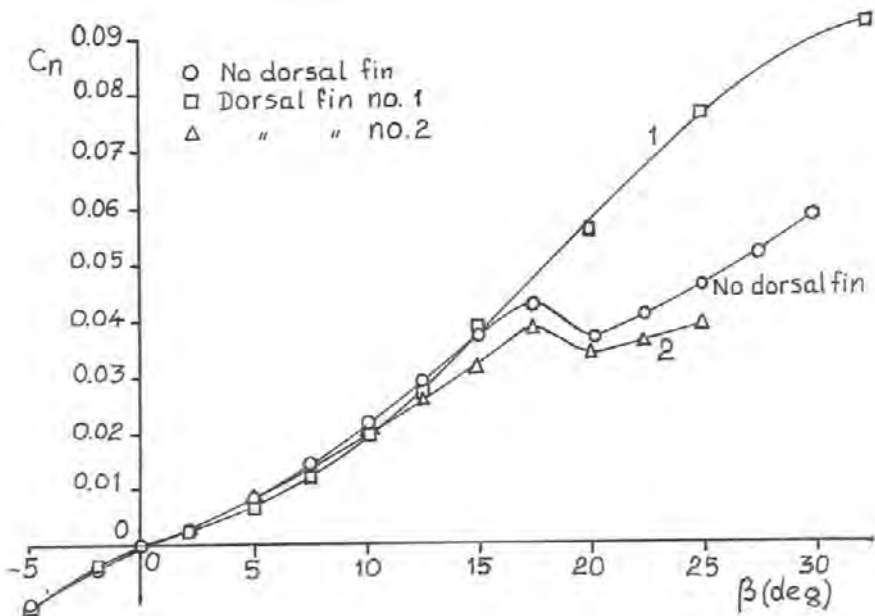
Figure 32.7 - Effect of a dorsal fin on the yawing moment coefficient (1). Source: NLL Report A-1374
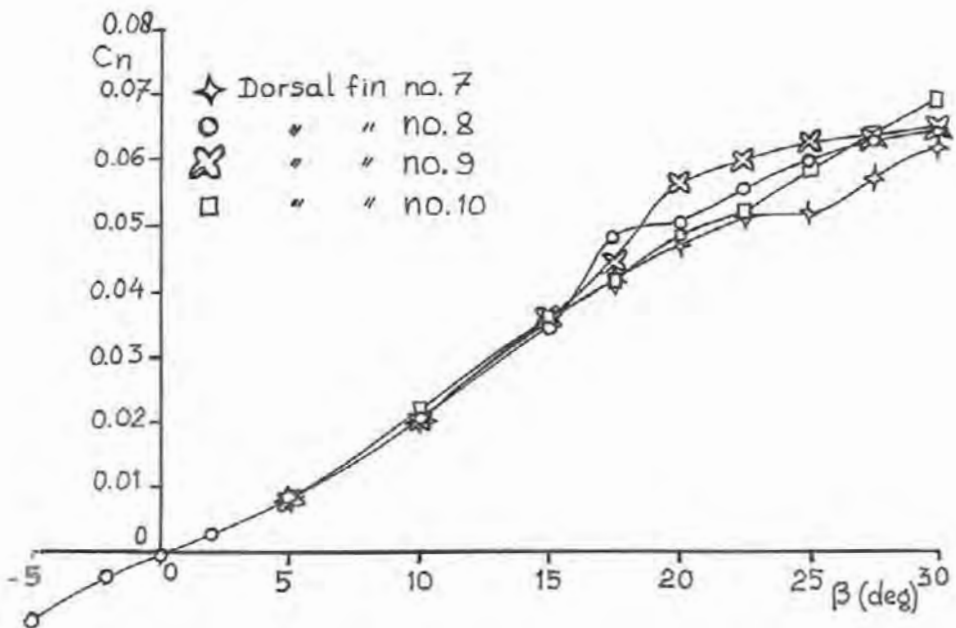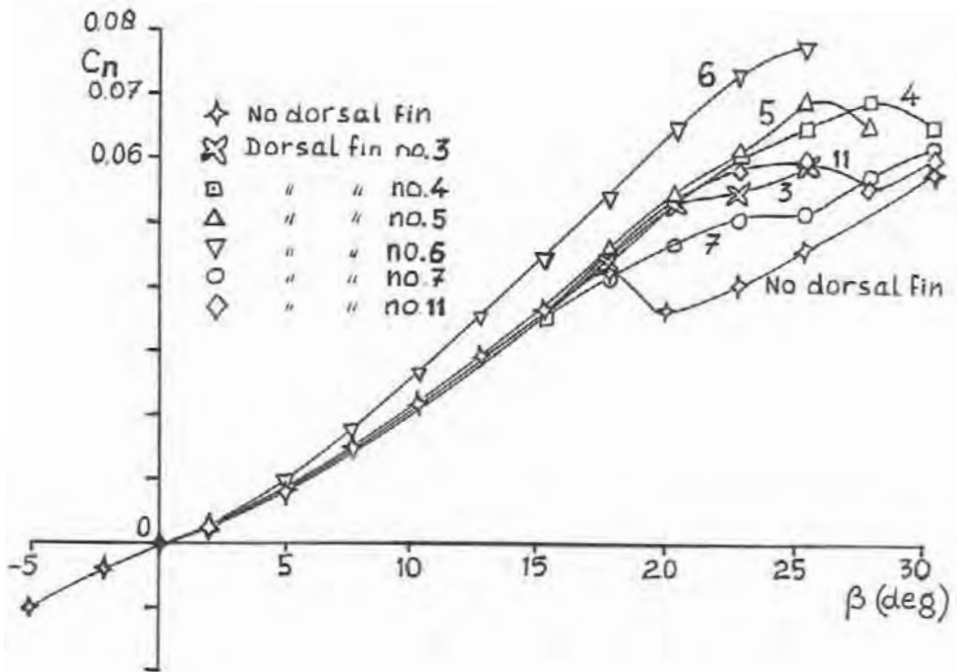
Figure 32.8 - Effect of a dorsal fin on the yawing moment coefficient (2). Source: NLL Report A-1374
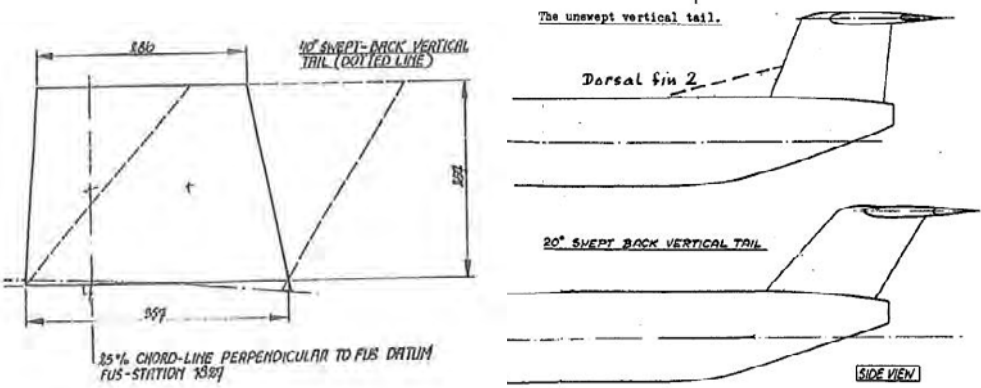
Figure 32.9 - Side view of three vertical tail surfaces and a dorsal fin investigated during the development of the Fokker F-28. Source: NLR Report A-1582

Instead of a lightly-swept leading edge in combination with a dorsal fin also a fully-swept-back leading edge on a vertical tail surface may produce favourable sideslip characteristics. This was already demonstrated by fin no.6 in figure 32.8. Further proof is given in figures 32.9 to 32.13 which show test results of an investigation on three tail configurations with these differences in leading-edge geometry, performed during the development of the Fokker F-28.

In figure 32.10 and 32.11 yawing moment vs. sideslip angle is presented for two aircraft angles-of-attack for the three configurations tested. For the linear regime, the three curves practically coincide. At higher side-slip angles above $\beta = 15$ deg, it appears that for zero angle-of-attack applying fin sweep or adding a dorsal fin has nearly the same favourable effect on the yawing moment curve.
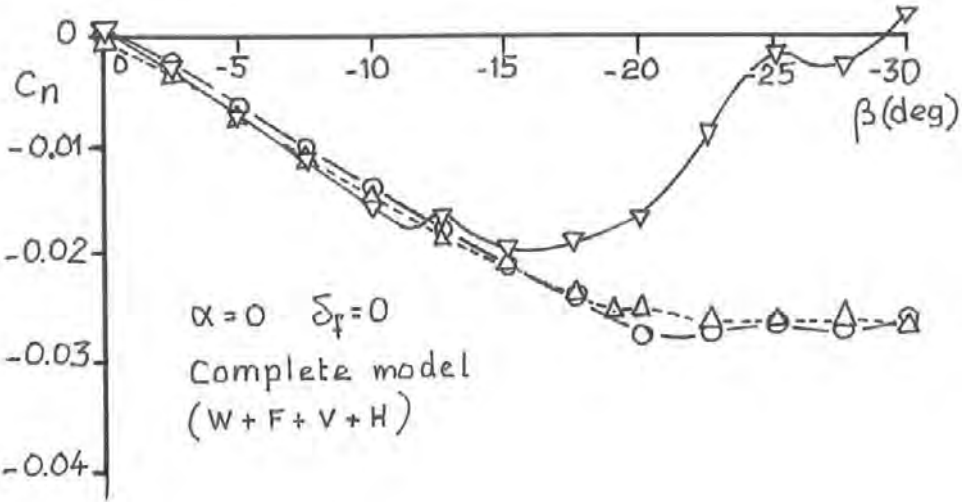
Figure 32.10 - Effect of sweep angle on vertical tailplane lift curve. Source: NLR Report A-1582
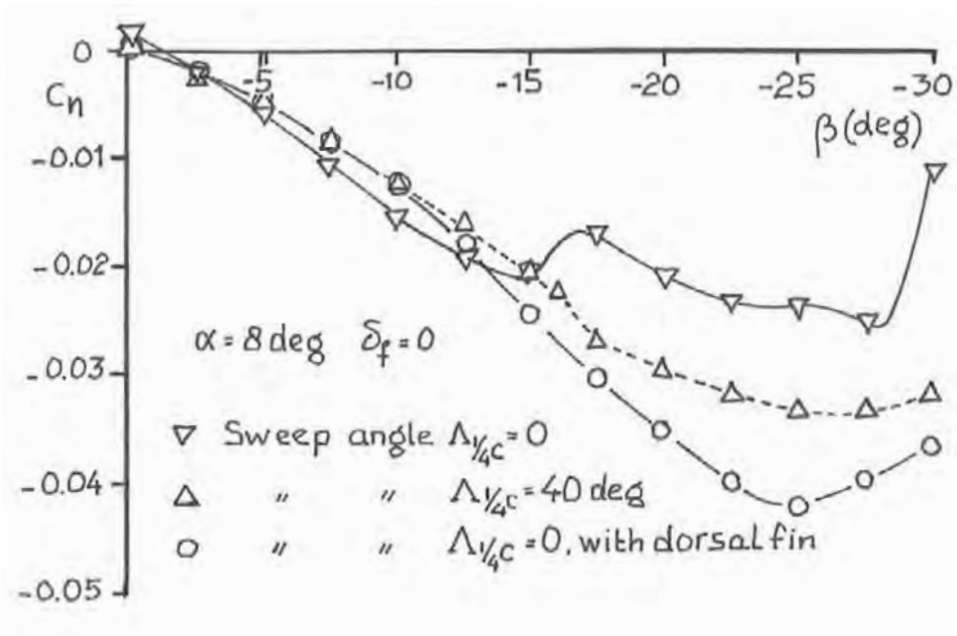
Figure 32.11 - Effect of sweep angle on vertical tailplane lift curve. Source: NLR Report A-1582
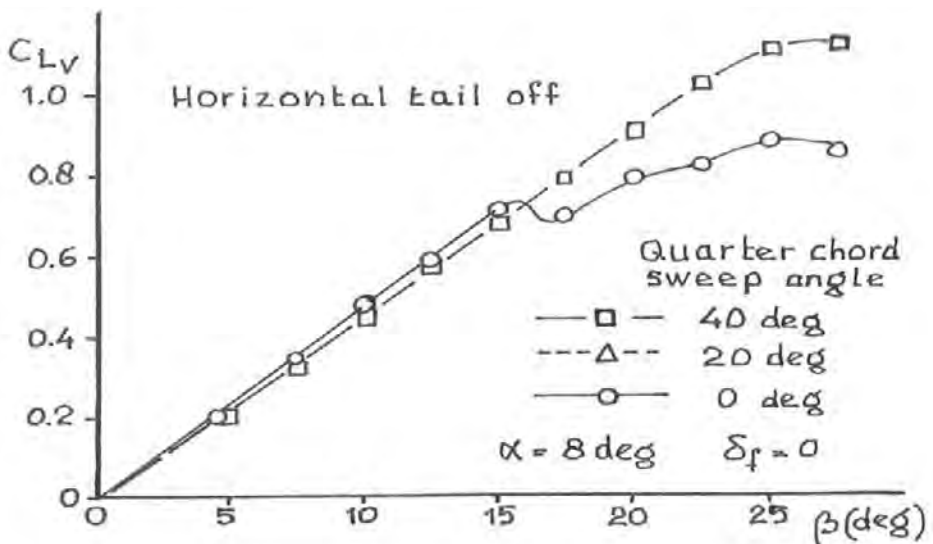
Figure 32.12 - Effect of the sweep angle and of the horizontal tail plane on the lift (side force) of the vertical tailplane in sideslip. Source NLR Report A-1582
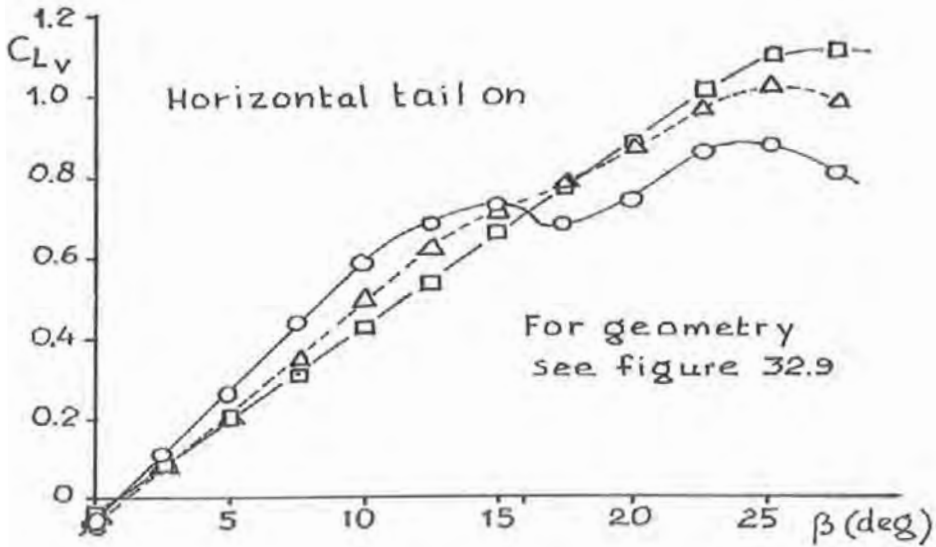
Figure 32.13 - Effect of the sweep angle and of the horizontal tail plane on the lift (side force) of the vertical tailplane in sideslip (b). Source NLR Report A-1582

But, when the aircraft angle-of-attack is increased to 8 deg, the lightly-swept tailplane with a dorsal fin performs better than the fully-swept-back vertical tail surface, although also the latter performs better than the basic tail surface without dorsal fin.

In figures 32.12 and 32.13 the tail contribution to the yawing moment has been converted to a vertical tail lift curve both with and without horizontal tail surface. Again it is clear that a dorsal fin or a high leading-edge sweep angle improves the sideslip characteristics of tail surfaces.

The above shows that also on low-speed aircraft sweep on the fin may be beneficial

Figures 32.14 and 32.15 present an overview of vertical tailplane shapes found on various aircraft. Note that the maximum aspect ratios used are:

A_V = 1.9 for low-set tailplanes

A_V = 1.5 for T-tails (indicated by combined solid and broken lines in figures 32.14 and 32.15)

The vertical tail aspect ratio is lower on T-tail aircraft because the effectiveness of the vertical tail increases due to the horizontal tailplane functioning as an endplate. Also, the vertical tail surfaces on T-tails have less taper, so that a sufficiently large tip chord provides space and stiffness to carry the horizontal tail.
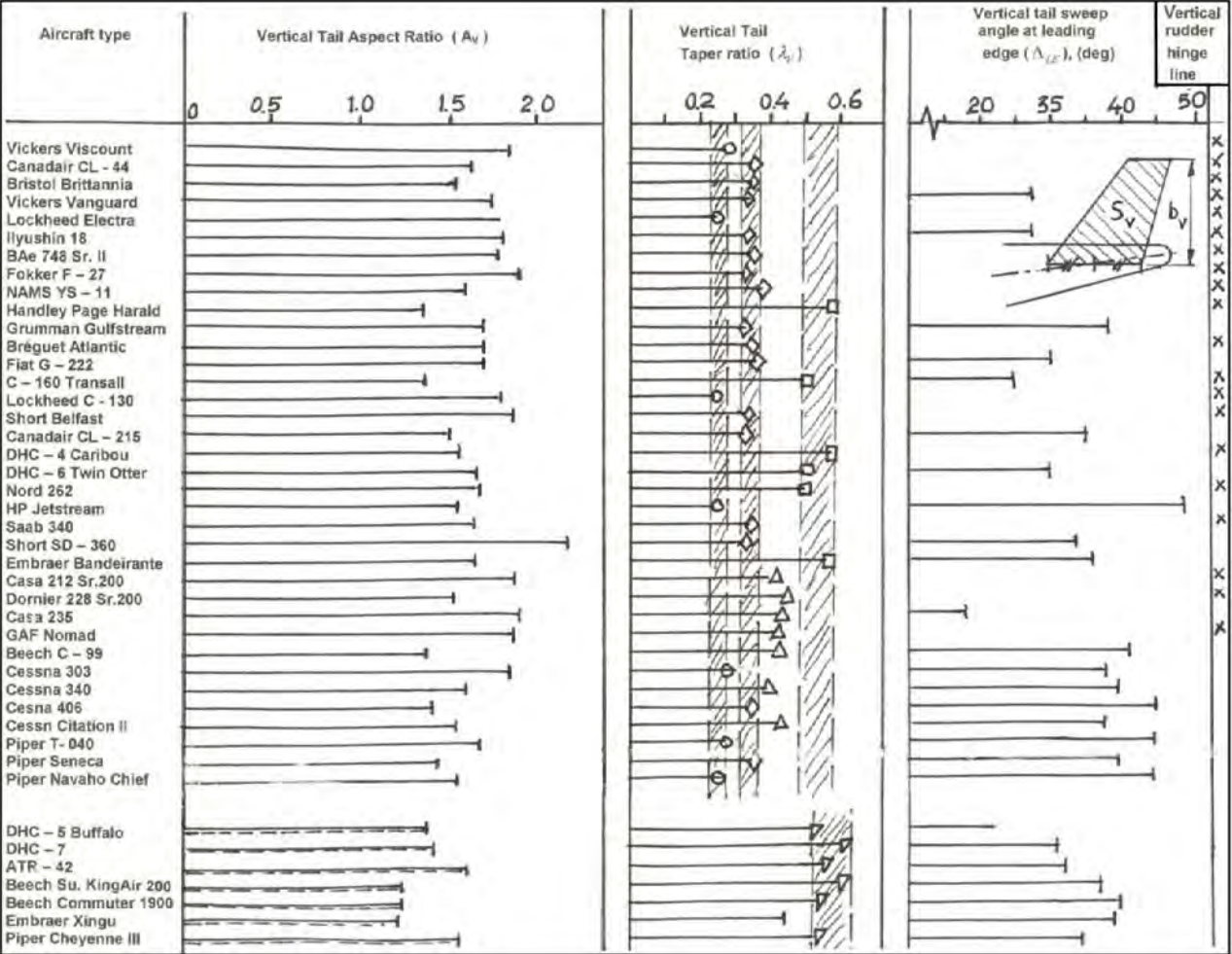
Figure 32.14 - Vertical tailplane data of propeller aircraft
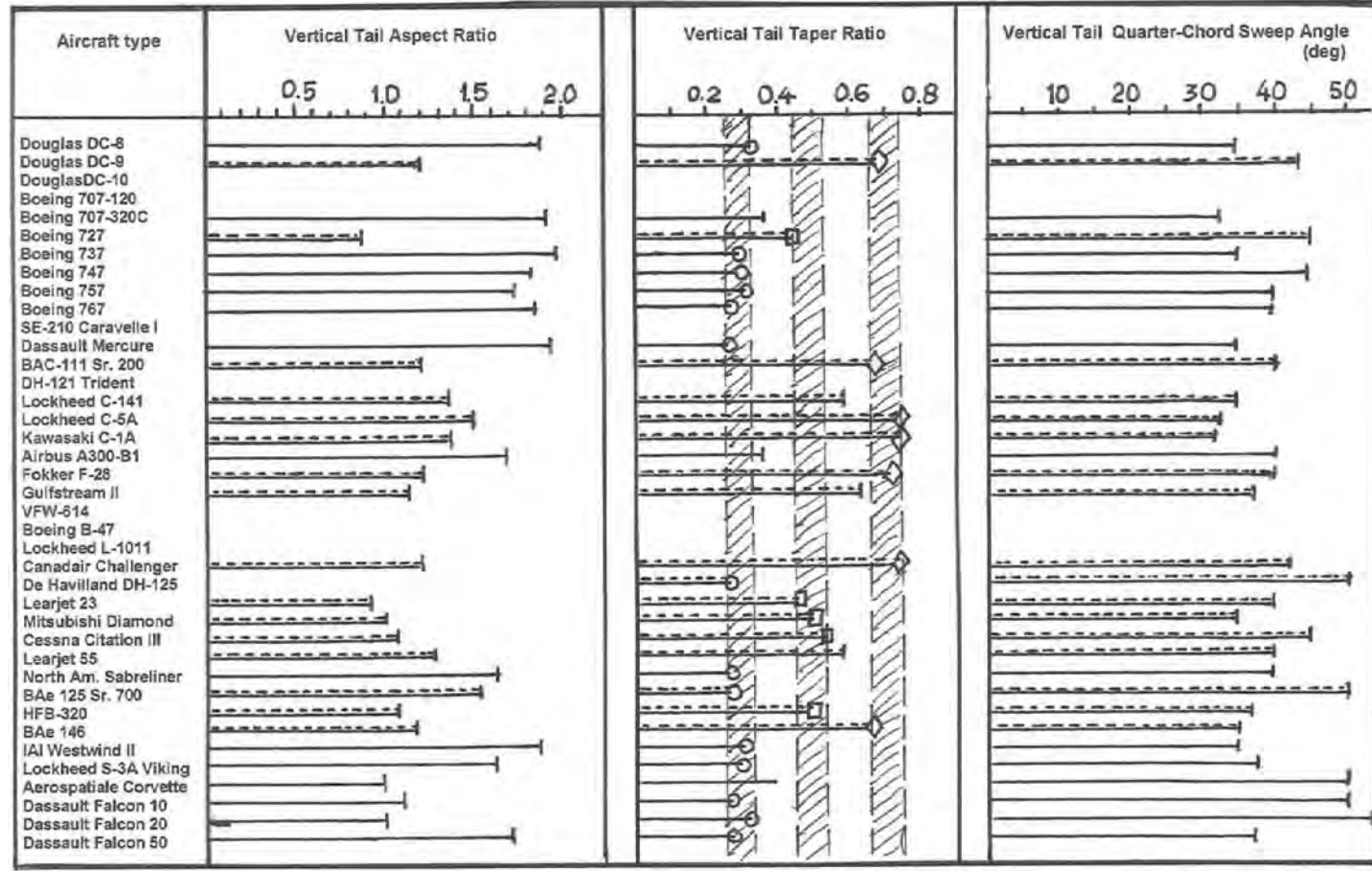
Figure 32.15 - Vertical tailplane data of jet aircraft

33 *Control surface design*

Control surfaces perform three functions:

1. Control surfaces provide means to achieve a steady state of equilibrium (trim) either at zero or at non-zero control force.

2. Control surfaces allow manoeuvring up to maximum roll, pitch and yaw rates. Also combinations of manoeuvres should be possible, for example de-crabbing in a cross-wind landing.

3. Control surfaces are used to counteract disturbances such as gusts, both small and large, which might otherwise cause the aircraft to deviate from its intended flight path (flight path tracking).

In order to obtain a **maximum lift force** due to control deflection a deep control surface may seem attractive. However, increasing the control-surface-chord-to-airfoil-chord ratio decreases the linearity between lift force (and hinge moment) and control-surface angle. This is illustrated in figure 33.1 for the rudder on a T-tail.

Note that the maximum side-force coefficient due to rudder deflection is not higher than $C_{L_v} = 0.8$ due to the low aspect ratio and is fairly independent of fin shape. Increasing the rudder-to-fin chord ratio much above $c_r/c_v = 0.30$ has no worthwhile effect on the maximum lift. Further examples of vertical tailplane lift (or side force) curves are shown in figure 33.2.

	F-29-1-1 F-29-2-2	SKV-LST-2
A_v	1.02	0.71
λ_v	0.77	0.80
$\Lambda_{1/4c}$	40 deg	40 deg
$\overline{V}_v$	0.1047	0.995
c_r/c_v	0.28	0.16 / 0.31
Based on exposed area		

Figure 33.1 - Side force due to rudder deflection – (I)
Source: Fokker Report L-29-118, L-29-137, L-307-46

	Boeing 737	F-29-2-5
A_v	1.81	1.80
λ_v	0.302	0.337
$\Lambda_{1/4c}$	35 deg	35 deg
$\overline{V}_v$	0.0891	0.0906
c_r/c_v	0.25	0.25
Based on exposed area		
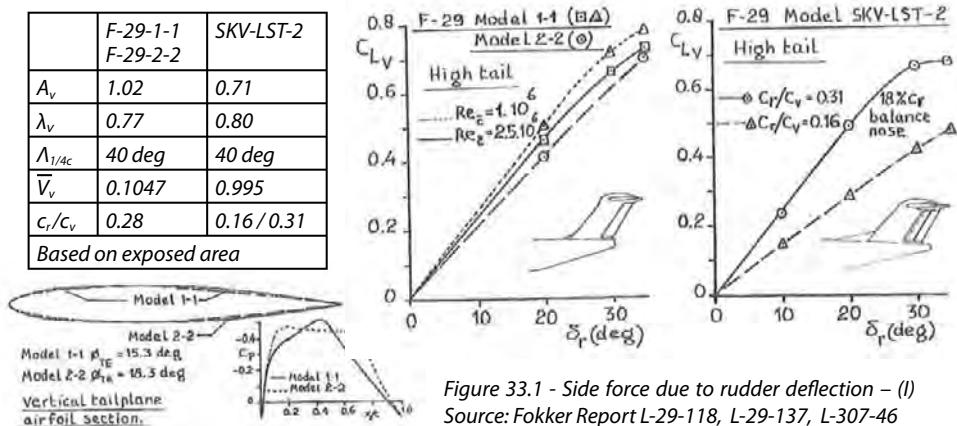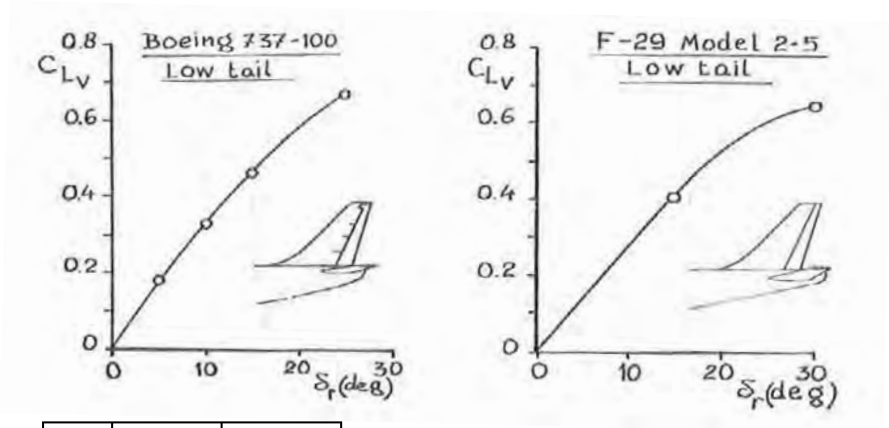
Figure 33.2 - Side force due to rudder deflection – (II)
Source: Fokker Report L-29-150

On a swept airfoil the root of the rear spar is a heavily loaded structural element. To maximise the spar height may therefore seem attractive. The resulting increase in the section tail angle will however decrease the aerodynamic effectiveness of the rudder as illustrated in figure 33.1. A compromise has to be made here.
In figure 33.1 the rudder on model 1-1 is more effective at $Re = 10^6$ than at $Re = 2.5 \times 10^6$. This is most probably due to deformation of the rudder brackets on the wind tunnel model at the high dynamic pressure necessary to achieve the high Reynolds number.

Until the widespread use of irreversible control systems obtaining satisfactory or even acceptable control forces at the cockpit controls has been a serious design challenge. With increasing aircraft weight and flight speed keeping control forces at acceptably low levels became a major element in aerodynamic design.
Developments in this field took two directions:
1. The control surface was extended in front of the hinge line and different cross sections were developed for these aerodynamic balances. Two types of balance were developed: the horn balance (the oldest type) and the long-span overhang balance.
2. Small balance tabs were used, varying in complexity from geared tabs to spring tabs.

The newest generation of large transport aircraft has irreversible control systems and no aerodynamic balance on the control surfaces (except the Boeing 737 family) to minimise drag. However for small propeller aircraft, business jets and the new class of Very Light Jets (VLJ's) manual control systems with aerodynamic balance on the control surfaces will still remain attractive.

The type of aerodynamic balance on control surfaces has a large effect on the linearity of the hinge moment coefficient vs. angle-of-attack and vs. control surface deflection.

$$C_h = C_{h_0} + \frac{\partial C_h}{\partial \alpha}\alpha + \frac{\partial C_h}{\partial \delta}\delta \qquad \text{(seldom applies at large angles)}$$

Linearity of the hinge-moment relations is particularly important for rudders because the rudder may be deflected to its maximum angle both to the weather side (during flight with a failed engine) and to the lee side (during side slips and cross-wing take-offs and landings). Non-linearities in hinge moment coefficients may cause large variations in control forces.

Large overhang balances also limit the maximum control surface deflections. If the leading edge of the balance nose protrudes outside the section contour overbalance and control lock may occur.
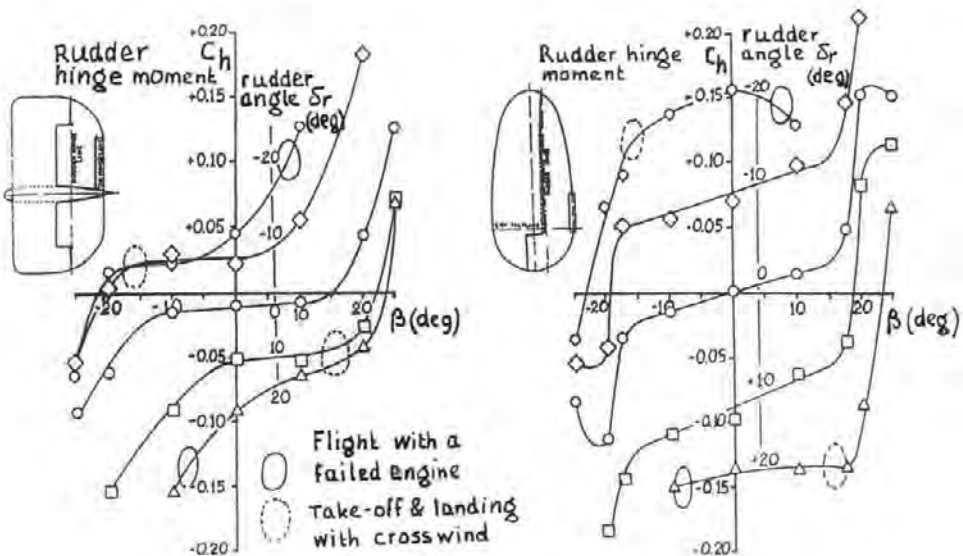
Figure 33.3 - The effect of two types of rudder balancing over the range of rudder hinge moments. Left: Handley-Page Halifax, Right: Avro Lancaster. Source: ARC R&M 2479

This is illustrated in figure 33.3. The rudder hinge moment coefficients are shown for two British four-engined World War II bombers, the Handley Page Halifax and the Avro Lancaster (fig. 33.4).

In both graphs representative conditions are indicated for flight with a failed engine (the drawn ellipses) and for a crosswind take-off or landing (the dotted ellipses).

The data on the Halifax, equipped with long-span overhang balances, show very non-linear hinge-moment curves at the larger rudder angles. This led to low rudder pedal forces in evasive sideslip manoeuvres resulting in a number of cases of overstressing. The Halifax rudders were later modified.

Figure 33.4 - Avro Lancaster. Source: Ian Nightingale

The Lancaster, equipped with shielded horn balances did not have this problem as the rudder hinge-moment coefficient showed a very regular pattern and consequently rudder pedal forces were sufficiently high to prevent overstressing.

On both aircraft a sudden hinge-moment reversal could occur leading to rudder lock when the angle-of-sideslip surpassed 22-24 deg. However the chance that this happened inadvertently was much larger on the Halifax than on the Lancaster.

Dorsal fins not only increase the maximum sideslip angle which can be reached before control is lost. But, as both effects are caused by thickening of the boundary layer and flow separation, dorsal fins also increase the sideslip angle where a significant rudder pedal force lightening and eventually rudder lock occurs.

The effect of a dorsal fin on the hinge moment characteristics is shown in figure 33.5. This figure shows wind tunnel test data obtained during the development of the Fokker F-27.

Figure 33.5 - Effect of a dorsal fin on the rudder hinge moment - Fokker F-27. Source: NLL Report A - 1394

Some significant characteristics of elevators were already discussed in chapter 31. Also on horizontal tail surfaces large variations occur in angle-of-attack and control deflection. In particular when some ice accretion is taken into consideration this may heavily influence the choice of primary design parameters for the horizontal tailplane and may also effect the elevator control force characteristics.

Contrary to elevator and rudder, which are attitude controls, ailerons are primarily rate controls. Therefore their effect increases linearly with speed unless compressibility effects or aeroelastic deformation causes a decrease in achievable roll rates. This is illustrated in figures 33.6 and 33.7 where peak roll rates for aileron-alone roll manoeuvres are presented for the Fokker F-28 Mk 1000.
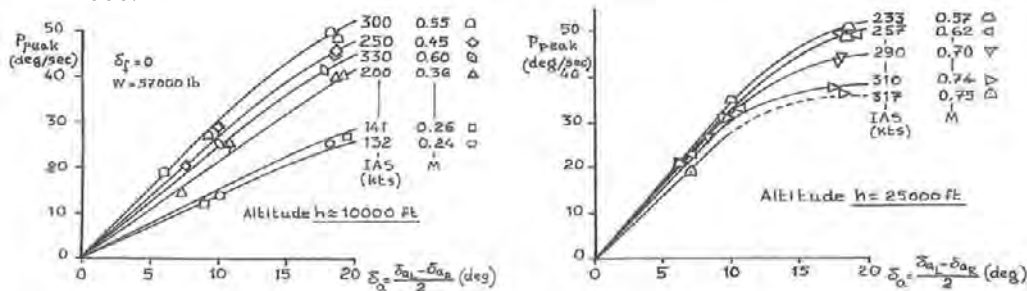
Figure 33.6 - Peak roll rates in aileron-alone roll manoeuvres vs. aileron angle - Fokker F-28. Source: Fokker Report V - 28 – 75.
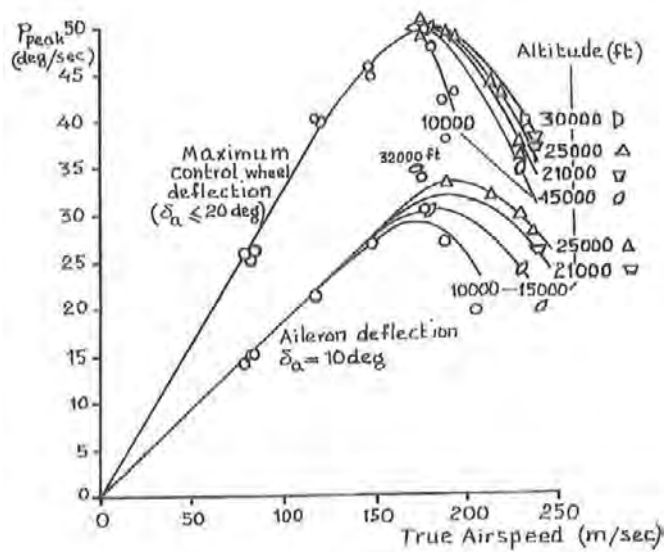
Figure 33.7 - Peak roll rate for aileron-alone roll manoeuvres as a function of altitude and true airspeed - Fokker F–28 Mk 1000. Source: Fokker Report V – 28 – 75.

Figure 33.8 shows the decrease in aileron effectiveness due to aeroelastic deformation as a function of Mach number and dynamic pressure. The data in this figure were used to convert the aileron rolling moments as derived from flight test data into rolling moments for the equivalent rigid wing. These rolling moments are compared to the wind tunnel test data in figure 33.9. In both cases the aileron effectiveness decreases significantly at high Mach numbers.

Note that on the outboard part of high speed wings the pressure distribution should allow aileron deflection without causing flow separation. Neglecting this requirement may lead to a lengthy flight test development for finding a vortex generator configuration that will remedy unsatisfactory high-speed roll control characteristics.
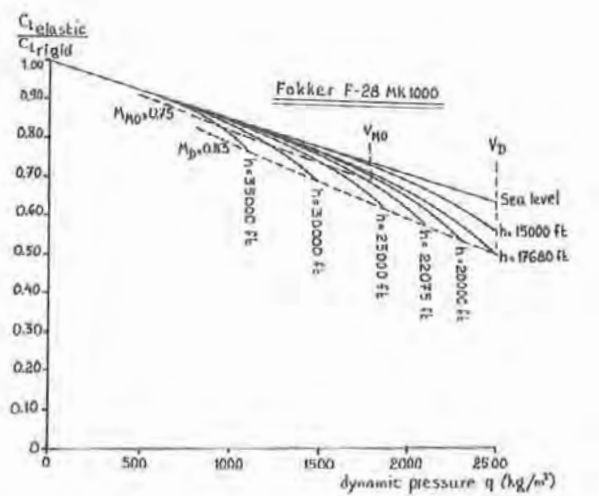
Figure 33.8 - Effect of wing torsional deformation on aileron effectiveness - Fokker F–28 Mk 1000. Source: Fokker Reports V-28-75 and X-28-392, issue 2.
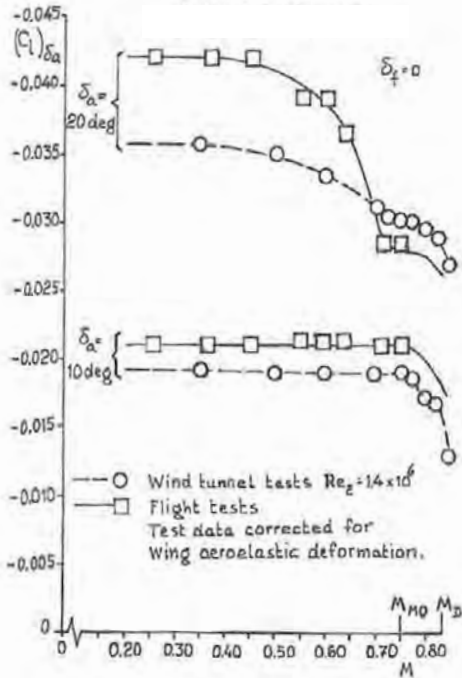
Figure 33.9 - Comparison of aileron effectiveness from wind tunnel and flight tests – Fokker F–28 Mk 1000. Source: Fokker Report V-28-75.

At high lift coefficients large aileron deflections, even with assistance from roll-control spoilers, may cause significant flight path disturbances with large adverse yaw. This is illustrated in figures 33.10 to 33.12. Although the control surfaces are fully deflected the roll rate is not constant because when sideslip occurs the rolling-moment-due-to-sideslip counteracts the rolling-moment-due-to-aileron-deflection. Even in this extreme flight condition no fin stall or rudder lock may occur.

Figure 33.10 - Aileron-alone roll manoeuvre – Fokker F–28 Mk 6000 (I). Source: Fokker Report V-28-75.
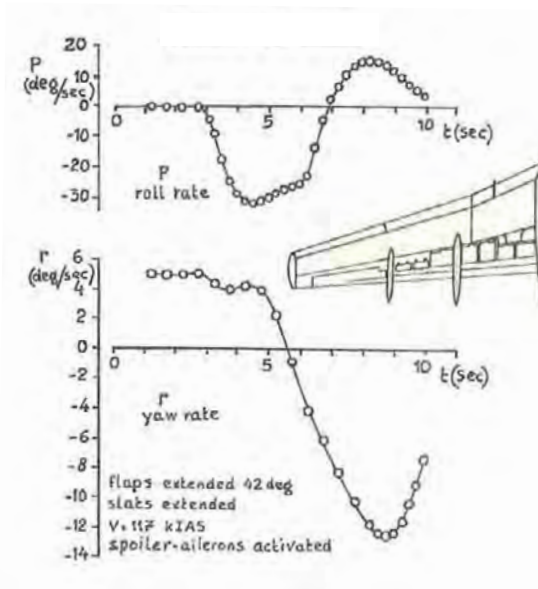
Figure 33.11 - Aileron-alone roll manoeuvre – Fokker F–28 Mk 6000 (II). Source: Fokker Report V-28-75.
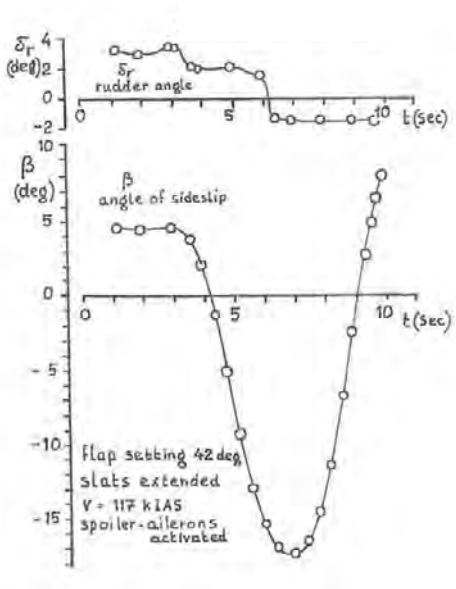
Figure 33.12 - Aileron-alone roll manoeuvre – Fokker F–28 Mk 6000 (III). Source: Fokker Report V-28-75.

Fokker 100 ailerons
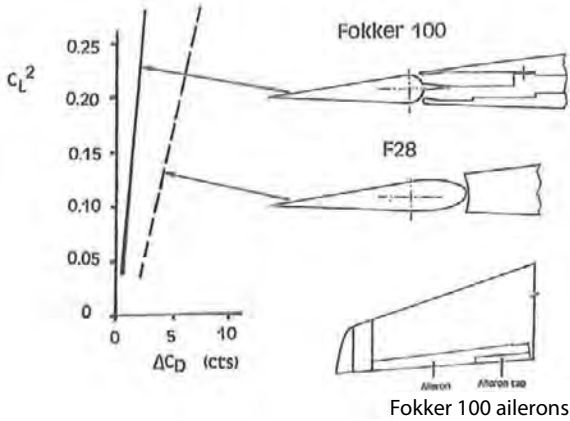
Figure 33.13 - Aileron geometry and associated aileron drag – Fokker F-28 and Fokker 100. Source: ICAS-88, Paper 6.1.2.

When supercritical airfoil sections, together with irreversible control systems, were applied in high-speed wing designs rear loading became an accepted element of modern wing design. On earlier generations of aircraft rear loading was avoided because the aileron hinge moments in the neutral aileron position tended to produce aileron upfloat through control cable stretch.

When it was decided to apply some rear loading in the wing design of the Fokker 100 wind tunnel tests showed that the original aileron with an overhang balance nose produced more drag than on the F-28. An alternative kind of aerodynamic balance, an internal balance plate which prevents leakage through the aileron gap, lowered the aileron drag to an acceptable level as shown in figure 33.13. The pressure difference over the balance plate also helps to keep the aileron at the small down rig angle in the neutral position. Figure 33.14 shows that at large aileron angles the hinge moment is slightly higher than with the F-28 type of overhang balance. The flying tab, which comes into operation after one or both hydraulic systems fail is however powerful enough to produce sufficiently large aileron deflections for flight in emergency conditions.
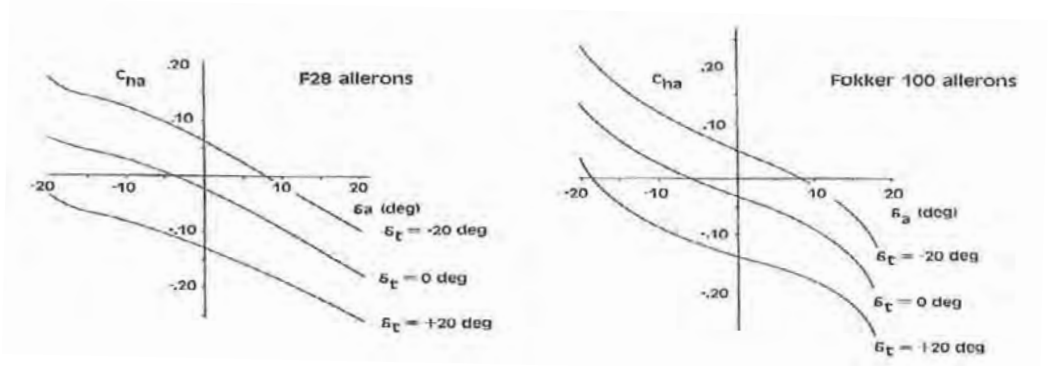
Figure 33.14 - Aileron hinge moments – Fokker F-28 and Fokker 100.Source: ICAS – 88, Paper 6.1.2.

34 *Lift spoiling control surfaces (spoiler panels)*

Spoiler panels act in the same way as split flaps except that they are usually mounted on the wing upper surface in front of the flaps.

Figures 34.1 and 34.2 illustrate the flow pattern behind spoiler panels, both with flaps retracted and extended. In the latter case the widening of the flap gap causes the complete flow over the flap upper surface to separate.

1 Separation Upstream of Hingeline
2 Reattachment on the Spoiler
3 Separation at Spoiler Trailing edge
4 Separation at the Cove lip
5 Reattachment(spoiler reversed flow)
6 Separation at the Flap Leading edge
7 Separation at Flap Trailing edge
8 Reattachment in the Wake
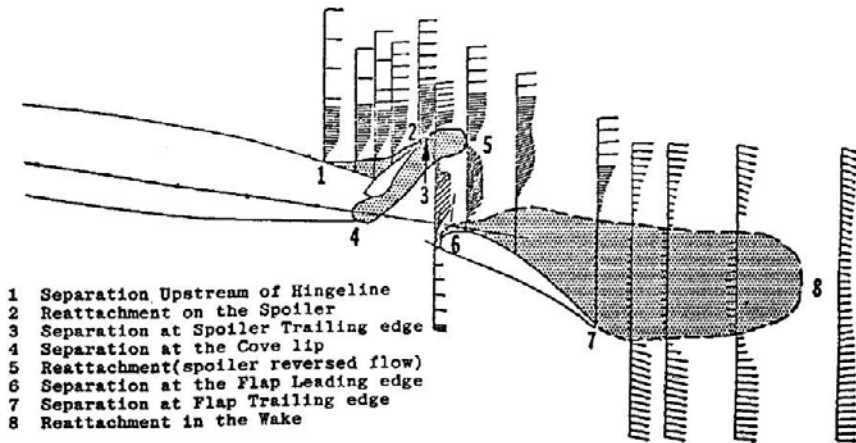
Figure 34.1 - Separated flow patterns: flap down, deflected spoiler. Source: AIAA Paper No 79-1873
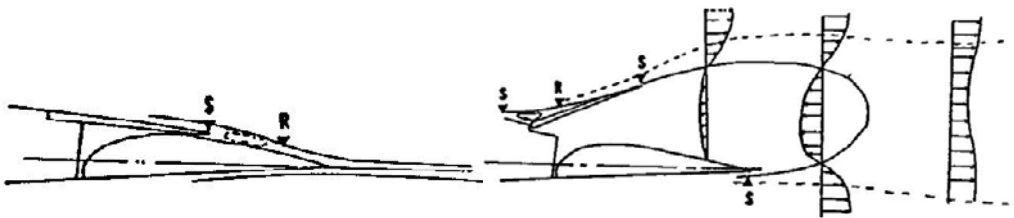
Figure 34.2 - Small (left) and large (right) spoiler deflection. Source: AIAA Paper No 79-1873

Just as flap and trailing-edge control surface deflection, upward **spoiler deflection** on an airfoil section causes:

1. a **decrease** in **lift**.
2. a **change** in **pitching moment**, both when considering the airfoil section characteristics and when considering the aircraft's behaviour.
3. an **increase** in **drag**.

Spoiler panels are used on transport aircraft for three functions:

1. for **roll control**
2. as **speed brakes** in flight
3. as **lift dumpers** during decelerating ground runs in landings or aborted take-offs.

Contrary to plain flap control surfaces, the change in aerodynamic characteristics with increasing deflection is far from linear and varies strongly with angle-of-attack and flap angle.

In particular for small spoiler deflections this may lead to large variations in airfoil section lift, drag or pitching moment, for a given spoiler angle. When applied as a roll control device on a wing this produces large variations in rolling moment for a given spoiler deflection. This effect is strongest with flaps in the landing position as shown in figures 34.3 to 34.5.
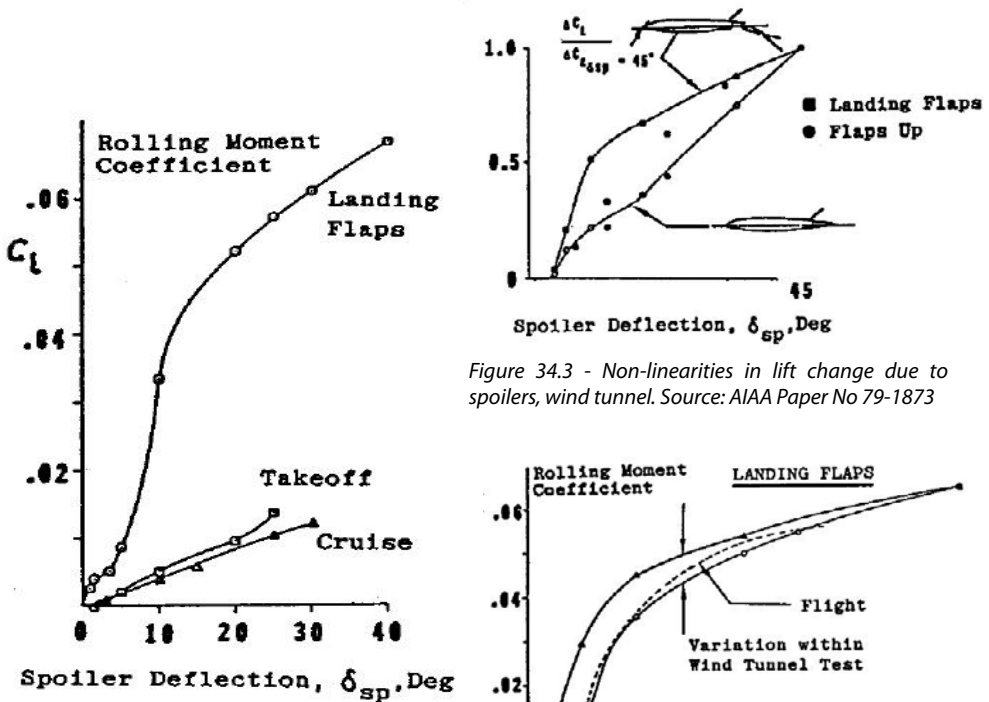
Figure 34.3 - Non-linearities in lift change due to spoilers, wind tunnel. Source: AIAA Paper No 79-1873

Figure 34.4 - Typical spoiler effectiveness characteristics, wind tunnel. Source: AIAA Paper No 79-1873
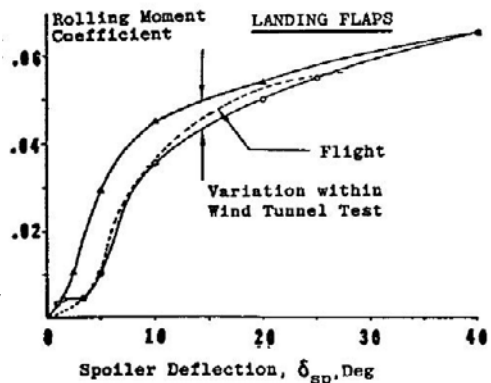
Figure 34.5 - Wind tunnel to flight comparison of spoiler effectiveness. Source: AIAA Paper No 79-1873
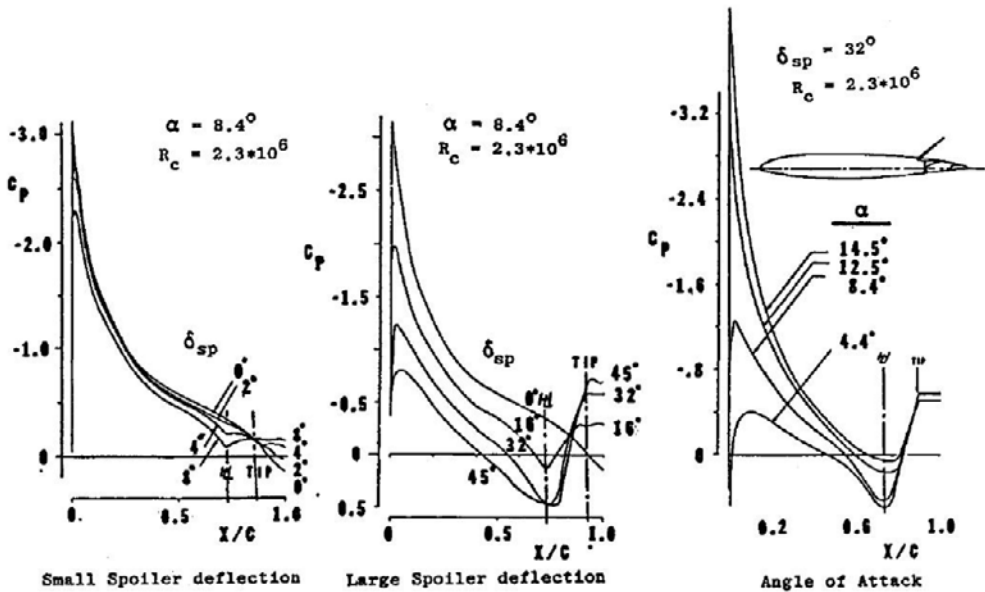
Figure 34.6 - Effects of spoiler deflection and angle of attack on upper surface pressures, flaps up. Source: AIAA Paper No 79-1873

In figure 34.6 the upper surface pressure distribution is shown on an airfoil section with a deflected spoiler panel.

For each of the three control functions mentioned above only one or two of the aerodynamic effects mentioned are required. Unfortunately, the remaining effect(s) can not be eliminated. Consequently:

1. For roll control through spoiler deflection on one wing half also the overall lift of the aircraft is affected.
2. With symmetric deflection of spoiler panels as speed brakes, where primarily an increase in drag is sought, also the wing lift is affected and the longitudinal behaviour of the aircraft.
3. Spoiler deflection in the lift dumper function also produces a change in the pitching moment and hence may either increase or decrease the nose wheel load.

These unintended effects require often a complicated mixing of the various functions and highly non-linear relations between control wheel force and individual panel deflection angles.

Also in many cases the variety in functions and the non-linear aerodynamics necessitate the division of spoiler panels in several separate components.

435

On many high-speed transport aircraft the primary roll control devices are two sets of ailerons. The first set, usually positioned behind the (inboard) wing-mounted engines, is used over the complete flight envelope. The second set, positioned outboard of the take-off and landing flaps, is often only operative with the flaps deflected. At high dynamic pressures the structural deformation of thin, swept wings cause outboard ailerons to lose much of their effectiveness with even the possibility of aileron reversal. For this reason some aircraft have split outboard ailerons with only the inboard part being operative at high speeds, such as the Airbus A330/A340.

Spoiler panels are positioned between the all-speed and low-speed ailerons and between the all-speed ailerons and the fuselage.

Figures 34.7 and 34.8 present the spoiler panel distribution on the Airbus A310 and on the Boeing 747.

The three spoiler panel functions are indicated in figure 34.7 for the Airbus A310. On the A310 the outboard ailerons have been deleted with part of the high-speed roll-control function being performed by outboard spoiler panels. Spoiler panels, because of their more forward hinge position, produce less torsional deformation than ailerons.

The aerodynamic characteristics of some spoiler panels of the Boeing 747 are shown in figures 34.9 to 34.15. These figures illustrate that the lift, drag and pitching and rolling moments are interrelated and are strongly non-linear with spoiler deflection, flap deflection, angle-of-attack, Mach number and dynamic pressure (aeroelastic effects).

This required in turn complicated mixing schedules for the relation between control wheel deflection and speed brake and lift dumper controls and each individual spoiler panel. These mixing schedules are shown in figures 34.13 to 34.15.

The mixing unit that made this mixing schedule possible was a mechanical device. Because of the complex design requirements this mixing unit was one of the first aircraft control systems where in newer designs digital electronics were introduced.
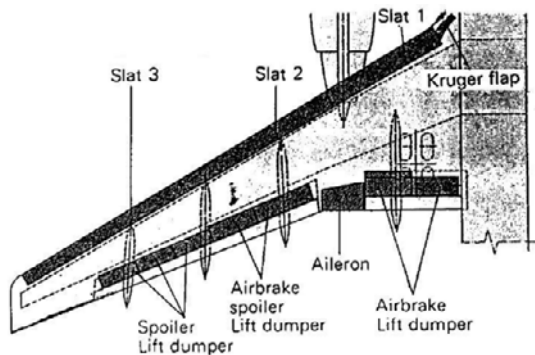
Figure 34.7 - Wing arrangement of Airbus A310.
Source: Interavia
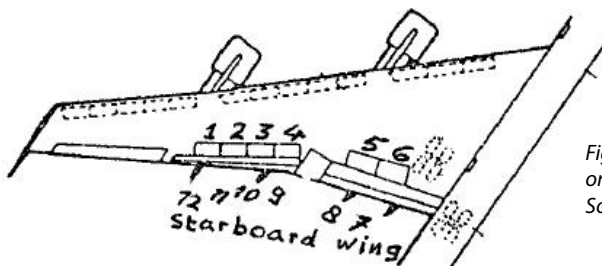
Figure 34.8 - Wing panels on starboard wing. Source: NASA CR-1756
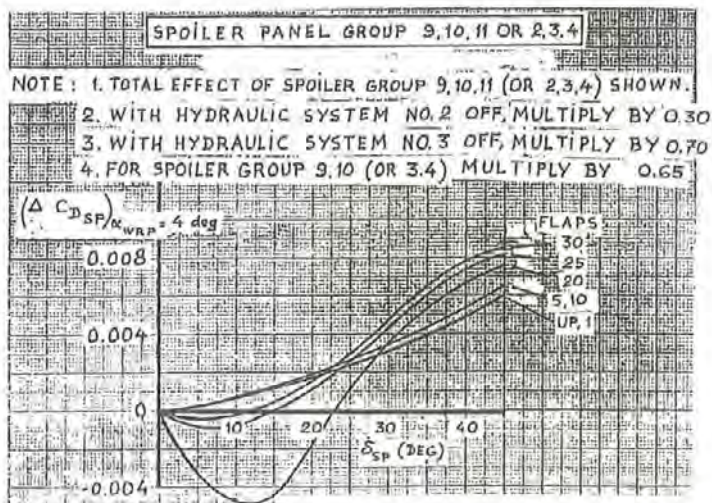
Figure 34.9 - Effect of flap setting and spoiler angle on the change in low-speed drag due to spoiler panel deflection at 4 deg angle-of-attack - Boeing 747-100. Source: NASA CR–114494
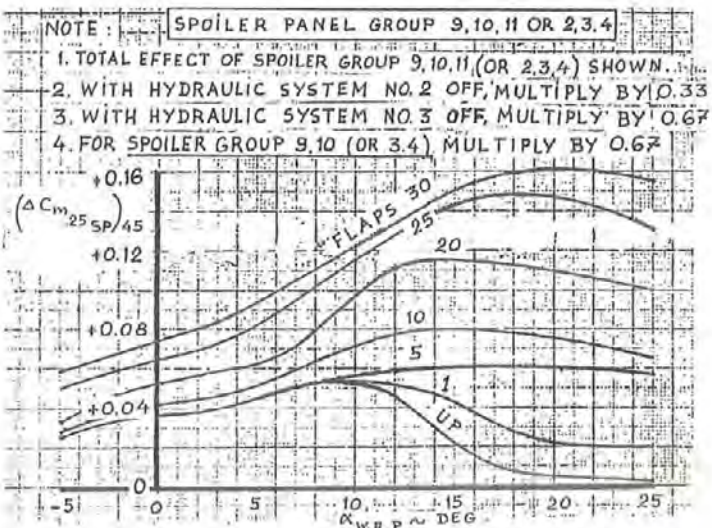
Figure 34.10 - Effect of flap setting and angle-of-attack on the change in low-speed pitching moment due to spoiler panel deflection to 45 deg. Source: NASA CR–114494
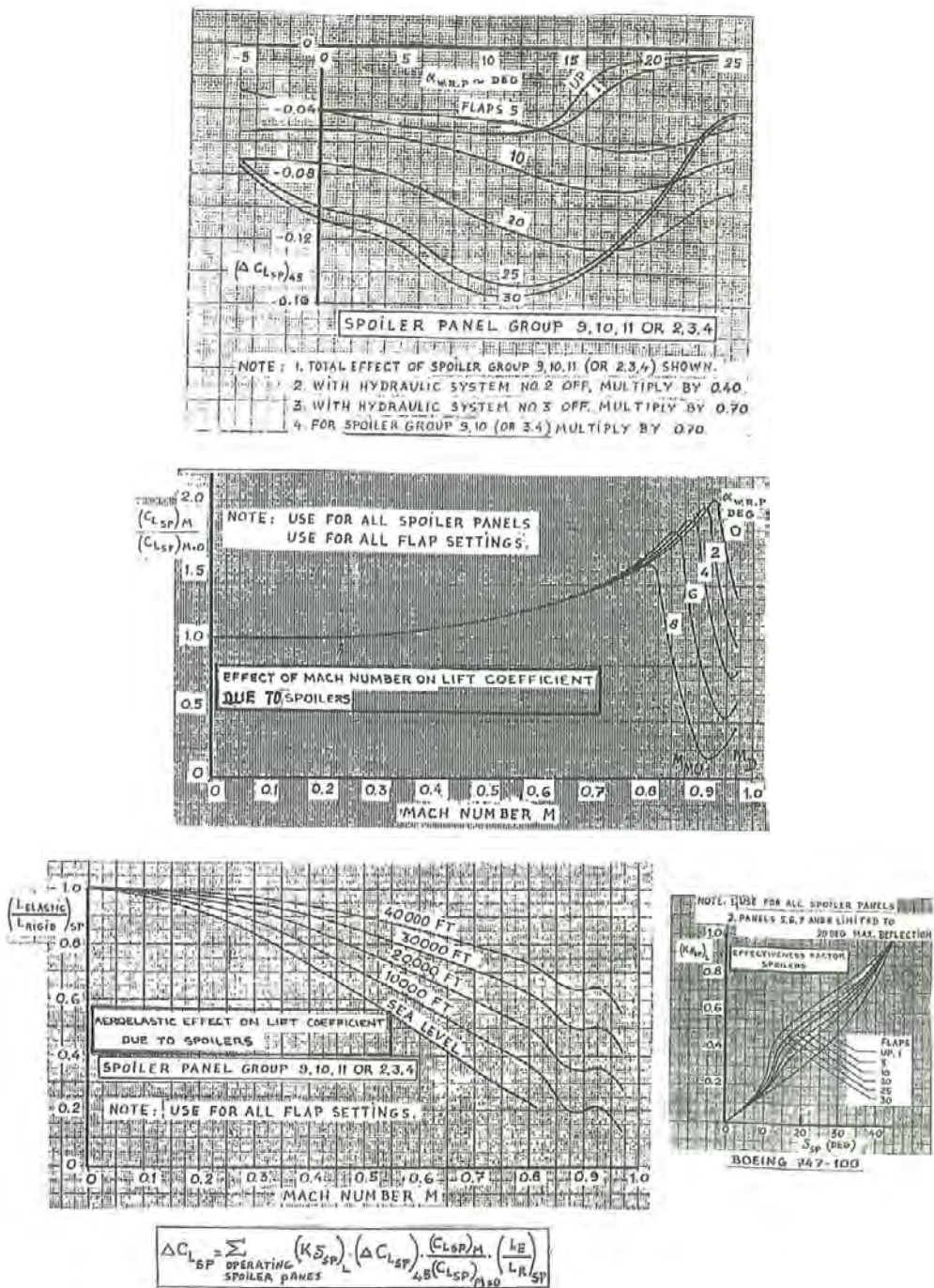
Figure 34.11 - Effect of angle-of attack, flap setting, Mach number, dynamic pressure and spoiler angle on the change in lift due to spoiler panel deflection - Boeing 747 – 100. Source: NASA CR-114494
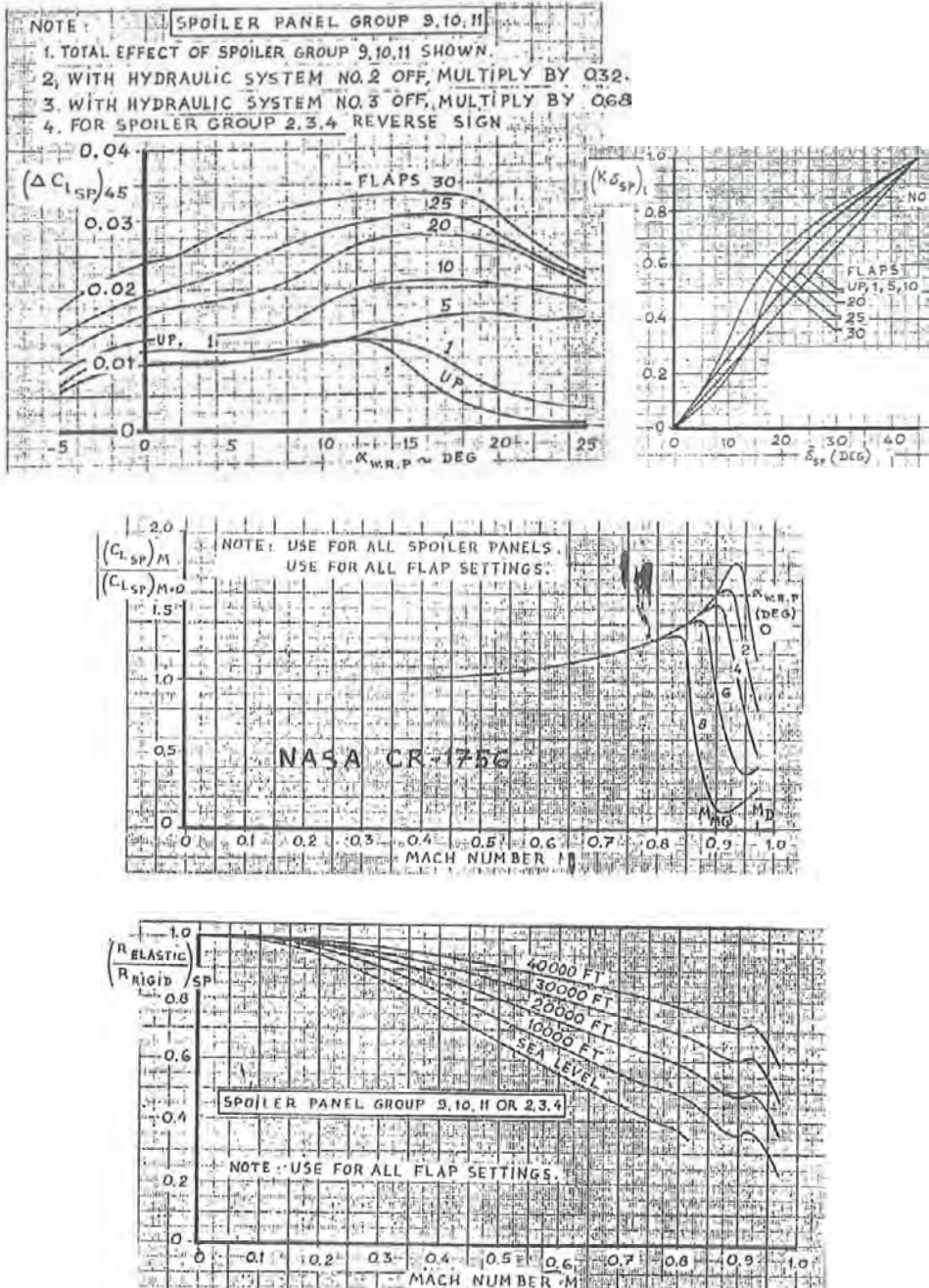
Figure 34.12 - Effect of angle-of-attack, flap setting, Mach number, dynamic pressure and spoiler angle on the change in rolling moment due to spoiler panel deflection - Boeing 747-100. Source: NASA CR–114494

439
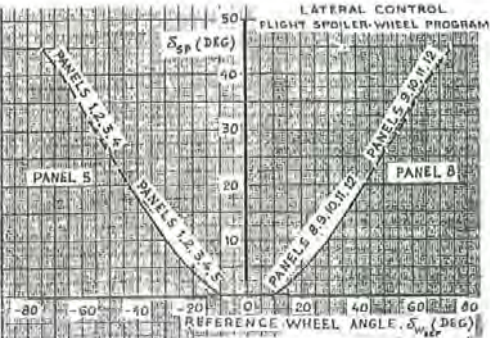
Figure 34.13 - Gearing between control wheel and roll control surfaces - Boeing 747-100. Source: NASA CR–114494
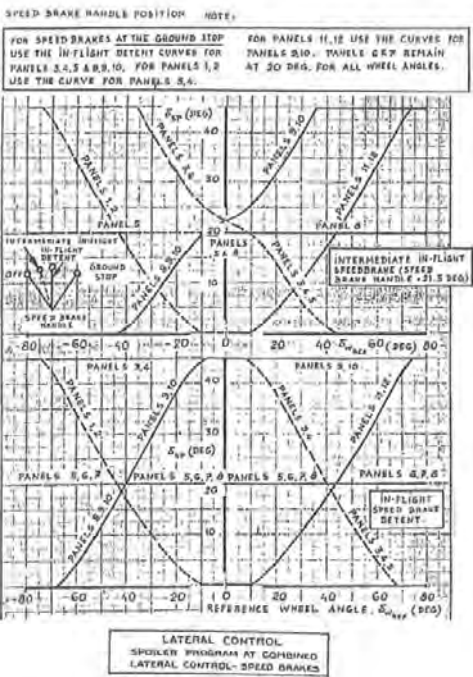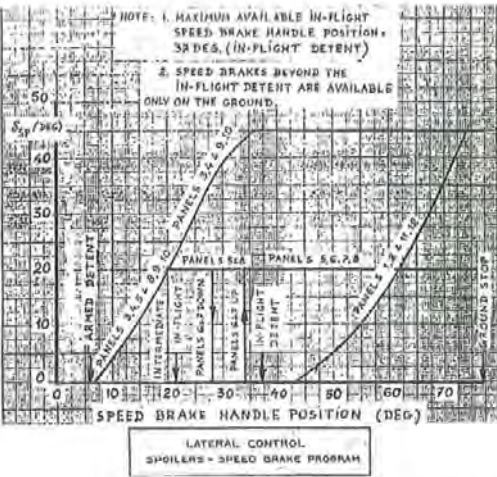
Figure 34.14 - Speed brake / lift dumper programme. – Boeing 747-100. Source: NASA CR–114494.

Figure 34.15 - Relation between control wheel angle and spoiler panel deflection in combined roll control and speed brake / lift dumper operation – Boeing 747-100. Source: NASA CR–114494.

35 *Control surface actuation*

Until the beginning of the Second World War control surface actuation on aircraft occurred almost exclusively by the pilot exerting a force at his control column (stick) or rudder pedals via a cable or push-pull-rod system. This caused a deflection of either the main control surface, the control tab (if the tab is a servo or flying tab) or a combination of both. This is called a **manual control system**. It is used today mostly on small, slow to medium-speed aircraft, because it is reliable as well as relatively simple to design and build (and therefore cost-effective).

For large and/or fast-flying aircraft manual control systems have the following disadvantages:

1. To prevent excessively high control forces a very high degree of aerodynamic balancing has to be developed including the use of complicated (spring-) tab systems. Very low values for the hinge moment coefficients C_{h_α} and C_{h_δ} have to be realised but no overbalancing may occur. This aerodynamic balancing is very difficult to obtain over the complete flight envelope for all aircraft configurations. Furthermore, to realise consistency in aerodynamic characteristics on production aircraft very high demands are put on production standards and on control system rigging procedures.
2. Taking static aero-elastic deformation effects into account can make the control system very complex.
3. To prevent flutter large counter weights are required for static and dynamic mass balancing.

In response to these problems, so-called **booster systems** were developed during and immediately after the Second World War. Booster systems are a mixture of manual and hydraulic control systems in which the pilot's control forces are multiplied by a constant factor through hydraulic actuators (boosters). Such systems are **fully reversible, i.e. all the (non-linear) characteristics of the aerodynamic hinge moments of the control surfaces are being fed-back to the pilot**. With such systems the level of control forces can be lowered considerably, which eliminates the very stringent requirements for aerodynamic balancing. The variations in control force due to changes in aircraft configuration,

Mach number or dynamic pressure remain however. The Fokker F-28 and the Fokker 100 have booster control systems in the elevator circuit.

In the late 1940's **fully irreversible hydraulic control systems** were developed. On such systems the control surfaces are actuated through one or more hydraulic actuators. The hydraulic flow control valve (and so the force exerted by the actuators) is controlled by the pilot through the cockpit flight controls.

The **control forces as felt by the pilot stem from a so-called "feel unit"** implemented in the control system. In its simplest form, this comprises of a spring box, which will give the pilot only stick displacement feedback.
In order to obtain velocity feedback, the free-stream dynamic pressure is usually fed into the system. This produces the so-called "q-feel".

Hydraulic systems are considered to be less reliable than manual systems. The failure rate of one system is assumed to be one failure per 10^3 to 10^4 flight hours. Therefore, multiplex systems are usually applied in order to prevent a serious degradation in flight characteristics after a single failure. The risk of serious degradation in flight characteristics by a single failure in the control system is also minimised by splitting the control surfaces themselves into two or more parts.
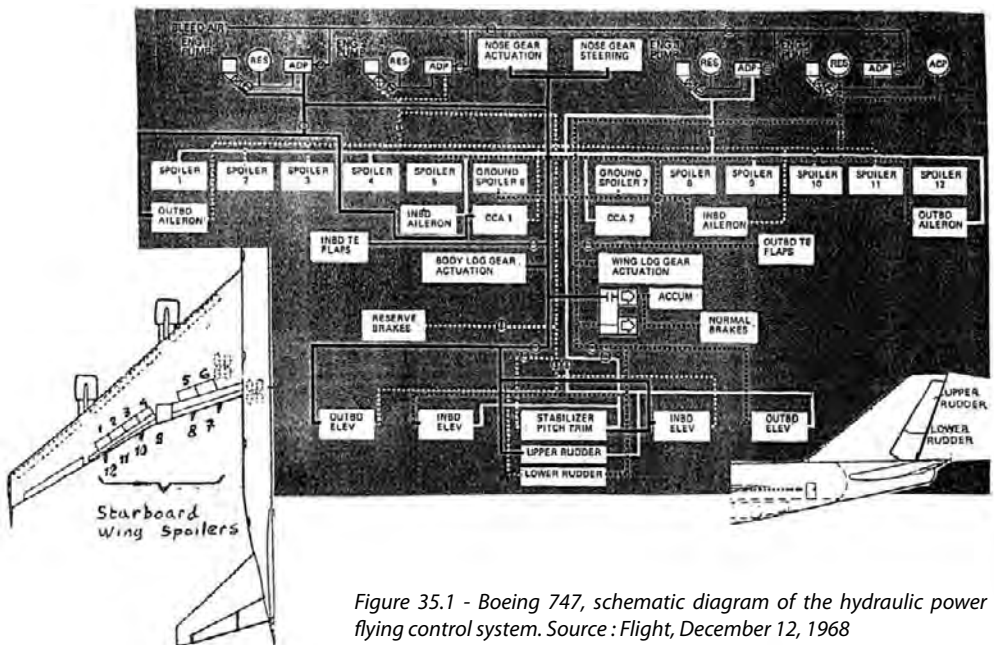
Figure 35.1 - Boeing 747, schematic diagram of the hydraulic power flying control system. Source : Flight, December 12, 1968

Each of these parts is either partly or completely driven by (a) separate system(s). As an example the diagram of the hydraulic system of the Boeing 747 is shown in figure 35.1.

From this figure it becomes clear that if system 3 fails, spoiler 4 will not deploy, but spoilers 2 and 3 will still be operative. This explains the multiplication factor of 0.68 in figure 34.12.

A combination of electric and hydraulic actuation schemes is also possible. Figure 35.2 shows how this was applied on the Vickers VC-10. Note for example in this figure how the rudder is divided into three panels, which are driven by multiple systems. The whole scheme has two hydraulic systems, each powered by two engines with separate pumps and two electrical systems each fed by two separate generators. The latter can in an emergency be coupled so a single generator can power all eleven electrical power control units. Notice also the ram-air backup systems that can be used to generate both electric power and pressure for hydraulic system B.

In figure 35.3 a part of an article is reproduced which describes the design philosophy of the VC-10 control system more in detail.
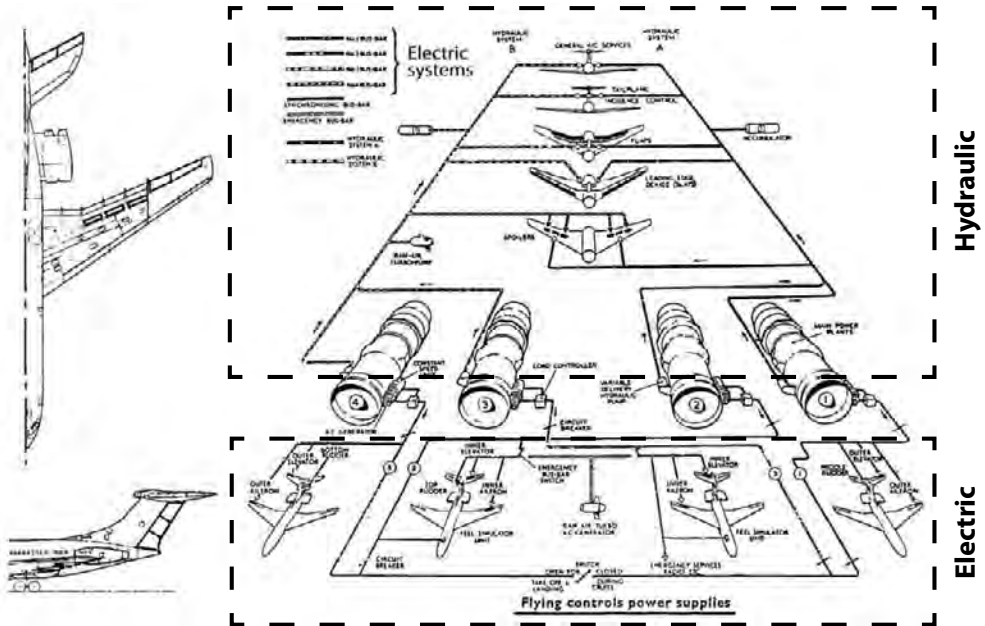
Figure 35.2 - Vickers VC-10 flying controls power system architecture. Source : Aircraft Engineering, June 1962

Another reason for splitting control surfaces is to minimise the risk of inadvertent control surface operation: if there were for example only one spoiler panel inadvertent deployment would cause an unacceptable flight path disturbance. (This is also one of the reasons why few civil airliners have an all-flying-tail. If either the stabiliser or the elevator fails or a run-away occurs, the other element is still controllable.)

With the aid of figures 35.4 to 35.6 the control surface actuation of some other aircraft are discussed.

In figure 35.4 the control surface actuation of the Boeing 767 is shown. Compared to the Boeing 747 the system architecture could be simplified to three hydraulic systems.

In figure 35.5 the control system of a smaller aircraft, the Boeing 737-200, is presented. Apart from the addition of an extra outer wing spoiler panel the same system is used on the latest -737 versions. The Boeing 737 has two hydraulic systems with a third auxiliary hydraulic system for the rudder. The stabiliser is moved by two electric motors but can in an emergency also be moved manually with the cockpit trim wheel. In case of a double hydraulic failure both elevator and ailerons can be controlled manually. On the elevator a geared tab, which is normally locked in a neutral position, becomes then operative. On the ailerons a geared tab is operative in all modes of operations.

In figure 35.6 the control system lay-out is shown of the Fokker F-28 and Fokker 100. These aircraft have two hydraulic systems. Stabiliser, elevator and rudder are each powered by both systems. The stabiliser has as a third control mode an auxiliary electrical system. When both hydraulic systems have failed elevator and rudder are both manually operated via the control column and the rudder pedals. These control systems have no tabs, only overhang balances.
Each aileron is driven by a single hydraulic system. An anti-upfloat cable connects both ailerons. When a hydraulic system fails a flying tab, which normally is locked in a neutral position, is unlocked and is then directly driven from the control wheel. The aileron is then driven by a combination of aerodynamic forces from the flying tab and the remaining hydraulic system through the anti-upfloat cable. When both hydraulic systems fail both ailerons are operated through the flying tabs directly from the cockpit.
Stabiliser, rudder and ailerons are operated by irreversible systems. The elevator is operated by a booster system with a boost ratio B.R.=4.0 and 4.8 respectively.

The keynote of the VC10 design philosophy has been safety. In the case of the flying controls this was combined with the need for adequate controllability and pleasant handling characteristics at all times. These qualities themselves go a long way to improve safety by reducing pilot fatigue and hence his liability to produce errors of judgment or technique.

One of the first questions that required resolving was whether a manually- or a power-operated control system should be employed, or indeed a powered system with manual reversion.

A manually-operated system was attractive from many points of view. It carried on the type of system which had been almost universally employed in the past, and of which a vast amount of experience had been accumulated. It was mechanically uncomplicated, reliable, required a minimum of servicing, and gave the pilot the type of system he was most familiar with. On the other hand, to mass balance the control surfaces to prevent flutter some 1,000 lb. of additional weight would have been needed. And to keep the control forces within reasonable bounds would - on an aircraft of this size - have involved exceedingly close aerodynamic balancing of the control surfaces. This in turn would almost certainly have resulted in prolonged flight testing - to develop satisfactory characteristics - and necessitated the stringent application of very tight manufacturing tolerances to ensure repeatability of the control characteristics.

The power control system might at first sight have appeared to be intrinsically heavier, due to the weight of the jacks and associated power supply systems. If, however, the power control units could be made sufficiently stiff and provide adequate damping in the failure case to eliminate the need for mass balancing of the control surfaces, some 1,000 lb. weight could be saved. Closer examination showed that this was enough largely to offset the weight of the power system. To produce a sufficiently high standard of safety with the powered system, duplication or indeed multiplication of many of the units would be necessary, and the consequent first costs and maintenance requirements would be appreciably higher than for the manual system. But the control hinge moment characteristics would no longer be so critical, and a great deal of the system development could be handled on ground rigs, saving precious flying hours.

These and many other pros and cons were tabulated for the manual system and a variety of types of power control systems, involving both electrical, hydraulic and mixed power systems. The final decision, bearing in mind the flight development time available for the aircraft, was for a straight-power control system involving split control surfaces, and having no manual reversion.

The reason for deleting manual reversion was that the additional complications involved in incorporating it probably introduced more hazards than its omission. Experience on the Valiant showed that the majority of the teething troubles associated with its power control system could be traced to the manual reversion feature: Part of the basic philosophy in the design of the flying control system was to obtain good controllability of the aircraft in the power system failure cases.

This was achieved by splitting each of the aircraft control surfaces by the use of duplicating electrical and hydraulic power supplies. Electrical and hydraulic power supply systems were split, and each had four-power sources, one on each engine, this being part of the philosophy of the design of these systems and was not a result of the use of a powered flying control system although it fitted in with the requirements of the latter.

The general arrangement of the power supplies for the controls is shown [in figure 35.2]. There are two electrical systems, engines 1 and 3 powering one, and engines 2 and 4 the other. Should any generator in either supply system fail, the other generator will supply sufficient power to keep all the power control units operative.

Under certain flight conditions, other than takeoff or landing, the two systems can be automatically commoned to form a single system in the event of failure of a power source. In this context, with suitable shedding of non-essential loads, one generator alone is capable of providing sufficient power to operate all eleven power control units.

In a similar manner, two separate hydraulic systems are provided, engines 1 and 2 providing power for system A, and engines 3 and 4 for system B.

Both electrical and hydraulic systems have ram air turbines as a standby to cope with the extremely remote possibility of the stopping of all four main propulsive engines.

The interests of safety are further advanced by arranging for the hydraulic systems to provide some roll and pitch control, whilst the rest is provided by the electrical systems.

Thus, roll control is provided by four ailerons moved by power control units operated by the electrical systems, and by six spoiler sections moved by hydraulic jacks.

Pitch control is by four independent elevators and associated electrical system power control units, whilst the variable incidence trimming tailplane (which can be used to control the aircraft in pitch) is powered by two hydraulic motors. The rudder is in three sections, each with its own control unit.

The power control units operating the ailerons, elevators and rudders are self-contained units each consisting of an electric motor, variable displacement hydraulic pump and an hydraulic jack. Control of these units and the spoiler jacks is through duplicated cable runs.

The spoilers have a dual function, operating either in

Figure 35.3 (I)- Vickers VC-10 - The Flying Control System. Source: Aircraft engineering, June 1962

conjunction with the ailerons to provide lateral control, or in unison when functioning as speed brakes. A mechanical 'mixing box' is provided in the control run to enable these two functions to be combined.

This control system was designed as a completely integrated system, with the autopilot elements integrated with and acting directly upon the power control units. This is fully described in the article on automatic landing. This is true also of the yaw damping applied to the rudder.

It was a design aim to avoid the use of synthetic stability aids if possible. This was not completely possible on a high-altitude, swept-wing aircraft like the VC10 which has an inherent tendency towards poor Dutch roll characteristics under some flight conditions and it was necessary to compromise to the extent of making the aircraft flyable without synthetic stability under all conditions, but reliant on yaw damping to provide pleasant handling characteristics.

With the use of a complete power control system such as this, there is no feed-back of aerodynamic force from the control surface to the pilot. It was, therefore, necessary to provide duplicated synthetic feel. Each half of the system consists of an electric motor, hydraulic pump and reservoir, and one aileron, one elevator and one rudder control unit and feel jack. The function of the control units is to regulate the hydraulic pressure in the feel jacks as a function of dynamic pressure, and, in the case of the elevator and aileron units, of altitude as well. Under given conditions of speed and altitude, the feel forces are directly proportional to control deflection. The pilot's feel in each of the three channels is derived from a pair of jacks. Each pair of jacks is connected to the appropriate control circuit via a differential linkage. In the event of failure of one half of the artificial system, this linkage ensures that the pilot's feel remains unaffected.

Figure 35.3 (II) - Vickers VC-10 - The Flying Control System. Source: Aircraft engineering, June 1962
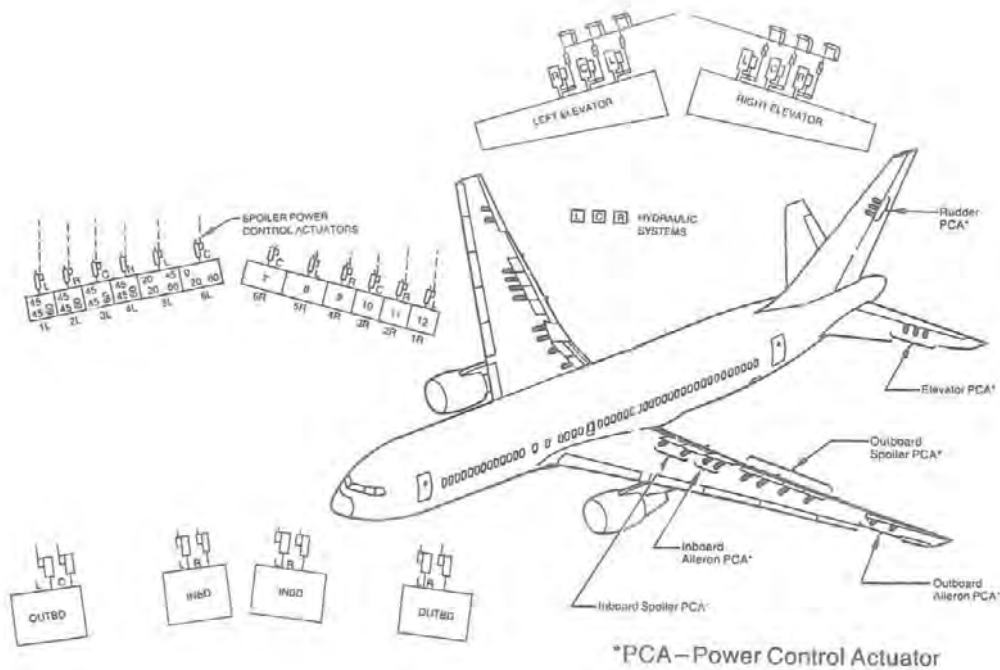
Figure 35.4 - Control surface actuation on the Boeing 767.
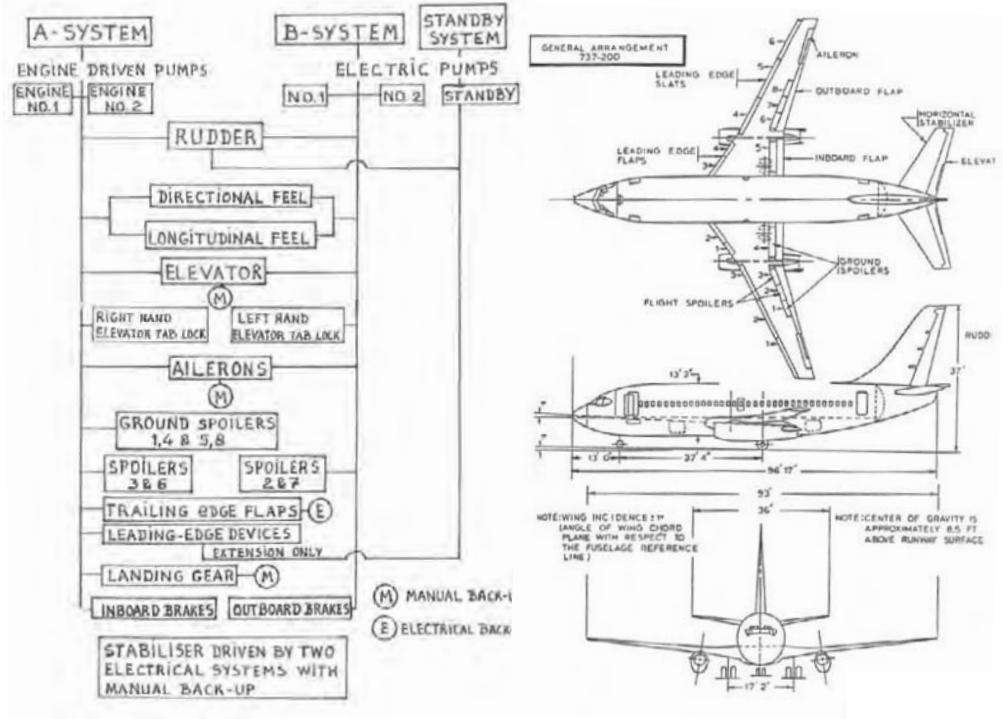
Figure 35.5 - Control surface actuation on the Boeing 737-200.

Fly-by-wire

In the foregoing classical control systems were discussed. With the advent of digital electronics new developments have taken place.

Digital electronics in primary aircraft control systems ("fly-by-wire") found their first application in supersonic combat aircraft, such as the F-16. When the reliability of such systems had been established they were introduced in civil aircraft.

Electronics had been applied in aircraft control systems before. Manufacturers and operators were familiar with sophisticated autopilots and blind-landing systems. But they were considered as "add-ons", although a modern Automatic Flight Control and Augmentation System (AFCAS) as applied in the Fokker 100 may be considered as a "half" fly-by-wire system.

Fly-by-wire is a generic term which indicates several degrees of sophistication. The simplest form is electronic signalling. This means that all mechanical connections between cockpit controls and control surface actuators have been replaced by (non-moving) electrical cables and the associated equipment. The pilot will hardly notice the difference. The aircraft will react directly to the pilot's control inputs.

Full fly-by-wire systems however fundamentally change the relation between the pilot's control inputs and the aircraft behaviour. The intermediate factor, control surface deflections, is no longer noticeable to the pilot. The pilot no longer commands a certain control surface deflection but a certain normal acceleration or pitch or yaw rate with the system computing the required control surface deflections. Fly-by-wire technology also allows the incorporation of various operational safety limits in the control systems in a far better way than the previous relatively primitive and crude mechanical systems could.

Figure 35.6 - Control surface actuation on the Fokker F-28 and Fokker 100.

Although fly-by-wire technology may at first glance be a subject purely related to system design there is a direct relation with aerodynamic design. Airworthiness Requirements on the determination of the maximum lift coefficient, the minimum stick-force-vs.-speed gradient at aft centre-of-gravity position, the relation between V_{MO}/M_{MO} and V_D/M_D, the allowable centre-of-gravity range etc. have to be scrutinised and/or reconsidered. This requires extensive discussions with the authorities to come up with Special Conditions that satisfy all parties involved. These may later lead to modified or new general airworthiness requirements.

The first civil transport aircraft in which true fly-by-wire technology was applied was the Airbus A320.

Figures 35.7 and 35.8 show the various control laws and the arrangement of the control surface actuation. For a more detailed description of the system the reader is referred to the original publications.

Identical systems are used in the Airbus A330 and A340. The high similarity in handling characteristics between these three aircraft types allows very short pilot conversion courses for cross-qualification on any of the three types.

Figure 35.7 - Fly-by-wire control laws on the Airbus A320. Source: Flight international, 12 December 1987.

» Key: ELAC, Elevator and Aileron Computer (system contains two ELACs) ; SEC, Spoiler and Elevator Computer (system contains three SECs) ; FAC, Flight Augmentation Computer (two in system, for yaw command, yaw damping, rudder trim, rudder travel limitation) ; GND-SPL, ground spoiler (lift dumper) ; LAF, load alleviation function (gust alleviation) ; SPD-BRK, speed brake ; ROLL, ailerons and spoilers for lateral control ; L.Ail, R.Ail, left and right ailerons ; Norm CTL, surfaces normally controlled by the numbered ELACs and SECs ; THS Actuator, trimmable horizontal surface actuator (triple tailplane trim motor) ; L.Elev, R.Elev, left and right elevator surfaces ; M, direct mechanical control.
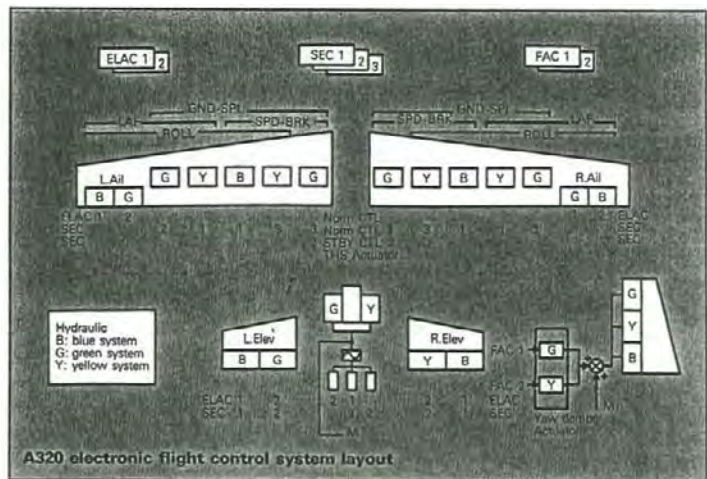
Figure 35.8 - Control surface actuation on the Airbus A320. Source: Interavia 1, 1988

A second development which took place in fly-by-wire technology on a civil transport aircraft was demonstrated on the Boeing 777. It was less a matter of technological progress than that it illustrated that fly-by-wire is so new that a common opinion on basic principles has not been reached yet.

Whereas Airbus aircraft use sidestick control for pitch and yaw with mainly control force as an input with limited sidestick movement Boeing uses a feed-back system through the computers which rotates the control wheel and moves the control column so that the pilot has the impression of operating a conventional control system. It complicates the control system design and only the future will prove if new generations of pilots will see this as superior to the Airbus approach.

Another difference in design philosophy between Airbus and Boeing is that Airbus uses hard limits in roll angle or normal acceleration to prevent surpassing the flight envelope boundary whereas Boeing utilises envelope protection. At reaching the flight envelope boundary control forces rise sharply but when the pilot persists in an emergency a higher angle-of-attack or roll angle can be achieved.

Figure 35.9 shows the surface control actuation arrangement on the Boeing 777.
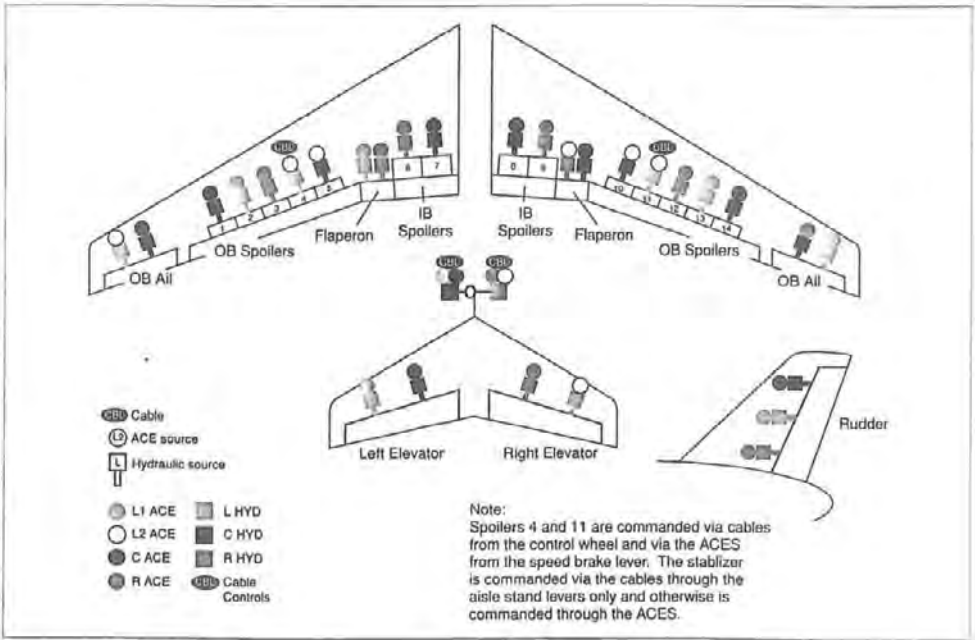
On the Model 777, Actuator Control Electronics (ACE) units provide control inputs to the hydraulic actuators for each flight control surface.

Figure 35.9 - Control surface actuation on the Boeing 777. Source: Boeing Airliner October-December 1994.

The deflection rates of primary and secondary control surfaces (slats, flaps, speed brakes) should be as follows:

The deflection rates should be high enough to give the pilot a feeling that he is really "in control" of the aircraft. Typically, full control surface deflection should be achieved in 0.4 to 0.5 second for roll control surfaces and 0.6 to 0.8 second for pitch and yaw controls. For primary control surfaces, this means that they should have deflection rates of 50 to 60 deg/sec and 35 to 45 deg/sec respectively.

The deflection rates should be high enough to compensate for trim changes occurring in normal operation. This applies to elevators but more in particular to stabilisers. The latter require trim rates of about 0.5 deg/sec at low speed and 0.15 to 0.2 deg/sec at high speed.
However, stabilisers and flaps should have sufficiently low deflection rates so that the pilot can cope with the trim changes caused by flap deflection or change in stabiliser setting. These trim changes may be deliberate (for example flap extension or retraction) or due to inadvertent operation. (for example a "run-away" on a trimmable stabiliser).

36 *Propeller slipstream effects*

Basic propeller theory

Propellers generate thrust by adding momentum to a streamtube that flows through the propeller disc area. Generating propeller thrust can be compared to generating wing lift. In both cases a streamtube is deflected over the induced downwash angle ε. Each propeller blade may be compared to a wing and deflects a streamtube such that a resultant force is created in the desired direction. This is shown in figure 36.1. At the bottom to the right the position of the propeller blade is shown.
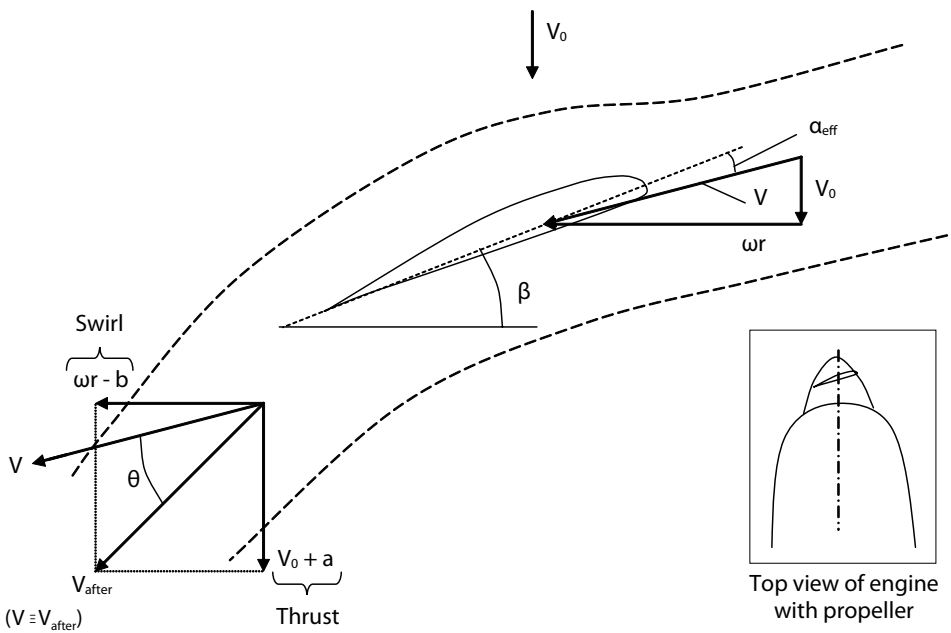
Figure 36.1 - Schematic overview of propeller airflow

The direction of the oncoming streamtube is defined for each blade segment by the vector summation of forward speed V_0 and the radial velocity of the blade segment $v = \omega r$ where ω is the propeller rotational speed and r the distance to the propeller axis. The concept of the blade segment is illustrated in figure 36.2.
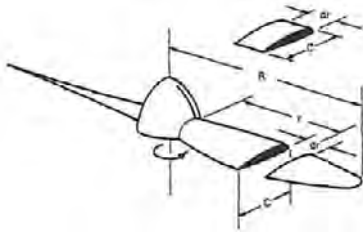
Figure 36.2 - Propeller blade element
Source: Fokker report A-225
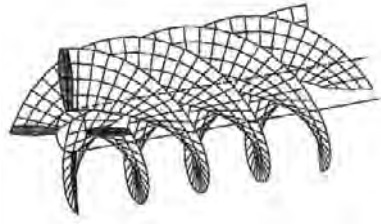
Figure 36.3 - Propeller wake helix
Source: AGARD CP-366, paper 5

The propeller deflects the part of the streamtube behind the blade segment over the induced angle θ. This deflection does not cause an induced drag but an induced *thrust* resulting from the increased impulse in **flight direction** (seen in flight direction, the velocity in the tube behind the propeller blade is increased with respect to the free stream velocity). The deflection of the flow over the angle θ is (in the aircraft frame of reference) experienced as a rotation or **swirl** with angle θ of the flow behind the propeller. The swirl is an energy loss (again seen in flight direction) and should therefore be minimised.

The picture presented above is a simplification of the real flow and should only be considered in principle. In real flow the radial velocity varies along the blade span. This explains the strong twist in propeller blades. Also the finite blade span and the flow fields of other propeller blades cause induced velocities comparable to those on a triplane or quadruplane wing. However the general conclusion concerning thrust and swirl are valid. Figure 36.3 shows the wake helix behind a four-bladed propeller.

Another way of visualizing how a propeller blade segment generates thrust is shown in figure 36.4. While the propeller segment creates lift and drag according to the standard definitions, the interesting parameters are thrust and radial force. The latter is a direct measure for the engine power required. In general, the goal is to maximise thrust while keeping the power to a minimum.
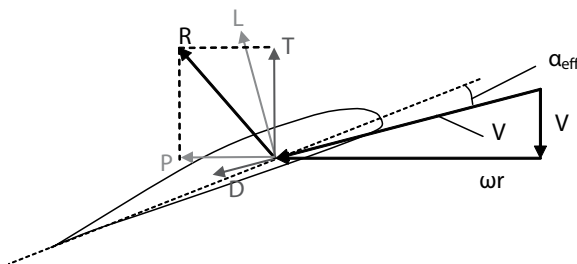
Figure 36.4 - Forces generated by a propeller segment

The stream tube behind a propeller in which the velocity of the axial flow is higher than the undisturbed flow and a rotational velocity is present is called the **propeller slipstream**.

Slipstream effects

Aircraft components which are located behind the propeller and are placed in the slipstream experience the slipstream as a variation in the oncoming airflow. Therefore, the oncoming flow is no longer homogeneous with parallel streamlines and so the pressure distribution (and consequently lift, drag and pitching moment) may differ considerably from a situation in which these components would be located outside the slipstream.

A simplified model of propeller slipstream is offered by the momentum theory where the propeller is represented by an actuator disc. In this theory slipstream rotation or swirl is neglected and the axial velocity is assumed to be constant over the slipstream cross-section. Slipstream contraction is incorporated.
The part of the wing covered by the slipstream experiences a higher dynamic pressure and will produce more lift than the adjacent parts of the wing. This is illustrated in figure 36.5.
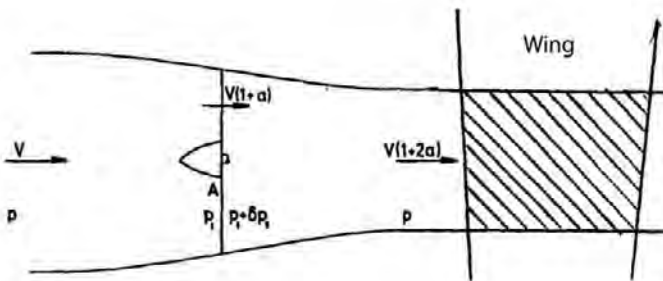
Figure 36.5 - Increase in average dynamic pressure over the part of the wing covered by the slipstream. Source: AGARD CP-366, paper 8

In real flow the wing lift is not only affected by the increased dynamic pressure in the slipstream but also by the slipstream rotation. The latter causes a variation in the local angle-of attack on the wing part covered by the slipstream. On one side of the propeller axis where the flow moves down the local-angle-of-attack is decreased. This will counteract the effect of the increased dynamic pressure on the lift on that part of the wing. On the other side of the propeller axis the slipstream swirl will produce an increase in local angle-of-attack which, together with the increased dynamic pressure, will produce a peak in the spanwise lift distribution. This is illustrated in figure 36.6 which shows the
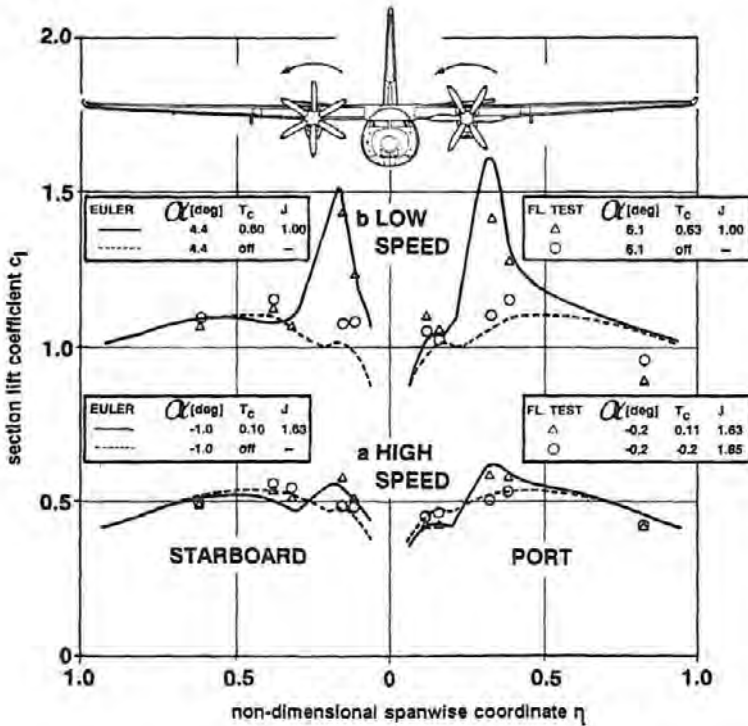
Figure 36.6 – Spanwise lift distribution of the Fokker 50. Comparison of theory and experiment. Source: AIAA Paper 90-3084.

spanwise lift distribution of the Fokker 50 for two flight conditions, calculated with a programme based on Euler equations. The calculated data are compared with local lift coefficients derived from pressure measurements on ten wing stations on the full-scale aircraft.

In figure 36.7 the spanwise dynamic pressure distribution at the horizontal tail is presented. Although the data were obtained from tests on an F-27 model the propellers rotated in the same direction as on the Fokker 50. The shift of the slipstream tube towards starboard is caused by the slipstream swirl.

The effect of propeller slipstream on wing lift is clearly shown in figure 36.8. When the thrust coefficient C_T is increased from $C_T = 0$ to $C_T = 1.39$, the lift curve slope increases and $C_{L_{max}}$ increases by about 60%.
Note that this increase in $C_{L_{max}}$ due to engine power can not be used for performance certification as the certified $C_{L_{max}}$ has to be determined in a zero-thrust condition. Additional lift due to slipstream does however give an extra safety margin during low-speed flight.
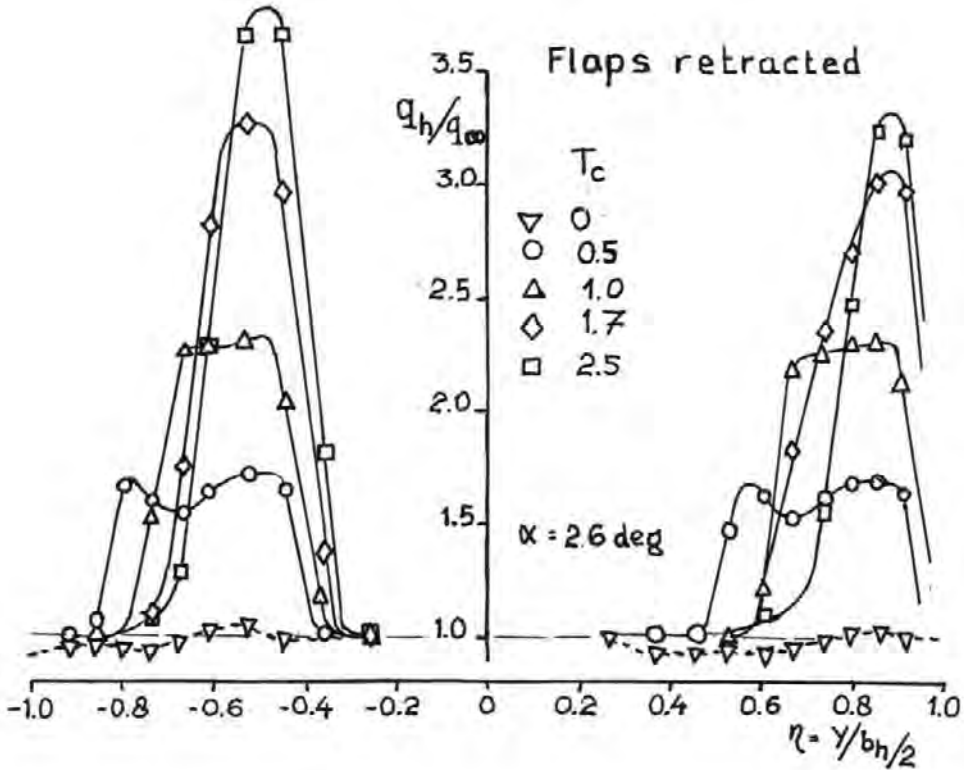
Figure 36.7 – Spanwise dynamic pressure distribution at the horizontal tailplane location as a function of thrust coefficient. Fokker F-27. Source: Fokker Report L-27-190

Many of the figures in this chapter stem from research on a STOL version of the Fokker F-27. After an extensive wind tunnel and a short flight test programme further development was cancelled because the gain in performance and the added complexity relative to the basic F-27 did not justify further expenditure.

C_T is defined as:

$$C_T = \frac{T}{\frac{1}{2}\rho V^2 S}$$ (36.1)

From figure 36.8, it can be concluded that C_{L_α} increases linearly with C_T. ($C_L = 0$ at α = -23 deg for all C_T-values neglecting the propeller normal force.)

Therefore:

$$\frac{dC_L}{d\alpha} \approx \left(\frac{dC_L}{d\alpha}\right)_{C_T=0} \left(1 + kC_T\right)$$ (36.2)

where *k* is a constant.

457
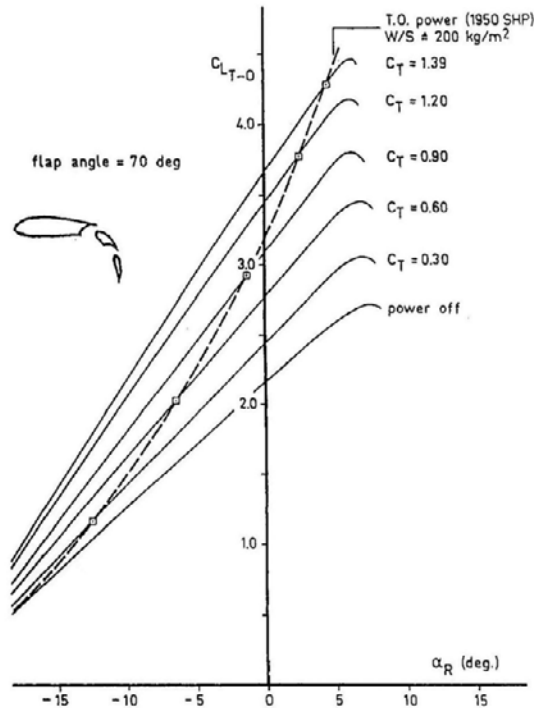
Figure 36.8 - Lift curves of F-27 STOL. Tail-off, n = 1.
Source: AGARD CP-160, Paper No. 10

Three power effects can be distinguished that affect the longitudinal stability and control of propeller aircraft:

1 – Propeller forces

Since Power = Thrust x Velocity or P = TV, the propeller thrust will increase, when the velocity of the aircraft is reduced. (The engine power remains nearly constant.) This increase in thrust may be destabilising depending on whether the thrust line is located beneath or above the centre of gravity of the aircraft. This is especially important at very low speeds, when the propeller thrust is at its maximum.

The propeller normal forces (C_{N_p}) will become quite substantial if the propeller is at a high effective angle of attack. Since the point of application is usually ahead of the centre-of-gravity, these too will often have a destabilising effect.

2 – Increase in wing lift, tail-off pitching moment and downwash

The increase in local wing lift due to the slipstream causes an increase in the downwash behind the wing – this is not limited to the slipstream tube, but occurs in the whole flow field. Therefore, the tail (also a T-tail) will experience a larger downwash, which will reduce the contribution of the tail to the longitudinal stability of the aircraft.

Usually the increase in wing lift, particularly when the flaps are deflected, will increase the tail-off pitching moment in a nose-down sense.

3 – Change in horizontal tail lift due to the increased dynamic pressure in the slipstream

If the horizontal tail is partly or completely immersed in the propeller slipstream, it will experience a higher average dynamic pressure. This will result in a larger effective tailplane lift curve slope, and increase the tailplane contribution to stability.

Whether the tail is actually in the slipstream, depends on many parameters, such as angle of attack, flap deflection and power setting.

In order to analyse the effect that the downwash has on stability, consider figure 36.9: This figure shows the linear relationship between downwash angle ε and lift coefficient C_L (as would be expected) but also that the slope

$$\left(\frac{d\varepsilon}{dC_L}\right)_{C_T=\text{constant}} \approx \text{constant.} \tag{36.3}$$

Furthermore, the ε-vs.-C_L curve shifts only slightly with increasing C_T. This shift occurs because the spanwise lift distribution deviates more and more from a near-elliptical distribution with increasing C_T.

The dashed line shows the line for constant power, for which holds

$$C_T \approx \frac{1}{V^3} \tag{36.4}$$

which is found by combining the equation $P = TV$ and equation (36.1). Therefore, when flying at constant power and C_L is increased (because the airspeed is reduced in rectilinear flight), ε increases more than according to the ε-vs.-C_L curve for C_T = constant as one moves to higher thrust levels.

A similar effect can be seen in the lift curves in figure 36.8.
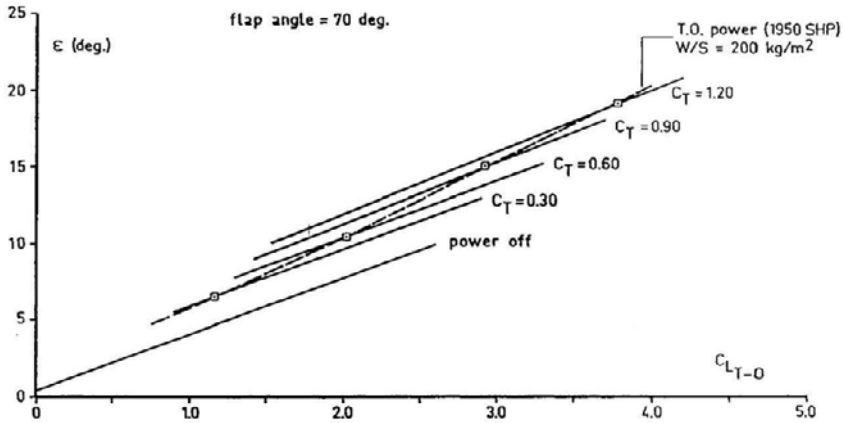
Figure 36.9 - Downwash angles at varying power settings for F-27 STOL, tail off.
Source: AGARD CP-160, paper 10

Because the wing lift curve slope C_{L_α} increases with increasing C_T (see equation 36.2), the downwash gradient $\dfrac{d\varepsilon}{d\alpha}$ also increases with C_T. Writing it as:

$$\frac{d\varepsilon}{d\alpha} = \frac{d\varepsilon}{dC_L}\frac{dC_L}{d\alpha} \tag{36.5}$$

and combining it with equations (36.2) and (36.3) yields:

$$\left(\frac{d\varepsilon}{d\alpha}\right)_{C_T=\text{constant}} = \frac{d\varepsilon}{dC_L}\left\{\left(\frac{dC_L}{d\alpha}\right)_{C_T=0}\left(1+kC_T\right)\right\} \tag{36.6}$$

In effect, equation (36.6) says that, when flying at constant airspeed and power setting (that is, with C_T = constant), the higher the power setting is chosen and so the thrust, **the more the contribution of the horizontal tailplane to the longitudinal stability of the aircraft decreases**.
This applies in particular when the tailplane is outside the slipstream.

On propeller-driven aircraft two types of longitudinal stability at constant power setting exist:

- The response of the aircraft to a change in angle-of-attack at constant speed (and constant C_T) such as in a turn or pull-up manoeuvre.
- The response of the aircraft to a change in angle-of-attack due to a change in speed in rectilinear flight (and a change in thrust coefficient C_T).

On jet aircraft there is hardly any difference between these two state variations because of the limited effect of changes in C_T.

Figure 36.10, illustrates the different changes in tailplane angle-of-attack (α_h) when the aircraft angle-of-attack (and the lift coefficient) is changed at constant C_T or due to speed (and C_T) variations in rectilinear flight. At constant C_T, it is a stable aircraft. A change in aircraft-tail-off lift coefficient results in a significant change in tailplane angle-of attack α_h, and a change in tail force and thus a restoring moment is produced.

The dashed line, indicating the change in α_h when the aircraft lift coefficient changes due to speed variations in rectilinear flight at constant power, has a minimum at about $C_L = 3$. At that minimum, the slope of the α_h-vs.-C_L curve is zero. Physically, this means that the tail contribution to the stability of the aircraft is insignificant. The tailplane lift coefficient is independent of aircraft angle of attack.
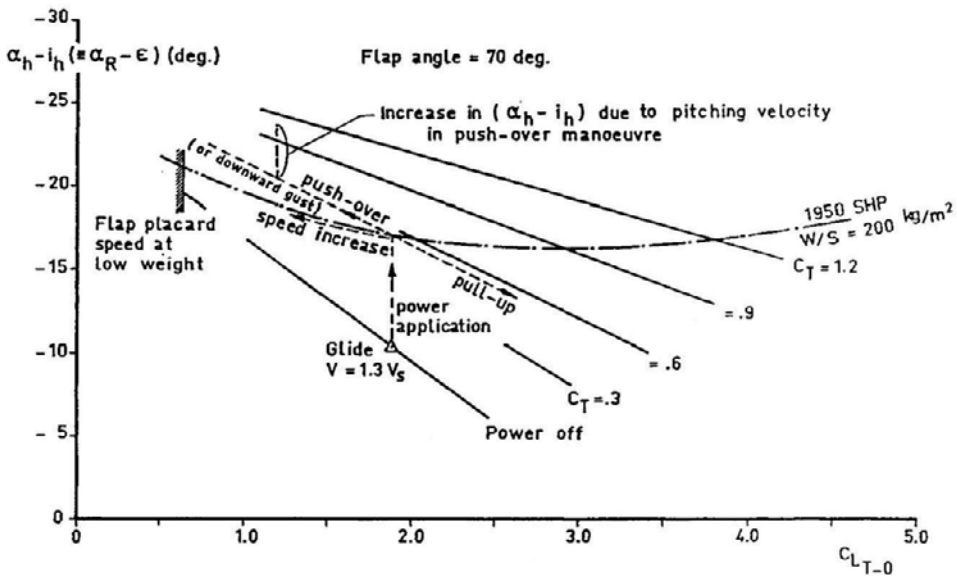
Figure 36.10 - The variation of tailplane angle of attack versus C_L. F-27 STOL, tail off
Source: AGARD CP-160, paper 10

Figure 36.10 also shows the tailplane angle-of-attack in a push-over manoeuvre. First, maximum power is applied. If the aircraft was allowed to accelerate α_h would develop along the curve marked "speed increase".

When, after power application, the nose of the aircraft is pushed down to the required load factor (n < 1.0), α_h develops along the curve marked "push-over".

However, due to the pitching movement of the aircraft, the tailplane, being positioned behind the centre-of-gravity, experiences an additional increase in negative angle-of-attack as indicated in the figure.

This manoeuvre is performed during flight testing as part of the certification programme to verify that even with such a manoeuvre the tailplane is still functioning properly.

In figure 36.11 the pitching moment is presented for the aircraft-less-tail for a range of thrust coefficients. At constant thrust coefficient the slope of the C_m-vs.-C_L curve is hardly affected by the thrust coefficient. Due to the large flap angle the propeller slipstream is strongly deflected downwards shifting the pitching moment curves towards more negative pitching moments with increasing thrust coefficient. For a more forward moment reference centre (or centre-of gravity) than x = 30% m.a.c. , the maximum negative pitching moment, which has to be balanced by tailplane lift, would be even larger.

The broken curve in the figure indicates the tail-off pitching moment curve for constant power in rectilinear flight.
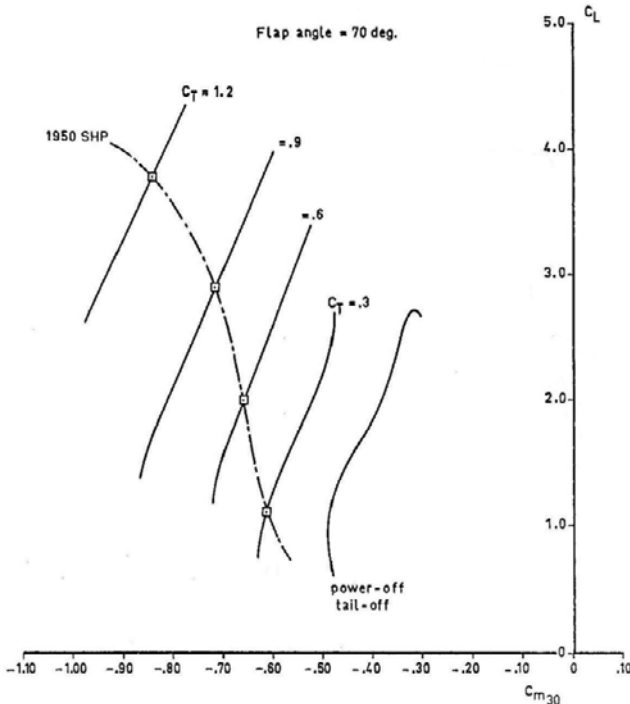
Figure 36.11 - C_m versus C_L for the aircraft-less-tail for different thrust coefficients, F-27 STOL. Source: AGARD CP-160, paper 10

Pitching moment equilibrium is described by the equation:

$$C_m = 0 = C_{m_0} + \left(\frac{dC_L}{d\alpha}\right)_{T-O} (\alpha - \alpha_0)\frac{x_{C.G.} - x_{A.C.}}{\bar{c}} - C_{L_{\alpha_h}}(\alpha - \varepsilon + i_h)\frac{S_h l_h}{S_w \bar{c}}\frac{q_h}{q} \tag{36.7}$$

with $(\delta_e = 0)$ and where

$$\alpha_h = \alpha - \varepsilon + i_h = \alpha\left(1 - \frac{d\varepsilon}{d\alpha}\right) - \varepsilon_0 + i_h \quad \text{or} \quad \alpha_h - i_h = \alpha\left(1 - \frac{d\varepsilon}{d\alpha}\right) - \varepsilon_0 \tag{36.8}$$

$\frac{d\varepsilon}{d\alpha}$ is given by equation 36.6.

In figure 36.12 the tail-on pitching moment curves as measured in the wind tunnel are shown for flight at power off with the stabiliser in the neutral position and at constant power (1950 SHP) for two stabiliser settings, $i_h = 0$ and $i_h = 5$ deg, stabiliser nose up. The curve for the latter stabiliser setting is almost parallel to the tail-off curve in figure 36.11. This is in line with the small variation in stabiliser angle-of-attack over a large C_L-range shown in figure 36.10. With the known stabiliser lift curve slope and the stabiliser angles-of attack from figure 36.10 the tail-on pitching moment curve could be estimated for the stabiliser setting $i_h = 0$.
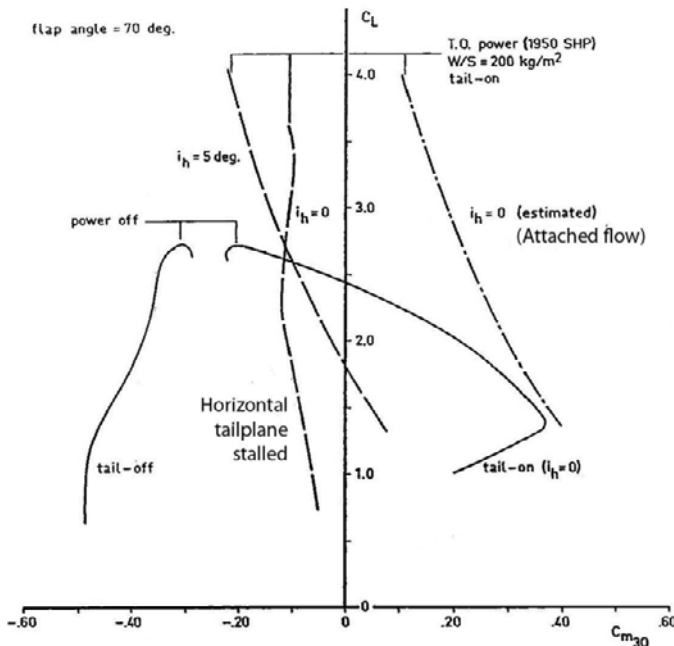
The difference between the estimated and the measured pitching moment curve indicates that in the wind tunnel tests the flow over the stabiliser had separated over the complete C_L-range.

Figure 36.12 - Pitching moment curves for F-27 STOL.
Source: AGARD CP-160, Paper No. 10

Negative tailplane stall

This is another example of negative tailplane stall. The strong downwash on high-powered propeller aircraft with effective wing flaps can cause very large negative tailplane angles of attack (in the order of -20 deg) which may lead to separated flow on the lower side of the tailplane.

During the short test programme flown on the F-27 prototype in the STOL configuration the aircraft had an adjustable stabiliser coupled to the flaps. When the flaps were progressively extended the stabiliser setting was changed from -1 deg to + 4 deg. Also, contrary to the wind tunnel model, the stabiliser on the prototype had the negative leading-edge camber (figure 36.13) used on the production aircraft. But even then erratic elevator control forces during gradual push-overs gave warning of impending negative tailplane stall. This was another reason why the programme was *discontinued*.
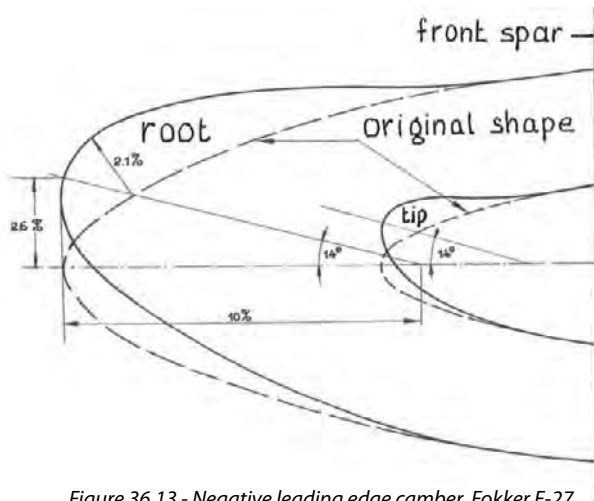
Figure 36.13 - Negative leading edge camber. Fokker F-27
Source: Fokker report L-27-88

Although the standard F-27 has single-slotted flaps with a maximum deflection of 40 deg the inboard flaps deflect only to two-thirds of the outboard flap angles to limit the maximum negative tailplane angles-of-attack in extreme flight conditions.

As mentioned before, the strong downwash is not limited to the slipstream tube. It occurs in the whole flow field since it is caused primarily by the lift produced by the wing. Therefore many propeller aircraft have a T-tail – not so much to locate it outside of the propeller slipstream, but to locate is as far as possible away from the wing trailing vortex sheet.

During the wind tunnel test programme for the STOL version of the Fokker F-27 also a tail configuration was tested with the stabiliser placed 3.6 m (full-scale) above the standard stabiliser position.

In figure 36.14 the stabiliser angle-of-attack as a function of tail-off lift coefficient is shown for the model both with the high and with the low tail for the high-constant-power condition.

At low C_L-values the stabiliser angle-of-attack is nearly independent of power setting and tail location. As the lift coefficient is low, so is the downwash. The high negative **tailplane** angle-of-attack is mainly caused by the large negative **aircraft** angle-of-attack (see figure 36.8).
However, at higher C_L, there is a significant difference in tailplane angle of attack depending on power setting and tail location; yet at both locations, the tail was located outside of the slipstream. The difference is caused by the fact that the low tail is located closer to the trailing vortex sheet from the wing, and thus experiences far more powerful downwash effects.
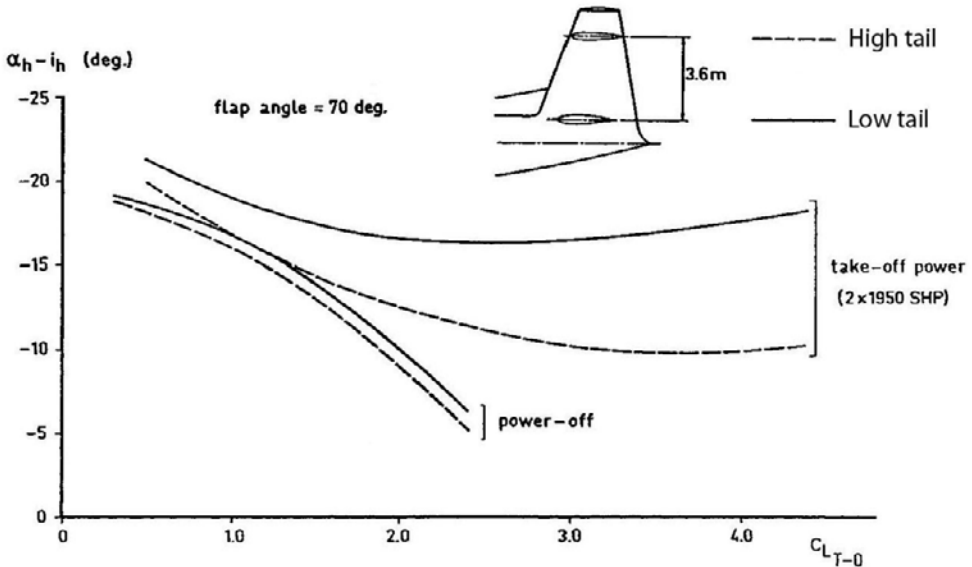
Figure 36.14 - C_L vs $(\alpha_h - i_h)$ for two tail locations and two power settings, F-27 STOL
Source: AGARD CP-160, Paper No. 10

The analysis presented above indicates that the oncoming flow of a horizontal tailplane differs from the undisturbed flow due to three flow phenomena:

1. The **wing and engine nacelle wake**, characterised by a lower average dynamic pressure than the undisturbed flow. A low-set stabiliser may, with the wing flaps retracted or at a take-off setting, exhibit a diminishing effectiveness at high angle-of-attack if the stabiliser is immersed in the wing wake.
2. The **propeller slipstream**, characterised by swirl and an increased average dynamic pressure relative to the outer flow and by an inflow of the outer flow on the slipstream boundary. The latter may further complicate the tailplane contribution to stability and control.
3. The **downwash** which is a direct consequence of the wing producing lift and is primarily tied to the lift coefficient with or without the presence of propeller slipstream.

Propeller slipstream effects are closely related to the flight handling qualities of an aircraft. In the following some longitudinal control characteristics of the Fokker F-27 are discussed.

When the controls are moved a pilot experiences both a control displacement and a control force. The control-displacement-vs.-speed relation is directly related to the neutral point, stick fixed. On the other hand, the control-force-vs.-speed relation is tied to the neutral point, stick free.

In figure 36.15 the effect of varying power on the stick-free stability is shown, at both forward and aft centre of gravity positions.

At the forward centre of gravity with idling engines the stick forces are high, in fact care has to be taken that in certain flight regimes the control force does not surpass the maximum allowable control forces specified in the airworthiness regulations.

By applying power, the control forces and force gradients become lower. Then the other certification requirement becomes a limiting factor: FAR/CS 25 states that the average control force gradient around a given trim speed should be at least 1 lb_f / 6 kts. This applies in particular at the aft centre-of-gravity.

The control displacement is presented in figure 36.16. The effects as seen in figure 36.16 can also be distinguished here: at higher power levels, the stability of the aircraft diminishes. At take-off power and the most aft centre-of-gravity position the stick-fixed stability of the aircraft is negative.
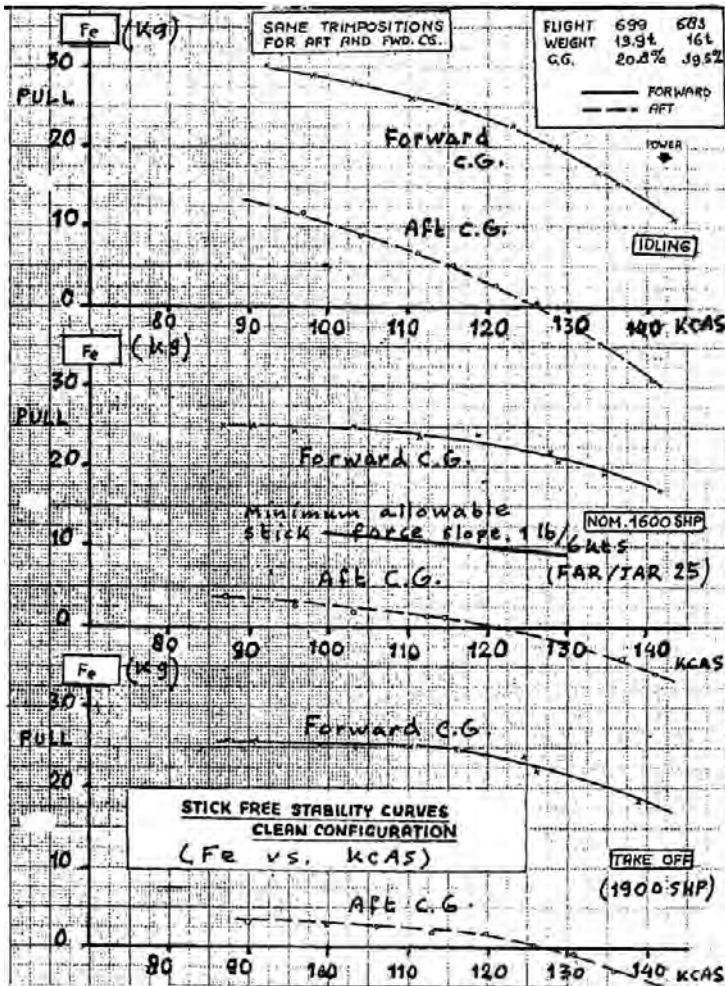
Figure 36.15 - Stick force versus airspeed at various power settings, F-27, clean.
Source: Fokker report V-27-49

Nowhere do the airworthiness requirements refer to control displacement. All requirements on stability and manoeuvrability mention only control forces. Usually stick-fixed instability also leads to stick-free instability. On the F-27 however a provision is used on the elevator which ensures stick-force stability in all flight conditions.

The F-27 elevator is equipped with three trailing-edge tabs. The left elevator half has an inner and an outer tab, the right elevator half has only an outer tab. The left inner tab is the true trim tab adjustable from the cockpit. The two outer tabs have a fixed setting of 5 deg trailing-edge up. When the aircraft is trimmed for zero stick force by appropriate trim tab deflection a decrease in
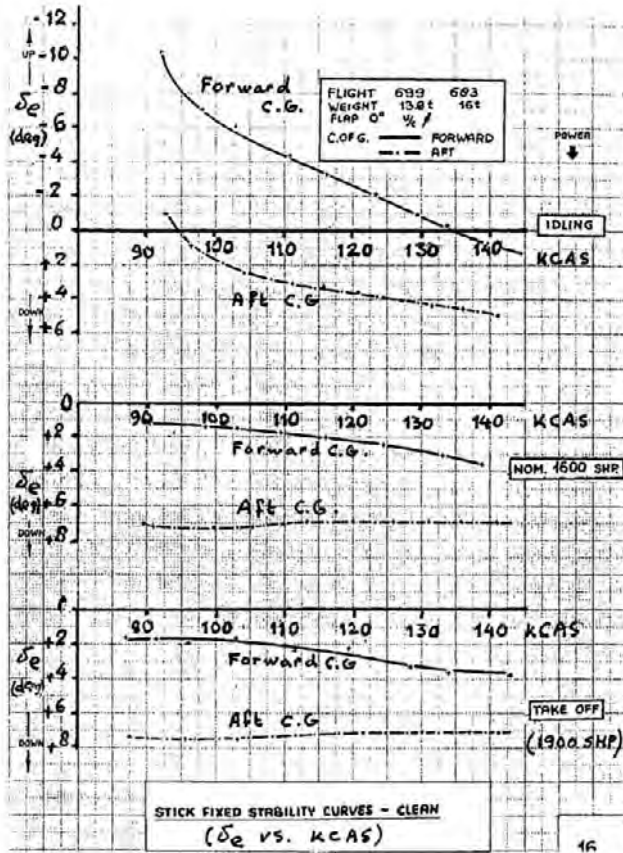
Figure 36.16 - Elevator deflection versus airspeed at various power settings, F-27, clean. Source: Fokker report V-27-49

speed at constant throttle setting will produce a higher dynamic pressure at the fixed outer tabs, being immersed in the propeller slipstream, than at the trim tab. This will force the elevator down more than required for trim in the new flight condition. This is due to the chosen fixed trailing-edge up trim setting. The pilot will have to apply a pull force to maintain longitudinal equilibrium experiencing positive stick-free stability even if the elevator is deflected slightly down relative to the original trimmed condition.

When the flaps are deflected the region with the highest downwash moves down, away from the stabiliser. The stability improves as is shown in figures 36.17 and 36.18. Only at the lowest airspeeds at a high power setting and aft centre-of-gravity position the upwards deflected fixed tab produces positive stick-free stability whereas the stick-fixed stability is indifferent.

At the most forward centre-of gravity position and idling engines large upward elevator deflections are required to reach low flying speeds as shown in figure 36.17. With a maximum elevator deflection δ_e = -25 deg the angle-of-attack for maximum lift can just be reached.
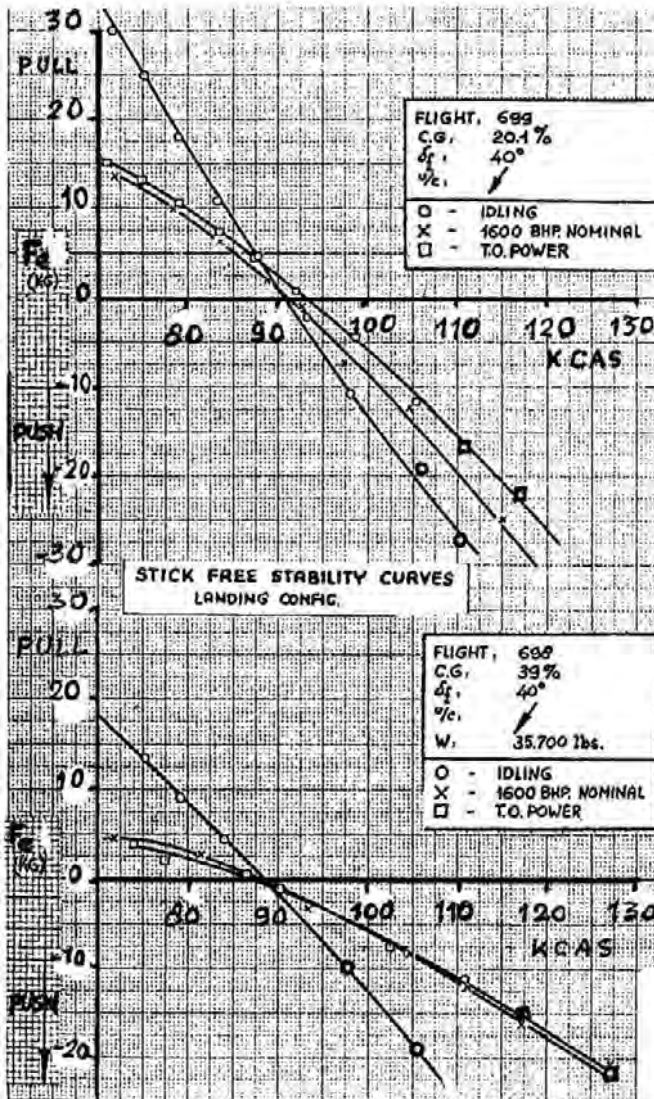
Figure 36.17 - Stick force versus airspeed at various power settings, F-27, landing. Source: Fokker report V-27-49
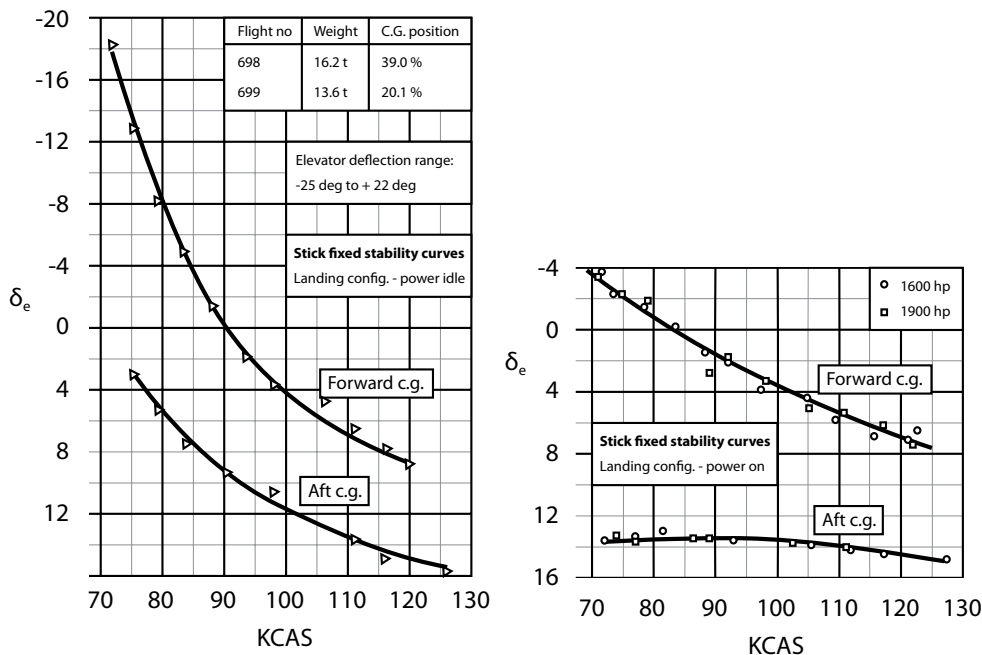
Figure 36.18 - Elevator deflection versus airspeed at various power settings, F-27, landing.
Source: Fokker report V-27-49

Another example of an aircraft programme where the design of the longitudinal control system was a true challenge was the Saab 2000 (figure 36.19). A successor to the successful Saab 340, it was designed to fly at 360 knots, nearly jet aircraft speed, for which it needed very powerful engines. Those in turn caused very strong slipstream effects. In view of the positive experience with the Saab 340, originally the use of a manual control system was envisaged. Initial flight test results however necessitated a redesign of the entire control system leading to the introduction of a simplified fly-by-wire system. This delayed the entry into service by a year, to late mid 1994.

Figure 36.19 - Saab 2000. Source: Christian Waser

Directional stability and control

Propeller slipstream does not only affect the flow over the horizontal tail but also over the vertical tail and therefore the directional stability and control of the aircraft.

Figure 36.20 shows the mechanism by which a crossflow is induced at the vertical tail by considering the various components that make up the lift distribution over the wing. It is shown for both (when seen from the rear) clockwise ("outboard up") and counterclockwise ("inboard up") propeller rotation.

In part 2 in figure 36.20, the increase in wing lift due to the wing being immersed in the slipstream is shown. In part 3 the swirl causes a large amount of additional lift at the side where the propeller blade moves upwards due to the local change in angle of attack. The resulting large local lift gradient causes a strong trailing vortex (part 4) at that point . This causes in the flow above the trailing vortex sheet in turn a crossflow *towards the engine.* It is clear from the figure that the "inboard up" propeller, which
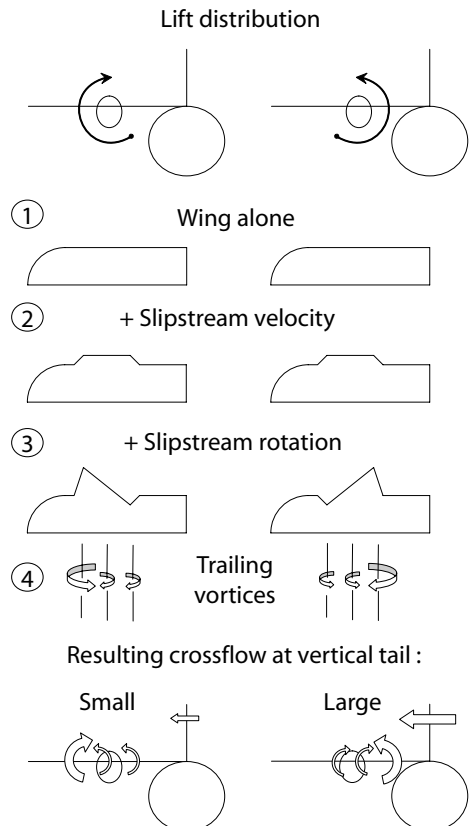
Figure 36.20 - Cross flow at the vertical tail induced by a propeller.
(Adapted from NLL report A-1508B, 1962)

471

has the strong trailing vortex nearest to the fuselage, produces the strongest crossflow over the vertical tail.

Now consider a twin-engined propeller aircraft whose propellers rotate in the same direction (co-rotating propellers, such as found on most civil aircraft). If the "outboard up" engine fails, the propeller of the remaining "inboard up" engine produces a strong crossflow **at zero sideslip** over the tail increasing the direct yawing moment from the operating engine. To compensate for this a large rudder deflection is required. If the "inboard up" engine fails, a much smaller rudder deflection is required because the crossflow caused by the slipstream of the operating engine is much smaller. For this reason, the "outboard up" engine is called the **critical engine**.

The required vertical tail size is heavily influenced by these slipstream effects. Because of the crossflow over the vertical tail, the side force the vertical tail and the rudder must be able to generate to produce a balancing yawing moment in flight with the critical engine inoperative is much larger than the propeller static moment. See for instance figure 36.21. In this figure, the "calculated" line represents the propeller static moment (thrust x moment arm). The measured yawing moment coefficients are all higher, particularly if the vertical tail is fitted. The yawing moment from the experiment at zero sideslip with the operating "inboard up" engine close to the fuselage differs from its calculated value as much as 50% .

Two spanwise engine positions are compared in figure 36.21 both for propellers rotating clockwise and anticlockwise. On this configuration **placing the engines further outboard does not lead to a larger yawing moment**. There are certain advantages in placing the propeller further outboard : it reduces both the cabin noise and the crossflow over the vertical tail. However, if an engine fails, the additional lift it produces is lost and a larger rolling moment will have to be compensated for.

In figure 36.22, the effect is illustrated that flaps have on the yawing moment. When the tail is not installed on the aircraft, actual and theoretical yawing moments show relatively little difference. However, once the tail is fitted on the aircraft, a large difference can be distinguished if the flaps are deployed. Not only does the yawing moment increase, it also becomes nearly constant regardless of the propeller position.

$$T_{C_{eff}} = \frac{T_{eff}}{\frac{1}{2}\rho V^2 S_{prop}}$$

$$S_{prop} = \frac{\pi}{4} D_{prop}^{\ 2}$$

$$C_n = \frac{N}{\frac{1}{2}\rho V^2 S_w b_w}$$

Flaps up:

α = 5.0 deg

$\left(C_L\right)_{T_C=0} = 0.75$

Flaps down:

(δ_f = 30 deg)

α = 5.8 deg

$\left(C_L\right)_{T_C=0} = 2.00$
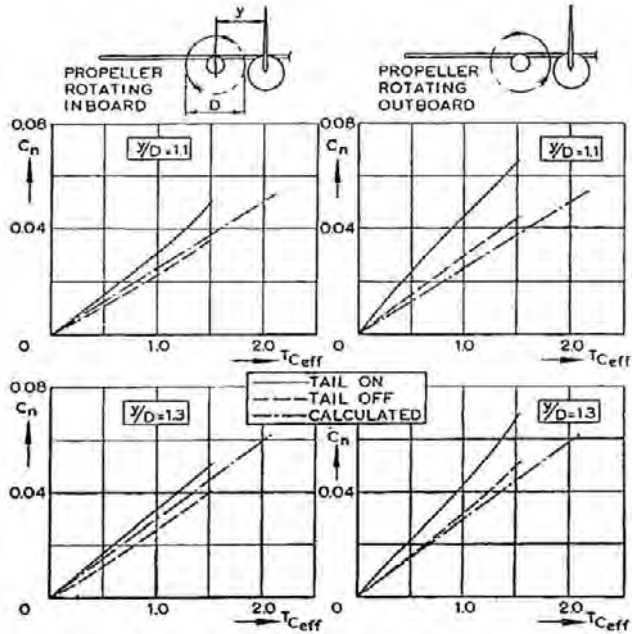
Figure 36.21 - C_n versus T_C for two engine nacelle positions with propellers rotating both clockwise and anti-clockwise. Source: NLL report A-1508B, 1962
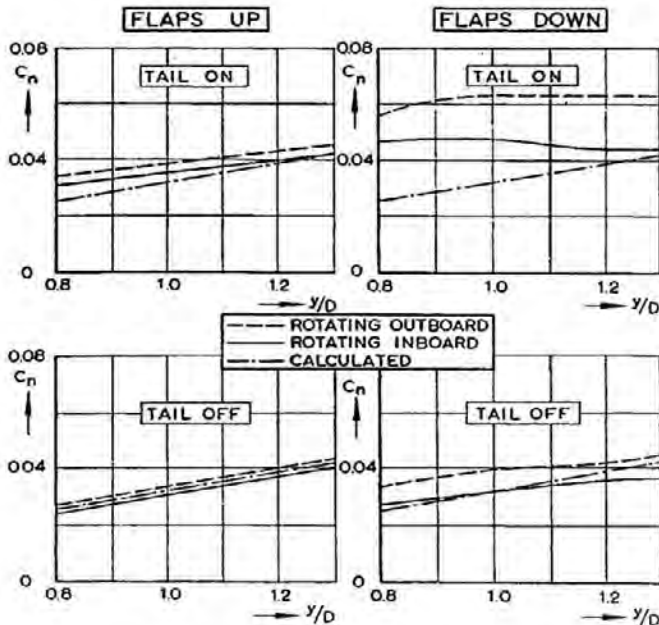
Figure 36.22 - C_n versus lateral propeller position for flaps up and down and tail on and off. Source: NLL report A-1508B, 1962

473

The examples presented are related to a high-wing configuration. Although the flow phenomena occur likewise on a low-wing configuration they will quantitatively be less important because of the larger vertical distance between the trailing vortex sheet and the vertical tailplane.

Clearly, the configuration with tail installed and flaps down is the critical configuration for a high-wing aircraft. Apparently the flap tip vortex, which is close to the fuselage, is "pulled" onto the fuselage by the mirror vortex in the fuselage. This is illustrated in figure 36.23. With the flap tip vortex now lodged close to the vertical tail, there is a stronger crossflow there, which induces a larger yawing moment.

Flap tip vortex, very strong vortex due to large lift production

More powerful crossflow because stronger vortex, closer to tail

Vortex is mirrored in fuselage, which causes original to move upwards
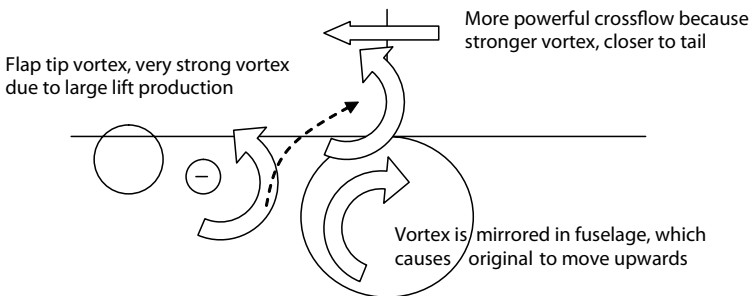
Figure 36.23 - Schematic representation of flap tip vortex moving onto fuselage

In the extreme case of propeller "inboard up", flaps down, the aircraft yawing moment, with the vertical tail size used on the model, can become twice as large as would be expected from the propeller static moment, as shown in the top-right part of figure 36.22.

The cross flow has its origin in the propeller slipstream and is independent of the size of the vertical tail. This means that a larger vertical tail also produces a larger yawing moment at zero sideslip in flight with an inoperative engine. To obtain the required minimum control speed a careful balance must be struck between the yawing moment from the operating engine and from sideslip and rudder deflection. Only then can the required fin size be determined.

Lateral stability

Due to propeller slipstream rotation and the resulting non-symmetric spanwise lift distribution, even with a symmetric power condition (see figure 36.6), power application will produce a rolling moment.

In a sideslip the slipstream will, when seen from above, not flow in line with the propeller axis but move to leeward as indicated in figure 36.24. This produces an additional shift in the lift peaks in the spanwise lift distributions which causes an additional rolling moment counteracting the basic rolling moment due to sideslip. At high thrust coefficients this may lead to lateral instability.

When the Fokker F-27 was developed into the Fokker 50 the engine power was increased considerably and this lateral instability was shown in the wind tunnel tests. This was unacceptable as the airworthiness requirements state that if in certain flight conditions the aircraft is banked and develops a sideslip and the pilot releases the controls the aircraft must show a tendency to raise the windward wing. A positive lateral stability is required.

This was realised on the Fokker 50 by the application of horn balances on the ailerons at 45 deg dihedral. As horn balances are sensitive to a change in angle-of-attack the 45 deg dihedral made them also sensitive to sideslip. In a sideslip the windward aileron will, with free controls, deflect downwards thus raising the wing. A shielded horn balance is used to prevent ice accretion on the horn in icing conditions.
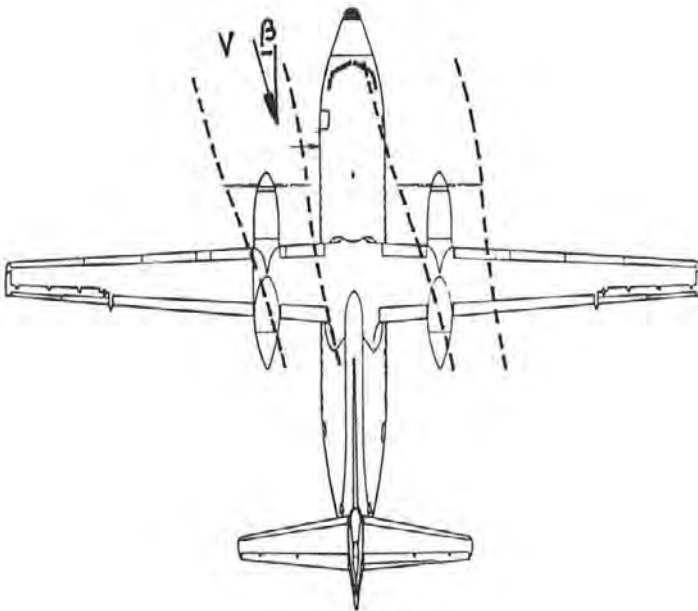
Figure 36.24 - Propeller slipstream in sideslip

PART 8

ENGINE INTEGRATION

37 *Engine intakes*

Engine development has been one of the main drivers in the development of aviation in general. Indeed, it was their engine and propeller, together with their understanding of flight control that allowed the Wright brothers to turn Octave Chanute's glider into a practical aircraft. Even today, an important part of the efficiency improvements in new aircraft (such as the Boeing 787 or Airbus A350) are found in the propulsion system – which shows that in this field development has not yet reached a plateau.

The following chapters deal with various aerodynamic aspects of the design of a propulsion system – engine intakes and exhausts and thrust reversers.

General aspects of intake design

As on most aircraft components the design of an engine intake requires compromises. This applies both to the internal and the external geometry because there are conflicting requirements with regard to optimum engine operation over the complete flight envelope.

In figure 37.1 the various characteristics of a subsonic engine intake and the intake flow are indicated. Note in particular three significant cross-sectional areas of the streamtube entering the compressor: the area at infinity, A_∞, the throat area, A_{TH} and the highlight (American hilite) area, A_{HL}.
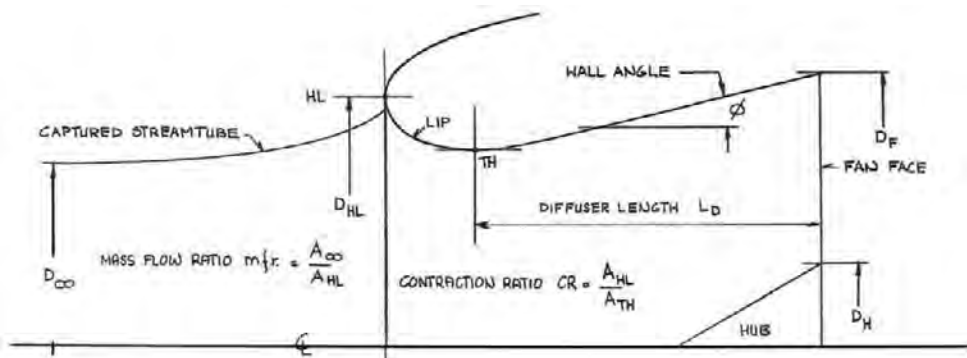
Figure 37.1 - Characteristics of a subsonic engine intake and the intake flow.
Source: Fokker report L-29-132
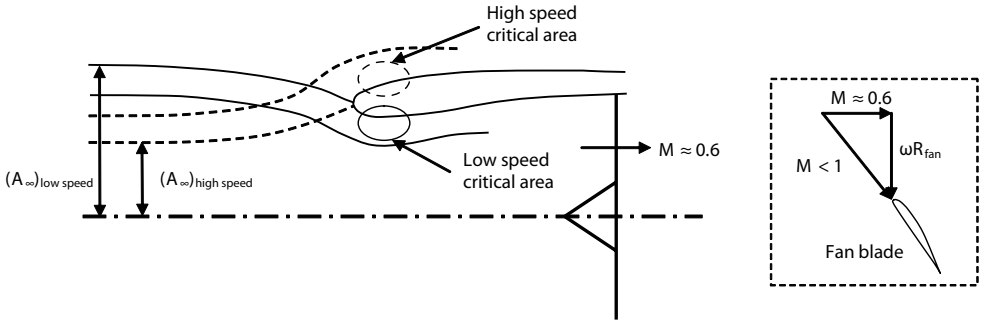
Figure 37.2 - Critical areas on the intake for high-speed and low-speed airflow

Design requirements for high speed operation in climb and cruise

For cruise the emphasis in the design effort is on minimising the drag. In order to obtain this, the supervelocities on the external surface of the engine should be as low as possible. This requires the mass flow ratio A_∞ / A_{HL} to be as near to unity as other design requirements permit so that the stagnation point is close to the highlight. In this flight condition, the supervelocities on the **outside** of the intake will be critical, as is indicated in figure 37.2. This is one of the design requirements that determines the intake area.

The **interior** intake geometry also requires attention however, as the highest velocities will occur near the throat area. Due to the streamwise wall curvature the velocity distribution over the throat area will not be uniform. The highest velocities occur near the wall. In order to prevent strong shockwaves on the intake wall or even separation at that point experience has shown that the average throat Mach number (M_{TH}) should be $M_{TH} < 0.8$. The average throat Mach number is calculated with the one-dimensional isentropic flow relations for the mass flow through the intake. The relation between throat area A_{TH} and average throat Mach M_{TH} number for a given mass flow m is given in equation 37.1.

$$A_{TH} = \frac{\dot{m}\sqrt{T_T}}{P_T}\left[M_{TH}\left(1+\frac{\gamma-1}{2}M_{TH}^{\,2}\right)^{\frac{(\gamma+1)}{2(1-\gamma)}} * \sqrt{\frac{\gamma}{R}} \right]^{-1} \qquad (37.1)$$

where R is the universal gas constant.

Figure 37.3 shows the theoretical relation between throat Mach number and relative mass flow ratio $\dot{m}/\dot{m}^*$ where $\dot{m}^*$ denotes the mass flow ratio when $M_{TH} = 1.0$. Note that at high throat Mach numbers small variations in mass flow have a strong effect on the throat Mach number.
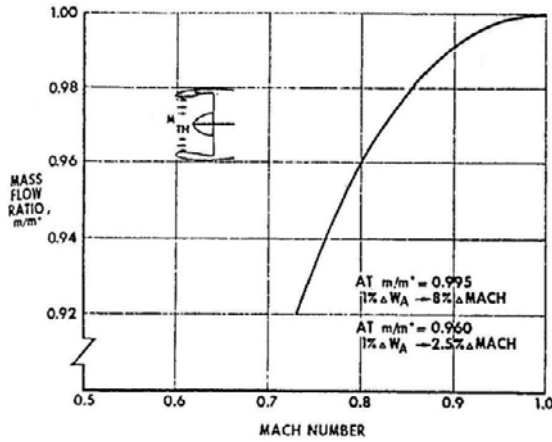
Figure 37.3 - Mass flow ratio in relation to throat Mach number.
Source: ASME paper 69-GT-41

Modern transport aircraft have cruise speeds near M = 0.8. With M_{TH} = 0.8 the mass flow ratio A_∞ / A_{HL} will then be equal to the reciprocal of the contraction ratio $1/(A_{HL}/A_{TH})$ according to the law of mass conservation $(\rho VA)_\infty = (\rho VA)_{TH}$ and the stagnation point will be at the highlight as desired.

In figure 37.4 the exterior pressure distribution over the top section of the engine nacelle mentioned in figure 37.5 is shown. With $1/(A_{HL}/A_{TH})$ = 0.743, a mass flow ratio A_∞ / A_{HL} = 0.774 and a freestream Mach number M = 0.75, the intake is correctly sized for the required mass flow. But nevertheless a small region with supersonic velocities is present at the leading edge.
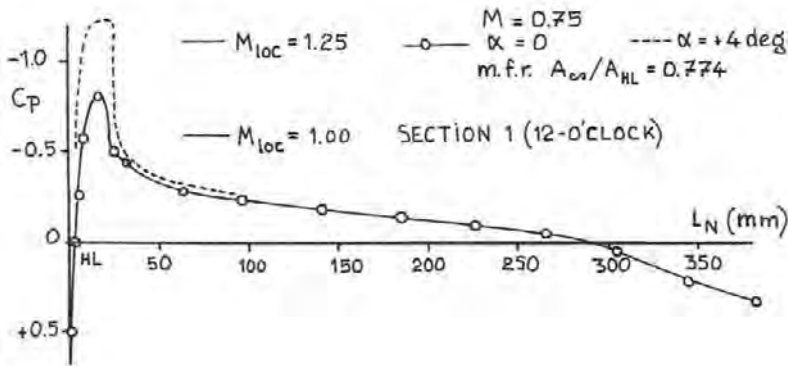
Figure 37.4 - Pressure distribution over the top section of an engine nacelle in cruise.
Source: Fokker Report L-29-174.
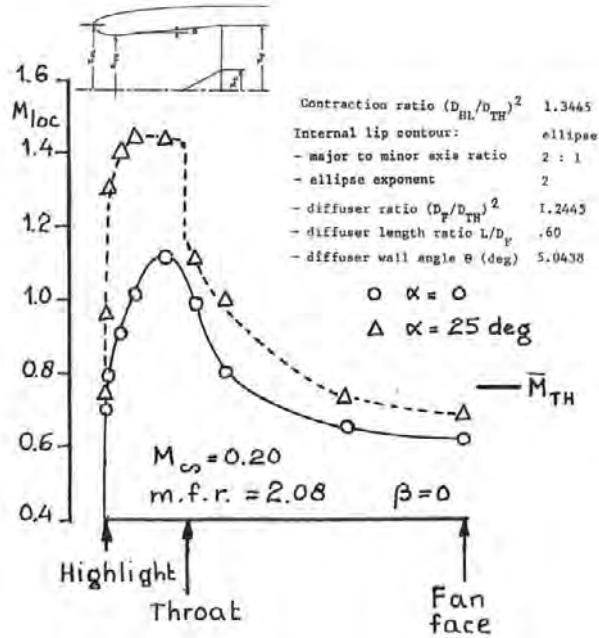
Figure 37.5 - Local Mach number distribution on the lower intake wall.
Source: Fokker Report L-29-174.

Design requirements for take-off and initial climb.

At low speeds, the mass flow ratio will be far greater (M.F.R. > 1.0). This will cause the highest supervelocities to occur on the inside of the intake near the throat area (see figure 37.2). In figure 37.5 the pressure distribution is shown on the lower intake wall of an intake model investigated by Fokker/NLR in 1982. At a free-stream Mach number M = 0.20 and an average throat Mach number $M_{TH} = 0.76$ the peak Mach number varies between $M_{loc} = 1.12$ and 1.44 for angles-of-attack between α = 0 and α = 25 deg.

If this limitation on average throat Mach number is surpassed a large decrease in inlet pressure recovery, and therefore engine efficiency, will result. This effect can be distinguished in figure 37.6.
This maximum throat Mach number is critical at low speed because the required engine mass flow is largest at take-off and initial climb. Limiting the throat Mach number is therefore the major design requirement that determines the intake area.

Most engines undergo during the life of the programme successive development steps at which thrust and mass flow increase. In order not to have to redesign
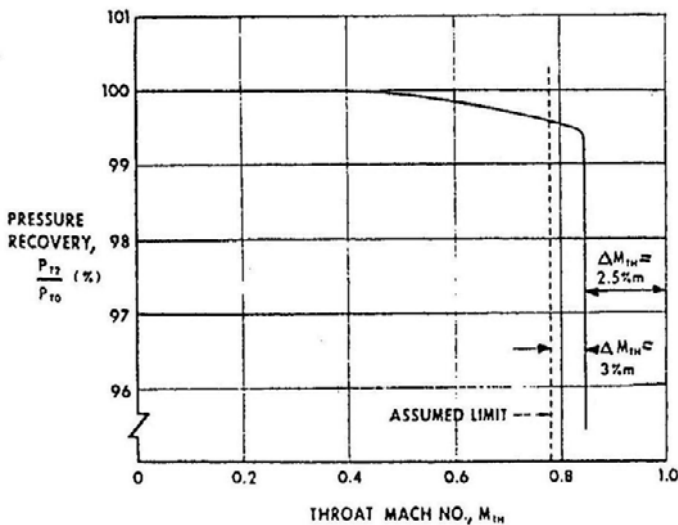
Figure 37.6 - Inlet pressure recovery versus throat Mach number.
Source: ASME Paper No 69-GT-41

the engine cowling at each development step it is common practice to size the intake such that some mass flow growth is possible. In figure 37.6 it is assumed that a growth in throat Mach number of 3% may occur and therefore the design maximum throat Mach number was fixed at M = 0.78. In the figure is also indicated that if the throat Mach number would be increased a further 2.5% the intake would be fully choked.

In figure 37.7 the inlet pressure ratio as a function of the average throat Mach number is shown for the intake model mentioned in figure 37.5. Note that the lower scale indicating $(A_\infty / A_{HL})/(A_\infty / A_{HL})_{crit}$ where $(A_\infty / A_{HL})_{crit}$ is the mass flow ratio for $M_{TH} = 1.0$ shows the same relation with the throat Mach number M_{TH} as figure 37.3.
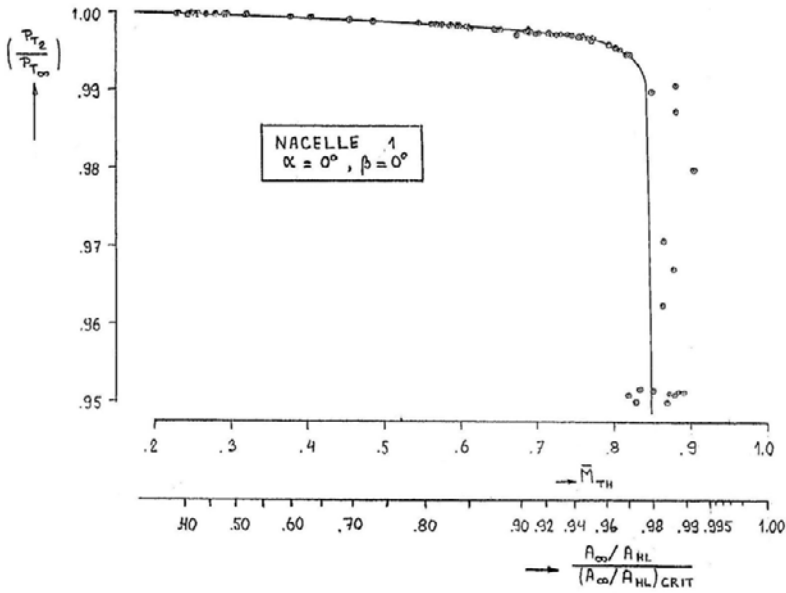
Figure 37.7 - Inlet pressure recovery versus throat Mach number and relative mass flow ratio. Source: Fokker report L-29-174

A second cause of total pressure losses in take-off and low-speed flight is boundary layer growth and separation on the inside of the intake lip as indicated in figure 37.8.

In figure 37.9, the effect is shown of intake contraction ratio, the ratio between the highlight and the throat area (A_{HL}/A_{TH}), on the inlet pressure recovery at static freestream conditions. The losses rise sharply with decreasing contraction ratio.

The reason for these losses differs from the losses due to a high throat Mach number. The latter are larger for higher contraction ratios because of the stronger wall curvature at the throat. The effects referred to in figures 37.8 and 37.9 are caused by the decreasing leading-edge radius and diminishing outward leading edge camber. This can be compared to the stall on an airfoil section with diminishing leading-edge radius and camber.

As was mentioned before, intake areas should be sized with a margin for variations in the maximum airflow. This may be either for a new engine under development when the mass flow requirements may still not be fixed or for a further development of the engine.
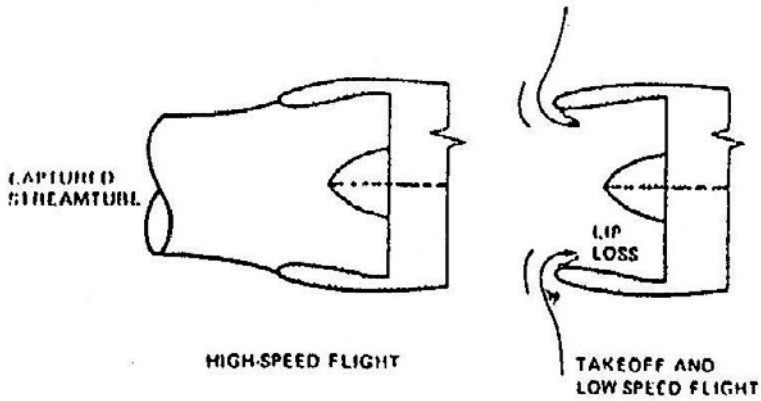
Figure 37.8 - Captured streamtube comparison, lip loss becomes a factor in low speed flight. Source: ASME Paper No 69-GT-41
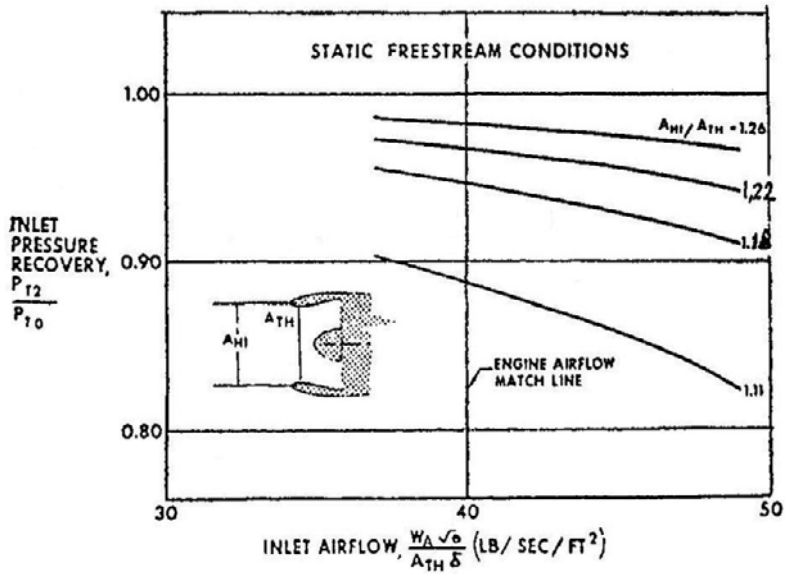
Figure 37.9 - Inlet pressure recovery for different contraction ratios. Source: ASME Paper No 69-GT-41

In figure 37.10 the corrected mass flow at climb rating for the Pratt &Whitney JT9D designed for the Boeing 747 is shown at a certain development stage. At the nominal mass flow the throat Mach number is $M_{TH} = 0.77$, a safe value. If the mass flow would be 5% higher however, the throat Mach number would be $M_{TH} = 0.85$ with a risk of intake choking losses.

In order to prevent some of these losses, some intakes feature a so-called auxiliary passage, shown in figure 37.11. Through this passage, air can enter the inlet and improve the airflow. Figure 37.12 shows that a significant improvement can be realised albeit at the price of added mechanical complexity.
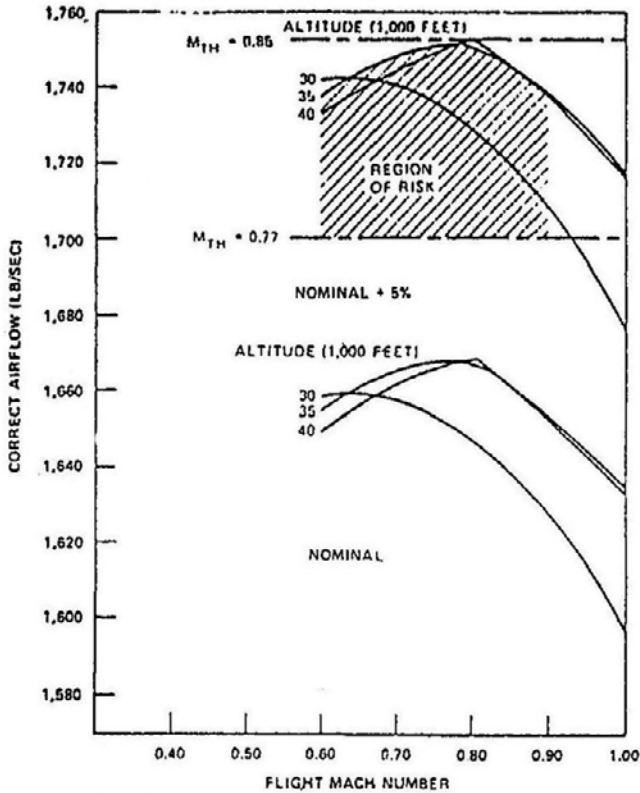
Figure 37.10 - JT9D corrected airflow at climb rating.
Source: ASME Paper No 69-GT-41
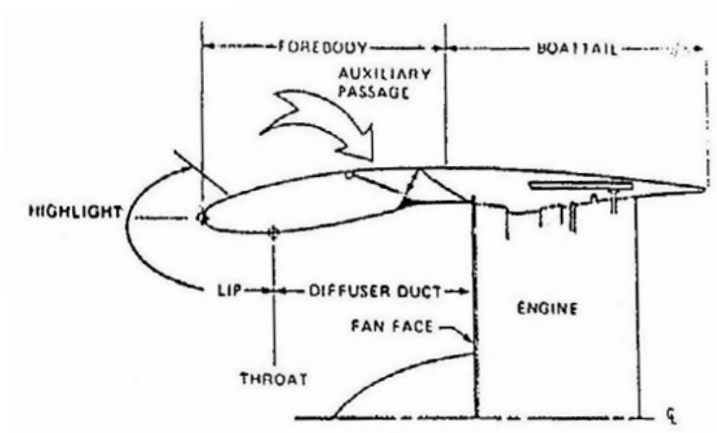
Figure 37.11 - Fan cowl with auxiliary passage.
Source: ASME Paper No 69-GT-41
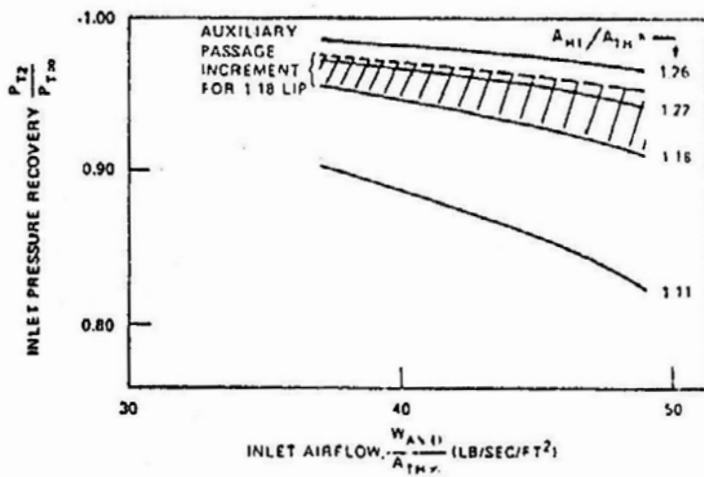
Figure 37.12 - Effect of lip area ratio on inlet pressure recovery at static free-stream conditions. Source: ASME Paper No 69-GT-41

In figure 37.2 it was shown that at the compressor blades the airflow velocity should not be higher than M = 0.6. In order to decelerate the airflow from the velocity at the throat to this Mach number the area behind the throat expands, forming a diffuser. The optimum diffuser angle θ, defined in figure 37.1 as the angle Φ, which produces the lowest total pressure loss, can be found with equation 37.1 and the coefficients K_1 and K_2 presented in figures 37.13 and 37.14.

The combination of figures 37.13 and 37.14 leads to an optimum value of θ of 5 degrees. Any larger values will induce separation.

Diffuser loss = $K_1 \cdot K_2 \cdot M_{TH}^2$

In figure 37.15 the increase in total pressure loss at increasing angles of attack is shown for a certain configuration, as a function of throat Mach number. Note that the losses are highest at high throat Mach numbers and angles-of-attack due to strong shocks forming on the lower inside of the intake. This is also shown in figure 37.5.
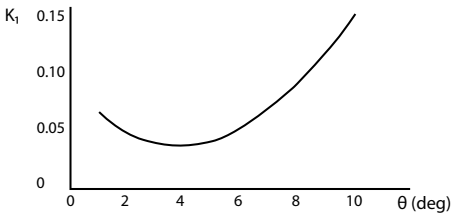
Figure 37.13 - K_1 as a function of θ
Source: ESDU Data Sheet 80037
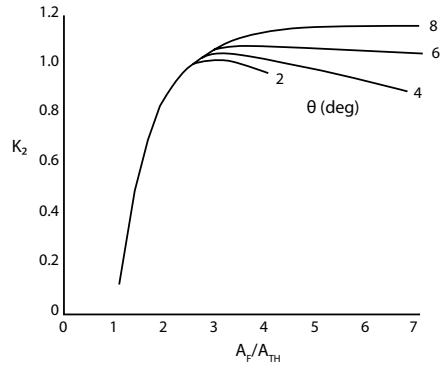
Figure 37.14 - K_2 as a function of θ and area ratio
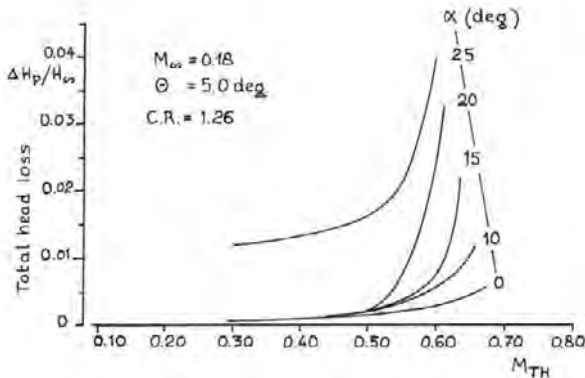
Figure 37.15 - Total-head (= total pressure) loss vs. M_{TH} and angle-of-attack α.
Source: SAE Paper 660732

Flight at near-sonic speeds

Since jet engines have reached the required thrust levels studies have been made to increase cruise speeds significantly above M = 0.80 to 0.85 at which transport aircraft are operated today.

To illustrate the challenges to be overcome some results are shown of a study performed in 1970-1971 for a transport aircraft flying at a cruise speed of M = 0.98.
The comparison in figure 37.16 between engine nacelles designed for M = 0.85 and M = 0.98 shows the principal differences. The nacelle designed for cruise at M = 0.98 has very thin intake lips but nevertheless an area of supersonic flow will exist over the upper surface behind the leading edge. This is acceptable as long as the local Mach number does not surpass M_{loc} = 1.15 to 1.20 but this still leaves little room for supervelocities due to wall curvature.
At take-off such thin intake lips will exhibit flow separation on the inboard side leading to significant thrust losses.

Figure 37.17 shows the inlet performance of the high-speed nacelle at very low speeds for intakes with various contraction ratios. The intake lip geometry is shown in the lower right-hand corner. It is evident that, particularly for a contraction ratio A_{HL}/A_{TH} = 1.1 the loss in intake efficiency is considerable.

TYPICAL MACH 0.85 ENGINE INSTALLATION

TYPICAL MACH 0.98 ENGINE INSTALLATION
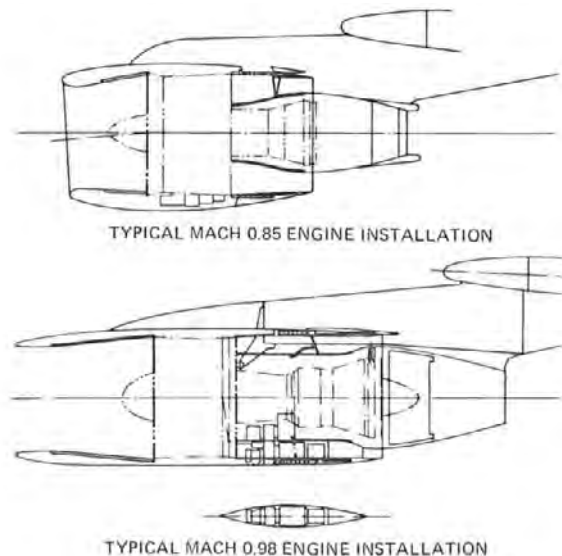
Figure 37.16 - Designs for M_{cruise} = 0.85 (top) and M_{cruise} = 0.98 (bottom) engine nacelles. Source: SAE Paper 710762
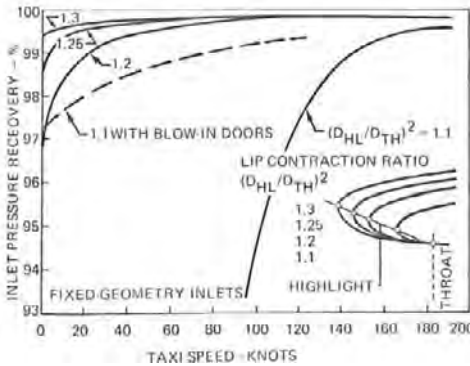
Figure 37.17 - Low speed inlet performance of near-sonic engine. Source: SAE Paper 710762
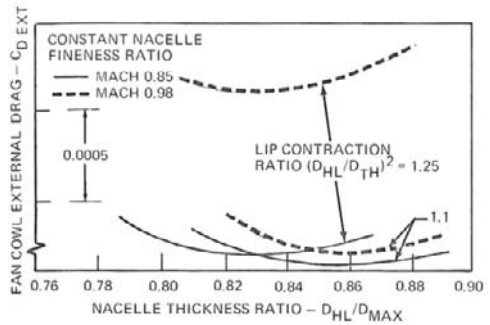
Figure 37.18 - Fan cowl drag at various thickness ratios. Source: SAE Paper 710762

The effect of contraction ratio on the external nacelle drag is shown in figure 37.18. Using a contraction ratio C.R. = 1.25 (which yields good characteristics in low speed flight) results in good performance for cruising at M = 0.85. However, at M = 0.98 the drag increase relative to an intake with a contraction ratio C.R. = 1.1 is almost 10 drag counts but the latter is less suitable for optimum low-speed operation as was shown above.

A possible solution is to use blow-in doors (termed auxiliary passage in figure 37.11). Figure 37.17 shows how the use of blow-in doors improves the low-speed characteristics of an intake with a contraction ratio C.R. = 1.1.

Flight with one engine inoperative

In order to maximise the load-carrying capability of a transport aircraft after an engine has failed every effort should be made to minimise the extra drag resulting from this flight condition.

When the engine fails at take-off the initial climb takes place at speeds near 1.2 V_S or 1.13 V_{SR}. The aircraft operates then at a high lift coefficient and angle of attack.

With engines on the wing there are then two additional drag sources and one possible drag source:

1. In order to balance the resulting yawing moment a large rudder deflection is required leading to extra drag from the vertical tailplane (**asymmetric drag**).
2. The failed engine will produce **windmilling** or **blocked-rotor drag**. This is the internal drag of the engine itself.

3. The resulting low mass flow ratio on the failed engine will produce higher supervelocities on the intake exterior surfaces and increased friction drag and possibly some wave drag. In combination with the high angle-of-attack, this may lead to flow separation, with additional drag, either on the lower inside or on the upper outside of the engine nacelle. The sum of these drag contributions is here termed **forebody drag**. When the basic external drag at mass flow ratios close to one is added the total drag is sometimes called **cowl drag**.

The first two drag sources are unavoidable but forebody drag deserves some attention. Forebody drag is built-up from two components, spillage drag and flow separation drag. Spillage drag, which primarily refers to the exterior drag is divided in additive or pre-entry drag and loss of leading-edge suction forces and is strongly dependent on mass flow ratio. Spillage drag also occurs when no shock waves or separation is present. For a further analysis of spillage drag reference is made to propulsion integration literature and design data such as ESDU Data Sheets.

To minimise shock wave strength in cruise and to prevent flow separation on an engine intake at take-off the intake is as far as possible aligned with the local flow. As intakes on wing-engines operate in the upwash (extensively discussed in chapter 25) in front of the wing the intake can operate at high angles of attack. This applies in particular to aircraft with powerful leading- and trailing-edge devices. Figure 37.19 presents the design operating envelope of the Boeing 747 engine inlet. The combination of high aircraft angles-of-attack and large upwash angles requires the intake to operate efficiently at local angles of attack of up to α = 30 deg.

Representative mass flow ratios for windmilling engines and engines with
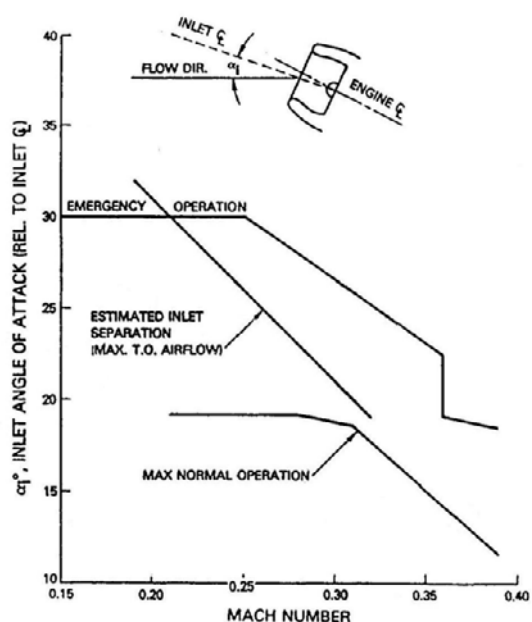
Figure 37.19 - Boeing 747 inlet flight envelope.
Source: AIAA Paper 84-2487

$M_0 = 0.25$
m.f.r. = 0.34
$\alpha_{inlet} = 0$ deg

$M_0 = 0.25$
m.f.r. = 0.34
$\alpha_{inlet} = 20.6$ deg
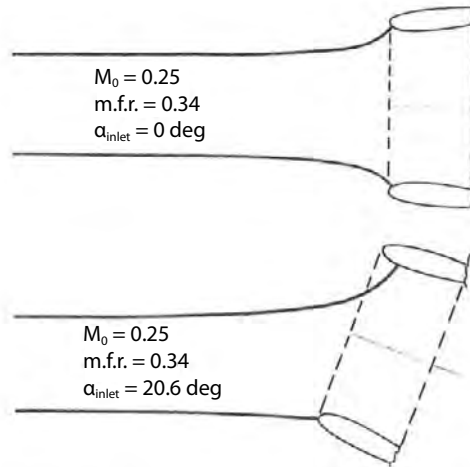
Figure 37.20 - Inlet flow field for windmill condition at zero angle of attack (top) and near separation angle of attack (bottom). Source: AIAA Paper No 84-2487

locked rotor are m.f.r. = 0.30 and 0.15. Figure 37.20 shows the shape of the streamtube and stagnation point position at $\alpha = 0$ deg and $\alpha = 20.6$ deg and m.f.r. = 0.34 for a given engine intake. At high α the stagnation point at the top has moved far inboard. This creates a leading-edge suction peak comparable to the suction peak on an airfoil.

On the other hand at the maximum thrust setting the operative engine(s) will at low speeds operate at a high mass flow (at around m.f.r. = 2.0). This will move the stagnation point on the lower outside further aft with increasing angle-of-attack leading to high local velocities on the lower inboard nacelle. This was shown before in figure 37.5.
Figure 37.21 illustrates the possible separated flow on upper and lower intake lip. In order to align engine intakes with the local flow in cruise and to maximise the intake efficiency at full thrust and minimise the added drag when an engine fails at high-angles of attack at low speed engine intakes are usually drooped 3 to 5 deg relative to the engine centre line (figure 37.22).
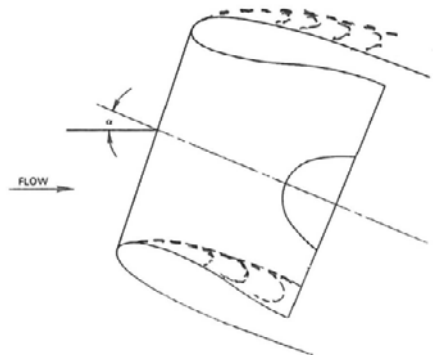
FLOW

Figure 37.21 - Flow separation on upper and/or lower intake lip at high angles-of-attack
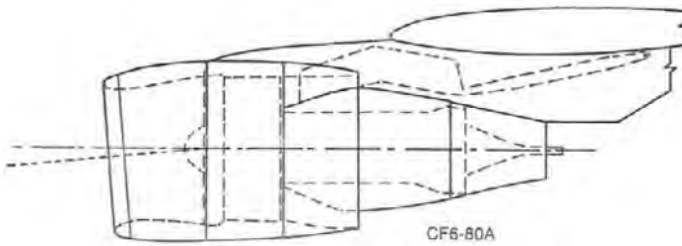
Figure 37.22 - Engine intake droop

In figure 37.23 the Mach number distribution is shown on the top inner and outer wall of an intake model at four angles-of-attack at M = 0.25 and m.f.r. = 0.34. At the highest angle-of-attack, α = 20.6 deg, the peak local Mach number M_{loc} = 1.05 for the particular Reynolds number.

Figure 37.24 shows that the maximum inlet angle of attack at which flow separation on the outside of the upper lip occurs is strongly Reynolds-number- and Mach-number dependent. To obtain reliable wind tunnel data for large aircraft tests have preferably to be performed at Reynolds numbers close to Re = 10^7 (With the maximum nacelle diameter as reference length).
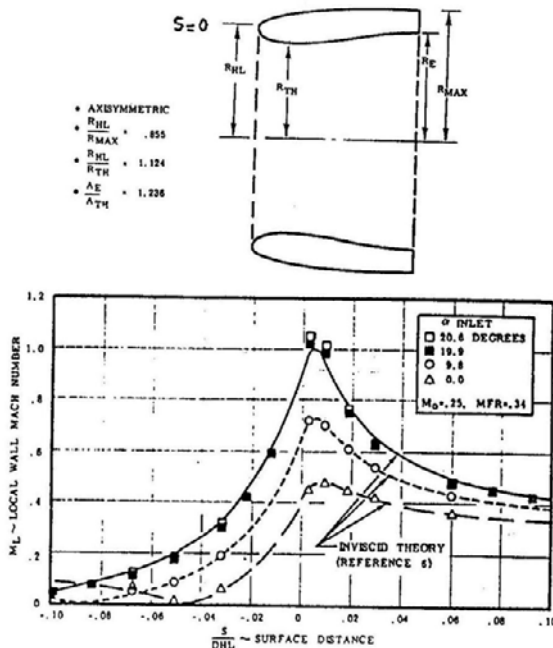
Figure 37.23 - Local Mach numbers near the wall at various angles of attack; model geometry (top) and inviscid theory/wall Mach number data comparison (bottom). Source: ICAS-1984-1.10.1
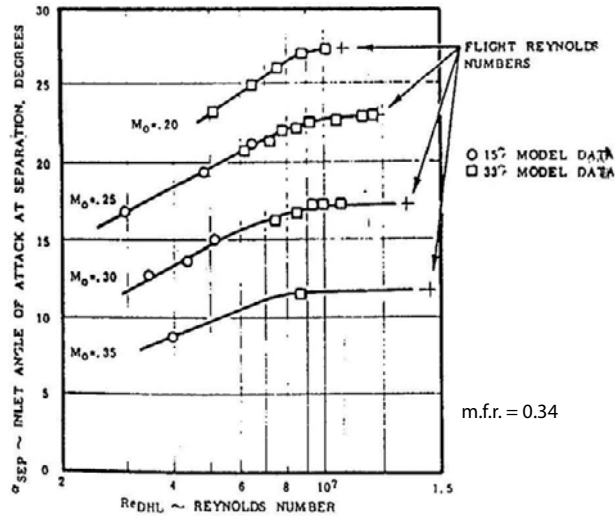
*Figure 37.24 - Relation between Mach and Reynolds
number and angle of attack. Source: ICAS-1984-1.10.1*

Engine intakes must not only be tolerant concerning high angles-of-attack, also large sideslip angles must be tolerated to enable operation with high crosswinds without engine surge. This requires also carefully shaped intake lips on the intake sides.

In the foregoing the attention has been focussed on the internal flow offered to the engine and on both internal and external flow separation.
But as was mentioned before variations in mass flow ratio also affect the cowl drag at low angles-of-attack, particularly at higher Mach numbers. In figure 37.25 drag data are presented for an engine with the intake described in figure 37.5. The data were derived from circumferential total pressure measurements at the nacelle exhaust position (see figure 37.27). Figure 37.25 shows that at low Mach numbers mass flow ratio variations show little effect on drag. The intake lip suction losses are minimal in these conditions. At high Mach numbers the drag rise is considerable. If this nacelle were operated at $M = 0.85$ an engine failure, reducing the mass flow ratio to m.f.r. $= 0.40$ would double the nacelle drag due to strong shocks around the intake lips. (The nacelle was designed for $M = 0.75$ to 0.77.)

This drag increase at higher Mach numbers has also to be considered in flight planning of day-to-day operation in relation to Extended Twin-Engine Operations (ETOPS).
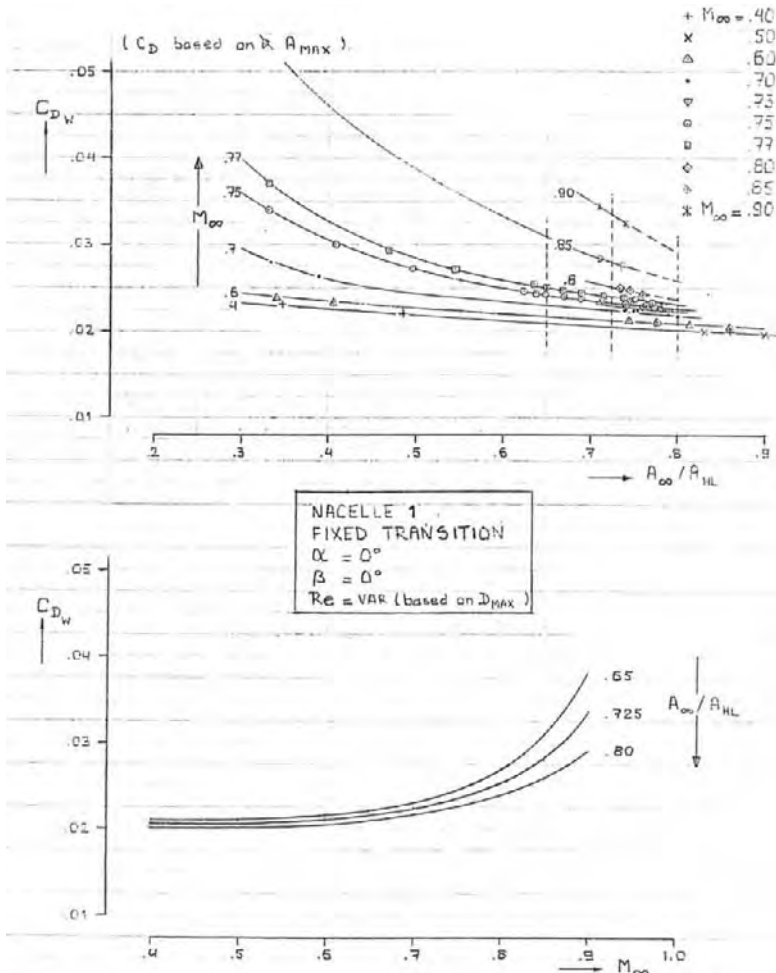
Figure 37.25 - The effect of mass flow ratio and Mach number on cowl drag.
Source: Fokker report L-29-174

The above illustrates that an engine intake has to be carefully tailored to both the engine and the aircraft design requirements.

In order to investigate the intake behaviour in the flow field of the complete aircraft flow-through engine nacelles with different mass-flow ratios may be tested. Because flow-through nacelles do not add or withdraw energy from the flow (apart from boundary-layer effects) the cross sectional area of the stream tube flowing through the nacelle is the same infinitely far in front of and behind the nacelle. Due to the sharp nacelle trailing edge there is no expansion or contraction of the exhaust flow and the static pressure in the exhaust plane is equal to the static pressure of the undisturbed flow. Consequently the intake

mass- flow ratio is determined by the ratio between highlight and exhaust area. This is illustrated in figure 37.26a. The rear end of the nacelle does not conform to the real nacelle lines so overall test data on the complete aircraft must be considered carefully. But in general this is a cost-effective way of performing part of the design and analysis of the intake.

On the flow through the real engine nacelle energy is added in the gas generator. Therefore, contrary to the flow-through nacelle, the flow conditions in front of and behind the nacelle are totally different as indicated in figure 37.26b. However, experience has taught that, unless the nacelle is very short, there is very limited interference between the intake and exhaust outer flow and intakes and exhausts can be studied separately.
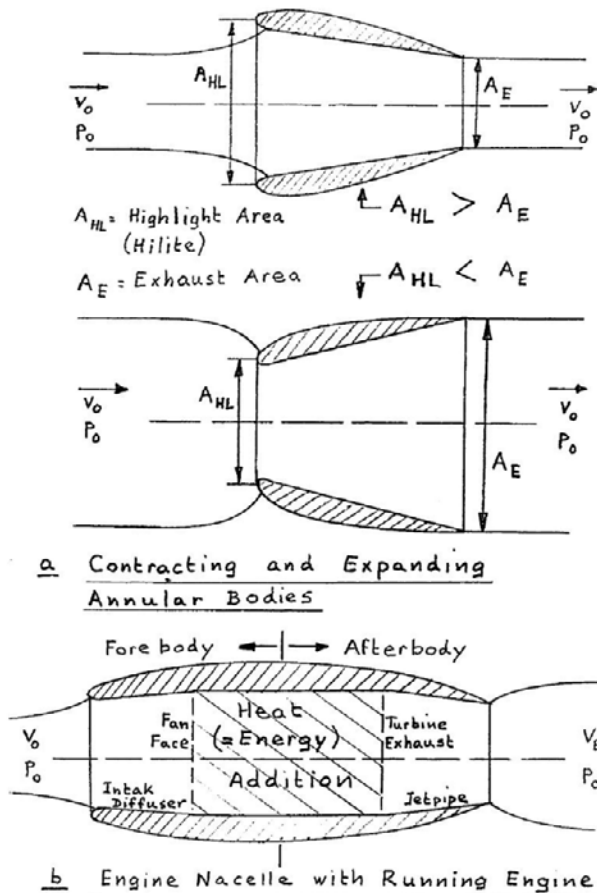
Figure 37.26 - Some characteristics of engine nacelle investigations in the wind tunnel.
   a. Variation of the mass flow ratio of flow-through nacelles
   b. The difference between flow-through nacelles and real engines or turbine-powered simulators (TPS)

Today turbine-powered simulators, mini jet engines powered by compressed air supplied by an external source, are used routinely in a number of places in the world. These approach the flow conditions at intake and exhaust of the real power plant. Nevertheless there will remain place for separate intake test rigs such as the one shown in figure 37.27, developed by NLR in the Netherlands. The limited use of moving parts and simple calibration facilitates the testing of different intake configurations in quick succession and makes these test rigs cost-effective.

Although the approach concerning analysis and design of a jet engine intake based on one–dimensional flow and average throat Mach number M_{TH} may seem outdated it is still a reliable starting point for initial sizing studies.
Modern CFD methods allow the detailed analysis of the internal and external flow of engine intakes, the wall pressure distributions and related boundary layer conditions. But due to the usually extensive preparation required and the limited flexibility there is still room for simple methods for feasibility and preliminary design studies.
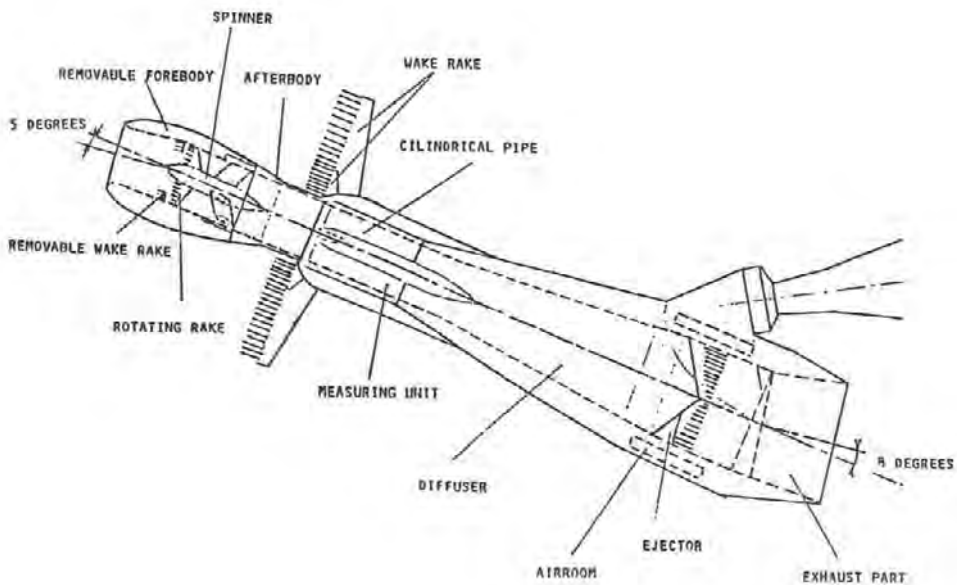
Figure 37.27 - Wind tunnel test rig for engine inlet investigation.
Source: Fokker report L-29-174

38 *Engine Exhausts*

Just as for the engine intake geometry the optimum configuration of the engine exhaust is determined by a number of requirements which stem from both the internal and the external flow.

Compared to basic one-dimensional jet engine theory the real gas flow through and over engine exhausts shows a number of differences:

- Both internal and external flow have boundary layers.

- Because of the boundary layer and streamwise wall curvature the internal flow is not one-dimensional. The axial velocity varies over each cross-section.

- Despite the application of nozzle guide vanes or stators to reduce swirl, a certain degree of rotation will be present in the exhaust. This also leads to the internal flow not being one-dimensional.

- Because of the difference in velocity between external and engine exhaust flow or, on a by-pass engine, between the fan and the core flow mixing occurs on the flow boundaries. This leads to an exchange of energy between external and internal flow and between fan and core flow.

Exhaust efficiency coefficients

In order to incorporate the above-mentioned effects in the standard propulsion analysis methods use is made of the **velocity coefficient** C_V and the **mass flow coefficient** or **discharge coefficient** C_D. C_V and C_D are defined in equations 38-1 and 38-2. These coefficients can be considered as corrections to the ideal velocity when the exhaust flow expands to ambient pressure and to the ideal mass flow which at a given pressure ratio passes through a given exhaust area.

$$C_V = \frac{V_{actual}}{V_{ideal}} \qquad \text{where} \qquad V_{actual} = \frac{F_{actual}}{\dot{m}_{actual}V_{ideal}} \qquad (38\text{-}1)$$

$$C_D = \frac{\dot{m}_{actual}}{\dot{m}_{ideal}} \tag{38-2}$$

The ratio between the ideal gross thrust and the real gross thrust is the thrust coefficient, which is equal to the product of C_V and C_D as given in formula 38-3.

$$C_T = \frac{F_{actual}}{\dot{m}_{ideal}V_{ideal}} = \frac{F_{actual}}{F_{ideal}} = C_V C_D \tag{38-3}$$

For a turbofan:

$$C_T = \frac{\left(F_{actual}\right)_{fan+core}}{\left(F_{ideal}\right)_{fan} + \left(F_{ideal}\right)_{core}} \tag{38-4}$$

The idealized mass flow and velocity can be computed with gas dynamics theory. For an unchoked nozzle (subsonic flow in the throat so $p_0/p_T > 0.528$ for $\gamma = 1.4$ for cold flow and $p_0/p_T > 0.4796$ for $\gamma = 1.33$ for hot flow):

$$V_{ideal} = \sqrt{\frac{2\gamma\,RT_T}{\gamma - 1}\left[1 - \left(\frac{p_T}{p_0}\right)^{\frac{1-\gamma}{\gamma}}\right]} \tag{38-5}$$

$$\dot{m}_{ideal} = A_e p_T \sqrt{\frac{2\gamma}{\gamma - 1}\frac{1}{RT_T}\left[\left(\frac{p_0}{p_T}\right)^{\frac{2}{\gamma}} - \left(\frac{p_0}{p_T}\right)^{\frac{\gamma+1}{\gamma}}\right]} \tag{38-6}$$

For a choked nozzle (Mach = 1 in the throat so $p_0/p_T > 0.528$ or $p_T/p_0 > 1.89$):

$$V_{ideal} = \sqrt{\frac{2\gamma}{\gamma - 1}RT_T} \tag{38-7}$$

$$\dot{m}_{ideal} = \left(\frac{2}{\gamma + 1}\right)^{\frac{\gamma+1}{2(\gamma-1)}} A_e p_T \sqrt{\frac{\gamma}{RT_T}} \tag{38-8}$$

Where A_e is the exhaust area.

The **actual mass flow can be measured** in test rigs using a venturi tube, the **idealized thrust can be computed** and the **actual thrust can be measured** or derived from total pressure rake measurements with wall static pressure tappings. The only quantity that cannot be measured is the **actual velocity**, **but it can be calculated** from the other quantities.

The importance of the thrust coefficient has increased considerably with the introduction of high-bypass ratio engines (bypass ratios 5 and up). The net thrust is the difference between gross thrust and intake momentum drag:

$$T = \dot{m}V_e - \dot{m}V_\infty \qquad\qquad (38\text{-}9)$$

The larger mass flows combined with lower average exhaust velocities lead to the **net thrust becoming more and more a relatively small difference between two large quantities**.

Therefore great care has to be applied to the exhaust coefficients being as close to 1.00 as possible in the various operating regimes: take-off, climb and cruise.

Effect of the ambient pressure

In the choked flow equations 38-7 and 38-8, the ambient pressure p_0 is not present. This means that if the exhaust is choked, the ambient pressure has no influence at all on the flow conditions in the exhaust.

But if the flow is not choked the ambient pressure does have an effect on the conditions in the exhaust (formulas 38-5 and 38-6). The aircraft has an impact on the local pressures in the vicinity of the exhaust and therefore it is important to know the influence of the aircraft flow field. This is usually investigated on large-scale wind tunnel models.

To determine the actual efficiency of the engine, it seems desirable to test it over its complete operating envelope in flight. The extent and accuracy of the required test equipment however does not per se produce more accurate data than a combination of wind tunnel tests and a full-scale engine test in an altitude test facility. Altitude test facilities enable the measurement of the engine performance over the range of ambient pressures and temperatures and flight Mach numbers that occur over the engine operating envelope. Figure 38.1 shows an Airbus A380 engine being tested in flight on an Airbus A340. Because of the high costs involved the need for flight tests is only seen for engines with a significant degree of new technology. For example no separate engine flight tests were performed for the Rolls-Royce Tay used on the Fokker 100.

Figure 38.1 - Airbus A340 fitted with the engine of the A380. Source: Jorge Abreu

Figure 38.2 shows the difference between choked and unchoked flow for a convergent nozzle. If the nozzle pressure ratio is increased the effective flow area increases. Note that in particular when the flow in the nozzle is unchoked with the pressure ratio being lower than 1.89 the losses can be considerable. For most engines the nozzle pressure ratios are of the order of 1.5-2.0 in take-off and 2.5-3.0 in cruise at M = 0.8. A convergent-divergent nozzle can increase the thrust in unchoked conditions, as is shown in figure 38.3. On civil transport aircraft (fixed) nozzle divergence ratios of only a few percent are used.
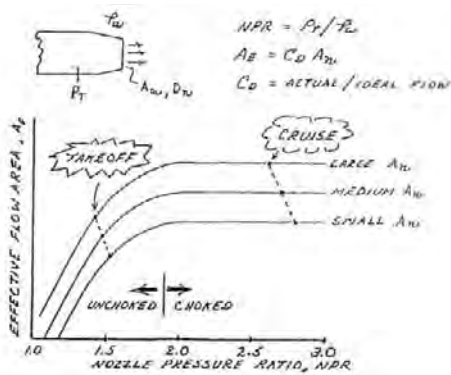
Figure 38.2 - The convergent nozzle
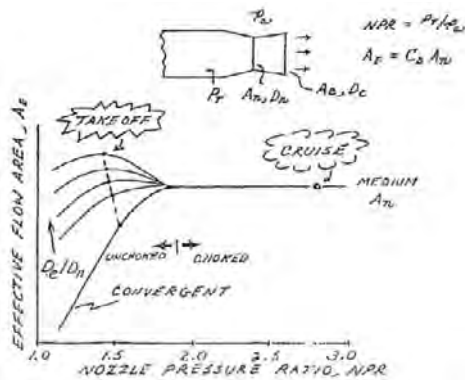
Figure 38.3 - The convergent-divergent nozzle
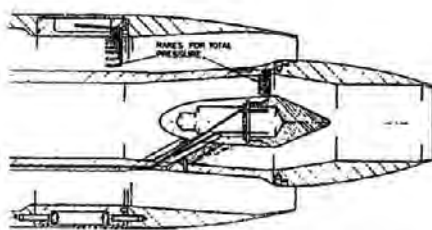
Figure 38.4 - Effect of flight Mach number and fan nozzle pressure ratio on total gross thrust. Layout of the model. Source: ICAS Paper No. 76-32
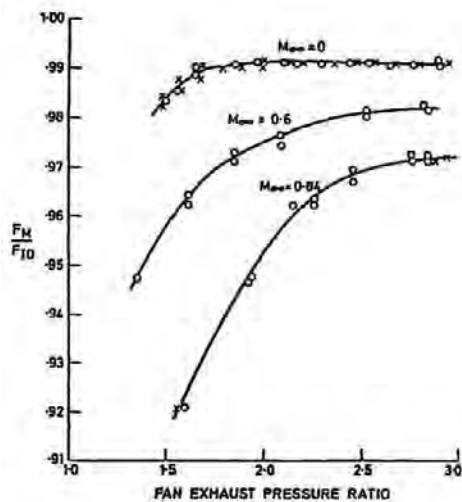
Figure 38.5 - Effect of flight Mach number and fan nozzle pressure ratio on total gross thrust. Typical test results. Source: ICAS Paper No. 76-32

In figure 38.4 the cross-section is shown of a typical engine exhaust simulator with separate fan and core nozzle for the determination of engine nozzle coefficients. Figure 38.5 shows how the gross thrust differs from the ideal thrust as a function of the flight Mach number and fan exhaust pressure ratio. The core pressure ratio has a fixed relation to the fan pressure ratio in this kind of tests depending on the particular engine simulated but is of the order of 80% of the fan pressure ratio. The losses decrease with increasing pressure ratio mainly due to the increase of the discharge coefficient. Note that the main reason for variation in the exhaust pressure ratio is due to the ambient pressure decreasing with altitude. Therefore, as was mentioned before, low pressure ratios in the order of NPR = 1.5 – 1.7 refer to take-off and NPR = 2.4 – 2.6 to cruise conditions.

Test data from the General Electric CF-6-50

Originally the General Electric CF-6-50 engine was designed with thrust reversers on both the fan and the cowl. When operational experience indicated that the core thrust reverser could be deleted the core cowl was redesigned as shown in figures 38.6. The shortening of the core cowl reduced the pressure drop in the core nozzle and reduced the scrubbing drag of the core cowl. The difference in the overall gross thrust coefficient C_T between the two nozzles is shown in figures 38.7 and 38.8 for the two wind tunnel models for M = 0, take-off at M = 0.25, holding at M = 0.60 and Cruise at M = 0.82. In figure 38.9 the gross thrust is compared from tests on both nozzle configurations on an actual engine in a Sea Level Static Test Bed. The data show an improvement of ΔC_T = 0.0035 - 0.0050 in overall thrust coefficient over the complete operating envelope. This may not seem much at first glance but as is indicated I figure 38.8 in cruise this means an increase in net thrust of ΔF_N = 1%.

This example illustrates the possible effect of differences in exhaust nozzle and fan cowl geometry on nozzle performance.
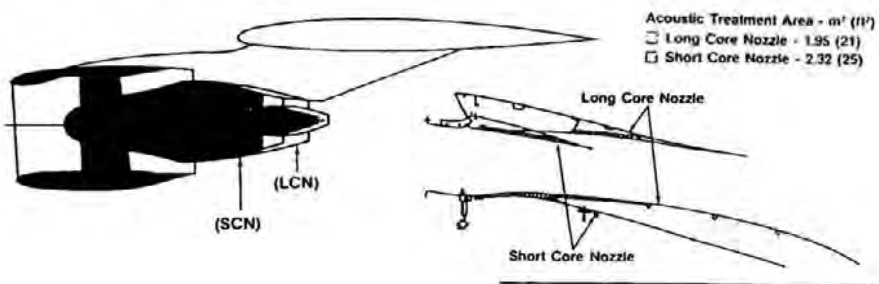
Figure 38.6 - CF6-50 long core nozzle (LCN) and short core nozzle (SCN) installation.
Source: AIAA Paper No. 80-1196
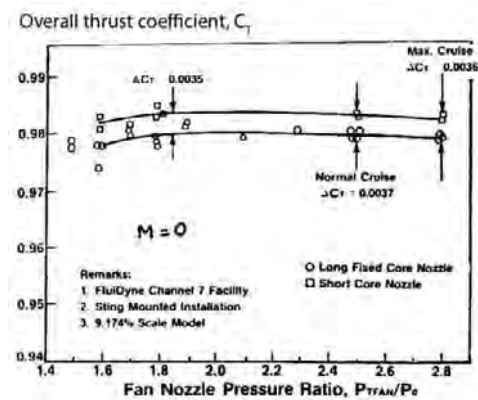
Figure 38.7 - Scale model isolated nacelle static test data. Source: AIAA Paper No. 80-1196
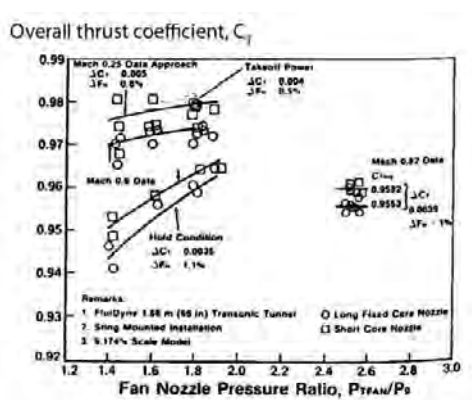
Figure 38.8 - Scale model isolated nacelle wind tunnel test data. Source: AIAA Paper No. 80-1196
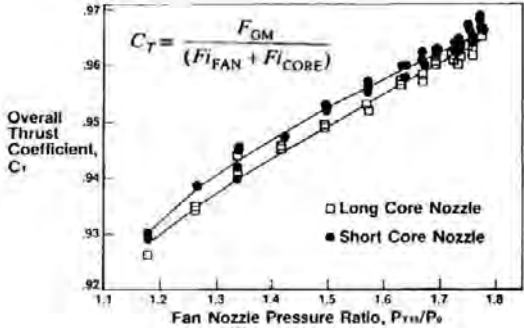
Figure 38.9 - Overall gross thrust coefficient. Actual engine test cell data. Source: AIAA Paper No. 80-1196

Fan and core flow interaction

The following figures show the interaction between the fan and the core flow at static conditions of the nacelle presented in figure 38.10. The velocity coefficient including and excluding the core flow is shown in figure 38.11. Figure 38.12 shows that if the core flow is sub-critical ($p_T/p_0 < 1.89$) and the fan pressure ratio is higher than the core pressure ratio, the discharge coefficient of the latter deteriorates rapidly with increasing fan pressure ratio.
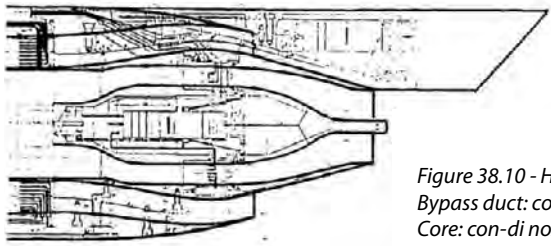
Figure 38.10 - High-bypass ratio engine nozzle.
Bypass duct: convergent nozzle.
Core: con-di nozzle (1.5% div)
Source: Fokker Report L-29-198
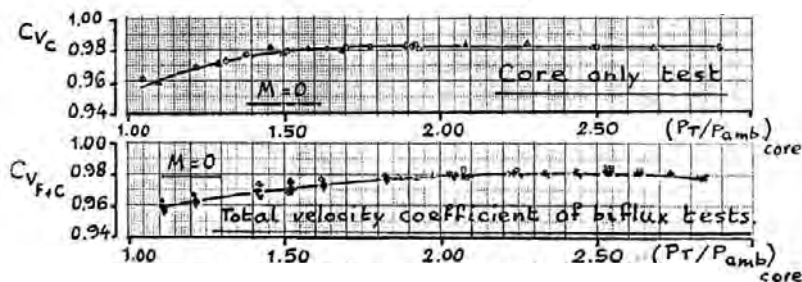
Figure 38.11 - Velocity coefficients of the model shown in figure 38.10
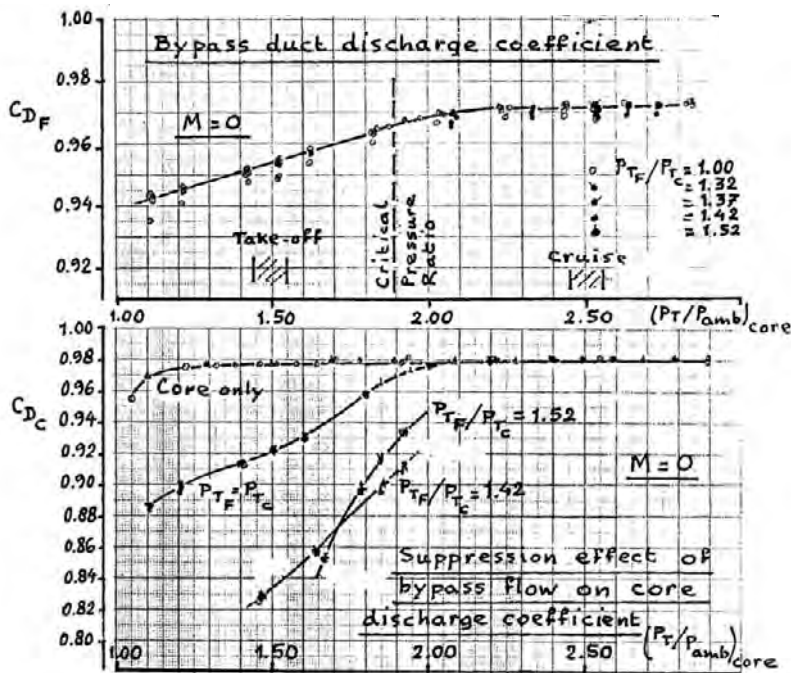
Figure 38.12 - Discharge coefficients of the model shown in figure 38.10
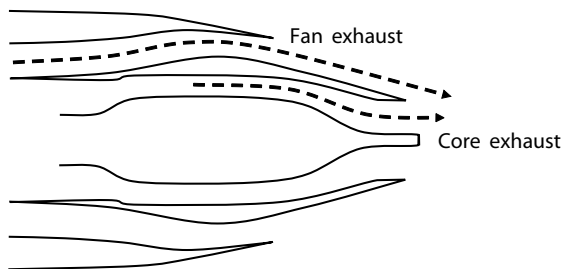
Figure 38.13 - Fan and core flow interference.
Source: Fokker Report L-29-198

A high fan pressure ratio indicates high fan exhaust flow velocities. As is shown in figure 38.13 the fan flow is directed towards the core exhaust and flow suppression occurs on the core flow. This reduces the mass flow from the core and consequently the discharge coefficient deteriorates. This situation exists in particular during take-off and initial climb.

Boeing 767 test data

Figure 38.14 to 38.18 present test data from an investigation to determine the most suitable exhaust configuration for the General Electric CF-6 engine on the Boeing 767.

Figure 38.14 shows the four different core nozzles which were investigated, two convergent and two convergent-divergent nozzles. Velocity and discharge coefficients for both fan and core nozzles are shown in figures 38.15 to 38.18. These test data clearly indicate that some nozzles have their optimum at low nozzle pressure ratios others at high pressure ratios. This means that optimum nozzle performance is determined by the relative importance of field or cruise performance. Field performance gets in general more emphasis on short-range aircraft, so a nozzle with good performance at low nozzle pressure ratios will be preferred here. For long-range aircraft nozzles will be preferred which show good performance at high nozzle pressure ratios.
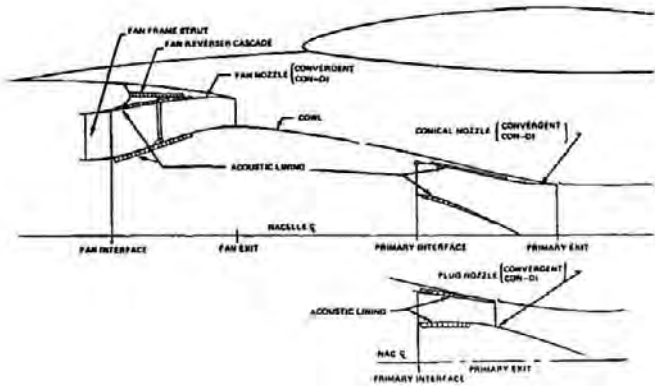
Figure 38.14 - Fan and primary nozzle configurations. Source: SAE Paper No. 800731
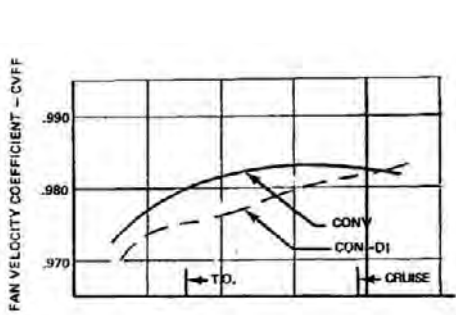
Figure 38.15 - Fan nozzle performance characteristics I. Source: SAE Paper No. 800731
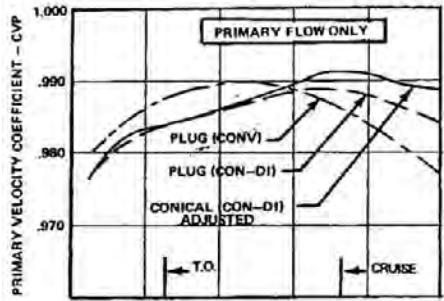
Figure 38.16 - Primary nozzle performance characteristics I. Source: SAE Paper No. 800731
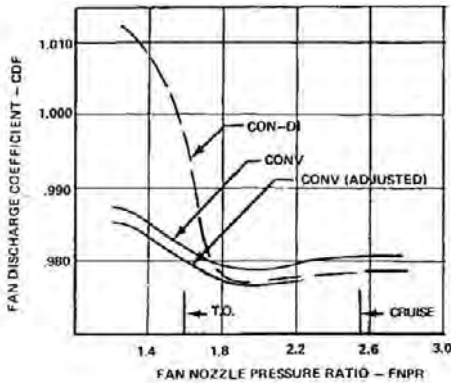
Figure 38.17 - Fan nozzle performance characteristics II. Source: SAE Paper No. 800731
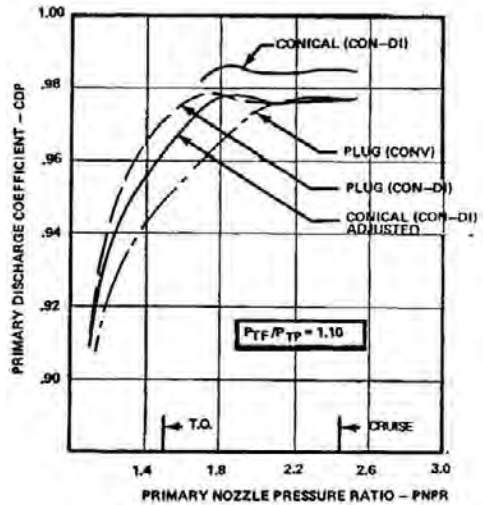
Figure 38.18 - Primary nozzle performance characteristics II. Source: SAE Paper No. 800731

Boat tail drag

In figure 37.19 a high-bypass-ratio engine nacelle is shown. Both the fan cowl and the core cowl are tapered towards the exhaust nozzle. If the exhaust pressure ratio is supercritical, which means that the static pressure in the exhaust plane is higher than the ambient pressure, the flow will expand.. This can create severe adverse pressure gradients on the fan cowl but more particular on the core cowl which may lead to flow separation as illustrated in figure 38.20. This pressure gradient is shown in figure 38.21 for different nozzle pressure ratios. In figure 38.22 the drag is presented as a function of local wall curvature and the figure shows that excessively high drag may occur when the radius of curvature is very small. This drag is termed boat tail drag because the side or top view of an engine exhaust resembles the stern of a motor yacht. In high speed flight

Figure 38.19 - Typical high bypass engine nacelle.
Source: AIAA Paper No. 81-1694

the fan is choked and compression waves are present. The compression waves are bounced back as expansion wave and vice versa, leading to the diamond shockwaves illustrated in figure 38.23. The drag increases because of the enthalpy losses due to the shockwaves and additionally the shockwaves may
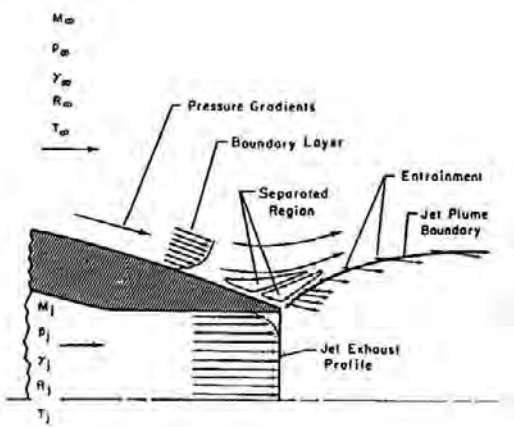
Figure 38.20 - Schematic of nozzle afterbody flow. Source: AIAA Paper No. 81-1694
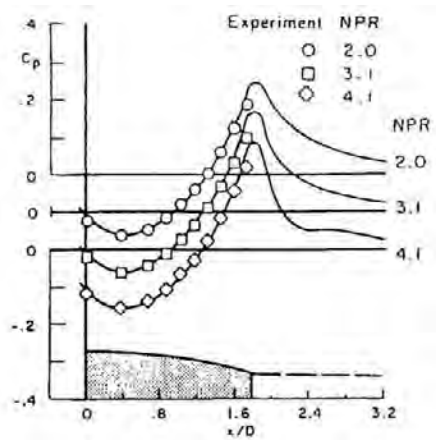
Figure 38.21 - Comparison of predictions with experiment. Source: AIAA Paper No. 81-1694
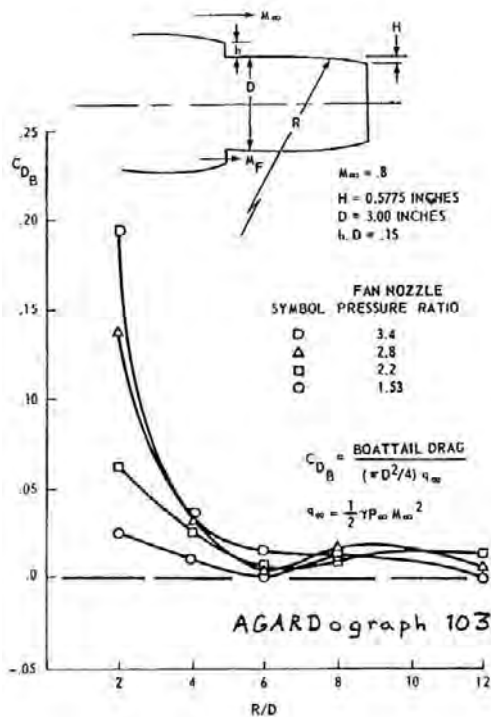
Figure 38.22 - Boat tail drag coefficient versus radius of curvature. Source: AGARD graph 103
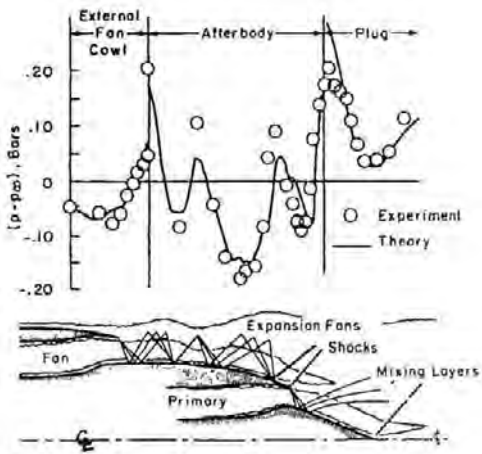
Figure 38.23 - Boat tail effects on the external flow on nacelle afterbody. Source: AIAA Paper No. 81-1694

39 *Thrust reversers*

The main function of thrust reversers is to decrease the ground roll distance, either after landing or in an aborted take-off. Thrust reversers are also used for taxiing backwards from the gate on reverser thrust ("power backing"). This is used by many operators in order to reduce operating costs. On most civil aircraft thrust reversers are operated only on the ground.

There are two basic types of thrust reversers in use:

- Bucket- or target-type thrust reversers
- Cascade thrust reversers

Figure 39.1shows a target-type thrust reverser on the Boeing 737 and in figure 39.2 the vanes of a cascade thrust reverser are visible on the Boeing 767.
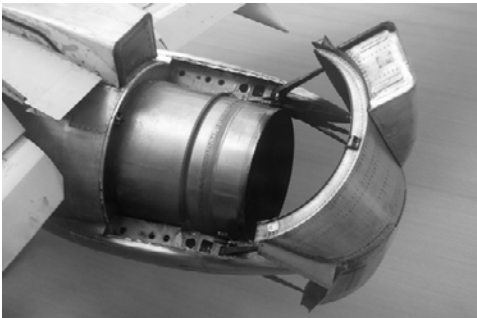
Figure 39.1 - Target type thrust reverser.
Source: Bruce Leibowitz
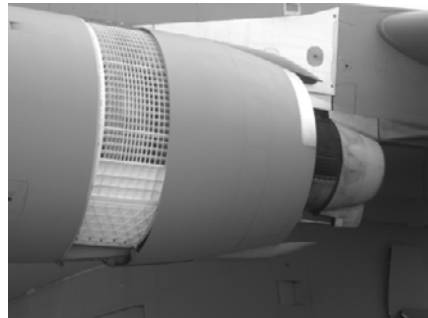
Figure 39.2 - Cascade type thrust reverser.
Source: Ronald Slingerland

Both the FAA and EASA do not allow the use of thrust reversers to reduce the certified accelerate-stop or landing distance on a dry runway but under certain provisions do allow their use in determining the certified required runway length on wet runways. In general however their main effect lies in decreasing the ground roll distance on wet and icy or snow- covered runways (figure 39.4) in day-to-day operation, lessening brake wear and providing an extra element of safety.
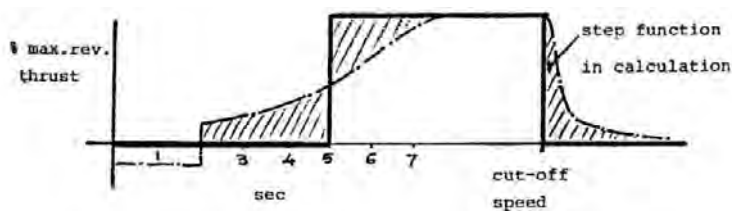
Figure 39.3 - Reverse thrust applied in calculating the data of figure 39.4.
Source: Fokker Report PDI-78-07
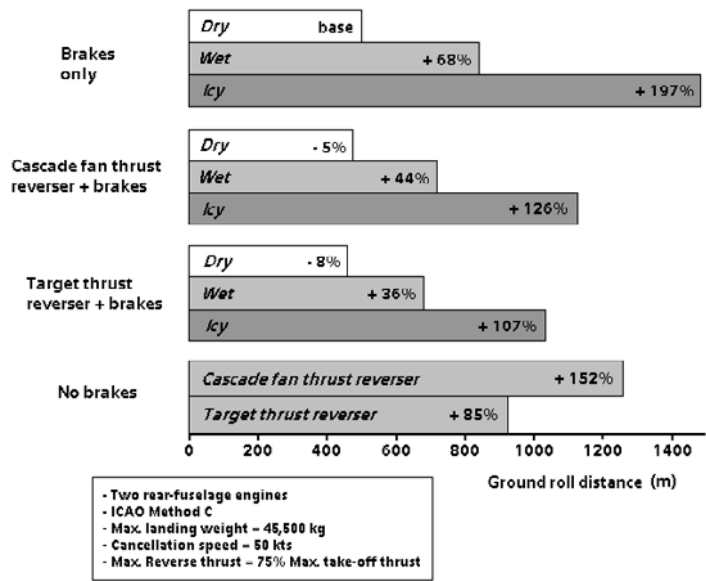
Figure 39.4 - Effect of runway conditions on landing ground roll (SL/ISA).
Source: Fokker Report PDI-78-07

The effect of cascade fan and target thrust reverser on the landing ground roll for three specified conditions.

Figure 39.3 shows the step function and table 39.1 gives the assumptions applied in the reverse thrust calculations performed to obtain figure 39.4. The figure illustrates that at dry-runway conditions (runway-to-tire friction coefficient $\mu = 0.53$) the reduction with thrust reversers is very small (5 to 8%, which means up to 50 m). At typical wet-runway conditions ($\mu = 0.25$) the reduction is reasonable (14 to 19%, which means up to 200 m). And at typical icy-runway conditions ($\mu = 0.10$) the reduction is significant (24 to 30%, or up to 540 m).

The following assumptions are made for the calculation:

- Reverser efficiency of a cascade fan   45%
  Reverser efficiency of a target thrust reverser   40%
- Delay time after touchdown of main wheels:
  Lift dumpers / brakes / selection of thrust reverser after 1 sec.
  Full thrust reverse after 5 sec.
- Cut-off speed: 50 kts.
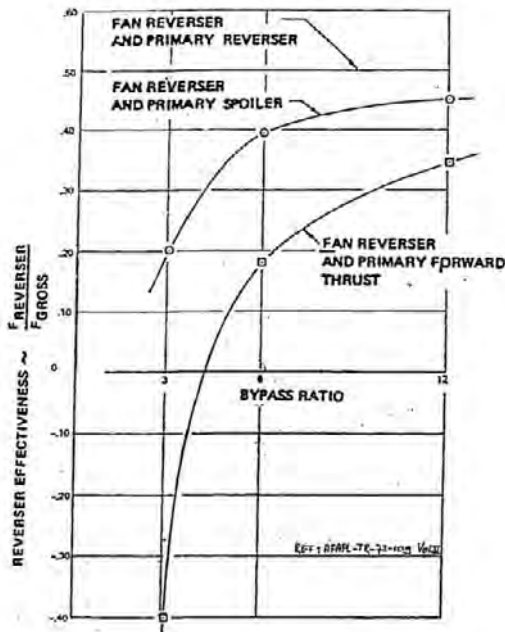
Figure 39.5 - Effect of primary reverse thrust mode on reverser effectiveness $(\eta_R)_{basic}$ = 50%. Source: AFAPL-TR-72-109 Vol. II

On bypass engines with separate fan and core exhausts the question arises if the need exists to apply reversers to both fan and core flow. In figure 39.5 a graph is shown of the effect of bypass ratio on total reverse thrust when a reverser is fitted only to the fan flow. Notwithstanding the low overall effect (in the particular example reverser efficiency η_{TR} = 18% for BPR = 6) thrust reversers are seldom applied to core exhausts because of the added weight and complexity and the wear and resulting additional maintenance costs.

Cascade thrust reversers can be of the clamshell door or of the blocker door type with external or internal cascade baffles as illustrated in figures 39.6 to 39.10. Cascade reversers have the advantage that the exhaust flow can be better directed in optimum directions. They are however heavier, more complex and require more maintenance.
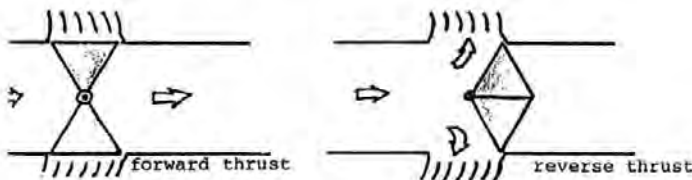
Figure 39.6 - Cascade thrust reverser schematic. Source: Fokker Report PDI-78-07
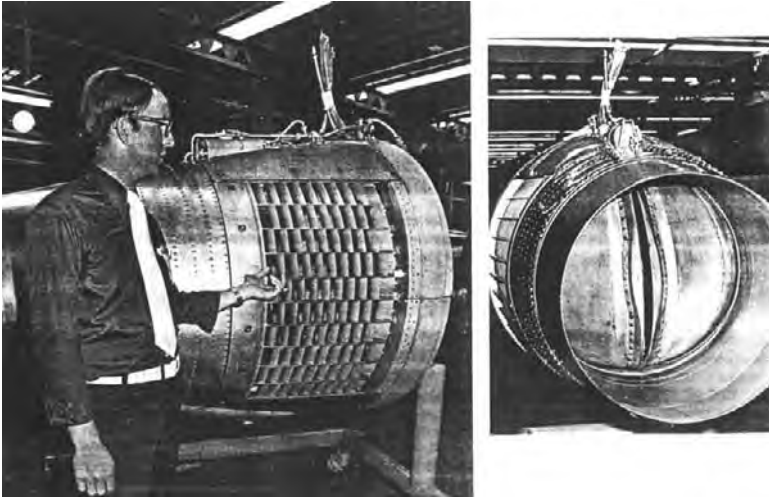
Figure 39.7 - Boeing 727 cascade thrust reverser. Source: Shell Aviation News No. 437, 1976

In the design of thrust reversers three design goals can be recognized:

A. The maximization of reverse thrust (usually not more than 50% reverse thrust is realised).
B. The minimization of the risk of ingestion of the hot exhaust gas and foreign objects.
C. The minimization of adverse effects on stability and control.

Requirements B and C oppose requirement A. Exhaust flow which is directed more forward increases the chance of re-ingestion. As illustrated in figure 39.8, re-ingestion means that exhaust gasses are sucked into the engine intake which disturbs the proper functioning of the engine. There is also a risk that stones and dirt are blown into the intake known as foreign object ingestion (FOI) resulting in foreign object damage (FOD).
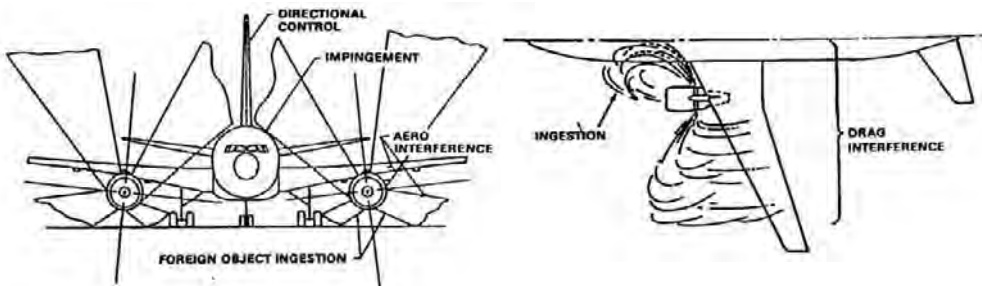
Figure 39.8 - Reverser plume design considerations. Source: AIAA Paper No. 86-1536
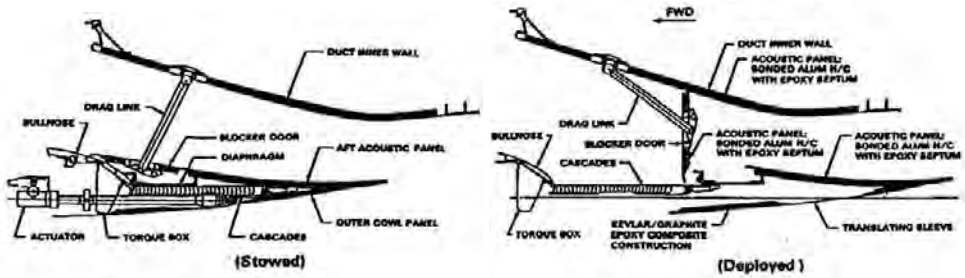
Figure 39.9 - Fan duct thrust reverser for the Boeing 767 GE CF-6 turbofan

Varying the shape and orientation of the cascade baffles on cascade thrust reversers allows a large degree of freedom in distributing the amount and direction of the reversed flow as is shown in figures 39.6 to 39.10.
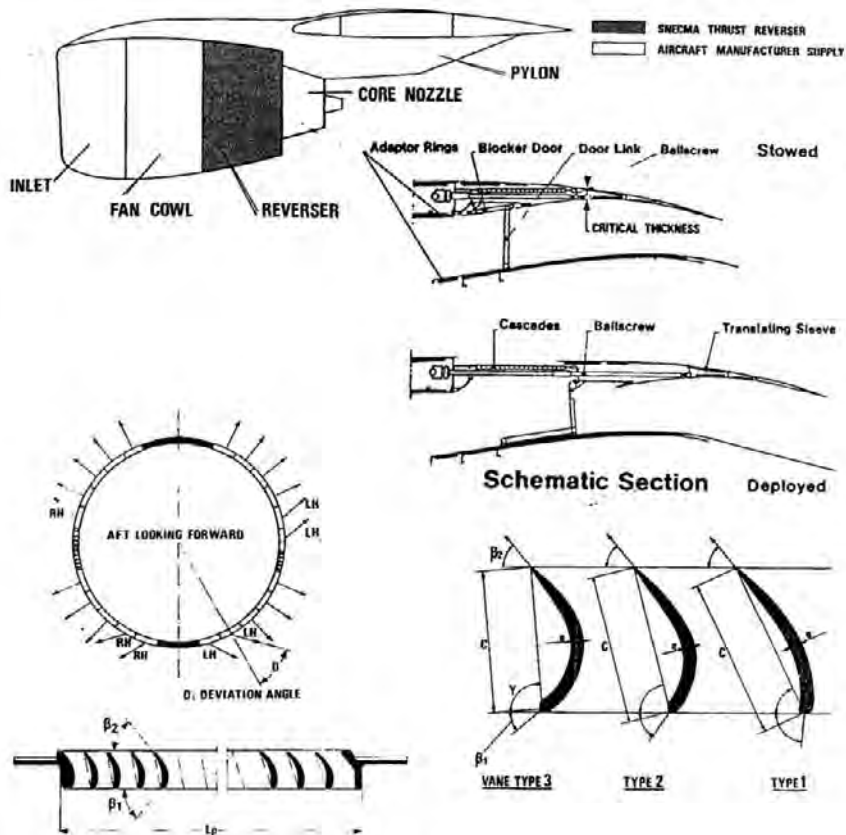
Figure 39.10a - CFM56 Thrust reverser. Source: J. Renvier / SNECMA, 4th seminar on Gas Turbine Technology, Bangalore (India), November 1979
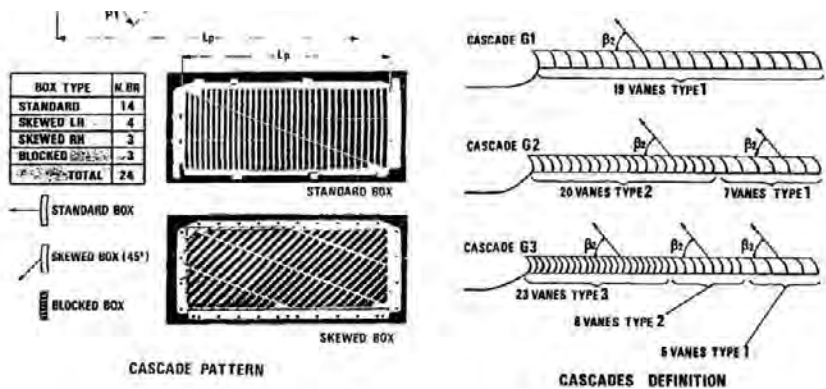
Figure 39.10b - CFM56 Thrust reverser. Source: J. Renvier / SNECMA, 4th seminar on Gas Turbine Technology, Bangalore (India), November 1979

Target-type thrust reversers have much less control over the direction of the exhaust flow. In particular rear-fuselage-mounted engines may cause problems both with rudder control because or diminishing rudder effectiveness and with nose wheel steering because of reduced nose-wheel loads. Examples of target type thrust reversers are given in figures 39.11 to 39.14.
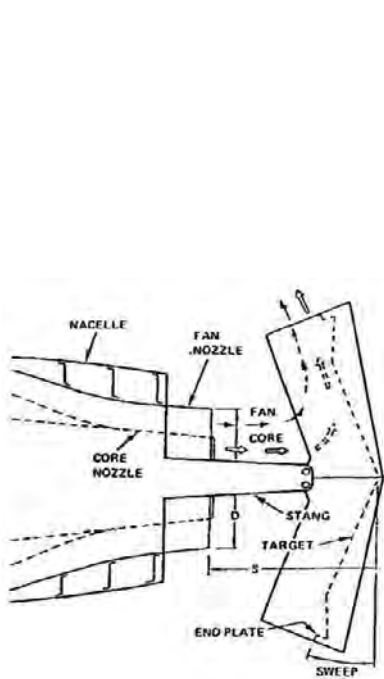
Figure 39.11 - Geometry of a target type thrust reverser. Source: AiResearch TFE-731
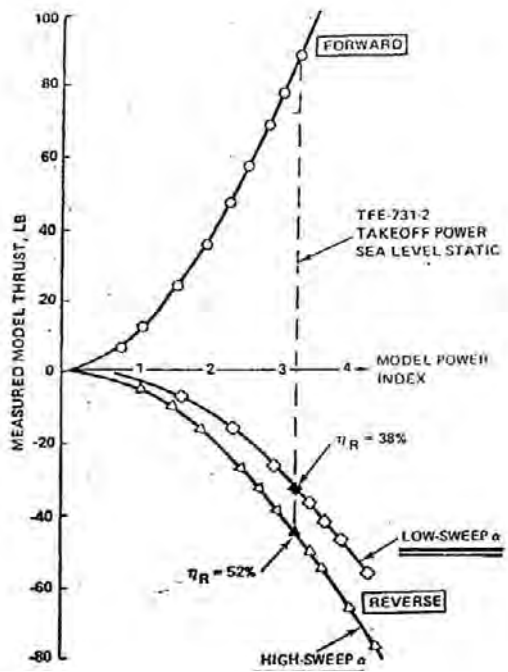
Figure 39.12 - Model reverse effectiveness. Source: AiResearch TFE-731
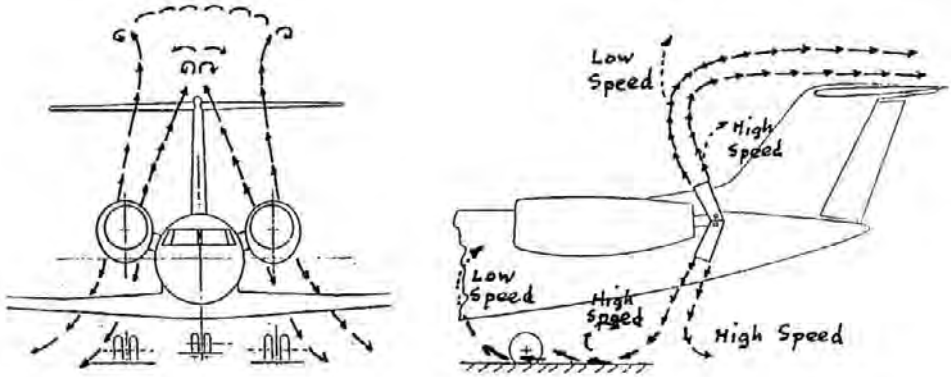
Figure 39.13 - Reverse thrust plume shape on rear-fuselage mounted engines. Target type thrust reverser. Source: SAE Paper No. 750506
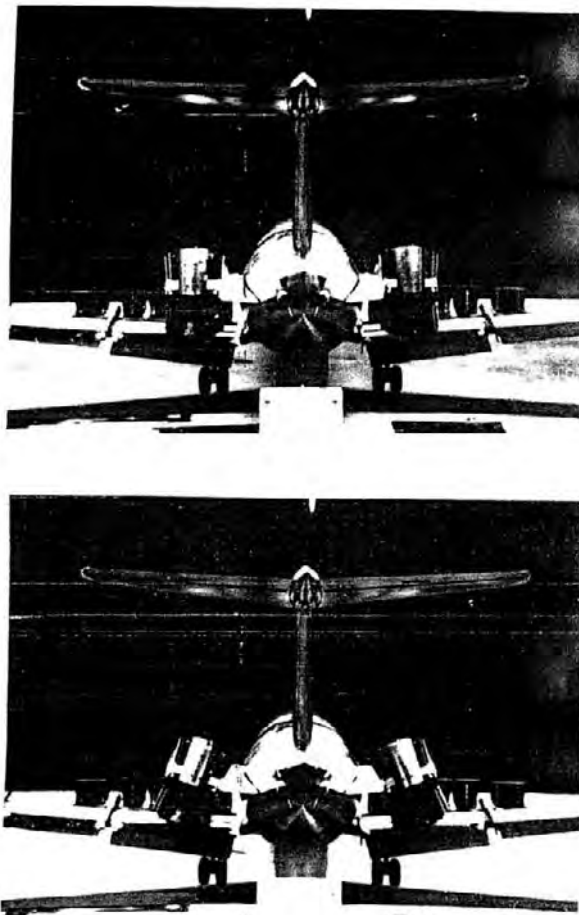
Figure 39.14 - Wind tunnel tests on a Fokker 100 model into the effects of thrust reverser door 'clocking' on re-ingestion and directional stability and control

On the Fokker 100 a small deflector plate, fitted on the inboard side of the exhaust nozzle considerably improves directional stability and control with a thrust reverser deployed as shown in figures 39.15 and 39.16.
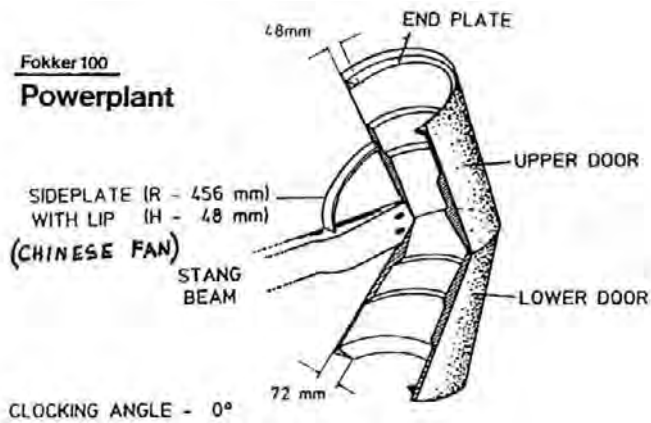
Figure 39.15 - Fokker 100 thrust reverser door configuration
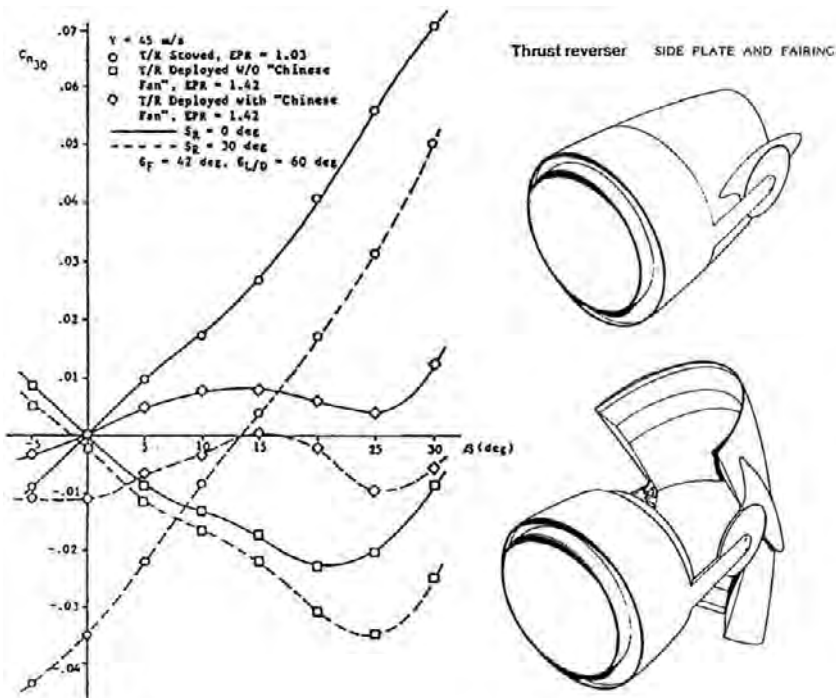
Figure 39.16 - The effect of the 'Chinese Fan' on the directional stability and control with thrust reverser deployed for the Fokker 100. Source: ICAS-88-6.1.2

Re-ingestion boundaries have to be determined very carefully both in wind tunnel and in full scale tests to determine safe minimum thrust reverser operating speeds (figures 39.17 to 39.21).
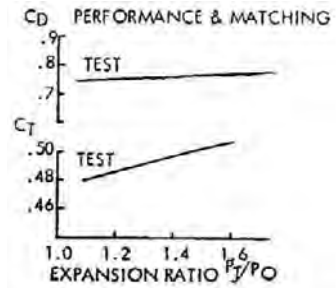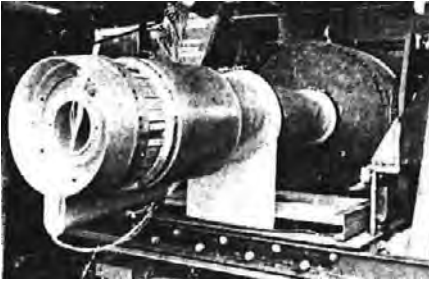
Figure 39.17 - Cascade type thrust reverser. Source: T.M.D. Sutton, Rolls Royce. Aircraft Engineering, March 1976
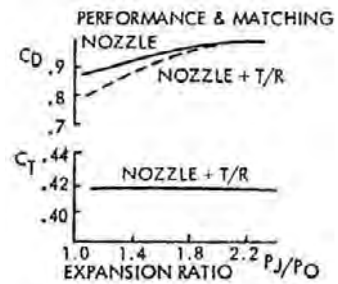
Figure 39.18 - Target type thrust reverser. Source: T.M.D. Sutton, Rolls Royce. Aircraft Engineering, March 1976
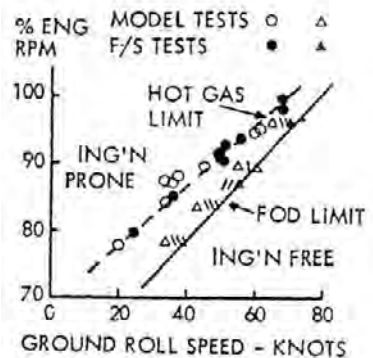
Figure 39.19 - Rear-fuselage-mounted engines model

517
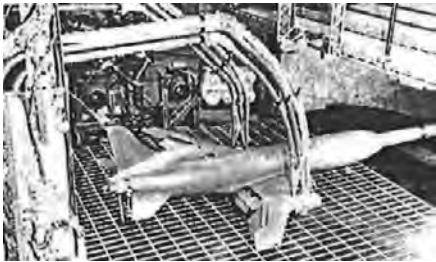
Figure 39.20 - Model with engines mounted under the wing - Lockheed 1011.
Source: T.M.D. Sutton, Rolls-Royce. Aircraft Engineering, March 1976
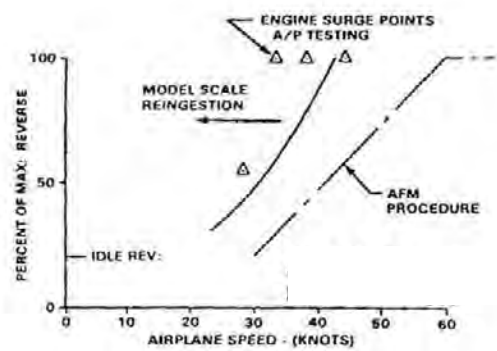
Figure 39.21 - Comparison of model to full-scale ingestion/surge
data for the Boeing 767 / GE CF-6. Source: AIAA Paper No. 97-1921

PART 9

AIRCRAFT PERFORMANCE

40 *Subsonic cruise drag*

Many design parameters concerning performance determine the limits of the flight envelope, such as the maximum lift coefficient and the buffet boundary. Aircraft drag however is of interest in day-to-day operation.

At first sight the present knowledge of boundary layer behaviour, the reduction of areas with flow separation and the ability to calculate the spanwise lift distribution and thus the induced drag would make accurate drag prediction a routine activity. But although 100 years of aviation have tremendously increased knowledge in aircraft design, accurate drag estimation still presents a challenge.

The challenge remains because, although the prediction aids, both in terms of CFD and wind tunnel test techniques, have developed tremendously, so have the customer demands and the commercial requirements.

The customer, particularly a launching customer, requires detailed performance guarantees with small margins and a tight delivery schedule. In the performance guarantees drag plays an important role. Investors and the manufacturer's management demand, because of the huge financial obligations, that the development process runs smoothly and according to planning. Nowadays hand-built prototypes are not produced, the first aircraft is built in production jigs. Modifications to a prototype, required because of disappointing performance which was not unusual in the past, has enormous ramifications for the continued business success of the airframe company. All this makes that accurate drag prediction is of paramount importance particularly for medium- and long-range aircraft.

In Chapter 27 the drag in take-off and landing configuration was considered.
In the present chapter the drag in the climb and cruise configuration will be analysed.

The drag in the clean configuration consists of zero-lift drag, lift-dependent drag, compressibility drag and trim drag. Modern transport aircraft are well-streamlined and due to the extensive use of CFD the interference in the flow over adjacent bodies is minimised. The classical approach of calculating the zero-lift drag by dividing the aircraft in a number of basic components and analysing the drag of each component separately is therefore justified, certainly

in the initial design phase.

The drag of each component consists of friction drag, pressure drag and compressibility drag. Also each design organisation considers some small additional drag sources such as fuselage upsweep drag, induced drag due to wing twist or unaccounted drag due to previous experience. The friction drag is assumed to be equal to the friction drag of a smooth, flat plate with zero pressure gradient with the same characteristic length as the component considered. The ratio between the actual drag of this component and the flat plate drag is termed the shape factor. This shape factor expresses the effect of the supervelocities and the resulting pressure gradients on the body on the friction drag and of the boundary layer displacement thickness on the pressure drag. As the name implies the shape factor is determined by the geometry of the body. Large collections of shape factors have been obtained from computations and wind tunnel tests and can be found in standard data bases such as ESDU Data Sheets or the USAF Datcom. Most design organisations develop their own version of such data based on their particular experience.

Real aircraft surfaces are not perfectly smooth. The surface disturbances, which are sources for additional drag, can be grouped under two headings: excrescences and roughness.

Excrescences are parts on the surface of which the individual drag can be identified such as antennae, instrument probes, external hinges, strobe lights, control surface gaps, etc. A complication in the determination of the drag of these individual parts is formed by their position , partly or completely, in the boundary layer. This requires the estimation of the local boundary-layer conditions in order to estimate the average local dynamic pressure in the flow around the excrescence.

Roughness is the collective term used to indicate smaller surface disturbances such as waviness, production gaps and mismatches, misaligned inspection covers and latches, rivets and similar small protuberances.

Johann Nikuradse, a German researcher, measured in 1932 the resistance a fluid experiences when flowing through a pipe of which the walls were covered with evenly distributed sand of various grain sizes and with varying speeds. He found that, for each grain size, the drag would decrease with increasing Reynolds number according to the friction drag law for a fully turbulent boundary layer on a smooth wall until a certain Reynolds number(speed) was reached. But above this critical Reynolds number drag increased slightly and then remained constant for a given grain size. Later researchers have investigated other forms of distributed roughness with similar results.

This can be explained as follows:

At low Reynolds numbers, as long as the roughness elements remain within the laminar sublayer of a turbulent boundary layer, their additional drag is mostly friction drag which remains constant with increasing Reynolds number. When a Reynolds number is reached where the roughness element emerges from the laminar sublayer the element starts developing a wake which produces pressure drag. With further increase in Reynolds number the element protrudes further into the outer boundary layer and the pressure drag will rise.

On the surface of an aircraft the distributed-roughness elements have different sizes. With increasing Reynolds number progressively more elements will protrude in the outer boundary layer. The total effect of this increase in pressure drag of all these minute disturbances is a perceived change in friction drag. Instead of an decrease in drag with increasing Reynolds number the drag will, after a given Reynolds number, be determined by the average roughness height and remain constant. This is illustrated in figure 40.1
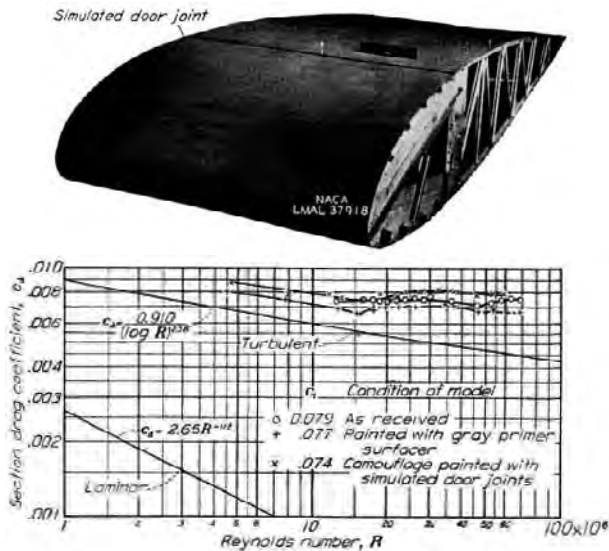
Figure 40.1 - Variation of the drag coefficient with Reynolds number for a practical-construction wind tunnel model based on the NACA 23016 airfoil section together with laminar and turbulent skin-friction coefficients for a flat plate. Source: NACA Report 824

Therefore the surface quality of an aircraft component is often compared to the surface roughness in Nikuradse's experiments and expressed as "equivalent sand roughness". Many wind tunnel experiments and analyses of flight test data

have led to the conclusion that on modern aircraft the equivalent sand-grain roughness lies between 0.0005 and 0.0020 inches or between 0.012 and 0.050 mm.
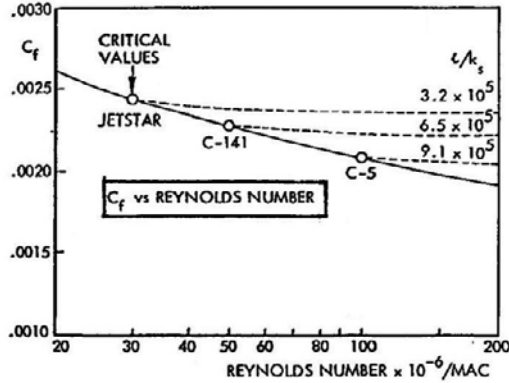
Figure 40.2 - Effect of distributed roughness on skin friction drag. Source: AGARD LS-37

On the latest generation of transport aircraft large parts are produced in carbon composites lacking rivets and the associated waviness. Also, the widespread use of Computer Aided Design and Manufacture has improved production tolerances leading to much smaller production gaps than earlier generations of aircraft. This may justify the use of lower equivalent sand-grain sizes between 0.0004 and 0.0010 inches in drag predictions.

Distributed-roughness drag is directly related to the ratio between boundary-layer thickness and average equivalent sand-roughness height. This means that at low Reynolds numbers with small characteristic lengths l and thin boundary layers even a small equivalent sand-roughness height k_s will cause additional drag. The "cut-off Reynolds number", the **critical Reynolds number above which the friction drag can be assumed to be constant**, does not depend on k_s but on the ratio k_s/l, the r**elative equivalent sand-roughness height**.

Figure 40.3 - Cut-off Reynolds number as a function of relative equivalent sand-roughness height. Source: AFFDL-TR-73-146, Vol. I, II, III

This leads to the conclusion that in most cases the drag coefficient of an aircraft in climb and cruise can be assumed to be independent of the Reynolds number because the cut-off Reynolds number is sufficiently high. However the value of the drag coefficient depends on the cut-off

Reynolds number and thus in practice on aircraft size. This is illustrated in figure 40.2. The cut-off Reynolds number as a function of the relative equivalent sand-roughness height is presented in figure 40.3.

The above is repeated in figure 40.4 which is an excerpt of an presentation on drag prediction by J.C.Callaghan of the McDonnell Douglas Company from 1974.

A good approximation to a clean configuration (high lift systems retracted) low speed drag polar is that represented by the classical parabolic polar

$$C_D = C_{D_0} + \frac{C_L^2}{\pi Ae} \tag{40-1}$$

Where C_{DO} is the drag at zero lift, and $C_L^2/\pi Ae$ is the lift dependent drag. In the strict sense, the drag polars are not parabolic; in practical sense, however, this representation is a reasonable one.

The zero-lift parasite drag with the high lift system retracted is estimated by empirical methods which rely heavily on wind tunnel and flight test data gathered during previous transport development programs. The basic equivalent parasite drag for the individual airplane components is defined as

$$\left(C_{D_0}\right)_{comp} = C_f K \frac{S_{wet}}{S_{ref}} \tag{40-2}$$

Where C_f is the flat plate skin friction coefficient, including the effects of roughness, and K is a form factor which accounts for the effects of thickness, supervelocities, and pressure drag. S_{wet}/S_{ref} is the ratio of wetted area to the reference area.

The flat plate skin friction coefficient can be obtained from various sources for fully turbulent flow and are based on the characteristic length of each component. The characteristic length for a body (fuselage, nacelle) is the overall length and for aerodynamic surfaces (wing, tail, and pylon) it is the exposed mean aerodynamic chord. Roughness effects are due to excrescences such as protruding rivets, steps, gaps and bulges in the skin, etc, which result from typical manufacturing procedures. This is accounted for by an equivalent roughness. This equivalent roughness has been determine by equating the flight test zero lift parasite drag for the DC-8, DC-9 and DC-10 to a detailed estimate of the parasite drag and solving for roughness. This value has been determined to be 0.00095 inch and is, within the accuracy of the flight data, a constant value.

The form factor for aerodynamic surfaces is a function of average thickness ratio and of the sweep of the surface, and may be determined from a data base or appropriate two- or three-dimensional wind tunnel data. The form factor for aerodynamic bodies is a function of overall body fineness ratio and may also be determined from a data base or appropriate wind tunnel data.

An additional miscellaneous excrescence drag is due to the protuberances such as light and antenna fairings, drain masts, probes, unavoidable mismatches, holes, air-conditioning system, etc, which all aircraft are required to have.

Figure 40.4 - Clean configuration drag. Source: AGARD LS-67, 1974, lecture 2

Figure 40.5 presents an excerpt from an article by D. Gyorgyfalvy of Boeing from 1965 on the drag due to distributed roughness.

Based on this result, the equivalent sand-grain roughness of the fuselage surface can be estimated. Equivalent sand-grain roughness K_s is defined as that size of sand grains, distributed on the surface with minimum spacing, which would produce the same skin friction as the original surface with an arbitrary roughness. Nikuradse has determined the relation between the wall law constant B and the roughness Reynolds number $R_{k_s} = k_s U_t / v_0$ for pipes with various sand-grain roughness. From this relation we may conclude that the range of $B = 3$ to 4, characteristic to the fuselage surface, has a corresponding $R_{ks} = 14$ to 9. Thus, we find that the sand-grain size equivalent to the fuselage surface roughness is approximately $k_s = 0.0014$ to 0.022 inch.

Although this value seems very small, it is several times greater than the admissible roughness height, i.e., the maximum size of roughness elements that still do not increase the friction. This limit is set as $R_{Kadm} = 4$, which corresponds to approximately $k_{adm} = 0.00056$ inch.

Figure 40.5 - Determination of equivalent sand-grain roughness.
Source: Journal of Aircraft, Nov-Dec 1965
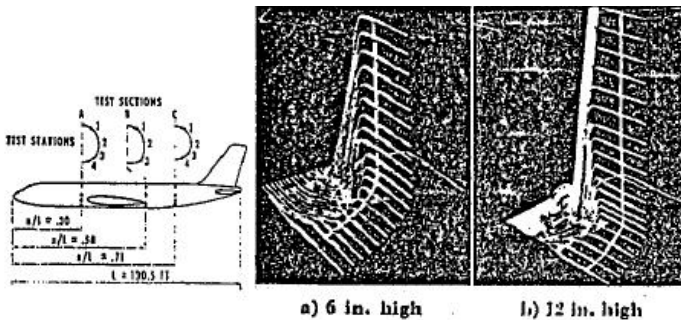
Figure 40.6 - Boundary layer rakes used.
Source: Journal of Aircraft, Nov-Dec. 1965

Much basic experimental research was recently carried out on flat plates in large American and British supersonic wind tunnels to obtain friction coefficients at very high Reynolds numbers. The results are within the boundaries given by the various approximate turbulent theories, but the question remains whether these calculations are valid for a slender wing.

In an attempt to find an answer, our colleagues of NASA have prepared a flight program of boundary-layer measurements at various locations on the upper surface of the experimental North American B-70 bomber. In France, we at ONERA, in cooperation with the French Air Ministry and the Dassault company, have tried similar tests on a Mirage 4 bomber. The friction drag coefficients in flight were deduced from the boundary-layer measurements made with a rake (26 pitot tubes, 1 static, 5 stagnation temperature probes, 1 wall temperature) mounted on the wing upper surface 17 ft behind the leading edge. The subsonic results obtained in flight at Mach number of about 0.85 ($Re_d \approx 70 \cdot 10^5$) are compared with a calculated turbulent friction coefficient (adiabatic flat plate) in fig 40.10. The agreement is excellent if we assume an equivalent sand roughness on the wing surface ($K \approx 0.002$ inch). We have plotted on the same figure some boundary-layer measurements made by a pitot traverse, at a similar location on the wing of a 1/10 scale model tested at low speed. With a natural transition, the values agree with a transitional boundary-layer calculation, whereas a fixed transition, by means of roughness along the leading edge, gives experimental results in accordance with the turbulent calculation on a smooth plate.

Figure 40.7 - Flight test analysis of roughness effects on actual aircraft.
Source: Journal of Aircraft, May-June 1968

Figure 40.7 contains an excerpt and figures 40.8 to 40.11 contain some test results from an article by Ph. Poisson-Quinton of ONERA from 1968.
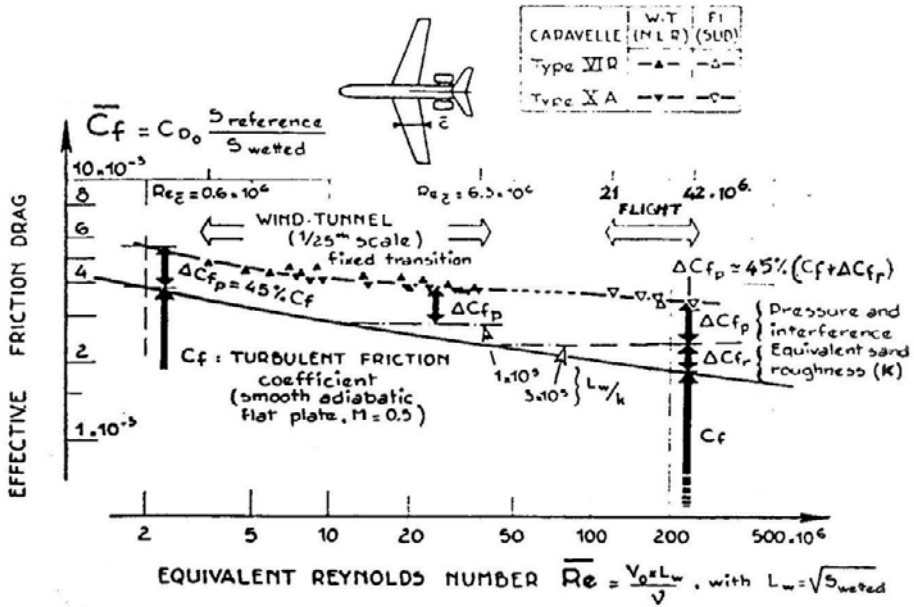
Figure 40.8 - Wind-tunnel-to-flight correlation of minimum drag for two types of "Caravelle": effective friction drag vs. equivalent Reynolds number. Source: Journal of Aircraft May-June 1968
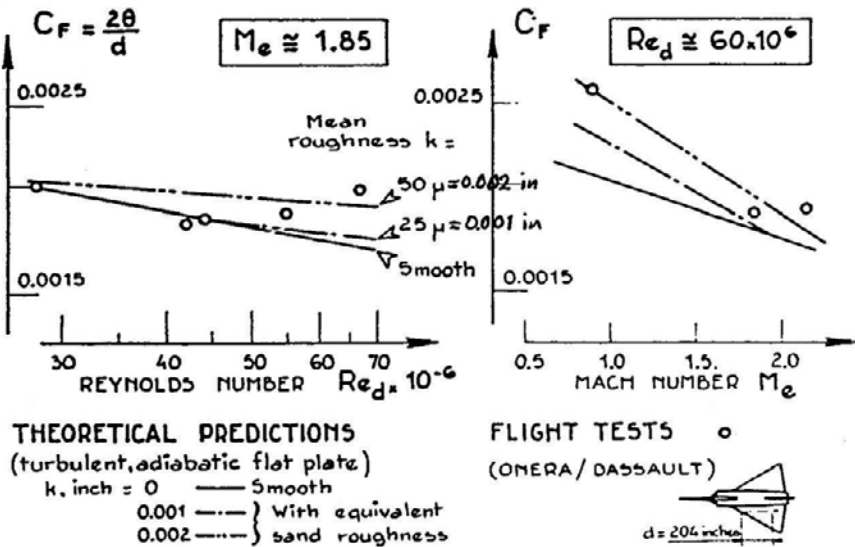
Figure 40.9 - Reynolds and Mach number effects on the mean friction drag coefficient. Source: Journal of Aircraft May-June 1968
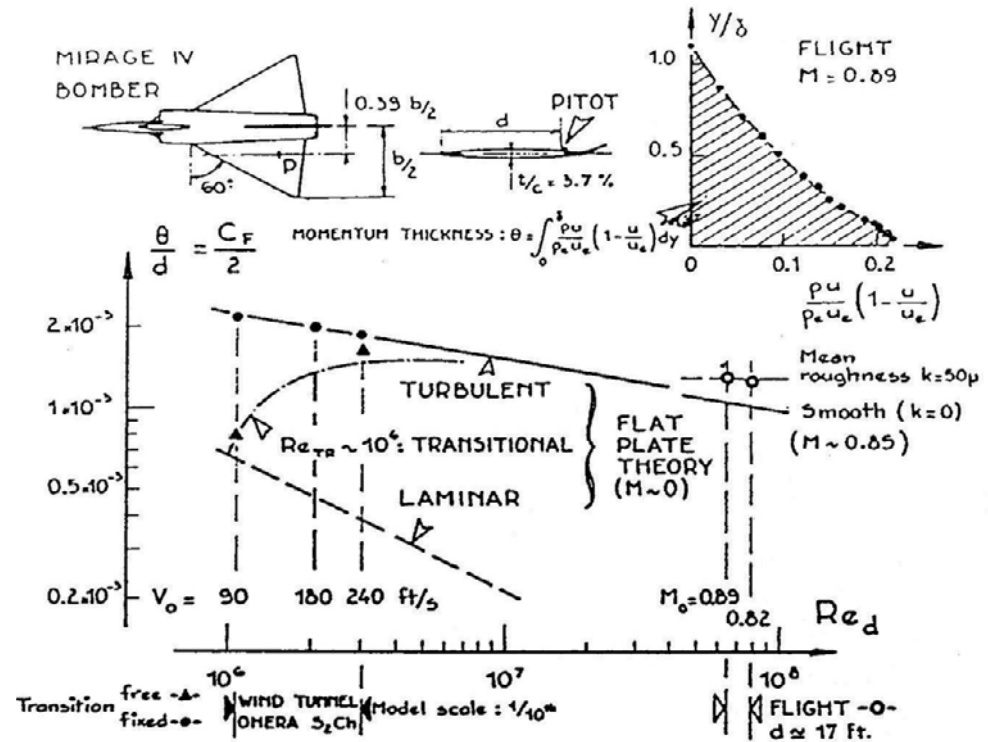
Figure 40.10 - Mean friction drag coefficients obtained by boundary-layer measurements on the delta wing of the Mirage 4 bomber in flight and on wind tunnel models. Subsonic tests: 0.1 < M < 0.9. Source: Journal of Aircraft, May-June 1968
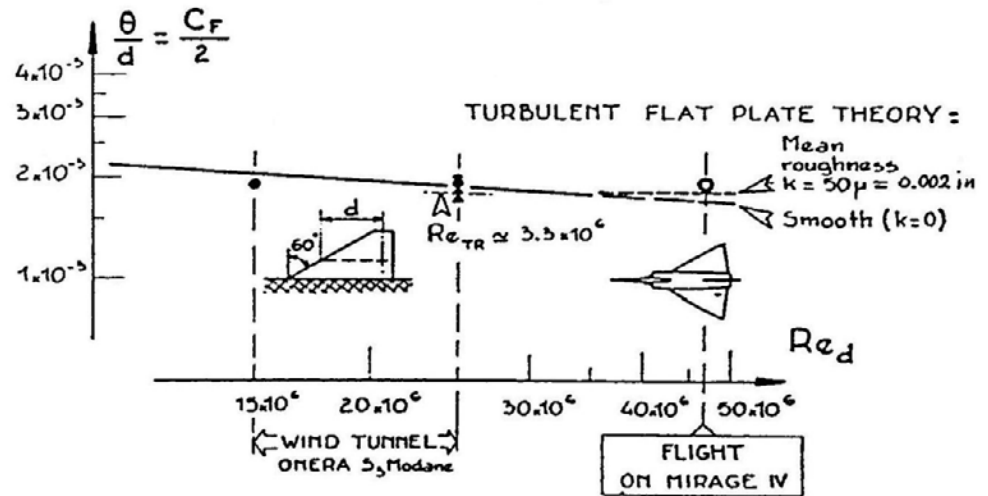
Figure 40.11 - Mean friction drag coefficients obtained by boundary-layer measurements on the delta wing of the Mirage 4 bomber in flight and on wind tunnel models. Supersonic test and comparisons with theoretical predictions: M ~ 2.15. Source: Journal of Aircraft, May-June 1968

Figures 40.12 and 40.13 show the difference in section drag of a wing section of the Boeing 727 wing as measured in the wind tunnel and in actual flight tests.
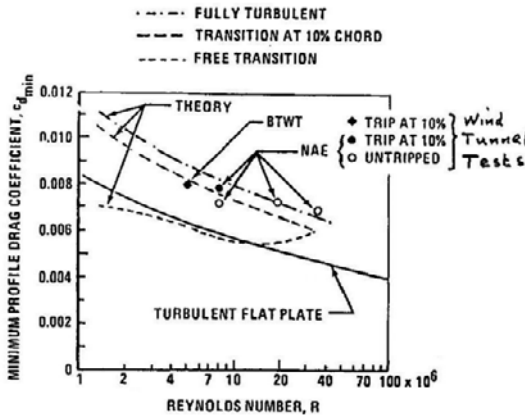
Figure 40.12 - Two dimensional data correlations (minimum profile drag). Source: AIAA Paper No. 71-289
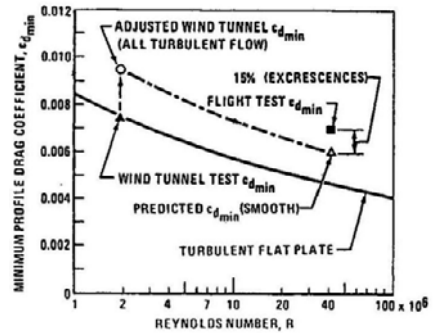
Figure 40.13 - Flight and wind tunnel data correlations (minimum profile drag), Boeing 727 wing. Source: AIAA Paper No. 71-289

The drag of different aircraft can be compared by relating the drag coefficient not to the reference wing area but to the total wetted area. In this way an equivalent skin friction drag coefficient is defined. The product C_{D_o} x S_W is sometimes called "parasite drag or equivalent flat plate area" when it is compared to the drag of a flat plate perpendicular to the flow with $C_D = 1.0$.

Such comparisons are shown in figure 40.14 to 40.17 for a number of both old and modern bomber, transport and read-loaded transport aircraft. The equivalent skin friction coefficient may vary between $\overline{c}_f = 0.0020$ and 0.0080.
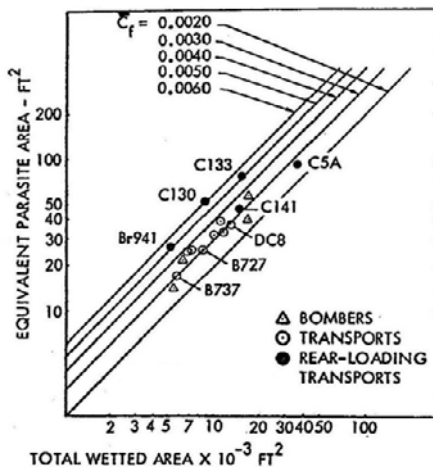
Figure 40.14 - Equivalent parasite area and skin friction drag coefficients for several types of aircraft. Source: AGARD CP-124 lecture 1
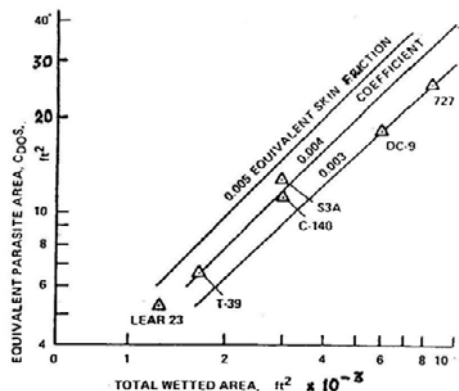
Figure 40.15 - Subsonic parasite drag area ($C_{D_0}S$). Source: AIAA Paper No. 76-931

529
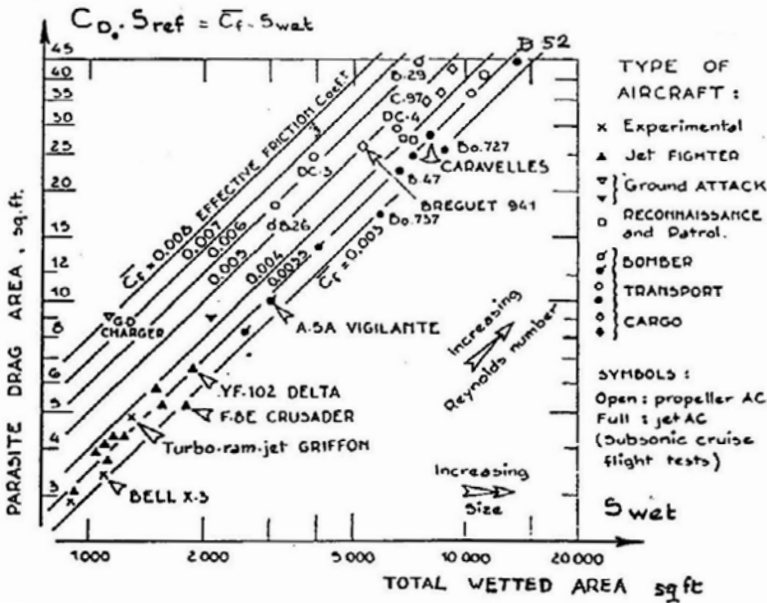
Figure 40.16 - Parasite drag area and skin friction coefficient for several types of aircraft.
Source: Journal of Aircraft, May-June 1968

For modern transport aircraft the equivalent skin friction drag coefficient varies between $\bar{c}_f = 0.0040$ for small aircraft, and $\bar{c}_f = 0.0025$ for large aircraft. When considering figure 40.16 which shows many old aircraft, the equivalent skin friction drag coefficient is much higher than for modern aircraft . This illustrates not only the effect of World war II excrescences such as gun turrets but also the large improvements in production techniques leading to much smoother surfaces and a large reduction in skin friction drag.

The impression may exist that the flat-plate friction drag for a fully turbulent boundary layer and shape factors are well defined parameters as is often suggested in textbooks and in design handbooks. However, all numerical data used in drag analysis are based on experiments and show in many cases considerable scatter. The skin friction law for a turbulent boundary layer has been formulated by several researchers. Between the various laws presented in figure 40.18 differences exist of the order of 4 percent. A curve often used is the one formulated by von Karman and Schoenherr. Figure 40.19 illustrates the spread in data points on which this curve is based.
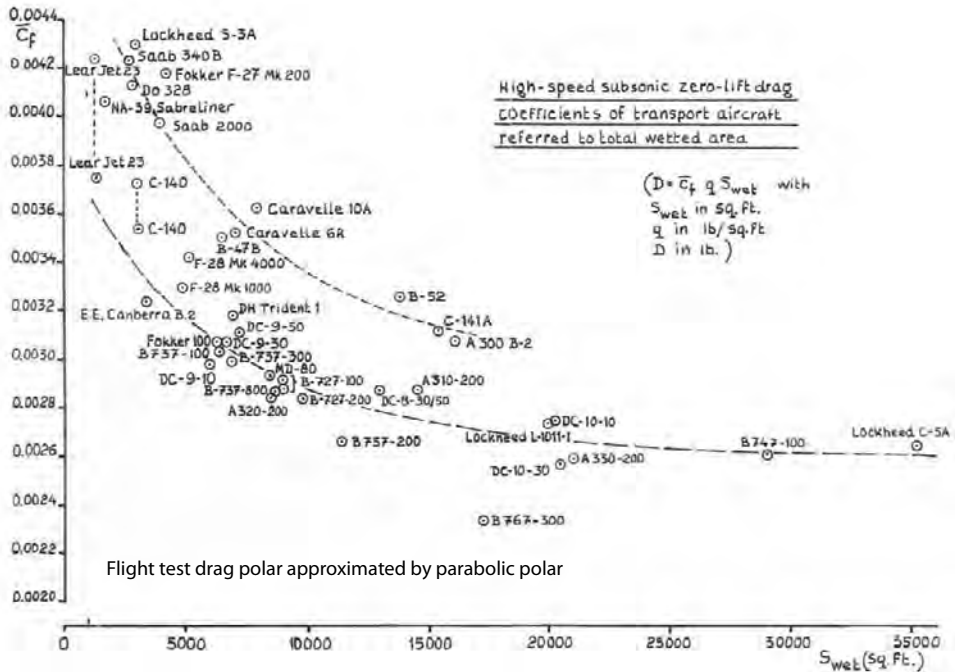
Figure 40.17 - High-speed subsonic zero-lift drag of transport aircraft referred to total wetted area
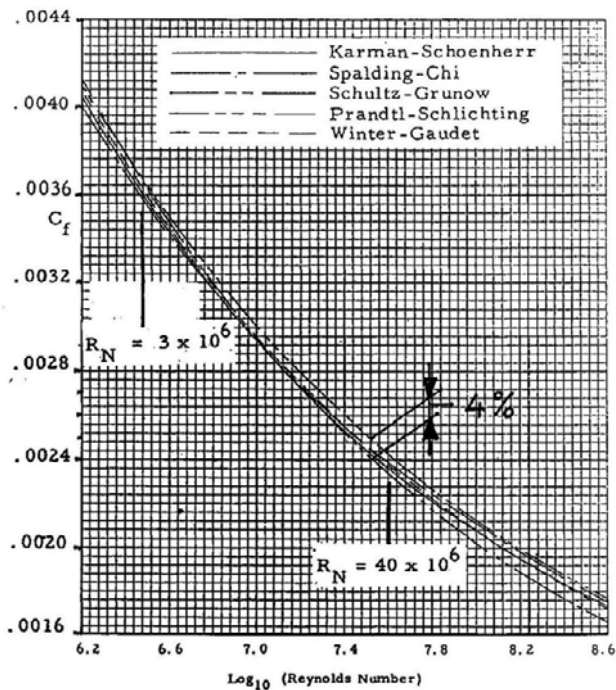
Figure 40.18 - Comparison of empirical flat plate skin friction curves for incompressible turbulent flow. Source: NASA CR-2333

531
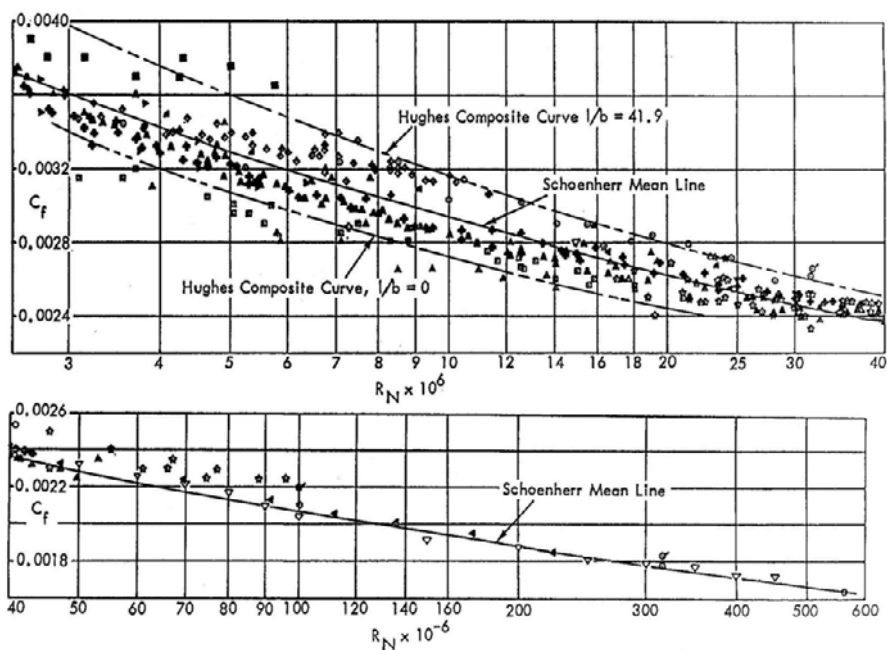
Figure 40.19 - Summary of experimental research on flat plate skin friction, incompressible flow. Source: NASA CR-2333

A shape factor is the ratio between the actual drag of a body and the corresponding flat plate. The actual drag is mostly obtained from wind tunnel tests with the usual test (in)accuracy. It is therefore important to know the flat plate drag curve used in the determination of the shape factor. This is not always possible with generalised data bases . For this reason the larger design organisations build up their own form factor data bases which are regularly updated. Figures 40.20 to 40.24 show examples of collections of form factors of airfoil sections and bodies of revolution. Figure 40.22 is of interest because it compares estimated drag data, obtained with the Lockheed in-house method, no doubt based on experimental data, with (other) wind tunnel test data.
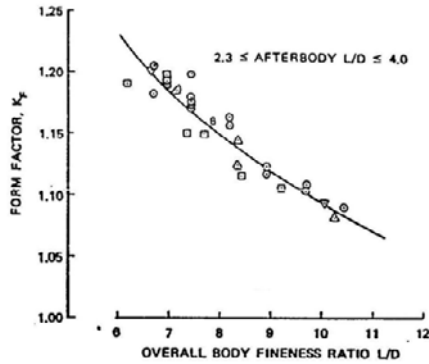
Figure 40.20 - Fuselage form factors. Source: Douglas Paper 7026
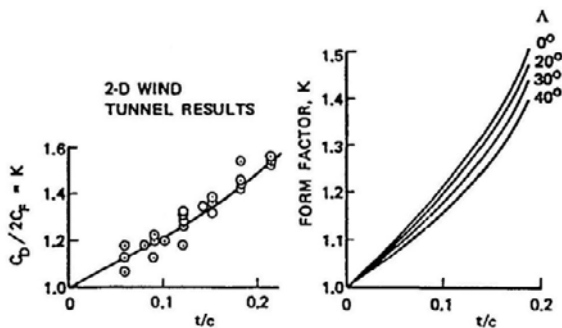
Figure 40.21 - Wing form factors for conventional-type airfoil shapes. Source: Douglas Paper 7026
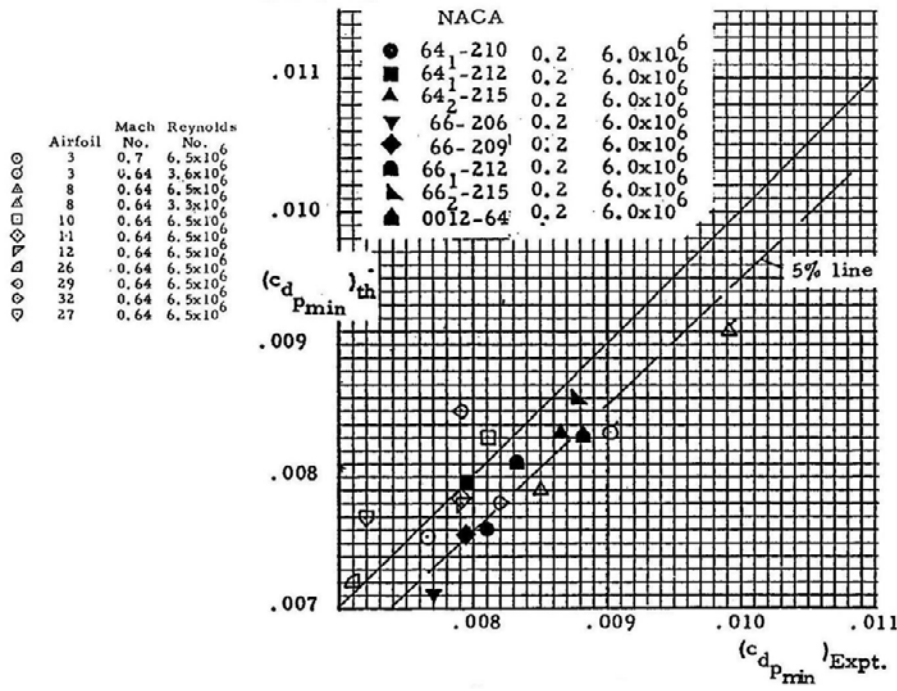
Figure 40.22 - Correlation of airfoil minimum profile drag. Source: NASA CR-2333
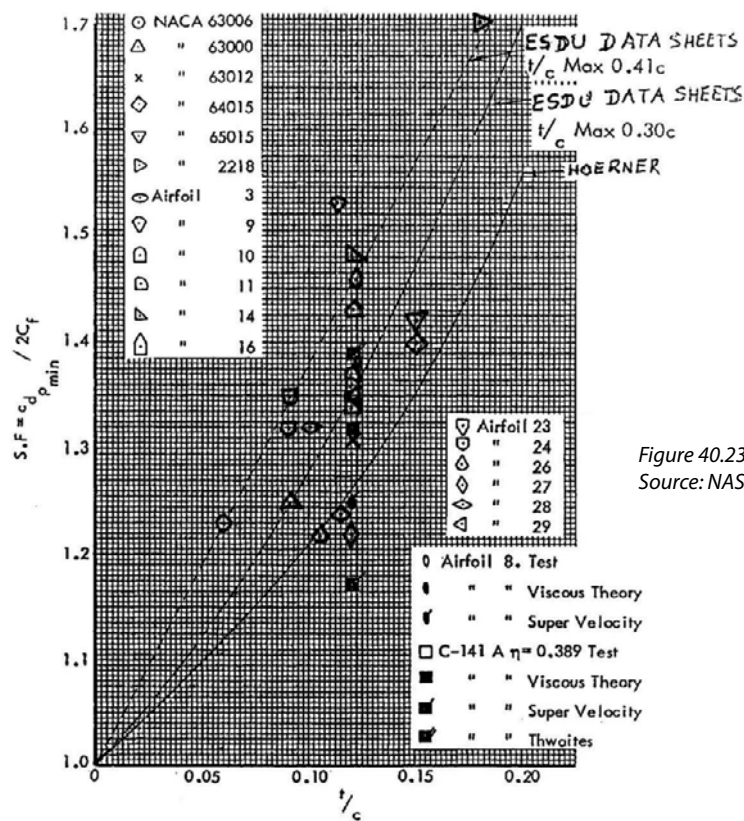
Figure 40.23 - Airfoil shape factors. Source: NASA CR-2333
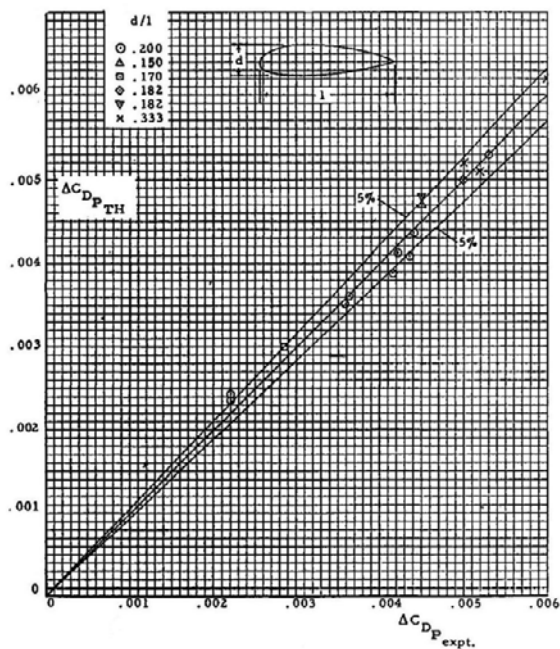
Figure 40.24 - Fuselage profile drag, bodies of revolution. Source: NASA CR-2333, A.D. Young R&M 1874, 1939
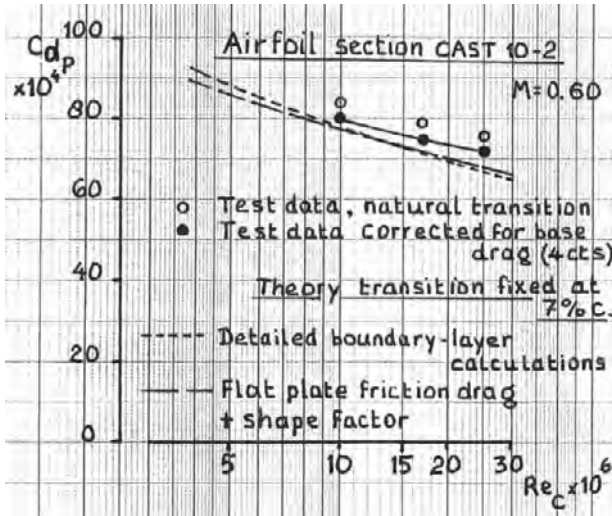
Figure 40.25 - Airfoil section drag-comparison between theoretical and measured drag.
Source: Fokker Report A-140

Notwithstanding the availability of modern three-dimensional boundary-layer computation methods these do not necessarily produce better drag predictions than the simple classical methods discussed above. This is illustrated in figures 40.25 and 40.26. In figure 40.25 the drag of a supercritical airfoil section, section CAST 10-2, calculated with a modern boundary-layer programme and with the standard Fokker preliminary-design drag prediction programme is compared with experimental data. The test data were obtained in the Lockheed blow-down facility. Both theoretical curves lie close together but differ from the test data although the difference is small.
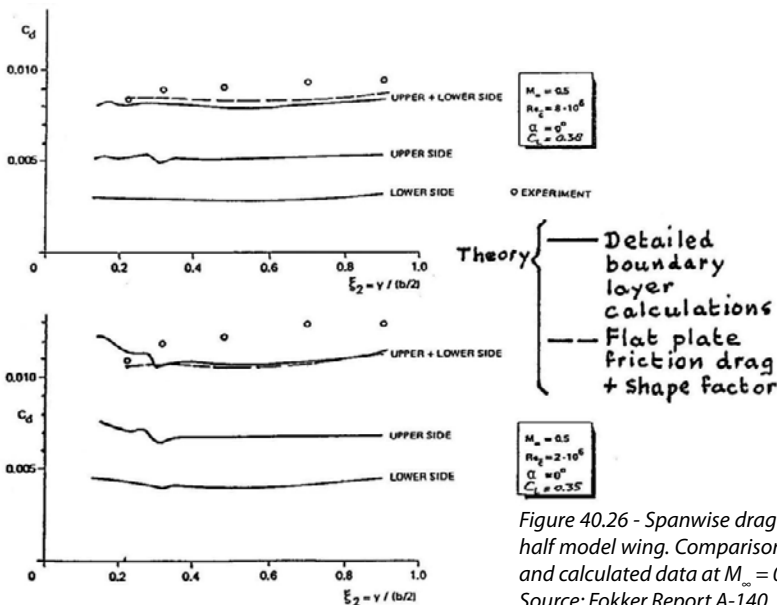
Figure 40.26 - Spanwise drag distribution on a half model wing. Comparison of experimental and calculated data at $M_\infty = 0.5$.
Source: Fokker Report A-140

Figure 40.26 shows a similar comparison for a wind tunnel halfmodel. Also here the theoretical curves lie close together and the drag from the experiment is higher than calculated, particularly for the low Reynolds number.

In figures 40.27 to 40. 30 the zero-lift drag build-up of four transport aircraft is presented as estimated by three design organisations. Although the uncertainties mentioned above could give the impression that the accuracy of drag prediction is unacceptably low these figures show otherwise. Fortunately, many of the uncertainties cancel out each other making the final result acceptable or satisfactory.

Components	Boeing				Fokker					
			Smooth				Smooth		Rough, k=0.001 in.	
	S_{wet} (m²)	Shape factor λ	c_f x 10⁴	C_{D_p} x 10⁴	S_{wet} (m²)	Shape factor λ	c_f x 10⁴	C_{D_p} x 10⁴	c_f x 10⁴	C_{D_p} x 10⁴
Wings	255.76	1.317	23.9	57.4	264.07	1.305	24.1	59.1	25.9	63.7
Fuselage	425.59	1.064	17.3	55.8	435.30	1.049	17.7	57.8	17.7	57.5
Vertical tail	38.55	1.150	22.5	7.1	68.21	1.163	22.2	12.5	23.5	13.2
Centre nacelle	51.10	1.410	20.6	10.6	14.10	1.179	23.4	2.7	25.0	2.9
Horizontal tail	65.68	1.228	25.2	14.5	68.13	1.252	25.3	15.4	27.5	16.7
Nacelles	39.86	1.300	23.0	8.5	41.20	1.179	23.4	8.1	25.0	8.7
Pylons	9.66	1.378	23.9	2.3	8.20	1.319	24.2	1.9	26.1	2.0
Flap track fairings	9.75	1.000	25.4	1.8	8.80	1.028	23.8	1.5	25.6	1.7
Total	895.95			158.0	908.01			159.0		166.3

Excrescences, roughness, .. 17.7 11.6
Interference drag, unknown, .. 4.8 3.6
Trim drag 1.0

$$C_{D_0} = 0.01805 \qquad C_{D_0} = 0.01825$$

Flight tests: $C_{D_0} = 0.01770$

M = 0.70 ; Re/m = 6.5x10⁶ ; S_{ref} = 140.3m²

Figure 40.27 - Estimated and flight-test derived subsonic zero-lift drag of the Boeing 727-200

Components	S_{wet} (m²)	Shape factor λ	Smooth Re/m = 6.0 x 10⁶ c_f x 10⁴	C_{D_p} x 10⁴	Rough, k = 0.001 in. c_f x 10⁴	C_{D_p} x 10⁴
Wings	150.12	1.270	25.9	52.9	28.3	57.7
Fuselage	301.64	1.056	18.8	64.1	19.0	64.6
Nacelles	46,18	1.226	25.3	15.3	27.1	16.4
Stub wings	5.68	1.217	24.3	1.8	27.1	2.0
Boundary layer fences	1.48	1.000	31.6	0.5	34.0	0.6
Flap track fairings	7.96	1.104	23.4	2.2	24.5	2.3
Anti-shock body	0.48	1.126	23.0	0.1	23.0	0.1
Vertical tailplane	31.56	1.201	25.2	10.2	27.1	11.0
Horizontal tailplane	41.13	1.236	27.8	15.1	30.7	16.7
Total				162.2		171.5

Excrescences: aircraft-size dependent	0.07 x 171.5	12.0
aircraft-size independent	$\Delta D/q = 0.40$ m²	4.3
Trim drag		0
Unaccounted drag 2% (previous experience)		3.8
		$C_{D_0} = 0.01916$
M = 0.50 ; S_{ref} = 93.5 m²	Flight tests: $C_{D_0} = 0.01880$	

Figure 40.28 - Estimated and flight-test derived subsonic zero-lift drag of the Fokker 100

Components	S_{wet} (m²)	Shape factor λ	Rough, k = 0.001 in. c_f x 10⁴	C_{D_p} x 10⁴
Centre Wing	25.10	1.756	28.5	18.0
Outer Wings	92.00	1.569	30.6	63.1
Fuselage	178.50	1.064	19.8	53.7
Nacelles	34.88	1.347	27.3	18.4
Vertical tailplane	30.64	1.389	32.2	19.6
Horizontal tailplane	48.48	1.120	24.1	18.7
Total	409.59			191.4

Excrescences: Control surface gaps	12.6
Excrescences: Engine nacelle intakes and exhausts	14.3
Excrescences: Other	6.4
Extra drag due to excrescences in the slipstream	2.1
Trim drag	-2.3
Unaccounted drag 2% (previous experience)	3.9
	$C_{D_0} = 0.02284$
Flight tests (parabolic drag polar): $C_{D_0} = 0.02330$	
M = 0.50 ; S_{ref} = 70.00 m²	

Figure 40.29 - Estimated and flight-test derived subsonic zero-lift drag of the Fokker 50

Components			Smooth $Re_c = 12.0 \times 10^6$	
	S_{wet} (m^2)	Shape factor λ	$c_f \times 10^4$	$C_{D_p} \times 10^4$
Wings	70.18	1.344	28.9	68.1
Fuselage	128.00	1.535	18.2	89.4
Horizontal tailplane	18.06	1.270	29.8	17.0
Vertical tailplane	22.12	1.271	27.3	19.2
Dorsal fin	-	-	-	2.0
Nacelles	25.80	1.261	20.5	16.6
Landing gear fairing	-	-	-	7.3
Total	264.16			219.6

Interference	17.1
Engine intakes	4.5
Wing flap and control surface gaps	14.4
Excrescences	18.8
Roughness	5.1
Engine bypass duct, cooling airco	15.9
Unaccounted (Buffer)	10.0

$$C_{D_0} = 0.03055$$

Parabolic drag polar $0.3 < C_L < 0.7$ from flight tests:
$$C_D = 0.0305 + 0.0308\, C_L^2 \ (e = 0.94)$$

M = 0.20 $S_{ref} = 40.0$ m^2

Figure 40.30 - Estimated and flight-test derived subsonic zero-lift drag of the Dornier 328

If wind tunnel test data are available for the configuration under study the model drag can be used as a starting point. The advantage here is that shape factors need not be estimated but can be determined by calculating the model drag with a standard method and adjust the shape factors for the different model components to reproduce the measured drag. For this reason it is worthwhile to investigate the model in successively more complete configurations starting with the fuselage or wing fuselage alone. The drag measurement must however have a high accuracy. If the tunnel and calculated data seem reliable an extrapolation to full-scale Reynolds numbers is performed and the additional drag of the parts not represented on the model such as excrescences and the effect of roughness is added. This is illustrated in figures 40.31 and 40.32.
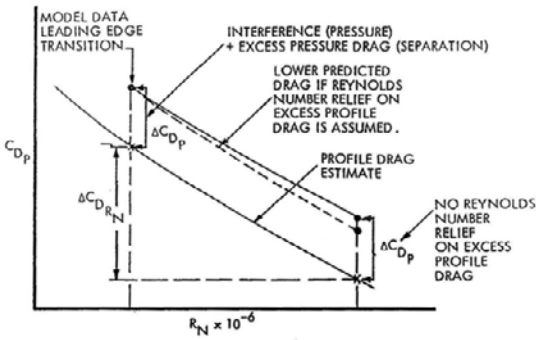
Figure 40.31 - Extrapolation of model data to full scale. Source: AGARD LS-37, Paper No. 4, 1969
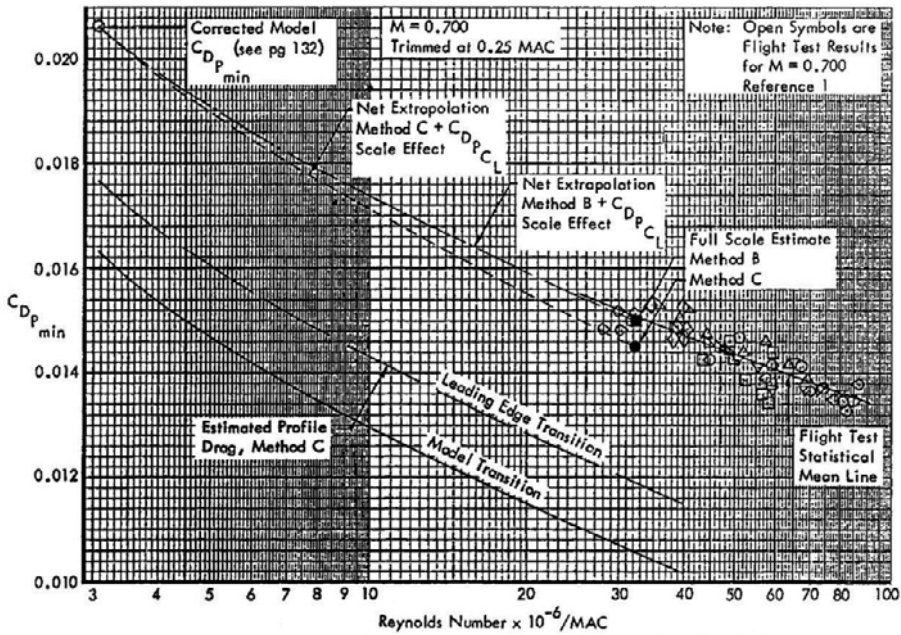
Figure 40.32 - Correlation of minimum profile drag. Lockheed C-141. Source: NASA CR-2333
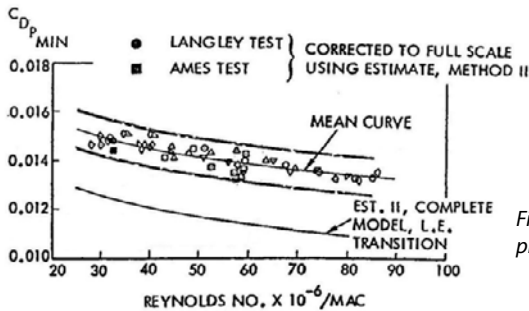
Figure 40.33 - Correlation of C-141 minimum profile drag. Source: AGARD LS-124 Lecture 1
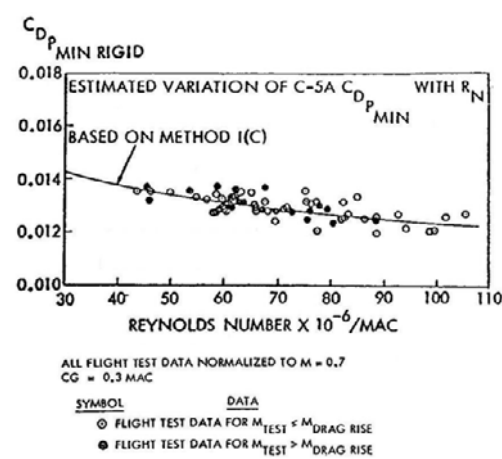
Figure 40.34 - Correlation of C-5 equivalent rigid flight test profile drag with the rigid estimate based on wind tunnel data.
Source: AGARD CP-124 Lecture 1
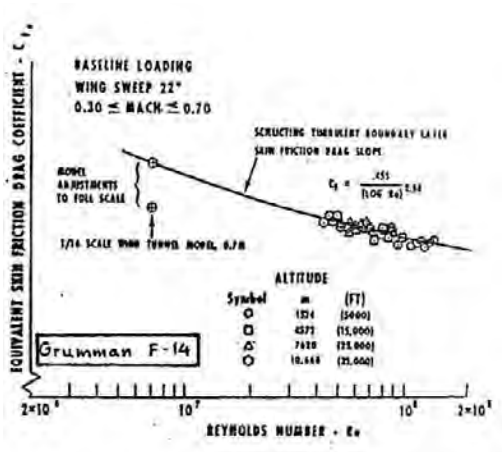
Figure 40.35 - Subsonic equivalent skin friction drag. Source: AGARD CP-124 Lecture 4

To obtain maximum accuracy in drag prediction it is advisable to use all available data and to continuously compare drag data from different sources, both from calculations and from wind tunnel tests and to incorporate experience from previous programmes.

Figure 40.32 and also figures 40.33 to 40.35 show minimum drag coefficients as a function of Reynolds number for the Lockheed C-141 and C-5A and the Grumman F-14. The very detailed analysis performed on the full-scale drag data of these aircraft led to the conclusion that, if all the differences between the wind tunnel model and the real aircraft were incorporated, the drag varied up to the highest Reynolds number according to the friction drag curve for a fully turbulent boundary layer. The conclusion from the Lockheed investigation was

that the **constant value** for the **minimum drag coefficient** found in the initial analysis was **not so much caused by surface roughness** but by variations in the aeroelastic deformation of the full-scale aircraft with varying dynamic pressure. This resulted in variations in the spanwise lift distribution and in the wing-twist contribution to the zero-lift drag.

This detailed analysis of the full-scale minimum drag coefficient is not affordable for civil transport aircraft during the certification period as aircraft have to be delivered and performance information has to be available.

Therefore some manufacturers collapse the flight test data to a given reference flight condition for each Mach number and provide corrections for different flight conditions based on Reynolds number variations. Other manufacturers use a single drag polar for each Mach number independent of weight and altitude.

- Boeing defines as the reference condition a W/δ -value as a function of altitude. Corrections are provided in the performance information for different W/δ -values and temperatures. These corrections are limited to $\Delta C_D = \pm 0.0003$ to 0.0005. This means that part of the effect of Reynolds number variations is incorporated in the data for the reference condition.
- McDonnell-Douglas used up to the MD-11 for each Mach number a single drag polar for all flight conditions. McDonnell-Douglas always adhered to the equivalent sand-roughness concept.
- Airbus provides basic performance data for a reference Reynolds number (Although the drag at constant C_L decreases slightly with increasing subsonic Mach number) with corrections for different Reynolds numbers.
- Fokker used a single drag polar for each Mach number identical to McDonnell-Douglas.
- Saab provided data for a reference altitude h = 15000 ft with the minimum drag decreasing with increasing subsonic Mach numbers. Altitude corrections of up to $\Delta C_D = -0.0010$ and $+0.0012$ were provided for altitudes between Sea Level and h = 35,000 ft.
- Dornier used for the Do 328 a reference condition M = 0.20 and Re = 12 x 10^6 with corrections based on Reynolds number variation for different flight conditions.

Each manufacturer provides data for trim drag variations due to different centre-of-gravity positions.

The above illustrates that there is no uniform opinion on the role of the Reynolds number on full-scale drag. This will reflect in the preliminary design methods used by the different design organisations.

Subsonic drag can be divided in zero-lift drag, lift-dependent drag and trim drag.

The lift-dependent drag consists of two parts: the lift-dependent form drag and the induced drag. The lift-dependent form drag contains a friction drag and a pressure drag component. The induced drag has its origin in the spanwise lift distribution of finite-span wings. It should be noted here that induced drag forms a part of the lift-dependent drag and that the two are not identical.

For preliminary design purposes, when working with a parabolic drag polar, the lift-dependent drag coefficient can be expressed in the form $C_{D_i} = (P+Q/A)\,C_L^2$. In figure 40.36 some varieties of this equation are presented together with the actual slope of the linearised C_D-vs.-C_L^2 drag polar of a number of modern and less-modern aircraft.

Symbol	Aircraft type	$S_{w_{ref}}$ (m²)	A_{ref}	Valid for C_L-range
✳	Learjet 23	21.5	5.02	0.2-0.8
✳	Lockheed Jetstar	50.4	5.44	0 - 0.7
+	DH 121 Trident 1	116.1	6.35	0.4-1.0
▽	DC-10-10	329.8	6.80	0.25-0.65
✕	Lockheed L-1011-1	321.1	6.95	0.25-0.6
◁	B 747-100	511.0	6.95	0.3-0.6
◁	F-28 Mk 1000	76.4	7.27	0.2-0.8
◀	DC-10-30	338.8	7.50	0.25-0.65
⊙	B 727-100	141.2	7.68	0.2-0.6
⊘	B 727-200	141.2	7.68	0.2-0.5
✶	F-28 Mk 4000	79.0	7.97	0.2-0.8
✸	F-28 Mk 6000	79.0	7.97	0.2-0.8
△	B-757-200	170.9	8.43	0.2-0.7
⬡	A-300 B2	235.4	8.56	0.25-0.7
○	Fokker 100	93.5	8.43	0.25-0.9
⊕	DC-9-30	93.0	8.21	0.2-0.8
⊖	DC-9-50	93.0	8.71	0.2-0.8
▣	B-737-100 ADV.	89.6	9.00	0.2-0.7
▢	B-737-300	91.0	9.16	0.2-0.8
⬒	DC-9-80	112.4	9.62	0.25-0.7
△	A-310-200	196.9	9.62	0.25-0.8
◯	B 767-200	276	8.20	0.1-0.7
◐	Airbus A-320	108.7	10.58	0.3-0.9
⬙	Dornier 328	40.0	11.00	0.3-0.9
⬚	Saab 340B	41.8	11.00	0.2-1.0
⬛	Saab 2000	55.7	11.00	0.2-1.0
⬤	B 757-300	125.7	9.52	0.2-0.7
☒	B 777-300	426.4	8.75	0.2-0.7
⬢	A 330-300	350.0	9.61	0.2-0.7

$$\frac{1}{\pi A_{ref}\,e} = \frac{1.02}{\pi A_{ref}} + 0.0090$$

$$\frac{1}{\pi A_{ref}\,e} = \frac{1.02}{\pi A_{ref}} + 0.0075$$

$$\frac{1}{\pi A_{ref}\,e} = \frac{1.05}{\pi A_{ref}} + 0.0070$$

Average C.G. position
M > 0.40
No compressibility effects.

$S_{w_{ref}} = S_{w_{trapezium}}$

Flight test drag polar approximated by parabolic polar

Figure 40.36 - High-speed subsonic lift-dependent drag coefficient of transport aircraft

At Mach numbers below the drag rise the maximum lift-drag ratio $(L/D)_{max}$ is found when

$$C_D = 2C_{D_0} \qquad (40\text{-}3)$$

when the drag polar can be written as a parabolic polar

$$C_D = C_{D_0} + \frac{C_L^2}{\pi A e} \qquad (40\text{-}4)$$

As the aspect ratio A is defined as

$$A = \frac{b^2}{S_{ref}} \qquad (40\text{-}5)$$

then, at $(L/D)_{max}$,

$$C_{D_0} = \frac{C_L^2}{\pi b^2 e} S_{ref} \qquad (40\text{-}6)$$

With

$$C_{D_0} S_{ref} = \overline{c_f} S_{wet} \qquad (40\text{-}7)$$

and

$$k = \frac{\overline{c_f}}{0.0030} \qquad (40\text{-}8)$$

then

$$\frac{C_L^2}{\pi b^2 e} S_{ref}^2 = 0.0030 k S_{wet} \qquad (40\text{-}9)$$

and

$$C_D S_{ref} = 2 C_{D_0} S_{ref} = 2 \cdot 0.0030 k S_{wet} \qquad (40\text{-}10)$$

As

$$C_L S_{ref} = b\sqrt{0.0030 \pi e}\sqrt{k S_{wet}} \qquad (40\text{-}11)$$

so

$$\boxed{\frac{C_L}{C_D} = \frac{\sqrt{0.0030 \pi e}}{0.0060} \frac{b}{\sqrt{k S_{wet}}} = 16.18 \frac{b}{\sqrt{k S_{wet}}}} \qquad (40\text{-}12)$$

for $e = 1.0$.

Figure 40.37 shows a survey of lift-drag ratios in cruise flight for a number of modern transport aircraft and some older bomber configurations correlated with the aid of the equation given above.
Note that at the Mach number for $(ML/D)_{Max}$ 15 drag counts are incorporated to include the initial drag rise in the design cruise condition.

Figure 40.38 gives an impression of the accuracy which in 1974 was thought to be achievable in estimating the lift-drag ratio in cruise flight prior to first flight. It is not clear if this accuracy has since increased.
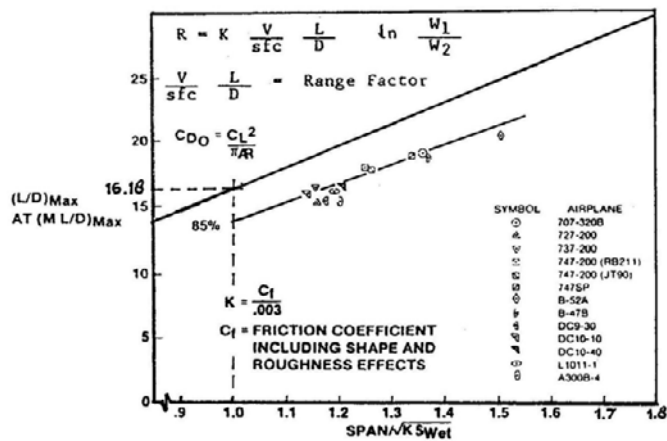
Figure 40.37 - Aerodynamic efficiency at $(M L/D)_{max}$. Source: AGARD R-712, Paper No. 6
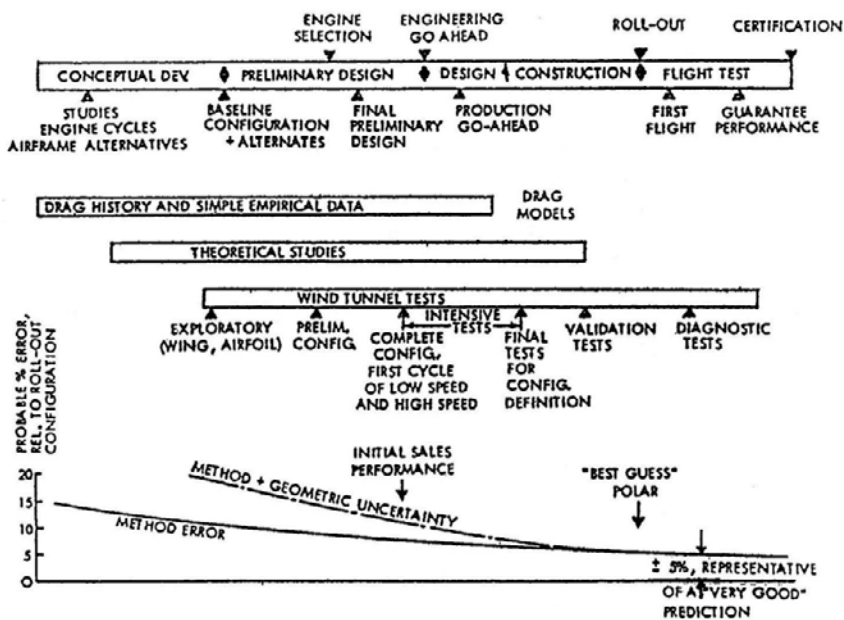
Figure 40.38 - Drag - airplane development schedule. Source: AGARD LS-67, Paper No. 4

Winglets

It has been known for a long time that the lift curve gradient of a lifting surface is increased and the induced drag is lowered when one or two endplates are fitted. These effects can be noticed on the fins of T-tails and on horizontal tailplanes with twin fins and rudders.

Only with the development of CFD methods has it become possible to analyse the flow around such configurations in greater detail. The first computer programmes that allowed investigations on non-planar lifting surfaces were developed around 1968 among others by Lundry and Giessing.

When after the two oil crises in the 1970's a strong interest developed in ways to reduce the drag of existing aircraft several research programmes were executed on different types of non-planar wing tip extensions which were popularly named "winglets".

Theory and wind tunnel tests had shown that such winglets did indeed lower the drag relative to the unmodified wings. It became less clear however what were the optimum shape and inclination of winglets and how did they compare to a wing span extension.

Elementary lifting surface computations show that non-planar winglets increase wing root bending moments less than straight wing tip extensions but winglets require attention in the following areas:

• The inner corner between wing upper surface and inner winglet surface should have an ample radius of curvature as illustrated in figure 40.39 to prevent high local supervelocities and flow separation near the trailing edge. Figures 40.40 and 40.41 show the spanwise lift distribution and the chordwise pressure distribution on a number of wing and winglet stations as determined in wind tunnel tests on a Boeing 747-200 equipped with winglets. Note the increase in supervelocities near the wing trailing edge adjacent to the winglet.
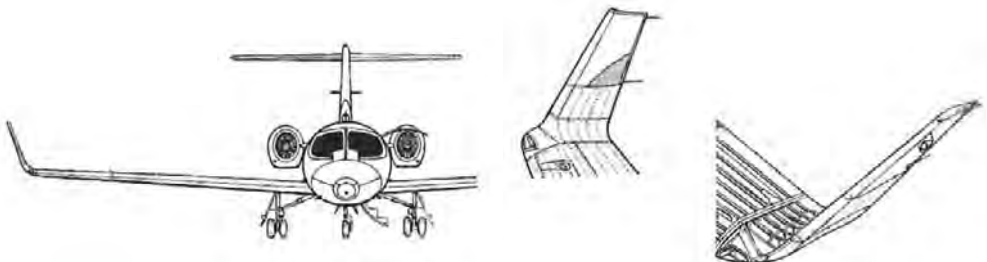
Figure 40.39 – Preferred shape of the wing-tip-to-winglet connection to minimise interference effects. Learjet 28/29. Source: Flight International, 10 February,1979

• The effectiveness of winglets is to a large degree determined by their toe-in or toe-out angle because of the mutual interference of the pressure distribution on wing and winglet. Therefore they can be optimised for only a limited range of lift coefficients and thus have to be designed either to improve cruise performance or field performance. In other operating conditions the drag may even increase.
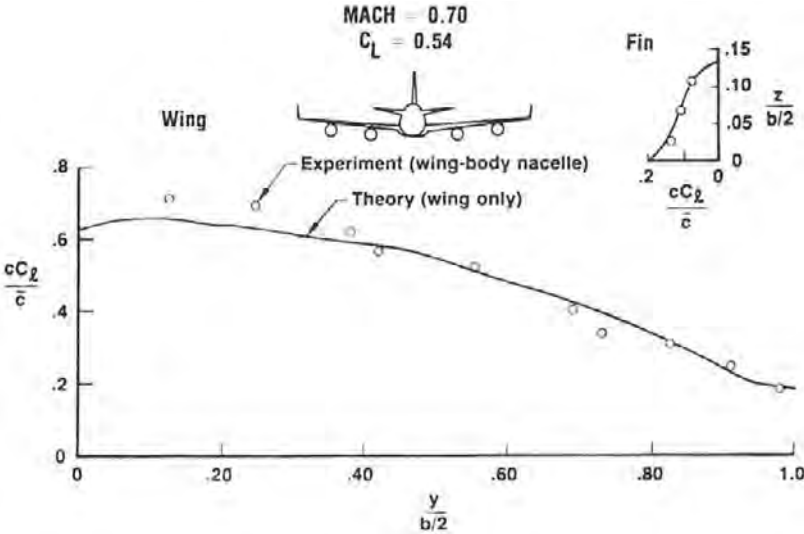
Figure 40.40 – Spanwise lift distribution on a Boeing 747-200 model equipped with winglets. Source: AIAA Paper No.76-940.
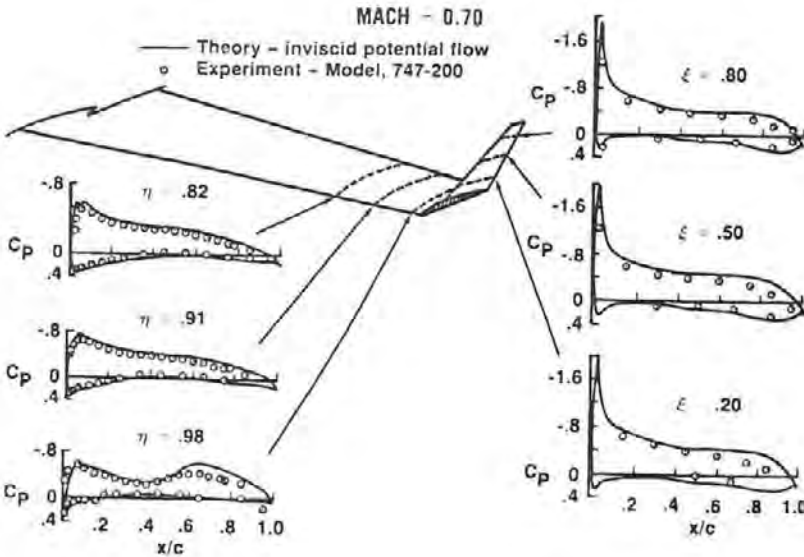
Figure 40.41 – Pressure distribution on a Boeing 747-200 model equipped with winglets. Source: AIAA Paper No. 76-940.

In comparing different shapes of winglets not only the theoretical effect on induced drag has to be considered but also the additional friction drag. Figure 40.42 shows the drag increase at low lift coefficients due to the addition of winglets on the Boeing 747-200 as found in the previously mentioned wind tunnel tests.
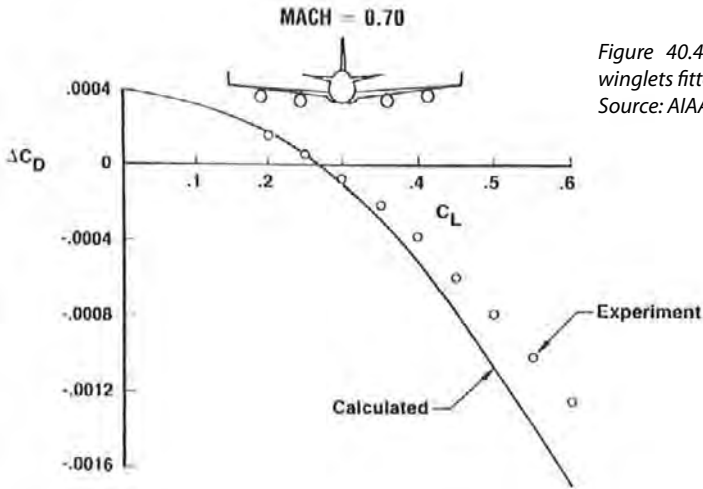
Figure 40.42 – Change in drag due to winglets fitted on a Boeing 747-200 model. Source: AIAA Paper No. 76-940.

In figures 40.43 and 40.44 the geometry is presented of a wing tip extension and several winglets investigated on a windtunnel halfmodel of the McDonnell-Douglas DC-10.
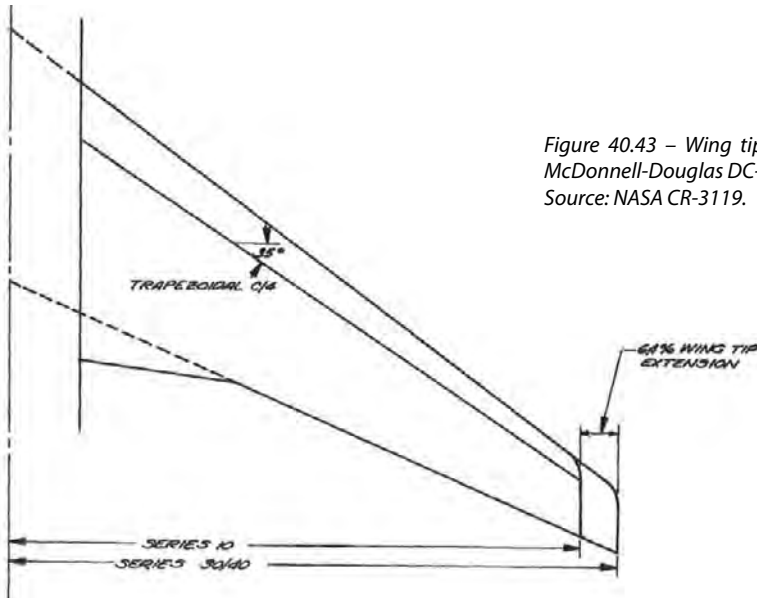
Figure 40.43 – Wing tip extension on the McDonnell-Douglas DC-10 Source: NASA CR-3119.
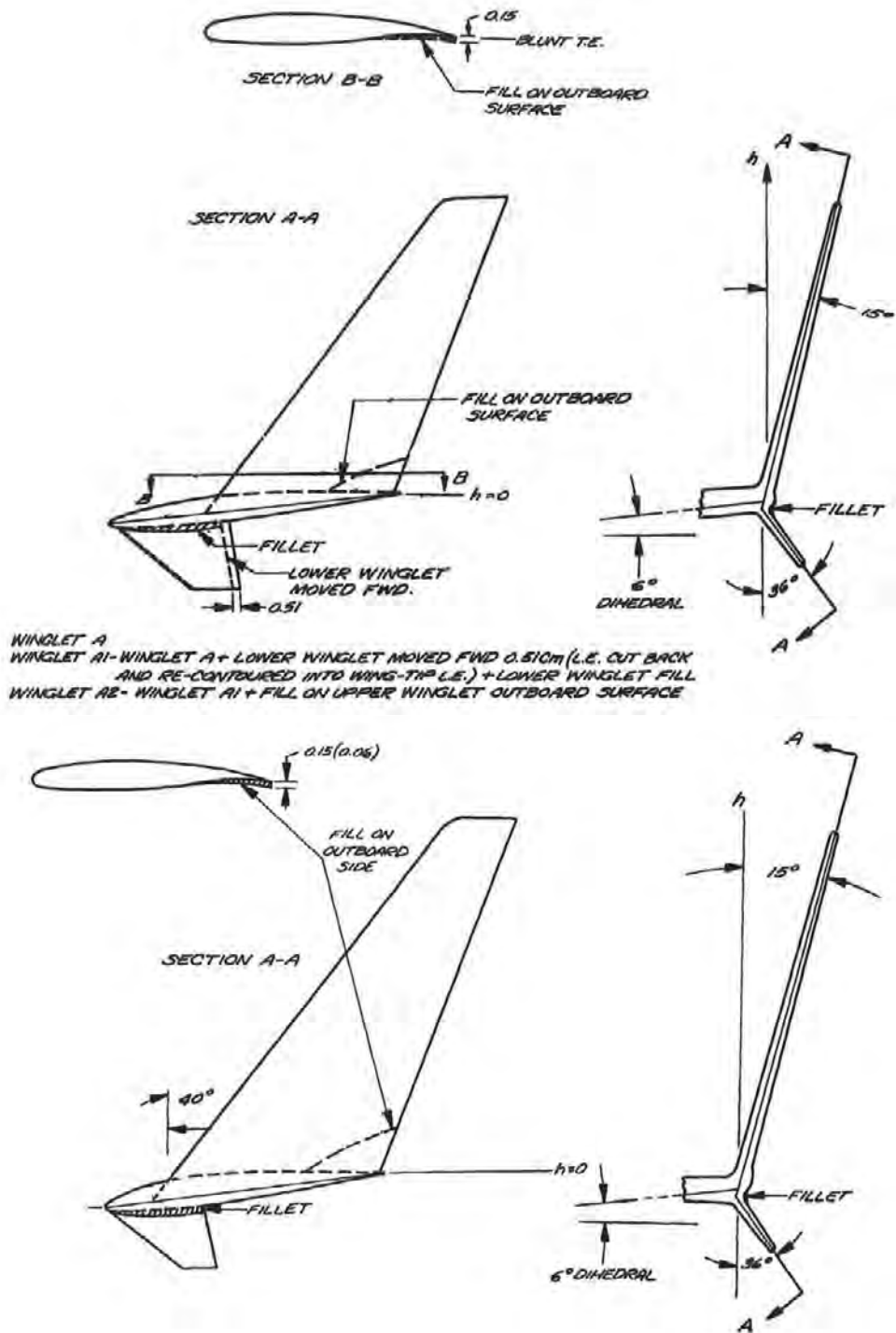
Figure 40.44 – Different winglet shapes investigated on a DC-10 wind tunnel model. Source: NASA CR-3119.

Figure 40.45 shows that for the DC-10 wing a span extension leads to a larger increase in wing root bending moment than fitting winglets. However as has been shown in other investigations this difference in wing root bending moment is sensitive to the spanwise lift distribution on the outer wing and different wing designs may lead to different conclusions concerning optimum wing tip devices.
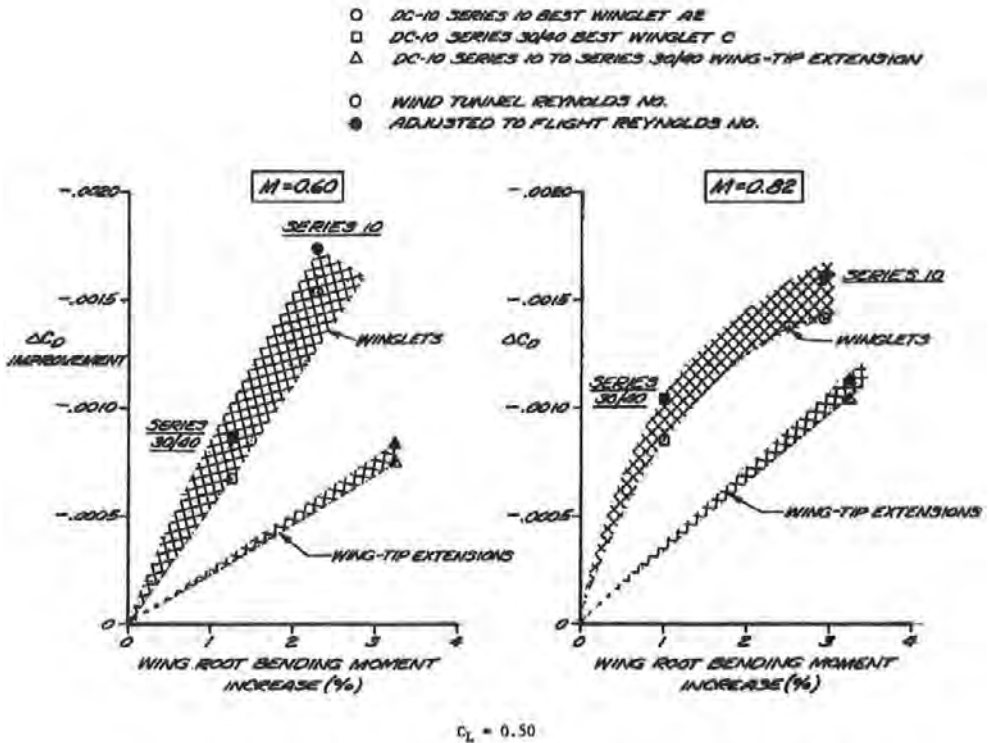
Figure 40.45 – Effect of a wing tip extension and winglets on the drag and wing root bending moment of the McDonnell-Douglas DC-10. Source: NASA CR-3119.

Furthermore the wing strength (and weight) is not always determined by the overall wing lift in limiting load conditions. In particular the strength of the outboard wing may be determined by control surface deflections or roll manoeuvres. By adapting these load conditions the increase in critical wing bending moments due to wing tip devices can be minimised. The latter is illustrated in figure 40.46 where re-orientating the blended winglets on the Boeing 737-800 together with limiting the spoiler panel deflection in certain flight conditions allowed the fitting of winglets with a minimum increase in wing bending moment and consequently minimum structural modifications.

Fitting wing tip devices on existing aircraft also requires checking their effect on the flutter boundary and a number of stability and control characteristics. These may all in one way or another limit the attractiveness of such a modification and this explains the wide variety in winglet shapes in use.

Application of wing tip devices will be more successful when their design forms an integral part of the total wing design or of an extensive wing redesign rather than of a retrofit programme. That the preferred device may than be a span extension, albeit of an unconventional shape is illustrated in figure 40.47 for the Boeing 767-400ER (and 777-200LR and – 300ER).

Finally, winglets may be applied to limit wing span when requirements exist concerning parking or manoeuvring in confined space. The latter forced McDonnell-Douglas to apply winglets to the C-17.

Design conditions typically vary throughout the wingspan:
■ Inboard wing : symmetric 2.5-g maneuver
■ Midwing : 2.5-g speed brakes deployed
■ Outboard wing : roll, gust or sideslip maneuver
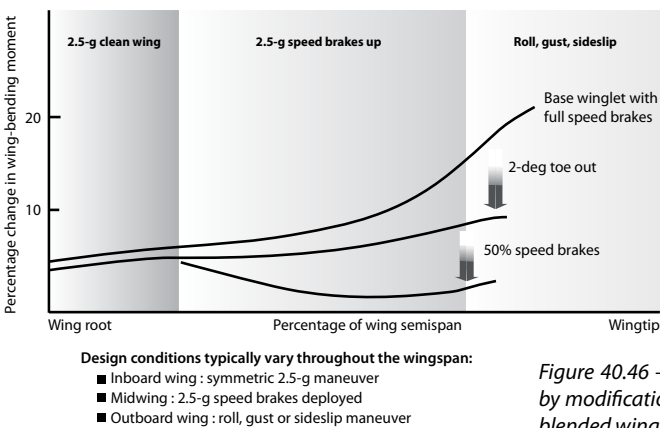
Figure 40.46 – Wing bending moment alleviation by modifications to the Boeing 737-800 wing with blended winglets. Source: Aero Magazine no.17.
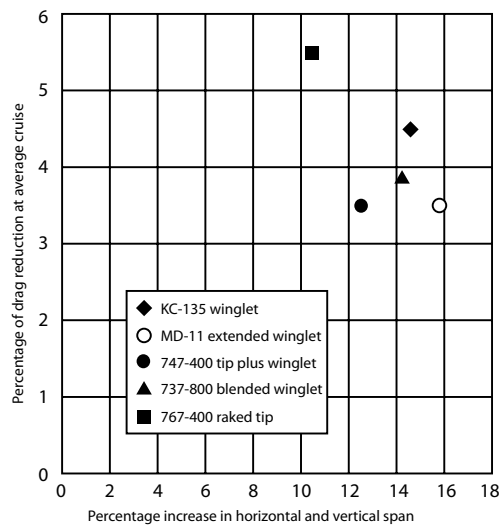
Figure 40.47 – Drag reduction of wing tip devices. Source: Aero Magazine no.17.

41 *Breguet's range equation*

In this chapter the Breguet range equation is discussed. This equation was originally derived for piston-engined propeller aircraft. Later a version for jet aircraft was produced which is still useful today for many analyses.

First the main assumptions are given after which the equation is derived.

Assumptions
- The engine specific fuel consumption C_T is constant
- Cruise takes place at a constant airspeed and Mach number
- The lift-drag ratio is constant

Derivation

Over a time period Δt, in cruise the decrease in weight through fuel consumption is:

$$-\Delta W = -\Delta W_{fuel} = C_T T \Delta t = C_T \frac{D}{L} W \Delta t \tag{41.1}$$

Furthermore:

$$\Delta S = V \Delta t = Ma \Delta t \tag{41.2}$$

So:

$$-\Delta W = C_T \frac{D}{L} W \frac{\Delta S}{Ma} \tag{41.3}$$

And:

$$\Delta S = -\frac{1}{C_T} Ma \frac{L}{D} \frac{1}{W} \Delta W \tag{41.4}$$

The cruise range can then be written as:

$$R = \int_{start}^{end} \Delta S = \int_{start}^{end} \frac{1}{C_T} Ma \frac{L}{D} \frac{1}{W} \Delta W \tag{41.5}$$

Resolving the integration results in Breguet's range equation:

$$R = \frac{aM}{C_T} \frac{L}{D} \ln \frac{W_{start}}{W_{end}}$$

(41.6)

Climb

The assumption of a constant lift - drag ratio means the lift coefficient also is constant. But because of fuel being burned the aircraft weight decreases and as the Mach number is constant the only parameter that can change is the density. Consequently the aircraft will perform a continuing climbing cruise as shown in figure 41.1.
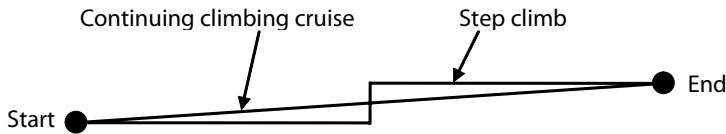
Figure 41.1 - Step climb

Most aircraft do not follow such a flight pattern because of air traffic control restrictions, but perform a step climb such as depicted in figure 41.1. The Breguet range equation is a good approximation because it is more or less the average of the step climb. Strictly speaking the above is only valid for flight above the tropopause where the temperature is constant.

Maximum range

In order to maximize the range it is not only the lift-drag ratio that must be maximized, the airspeed and specific fuel consumption, which are dependent on the Mach number, must also be taken into account.

During cruise, the thrust is equal to the drag:

$$T = D$$

(41.7)

The power required to propel the aircraft is:

$$DV = TV$$

(41.8)

The fuel flow is equal to the specific fuel consumption multiplied by the thrust:

$$m_{fuel} = \frac{C_T T}{g} \tag{41.9}$$

The total amount of energy delivered is equal to the fuel flow multiplied by the total propulsive efficiency η and the caloric value of the fuel H:

$$E_{delivered} = \frac{C_T T}{g}\eta H \qquad \text{per unit time} \tag{41.10}$$

The amount of energy required and delivered must be equal:

$$TV = \frac{C_T T}{g}\eta H \tag{41.11}$$

Eliminating the thrust from the equation and rewriting it gives:

$$\frac{V}{C_T} = \frac{\eta H}{g} \tag{41.12}$$

This expression can then be inserted in the Breguet formula:

$$R = \frac{\eta H}{g}\frac{L}{D}\ln\frac{W_{start}}{W_{end}} \tag{41.13}$$

As the caloric value of kerosene is a fixed value, the expression to be maximized in order to achieve maximum range is:

$$\left(\eta\frac{L}{D}\right)_{max} \Rightarrow R_{max} \tag{41.14}$$

Additional fuel requirements

When using the Breguet equation to estimate a range some extra weight has to be incorporated for take-off, climb and approach fuel and also the reserve fuel must be included. Reserve fuel constitutes typically 4 to 5% of the take-off weight for long-range flights.

Figures 41.2 and 41.3 show the fuel consumption of a hypothetical 130-seater for two flight lengths, 500 and 1700 N.M.
On the shorter trip almost half the fuel used is consumed during the climb in which only 20 percent of the total flight distance is covered. On a trip length of

300 N.M. the cruise part would be only 30 percent of the total trip length, the minimum acceptable distance from an air traffic control point of view if the aircraft would climb to 35,000 ft.

This illustrates that the Breguet range equation primarily has significance for medium and long-range flights.
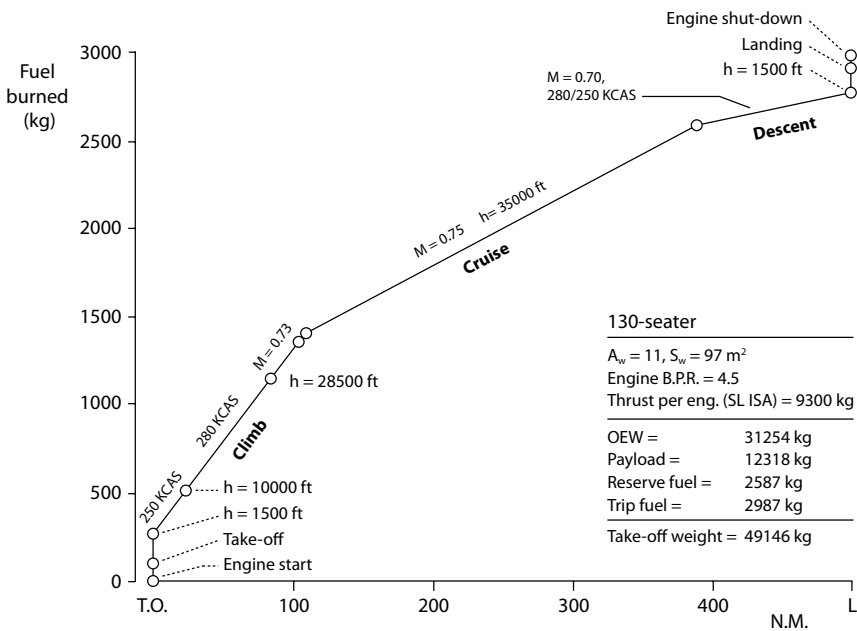
Figure 41.2 - Fuel consumption on a 500 N.M. trip
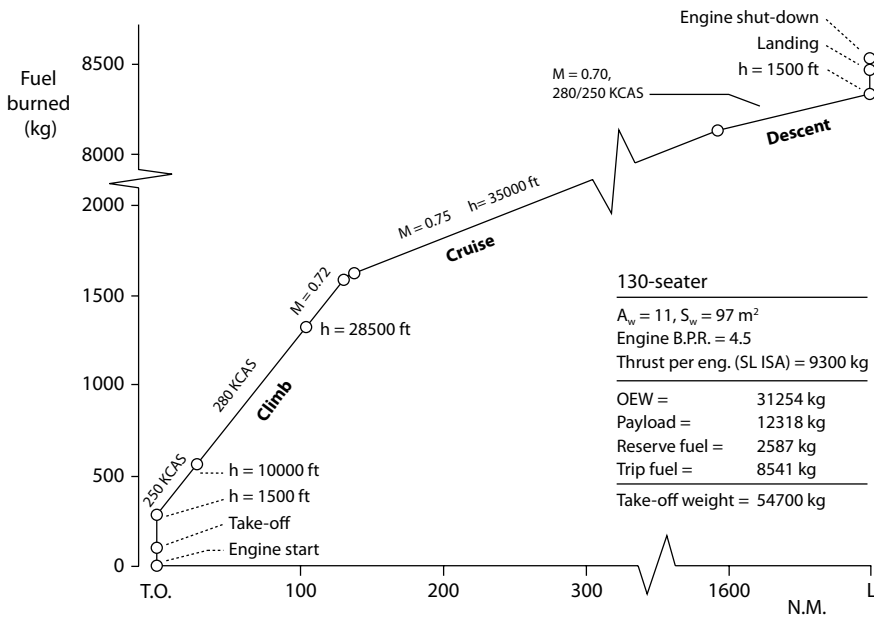
Figure 41.3 - Fuel consumption on a 1700 N.M. trip

42 *Aircraft weight*

Estimating the weight of an aircraft in the preliminary or initial design phase is one of the most challenging tasks in the development of a new aircraft programme. Strict weight control with periodic reviews and weight saving actions are standard activities during the detail design phase. It is however, at the beginning of the design process, when many technical decisions have not been taken yet, that the risk of underestimating the final aircraft weight is greatest. Most aircraft have undergone a significant increase in take-off weight between the issue of the first type specification and the first flight. As was discussed before, the Boeing 747 had severe weight problems; it suffered from a 29% increase in weight from the first concept to the final certification. The Airbus A380 has also suffered from weight problems, but in this case the increase is about 1 to 2%. This is still significant for a long-range aircraft as the payload is only 10% of the take-off weight.

Weight growth may also occur in an indirect way. For example, if flight tests indicate that the aircraft drag is higher than predicted and the range guarantee can not be realized the fuel weight has to be increased. This necessitates an extensive check of the strength calculations and possibly a local strengthening due to increased Maximum Take-off Weight (MTOW).

The severity of such a development is illustrated by the initial development of the Canadair Challenger, a mid-sized business jet.
The aircraft was launched in 1976. At the configuration freeze in April 1977 the guaranteed range with 5 passengers and NBAA reserves was 3600 N.M. cruising at Mach = 0.80. The aircraft was certified in the Autumn of 1980 at a MTOW of 33000 lb but showed a disappointing range performance.
After a switch to a different engine a new version was certified in March 1983 with a range with NBAA reserves of 3500 N.M. when cruising at Mach = 0.74. But MTOW had gone up to 41500 lb and the price had gone up from U.S. $ 7.0m to U.S. $ 10.2m in standard configuration.

Successive weight steps, usually accompanied with an increase in engine power or thrust, is a normal development over the life of an aircraft programme. Most airlines show a constant growth in required capacity and maximum range.

However this process should be a controlled process based on developing market requirements and not due to shortcomings in the initial design .

Figure 42.1 shows the increase in range and thus in weight over a number of years for several transport aircraft families.
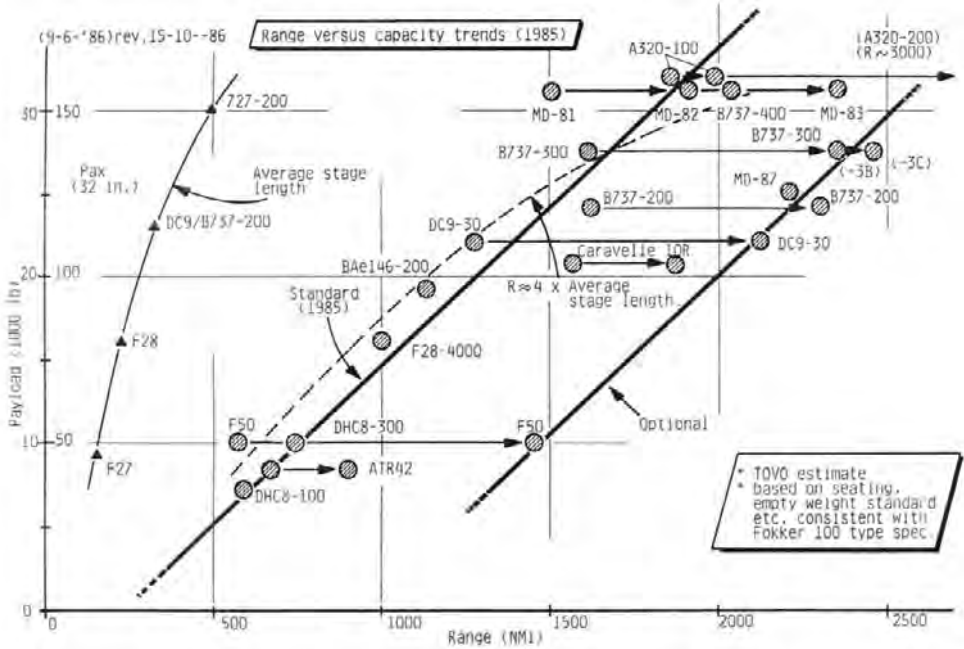
Figure 42.1 – Range increase over the years of several transport aircraft families

Weight determination

A first estimate of the aircraft weight can be obtained by considering the following:

The take-off weight is built up by adding the operational empty weight, the weight of the payload, the fuel for take-off, climb, and descent, the cruise fuel and the reserve fuel.

$$W_{TO} = W_0 + W_p + W_{f,to-la} + W_{f,cr} + W_{f,reserve} \qquad (42.1)$$

Neglecting the fuel consumed in descent and landing the weight at the top of the climb is:

$$W_{TO} - W_{f,to-la} \approx W_{TO} - W_{f,to-cl} = W'_{TO} \qquad (42.2)$$

Combining equations (42.1) and (42.2) gives:

$$W_{TO}^{'} = W_0 + W_p + W_{f,cr} \tag{42.3}$$

The Breguet range equation can be written as:

$$R = \frac{aM}{C_T} \frac{L}{D} \ln \frac{W_{TO}^{'}}{W_{TO}^{'} - W_{f,cr}} \tag{42.4}$$

Or:

$$\frac{RC_T}{aM \frac{L}{D}} = \ln \frac{W_{TO}^{'}}{W_{TO}^{'} - W_{f,cr}} \tag{42.5}$$

So:

$$-\frac{RC_T}{aM \frac{L}{D}} = \ln \frac{W_{TO}^{'} - W_{f,cr}}{W_{TO}^{'}} \tag{42.6}$$

And:

$$e^{-\frac{RC_T}{aM \frac{L}{D}}} = 1 - \frac{W_{f,cr}}{W_{TO}^{'}} \tag{42.7}$$

Or:

$$\boxed{\frac{W_{f,cr}}{W_{TO}^{'}} = 1 - e^{-\frac{RC_T}{aM \frac{L}{D}}}} \tag{42.8}$$

The range, Mach number and speed of sound (= altitude) are operational requirements, whereas the specific fuel consumption and lift-drag ratio correspond to a certain technology level. Equation (42.8) shows that the ratio of the fuel weight to the take-off weight is only a function of operational requirements and the technology level and not of the empty weight.

Equation (42.3) can be rewritten as:

$$1 = \frac{W_0}{W_{TO}^{'}} + \frac{W_p}{W_{TO}^{'}} + \frac{W_{f,cr}}{W_{TO}^{'}}$$

(42.9)

Payload is a part of the specification, which means it is not a fraction but a fixed value. Combining equations (42-8) and (42-9) gives:

$$1 - \frac{W_{f,cr}}{W_{TO}^{'}} = e^{-\frac{RC_T}{aM^{L}/_D}}$$

(42.10)

This can rewritten as:

$$W_{TO}^{'} = \frac{W_p}{e^{-\frac{RC_T}{aM^{L}/_D}} - \frac{W_0}{W_{TO}^{'}}}$$

(42.11)

Equation (42.11) shows how the take-off weight can be found for a given empty weight. There are three unknowns in this equation: the empty weight, the take-off weight and the fuel weight. To solve these unknowns two equations have been discussed: the Breguet range equation and the summation of weights. A third equation, required to determine the weights, is lacking. Finding the empty weight of the airplane by performing a detailed calculation is hardly feasible in the preliminary design phase.

In figures 42.2 and 42.3 the relation is presented between empty weight and take-off weight for comparable aircraft . These figures show that for a **certain aircraft category** the **empty weight fraction** is more or less constant and almost independent of aircraft size but is **dependent on range**. For a long range aircraft, the empty weight fraction would be about 45% and the fuel fraction about 45%, leaving 10% for the payload. Short haul aircraft have fuel fractions of about 20% to 25%, empty weight fractions of 50% to 60% and a payload fraction of about 25% to 30%.

For a new aircraft design these simple statistics loose their meaning if the new design does not have comparable predecessors. The above is only valid for conventional configurations and a large increase in take-off weight far outside the existing weight brackets may produce erroneous results.
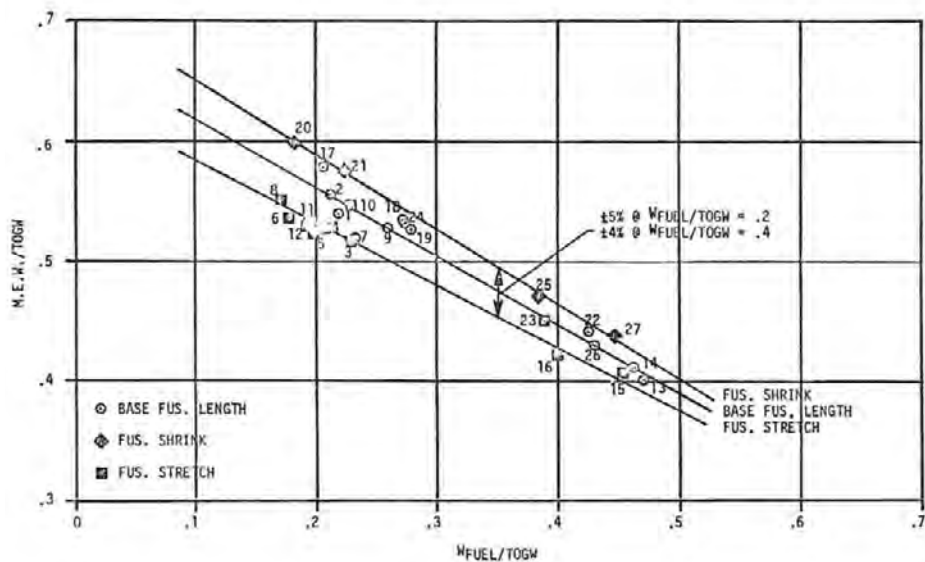
Figure 42.2 - Empty weight over take-off weight versus fuel weight over take-off weight.
Source: S.A.W.E. Journal
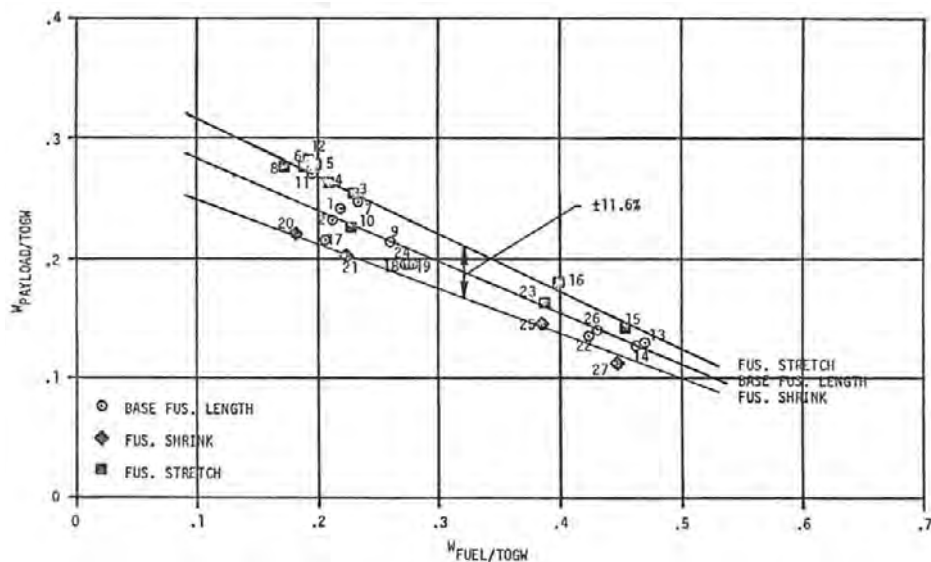
Figure 42.3 - Payload weight over take-off weight versus fuel weight over take-off weight.
Source: S.A.W.E. Journal

	MODEL	M.E.W.	$W_{PAYLOAD}$	W_{FUEL}	TOGW	N_P	$\dfrac{M.E.W.}{TOGW}$	$\dfrac{W_{PAYLOAD}}{TOGW}$	$\dfrac{W_{FUEL}}{TOGW}$
1.	F-28	33,505	15,000	13,495	62,000	60	.540	.242	.218
2.	DC-9-10	48,075	20,000	18,225	86,300	80	.557	.232	.211
3.	DC-9-30	55,930	27,500	24,570	108,000	110	.518	.255	.228
4.	DC-9-40	60,243	30,000	23,757	114,000	120	.528	.263	.208
5.	DC-9-50	63,314	33,750	23,936	121,000	135	.523	.279	.198
6.	DC-9-80*	75,064	38,750	26,186	140,000	155	.536	.277	.187
7.	DAC-111	51,762	24,750	23,138	99,650	99	.519	.248	.232
8.	737-200	57,452	28,750	17,798	104,000	115	.552	.276	.171
9.	727-100	84,850	34,500	41,650	161,000	138	.527	.214	.259
10.	727-200	95,695	39,500	39,805	175,000	158	.547	.226	.227
11.	MERCURE 100	66,670	33,750	24,180	124,600	135	.535	.271	.194
12.	ASMR**	81,951	43,500	29,549	155,000	174	.529	.281	.191
13.	707-320	125,176	40,500	146,324	312,000	162	.401	.130	.469
14.	DC-8-55	133,471	41,250	150,279	325,000	165	.411	.127	.462
15.	DC-8-62	136,065	47,250	151,685	335,000	189	.406	.141	.453
16.	DC-8-63	147,900	62,750	139,350	350,000	251	.423	.179	.398
17.	A300B2	180,800	67,250	63,950	312,000	269	.579	.216	.205
18.	A300B4	185,800	67,250	93,950	347,000	269	.535	.194	.271
19.	DC-10-10	226,750	83,750	119,500	430,000	335	.527	.195	.278
20.	DC-10-TWIN*	202,893	74,750	61,357	339,000	299	.599	.221	.181
21.	DC-X-200*	160,660	56,500	61,840	279,000	226	.576	.203	.222
22.	DC-10-40	249,000	77,000	239,000	565,000	308	.441	.136	.423
23.	DC-10-STRETCH*	265,880	95,500	228,620	590,000	382	.451	.162	.387
24.	L-1011-1	229,014	83,750	117,236	430,000	335	.533	.195	.273
25.	L-1011-500*	233,196	72,500	190,304	496,000	290	.470	.146	.384
26.	747-200	333,567	108,750	332,683	775,000	435	.430	.140	.429
27.	747-SP	290,300	75,000	294,700	660,000	300	.440	.114	.447

M.E.W. = Manufacturer's Empty Weight (Pounds)
$W_{Payload}$ = Operational Items + Payload = 250 Lb/Passenger
W_{Fuel} = Fuel Weight (Pounds) = TOGW - M.E.W. - $W_{Payload}$
TOGW = Maximum Design Takeoff Weight (Pounds)
N_p = Number of Passengers, All Economy @ 34" Basic Seat Pitch
     Abreast Seating = 5AB (F-28, DC-9, BAC-111), 8AB (A300), 9AB (DC-10, L-1011), 10AB (747), 6AB (All Others)

* Proposed Aircraft
** Proposed Stretch of Mercure 100

Figure 42.4 - Weight data used for figures 42.2 and 42.3. Source: S.A.W.E. Journal

The ground rules used to produce figures 42.2 and 42.3 are given in figure 42.4. For the purpose of comparison all aircraft were assumed to have a standard cabin arrangement. This is a simplification but does not affect the general conclusions given above.

Growth factor:

The growth factor is an indicator of the ratio between the increase in weight of a particular weight component and of the overall take-off weight. It is, particularly for long-range aircraft, a reminder of the sensitivity of the total empty aircraft weight to an ,at first glance insignificant, weight increase of a particular element in the structure or equipment. It shows how sensitive the take-off weight is to increases in payload weight, fuel weight or empty weight. These weights change because of for example higher-than-expected fuel consumption or a lower lift-drag ratio. At constant take-off weight, fixed by the strength considerations, the payload may suffer accordingly.

The growth factor with respect to the payload can be found by re-writing equation (42.3) as follows:

$$W_{TO}^{'} = \frac{W_0}{W_{TO}^{'}} W_{TO}^{'} + \frac{W_{f,cr}}{W_{TO}^{'}} W_{TO}^{'} + W_p \tag{42.12}$$

Or:

$$W_{TO}^{'} \left(1 - \frac{W_0}{W_{TO}^{'}} - \frac{W_{f,cr}}{W_{TO}^{'}} \right) = W_p \tag{42.13}$$

And:

$$W_{TO}^{'} = \frac{1}{1 - \dfrac{W_0}{W_{TO}^{'}} - \dfrac{W_{f,cr}}{W_{TO}^{'}}} W_p \tag{42.14}$$

From the empirical data for the class of aircraft considered:

$$\frac{W_0}{W_{TO}} \approx const. \tag{42.15}$$

And thus:

$$\frac{W_0}{W_{TO}^{'}} \approx const. \tag{42.16}$$

Furthermore, with a constant lift-drag ratio:

$$\frac{W_{f,cr}}{W_{TO}^{'}} = 1 - e^{-\frac{RC_T}{aM^{L}/_D}} = const. \tag{42.17}$$

Then combining equations (42.3) and (42.14) results in the growth factor:

$$\boxed{\frac{dW_{TO}}{dW_p} \approx \frac{dW_{TO}^{'}}{dW_p} = \frac{W_{TO}^{'}}{W_p}} \tag{42.18}$$

Such an equation can also be derived for $\dfrac{dW_{TO}}{dW_0}$ and $\dfrac{dW_{TO}}{dW_{f,cr}}$.

Example 42-1:

Consider as part of the specification of an airplane comparable to an Airbus A300 the following characteristics:

h > 36000 ft (a = 295 m/s)
M = 0.80
C_T = 0.65 kg/kg.hr
L/D = 18
W_P = 25000 kg (200 passengers + cargo)
R = 2778 km (1500 nm)

For this specification the take-off weight, empty weight and fuel weight are computed for a certain empty weight fraction. The results are given in table 42.1. To take into account a 3% reduction in weight at top of climb, equation (42.11) is rewritten as:

$$W_{TO} = \frac{1}{0.97} \frac{W_p}{e^{\frac{RC_T}{aM L/D}} - \frac{W_0}{W_{TO}} \frac{1}{0.97}}$$

Table 42.1 shows the effect of an increase in empty weight. If the empty weight fraction grows with 4%, the take-off weight increases by 5.8% and the empty weight by 10%. The fuel weight grows as much as the take-off weight as it is independent of the empty weight.

W_0/W_{TO}	W_{TO} (kg)	W_0 (kg)	W_f (kg)
0.50	69079	34539	9549
0.52 (+4%)	73112 (+5.8%)	38020 (+10.0%)	10094 (+5.7%)
0.54 (+8%)	77654 (+12.4%)	41933 (+21.4%)	10720 (+12.3%)

Table 42.1 - Results of example 42-1

Example 42-2:

Now the influence of a reduction in payload for the same aircraft as in example 42-1 is shown by calculating the weights. The conditions remain the same except that the empty weight fraction is specified and the payload is changed:
$W_0/W_{TO} = 0.52$
$W_P = 15000$ kg

In order to find the weights equation (42.9) is used. The results are:
$W_{TO} = 43869$ kg
$W_0 = 22812$ kg
$W_f = 6057$ kg

Note that this is an academic exercise as the payload is a part of the specification and will not be changed as dramatically as in this example.

Example 42-3

Now the empty weight is increased by 500 kg, the specific fuel consumption is increased by 3% and the lift-drag ratio is reduced by 3%. These variations may easily occur during engine and aircraft development. The other conditions are the same as in example 42-2.

$W_0 = 23312$ kg	$(= 22812$ kg $+ 500$ kg$)$
$C_T = 0.670$ kg/kg.hr	$(= 1.03 \cdot 0.650)$
$L/D = 17.48$	$(= 0.97 \cdot 18)$

If the maximum take-off weight remains 43869 kg the payload decreases to 14229 kg. This means a 5% loss in payload weight and thus revenue.

Example 42-4

Now the range is increased, the other parameters are the same as in example 42-2: $h = 3704$ km (2000 nm)

This leads to:
$W_{TO} = 48592$ kg
$W_0 = 25268$ kg
$W_f = 8324$ kg

Example 42-5

Now the empty weight found in example 42-4 is increased by 500 kg and the specific fuel consumption and lift-drag ratio are modified as was done in example 42-3. For a take-off weight of 48592 kg, the result of example 42-4, the payload and fuel weights become:
$W_P = 14112$ kg
$W_f = 8712$ kg

This corresponds to an increase in fuel weight of 4.7% compared to example 42-4 and a decrease in payload weight of 6%.

Weight definitions

Figure 42.5 presents an overview of the different weight definitions in use. Some of the definitions show subtle differences such as "basic weight" and "basic operating weight". The first is the empty weight of the aircraft including fixed equipment. The second definition also includes equipment that can be removed. Galleys, for example, are standard items that can be removed, but are necessary to operate the airplane. The food and drinks filling these galleys however, are part of the operators' items. Note that especially on long range flights food and drinks can be a considerable part of the total aircraft weight.

Airframe Structure	Powerplant	Airframe equipment and services		Operators items	Payload	Fuel	Main groups
		Fixed equipment	Removable equipment				
Basic Empty Weight							Typical Weights
Manufacturers Empty Weight				Load			
Basic Operational Empty Weight					Useful load		
Zero Fuel Weight						Fuel Weight	
Gross Weight							

Figure 42.5 - Weight definitions

Payload-range diagram

A payload-range diagram shows the commercial operating envelope of an aircraft in terms of weight. An important operational characteristic is that payload can be exchanged for fuel and vice versa in order to have some range flexibility, provided the fuel tank capacity is adequate. The slight increase in range after point C in figure 42.6 obtained by decreasing the payload (and weight and drag) is only of interest for ferry or positioning flights.
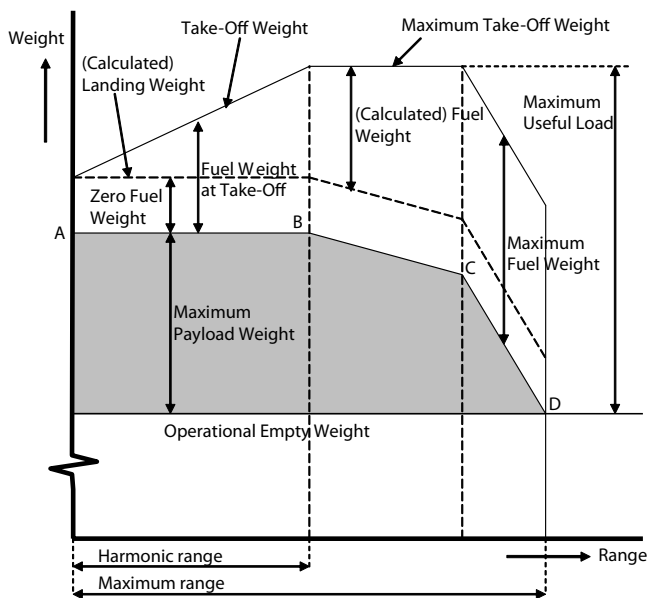
Figure 42.6 - Payload-range diagram
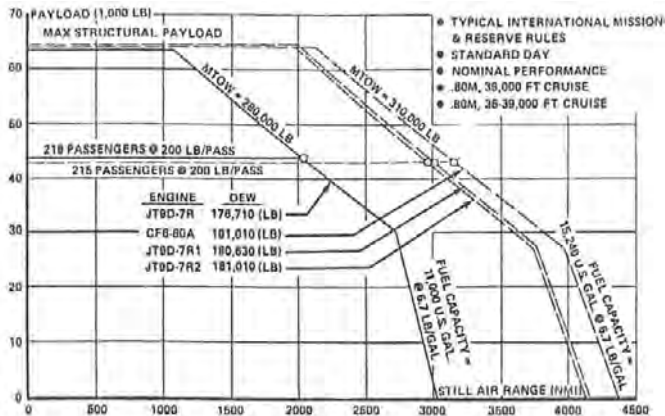
Figure 42.7 - Payload range diagram Boeing 767-200.
Source: Air et Cosmos No. 741, November 25, 1978

The limits of applicability of simple weight estimation methods

Just as drag estimation weight estimation has to be performed with great care when using simple methods. Such methods should only be used to study trends while keeping a sharp eye on the limits of the validity of the numbers involved. Some examples will be given here below:

Figure 42.8 suggests there is a linear relationship between number of passengers and maximum brake release weight for short-to-medium range aircraft up to 150 seats. The maximum brake release weight is about 1000 lb per passenger. This only holds for this class of aircraft. For the Boeing 747 for example it would be 1700 lb per passenger because of the much smaller part of the take-off weight being taken up by the payload. Within a certain class of aircraft the weight fraction can be considered approximately constant, but only within that class. The kind of data as shown in figure 42.8 should only be used to obtain a first impression of the aircraft weight.

Stretches and shrinks of an aircraft should be considered differently from the baseline aircraft. If an aircraft is lengthened or "stretched" it becomes more efficient from a structural point of view as the strength distribution found during static and fatigue testing of the aircraft is known in much greater detail than during the design of the basic version. This is shown in figure 42.9 where the stretched version of the De Havilland Dash-8-100, the Dash-8-300, has a lower operating weight per passenger than the Dash-8-100. The same holds for the ATR-42 to -72 and the British Aerospace 146-100 to -300 stretches. The line between the Fokker F-28-4000 and the F-100 is shallower. The reason for this is the generation difference. In the 20 years between these two aircraft many changes were made leading to a much heavier aircraft. Shortening or "shrinking" an aircraft however leads to an overweight aircraft as only two barrels are cut out from the original fuselage in front and behind the wing. Note the lines for a "shrink" in figure 42.2 which increases the empty weight and vice versa for a "stretch".
Baseline aircraft should be compared with baseline aircraft and notice should be taken of the differences between aircraft generations.
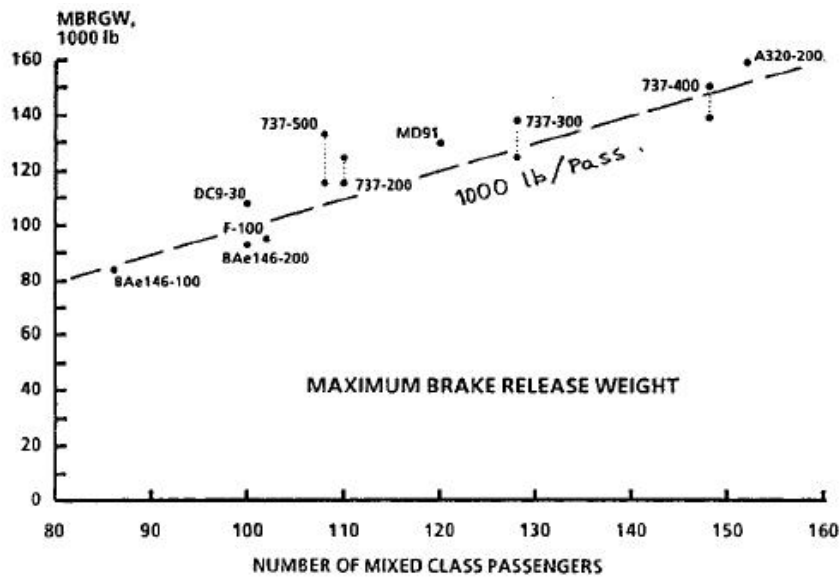
Figure 42.8 - Maximum brake release weight versus number of passengers
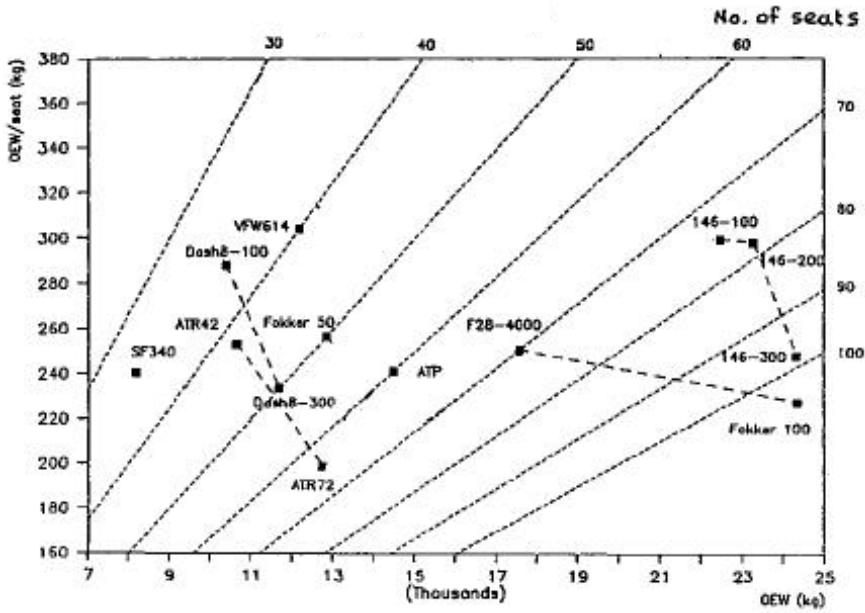
Figure 42.9 - Operating empty weight comparison

Weight estimation by means of more detailed computations.

Once a first impression exists of the basic aircraft weights the weight estimation process rises to the next detail level.

From the above it is clear that the most demanding task in weight estimation is the determination of the Manufacturers Empty Weight (MEW) or Operating Weight Empty (OWE). It is not so much a demanding task because of its complexity but because of the large number of elements which have to be analysed, each with its own numerical inaccuracy.

In the detail design phase the weight department in a design organisation is mainly involved in a complicated book-keeping process. The weight of each part is meticulously calculated from production drawings, real or virtual. At the same time the department functions as a watch dog which alarms management if somewhere target weights are exceeded.

In the initial design phase, when many details are not yet known, weight estimation requires insight and experience. On the one hand there is the temptation to collect as many weight data as possible to derive statistical averages. On the other hand, just as with drag estimates, all data have to fit in a closed system to prevent double or incomplete bookkeeping. Therefore, again just as for drag estimation, each design organisation builds up its own weight estimation methodology built on in-house experience. This methodology is regularly checked and updated by comparing calculated weight break-downs with detailed reliable weight break-downs of actual aircraft.

The equations and formulae used at this stage are, certainly for the larger airframe components, of a semi-statistical nature. Basic equations for bending and torsion calculations with elementary load assumptions are calibrated with actual weight data for a number of configurations and collected in a common frame of reference.

In order to do a detailed computation on aircraft weight, the manoeuvre and gust load envelopes as shown in figures 42.10 and 42.11 are required. These determine for example the wing weight. Which one of the two envelopes produces the maximum loads depends on the aircraft size and flight condition and aircraft configuration. The load envelopes depend partly on specific speeds chosen during the design from commercial and operational considerations and partly on airworthiness requirements. Although figure 42.11 is no longer shown in the present issue of FAR 25 or in CS 25 the figure is in line with the context of paragraph 25.335.
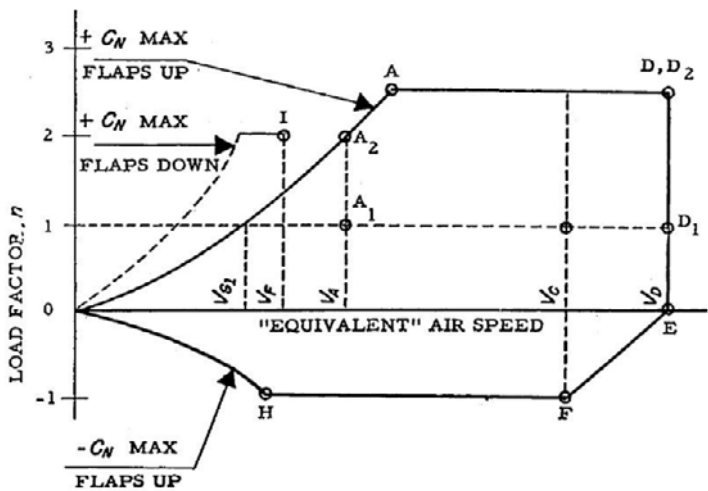
Figure 42.10 - Manoeuvre envelope. Source: FAR 25-335
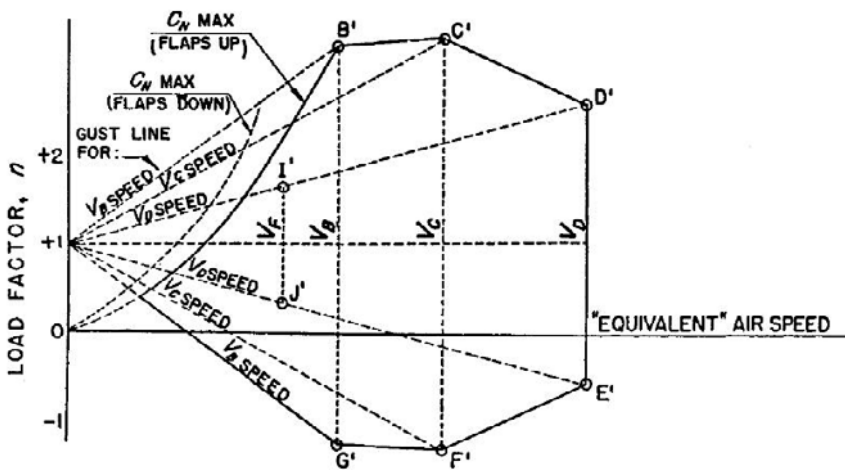
Figure 42.11 - Gust envelope. Source: Earlier issues of FAR 25-335

Figures 42.12 to 42.15 show flight envelopes of four different aircraft. Each flight envelope is characterised, from a weight-strength point of view, by the following quantities:

- Maximum Operating Speed, V_{MO}.
- Maximum Operating Mach Number, M_{MO}.
- Maximum Dive Speed, V_D.
- Maximum Dive Mach number, M_D.
- Maximum dynamic pressure at the cross-over altitude V_{MO}/ M_{MO}.
- Maximum dynamic pressure at the cross-over altitude , V_D/ M_D.
- Maximum altitude. (Determines the maximum cabin overpressure and fuselage weight.)
- The maximum speed (placard speed) for each low speed configuration.
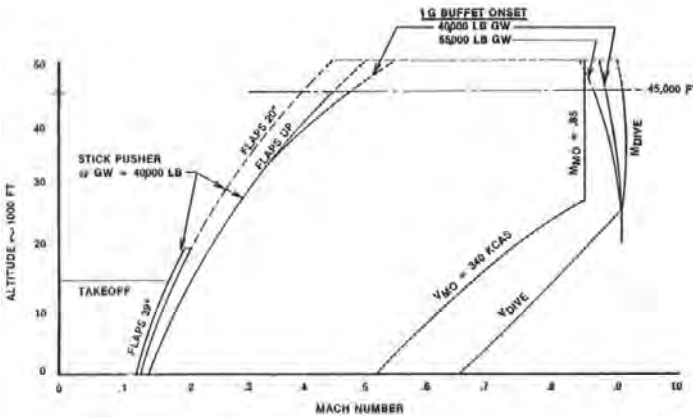
Figure 42.12 - Flight envelope Gulfstream IV
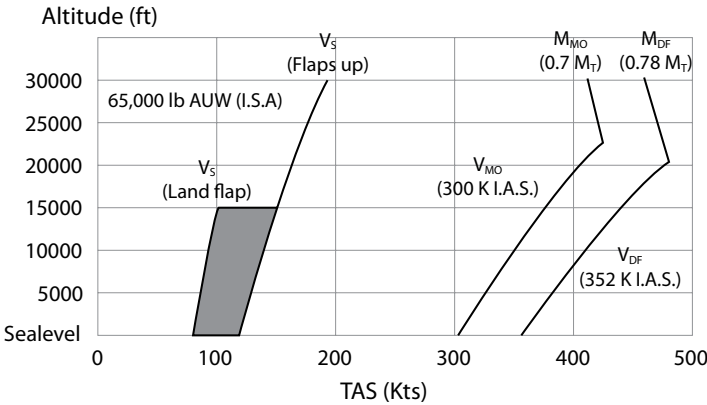
Figure 42.13 - Flight envelope British Aerospace 146-100
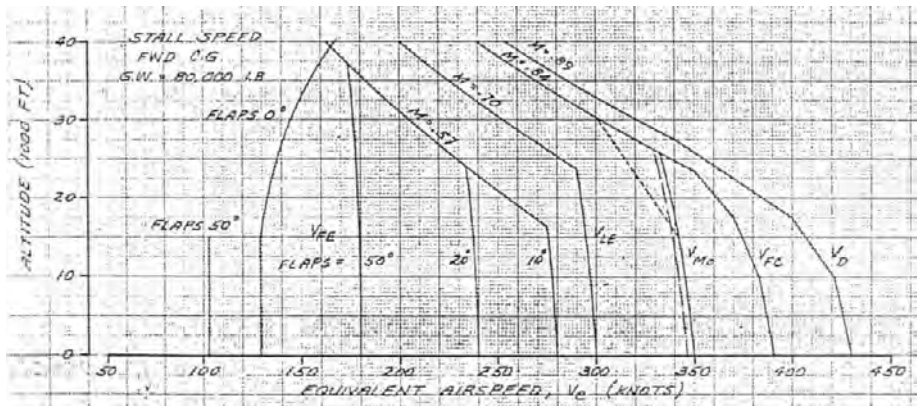
Figure 42.14 - Flight envelope DC-9-10
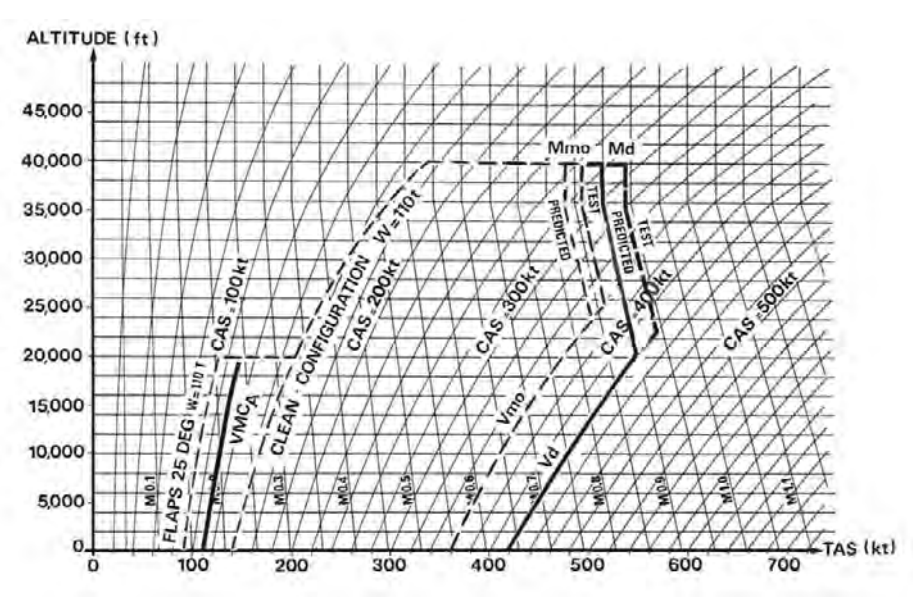
Figure 42.15 - Flight envelope Airbus A300 B2

573

From an operational point of view it would be desirable to choose the operational speeds as high as possible. It will be clear however that a balance must be struck between operational requirements and weight.

An example of a semi-empirical relationship between some physical parameters and the weight of a component is shown in figure 42.16 for wings. The parameters used: aircraft weight, normal load factor, wing area and span, and the inverse of the root thickness clearly indicate that the physical model for this weight equation is a slender beam under bending loads fixed at one end. Because this is not a simple relationship a new quantity γ is defined incorporating the parameters mentioned above. This quantity γ is then determined for a number of comparable wings and plotted on a double-logarithmic scale. The slope of the resulting curve produces the odd power in the weight equation.

In figure 42.17 wing-weight equations are presented for three different types of aircraft. The same parameters as used in the wing-weight equation in figure 42.16 can be recognised but in a more complicated form.

Many studies have been performed into wing-weight equations of varying complexity but accuracy hardly improves when more variables are included. In practice each design organisation believes in its own semi-empirical correlation.
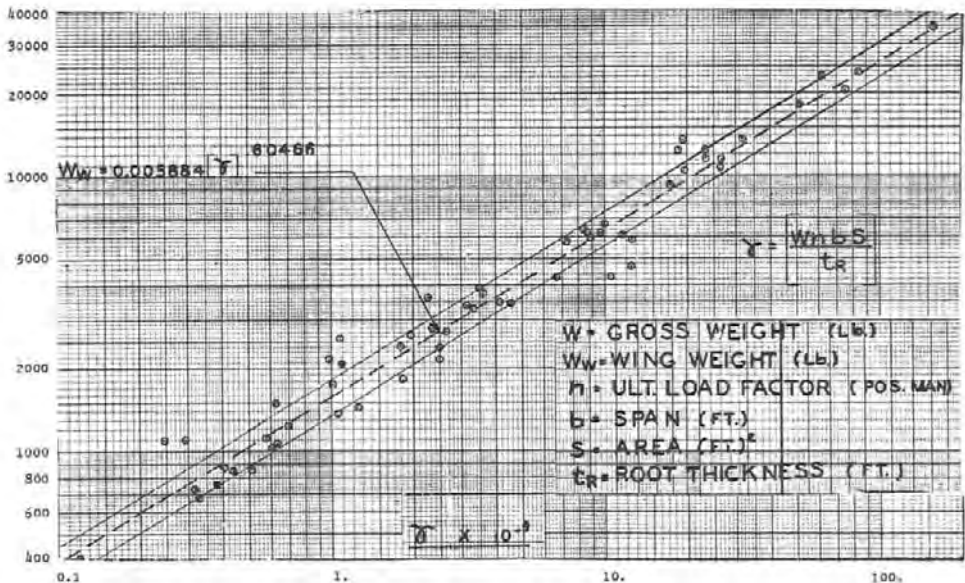
Figure 42.16 - Wing weight prediction. Source: Aerospace vehicle design Vol. 1. Aircraft Design, K.D. Wood
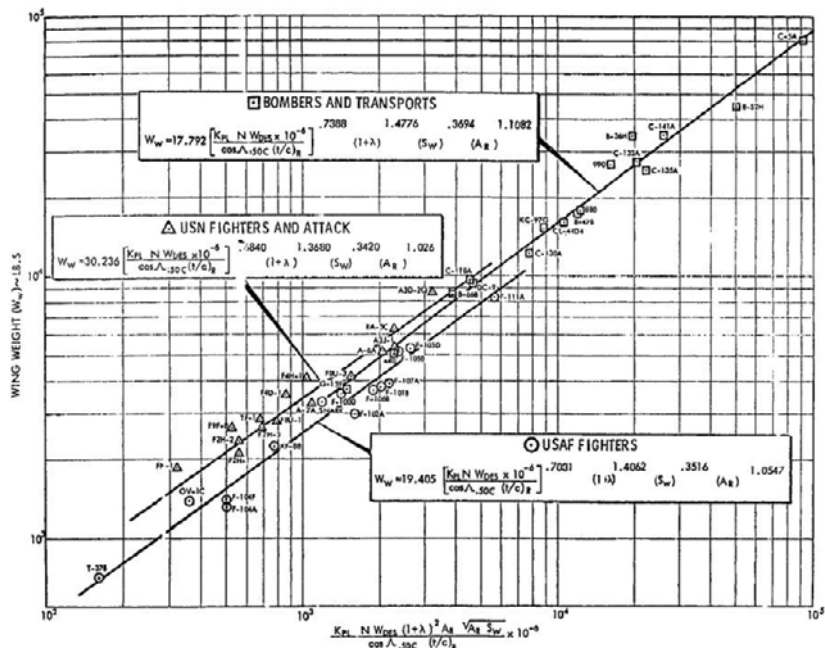
Figure 42.17 - Wing weight versus wing-root bending stress parameter.
Source: The derivation and application of analytical-statistical weight
prediction techniques - R.S. St. John, 1969
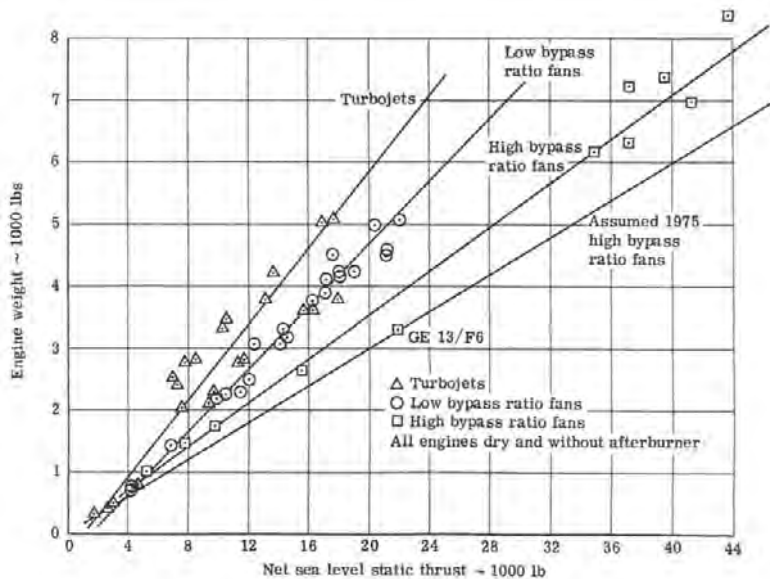
Figure 42.18 - Dry engine weight. Source: NASA CR 2320

The weight of wings, fuselages and, to a lesser degree, tail surfaces has been studied extensively and weight estimates are reasonably accurate. But the data correlations of other aircraft components are far less accurate. In many cases the weight of a particular system is correlated to the aircraft weight and/or a simple geometric characteristic.

Figure 42.18 shows a graph where engine weight is a linear function of sea level static thrust with an (approximate) dependency on by-pass ratio.

In figures 42.19 to 42.28 the weight breakdown of a number of turbine-powered aircraft are presented.

In figures 42.24 and 42.26 to 42.28 the engine nacelles and surface controls are part of the structures group.

The structure weight varies between 55 % and 60 % of the Operational Empty Weight.

The wing weight is normally 11 % of the Maximum Take-Off Weight +/- 10 %.

The relatively high systems weight of the Airbus A320 is indicative of the growing reliance on electric power on modern transport aircraft.
But also when the Fokker F-27 Mk 500 was developed into the Fokker 50 the combined weight of the instrument, electrical and electronic groups rose from 900 kg to 1203 kg. Similarly, when the F-28 Mk 4000 was developed into the Fokker 100 the combined weight of these groups increased from 797 kg to 1596 kg.

Item	Weight, lb (kg)	
Wing	18 520	(8 401)
Horizontal tail	1 930	(875)
Vertical tail	2 220	(1 007)
Body	22 380	(10 152)
Main landing gear	6 520	(2 957)
Nose landing gear	1 140	(517)
Nacelle and strut	2 220	(1 007)
Total structure	54 930	(24 916)
Engine (JT8D-9)	9 680	(4 391)
Engine accessories	270	(122)
Engine controls	120	(54)
Starting system	150	(68)
Fuel system	1 210	(549)
Thrust reverser	1 580	(717)
Total propulsion group	13 010	(5 901)
Instruments	830	(376)
Surface controls	2 970	(1 347)
Hydraulics	1 430	(649)
Pneumatics	—	—
Electrical	2 420	(1 098)
Electronics	1 830	(830)
Flight provisions	890	(404)
Passenger accommodations	8 820	(4 001)
Cargo handling	1 090	(494)
Emergency equipment	1 100	(499)
Air-conditioning	1 710	(776)
Anti-icing	490	(222)
Auxiliary power unit	850	(386)
Total fixed equipment	24 430	(11 081)
Exterior paint	100	(45)
Options	730	(331)
Manufacturer's empty weight	93 200	(42 276)
Standard and operational items	5 800	(2 631)
Operational empty weight	99 000	(44 906)
Maximum Take-Off Weight	**172500**	**(78245)**

Figure 42.19 - Boeing 727-200 aircraft weight breakdown. Source: NASA CR 134800

	747-100	**747 SP**	**Weight change**
Wing	88,537 lb	76,100 lb	12,437 lb
Horizontal tail	8,000 lb	8,000 lb	-
Vertical tail	3,937 lb	5,420 lb	+1,483 lb
Body	70,684 lb	59,515 lb	-11,169 lb
Main undercarriage	27,464 lb	25,650 lb	-1,814 lb
Nose undercarriage	3,180 lb	3,410 lb	+230 lb
Nacelle and strut	10,444 lb	10,444 lb	-
Propulsion	45,541 lb	44,244 lb	1,297 lb
Systems and equipment	35,162 lb	31,431 lb	3,731 lb
Interior	29,381 lb	24,743 lb	4,638 lb
Upper deck	2,670 lb	2,670 lb	-
Operating items	34,100 lb	23,373 lb	10,727 lb
Operating empty weight	359,100 lb	315,000 lb	44,100 lb

Figure 42.20 - 747SP/747-100 Structural weight comparison. Source: Flight, September 20, 1973

	747-100	**747 SP**
Taxi gross weight	738,000 lb	653,000 lb
Landing weight	564,000 lb	450,000 lb
Zero-fuel weight	526,500 lb	410,000 lb
Operating empty weight	359,100 lb	315,000 lb
Engines	JT9D-7A	JT9D-7A
Thrust	46,150 lb	46,150 lb
Seats	385 (= 77,000 lb)	288 (= 57,600 lb)

Figure 42.21 - 747SP Characteristics. Source: Flight, September 20, 1973

	Domestic all-economy (32in pitch)	**Domestic all-economy (33 in / 34 in pitch)**	**Regional mixed class**	**International mixed class**
Take-off weight	520,000 lb	520,000 lb	600,000 lb	*710,000 lb
Landing weight	505,000 lb	505,000 lb	525,000 lb	564,000 lb
Zero-fuel weight	475,000 lb	475,000 lb	485,000 lb	526,500 lb
Operating empty weight	345,600 lb	344,600 lb	357,500 lb	363,700 lb
Passenger capacity	537	500	461	382
Powerplant	JT9D-7 (derated)	JT9D-7 (derated)	JT9D-7 (derated)	JT9D-7 (derated)
Thrust (sea-level, static)	43,500 lb (dry)	43,500 lb (dry)	43,500 lb (dry)	45,500 lb (dry)
The JAL 747SR will seat 498 Initially. * 735,000 lb available (747B is certificated at 775,000 lb).				

Figure 42.22 - 747SR principal data. Source: Flight, November 9, 1972

COMPONENT	DHC 5 (CIVIL)			DHC 6		DASH 7	
	WT - LB	% G.W. 41,000	% G.W. 49,200	WT - LB	% G.W.	WT - LB	% G.W.
WING STRUCTURE	4571	11.1	9.3	1212	9.7	4879	11.1
TAIL STRUCTURE	1071	2.6	2.2	300	2.4	1427	3.2
FUSELAGE STRUCTURE	4952	12.1	10.1	1758	14.0	4606	10.5
LANDING GEAR	1896	4.6	3.8	607	4.9	1713	3.9
NACELLE STRUCTURE	1654	4.0	3.4	220	1.8	1841	4.2
FLYING CONTROLS	424	1.0	0.9	144	1.2	704	1.6
ENGINES	2238	5.5	4.5	648	5.2	2386	5.4
PROPELLERS	1568	3.8	3.2	269	2.2	1441	3.3
POWER PLANT SYSTEMS	1285	3.1	2.6	334	2.7	872	2.0
ELECTRICS	1008	2.5	2.0	355	2.8	1651	3.8
HYDRAULICS	454	1.2	0.9	44	0.4	492	1.1
STRUCTURE PROVISIONAL AVIONICS STANDARD	48	0.1	0.1	14	0.1	154	0.4
AVIONICS – TYPICAL	532	1.3	1.1	190	1.5	639	1.5
INSTRUMENTS	145	0.4	0.3	70	0.6	212	0.5
DEICING	230	0.6	0.5	163	1.3	178	0.4
AIR CONDITIONING/HEATING	363	0.9	0.7	104	0.8	550	1.2
CREW SEATS	125	0.3	0.3	52	0.4	119	0.3
PASSENGER SEATS	681	1.4	1.2	307	2.4	1018	2.3
FLIGHT COMPARTMENT FURNISHINGS	20	–	–	30	0.2	84	0.2
CABIN FURNISHINGS	768	1.9	1.6	310	2.5	1077	2.4
BAGGAGE COMPARTMENT / FURNISHINGS	–	–	–	–	–	84	0.2
MISC. O_2 ETC.	166	0.4	0.3	–	–	104	0.2
TOILET & BUFFET	–	–	–	–	–	369	0.8
EXTERIOR PAINT	120	0.3	0.2	70	0.6	150	0.3
A.P.U.	123	0.3	0.2	–		–	
MANUFACTURE VARIATION	290	0.7	0.6	–		–	
TRAPPED FUEL	107	0.6	0.5	89	0.7	280	0.6
FULL OIL	120						
STANDARD BASIC WEIGHT	24,858	60.6	50.5	7290	58.4	27,030	61.4
FLIGHT CREW, BAGS	560	1.4	1.1	470	3.7	470 180	1.5
ATTENDANTS, SUPPLIES							
OPERATIONAL WEIGHT EMPTY	25,418	62.0	51.6	7760	62.1	27,680	62.9
PASSENGERS @ 200 LB	8,800 (44)	21.5		3800 (19)	30.4	10,000	22.7
ZERO FUEL WEIGHT	34,218	83.5		11,560	92.4	37,680	85.6
MISSION FUEL - MAX. PASS.	6,782	16.5		940	7.5	6,320	14.4
GROSS WEIGHT	41,000	100.0		12,500	100.0	44,000	100.0
MAXIMUM GROSS WEIGHT	41,000			12,500		44,000	
TRANSPORT	49,200			–		–	
MAXIMUM ZERO FUEL WEIGHT	40,000			NO RESTRIC.		39,000	
MAXIMUM LANDING WEIGHT	40,000			12,300		42,000	
WING AREA	945 FT^2			420 FT^2		860 FT^2	
MAXIMUM WING LOADING		43.4	52.1	29.8		51.2	

Figure 42.23 - Weight summaries of three De Havilland Canada aircraft.
Source: AIAA professional studies series – A case study on the De Havilland STOL commuter aircraft

ATR - 42		
Item	*Weight [kg]*	*% MTOW*
Wing	1565	9.69
Fuselage	2587	
Horizontal tailplane	220	
Vertical tailplane	322	
Landing gear	534	
Engine nacelles	366	
Flight controls	195	
Structure	**5788**	**35.84**
Equipped engines	1212	
Engine controls	37	
Engine instrumentation	10	
Fuel system	89	
Propulsion	**1347**	**8.34**
Hydraulic generation	91	
Hydraulic distribution	50	
Air conditioning	287	
De-icing	75	
Fire protection	25	
Cockpit furnishing	79	
Auto-flight system	26	
Navigation	164	
Communication	94	
Electric generation	310	
Electric distribution	213	
Systems	**1414**	**8.76**
Furnishing	845	
Oxygen	31	
Lighting	90	
Water installation	11	
Furnishings	**977**	**6.05**
Manufacturer's Empty Weight	***9526***	***58.98***
Pantry structure	45	
Passenger seats	322	
Other standard items	34	
Standard items	**401**	**2.48**
Delivery empty weight	***9927***	***61.47***
Operational items	**326**	**2.02**
Operational empty weight	***10253***	***63.49***
Maximum take-off weight (MTOW)	***16150***	***100***

Figure 42.24 - Weight breakdown ATR-42

Airbus A320-200		
Item	*Weight [kg]*	*% MTOW*
Wing	8801	11.97
Fuselage	8938	
Horizontal tailplane	625	
Vertical tailplane	463	
Landing gear	2275	
Pylons	907	
Structure	**22009**	**29.94**
Equipped engines	6621	
Bleed air system	249	
Engine controls	29	
Engine instrumentation	0	
Fuel system	299	
Propulsion	**7198**	**9.79**
Auxiliary power unit	223	
Hydraulic generation	547	
Hydraulic distribution	319	
Air conditioning	664	
Anti-icing	30	
Fire protection	85	
Flight controls	772	
Instruments	71	
Auto-flight system	101	
Navigation	415	
Communication	186	
Electric generation	343	
Electric distribution	1032	
Systems	**4788**	**11.96**
Furnishing	2431	
Oxygen	103	
Lighting	200	
Water installation	79	
Furnishings	**977**	**6.05**
Manufacturer's Empty Weight	***36808***	***50.08***
Standard and Operational items	**3215**	**4.37**
Operational empty weight	***40023***	***54.45***
Maximum take-off weight (MTOW)	***73500***	***100***

Figure 42.25 - Weight breakdown Airbus A320-200

Fokker F-28 Mk 4000		
Item	*Weight [kg]*	*% MTOW*
Wing group	3419	10.32
Horizontal tail group	414	
Vertical tail group	322	
Fuselage group	3571	
Landing gear group	1365	
Surface control group	633	
Nacelle group	379	
Structure	**10103**	**30.49**
Propulsion	**2438**	**7.36**
Aux. power unit group	172	
Instrument group	151	
Hydraulic group	176	
Electrical group	483	
Electronic group	407	
Air cond. & anti-icing gr.	506	
Systems	**1895**	**5.72**
Furnishings	**1481**	**4.47**
Manufacturer's Empty Weight	***15917***	***48.03***
Pantry structure	149	
Passenger seats	798	
Other standard items	178	
Standard items	**1125**	**3.39**
Delivery empty weight	***17042***	***51.42***
Operational items	**505**	**1.52**
Operational empty weight	***17547***	***52.94***
Maximum take-off weight (MTOW)	***33140***	***100***

Figure 42.26 - Weight breakdown Fokker F-28 Mk 4000

Fokker 100		
Item	*Weight [kg]*	*% MTOW*
Wing group	4669	10.08
Horizontal tail group	491	
Vertical tail group	365	
Fuselage group	4758	
Landing gear group	1459	
Surface control group	654	
Nacelle group	839	
Structure	**13235**	**28.87**
Propulsion	**4182**	**9.12**
Aux. power unit group	196	
Instrument group	174	
Hydraulic group	233	
Electrical group	758	
Electronic group	664	
Air cond. & anti-icing gr.	730	
Systems	**2755**	**11.25**
Furnishings	**2009**	**4.38**
Manufacturer's Empty Weight	***22181***	***58.98***
Pantry structure	187	
Passenger seats	979	
Electronic instruments	0	
Other standard items	326	
Standard items	**1492**	**3.25**
Delivery empty weight	***23673***	***51.63***
Operational items	**807**	**1.76**
Operational empty weight	***24480***	***53.39***
Maximum take-off weight (MTOW)	***45850***	***100***

Figure 42.27 - Weight breakdown Fokker 100

Fokker 50		
Item	*Weight [kg]*	*% MTOW*
Wing group	2083	10.00
Horizontal tail group	269	
Vertical tail group	260	
Fuselage group	2338	
Landing gear group	1032	
Surface control group	232	
Nacelle group	420	
Structure	**6634**	**31.86**
Propulsion	**2163**	**10.39**
Aux. power unit group	0	
Instrument group	137	
Hydraulic group	99	
Electrical group	571	
Electronic group	495	
Air Conditioning	297	
De-icing group	143	
Systems	**1742**	**8.37**
Furnishings	**1139**	**5.47**
Manufacturer's Empty Weight	***11678***	***56.53***
Pantry structure	59	
Passenger seats	478	
Electronic instruments	0	
Other standard items	152	
Standard items	**689**	**3.30**
Delivery empty weight	***12367***	***59.40***
Operational items	**370**	**1.78**
Operational empty weight	***12737***	***61.18***
Maximum take-off weight (MTOW)	***20820***	***100***

Figure 42.28 - Weight breakdown Fokker 50

PART 10

SAFETY AND REGULATIONS

43 *Certification regulations and design rules*

Certification regulations

Regulations describe the **minimum** requirements with which a design must **comply** in order to c**onvince airworthiness authorities** that an **acceptable safety standard** is **achieved**.

Any civil transport aircraft with a maximum take-off weight MTOW > 12500 lb (5700 kg), for which today, summer 2008, airworthiness certification is sought for operation in the Western world, must comply with the US Federal Aviation Regulations FAR 25, Amendment 25-120 and the EU Certification Specifications for Large Aeroplanes CS-25, Amendment 2.

The first certification regulations were written in the 1920's. Initially each country with an aviation industry of some significance developed its own regulations. Although formerly most countries kept their national regulations after the Second World War many Western countries, but not the UK and France, in practice adopted the US regulations.

The regulations have evolved hand-in-hand with the development of aircraft and aircraft systems. For example, the introduction of jet engines shortly after the Second World War meant new regulations had to be written. To maintain or even improve a certain safety level, regulations are continuously revised and adjusted. The introduction of a new system in an aircraft sometimes means a temporary reliability level standstill, or even decrease. Usually this improves after a while. Such a development is illustrated in figure 44.1, showing the shutdown rate of gas turbine engines. Introduction of the high-bypass-ratio turbofan engine caused at first an increased shutdown rate but the second generation engines showed a marked improvement in reliability.

As an example of the evolution of airworthiness requirements and the responsible agency a short overview of the development in the US is presented here below:
• In 1926 the Aeronautics Branch of the Department of Commerce was established responsible for the certification of civil aircraft. The (simple) rules were published in Aeronautics Bulletin no. 7.
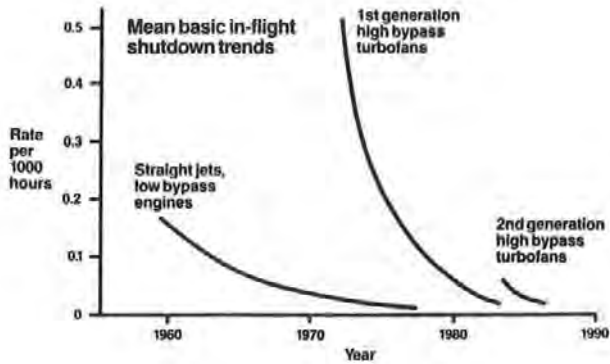
Figure 43.1 - Civil aero gas turbine engine trends. Source: Rolls-Royce/VSV, Delft, september 1985

- In 1934 the Aeronautics Branch was renamed Bureau of Air Commerce.
- In 1938 the aircraft certification agency was separated from the Bureau of Commerce and became the independent Civil Aeronautics Authority CAA.
- In 1940 The Authority was split in two separate agencies with the Civil Aeronautics Administration (new CAA) becoming responsible for aircraft certification. This agency introduced in 1942, as part of the new Civil Air Regulations, new certification regulations for large transport aircraft CAR 4 with later amendments CAR 4A and CAR 4B.
- In 1958, partly due to the introduction of jet airliners a new agency responsible for aircraft certification was created, the Federal Aviation Agency. This agency introduced new regulations for turbine-powered aircraft, Special Regulation SR 422, later amended by SR 422A and SR 422B.
- In 1967 as part of the establishment of the new Department of Transportation the Federal Aviation Agency was renamed Federal Aviation Agency.
- On December 31st 1964 the Federal Aviation Agency (FAA) completed the reorganization of their aviation regulations into one set of rules: the Federal Aviation Regulations (FAR). It is an extensive set of regulations that is set-up as follows:

Chapter 1	Subchapter A	Definitions
	Subchapter B	Procedural rules
	Subchapter C	Aircraft
	Subchapter D	Airmen
	Subchapter E	Airspace
	Subchapter F	Air traffic and general operating rules
	Subchapter G	Certification and operations
	Subchapter H	Schools

Subchapter I   Airports
Subchapter J   Navigational facilities
Subchapter K   Administrative regulations
Chapter 2, 3, 4 and 5 handle economics and space transportation.

For certification of large transport aircraft FAR 25, which is basically a combination of CAR 4B and SR 422B, is applicable.

In Europe a slightly different development took place. Under the pressure of international aircraft development programmes the airworthiness authorities of a number of European countries started in 1970 a collaborative programme to unify national airworthiness regulations in a body called the Joint Airworthiness Authorities. In 1987 this work had proceeded so far that the establishment of a formal certification body was warranted, recognised by the member states, the Joint Aviation Authority JAA. The JAA has formulated Joint Aviation Requirements (JAR) of which JAR-25 is comparable to the FAA FAR 25.

Following intensive discussions between the FAA and the JAA, the latter adopted FAR-25 as the Basic Code. On a small number of subjects there are still differences but as both sets of requirements maintain the same numbering system of all paragraphs differences are easily recognisable.

In 2003 the European Union established the European Aviation Safety Agency (EASA) which succeeded the European Joint Aviation Authorities JAA. The Joint Aviation Requirements (JAR) were adopted integrally and are now termed Certification Specifications (CS) so JAR-25 is now CS-25. The Certification Specifications now apply to all EU Member States.

Besides FAR 25 and CS-25 for large transport aircraft (MTOW > 5700 kg) FAR 23 and CS-23 are relevant to the aerodynamic design of small transport aircraft (MTOW < 5700 kg).

For the aerodynamic design of large transport aircraft the most important parts of CS-25 are (comparable to FAR 25):
    Subpart B – Flight
    Subpart C – Structure
    Subpart D – Design and Construction
    Subpart F – Equipment, both from
    Book 1 – Airworthiness Code and
    Book 2 – Acceptable Means of Compliance (AMC).

Subpart B – Flight contains the following paragraphs:

General with the following sub-paragraphs:
CS 25.20   Scope
CS 25.21   Proof of compliance
CS 25.23   Load distribution limits
CS 25.25   Weight limits
CS 25.27   Centre of gravity limits
CS 25.29   Empty weight and corresponding centre of gravity
CS 25.31   Removable ballast
CS.25.33   Propeller speed and pitch limits

Performance with the following sub-paragraphs:
CS 25.101 General
CS 25.103 Stall speed
CS 25.105 Take-off
CS 25.107 Take-off speeds
CS 25.109 Accelerate-stop distance
CS 25.111 Take-off path
CS 25.113 Take-off distance and take-off run
CS 25.115 Take-off flight path
CS 25.117 Climb: general
CS 25.119 Landing climb: all-engines-operating
CS 25.121 Climb: one-engine-inoperative
CS 25.123 En-route flight paths
CS 25.125 Landing

Controllability and manoeuvrability with the following sub-paragraphs:
CS 25.143 General
CS 25.145 Longitudinal control
CS 25.147 Directional and lateral control
CS 25.149 Minimum control speed

Trim with the following sub-paragraph:
CS 25.161 Trim

Stability with the following sub-paragraphs:
CS 25.171 General
CS 25.173 Static longitudinal stability
CS 25.175 Demonstration of static longitudinal stability
CS 25.177 Static directional and lateral stability
CS 25.181 Dynamic stability

Stalls with the following sub-paragraphs:
CS 25.201 Stall demonstration
CS 25.203 Stall characteristics
CS 25.207 Stall warning

Ground handling characteristics with the following sub-paragraphs:
CS 25.231 Longitudinal stability and control
CS 25.233 Directional stability and control
CS 25.235 Taxiing conditions
CS 25.237 Wind velocities

Miscellaneous flight requirements with the following sub-paragraphs:
CS 25.251 Vibration and buffeting
CS 25.253 High-speed characteristics
CS 25.255 Out-of-trim characteristics

The most significant sub-paragraphs in Subparts C, D and F are:

Subpart C – Structure with the following paragraphs:

General with the following sub-paragraphs:
    CS 25.301 Loads
    CS 25.303 Factor of safety
    CS 25.305 Strength and deformation
    CS 25.307 Proof of structure

Flight loads with the sub-paragraph:
    CS 25.321 General

Flight manoeuvre and gust conditions with the following sub-paragraphs:
    CS 25.331 Symmetric manoeuvring conditions
    CS 25.333 Flight manoeuvring envelope
    CS 25.335 Design airspeeds
    CS 25.337 Limit manoeuvring load factors
    CS 25.341 Gust and turbulence loads
    CS 25.343 Design fuel and oil loads
    CS 25.345 High lift devices
    CS 25.349 Rolling conditions

Subpart D – design and construction with the following paragraph:

Control system with the following sub-paragraph:
    CS 25.671 General

Subpart F – Equipment with the following paragraph:
General with the following sub-paragraph:
    CS 25.1309 Equipment, systems and installations

Special conditions

For any new application for a certificate of airworthiness the authorities are entitled to formulate new design or proof-of-compliance requirements for the particular application, termed **special conditions**, if certain design characteristics according to the authorities are not covered by the existing regulations. This was for example the case for the fly-by-wire control system of the Airbus A320.

Design rules

Airworthiness regulations exist in the first place to guarantee an acceptable level of safety and are not intended to improve the economic or operational performance of a transport aircraft. Contrary to this, design rules are guidelines for the design process which, when strictly followed, will result in a satisfactory design. Design rules thus cover either design aspects not mentioned in the airworthiness regulations or define **satisfactory** characteristics contrary to minimum acceptable characteristics as laid down in the regulations. They are goals, which are not necessarily achieved completely.

From this description it is clear that:
- **Design rules incorporate** relevant **regulations**.
- **Design rules** incorporate **a design organisation's** previous **experience** not necessarily shared by other designers.

Over the years, the airworthiness regulations have continuously been extended and improved with the result that the gap between minimum acceptable and satisfactory aircraft characteristics is constantly diminishing.
This process is carefully monitored by the aircraft industry. The ever-increasing extent of the airworthiness regulations makes the task of finding a commercially attractive compromise between the various types of design requirements more and more demanding. On the other hand, airworthiness regulations should not be used as design rules on their own.

Airworthiness regulations and design rules should be considered **separately** from the **Performance Specification** which in itself contains aerodynamic design requirements. From the performance specification the design values for $C_{L_{max}}$, L/D, buffet boundary, etc. are derived taking the airworthiness regulations into account. But airworthiness regulations are not so much a **stimulus** for an **optimum design in the commercial sense** but more a **constraint**.
The performance specification is entirely the **responsibility of the designer / manufacturer**.

Regulations aimed at safety and requirements on aircraft handling characteristics can be interconnected because for example "pleasant" handling characteristics and good stability lead to lower pilot fatigue and allows the pilot to divide his attention between actually flying the aircraft and performing other cockpit tasks and keeping an eye on the outside world thus enhancing flight safety.

Due to the differences in operation this was recognised by the military far earlier than by civil operators. Formal design requirements on flight handling characteristics were formulated by the military and later informally adopted by individual civil aircraft manufacturers as guidelines.

Quantification of flight handling characteristics was pioneered by the military, in particular in the US, because of their interest in manoeuvrability and tracking performance.

The most extensive set of military design rules for flight handling characteristics is:

> Military Specification   MIL- F- 8785-C

The civil aircraft industry has for a long time used this Mil. Spec. as a guideline for its own activities. In the 60's the American Society of Automotive Engineers (SAE) formulated a set of design rules for transport aircraft: Aerospace Recommended Practice ARP 842 based on MIL-F-8785 and the civil regulations CAR 4B. In 1984 an update was produced:

> Aerospace Recommended Practice ARP 842C

In this set of design rules for flight handling also attention is paid to **failures in control systems**.

The latter is a matter of increasing importance as the use of transport aircraft is more and more intensified and passengers (and operators) expect that, when a single in-flight failure occurs the aircraft can nevertheless fulfil its flight plan. This in turn requires the control systems to be designed such that the aircraft capabilities in critical flight conditions such as a night approach and landing in stormy weather are hardly affected.

The items addressed in SAE ARP 842C can be divided in items concerning:
   • Static equilibrium in extreme conditions
   • Manoeuvrability
   • Tracking

This is in line with what was said about flight handling requirements in chapter 33 on control surface design.

44 *Take-off performance regulations*

In chapter 43 the certification regulations for large civil transport aircraft were explained. A large part of the regulations defines the flight tests required to be performed in order to obtain the basic data from which the take-off limitations can be calculated for inclusion in the official flight manual. In the present chapter the certification requirements concerning the take-off are considered more in detail.

Certification tests are performed to determine the performance and flight handling characteristics of the aircraft in order to guarantee a satisfactory level of safety in its commercial day-to-day operation.
Commercial aviation started later in the USA than in Europe but developed at a much faster pace. This was to a large extent due to the full support of the U.S. government.
At the same time however, there was public concern about the safety of flying and the government was under pressure to take measures to enhance flight safety. This produced a dualism in the responsibilities of the government agency which on the one hand is to stimulate the growth of civil aviation but on the other hand is, to introduce regulations, which enhance flight safety.
The consequence of this situation is that, whenever new rulemaking is considered, the FAA and all its predecessors have and had extensive dialogues with all parties concerned. In many cases detailed studies were performed of the existing situation with analyses of the probability of a particular occurrence and how improvements could be realised. The origin of the quantified requirements in the present regulations may not be immediately visible but each of them is the result of detailed studies.
Although in the past many countries originally had their own regulations, at present most countries have adopted the FAA regulations as described in the previous chapter.

Engine failure during take-off has for many years been regarded as one of the most serious causes of accidents.
The reason is two-fold: First, during take-off the engine operates at its most critical condition. Second, if an engine failure occurs the pilot has literally little time and space to react adequately.

The complexity of take-off performance certification is illustrated in figure 44.1. Although the figure gives an extensive overview, a number of significant speeds that have to be determined as well such as the minimum control speeds with one engine inoperative, both in the air (V_{MCA}) and on the ground (V_{MCG}), are not presented in this figure.

In order to maximise the operational flexibility transport aircraft are certified for a range of take-off flap settings. For each flap setting a complete free-flight and field performance test programme has to be executed. This explains why a large part of the certification effort is for the take-off and initial climb phase.

Runway length is defined as the distance between the thresholds. The runway surface has adequate bearing strength for normal landings of the heaviest aircraft in its category. Some runways, where the space is available, have **stopways**, extensions past the threshold with lower bearing strength. These stopways may not be used for landing but, as the name implies, may be used to bring the aircraft to a standstill after a rejected take-off.

To increase the available take-off distance without actually lengthening the asphalt or concrete runway the area past the stopway may be cleared of obstacles to allow an unobstructed climb to 35 ft with a failed engine. The length of this area, the **clearway**, may, together with the stopway, not exceed 50 % of the runway length.
Figures 44.2 and 44.3 present the options in available take-off field length.
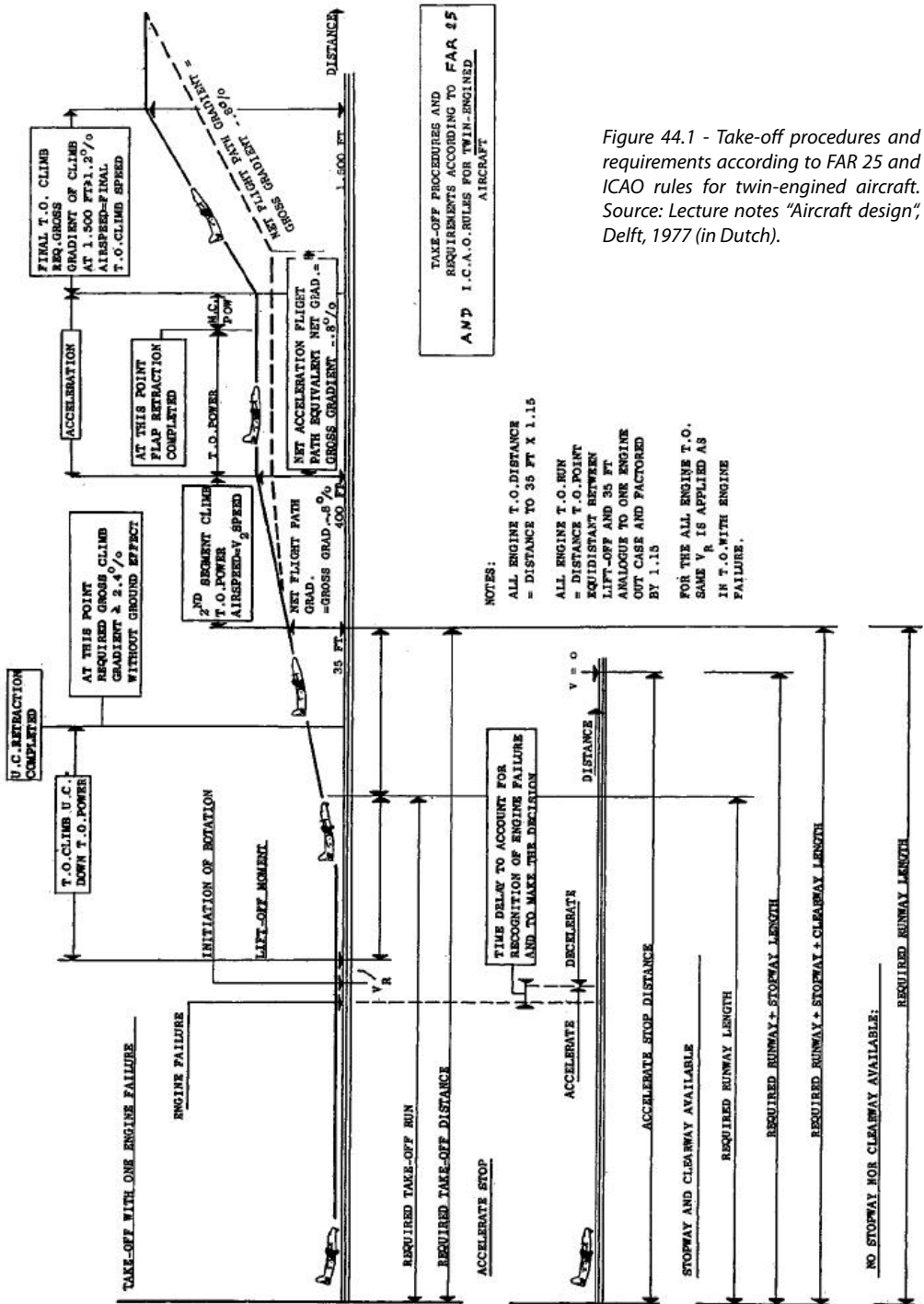
Figure 44.1 - Take-off procedures and requirements according to FAR 25 and ICAO rules for twin-engined aircraft. Source: Lecture notes "Aircraft design", Delft, 1977 (in Dutch).
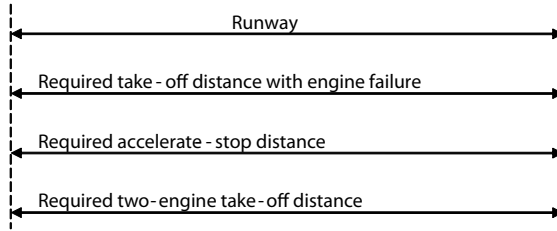
Figure 44.2 - Field length - no stopway nor clearway available.
Source: Lecture notes "Aircraft design", Delft, 1977 (in Dutch).
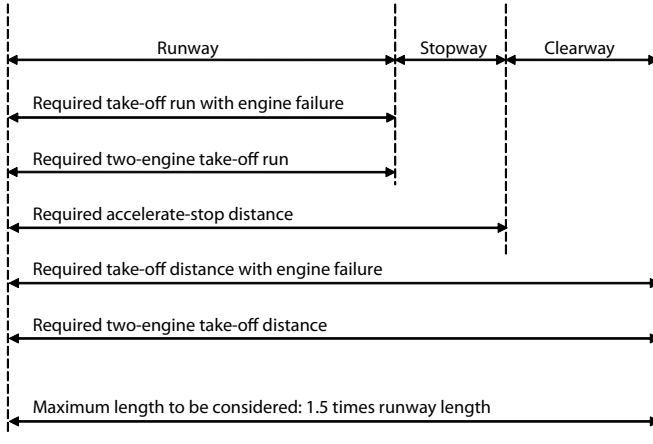
Figure 44.3 - Field length - stopway and / or clearway available.
Source: Lecture notes "Aircraft design", Delft, 1977 (in Dutch).

To determine the required runway length for a given combination of flap setting, weight, altitude and temperature three different situations have to be investigated. The three types of test that have to be performed will be discussed using figures 44.4 to 44.6.

In figure 44.4 the take-off with all engines operating is considered. The measured take-off distance is multiplied with a factor 1.15 to account for non-ideal conditions to obtain the required runway length.

The second test is one of two with a simulated engine failure just before reaching the decision speed V_1. In this test take-off is continued. The required runway length now is the distance covered when flying over the imaginary 35 feet high obstacle, see figure 44.5.

Finally, the third test concerns a simulated engine failure just before reaching the decision speed V_1, but then deciding to abort the take-off and apply full brakes. This is shown in figure 44.6.
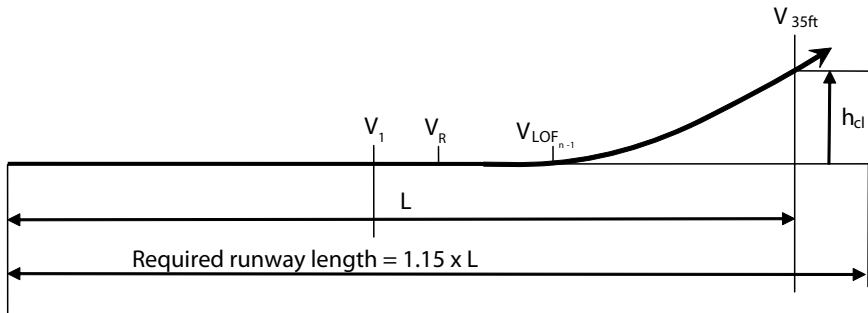
Figure 44.4 - Take-off with all engines operative.
Source: Lecture notes "Aircraft design", Delft, 1977 (in Dutch)
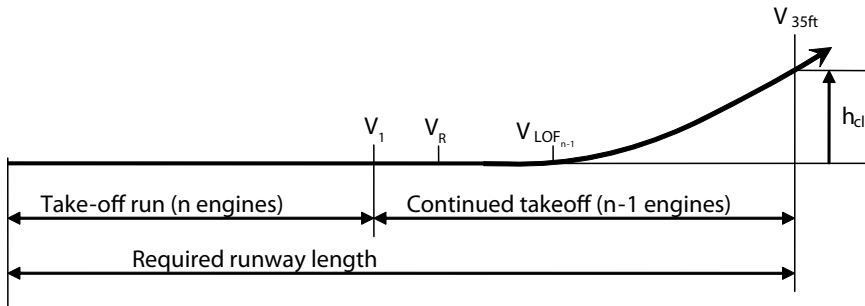
Figure 44.5 - Continued take-off with one engine inoperative at V1.
Source: Lecture notes "Aircraft design", Delft, 1977 (in Dutch)
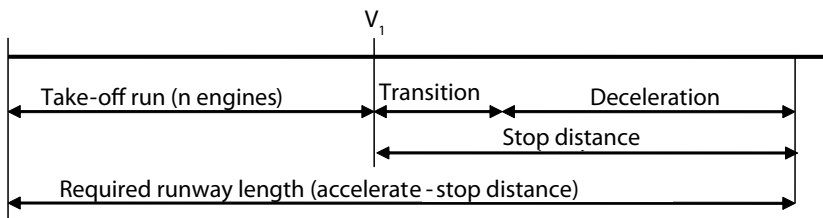
Figure 44.6 - Aborted take-off with one engine inoperative at V1.
Source: Lecture notes "Aircraft design", Delft, 1977 (in Dutch)

Definitions:

V_{FE}	engine failure speed
V_1	critical engine failure speed
V_R	rotation speed
V_{LOF}	lift-off speed
V_2	take-off safety speed
V_{2min}	minimum take-off safety speed
h_{cl}	clearance height (35 ft $\approx$ 10.76 m)
n	number of engines installed
n-1	number of engines operative after failure of one engine

When all three runway lengths have been determined, the longest runway would be the required runway length to be stated in the limitations section of the flight manual for the particular aircraft and atmospheric condition.

If the take-off distances for the two engine failure cases, determined in the flight tests, differ from each other this is rectified by adapting the decision speed V_1. This may be done by computation using the flight test data as shown in figures 44.7 to 44.9. On the abscissa the engine failure recognition speed is shown, on the ordinate the take-off length. Note that the take-off weight, flap deflection and atmospheric condition is the same for all three figures.

Figure 44.7 shows both a continued take-off after engine failure, as well as an aborted take-off. The shortest required runway length is achieved at that speed and runway length where the two curves (of continued and aborted take-off) intersect. This runway length is also called the **balanced field length**. Note that, for two-engined aircraft the balanced field length is (as far as is known) always longer than the field length with all engines operating because the effect on required runway length of 50% thrust loss at V_1 is much larger than the 15% margin on the runway length for the all-engine take-off.

Figure 44.8 shows a comparison between the required runway lengths for the three situations discussed if continuation of take-off after engine failure is more critical than aborting the take-off.

Figure 44.9 illustrates the case when the runway length for a take-off with all engines operating is limiting. As mentioned above this is not known to have occurred on twin-engined aircraft but may occur on three- and four-engined aircraft as an engine failure causes only a 33% or 25% thrust loss with consequently less effect on the required runway length.

If the take-off length with all engines operating determines the required runway length, V_1 may be adjusted to a higher speed to allow full use of the available runway length to bring the aircraft to a halt if the take-off is aborted.

Continued takeoff after engine failure

Take-off length

Required runway length, also: balanced field length

1.15L, all engines operative

Aborted take-off after engine failure

1.15L, all engines operative

Speed at engine failure V_1 V_R
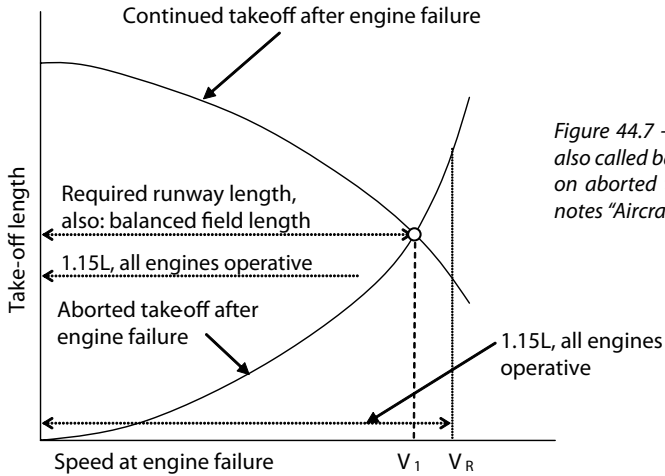
Figure 44.7 - Shortest required runway length, also called balanced field length, if dependence on aborted take-off is critical. Source: Lecture notes "Aircraft design", Delft, 1977 (in Dutch).

Continued takeoff after engine failure

Take-off length

Required take-off length

1.15L, all engines operative

Aborted take-off after engine failure

Speed at engine failure $V_1 = V_R$
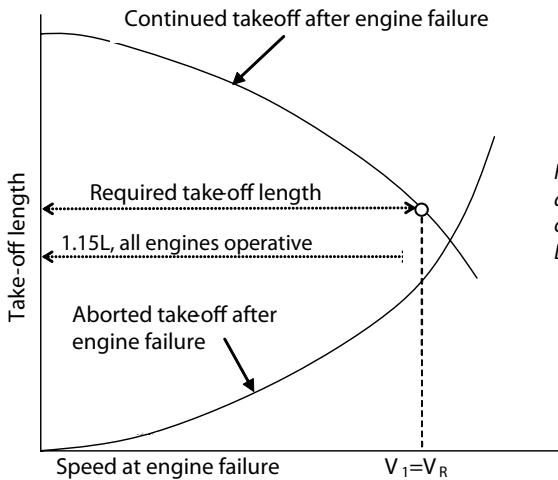
Figure 44.8 - Shortest required runway length at maximum V_1 and continuation of take-off is critical. Source: Lecture notes "Aircraft design", Delft, 1977 (in Dutch).

Continued takeoff after engine failure

Take-off length

Required take-off length
1.15L, all engines operating

Aborted take-off after engine failure

Speed at engine failure V_1 V_R
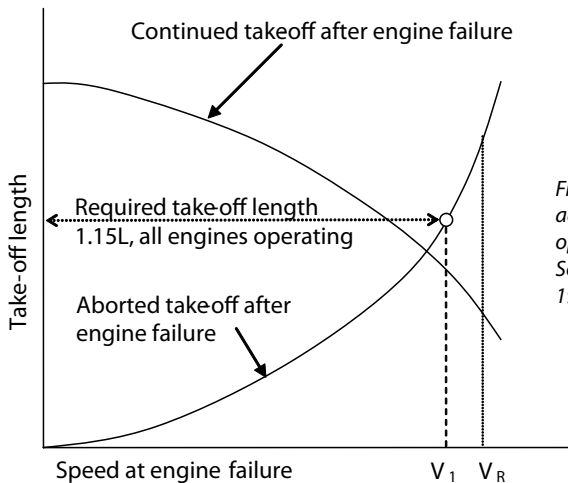
Figure 44.9 - Shortest runway length at adjusted V_1 (required runway length, all engines operative, then equal to aborted take-off). Source: Lecture notes "Aircraft design", Delft, 1977 (in Dutch).

The foregoing has illustrated the complexity of certification regulations regarding field performance. To illustrate this further, figure 44.10 shows one of the memory aids of Fokker's former performance specialists. The columns on the left explain the relevant flight conditions whereas the right part give the requirements on climb gradient the aircraft has to comply with.

Most important requirements for climb performance of civil transport aircraft with turbine engines

Class	Phase of flight	Flap setting for:	Under-carriage	Engine setting operative engine	No. in-operative engines	Calibrated air speed (CAS)	Height interval above runway	Aircraft weight	2-engined aircraft [%]	3-engined aircraft [%]	4-engined aircraft [%]	Notes
Climb gradient potential in take-off	Take-off	Take-off setting	Down	Take-off setting	1	V_{LOF}	$0 + h_{uu}$ (ft) (without ground effect)	Weight at V_{LOF}	≥ 0	≥ 0.3	≥ 0.5	Take-off gradient limits: runway length
Take-off flight path elements	Climb following take-off	Take-off	Up	Take-off setting	1	V_2 *	h_{uu} until 400 ft	Weight at h_{uu}	≥ 2.4	≥ 2.7	≥ 3.0	Take-off weight regardless of available runway length
-	Last climb segment of take-off	Cruise	Up	Max continued engine setting	1	$V_2 ≥ 1.25 V_s$	$h_{er} ≥ 1500$ ft	Weight at h_{er}	≥ 1.2	≥ 1.5	≥ 1.7	
Climb gradient potential in approach	"Approach" climb ***	Approach climb ***	Up	Take-off setting	1	$V ≤ 1.50 V_s$	0	Landing weight	≥ 2.1	≥ 2.4	≥ 2.7	Landing weight regardless of available landing length
	"Landing" climb	landing	down	Power available 8s after turning on engines	0	$V ≤ 1.3 V_s$	0	Landing weight	≥ 3.2	≥ 3.2	≥ 3.2	Landing weight of available landing length

Figure 44.10 - Most important requirements for climb performance of civil transport aircraft with turbine engines. Source: Federal Aviation Regulation Part 25, paragraphs 25.117 to 25.121

V_{LOF}	lift-off speed
V_2	take-off safety speed
V_s	stall speed
h_{uu}	height above runway, undercarriage retracted
h_{er}	height above runway, at the moment of finishing transition of take-off to cruise conditions
*	$V_2 ≥ 1.2 V_s$ for 2- and 3-engined turboprops and turbojet aircraft without V_s lowering influence by operative engines
**	flap setting chosen such, that $V_s ≤ 1.10 V_s$ for landing condition

Minimum unstick speed V$_{MU}$

Take-off performance is not only determined by the maximum lift coefficients, the lift-drag ratio, the engine characteristics and the brake performance. Other data that have to be obtained in certification flight tests are minimum control speeds, both on the ground and in the air and minimum unstick speeds (V$_{MU}$).

The minimum unstick speed is the minimum speed at which the aircraft is able to take-off within the certified take-off distance for the atmospheric and aircraft conditions under consideration.

This parameter had to be incorporated in the certification requirements with the introduction of jet transport aircraft. The certified take-off performance of propeller aircraft is based on maximum lift coefficients determined with idling engines or zero thrust. During take-off the propeller slipstream provides extra lift and often increases the stall angle so an early rotation does not necessarily cause an unsafe situation. Also on straight wings drag increase due to partial flow separation prior to the stall is insignificant.

If however, an early lift-off is attempted on a jet aircraft overrotation may lead to flow separation on the wing, either prior to or at the stall in ground effect, with a large increase in drag. This causes a loss of acceleration in the take-off run and initial climb-out. This occurred twice on the first certified civil jet transport aircraft, the De Havilland 106 Comet. In both cases the aircraft overran the threshold at the far end of the runway in an attempted take-off.

Also on early versions of the Boeing 707 the risk of overrotation existed necessitating the fitting of a ventral fin to limit the maximum achievable ground angle. On the highly swept wing with only part-span leading-edge flaps trailing edge separation started in ground proximity even at moderate angles of attack. This caused large variations in drag with only small variations in lift-off angle of attack well before reaching the angle-of-attack for maximum lift. This is illustrated in figure 44.11.

Figure 44.11 - Effect of the dorsal fin on the maximum ground angle of the Boeing 707. Source: Boeing Airliner July 1960.
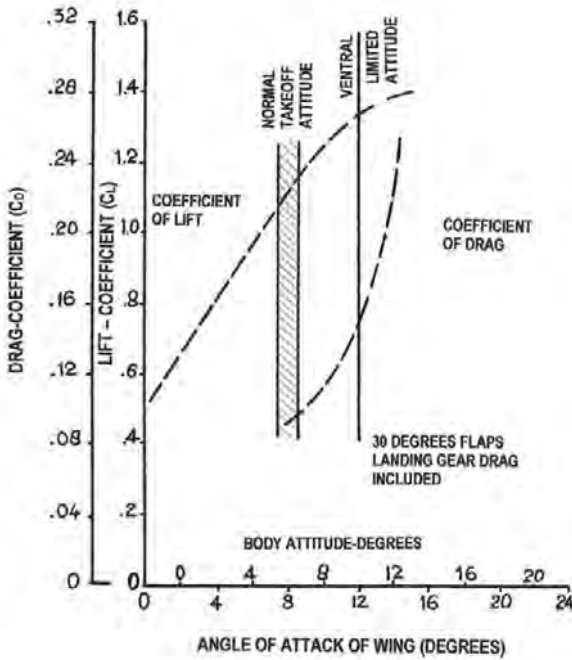
Swept wing

Increase of area with separated flow makes the viscous drag increase progressively

The ventral fin, in addition to improving directional stability at low speed, limits the maximum angle of rotation with the main gear wheels still on the runway during take-off. The size of the ventral fin varies between different models in accordance with airplane performance. As described in the article "707 Take-off Performance" (AIRLINER, for September 1959), rotating to an excessive angle-of-attack too early in the take-off run may extend the ground distance to take-off. Also excessive rotation, to the angle of where the aft body drags, may also decrease the climb-out immediately after take-off due to the increase in drag and the decrease in lift coefficient affecting wing performance.

On modern aircraft V_{MU} may be determined by three parameters:
1. wing stall in ground effect with the main wheels still on the ground
2. geometric limitations because the maximum usable C_L in ground effect is determined by the rear fuselage striking the runway
3. through a limited elevator capacity (the aircraft rotates so late that due to the aircraft's speed and acceleration the aircraft leaves the ground before the maximum lift coefficient in ground effect is reached.)

In figure 44.12 the lift curve for a flap setting $\delta_f = 20$ deg, both in free air and in ground effect with the main wheels just touching the ground, is presented for one of the wind tunnel models tested during the development of the Fokker 100. Also the drag polar in ground proximity is shown. At the wind tunnel Reynolds number Re = 3.1×10^6 the maximum lift coefficient in ground effect is reached $\alpha_R = 10.3$ deg.

An increase in angle-of-attack $\Delta\alpha_R = 0.5$ deg causes more than 60% increase in drag when the flow condition changes from fully attached flow to separated flow on the inboard wing. This illustrates the danger of overrotation in take-off, even when the aircraft is fully controllable.

During the initial flight tests with the Fokker 100 it turned out that at full-scale Reynolds numbers at the maximum ground angle $\alpha_R = 12.6$ deg only limited flow separation near the wing trailing edge was observed and the aircraft was geometry-limited for all take-off flap settings. Elevator capacity was checked and was found to be just sufficient not to affect V_{MU}.
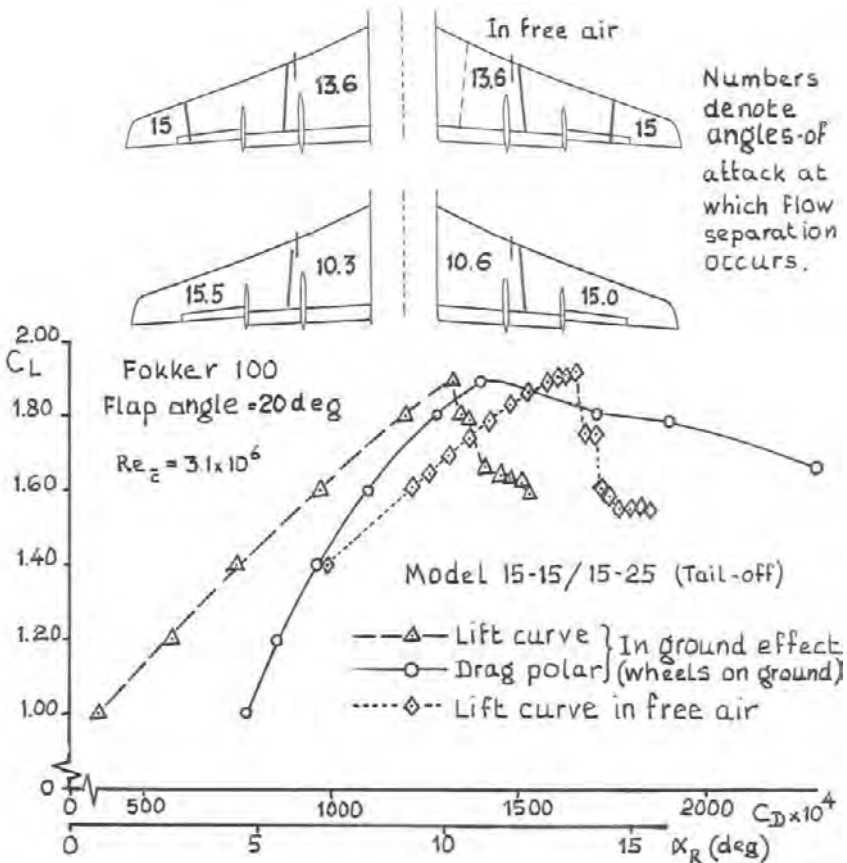
Figure 44.12 - Stalling characteristics in ground effect and free air of a Fokker 100 wind tunnel model. Source: Fokker Reports L-28-400 and L-28-566.

The situation was different on the Fokker F-28 Mk 4000. Ground runs showed flow separation on the inboard wing at $\alpha_R = 12.3$ deg to 11.5 deg, depending on flap angle as shown in figure 44.13. As the maximum ground angle was 15.7 deg V_{MU} was clearly determined by wing stall in ground effect. The maximum lift coefficient in ground effect was determined by making ground runs with successively increased angles-of-attack and recording the lift-off speed taking care to remain half a degree below the observed stall angle-of-attack.

The lift curves and the C_{Lmax} thus obtained but corrected for stabiliser setting, elevator deflection and the vertical component of the thrust are presented in figure 44.14 for the three take-off flap settings and compared to the free-air curves.
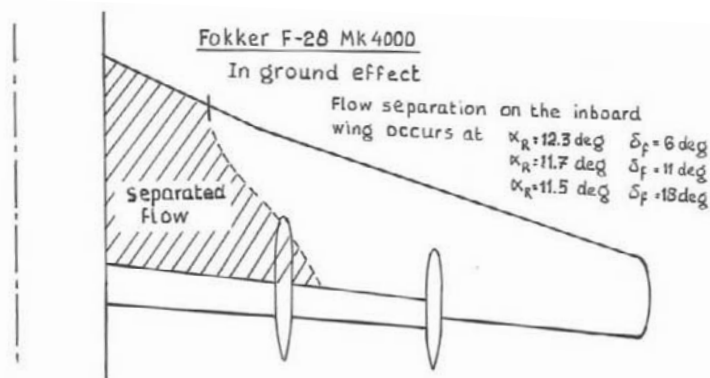
Figure 44.13 - Stalling characteristics in ground effect of the Fokker F-28 Mk 4000. Source: Fokker Reports H-28.40-27.002
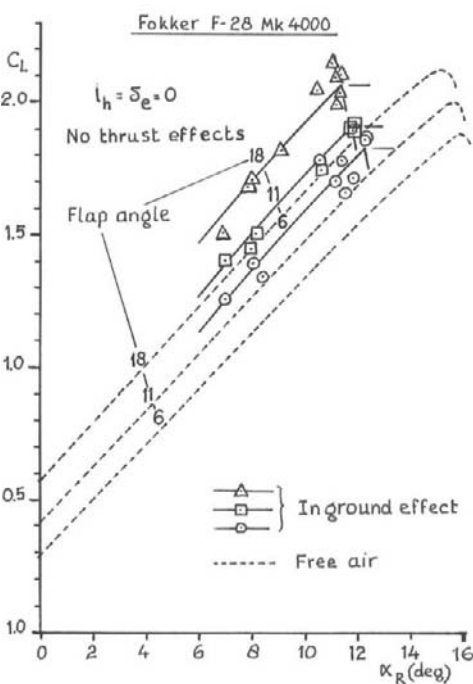
Figure 44.14 - Lift curves in ground effect and in free air of the Fokker F-28 Mk 4000.
Source: Fokker Reports H-28.40-27.002 and V-28-83.
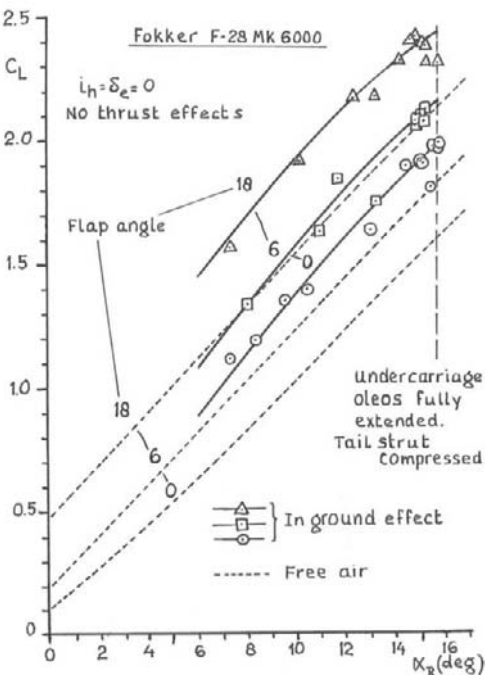
Figure 44.15 - Lift curves in ground effect and in free air of the Fokker F-28 Mk 6000.
Source: Fokker Report H-28.60-27.002.2

When the Fokker F-28 Mk 6000, the version equipped with slats, was developed it was clear that on this version V_{MU} would be geometry-limited. Flight tests were performed, similar to the V_{MU}-tests on the F-28 Mk 4000 albeit one year earlier. Because the aircraft would be able to lift off with the tail striking the runway the tail bumper was equipped with a wooden rubbing block.

Lift curves as obtained from the flight tests, both in ground effect and in free air are shown in figure 44.15.

As an illustration of a V_{MU}-test on a geometry-limited configuration figures 44.16 and 44.17 are presented showing the Airbus A340-600 and A380 taking-off at maximum ground angle.

Finally, a list of ground and flight tests to be performed related to aircraft performance is given in figure 44.18. This is presented to illustrate the extent of the evaluation and certification flight test programme devoted to performance.

For the complete certification flight test programme of a civil transport aircraft a large number of flights and flight hours (1,500 to 3,000 hrs) and the installation of much test instrumentation is required.

Figure 44.16 - Airbus A340-600 V_{MU} test. Source: Yannick Delamarre

Figure 44.17 - Airbus A380 V_{MU} test. Source: Airbus

List of performance ground and flight tests required for a certificate of airworthiness

1. Calibration of pitot-static system
   - with a towed static tube as a reference at low speed
   - with a towed static cone as a reference at high speed
   - calibration during ground runs.

2. Calibration of angle-of-attack and outside-air temperature sensors

3. Determination of stall speed and stall characteristics

4. Determination of minimum control speeds with one engine inoperative (V_{MCA} and V_{MCG})

5. Determination of the take-off performance
   - minimum unstick speed (V_{MU})
   - rotation speed (V_R)
   - lift-off speed (V_{LOF})
   - recognition time engine failure
   - runway length over 35ft obstacle
   - accelerate-stop length
   - take-off performance with an early rotation before the established V_R
These characteristics have to be determined with
   - all engines operative
   - one engine inoperative (for two-engined aircraft)
   - every flap setting for which the aircraft should be able to take-off

6. Landing performance over a 50 ft obstacle (for all landing flap settings)

7. Buffet-boundary at high Mach numbers

8. Climb performance in
   - take-off configuration (undercarriage up and down)
   - cruise configuration
   - approach configuration
   - landing configuration

9. Engine calibration in an altitude test facility

10. Determination of inlet and exhaust efficiency

Note:
Although the following subjects are in general not part of the basic certification procedure, with regard to field performance tests are also performed on
   - wet runways
   - runways with wet snow
   - the effect of failure of one of the braking devices of the aircraft

Figure 44.18 - List of performance-related ground and flight tests required for a certificate of airworthiness of a large civil transport aircraft

45 *Flight safety in civil aviation*

In the two previous chapters airworthiness regulations were explained. Those regulations were and are still being developed to make sure a certain safety level is reached and maintained in aviation. As with all forms of human activity expecting 100% safety in aviation is unrealistic. In contrast to other means of transportation however, aviation is the only one in which risk is (albeit grudgingly) accepted, failure rates are analysed and maximum "acceptable" failure rates are calculated.

Safety assessment is an essential part of aviation as it is related to both the willingness of passengers to fly and the acceptance of overflying aircraft by the population on the ground.

To assess safety, the following criteria are commonly used:

- Fatalities per 1000 million passenger-kilometres or passengers-miles
- Accidents per 1000 million passenger-kilometres or passengers-miles
- Fatalities per million aircraft-hours
- Accidents per million aircraft-hours
- Fatalities per million flights
- Accidents per million flights

Most often, the focus is on the number of accidents per flight or flight-hour.

Determining the safety level afterwards is a relatively easy task. Deciding beforehand what safety level should be achieved in aviation is far more difficult. It has to be related to the current technology level, to safety levels of other means of transportation, to air traffic density and many other factors. Despite many uncertainties the safety assessment is the basis for the current airworthiness regulations.

Using historical data, some of the earlier mentioned factors can be illustrated. Figure 45.1 shows the USA transportations fatalities in 1980, showing the number of air transport fatalities is relatively very low.

In the first years after the Second World War, many combat pilots became commercial airline pilots. But also maintenance standards and aircraft quality levels showed their origin to lie in wartime circumstances. This caused a number of accidents, but as peace conditions became established, authority overview increased and between 1947 and 1952 more pilots were trained specifically for commercial operations. This is reflected in the fatality rate in these years, see figure 45.2.
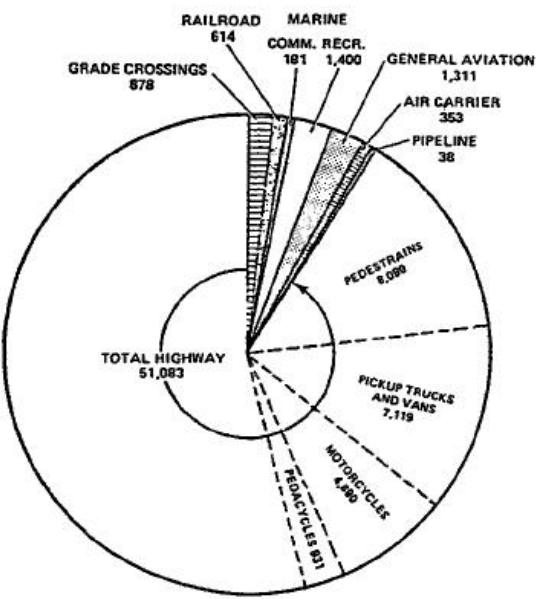
Figure 45.1 - Yearly accidents in the USA.
Source: Aviation Daily, 20-05-1980
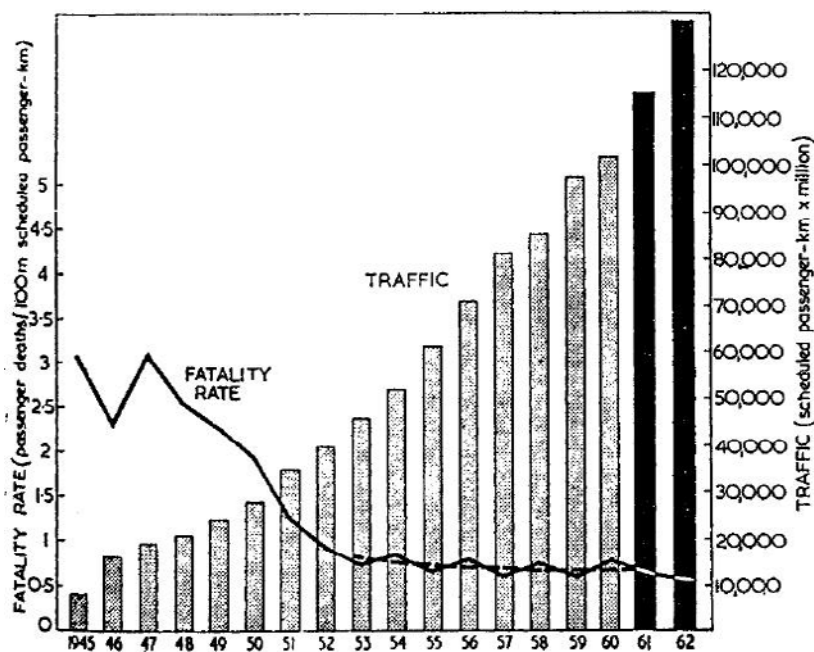
Figure 45.2 - ICAO World safety record (1961 and 1962 estimated).
Source: Flight international, 30 May 1963

The fatality rate in figure 45.2 shows only a gradual improvement between 1953 and 1962, but the situation changed after that year, as can be seen in figure 45.3. This figure shows the next step in the increase in flight safety: the introduction of jet engines. At first, jet engines meant a decrease in flight safety. Initially pilots were not aware of the fact that with the higher take-off and landing speeds coupled with the lack of propeller slipstream strict adherence to prescribed operating procedures was an absolute necessity.
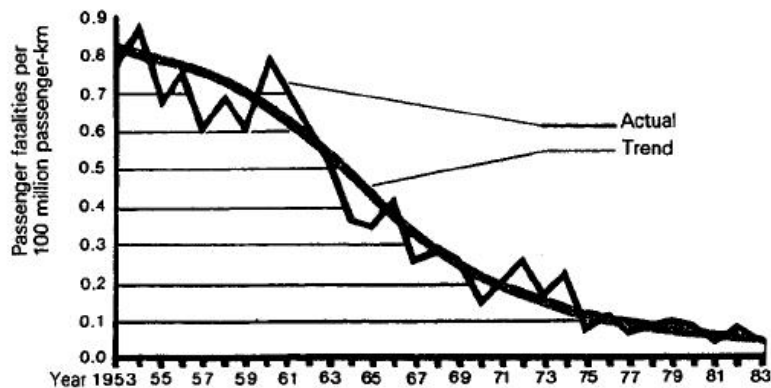
Figure 45.3 - World aviation accident rates. Source: Interavia 12/1984

New pilot training and procedural changes were necessary to teach the pilots to "fly according to the book", which eventually increased the safety level. This development is also illustrated in figures 45.4 to 45.7.
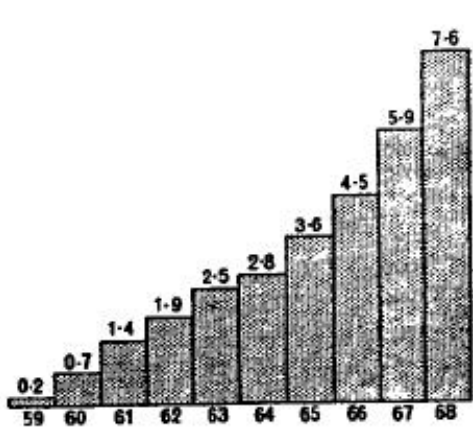
Figure 45.4 - Jet airliner flying hours per year (millions). Source: Flight International 6 January 1969
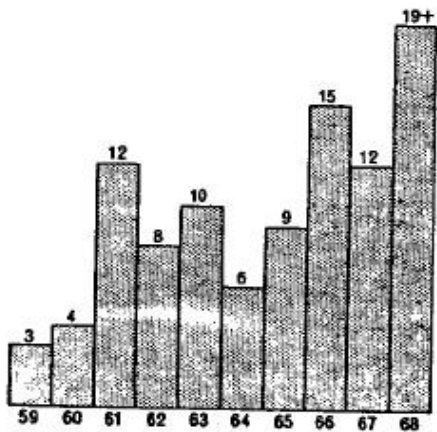
Figure 45.5 - Total losses, all circumstances. The 1968 figure does not include the aircraft destroyed at Beirut by the Isrealis on December 28. Source: Flight International 16 January 1969

611
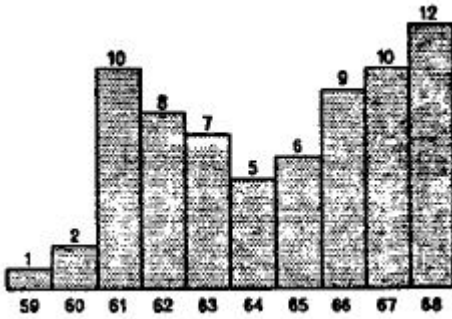
Figure 45.6 - Total losses on passenger revenue services. Source: Flight International 6 January 1969
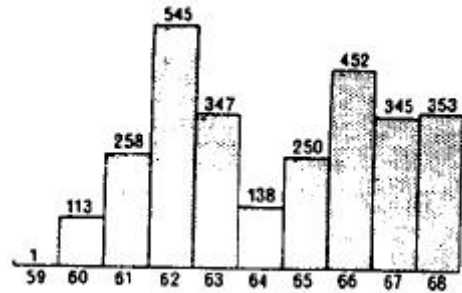
Figure 45.7 - Passenger fatalities. Source: Flight International 6 January 1969

A continuous decrease in the accident rate is necessary to prevent an increasing number of fatalities with an increasing number of flights.

This was described in 1984 by the International Civil Aviation Organisation (ICAO) as follows:

It is simple that if one killing per 100 million passenger-miles is acceptable to the industry today, it certainly is not going to be acceptable to the industry or to the public in 30 years' time, when the passenger-mileage volume will be so great that it will mean 10,000 people killed per year, and big, black air-crash headlines every other day.
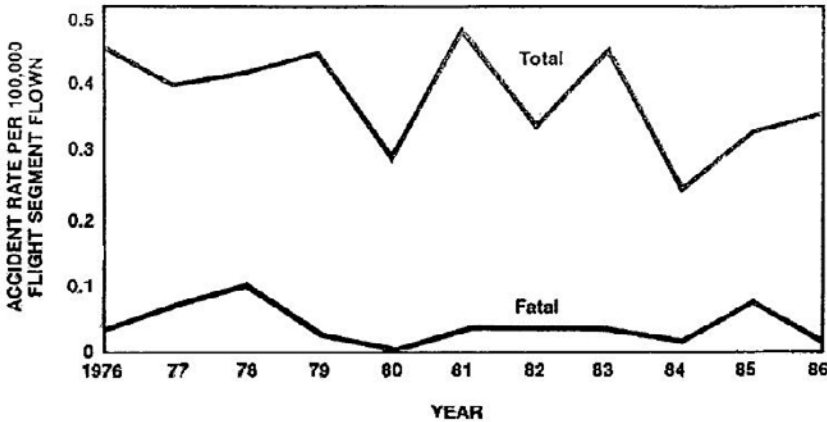
Figure 45.8 - Accident rates per 100,000 flight segments flown, U.S. scheduled air carriers operating under 14 CFR121, 1976-1986. Source: Aviation Week & Space Technology, July 13, 1987

That a slow improvement in commercial flight safety has occurred in the decade 1976-1986 is illustrated in figure 45.8.

Figure 45.9 gives an overview of a number of figures related to flight safety. Note that although more flights are performed every year, the number of passenger fatalities remains roughly the same.

When adding up worldwide passenger fatalities between 1950 and 1972, this amounts to 18,534 in 22 years. When comparing this to the 51,083 deaths in highway transport in the U.S. in 1980 alone (see figure 45.1), it can be stated that, although the comparison is not entirely valid when the total distance covered is not mentioned, air travel is a safe means of transport.

Year	Aircraft accidents	Passengers killed	Fatality rate per 100 million		Fatal accidents per 100 million		Fatal accidents per 100,000	
			Pass.-km	Pass.-miles	Km flown	Miles flown	Aircraft hours	Aircraft landings
1950	27	551	1·97	3·15	1·88	3·02	0·54	
1951	20	443	1·27	2·01	1·23	1·99	0·35	
1952	21	386	0·97	1·54	1·18	1·90	0·34	
1953	28	356	0·77	1·25	1·44	2·32	0·43	
1954	28	443	0·85	1·36	1·36	2·19	0·42	
1955	26	407	0·67	1·07	1·14	1·82	0·36	
1956	27[2]	552	0·78	1·25	1·06	1·71	0·34	
1957	31	507	0·62	0·99	1·09	1·76	0·36	
1958	30	609	0·72	1·15	1·02	1·65	0·34	
1959	28	613	0·63	1·00	0·91	1·46	0·31	
1960	34[2]	873	0·80	1·29	1·09	1·76	0·40	0·52
1961	25	805	0·69	1·11	0·80	1·29	0·31	0·38
1962	29	778	0·60	0·97	0·90	1·44	0·37	0·44
1963	31	715	0·49	0·78	0·90	1·46	0·39	0·46
1964	25	616	0·36	0·58	0·68	1·09	0·30	0·35
1965	25	684	0·35	0·56	0·61	0·98	0·29	0·33
1966	31[2]	1001	0·44	0·70	0·69	1·12	0·33	0·40
1967	30	678	0·25	0·40	0·57	0·91	0·29	0·35
1968	35	912	0·29	0·47	0·58	0·94	0·32	0·38
1969	32	946	0·27	0·43	0·48	0·77	0·27	0·34
1970	27	680	0·18	0·28	0·38	0·62	0·22	0·28
	29[3]	779	0·17	0·27	—	—	—	—
1971	31	859	0·22	0·35	0·44	0·71	0·27	0,33
	33[3]	967	0·20	0·32	—	—	—	—
1972	39	1089	0·24	0·38	0.57	0·92	0·34	—
	41[3]	1285	0·23	0·37	—	—	—	—

1. Data for 1970, 1971 and 1972 include the USSR.
2. Includes a mid-air collision counted as one accident.
3. Including the USSR.
4. Figures for 1972 include three collisions each counted as one accident.

Figure 45.9 - Accidents with passenger fatalities on scheduled air services, 1950-1972.
Source: Flight International, 18 January 1973

Between 1959 and 1978, the total fatal accident rate has decreased, though some aircraft types have contributed to this more than others, as can be seen from figure 45.10. This figure shows again that the first types of jet transport aircraft paid the "tuition fee" for learning how to operate jet transports. But also the operating environment played an important role. For some operators the changes, when they started operating jet aircraft, were much larger than for others.
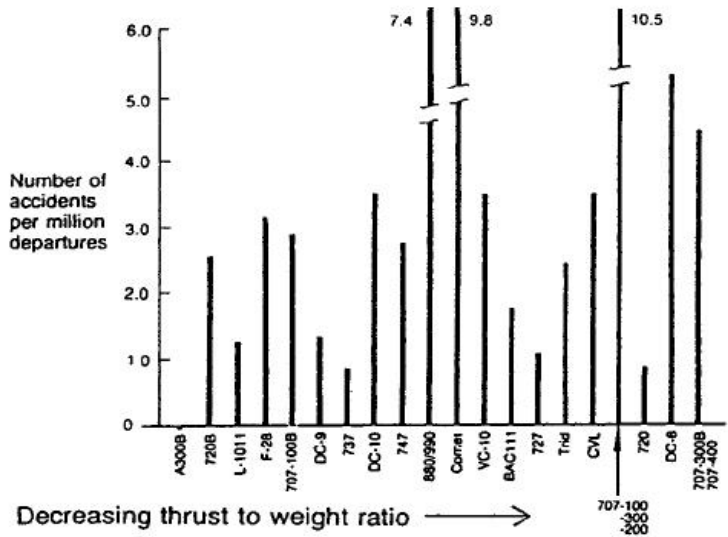
Figure 45.10 - Hull loss accident rate, world wide air carriers; all
operations 1959 - 1978. Source: Boeing airliner July-Sept 1980

Finally some recent flight safety statistics are presented.

Figure 45.11 shows that the number of flights is steadily increasing. The number
of fatal accidents is slightly decreasing, as shown from the vertical bars. This
means the safety level has increased in recent years as is confirmed in figure
45.12.
In figure 45.13 the most recent statistics are presented for U.S. FAR Part 121 and
Part 135 operators.
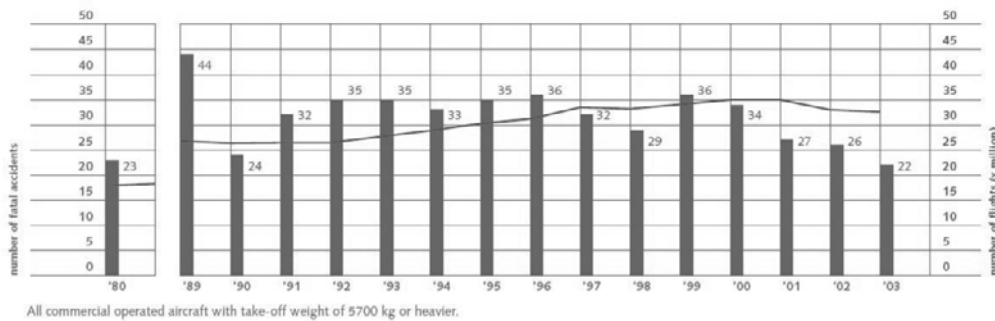
Figure 45.11 - Number of flights and fatal accidents, worldwide, 1989-2003 (only aircraft with MTOW > 5700 kg).
Source: Civil Aviation Safety Data, 1989-2003
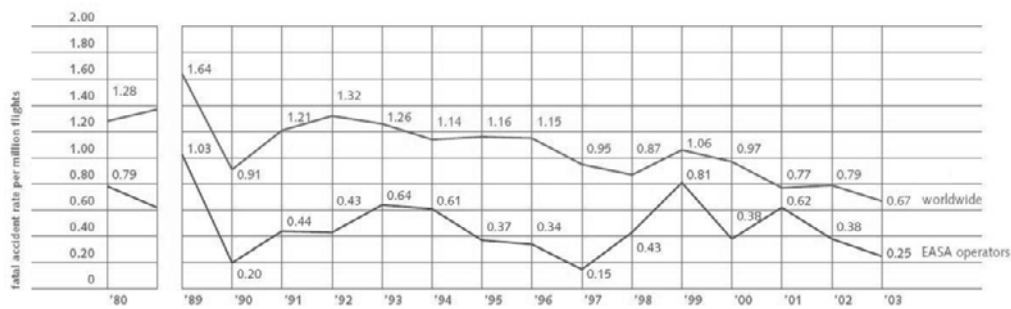
Figure 45.12 - Fatal accident rate, commercial operators, 1989-2003.
Source: Civil Aviation Safety Data, 1989-2003
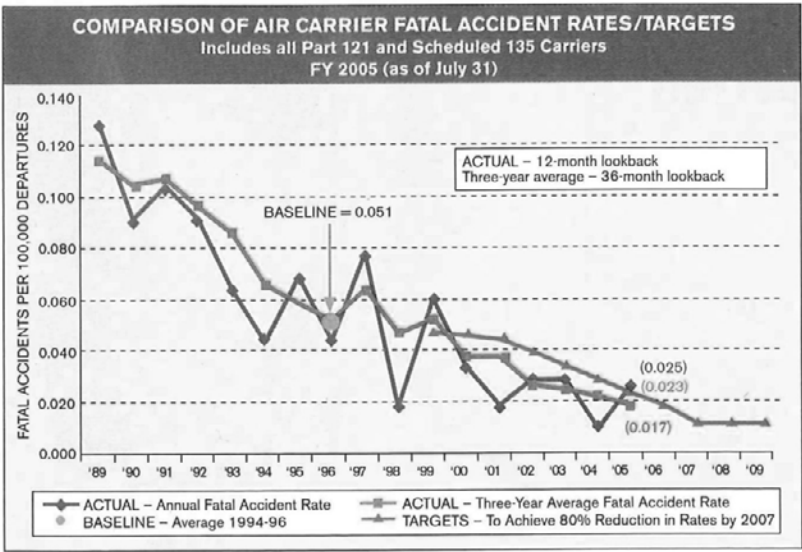
Figure 45.13 - The current US fatal accident rate of 0.017 per 100,000 departures
surpasses the 2005 goal of 0.023 per 100,000 departures.
Source: Aviation Week & Space Technology, August 22-29, 2005

The fatal accident rate can be considered per region. There are clearly large differences not only influenced by operating procedures within an operator, but also related to the intensity of inspections by the authorities, in short by political and cultural circumstances. A global overview of accident rates per continent is shown in figure 45.14.

615
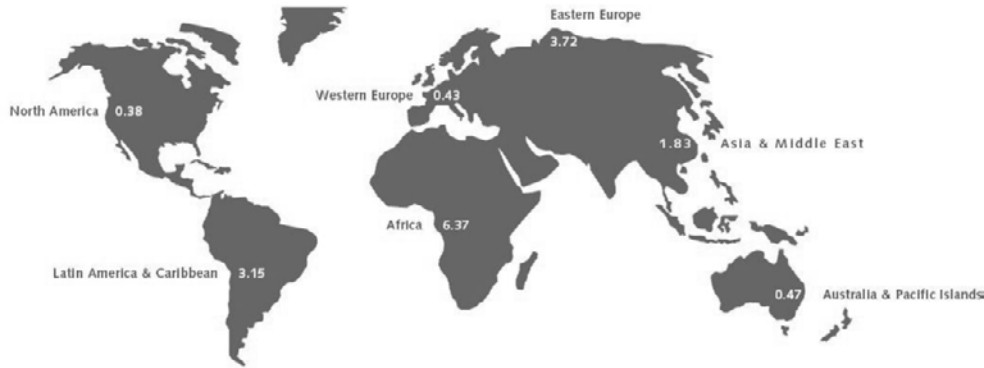
Figure 45.14- Fatal accident rate per region, domicile operator.
Source: Civil Aviation Safety Data, 1989-2003

In figure 45.15 the flight phase in which fatal accidents occur is shown. The landing is percentage-wise the phase in which most accidents happen. This can be explained as follows:

The average take-off develops, if no engine failure, tire burst or bird ingestion occurs, according to a fairly predictable pattern. Given the aircraft is properly loaded and trimmed before take-off, it climbs away from the ground and so increases its room to manoeuvre.

In a landing the situation is reversed. When the aircraft approaches the runway the room to manoeuvre literally and figuratively speaking diminishes. Approaches in mountainous areas under adverse Instrument Meteorological Conditions (IMC) with very low visibility and strong gusts and rain are far more usual than an aborted take-off at high speed. When in such circumstances on final approach the runway comes in sight the pilot has just a few seconds to judge the situation and to decide whether to continue the landing or make a go-around. It is usually in such conditions that accidents occur, not necessarily after touching down on the runway but also by flying into the ground in a non-precision approach, so-called Controlled Flight Into Terrain (CFIT).
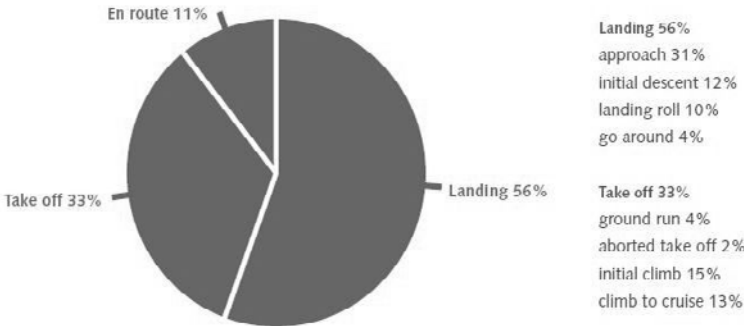
Figure 45.15 - Fatal accident and flight phase, worldwide, 1989-2003.
Source: Civil Aviation Safety Data, 1989-2003

Sometimes it is tried to group accidents per type, such as in figure 45.16. Such statistics should only be considered as indicative. Most accidents do not occur for one reason only, but happen as an accumulation of several occurrences. In this figure, the most significant event leading to the accident is shown.

Note that the percentage per type of occurrence and number of onboard fatalities is not linked. An explosion or fire occurs less often than undershooting or overrunning the runway, but it results in more onboard fatalities.

Figure 45.17 shows contributing factors in the causal chain of events leading to a fatal accident. Accidents are relatively often pilot-related. Human factors research may reduce this as a factor. This holds as well for the accidents related to maintenance and air traffic control.
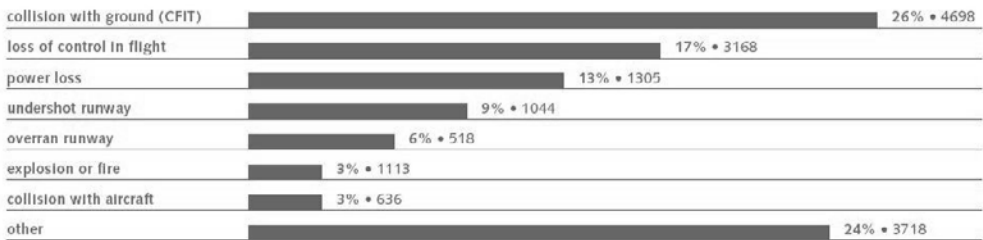
Figure 45.16 - Type of occurrences and fatalities, worldwide, 1989-2003 (percentage type of occurrence; number of on board fatalities). Source: Civil Aviation Safety Data, 1989-2003
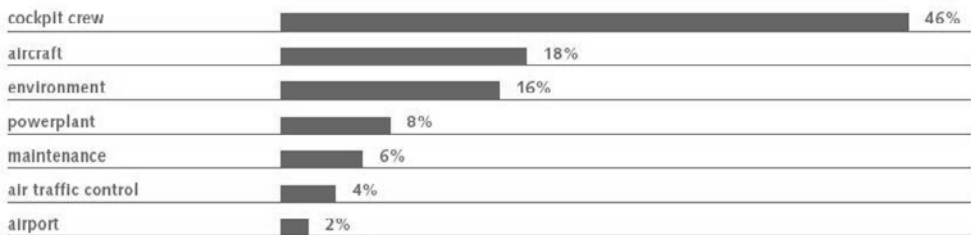
Figure 45.17 - Contributing factors in fatal accidents, worldwide, 1989-2003.
Source: Civil Aviation Safety Data, 1989-2003

One of the most demanding safety requirements in the certification regulations is section 25.1309 which states that the possibility that a single failure can become catastrophic, must be extremely improbable, which means a probability of less than 10^{-9} per flight hour. This number is not mentioned in the requirement but in the interpretative material AMJ 25.1309. This requirement is based on the reliability of critical flight systems and the probability and severity of their failure. These critical flight systems are described in figure 45.18, and the origin of the requirement is given in figure 45.19.

(a) The equipment, systems, and installations whose functioning is required by this subchapter must be designed to ensure that they perform their intended functions under any forseeable operating condition.

(b) The airplane systems and associated components, considered separately and in relation to other systems, must be designed so that —

(1) The occurrence of any failure condition which would prevent the continued safe flight and landing of the airplane is extremely improbable, and

(2) The occurrence of any other failure condition which would reduce the capability of the airplane or the ability of the crew to cope with adverse operating conditions is improbable.

(c) Warning information must be provided to alert the crew to unsafe system operating conditions and to enable them to take appropriate corrective action. Systems, controls, and associated monitoring and warning means must be designed to minimize crew errors which would create additional hazards.

(d) Compliance with the requirements of paragraph (b) of this section must be shown by analysis, and where necessary, by appropriate ground, flight, or simulator tests. The analysis must consider —

(1) Possible modes of failure, including malfunctions and damage from external sources.

(2) The probability of multiple failures and undetected failures.

(3) The resulting effects on the airplane and occupants, considering the stage of flight and operating conditions, and

(4) The crew warning cues, corrective action required, and the capability of detecting faults.

Figure 45.18 - Section 25.1309 - Equipment, systems, and installations.
Source: Federal Air Regulation Part 25.1309.

The approach taken by the world's regulatory agencies in establishing rational probability values for use in assessing the acceptability of a system design was as follows: Although the accident rate due to operation- and airframe-related causes was difficult to ascertain exactly because the causes of an accident are seldom simple, history indicated that the risk of a serious accident due to such causes was approximately 1×10^{-6} per hour of flight. History further indicated that about 10 percent of the total, or 1×10^{-7}, was attributable to system problems (power, control, avionics, etc.). It was thereby possible to require that the probability of an accident contributed to by an aircraft's systems be no greater than 1×10^{-7}, but this would have been an awkward requirement because it is not possible to say whether the requirement has been met until all systems are collectively analyzed.

Furthermore, if the requirement was not met, it might be difficult to decide which system or systems should be modified in order to meet it. For this reason it was decided to assume arbitrarily that there are 100 potential failure conditions in an airplane which could contribute significantly to the cause of a serious accident. The allowable risk of 10^{-7} was thus apportioned equally among these conditions, resulting in a risk allocation of 1×10^{-9} to each. The agencies therefore concluded that the acceptable upper-risk limit for an identified catastrophic system-related failure condition would be 1×10^{-9} for each hour of flight, and that failure conditions having less severe effects could be relatively more likely on an inverse scale.

Figure 45.19 - Origin of 10^9 requirement. Source: SAE Paper No 831406

To graphically describe different safety levels figure 45.20 has been prepared. It relates the severity of an effect to the probability of an occurrence, and also takes into account the capability of the aircraft and the ability of the crew to cope with the effect. It shows again that the accepted probability of catastrophic effects of a single system failure is 10^{-9} per flight hour, making the failure extremely improbable.
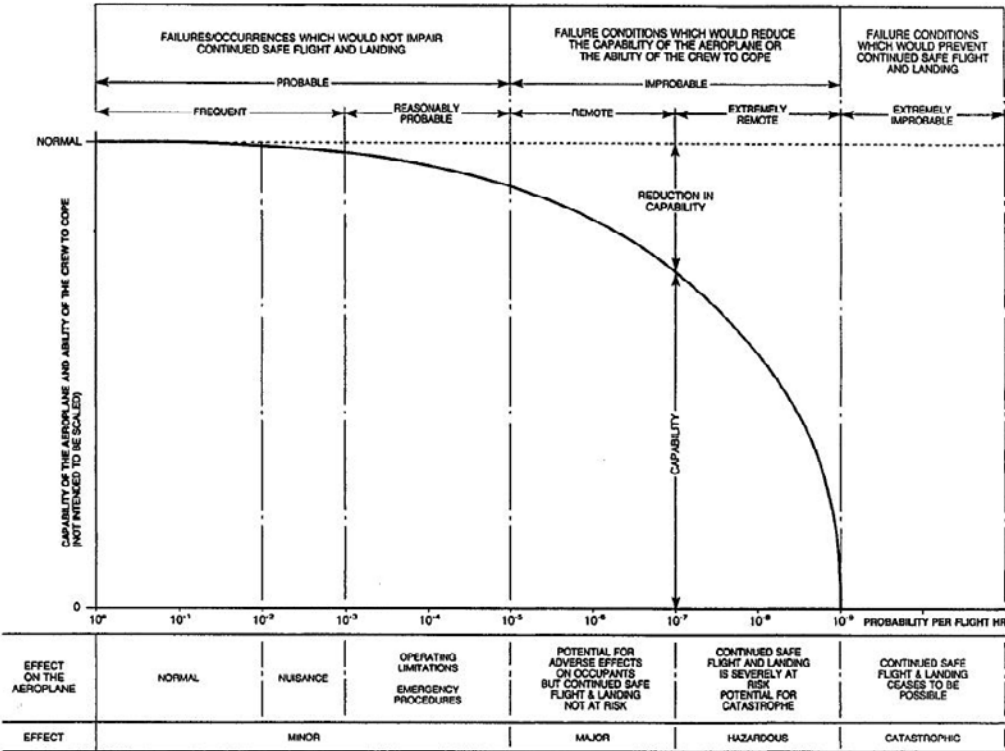
Figure 45.20 - Relationship between probablity and severity of failure condition. Source: SAE Paper No 831406

Section 25.1309 in the airworthiness regulations has been highly instrumental in improving the integrity of aircraft systems. However in today's civil aviation environment safety is only partly determined by the proper functioning of the technical equipment in the strict sense. The function of many pieces of equipment, both in the aircraft and on the ground is to aid the human operator in monitoring his working environment and attract his attention unambiguously and point to how to rectify the situation if something abnormal occurs. It is particularly in the complex combination of operating the aircraft and at the same time being part of a crowded air traffic system that a maximum situation awareness is demanded of both pilot and air traffic controller and their mutual understanding. Effort to fulfill these demands is of paramount importance if continued improvements in flight safety are to be achieved.

Sources

Aero Magazine
No. 17   Blended winglets for improved airplane performance, 1st Q. 2002.

Aeronautical Engineering Review
----------   Evans, R. E., Operational aspects of the SAC transition to jets, November 1956.

The Aeronautical Journal of the RAeS.
----------   Smith, J.P., The development of the Trident series, November 1969.

The Aeronautical Quarterly
-----------   Küchemann, D., The distribution of lift over the surface of swept wings, August, 1953.
-----------   Lock, R.C., Fulker, J.L., Design of supercritical aerofoils, November, 1974

The Aeroplane and Astronautics
-----------   March 25, 1960.

Aeronautics and Astronautics
-----------   Goodmanson, L.T., Gratzer, L.B., Recent advances in aerodynamics for transport aircraft, December 1973.

L'Aeronautique et L'Astronautique
-----------   Airbus Industrie A 310. No. 91 - 1981-6, page 15.
-----------   Deque, R., Puyplat, D., De l' A300 à l' A310. No. 93 - 1982-2.

Aerospace
-----------   Back, R.F., Wedderspoon, J.R., The A320 wing - Designing for commercial success, January 1986.

AFFDL Reports

AFFDL-TR-73   Methods for predicting the aerodynamic and stability and control -146, Vol. I, II, III. characteristics of STOL aircraft. (Douglas Aircraft Co.), 1973.

AGARD Conference Proceedings

CP-46   Aeroelastic effects from a flight mechanics standpoint, Paper no. 17.
Schoernack,W., Hässler,E., Theoretical investigation of aeroelastic influences on the lift distribution and the aerodynamic derivatives of swept wings at symmetric and antisymmetric stationary flight conditions,1969.

CP-102   Fluid dynamics of aircraft stalling, Paper no.10.
Smith, A.M.O., Aerodynamics of high-lift airfoil systems, 1972.
Fluid dynamics of aircraft stalling, Paper no.21.
Wimpress, J.K., Predicting the low-speed stall characteristics of the Boeing 747, 1972.

CP-124   Aerodynamic drag, Paper no. 1.
Paterson, J.H., MacWilkinson, D.G., Blackerby, W.T., A survey of drag prediction techniques applicable to subsonic and transonic aircraft design, 1973.
Paper no. 24.
Rooney,E.C., Development of techniques to measure in-flight drag of a U.S. Navy fighter airplane and correlation of flight measured drag with wind tunnel data, 1973.

CP-143   V/STOL Aerodynamics, Paper no.13
Ljungström, B.L.G., Experimental high lift optimisation of multiple element airfoils, 1974.

CP-150   Airframe / propulsion interference, Paper no. 20.
Rohling, W.J., The influence of nacelle afterbody shape on airplane drag, 974

CP-160   Take-off and Landing. Paper no. 10.
Obert, E., Low-speed stability and control characteristics of transport aircraft with particular reference to tailplane design, 1974.

CP-242   Performance prediction methods, Paper no.21.
Hopps, R.H., Danforth, E.C.B., Correlation of wind-tunnel and flight-test data for the Lockheed L-1011 Tri-Star airplane,1977.

CP-285	Subsonic / transonic configuration aerodynamics, Paper no. 11.
	Jupp, J.A., Interference aspects of the A310 high speed wing configuration, 1980
CP-336	Aerodynamics and Acoustics of Propellers. Paper no. 5.
	occi, A.J., Morrison, J.I., A review of ARA research into propeller aerodynamic prediction methods.
CP-339	Ground / flight test techniques and correlation. Paper no. 7
	Mavriplis, F., Comparison of prediction, wind tunnel and flight test data for the Canadair Challenger turbofan aircraft, 1982.
CP-348	Wind tunnels and testing techniques. Paper no.22.
	Saiz, M., Quemard, C., Essais dans la soufflerie F1 de l'ONERA – Comparaison vol-soufflerie, 1983.
CP-365	Improvement of aerodynamic performance through boundary layer control and high lift systems, Paper no. 3.
	Oskam, B., Laan, D.J., Volkers,D.F., Recent advances in computational methods to solve the high-lift multi-component airfoil problem, 1984.
	Paper no. 9.
	Dillner, B., May, F.W., McMasters, J.H., Aerodynamic issues in the design of high-lift systems for transport aircraft, 1984.

AGARD Lecture Series

LS-37	High Reynolds number subsonic aerodynamics, Lecture series 16, 1969.
	Little Jr.,B.H., Advantages and problems of large subsonic aircraft. Paper no.1
	Paterson, J.H., scaling effects on drag prediction. Paper no 4.
	Ryle, D.M.,. High Reynolds number subsonic aerodynamics, Paper no. 6.
LS-43	Assessment of lift augmentation devices. Paper no. 7.
	Gratzer, L.B., Analysis of transport applications for high-lift schemes, 1970.
LS-56	Aircraft performance – prediction methods and optimization. Paper no. 2.
	Williams, J., Airfield performance prediction methods for transport and combat Aircraft, 1972.

LS-67	Prediction methods for aircraft aerodynamic characteristics, Paper no. 2
	Callaghan, J.G., Aerodynamic prediction methods for aircraft at low speeds with mechanical high lift devices, 1974.
LS-67	Paper no.4,
	Bowes, G.M., Aircraft lift and drag prediction and measurement, 1974.

AGARD Reports

R-712	Special course on subsonic/transonic aerodynamic interference for aircraft.
	Rettie, I.H., Aerodynamic design for overall vehicle performance. Paper 6.
	Rettie, I.H., Interference problems in aircraft design. Paper 7, 1983

AGARDographs

| No.103 | Aerodynamics of power plant installation, 1965. |

AIAA Papers

AIAA-65-738	Shevell, R.S., Schaufele, R.D., Aerodynamic design features of the DC-9.
AIAA-69-830	Bates, R.E., Progress on the DC-10 development program, 1969.
AIAA-71-289	George-Falvy, D., Scale effect studies of airfoil profile drag at high subsonic speed, 1971. (Boeing 727)
AIAA-72-188	Rubbert, P.E., Saaris, G.R., Review and evaluation of a three-dimensional lifting potential flow analysis method for arbitrary configurations, 1972.
AIAA-73-792	Burdges, K.P., A synthesis of transonic, 2-D airfoil technology, 1973.
AIAA-73-778	O'Laughlin, B.D., Graham, E.L., S-3A development tests, 1973.
AIAA-74-939	Smith, A.M.O., High-lift aerodynamics, 1974
AIAA-75-996	Axelson, J. A. ,Estimation of transonic aircraft aerodynamics to high angles of attack, 1975. Also in : Journal of aircraft, June 1977.
AIAA-76-940	Ishimitsu, Kitchio, K., Aerodynamic design and analysis of winglets, 1976.

AIAA-79-0066	Blackerby, W.T., Johnson,W.K., Application of advanced technologies to improve C-141 cruise performance, 1979.
AIAA-79-1795	Sullivan, R.L., The size and performance effects of high lift system technology on a modern twin engine jet transport, 1979
AIAA-79-1873	Mack, M.D., Seetharam, H.C., Kuhn, W.G., Bright, J.T., Aerodynamics of spoiler control devices, 1979.
AIAA-80-1196	Dusa, D.J., Hrach, F.J., CF6-50 Short core exhaust nozzle, 1980.
AIAA-81-1694	Putnam, L.E., Mace, J., A survey of aftbody flow prediction methods, 1981.
AIAA-80-1391	Yu, N.J., Grid generation and transonic flow calculations for three-dimensional configurations, 1980.
AIAA-83-1368	Chen, A.W., Tinoco, E.N., PAN AIR Applications to aero-propulsion integration, 1983. Also in: Journal of Aircraft , March 1984.
AIAA-83-1845	Murillo,L,E., McMasters,J.H., A method for predicting low-speed aerodynamic characteristics of transport aircraft, 1983.
AIAA-83-2060	Rubbert, P.E., Tinoco E.N., Impact of computational methods on aircraft design, 1983.
AIAA-84-0381	Tinoco, E.N., Chen, A.W., Transonic CFD applications to engine/airframe integration, 1984.
AIAA-84-0614	Hallstaff, T.H., Brune, G.W., An investigation of civil transport aft-body drag using a three-dimensional wake survey method, 1984
AIAA-84-2487	Motycka, D.L., Welling,S.W., Lewis-Smith,F.A., Comparison of model and full scale inlet distortions for subsonic commercial transport inlets, 1984.
AIAA-85-4067	Shevell, R.S., Aerodynamic bugs: Can CFD spray them away? 1985.
AIAA-86-1536	Jackson, J., Development of the Boeing 767 thrust reverser, 1986.
AIAA-86-1811	Tinoco, E.N., Ball, D.N., Rice II, F.A., PAN AIR analysis of a transport high-lift configuration, 1986. Also in: Journal of aircraft, March 1987.
AIAA-87-0454	Yu, N.J., Kusunose, K., Chen, H.C., Sommerfield, D.M., Flow simulations for a complex airplane configuration using Euler equations, 1987.
AIAA-87-1921	Identical to Paper AIAA-86- 1536.

AIAA-87-2928	Field, G. G., MD-11 Design – Evolution, not revolution, 1987.
AIAA-90-3084	van den Borne, P.C.M., van Hengst, J., Investigation of Propeller Slipstream Effects on the Fokker 50 Through in-Flight Pressure Measurements., 1990.
AIAA-93-3140	van Dam, C.P., Vijgen, P.M.H.W., Yip, L.P., Potter, R.C., Leading-edge transition and relaminarization phenomena on a subsonic high-lift system, 1993.

AIAA Professional study series

| ---------- | Steiner, J.E., et al., Case study in aircraft design – The Boeing 727, 1978. |
| ---------- | Hiscocks, R. E., A case study on the De Havilland STOL commuter aircraft. |

Air et Cosmos

----------	Anon., American et Delta commandent le B.767, 25 novembre 1978.
----------	Anon., A.300-600: des résultats déjà très satisfaisants, 10 septembre 1983.
----------	Anon., L' A.300-600 consomme moins et va plus loin, 24 mars 1984.

Aircraft engineering

-----------	Hay, J.A., Vickers VC-10, Part one – Aerodynamic design, June 1962.
-----------	Prior, B.J., BAC One-Eleven – Aerodynamic design., May 1963.
-----------	Sutton, J.M.D., Thrust reverser design for airframe compatibility, 1976.
-----------	Smith, J.P., Considerations in the design of large twin engined transport aircraft, October, 1969.

A.R.C. Current Papers

| C.P. No. 1170 | Simper, J.I., Hutton, P.G., Results of a series of wind tunnel model breakdown tests on the Trident 1 aircraft and a comparison with drag estimates and full scale flight data, 1971 |

C.P. No. 1125   Taylor, C.R., Hall, J.R., Hayward, R.W., Super VC-10 cruise drag – A wind-tunnel investigation. Part I   Experimental techniques, 1970.

A.R.C. Reports & Memoranda

R.& M. No.1874   Young, A.D., The calculation of the total and skin friction drags of bodies of revolution at zero incidence, 1939.

R.& M. No. 2479   Warren, C.H.E., Kirk, J.A., Wind-tunnel investigation of fin and rudder accidents on heavy bombers (Halifax and Lancaster).

R.& M. No. 2849   Pearcey, H.H., Faber, M.E., Detailed observations made at high incidences and at high subsonic Mach numbers on Goldstein 1442/1547 aerofoil, 1950.

R.& M. No. 2908   Küchemann, D., Weber, J., The subsonic flow past swept wings at zero lift without and with body, 1956.

R.& M. No. 3346   Lock, R.C., An equivalence law relating three- and two-dimensional pressure distributions, 1962.

R.& M. No. 3608 I   Isaacs, D., Wind tunnel measurements of the low-speed stalling characteristics of a model of the Hawker Siddeley Trident I C, 1968.

R.& M. No. 3707   Browne ,G.C., Bateman, T.E.B., Pavitt, M., Haines , A.B., A comparison of wing pressure distributions measured in flight and on a windtunnel model of the Super VC-10,197.

ASME Papers

ASME 69-GT-52   Saylor, J.M., Hancock, J.P., C-5 engine inlet development , 1969.

Aviation Week (and Space Technology)

---------   Anon. PanAm 707 dives 29000 ft, February 9,1959.

---------   Anon. CAB opens hearings on PanAm 707 Atlantic dive; crew testifies, March, 23,1959.

---------   Anon. Maker strives to regain SN-600 pace, May 31,1971, page 221.

---------   Anon. French start SN-600 production, October 18,1971, page 17.

---------   Anon. Giant jet's teething problems easing, February 28,1972.

---------   Anon. Autopilot trim runaway. In article: Air Siam cancels acquisition plans for A-300B4 transport, October 20,1975.

---------   O'Lone, R.G., Swissair orders improved 747 version, June 16, 1980.

---------   Proctor, P., Boeing poised to offer stretched 747 versions, February 5,1996.

---------   Smith, B.A., Boeing revamps 747X wing design, March 12, 2001.

---------   Fiorino, F. Safety in numbers, August 22-29, 2005.

Boeing Airliner

---------   Anon., Flight improvement program, July 1960. (Boeing 707).

---------   Bartley, G., Model 777 primary flight control system, October-December 1994.

---------   Arnold, H., The new 737-600, -700, - 800. January-March 1996.

Canadian Aeronautical Journal

---------   Raymond, A.E., A Philosophy of jet transport design. (Douglas DC-8) October 1960.

Canadian Aeronautics and Space Journal

--------   Bauer, A.B., Smith, A.M.O., Hess, J.L., Potential flow and boundary layer theory as design tools in aerodynamics, February 1970.

---------   Eggleston,B., R & D in the evolution of the Dash 8, September 1984.

Douglas Flight Approach

---------   Anon., Flying the DC-10 – An experience in performance, December 1971.

---------   Anon., Proving the numbers: the take-off regime, parts 1 & 2, April 1972.

---------   Anon., The DC-10's high-lift wing, 1972.

Douglas Papers

Paper 7026   Lynch, F.T., Commercial transports – Aerodynamic design for cruise performance efficiency. – Transonic perspective symposium, February 1981.

--------- Callaghan, J.G., Oliver, W.R., Development of an advanced-technology high-lift system for an energy-efficient transport, 1979.

Flight International

--------- Anon., The Super VC-10, 1 April 1965.
--------- Harrison, N., Boeing 747, 12 December 1968.
--------- Hirst, M., Marsden, J., Longhorns into service, 10 February 1979.
--------- Hopkins, H., The state of the art – Flight-test Airbus A320, 12 December 1987.
--------- Kingsley-Jones, M., Have four engines, will travel far, 2-8 September 1998. (Airbus A340-500/-600).

Fokker Reports

A-140 Schoonveld, E.R., An analysis of recent two-dimensional airfoil drag data, 1982.
A-143 Volkers, D.F., A method for buffet onset prediction., 1982.
A-158 Obert, E., A data compilation on the high-lift characteristics of modern single- and multi-component two-dimensional airfoil sections, 1985.
A-166 Obert, E., Drag due to flap extension on multi-component airfoil sections, 1985.
A-173 Obert, E., A procedure for the determination of trimmed drag polars for transport aircraft with flaps deflected, 1986.
A-225 Jansen, M.H.E., An evaluation of methods for the calculation of the flow around a propeller at angle of attack, Part A and B, 1991.
H-0-83 Obert, E., An analysis of the low-speed zero-lift pitching moment, aerodynamic centre position and downwash characteristics of tail-off transport aircraft configurations, 1991.
H-28.40-27.001 Schuringa, Tj., Stalling speed determination; flap settings 0, 6, 11, 18, 25 and 42 deg; Influence of landing gear position. (F-28 Mk 4000), 1975.
H-28.40-27.002 Obert, E., Special performance items. Determination of VMU. (F-28 Mk 4000), 1975
H-28.60-27.002.2 Obert, E., Special performance items. Determination of VMU. (F-28 Mk 6000), 1974.

HX-28-S89-001	Boer, N., Koch, T., F-28 Mk0100 / Rolls-RoyceTay Mk620-15. Performance Engineers Manual, 1989.
L-27-204	Voogt, N., Prediction of transonic drag development for the F-27 root section, 1984.
L-28-88	Bergmeyer, P., Adaptation of the F-27 longitudinal control for further development of the aircraft, 1959. (in Dutch).
L-28-316	Voogt,N., Assessment of transonic drag reduction resulting from an F-28 wing leading edge reduction, 1983.
L-28-341	Voogt, N., Design computations for F-28 wing modification W10, 1983.
L-28-400	Boer. J. N., Aerodynamic characteristics of an F-28 Mk 0100 wind tunnel model, Model 15-15, 1984.
L-28-448	Kuijvenhoven, J.L., Numerical prediction of buffet onset for the Fokker 100, 1987.
L-28-566	van Rooy, L., Experimental investigation of aerodynamic characteristics of Fokker 100 and Fokker 70 configurations Model 15-25 in the HST wind tunnel,1994.
L-29-118	Hogenhuis, H, Willemse, W.H.A.R., Schoonveld, E., de Hay, L., van den Bovenkamp, N., Aerodynamic characteristics of a high-speed F-29 windtunnel model – Model 1-1, 1980.
L-29-132	van Hengst, J., Nacelle design for the CFM56-3 engine, 1981.
L-29-135	van den Bovenkamp, N., Hogenhuis, H., Warrink, B., Willemse, W., Aerodynamic characteristics of an HST model – Model 1-2, 1981.
L-29-137	Boer, J.N., van den Bovenkamp, N., Volkers, D.F., Aerodynamic characteristics of an HST model – Model 2-2, 1981.
L-29-150	Willemse, W.H.A.R., Boer, J.N., van den Bovenkamp, N., Schoonveld, E., Steeman, P., Aerodynamic characteristics of a high-speed F-29 windtunnel model – Model 2-5, 1981.
L-29-152	Warrink, B., Wake drag analysis of a high-speed windtunnel halfmodel – ' Model SKV-5½, 1981.
L-29-174	de Hay,L., van Hengst, J., Results of wind tunnel tests on an F-29 intake model, Model 9-1, 1982.
L-29-196	Boer, J.N., Aerodynamic characteristics of the two-dimensional HST-model, Model 12-1 fitted with high-lift devices, 1982.
L-29-198	Hogenhuis, H., Static nozzle tests in the K.A.T. on exhaust model 14, 1982.

L-29-202	Volkers, D.F., Boer,J.N., Aerodynamic characteristics of an F29 / MDF-100 halfmodel, Model 10-7, fitted with pressure taps on slats and flaps, 1983.
L-307-39	Boer, J.N., Results of the low-speed investigation on the NLR 7703 Mod section with leading- and trailing-edge high-lift devices, 1978.
L-307-46	Boer, J.N., Hogenhuis, H., Willemse, W.H.A.R., Aerodynamic characteristics of the low-speed model SKV-LST-2,1979.
L-307-97	Volkers, D.F., Results of the second low-speed investigation on the NLR 7703 Mod section with leading-and trailing-edge high-lift devices, 1980.
PDI 78-07	Clignett, P., The possible use of ground thrust reversers on the Super F-28, 1978.
V-27-49	Martin Box, J., Bergmeijer, P., Results of flight handling tests on the Friendship F1 prototype with R.-R. Dart Mk 528 engines,1959.
V-28-75	Obert, E., Flight test analysis of roll characteristics of the Fokker F-28 including a comparison between wind-tunnel- and flight-test-derived aileron control data, 1986.
V-28-83	Obert, E., Flight test analysis of the lift and pitching moment characteristics of the Fokker F-28 Mk 4000 and Mk 6000 including a comparison with windtunnel test data,1996.
WT-P-159	Broekhuizen, H.J., van Garrel, A., VTP-4: The aerodynamic integration of a wing mounted engine., 1996.

ICAS Conference Proceedings

Paper No.76 - 32	Seed, A.R., Design techniques for high by-pass ratio powerplant nozzle systems, 1976.
1978, Paper B2-01	da Dosta, A.L., Application of computational aerodynamics methods to the design and analysis of transport aircraft, 1978.
1978, Paper B3-01	Blackwell Jr., J.A., Scale effects on supercritical airfoils, 1978.
1980.Paper 12.2	Lundry, J.L., Recent advances in Boeing high-lift technology, 1980.
1984,Paper 1.10.1	Hoelmer, W., Younghans, J.L., Effect of Reynolds number on upper cowl flow separation,1984
1982,Paper 5.7.2	Nagel, A.L., Aerodynamic research applications at Boeing, 1882.

1988,Paper 6.1.2   Obert, E., The aerodynamic development of the Fokker 100, 1988.

Interavia
---------   Just, W., Sahliger, K., Aeroplane drag when approaching sonic speed. January, 1948.
---------   Geddes, J.Ph., Two years of 747 service, page 455, May 1972.
---------   Boeing 747SP. Shorter, faster, farther, July 1975.
---------   Lambert, M., Airbus Industrie's heavenly twins – A310 and A300-600, November 1980.
---------   Lambert, M., A320 fly-by-wire nears certification, January 1988.

Jahrbuch der Deutsche Gesellschaft für Luft- und Raumfahrt DGLR
Jahrbuch 1973   Béteille, R., Airbus A300, 1973.

Journal of Aircraft
----------   Kutney, J. T., Piszkin, S. P., Reduction of drag rise on the Convair 990 airplane, January-February 1964.
             Also: AIAA-63-276.
----------   Gyorgyfalvy, D., Effect of pressurization on airplane fuselage drag, November-december 1965.
----------   Shevell, R.S., Schaufele, R.D., Aerodynamic design features of the DC-9. November-December 1966.
----------   Poisson-Quinton, Ph., From wind tunnel to flight, the role of the laboratory in aerospace design, May-June 1968.
----------   Shevell, R.S., Aerodynamic anomalies: can CFD prevent or correct them? August 1986.

Journal of the Royal Aeronautical Society
----------   Ward, J.W., The behaviour and effects of laminar separation bubbles on aerofoils in incompressible flows, December 1963.
----------   Küchemann, D., Types of flow on swept wings, November 1953.

NACA Reports, Technical Notes and Research Memoranda.
Report 824   Abbott,I.H., von Doenhoff, A.E., Summary of airfoil data, 1945. (also in Theory of wing sections, 1949, 1959.)

Report 1091	Fischel, J., Naeseth, R.L., Hagerman, J.R., O'Hare, W.M., Effect of aspect ratio on the low-speed lateral control characteristics of untapered low-aspect-ratio wings equipped with a flap and with retractable ailerons, 1952.
Report 1098	Campbell, J.P., Mckinney, M. O., Summary of methods for calculating dynamic lateral stability and response and for estimating aerodynamic stability derivatives, 1952.
Report 1298	Skoog, R.B., Analysis of the effects of aeroelasticity on static longitudinal stability and control of a swept-wing airplane, 1957.
RM A9E31	Hemenover, A.D., Tests of the NACA 64-010 and 64A010 airfoil sections at high subsonic Mach numbers, 1949.
RM A50K28a	Demele, F.A., Sutton, F.B., The effects of increasing the leading-edge radius and adding forward camber on the aerodynamic characteristics of a wing with 35° of sweepback, 1951.
RM A52A10	Hunton, L.W., Effects of finite span on the section characteristics of two 45° swept-back wings of aspect ratio 6, 1952.
RM A52A31	Rolls, L.S., Matteson, F.H., Wing load distribution on a swept-wing airplane in flight at Mach numbers up to 1.11, and comparison with theory, 1952.
RM A54L08	Sutton , F.B., Dickson, J.K., The longitudinal characteristics at Mach numbers up to 0.92 of several wing-fuselage-tail combinations having sweptback wings with NACA four-digit thickness distributions, 1955.
RM A55C08	Walker, H.J., Maillard, W.C., A correlation of airfoil section data with the aerodynamic loads measured on a 45° sweptback wing model at subsonic Mach numbers, 1955.
RM A55C23	Hunton, L.W., A study of the application of airfoil section data to the estimation of the high-subsonic-speed characteristics of swept wings, 1955.
TN 1146	Purser, P.E., Spear, M.F., Tests to determine effects of slipstream rotation on the lateral stability characteristics of a single-engine low-wing aircraft model, 1946.
TN 2010	Brewer, J.D., Lichtenstein, J.H., Effect of horizontal tail on low-speed static lateral stability characteristics of a model having 45 degree sweptback wing and tail surfaces,1950.

TN 2228	Kelly, J.A., Effects of modifications to the leading –edge region on the stalling characteristics of the NACA 631-012 airfoil section, 1950.
TN 2288	Dods, J.B. Jr., Estimation of low-speed lift and hinge-moment parameters for full-span trailing-edge flaps on lifting surfaces with and without sweepback,1951.
TN 3497	Dods, J.B.Jr., Tinling, B.E., Summary of results of a wind-tunnel investigation of nine related horizontal tails, 1955.
TN 3871	Maki,R.L., Hunton, L.W., An investigation at subsonic speeds of several modifications to the leading-edge region of the NACA 64A010 airfoil section designed to increase the maximum lift,19…

NASA Contractor Reports

CR-1218	Lundry, J. L., A numerical solution for the minimum induced drag, and the corresponding loading, of non planar wings, 1968.
CR-1756	Hanke, C.R.,The simulation of a large jet transport aircraft. Vol. I Mathematical model,1971.
CR-2320	Morris, R.L., Hanke, C.R., Pasley, L.H., Rohling, W.J., The influence of wing loading on turbofan powered STOL transports with and without externally blown flaps, 1973.
CR-2333	McWilkinson, D.G., Blackerby, W.T., Paterson.J.H., Correlation of full scale drag predictions with flight measurements on the C-141 aircraft – Phase II, wind tunnel test, analysis, and prediction techniques, 1974.
CR- 3119	Gilkey, R. D., Design and wind tunnel tests of winglets on a DC-10 wing, 1979.
CR-114494	Hanke, C.R., Nordwall, D.R.,The simulation of a large jet transport aircraft. Vol. II. Modeling data, 1970.
CR-134800	Anon., Phase 2 program on ground test of refanned JT8D turbofan engines and nacelles for the 727 airplane. Volume 4. Airplane evaluation and analysis., 1975.

NASA Reports

CP-3020 – Vol.I.	Transonic symposium:Theory, application and experiment, Vol. I, Part I, page 79.
SP-347, Pt. 2	Tinoco, E.N., Transonic CFD applications at Boeing, 1989. Aerodynamic analysis requiring advanced computers, Part 2, page 979, 1975.

TM 78566	Olson, L.E., McGowan, P.R., Guest, C.J., Leading edge slat optimization for maximum lift, 1979.
TM 78786	Montoya, L.C., Flechner, S.G., Jacobs, P.F., Effect of an alternate winglet on the pressure and spanwise load distributions of a first generation jet transport wing, 1978.
TM 83556	Olsen, W., Shaw, R., Newton, J., Ice shapes and the resulting drag increase for a NACA 0012 airfoil, 1984.
TM X-1345	Blackwell, J.A., Jr., Brooks, E.N., Jr., Decker, J.P., Static aerodynamic characteristics of a model of a typical subsonic jet-transport airplane at Mach numbers from 0.40 to 1.20, 1967. (Boeing 720B)
TM X-3293	Hicks, R.M., Mendoza, J.P., Bandettini, A., Effects of forward contour modification on the aerodynamic characteristics of the NACA 641-212 airfoil section, 1975.
TM X-3160	Beasley, W.D., McGhee, R.J., Experimental and theoretical low-speed aerodynamic characteristics of the NACA 651-213, a=0.50, airfoil.
TN D-5971	Capone, F.J., Longitudinal aerodynamic characteristics of a twin-turbofan subsonic transport with nacelles mounted under the wings, 1970. (B 737).
TN D-7428	McGhee, R.J., Beasley, W.D., Low-speed aerodynamic characteristic of a 17-percent thick airfoil section designed for general aviation applications, 1973.
TN D-8512	Luckring, J.M., Theoretical and experimental analysis of longitudinal and lateral aerodynamic characteristics of skewed wings at subsonic speeds to high angles of attack, 1977.

NLL Reports

A -1374	F-27: Investigation of an aircraft model, scale 1:15. IV. Fuselage drag, characteristics of different horizontal and vertical tail surfaces, flight characteristics in take-off, landing and cruise, 195.. (In Dutch).
A -1394	van der V.., C.B., F-27 tail surface model (1 : 9). II. Investigation of the vertical tail surface, 1955. (In Dutch).
A -1485	Mannée, J., Windtunnel investigation of the slipstream effects on the stability and control characteristics of the complete F-27 model with various configurations of the horizontal tail, 1960.

A -1508 B   Mannée, J., Windtunnel investigation of the influence of the aircraft configuration on the yawing and rolling moments of a twin-engined propeller driven aircraft with one engine inoperative, 1962.

NLR Reports

A .1582   de Vries, O., Low-speed windtunnel investigation on a complete model of the F-28 on a scale 1 : 11.58 (Model 8 /4).

TR 69025 U   van den Berg, B., Reynolds number and Mach number effects on the maximum lift and the stalling characteristics of wings at low speed , 1969.

TR 70084 C   Kho, Y.G., Pot, P.J., Two-dimensional low-speed windtunnel investigation on a Fokker F-28 wing model with various types of slats, 1970.

TR 82044 C   Pot,P.J., 2-D low-speed wind-tunnel investigation of a supercritical airfoil NLR 7703 Mod with slat and flap (July / August 1978).

TR 82050 C   Pot,P.J., 2-D low-speed wind-tunnel investigation of a supercritical airfoil NLR 7703 Mod with slat and flap (April / May 1980).

TR 82057 C   de Bruin, A.C., The turbulent boundary layer on the SKV 5½ wind tunnel model, 1982.

TR 83059 C   Vogelaar, H.L.J., Wind-tunnel investigation on the two-dimensional F - 29 model 12-1 airfoil section with various high lift devices at various Mach and Reynolds numbers, 1983.

TR 84010 C   Rohne, P.B., van Zwieten, L.J., Data report of an investigation on semi-span model F-29-10-7 in the high-speed wind tunnel HST, 1983.

Proceedings of the Royal Society London

--------   Dykins, D.H., Jupp, J.A., McRae, D.M., Application of aerodynamic research and development to civil aircraft wing design, A 416, page 43 to 62. 1988.

RAE Reports

No. Aero 2219   Küchemann, D., Design of wing junction, fuselage and nacelles to obtain the full benefit of sweptback wings at high mach number,1947.

| No. Aero 2556 | Bateman, T.E.B., Lawrence, A.J.,Experimental investigation of the pressure distribution at the centre-section of a sweptback wing at high subsonic speeds, 1955. Also : ARC C.P. 367 . |
| TR 68108 | Isaacs, D., Wind tunnel measurements of the low-speed stalling characteristics of a model of the Hawker Siddeley Trident I C, 1968. |

SAE Papers

SAE 237-A	Dunn, O.R., Flight characteristics of the DC-8. SAE National Aeronautic Meeting, Los Angeles, Cal., October 10-14, 1960.
SAE S408	Harvey, S.T., Norton, D.A., Development of the model 727 airplane high lift system, April 21,1964.
SAE 660733	Viall, W.S., Aerodynamic considerations for engine inlet design for subsonic high-bypass fan engines, 1966.
SAE 670846	Schaufele, R.D., Ebeling, A.W., Aerodynamic design of the DC-9 wing and high-lift system, 1967.
SAE 700828	Archer,D.D., 747 flight test certification, 1970.
SAE 800731	Neal, B., Aerodynamic development of the engine nacelle combination for the Boeing 767 airplane,1980.

S.A.W.E. Journal

| -------- | Marsh, D. P., Quick mass properties estimating relationships for conceptual design. S.A.W.E. Journal |

SAWE Papers

| Paper No. 810 | St. John, R.S., The derivation and application of analytical-statistical weight prediction techniques, 1969. |

Shell Aviation News

| -------- | Olason, M.L., Norton, D.A., Aerodynamic design of Boeing's short haul jet, nos. 343,344, 1965. Also in : AIAA Paper 65-739. (No numbers). |
| -------- | Kolb, S.P., Developing a cascade thrust reverser, no. 437, 1976. |

Untersuchungen und Mitteilungen - Deutsche Luftfahrtforschung

| UM Nr.1167 | Göthert, B., Widerstandsanstieg bei Profilen im Bereich hoher Unterschallgeschwindigkeiten. Deutsche Versuchsanstalt für Luftfahrt E.V.,1944. |

VSV Congress

--------   The next generation of aircraft, evolution or revolution?
                             Pickerell, D.J., Advanced turbofans, Delft, September 1985.

Books

Bridgeman, W., The Lonely sky,1955.

Kuter, L.S., The great gamble: The Boeing 747, 1973.

Schlichting, H. & Truckenbrodt, E., Aerodynamik des Flugzeuges, 1960.

Toorenbeek, E., Synthesis of subsonic airplane design, 1976.

Wood, K.D., Aerospace vehicle design, Vol. I, Aircraft design, 1966, 1968.